

Biegelsen
Smith
Tong
EDITORS



VOLUME 295



VOLUME 295

Atomic-Scale Imaging of Surfaces and Interfaces

EDITORS

David K. Biegelsen
David J. Smith
S.Y. Tong

AD-A265 674



Atomic-Scale Imaging of Surfaces and Interfaces

DTIC
ELECTE
JUN 14 1993
S C D

DISTRIBUTION STATEMENT A

Approved for public release
Distribution Unlimited

BEST
AVAILABLE COPY

Atomic-Scale Imaging of Surfaces and Interfaces

Symposium held November 30-December 2, 1992, Boston, Massachusetts, U.S.A.

EDITORS:

David K. Biegelsen

Xerox Palo Alto Research Center
Palo Alto, California, U.S.A.

David J. Smith

Arizona State University
Tempe, Arizona, U.S.A.

S.Y. Tong

University of Wisconsin-Milwaukee
Milwaukee, Wisconsin, U.S.A.

Accession for	
NTIS CRA&I	<input checked="" type="checkbox"/>
DTIC TAB	<input type="checkbox"/>
Unannounced	<input type="checkbox"/>
Justification	
By	
Distribution /	
Availability Codes	
Dist	Avail and/or Special
A-1	

DTIC QUALITY INSPECTED 8

MRS

MATERIALS RESEARCH SOCIETY
Pittsburgh, Pennsylvania

93-13200


93 6 14 02 6

This work was supported in part by the Office of Naval Research under Grant Number N00014-93-0023. The United States Government has a royalty-free license throughout the world in all copyrightable material contained herein.

Single article reprints from this publication are available through University Microfilms Inc., 300 North Zeeb Road, Ann Arbor, Michigan 48106

CODEN: MRSPDH

Copyright 1993 by Materials Research Society.
All rights reserved.

This book has been registered with Copyright Clearance Center, Inc. For further information, please contact the Copyright Clearance Center, Salem, Massachusetts.

Published by:

Materials Research Society
9800 McKnight Road
Pittsburgh, Pennsylvania 15237
Telephone (412) 367-3003
Fax (412) 367-4373

Library of Congress Cataloging in Publication Data

Atomic-scale imaging of surfaces and interfaces / editors, David K. Biegelsen, David J. Smith, S.Y. Tong

p. cm.—(Materials Research Society symposium proceedings ; v. 295)
Includes bibliographical references and index.

ISBN 1-55899-190-5

I. Surfaces (Technology)—Congresses. 2. Scanning electron microscopy—Congresses. 3. Atomic structure—Congresses. I. Biegelsen, D.K. II. Smith, David J., 1948- III. Tong, S.Y. IV. Series: Materials Research Society symposium proceedings ; v. 295.

TA418.7.A855 1993
620'.44—dc20

93-15224
CIP

Manufactured in the United States of America

Contents

PREFACE	ix
MATERIALS RESEARCH SOCIETY SYMPOSIUM PROCEEDINGS	x
SCANNING TUNNELING MICROSCOPY FOR HYDROGEN-DESORPTION-INDUCED STRUCTURAL CHANGE OF Si(111) SURFACE Y. Morita, K. Miki, H. Tokumoto, T. Sato, T. Sueyoshi, and M. Iwatsuki	3
STEPS ON THE (110) SURFACE OF InP Yong Liang, William E. Packard, and John D. Dow	9
SCANNING TUNNELING MICROSCOPY ON CHARGE DENSITY WAVES IN LAYERED COMPOUNDS J.Th.M. De Hosson and G.P.E.M. Van Bakel	15
DESIGN OF ULTRA HIGH VACUUM SCANNING ELECTRON MICROSCOPE COMBINED WITH SCANNING TUNNELING MICROSCOPE Mikio Takai, Naoki Yokoi, Ryou Mimura, Hiroshi Sawaragi, and Ryuso Aihara	23
SCANNING TUNNELING MICROSCOPY PERSPECTIVE OF STRUCTURES ON REDUCED $\text{SrTiO}_3(001)$ SURFACES Yong Liang and Dawn A. Bonnell	29
SURFACE STRUCTURE AND ELECTRONIC PROPERTY OF REDUCED $\text{SrTiO}_3(100)$ SURFACE OBSERVED BY STM/STS Takuya Matsumoto, Hiroyuki Tanaka, Tomoji Kawai, and Shichio Kawai	35
*METASTABLE STRUCTURAL SURFACE EXCITATIONS AND CONCERTED ADATOM MOTIONS: A STM STUDY OF ATOMIC MOTIONS WITHIN A SEMICONDUCTOR SURFACE Jene Golovchenko, Ing-Shouh Hwang, Eric Ganz, and Silva K. Theiss	41
*MECHANISMS AND ENERGETICS OF SURFACE ATOMIC PROCESSES, AN ATOM-PROBE FIELD ION MICROSCOPE STUDY Tien T. Tsong	49
ATOMIC ARRANGEMENT OF Al NEAR THE PHASE BOUNDARIES BETWEEN $\sqrt{3}\times\sqrt{3}$ -Al AND 7×7 STRUCTURES ON Si(111) SURFACES Katsuya Takaoka, Masamichi Yoshimura, Takafumi Yao, Tomoshige Sato, Takashi Sueyoshi, and Masashi Iwatsuki	59
GROWTH AND SURFACE MORPHOLOGY OF THIN SILICON FILMS USING AN ATOMIC FORCE MICROSCOPE Rama I. Hegde, Mark A. Chonko, and Philip J. Tobin	65
*SOLVING INTERFACE STRUCTURES BY COMBINED ELECTRON MICROSCOPY AND X-RAY DIFFRACTION A. Bourret and G. Feuillet	71
QUANTITATIVE HREM STUDY OF THE ATOMIC STRUCTURE OF THE $\Sigma(310)/[001]$ SYMMETRIC TILT GRAIN BOUNDARY IN Nb Wayne E. King and Geoffrey H. Campbell	83
HRTEM OBSERVATIONS OF A $\Sigma=3$ $\{112\}$ BICRYSTAL BOUNDARY IN ALUMINUM D.L. Medlin, M.J. Mills, W.M. Stobbs, M.S. Daw, and F. Cosandey	91

*Invited Paper

ATOMIC STRUCTURE OF THE (310) TWIN IN NIOBIUM: THEORETICAL PREDICTIONS AND COMPARISON WITH EXPERIMENTAL OBSERVATION Geoffrey H. Campbell, S.M. Foiles, M. Rühle, and W.E. King	97
QUANTITATIVE HIGH-RESOLUTION ELECTRON MICROSCOPY OF GRAIN BOUNDARIES IN α -Al ₂ O ₃ T. Höche, P.R. Kenway, H.-J. Kleebe, and M. Rühle	103
COMPARISONS OF OBSERVED AND SIMULATED ATOMIC STRUCTURES OF Pd/Ni HETEROPHASE INTERFACES M.I. Buckett, J.P. Shaffer, and Karl L. Merkle	109
ATOMIC STRUCTURE OF $\Sigma=5$ (130) SYMMETRICAL TILT BOUNDARY IN STRONTIUM TITANATE V. Ravikumar and Vinayak P. Dravid	115
ASSESSMENT OF GaInAs/GaInAsP INTERDIFFUSION PROFILES OBTAINED USING STEM-EDX AND HREM R.E. Mallard, N.J. Long, G.R. Booker, E.J. Thrush, and K. Scarrott	121
ELECTRON MICROSCOPY CHARACTERIZATION OF EPITAXIAL GROWTH OF Ag DEPOSITED ON MgO MICROCUBES J. Liu, M. Pan, and G.E. Spinnler	127
REAL-TIME VIEWING OF DYNAMIC PROCESSES ON CdTe SURFACES AT ELEVATED TEMPERATURE David J. Smith, R. Vogl, and Ping Lu	133
AFM IMAGING OF THE CRYSTALLINE-TO-AMORPHOUS TRANSITION ON THE SURFACE OF ION-IMPLANTED MICA Ray K. Eby, Grant S. Henderson, Fred J. Wicks, and George W. Arnold	139
AFM IMAGINGS OF FERRITIN MOLECULES BOUND TO LB FILMS OF POLY-1-BENZYL-L-HISTIDINE Satomi Ohnishi, Masahiko Hara, Taiji Furuno, Wolfgang Knoll, and Hiroyuki Sasabe	145
ARTIFACTS IN ATOMIC FORCE MICROSCOPY OF NANOPOROUS AND MESOPOROUS FIDUCIAL SAMPLES H.W. Deckman and R.J. Plano	151
AI INDUCED RECONSTRUCTIONS ON THE Si(111) SURFACES STUDIED BY SCANNING TUNNELING MICROSCOPY Masamichi Yoshimura, Katsuya Takaoka, Takafumi Yao, Tomoshige Sato, Takashi Sueyoshi, and Masashi Iwatsuki	157
STRUCTURE OF THE $\Sigma=3$ (111) GRAIN BOUNDARY IN Cu-1.5%Sb Richard W. Fonda and David E. Luzzi	161
HIGH RESOLUTION ELECTRON MICROSCOPY OF $\Sigma=3$ NiSi ₂ ($\bar{1}11$)/($1\bar{1}5$) Si AND NiSi ₂ (2 $\bar{2}1$)/(001)Si INTERFACES Wen-Jauh Chen and Fu-Rong Chen	167
IMAGE SIMULATIONS OF Ge TWIN BOUNDARIES Stuart McKernan and C. Barry Carter	173
SURFACE STRUCTURE OF OXIDE CATALYST MICROCRYSTALS: HIGH RESOLUTION ELECTRON MICROSCOPY STUDY G.N. Kryukova, A.L. Chuvilin, and V.A. Sadykov	179
A MICROSTRUCTURAL STUDY OF REACTION-BONDED SILICON CARBIDE K. Das Chowdhury, R.W. Carpenter, and W. Braue	183

COMPOSITIONAL ANALYSIS AND HIGH RESOLUTION IMAGING OF GRAIN BOUNDARIES IN Pr-DOPED ZnO CERAMICS I.G. Solorzano, J.B. VanDer Sande, K.K. Baek, and H.L. Tuller	189
ATOMIC STRUCTURES AND DEFECTS OF AS-GROWN Nb _{1-x} S ₂ PLATELETS ON Nb SUBSTRATES Chuxin Zhou and L.W. Hobbs	195
A COMPACT NUCLEAR MICROPROBE WITH A LIQUID METAL ION SOURCE AND A TOROIDAL ANALYZER Mikio Takai, Ryou Mimura, Hiroshi Sawaragi, and Ryuso Aihara	201
IN-PLANE ASYMMETRIES ON THE Ge(111) c(2×8) SURFACE MAPPED WITH THE SCANNING TUNNELING MICROSCOPE P. Molinàs-Mata, J. Zegenhagen, M. Böhringer, N. Takeuchi, and A. Selloni	207
*EXPERIMENTAL OPTIMIZATION FOR IMAGING WITH PHOTOELECTRON DIFFRACTION J.G. Tobin, G.D. Waddill, Hua Li, and S.Y. Tong	213
LOW ENERGY PHOTOELECTRON HOLOGRAPHY ON GaAs R. Denecke, R. Eckstein, L. Ley, A. Bocquet, J. Riley, and R. Leckey	219
EFFECT OF THE ANGULAR MOMENTUM AND MAGNETIC QUANTUM NUMBERS ON AUGER AND PHOTOELECTRON SCATTERING D.E. Ramaker, H. Yang, and Y.U. Idzerda	225
IMAGING OF METAL/SEMICONDUCTOR INTERFACE BY BALLISTIC- ELECTRON-EMISSION MICROSCOPY (BEEM) E.Y. Lee, B.R. Turner, J.R. Jimenez, and L.J. Schowalter	231
*LOW ENERGY POINT SOURCE ELECTRON MICROSCOPY H.J. Kreuzer	235
ATOMIC FORCE MICROSCOPIC IMAGING OF BIOLOGICALLY IMPORTANT MATERIALS Lorraine M. Siperko and William J. Landis	243
CHARACTERIZATION OF INTERNAL INTERFACES BY ATOM PROBE FIELD ION MICROSCOPY M.K. Miller and Raman Jayaram	247
*THE ORIGINS OF HIGH SPATIAL RESOLUTION SECONDARY ELECTRON MICROSCOPY M.R. Scheinfein, J.S. Drucker, J. Liu, J.K. Weiss, G.G. Hembree, and J.M. Cowley	253
*REM AND RHEED STUDIES OF Pb ADSORPTION ON Si(111) Yasumasa Tanishiro, Masahiko Fukuyama, and Katsumichi Yagi	261
*THE SURFACE STRUCTURE OF OXIDES STUDIED WITH REFLECTED HIGH ENERGY ELECTRONS Tung Hsu	271
APPLICATION OF Z-CONTRAST IMAGING TO OBTAIN COLUMN-BY- COLUMN SPECTROSCOPIC ANALYSIS OF MATERIALS Nigel D. Browning and Stephen J. Pennycook	279
AUTHOR INDEX	285
SUBJECT INDEX	287
*Invited Paper	

Preface

The gap between *imagining* and *imaging* is getting ever smaller. Atomic-Scale Imaging of Surfaces and Interfaces, Symposium W at the 1992 MRS Fall Meeting in Boston, Massachusetts, brought together researchers using most state-of-the-art imaging techniques capable of resolving atomic features. Methods represented were scanning tunneling microscopy (STM), atomic force microscopy (AFM), low energy electron microscopy (LEEM), transmission (TEM) and reflection (REM) electron microscopy, scanning electron microscopy (SEM), atom probe field ion microscopy (APFIM or POSAP), high and low energy external source electron holographies and internal source electron holographies. Some highlights from the STM papers included discussions of the limitations and future potential of STM as well as current findings. Several papers presented work with STM at elevated temperatures. Jene Golovchenko reviewed STM work showing cooperative diffusion events (Pb on Ge) involving many tens of substrate atoms. Don Eigler focused on atomic manipulation and some of its uses to enable fundamental studies of small atomic clusters. From LEEM studies Ruud Tromp showed videos of 2d-faceted Ag island growth on Ge. In synchronization with the layer-by-layer growth on the islands, a sharpening-rounding transition occurred at the completion-initiation of each layer. Novel TEM work (e.g., by Murray Gibson, Bob Sinclair, Laurie Marks and Dave Smith, among others) included highly clean and stable *in situ* cross-sectional and plan view observations of changing surface and interface structure. A series of papers on cross-sectional TEM imaging of interfaces by Wayne King, Karl Merkle and others demonstrated great progress in structure refinements using correlations between atomistic simulations and experimental micrographs. Results from REM were reviewed by Yasumasa Tanishiro to show the efficacy of this tool for non-invasive use in deposition environments, and Tung Hsu demonstrated its usefulness for characterizing the atomic-scale morphology of oxide surfaces. Alain Bourret underlined the necessity of applying complementary methods (here TEM and grazing incidence x-ray diffraction) for a complete elucidation of more complicated interface structures. Mike Scheinfein described experiments clarifying the origin of fast secondary electron emission and indicated that under optimal conditions, near-atomic scale resolution may be possible in SEM. Hans Kreuzer discussed the state of the art and future of point source electron holographic imaging. Its low energy and lensless configuration promise many exciting possibilities. Several talks showed the usefulness of atom probe FIM for near atomic scale (~ 1 nm) chemical/structural analysis. Another area of considerable recent progress is internal source electron holography. Removal of multiple scattering effects is allowing experimental phase coherent diffraction data at multiple energies to be transformed back to the spatial domain. The images which result are chemically specific mappings representing an average site (central atom and near neighbors). Both LEED and photoelectron diffraction methods were treated.

The present volume represents a snapshot of the field of atomic-scale imaging. The various complementary techniques are evolving rapidly in their chemical and spatial resolution capabilities. No single technique is yet complete in its ability to image and identify atoms. The future seems bright and predictably unpredictable.

David K. Biegelsen
David J. Smith
S.Y. Tong

April 1993

MATERIALS RESEARCH SOCIETY SYMPOSIUM PROCEEDINGS

- Volume 258—Amorphous Silicon Technology—1992, M.J. Thompson, Y. Hamakawa, P.G. LeComber, A. Madan, E. Schiff, 1992, ISBN: 1-55899-153-0
- Volume 259—Chemical Surface Preparation, Passivation and Cleaning for Semiconductor Growth and Processing, R.J. Nemanich, C.R. Helms, M. Hirose, G.W. Rubloff, 1992, ISBN: 1-55899-154-9
- Volume 260—Advanced Metallization and Processing for Semiconductor Devices and Circuits II, A. Katz, Y.I. Nissim, S.P. Murarka, J.M.E. Harper, 1992, ISBN: 1-55899-155-7
- Volume 261—Photo-Induced Space Charge Effects in Semiconductors: Electro-optics, Photoconductivity, and the Photorefractive Effect, D.D. Nolte, N.M. Haegel, K.W. Goossen, 1992, ISBN: 1-55899-156-5
- Volume 262—Defect Engineering in Semiconductor Growth, Processing and Device Technology, S. Ashok, J. Chevallier, K. Sumino, E. Weber, 1992, ISBN: 1-55899-157-3
- Volume 263—Mechanisms of Heteroepitaxial Growth, M.F. Chisholm, B.J. Garrison, R. Hull, L.J. Schowalter, 1992, ISBN: 1-55899-158-1
- Volume 264—Electronic Packaging Materials Science VI, P.S. Ho, K.A. Jackson, C-Y. Li, G.F. Lipscomb, 1992, ISBN: 1-55899-159-X
- Volume 265—Materials Reliability in Microelectronics II, C.V. Thompson, J.R. Lloyd, 1992, ISBN: 1-55899-160-3
- Volume 266—Materials Interactions Relevant to Recycling of Wood-Based Materials, R.M. Rowell, T.L. Laufenberg, J.K. Rowell, 1992, ISBN: 1-55899-161-1
- Volume 267—Materials Issues in Art and Archaeology III, J.R. Druzik, P.B. Vandiver, G.S. Wheeler, I. Freestone, 1992, ISBN: 1-55899-162-X
- Volume 268—Materials Modification by Energetic Atoms and Ions, K.S. Grabowski, S.A. Barnett, S.M. Rossnagel, K. Wasa, 1992, ISBN: 1-55899-163-8
- Volume 269—Microwave Processing of Materials III, R.L. Beatty, W.H. Sutton, M.F. Iskander, 1992, ISBN: 1-55899-164-6
- Volume 270—Novel Forms of Carbon, C.L. Renschler, J. Pouch, D. Cox, 1992, ISBN: 1-55899-165-4
- Volume 271—Better Ceramics Through Chemistry V, M.J. Hampden-Smith, W.G. Klemperer, C.J. Brinker, 1992, ISBN: 1-55899-166-2
- Volume 272—Chemical Processes in Inorganic Materials: Metal and Semiconductor Clusters and Colloids, P.D. Persans, J.S. Bradley, R.R. Chianelli, G. Schmid, 1992, ISBN: 1-55899-167-0
- Volume 273—Intermetallic Matrix Composites II, D. Miracle, J. Graves, D. Anton, 1992, ISBN: 1-55899-168-9
- Volume 274—Submicron Multiphase Materials, R. Baney, L. Gilliom, S.-I. Hirano, H. Schmidt, 1992, ISBN: 1-55899-169-7
- Volume 275—Layered Superconductors: Fabrication, Properties and Applications, D.T. Shaw, C.C. Tsuei, T.R. Schneider, Y. Shiohara, 1992, ISBN: 1-55899-170-0
- Volume 276—Materials for Smart Devices and Micro-Electro-Mechanical Systems, A.P. Jardine, G.C. Johnson, A. Crowson, M. Allen, 1992, ISBN: 1-55899-171-9
- Volume 277—Macromolecular Host-Guest Complexes: Optical, Optoelectronic, and Photorefractive Properties and Applications, S.A. Jenekhe, 1992, ISBN: 1-55899-172-7
- Volume 278—Computational Methods in Materials Science, J.E. Mark, M.E. Glicksman, S.P. Marsh, 1992, ISBN: 1-55899-173-5

*Prior Materials Research Society Symposium Proceedings
available by contacting Materials Research Society*

MATERIALS RESEARCH SOCIETY SYMPOSIUM PROCEEDINGS

- Volume 279—Beam-Solid Interactions—Fundamentals and Applications, M.A. Nastasi, N. Herbots, L.R. Harriott, R.S. Averbach, 1993, ISBN: 1-55899-174-3
- Volume 280—Evolution of Surface and Thin Film Microstructure, H.A. Atwater, E. Chason, M. Grabow, M. Lagally, 1993, ISBN: 1-55899-175-1
- Volume 281—Semiconductor Heterostructures for Photonic and Electronic Applications, D.C. Houghton, C.W. Tu, R.T. Tung, 1993, ISBN: 1-55899-176-X
- Volume 282—Chemical Perspectives of Microelectronic Materials III, C.R. Abernathy, C.W. Bates, D.A. Bohling, W.S. Hobson, 1993, ISBN: 1-55899-177-8
- Volume 283—Microcrystalline Semiconductors—Materials Science & Devices, Y. Aoyagi, L.T. Canham, P.M. Fauchet, I. Shimizu, C.C. Tsai, 1993, ISBN: 1-55899-178-6
- Volume 284—Amorphous Insulating Thin Films, J. Kanicki, R.A.B. Devine, W.L. Warren, M. Matsumura, 1993, ISBN: 1-55899-179-4
- Volume 285—Laser Ablation in Materials Processing—Fundamentals and Applications, B. Braren, J. Dubowski, D. Norton, 1993, ISBN: 1-55899-180-8
- Volume 286—Nanophase and Nanocomposite Materials, S. Komarneni, J.C. Parker, G.J. Thomas, 1993, ISBN: 1-55899-181-6
- Volume 287—Silicon Nitride Ceramics—Scientific and Technological Advances, I-W. Chen, P.F. Becher, M. Mitomo, G. Petzow, T-S. Yen, 1993, ISBN: 1-55899-182-4
- Volume 288—High-Temperature Ordered Intermetallic Alloys V, I. Baker, J.D. Whittenberger, R. Darolia, M.H. Yoo, 1993, ISBN: 1-55899-183-2
- Volume 289—Flow and Microstructure of Dense Suspensions, L.J. Struble, C.F. Zukoski, G. Maitland, 1993, ISBN: 1-55899-184-0
- Volume 290—Dynamics in Small Confining Systems, J.M. Drake, D.D. Awschalom, J. Klafter, R. Kopelman, 1993, ISBN: 1-55899-185-9
- Volume 291—Materials Theory and Modelling, P.D. Bristowe, J. Broughton, J.M. Newsam, 1993, ISBN: 1-55899-186-7
- Volume 292—Biomolecular Materials, S.T. Case, J.H. Waite, C. Viney, 1993, ISBN: 1-55899-187-5
- Volume 293—Solid State Ionics III, G-A. Nazri, J-M. Tarascon, M. Armand, 1993, ISBN: 1-55899-188-3
- Volume 294—Scientific Basis for Nuclear Waste Management XVI, C.G. Interrante, R.T. Pabalan, 1993, ISBN: 1-55899-189-1
- Volume 295—Atomic-Scale Imaging of Surfaces and Interfaces, D.K. Biegelson, D.S.Y. Tong, D.J. Smith, 1993, ISBN: 1-55899-190-5
- Volume 296—Structure and Properties of Energetic Materials, R.W. Armstrong, J.J. Gilman, 1993, ISBN: 1-55899-191-3

*Prior Materials Research Society Symposium Proceedings
available by contacting Materials Research Society*

Atomic-Scale Imaging of Surfaces and Interfaces

SCANNING TUNNELING MICROSCOPY FOR HYDROGEN-DESORPTION-INDUCED STRUCTURAL CHANGE OF Si(111) SURFACE

Y. MORITA***, K. MIKI*, H. TOKUMOTO*, ***, T. SATO**, T. SUEYOSHI**
AND M. IWATSUKI**

*Electrotechnical Laboratory, Tsukuba, Ibaraki 305, Japan,

**JEOL Ltd., Akishima, Tokyo 196, Japan.

ABSTRACT

A scanning tunneling microscopy (STM) has revealed an atomic structure of Si(111)- $\sqrt{3}\times\sqrt{3}R30^\circ$ which is induced by the hydrogen desorption at about 500 °C. There exist domains with the $\sqrt{3}\times\sqrt{3}R30^\circ$ structures, indicating that each domain is formed by rearrangement of Si adatoms around each cluster present at room temperature. Near the domain boundary, the adatoms locate mostly at T_4 sites and occasionally at H_3 sites. The dynamic nature of the adatoms are predicted

INTRODUCTION

Determination of atomic structure of silicon surface is important in the fields of both surface science and silicon technology. As for Si(111)- 7×7 structure, which is stable at low temperature under thermal equilibrium condition, a model of dimer-adatom-stacking-fault (DAS) structure was proposed by Takayanagi et al [1] and confirmed by many experiments. Theoretical calculations for the DAS model were also performed in order to make clear why 7×7 is stable. Since the DAS structure is complicated and many atoms are involved, most theoretical calculations are simplified and some of them pay attention to the adatom arrangement on an unreconstructed Si(111) surface. Then, both 2×2 and $\sqrt{3}\times\sqrt{3}$ adatom arrangements are found to be energetically stable on the unreconstructed Si(111) surface, among which the former is more favorable than the latter [2,3]. However no experimental evidences for the existence of the 2×2 or $\sqrt{3}\times\sqrt{3}$ arrangements of Si adatoms have been reported so far except for a special case on the narrower terrace than the size of unit cell of the 7×7 structure [4].

Very recently, we have successfully found the $\sqrt{3}\times\sqrt{3}R30^\circ$ structure on the unreconstructed Si(111) surface in the temperature range of 500-580 °C utilizing the hydrogen-mediated-surfactant effect [5]. In this paper, we shall show STM observations of Si adatom rearrangement between T_4 and H_3 sites which is more visible at the domain boundary.

EXPERIMENTAL

The STM used in this experiment was designed to operate in ultrahigh vacuum (UHV) and at high temperature up to 900 °C [6]. An electrochemically etched W tip was used without any intentional cleaning but should be clean as a result of either sample flashing at 1200 °C by 10 mm apart or tip scanning over the hot sample surface. A sample was B-doped Si(111) (0.1-0.3 $\Omega\cdot\text{cm}$) with a misorientation angle of less than $\pm 0.1^\circ$. The sample was heated resistively in UHV, and its temperature was determined by an infrared pyrometer above 600 °C with an accuracy of $\pm 10^\circ\text{C}$ and by a calibrated power-temperature relationship for the present sample below 600 °C with an accuracy of $\pm 50^\circ\text{C}$. Before starting the experiment, the sample surface was checked to be clean by observing clear 7×7 structure.

The hydrogen terminated surface was prepared by the adsorption of H-atoms on Si surface in UHV chamber. The H-atoms were produced by dissociating H-molecules with a hot (1600 °C) W filament located at 20-30 mm apart from the sample surface. Initially the sample temperature was raised to about 900 °C which was higher than a (1x1)-(7×7) phase transition temperature and STM confirmed the complete disappearance of the 7×7 structure. Then the

*** Present address: National Institute for Advanced Interdisciplinary Research, Tsukuba, Ibaraki 305, Japan.

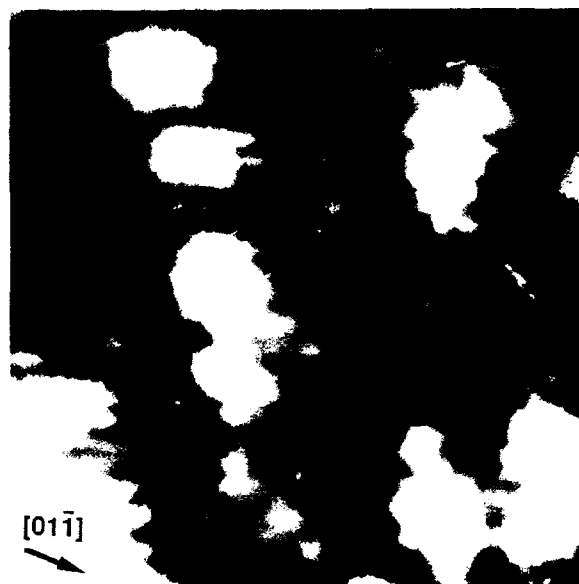


Fig. 1. A typical ($100 \times 100 \text{ \AA}^2$) STM image of an *as-prepared* Si(111) surface obtained at room temperature. The sample was biased at 1.7 V and the tunneling current was maintained at 0.2 nA. Strips seen on the clusters originate from raster scanning noises. The crystallographic direction is shown in the image.

sample temperature was quenched from 900 °C to room temperature within a few seconds while exposing H-atoms to the surface.

Figure 1 shows an STM image of *as-prepared* Si(111) surface obtained at room temperature. In this image, there are many white protrusions (we call these as clusters hereafter) and regular dots on the background terrace. The regular dots exhibit a threefold symmetry with a separation of 3.8 Å which is the same symmetry and periodicity as that of the topmost Si atoms on the Si(111)- 1×1 surface. The tunneling spectra for both the clusters and dots exhibited the band gaps of the order of 2 eV without any states in the gap originating from the presence of dangling bonds, etc., which is the same feature as the previous work [7]. These facts indicate that the clusters are formed by the agglomeration of hydrogenated Si adatoms and the flat terrace is terminated by mono-hydride forming a Si(111)- 1×1 :H surface.

With increasing temperature, the hydrogen atoms start to desorb from the cluster surface leaving Si atoms with monohydride behind. During this process, the clusters decompose into many monohydride adatoms and release agglomerated adatoms onto the surface. This type of the behavior has been confirmed by Boland, showing that the hydrogenated Si clusters decompose into the hydrogenated Si adatoms which spread over the H-terminated restlayers of the DAS structure in the presence of the 7×7 reconstruction [7]. However, the behavior for the present 1×1 case is somewhat different from the 7×7 case since there are no restlayers characterized by the presence of dimers. In order to make clear the behavior for the present case, we have measured the in-situ STM with keeping temperatures well below 580 °C above which the 7×7 structure appears.

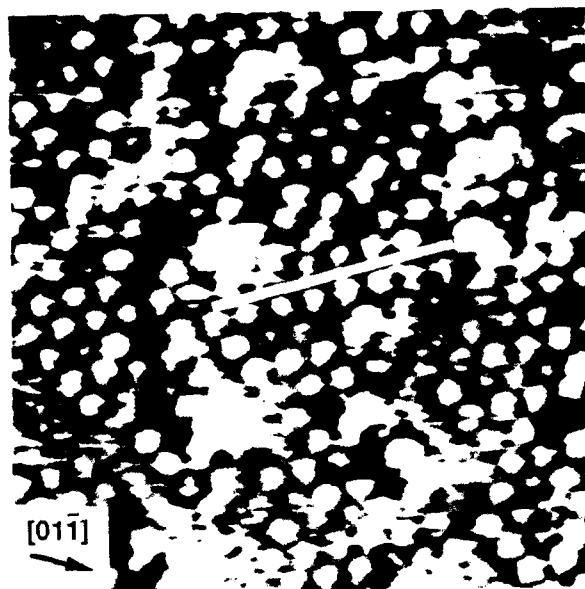


Fig. 2. A typical ($100 \times 100 \text{ \AA}^2$) STM image of the Si(111) surface obtained at 535°C after hydrogen desorption. The sample was biased at 0.7 V and the tunneling current was maintained at 0.2 nA . Several large bright protrusions may be due to the presence of the clusters which have not dissolved completely. The crystallographic direction is shown in the image. A line drawn in the image indicate a typical domain boundary between two $\sqrt{3} \times \sqrt{3}$ regions.

RESULTS

Figure 2 shows an STM image of the Si(111) surface obtained at 15 min later after setting to 535°C from room temperature. In this image, the clusters and 1×1 dots are not observed. Instead, the entire surface is covered by the regular dots which form threefold symmetry with separation of 6.6 \AA . This value is $\sqrt{3}$ times larger than that between top-most Si atoms on the Si(111)- 1×1 surface. The disappearance of the clusters indicates that the clusters decompose during the thermal desorption of the H-atoms and deliver Si atoms onto the surface. Comparing the direction of the dot arrangement with the crystallographic direction indicated in the figure, the registry of the dots indicates $\sqrt{3} \times \sqrt{3} R30^\circ$ structure.

The $\sqrt{3} \times \sqrt{3} R30^\circ$ structure on Si(111) surface is well known to be induced by the adsorption of group III metals [8]. If this is the case, the $\sqrt{3} \times \sqrt{3} R30^\circ$ structure should be conserved even at room temperature. This is, however, not the case because locally ordered $c(2 \times 4)$ and 2×2 structures have been obtained at room temperature [5]. In addition, the H-coverage after keeping 15 min at 535°C can be estimated as $1/300$ monolayers from the H-desorption kinetics based on the thermal desorption studies [9]. This means that almost all of hydrogen atoms have desorbed from the surface in the present case. Therefore we can conclude that the Si(111)- $\sqrt{3} \times \sqrt{3} R30^\circ$ structure shown in Fig. 2 is not caused by the adsorption of hydrogen atoms themselves but by the rearrangement of Si adatoms which had formed the

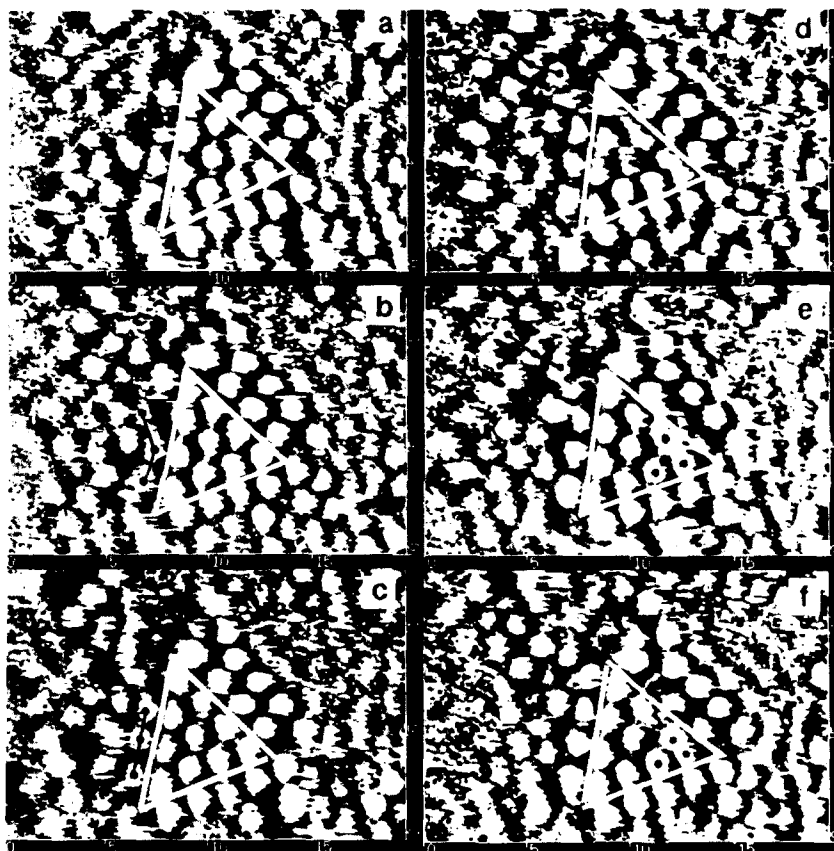


Fig. 3. Successive ($20 \times 13 \text{ \AA}^2$) STM images in the vicinity of the 9×9 reconstruction obtained at 504°C for every 10 seconds. The sample was biased at 0.7 V and the tunneling current was maintained at 0.2 nA . An half unit of 9×9 cell is surrounded by a white triangle. The dots and the networks are superimposed to the images in order to point out the typical adatom hopping of $\text{T}_4\text{-T}_4$ ((b) to (c)) and $\text{T}_4\text{-H}_3$ ((d) to (e) and (e) to (f)).

clusters on the Si(111) surface during H-desorption process. Here we noticed faint and fuzzy $\sqrt{3}\times\sqrt{3}R30^\circ$ dots than surrounding clear and bright ones in the $\sqrt{3}\times\sqrt{3}R30^\circ$ image shown in Fig. 2. This may be due to the existence of the H-atoms at the top of the adatoms since the STM dots originated from Si-H states are usually darker than those from the Si dangling bonds [7].

An interesting feature of the image is the presence of irregularity (domain boundary) of the arrangement of the dots, which is seen in the central part of the Fig. 2. The domain boundary was observed at many places on the $\sqrt{3}\times\sqrt{3}R30^\circ$ surface. This indicates that each domain is formed by rearrangement of Si adatoms around each cluster present at room temperature. However, there is a different boundary (phase boundary) between the $\sqrt{3}\times\sqrt{3}$ and DAS structures on the surface.

Figure 3 shows successive STM images of the Si(111) surface obtained at 504 °C. Each image was recorded for every 10 sec. In these images, there consist of fuzzy parts and atomlike dots. The fuzzy part can be ascribed to the mobile hydrogenated Si adatoms since the H-coverages can be estimated as about 0.1 monolayers based on the thermal desorption studies [5,9]. The dots can be divided into two groups: the adatoms in the half unit of 9×9 cell shown by white triangle and their surrounding dots. In the 9×9 cell, it is derived from the simple extension of the DAS model that the adatoms locate at the T_4 sites. From the relative position of the 9×9 and the surrounding atoms in the image, we can determine the registry of the surrounding atoms. Then we can see the surrounding adatoms mostly locate at T_4 sites and occasionally locate on H_3 sites [5]. In addition, it should be noticed that a few surrounding adatoms and 9×9 adatoms change their sites from one image to another.

DISCUSSION

We discuss the time-dependent behavior of the adatoms observed in Fig. 3. A total energy calculation shows that the T_4 is the more favorable site for the adatom than the H_3 site [10]. This predicted behavior is seen in the present results: the adatoms mostly locate at T_4 sites and occasionally at the H_3 sites. The adatoms near the domain boundary thermally fluctuate and hop mainly between two T_4 sites as shown by dots and networks in Fig. 3 (b) and (c), and occasionally between T_4 and H_3 sites by dots and networks in Fig. 3 (d) and (e).

Next we shall mention for the adatoms within the 9×9 cell. As shown by the dots in Fig. 3 (e) and (f) an adatom locating on T_4 site hops to H_3 site. On the other hand, in the central area of the $\sqrt{3}\times\sqrt{3}$ domain the adatoms hardly changed their sites. By comparing the structure of the $\sqrt{3}\times\sqrt{3}$ with that of the 9×9 , we notice that the former adatoms form the closest packed structure and there are no space to hop for the adatom. On the other hand the latter ones form the 2×2 structure and are not closest-packed. Therefore the adatoms forming local 2×2 structure within the 9×9 unit can hop to the adjacent H_3 site. In the vicinity of the domain boundary, there are a few missing-adatom sites and therefore the adatoms can hop among possible T_4 - T_4 and T_4 - H_3 sites.

CONCLUSIONS

We have shown the atomic structure of Si(111)- $\sqrt{3}\times\sqrt{3}R30^\circ$ and its dynamic nature at about 500 °C. There are many domains with the $\sqrt{3}\times\sqrt{3}R30^\circ$ structures and, in the central part of the domains, the adatoms locate at the T_4 sites stably. The adatoms fluctuate thermally and hop either among T_4 sites or among T_4 - H_3 sites. The adatoms within the 9×9 cell occasionally hop from T_4 to H_3 sites.

REFERENCES

- [1] K. Takayanagi, Y. Tanishiro, M. Takahashi, and S. Takahashi, *J. Vac. Sci. Technol. A* **3**, 1502 (1985).
- [2] J.E. Northrup, *Phys. Rev. Lett.* **57**, 154 (1986).
- [3] R.D. Meade and D. Vanderbilt, *Phys. Rev.* **B40**, 3905 (1989).
- [4] Th. Berghaus, A. Brodde, H. Neddermayer and St. Tosch, *Surf. Sci.* **181**, 340 (1986).
- [5] Y. Morita, K. Miki, and H. Tokumoto, (to be published)
- [6] S. Kitamura, T. Sato, and M. Iwatsuki, *Nature* **351**, 215 (1991).
- [7] J.J. Boland, *Surf. Sci.* **224**, 1 (1991).
- [8] For example, J. Nogami, S. Park, and C.F. Quate, *Phys. Rev.* **B36**, 6221 (1987).
- [9] G. Schulze and M. Henzler, *Surf. Sci.* **124**, 336 (1983).
- [10] J.E. Northrup, *Phys. Rev. Lett.* **53**, 683 (1984).

STEPS ON THE (110) SURFACE OF InP

YONG LIANG,*† WILLIAM E. PACKARD,* AND JOHN D. DOW*

*Department of Physics and Astronomy, Arizona State University, Tempe, Arizona 85287-1504, U.S.A.

†Laboratory for Research on the Structure of Matter, University of Pennsylvania, Philadelphia, Pennsylvania 19104, U.S.A.†

ABSTRACT

Three types of steps are observed on the cleaved InP(110) surface, using atomic-resolution ultra-high vacuum (UHV) scanning tunneling microscopy (STM). The step edges are oriented along the (110), (111), and (112) directions. Atomic models of monatomic-height (111) and (112) steps indicate that the edges of each of these unrelaxed steps should have pairs of dangling bonds. We propose that the bonds dimerize, causing the edges to relax and form periodic structures along the edge.

I. INTRODUCTION

In this paper we present scanning tunneling microscopy (STM) images of the InP(110) surface cleaved in ultra-high vacuum, and find atomic-resolution images of steps on this surface. Ebert *et al.* [1] have examined the InP(110) surface with STM, but the present paper is, we believe, one of the first STM efforts [2] to study such steps, which are important as nucleation sites for layered InP(110) growth, very likely determine essential physics of contact metallization, doubtless play a role in Schottky barrier formation, and getter defects. Here we present images of the flat (110) surface and of steps on the surface. We also propose a Dimerization Model of atomic relaxation at (112) step edges on the (110) surface.

II. EXPERIMENT

The images were obtained with a Pachyderm-4 ultra-high vacuum (UHV) scanning tunneling microscope equipped with a demountable sample holder containing six samples at one time. Each sample was cleaved in UHV (10^{-11} torr range) before being imaged with the tungsten tip of the STM. The microscope, cleavage method, and tip preparation are described in detail elsewhere [3].

III. RESULTS AND DISCUSSION

We imaged the (110) surface of InP with atomic resolution. An example of a flat (110) surface imaged by tunneling into the empty conduction band states is shown in Fig. 1. Similar images for the InSb(110) surface may be found in Ref. [3]. In all cases the expected 1×1 rectangular lattice was observed, and only one atomic species was imaged at a time, depending on the polarity of the sample bias: indium atoms for positive bias, and phosphorus atoms for negative bias.

In addition to flat terraces, steps on these surfaces were also observed. For InP(110), steps were found with edges running in the (110), (111), and (112) directions. An example showing all three step types on InP(110) is shown in Fig. 2, where a single triangular-shaped terrace was formed by intersecting (110), (111), and (112) steps. This intersection of steps on the (110) surface of InP was unanticipated. These steps are the result of the cleavage process and do not represent an equilibrium step configuration, as for some heat-treated samples. On Si and Ge (001)- 2×1 and (111)- 7×7 surfaces, the steps are normally created not by cleavage but by high temperature processing, namely under quasi-equilibrium conditions. Our steps on the InP(110) surface

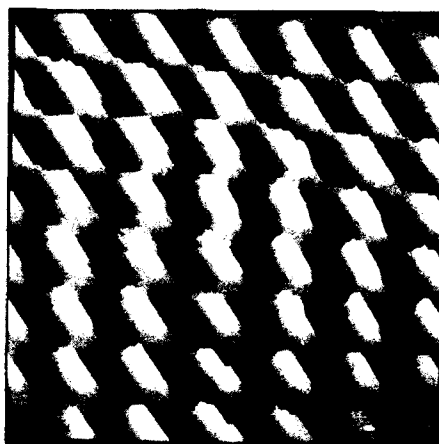


Fig. 1. STM image showing empty states on the flat, cleaved InP(110) surface: A $35 \text{ \AA} \times 35 \text{ \AA}$ image taken under +2.0 V sample bias with a tunneling current of 100 pA.

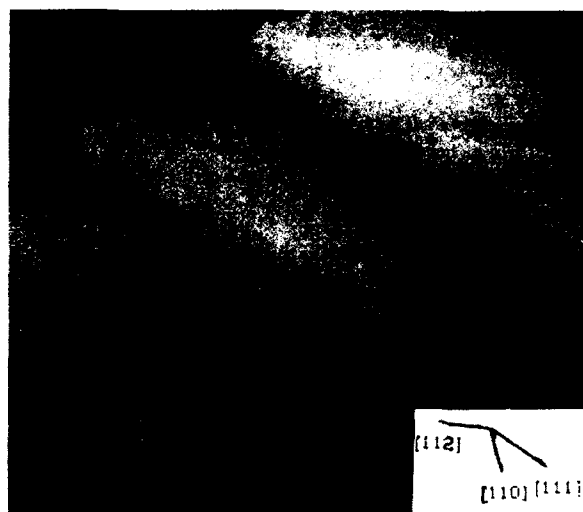


Fig. 2. Triangular terrace on the InP(110) surface, observed by STM at a voltage of +2.0 V and a current of 100 pA. A triangular structure formed by intersecting (110), (111), and (112) steps on the InP(110) surface is pictured. The region shown is $450 \text{ \AA} \times 450 \text{ \AA}$.

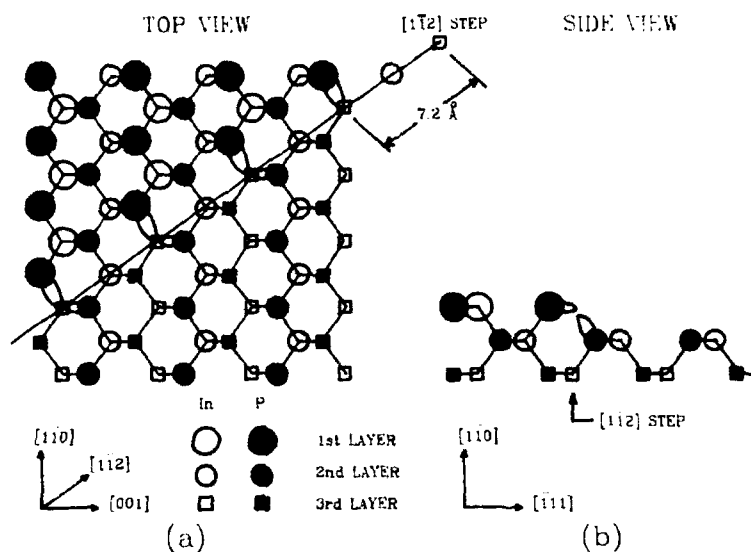


Fig. 3. Dimerization Model for a (112)-type step edge, the $[1\bar{1}2]$ step edge, *before any relaxation*. (a) Top view and (b) side view of the $[1\bar{1}2]$ step showing dangling bonds ("rabbit ears") *before* dimerization.

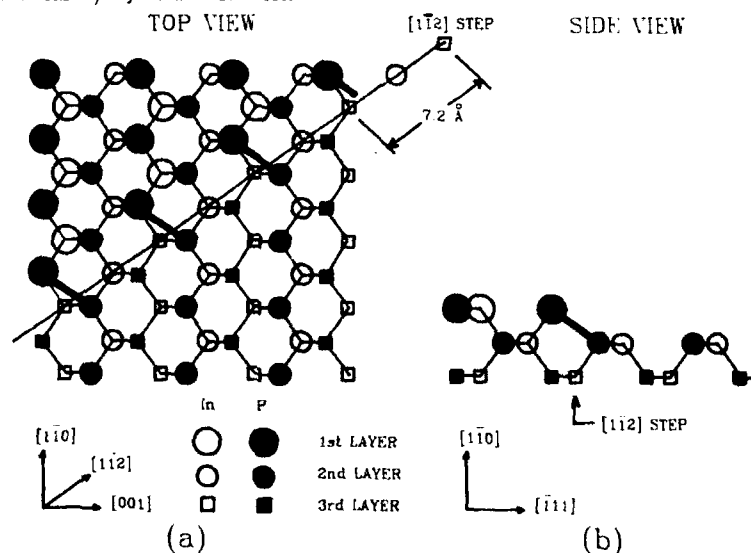


Fig. 4. Dimerization Model for a (112)-type step edge, the $[1\bar{1}2]$ step edge, *after dimerization*. For simplicity of presentation, the 29° rigid rotation [6] of the P anions up out of the surface has been omitted. (a) Top view and (b) side view of the $[1\bar{1}2]$ step showing dangling bonds *after* dimerization.

are not created in quasi-equilibrium, but by cleavage (a rather non-equilibrium event). If, on the one hand, step-intersections on the InP(110) surface were to occur at equilibrium, then those steps would have effective attractive interactions. On the other hand, if the step intersections are a result of cleaving, then the physics of their intersections should produce insights into the processes by which the cleaving energy is dispersed.

Simple geometric models of one-atom-high steps can be constructed from the zinc-blende (110) surface structure. Fig. 3 shows a (112)-type step, assumed to be one-atom in height, both top and side views. Note that there are two dangling bonds periodically repeated at the step-edge, one parallel to the surface and another directed at an angle of 55° with respect to the surface plane.

We propose that these bonds will dimerize and the step-edge will relax, forming the surface structure of Fig. 4. One implication of this Dimer Model of the (112)-type monatomic step is that the relaxed step-edge should be scalloped, showing a periodic structure of about 7.2 Å. We also propose that the (111) monatomic step exhibits similar dimerization, which should lead to a periodicity of 10.2 Å on the InP(110) surface. At the present we are unable to determine whether the dimerized atoms in monatomic steps are In pairs or P pairs; theoretical work on this question is in progress.

In recent studies of the InAs(110) surface, we have searched for and found such periodicities on monatomic steps — which will be reported soon [4]. Presumably the same edge-reconstruction effect will be present in InP. We note also that not all steps observed are monatomic, and that models of these larger steps need to be developed [5].

It is worth remarking that the InP(110) surface is considerably more difficult to image with STM than either InAs(110) or InSb(110). This was unanticipated, and, while at first we thought it might have been related to the quality of our samples, we now suspect that it may be related to the ionicity of the material, since InSb was easy to image and InAs intermediate. We currently have no explanation of this.

IV. CONCLUSIONS

For cleaved InP(110) surfaces we observed the expected 1×1 surface reconstruction which is consistent with the standard model of this surface: the anions rotate up out of the surface, almost in a rigid rotation, by about 29° [6]. In addition we observed steps running in preferred directions on this surface: Step edges were found to run in the (110), (111), and (112) directions. Model calculations are under way to determine the energetics of formation of the various steps.

Periodicity along the (111) and (112) steps is a natural consequence of the Dimer Models we have proposed for the step-edges' relaxation. Model calculations are underway to determine if the dimers along the (111) and (112) steps are III-III or V-V dimers. The study of these steps appears to be a very interesting scientific problem with technological implications.

Acknowledgements — We are grateful to the U.S. Office of Naval Research and the U.S. Army Research Office for their support of this work (Contract Nos. N00014-92-J-1425 and DAAL03-91-G-0054).

REFERENCES

† Present address.

- [1] Ph. Ebert, G. Cox, U. Poppe, and K. Urban, *J. Ultramicroscopy*, **42-44**, 871 (1992).
- [2] Y. Liang, Ph.D. Thesis, University of Notre Dame, 1991. Available from University Microfilms, Ann Arbor, Michigan.
- [3] Y. Liang, W. E. Packard, and J. D. Dow, *J. Vac. Sci. Technol. B*, **9**, 730 (1991).
- [4] Y. Liang, W. E. Packard, J. D. Dow, and G. J. Lapeyre, to be published.
- [5] See, for example, the polyatomic step in Fig. 2.
- [6] S. Y. Tong, A. R. Lubinsky, B. J. Mrstik, and M. A. Van Hove, *Phys. Rev. B* **17**, 3303 (1978); D. J. Chadi, *Phys. Rev. B* **18**, 1800 (1978); D. J. Chadi, *Phys. Rev. B* **19**, 2074 (1979). See also the recent controversy over whether the surface relaxation angle depends on ionicity or not: Arguing for a dependence on ionicity are R. V. Kasowski, M.-H. Tsai, and J. D. Dow, *J. Vac. Sci. Technol. B* **5**, 953 (1987); M.-H. Tsai, J. D. Dow, R.-P. Wang, and R. V. Kasowski, *Phys. Rev. B* **40**, 9818 (1989); *Superlatt. Microstruct.* **6**, 431 (1989). J. L. A. Alves, J. Hebenstreit, and M. Scheffler, *Phys. Rev. B* **44**, 6188 (1991), supported by low-energy positron diffraction data of X. M. Chen, G. R. Brandes, K. F. Canter, C. B. Duke, D. Paton, W. K. Ford, and D. L. Lessor, *Bull. Amer. Phys. Soc.* **37**, 167 (1992). Arguing against such a dependence are C. B. Duke, R. J. Meyer, and P. Mark, *J. Vac. Sci. Technol. B* **17**, 971 (1980); W. Chen, M. Dumas, S. Ahsan, A. Kahn, C. B. Duke, and A. Paton, *J. Vac. Sci. Technol. A* **10**, 2071 (1992); and A. Kahn, S. Ahsan, W. Chen, M. Dumas, C. B. Duke, and A. Paton, *Phys. Rev. Letters* **68**, 3200 (1992).

SCANNING TUNNELING MICROSCOPY ON CHARGE DENSITY WAVES IN LAYERED COMPOUNDS

J.Th.M. DE HOSSON and G.P.E.M. VAN BAKEL

Department of Applied Physics, University of Groningen, Zernike Complex, Nijenborgh 4, 9747 AG Groningen, The Netherlands.

ABSTRACT

Different layered transition metal dichalcogenides were subjected to scanning tunneling microscopy to reveal the electronic charge distribution associated with the charge density wave (CDW) part of the superstructure, in addition to the atomic corrugation. The observations presented display three regimes ranging from localized CDW centred around defects/impurities in the case of 1T-TiS₂, via an intermediate regime governed by overlapping envelope functions in 2H-NbSe₂, to a fully developed CDW system in 1T-TaSe₂ (as well in a large number of other compounds). The fact that these observations have been made in solids ranging from (dirty) semiconductor (1T-TiS₂) to semimetal (1T-TaSe₂) to metallic (2H-NbSe₂) points at the general applicability of the phenomenological Ginzburg-Landau theory, employed to describe the various regimes in which the formation of charge density waves and the accompanying periodic lattice distortions appear to act.

INTRODUCTION

The layered transition-metal dichalcogenides (LTMD) belong to a class of solids exhibiting a marked two-dimensional behaviour, despite their three-dimensional atomic structure. Because of this pseudo two-dimensional character, these materials manifest interesting physical and chemical properties like intercalation of electron-donating species in between layers, superconductivity and charge density waves (CDW) coexisting with periodic lattice distortions (PLD). These phenomena already have been given much attention in past research [1,2]. Mechanisms involved have been devised by means of both theoretical and experimental techniques. The scanning tunneling microscope (STM) adds the possibility of real-space observation of the surface of these solids. In fact, under certain circumstances, the STM measures the conduction electron charge density at the surface. This renders topographs representing the atomic structure. In addition, the charge density superimposed by the stationary charge density wave can be measured directly. This is of special interest because it enables the observation of the order parameter used in the description of phase transformations. This already has led to the confirmation of the domain-structure encountered in the nearly commensurate CDW/PLD [3,4,5,6], predicted earlier theoretically [7]. The effect of defects on CDW/PLD also has been treated theoretically in [8]. STM studies include the imaging of the atomic structure, CDW/PLD [9-13] and the effect of impurities in a number of cases [14-17].

Since the phase transformations in the sequence normal-ICDW-CCDW are 'weak' first-order transitions, McMillan [8] has employed the Ginzburg-Landau theory [18] to describe these phenomena. Recognizing the fact that experiments show three charge density waves that have components 120° apart, McMillan introduces a six-component order parameter consisting of three functions $\psi_i(\vec{r})$. These are related to the conduction electron charge density by:

$$\rho(\vec{r}) = \rho_0(\vec{r}) [1 + \alpha(\vec{r})] \quad (1)$$

where $\rho_0(\vec{r})$ is the charge density in the normal state and:

$$\alpha(\vec{r}) = \text{Re} \{ \psi_1(\vec{r}) + \psi_2(\vec{r}) + \psi_3(\vec{r}) \} \quad (2)$$

Now the free energy density must be constructed. The simplest form to start with is the 'Landau' part of the free energy density: $a\alpha^2 + b\alpha^3 + c\alpha^4 + \dots$, where the cubic term must be included to describe a first-order transition. This expression, however, does not permit a distinction between single and triple charge density waves. Therefore cross terms are added of the form $d(|\psi_1\psi_2|^2 + |\psi_2\psi_3|^2 + |\psi_3\psi_1|^2)$.

Now, the total energy can be minimized with respect to variations in the order parameter, i.e. the total energy of one layer (integration of Landau expression of the total energy over $d^2\vec{r}$), is minimized with respect to variation in $\delta\psi$. The variations may be written out explicitly and set to zero. Like the zero-field solutions in the Ginzburg-Landau theory [18], the solutions of $\psi(\vec{r})$ of this differential equation is, beside the trivial solution of $\psi(\vec{r}) = 0$, a plane wave $\psi(\vec{r}) = e^{i\vec{q} \cdot \vec{r}}$.

In the normal state the charge density is unaffected and uniform. However, impurities may give rise to fluctuations in the order parameter. As a consequence $\psi_i(\vec{r}) = \phi(\vec{r})e^{i\vec{k}_i \cdot \vec{r}}$ where $\vec{k}_i = \vec{q}_i$ for the incommensurate phase and $\vec{k}_i = \vec{K}_i/3$ for the commensurate phase. Both the coefficient $\phi(\vec{r})$ and the impurity potential $U(\vec{r})$ can be Fourier transformed, like:

$$\phi(\vec{r}) = \phi_0 + \sum_{\vec{q}} \phi_{\vec{q}} e^{i\vec{q} \cdot \vec{r}} \quad (3)$$

The contribution due to the impurity potential must be added to the free energy together with a change of ψ_0 by $\phi_{\vec{q}}$. Next, minimizing the total energy with respect to $\phi_{\vec{q}}$, $\psi_i(\vec{r})$ can be rewritten for one impurity at the origin as:

$$\psi_i(\vec{r}) = \phi_0 e^{i\vec{q}_i \cdot \vec{r}} - \frac{1}{2} U_0 \sum_{\vec{q}} \frac{e^{i(\vec{q} + \vec{q}_i) \cdot \vec{r}}}{g_{\vec{q}}} \quad (4)$$

Combining (Eq.4) with (Eq.1 and Eq.2) the expression for the charge density around one impurity is given by (assuming an elastic constant e_0 of the CDW):

$$\rho(\vec{r}) = \rho_0(\vec{r}) \left[1 - \sum_{i=1}^3 \frac{u_0 \cos(\vec{q}_i \cdot \vec{r}) f(r/\xi_{CDW})}{4\pi e_0 q_i^2} \right] \quad (5)$$

This equation is valid for $\vec{q}_i \cdot \vec{r} > 1$. The function $f(r/\xi_{CDW})$ is expressed as an integral :

$$f(r/\xi_{CDW}) = \int_1^\infty \frac{e^{-yr/\xi_{CDW}}}{\sqrt{y^2 - 1}} dy \quad (6)$$

EXPERIMENTS

Here STM results on a number of LTMD are presented, belonging to different regimes as far as crystal symmetry, electronic transport properties and CDW are considered.

The STM experiments were performed in air and at room temperature, using a Digital Instruments Nanoscope II instrument equipped with a type-A scanning head, capable of performing constant-height and constant-current scans of 600x600x450 nm in size.

STM on charge density waves in 1T-TaSe₂

Imaging of 1T-TaSe₂ revealed the characteristic superposition of atomic and CDW-corrugation, depicted in Fig.1. The measured angles between the lattices and the ratio of the lattice parameters agree with those observed earlier [9,12]. The simultaneous appearance of the two corrugations is due to the fact that the amplitudes of the two corrugations are about equal. This is not a general result of all the transition-metal dichalcogenides. It is to be mentioned that one of the CDW maxima is depressed with respect to the average amplitude, however the atomic lattice shows to be unaffected by this effect. This indicates that a disturbance of the CDW-corrugation does not necessarily have an effect on the atomic corrugation. The CDW-corrugation in this example is described well by the equations in the section of this paper concerning the Landau theory when only a periodic lattice potential is present. However, this does not hold for the missing CDW-maximum and this points at distortion of the CDW-lattice caused by the presence of defects.

STM on 1T-TiS₂

The STM-images obtained on 1T-TiS₂ (Fig.2) primarily consist of hexagonally arranged bright (i.e. elevated) spots, along with a number of characteristic features. These are grouped into three categories: one type consisting of an isolated black recession (type-1). In addition, another feature type is characterized by three protruding spots surrounded by three recessions (type-6), as well as type extending over 15 protruding sites (type-15).

In order to gain insight on the underlying mechanism responsible for the presence of the features, the densities (number of features observed per unit cell) of the three types were determined by counting the number of occurrences over approximately 2500 surface unit cells. The relative occurrences of type 1 : type 6 : type 15 are found to be close to 1:1:2. As a result it is assumed that, during the crystal growth process, some titanium atoms, which normally occupy the octahedral sites in the crystal, are displaced to, normally unoccupied, tetrahedral interstitial sites within the sandwich. Since there are two kinds of tetrahedral sites and one octahedral site, this would account for the fact that there are three observed feature types. The estimate for the respective feature density supports this explanation, because one of the features (type-15) has a density equal to the sum of the densities of the remaining type (type-1 and type-6). This would infer that type-15 corresponds to a vacancy in the titanium sublattice, whereas type-1 and type-6 correspond to titanium interstitials.

STM on 2H-NbSe₂

STM-topographs of 2H-NbSe₂ were reported before by Dahn et al. [19] and 'buckling of the surface with a period of several times the interatomic spacing' was mentioned. The STM-images presented here allow to make a more careful analysis of this buckling and its possible relation to charge density waves. From the constant height map, shown in Fig.3, it is clear that, apart from the atomic corrugation, whose lattice has the appropriate spacing and symmetry, a number of atomic sites displays larger tunneling probability (bright contrast) than the average amplitude, whereas an about equal number displays the opposite behaviour (dark contrast). Furthermore, there seems to be a correspondence between the tunneling current amplitudes of alternate atomic rows. To make this statement more quantitative, the auto correlation function was calculated. This (real) function shows the correlation between sites connected by a certain shift vector:

$$G(\vec{s}) = \int \int z(\vec{r}) \cdot z(\vec{r} + \vec{s}) d^2\vec{r} \quad (7)$$

If the tunneling current map consists of the superposition of three plane waves, then the auto correlation function will take the same form. The measured auto correlation values at the different nearest neighbour separations are listed in Table I, taking the values at the centre equal to 1. From this table it can be derived that the next-nearest neighbour correlation is larger than the nearest neighbour correlation.

Table I

Autocorrelation data 2H-NbSe₂ (origin, 1st, 2nd, 3rd nearest neighbour)

105°	1.00	0.386	0.448	0.404
345°	1.00	0.354	0.424	0.340
225°	1.00	0.368	0.452	0.340

The comparison is feasible because the envelope of the correlation function shows little decay over many interatomic distances. The values of the correlations cannot be taken as absolute because the correlation depends on both the corrugation of the super structure and the coverage of the surface area. Next to the auto correlation function, the two-dimensional Fourier transform was performed, the intensity map of which is shown in Fig.4. The spectrum can be divided into contributions from the atomic corrugation and the surface buckling, respectively. The atomic lattice has a well-defined period and the fundamental harmonic constituent gives rise to a hexagonally arranged set of bright spots. The spots outside this hexagon are due to the higher harmonics necessary to describe the observed current map. Inside the fundamental hexagon six clouds are visible, having the same symmetry as the spots belonging to the atomic lattice.

CALCULATION OF STM-IMAGES

Equation 5 is taken as a starting point for the calculation of STM topographs. To model the atomic corrugation a superposition of three plane waves is taken, with wave vectors being equal in size and having angular separation of 120° . The wave vectors add to zero, ensuring the maxima do coincide at a two-dimensional Bravais lattice (hexagonal). The charge density map obtained corresponds to the observed corrugation to a fair degree. The full expression for the calculated images is given by :

$$A_{lat} \sum_{i=1}^3 \cos[\vec{K}_i \cdot (\vec{r} + \vec{d}_{lat})] + A_{cdw} f\left(\frac{\sqrt{(|\vec{r}|^2 + z^2)}}{\xi_{cdw}}\right) \sum_{i=1}^3 \cos[\vec{q}_i \cdot (\vec{r} + \vec{d}_{cdw}) + \theta_{cdw}] \quad (8)$$

with conditions $\sum_{i=1}^3 \vec{K}_i = \vec{0}$ and $\sum_{i=1}^3 \vec{q}_i = \vec{0}$

The integral emerging in this expression is improper because of the integrand approaching infinity when y approaches 1 and the integration interval being infinite. However, the integrand can be approximated for low and high values of y and the contributions of the lower and upper part of the integration interval are readily estimated. The contributions of the intermediate values of y can be calculated numerically. This procedure can be carried out for various values of r/ξ_{cdw} . The function $f(r/\xi_{cdw})$ shows an asymptotic behaviour according to :

$$r/\xi_{cdw} \ll 1 : f(r/\xi_{cdw}) = \ln(1.12\xi_{cdw}/r) \quad (9)$$

$$r/\xi_{cdw} \gg 1 : f(r/\xi_{cdw}) = \left(\frac{\pi\xi_{cdw}}{2r}\right)^{1/2} e^{-r/\xi_{cdw}} \quad (10)$$

The numerically calculated values then can be checked against this asymptotic behaviour. The resulting expression for the charge density contains few parameters.

In all the calculations each set of the wave vectors, either \vec{K}_i or \vec{q}_i , consists of a star of vectors of equal length and 120° apart. The two vector sets have the same orientation. By taking the vectors composing the localized charge density wave as somewhat smaller than half the ones used to generate the atomic corrugation and adjusting the amplitude, location and correlation length, topographs are assembled that do resemble the observed features in the case of type 1 and type 6. For a full account of the parameters used, see Table II. For type 15, much smaller wave vectors were applied and also a phase shift was introduced, resulting in a topograph in reasonable agreement with the observed type feature. The calculated images are displayed in Fig. 5.

Table II
Parameters used in calculations on 1T-TiS₂ (type-1, type-6, type-15)

$ \vec{K} $	$2.131 \cdot 10^{10} \text{ m}^{-1}$	$2.131 \cdot 10^{10} \text{ m}^{-1}$	$2.131 \cdot 10^{10} \text{ m}^{-1}$
$ \vec{q} $	$0.852 \cdot 10^{10} \text{ m}^{-1}$	$0.852 \cdot 10^{10} \text{ m}^{-1}$	$0.320 \cdot 10^{10} \text{ m}^{-1}$
\vec{d}_{lat}	(0, 0) nm	(0, -0.197) nm	(0, -0.197) nm
\vec{d}_{cdw}	(0, 0) nm	(0, 0.492) nm	(0, 0) nm
θ_{cdw}	0	0	-1.100
ξ_{cdw}	0.224 nm	0.224 nm	0.352 nm
A_{cdw}/A_{lat}	-15	-15	15
z	0.209 nm	0.070 nm	0.141 nm

For all three features, the origin of the envelope function was chosen below the surface, at a distance in agreement with the assumed defect sites. The signs of the amplitudes correspond to the defect model in which type 1 and type 6 are ascribed to titanium interstitials and type 15 as a vacancy at a lattice site normally occupied by titanium. In fact the calculated images for type 1 and type 6 only differ in the position of the origin of the CDW system.

DISCUSSION

From the auto correlation function in the case of 2H-NbSe_2 , it was deduced that the next-nearest neighbour correspondence is larger than the nearest neighbour correspondence. The vector connecting next-nearest neighbours also connects alternate close packed atomic rows. Alternate atomic rows are connected by a plane wave having a wave vector half that of the atomic lattice. Now suppose the observed current map consists of a superposition of the atomic corrugation and an electronic density corrugation described by a superposition of three plane waves. These waves are described by wave vectors that are about one half of those describing the atomic corrugation. Their amplitudes are modulated by a modulation function containing spatial frequencies up to about one half of the fundamental spatial frequency of the atomic lattice. The resulting Fourier transform will consist of the fundamental hexagon due to the atomic lattice, a convolution of a hexagon, the size being one half that of the fundamental one, and the Fourier transform of the modulation function. If the uniform 'superlattice' having the double interatomic spacing is drawn in the observed image then it becomes clear that long range correlation between alternate rows is absent and phase shifts of π are seen to occur often. Therefore this is certainly not a superstructure with large coherence length. So the modulation function (or functions when each plane wave is contributing to the superlattice is modulated by its own function) will have to introduce phase shifts. Now attention is drawn to the feature present in the 2H-NbSe_2 map, resembling the type 6 feature in the case of 1T-TiS_2 . In the analysis of 1T-TiS_2 it became clear that the phases of the plane waves are essential in establishing a matching calculated feature. Since this feature occurs more than once in the current map, the modulation functions probably originate from several sources, possibly impurities/defects in or at the 2H-NbSe_2 crystal. On the other hand phase shifts are also present in nearly commensurate charge density waves [3,4,5,6] and a domain structure establishes in order to minimize total free energy. This, however, is not a very likely explanation for the observed phase shifts here, for the correlation length of the type 6 feature is short compared to the domain sizes encountered in incommensurate charge density waves (say 30 interatomic distances). Decomposition of the modulation is difficult for the number of sources is seen to be rather high compared to the more or less isolated features in 1T-TiS_2 .

CONCLUSIONS

From the STM observations made on stoichiometric 1T-TiS_2 several conjectures are established. It is seen that both the sulphur and titanium sublattices contribute to the STM topographs presented here. It is assumed that the crystal sites coincide with threefold symmetry sites in the topographs. In addition, the topographs show the presence of three distinct feature types, each centred around a distinct threefold symmetry site and occurring in single orientation only. From the relative occurrences and the possible assignments of threefold symmetry sites to crystal sites a novel model is established in which Frenkel pairs, consisting of vacancies in the titanium sublattice and occupation of the tetrahedral interstitial sublattice are responsible for the observed features. The existence of one titanium sublattice and two tetrahedral sublattices accounts for the fact that three feature types are observed. The model leaves only one assignment of symmetry sites to crystal sites open, the local maxima being assigned to sulphur and the local minima to titanium. A more extensive discussion can be found in [20].

The observations presented here display three regimes ranging from localized CDW/PLD centred around defects/impurities in the case of 1T-TiS_2 , via an intermediate regime governed by overlapping envelope functions in 2H-NbSe_2 , to a fully developed CDW/PLD system in 1T-TaSe_2 (as well in a large number of other compounds). The fact that these observations have been made in solids ranging from (dirty) semiconductor (1T-TiS_2) to semimetal (1T-TaSe_2) to metallic (2H-NbSe_2) points at the general applicability of the phenomenological Ginzburg-Landau theory, employed to describe the various regimes in which CDW/PLD formation appears to act.

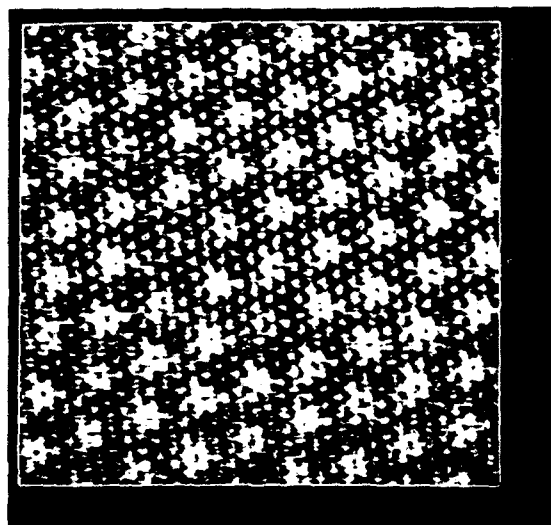


Fig. 1 STM current map of 1T-TaSe₂ at $V_{\text{sample}} - V_{\text{tip}} = 3.1$ mV and $I_{\text{setpoint}} = 2.4$ nA, scan size = 10 nm.

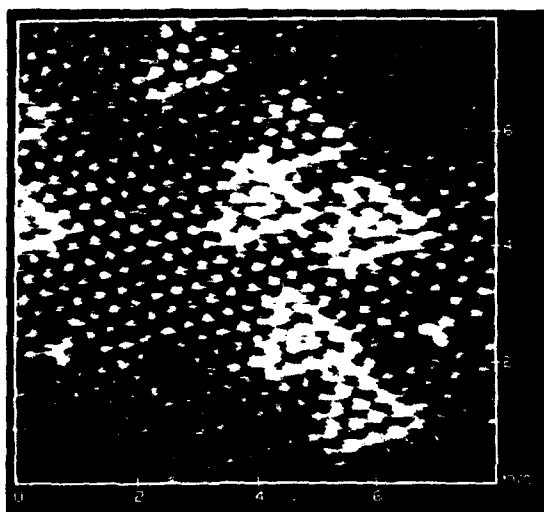


Fig. 2 STM topograph on 1T-TiS₂ at $V_{\text{sample}} - V_{\text{tip}} = 25$ mV and $I_{\text{setpoint}} = 1.3$ nA, scan size = 7.5 nm, filtered at $(0.25 \text{ nm})^{-1}$.

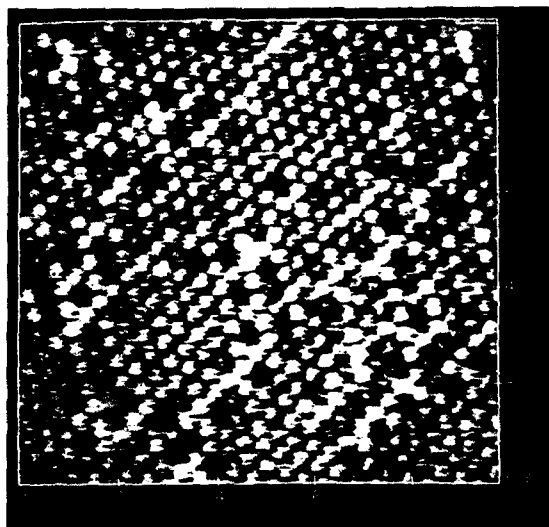


Fig. 3 STM current map on 2H-NbSe₂ at $V_{\text{sample}} - V_{\text{tip}} = 5.8$ mV and $I_{\text{setpoint}} = 1$ nA, scan size = 8.8 nm.

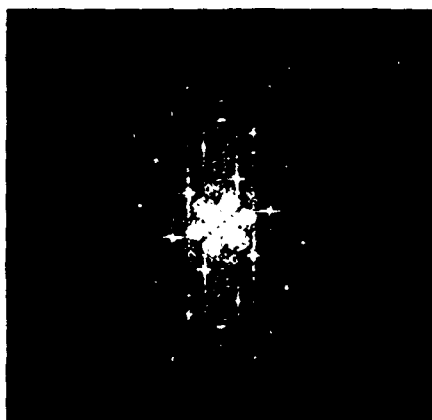


Fig. 4 Fourier-transform intensity plot of 2H-NbSe₂ STM current map (Fig. 3).

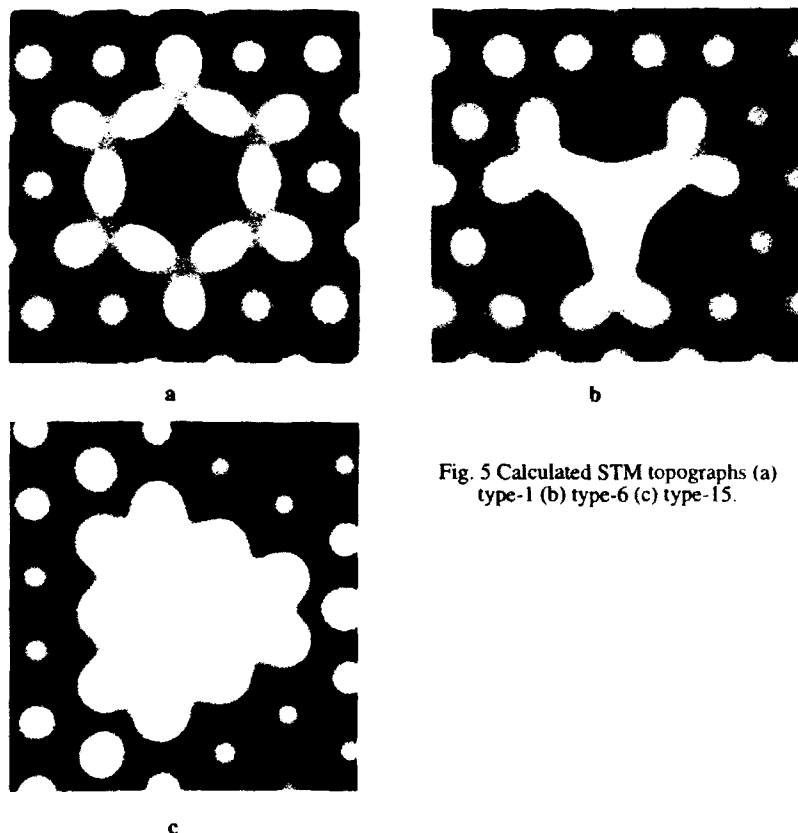


Fig. 5 Calculated STM topographs (a) type-1 (b) type-6 (c) type-15.

REFERENCES

- [1] R. H. Friend, A. D. Yoffe, *Adv. Phys.* 36, 1 (1987).
- [2] J. A. Wilson, *Phys. Status Solidi B* 86, 11 (1978).
- [3] B. Burk, R. E. Thomson, A. Zettl, J. Clarke, *Phys. Rev. Lett.* 66, 3040 (1991).
- [4] C. G. Slough, W. W. McNairy, C. Wang, R. V. Coleman, *J. Vac. Sci. Technol. B* 9, 1036 (1991).
- [5] X. L. Wu, C. M. Lieber, *Phys. Rev. Lett.* 64, 1150 (1990).
- [6] X. L. Wu, C. M. Lieber, *J. Vac. Sci. Technol. B* 9, 1044 (1991).
- [7] W. L. McMillan, *Phys. Rev. B* 14, 1496 (1976).
- [8] W. L. McMillan, *Phys. Rev. B* 12, 1187 (1975).
- [9] R. V. Coleman, B. Giambattista, P. K. Hansma, A. Johnson, W. W. McNairy, C. G. Slough, *Adv. Phys.* 37, 559 (1988).
- [10] C. G. Slough, B. Giambattista, A. Johnson, W. M. McNairy, C. Wang, R. V. Coleman, *Phys. Rev. B* 37, 6571 (1988).
- [11] R. E. Thomson, U. Walter, E. Ganz, J. Clarke, A. Zettl, P. Rauch, F. J. DiSalvo, *Phys. Rev. B* 38, 10734 (1988).
- [12] B. A. Parkinson, J. Ren and M.-H. Whangbo, *Am. Chem. Soc.* 113, 7833 (1991).
- [13] R. C. Barrett, J. Nogami, C. F. Quate, *Appl. Phys. Lett.* 57, 10, 992 (1990).
- [14] H. Dai, H. Chen, C. M. Lieber, *Phys. Rev. Lett.* 66, 24, 3183 (1991).
- [15] H. Chen, X. L. Wu, C. M. Lieber, *J. Am. Chem. Soc.* 112, 3326 (1990).
- [16] X. L. Wu, C. M. Lieber, *Phys. Rev. B* 41, 2, (1990).
- [17] X. L. Wu, C. M. Lieber, *Phys. Rev. Lett.* 61, 22 (1988).
- [18] V. L. Ginzburg, L. D. Landau, *Nuovo Cimento* 2, 1234 (1955).
- [19] D. C. Dahn, M. O. Watanabe, B. L. Blackford, M. H. Jericho, *J. Appl. Phys.* 63, 2, 315 (1987).
- [20] G.P.E.M. Van Bakel, J.Th.M. De Hosson, *Phys. Rev. B* 46, 2001 (1992).

DESIGN OF ULTRA HIGH VACUUM SCANNING ELECTRON MICROSCOPE COMBINED WITH SCANNING TUNNELING MICROSCOPE

Mikio Takai*, Naoki Yokoi*, Ryou Mimura**, Hiroshi Sawaragi**, and Ryuso Aihara**

*Faculty of Engineering Science and Research Center for Extreme Materials,
Osaka University, Toyonaka, 560 Osaka, Japan

**EIKO Engineering Co., Ltd., 50 Yamazaki, Nakaminato, Ibaraki 311-12, Japan

ABSTRACT

An ultra high vacuum (UHV) scanning electron microscope (SEM) combined with a scanning tunneling microscope (STM) has been designed and constructed to solve problems arising from STM surface imaging and nanofabrication using STM tips, such as difficulty in probe tip location and change in tip shape. The system facilitates to image and/or to modify a wide range of area from submicron down to subnanometer. A ZrO/W thermal emitter in a Schottky mode has been used for an electron gun to obtain a low energy spread with a high angular current density. Minimum beam spot diameters of 6 and 12 nm with currents of 100 pA and 4 nA are estimated by optical property calculation for high resolution (SEM) and high current (fabrication) modes, respectively.

INTRODUCTION

Scanning tunneling microscopes (STMs) have been widely used to investigate surface electronic states of conductive materials since their invention [1]. They have also been applied to localized material modification in a nanometer scale [2 - 7], though the mechanism of such a nanoscale modification was not yet clarified. Thus, the STM fabrication can provide in-situ modification of atomic surfaces during atomic scale monitoring. Difficulties in nanofabrication using STM tips are a probe-tip location, change in STM image and STM tip shape [7, 8], and low process rate. The probe tip location cannot be easily identified because of the extremely small processed area. The change in STM image during nanofabrication is often observed presumably due to the change in tip shape induced by the application of voltage bias pulses [7, 8]. Such difficulties can be overcome by the combination of a scanning electron microscope (SEM) column with a STM as in Fig. 1, which can facilitate the STM tip location in localized areas and in-situ monitoring of the STM tip shape. An UHV chamber for the STM improves the instability and contamination of modified atomic surfaces. Furthermore, an UHV SEM combined with a STM realizes in-situ fabrication (i.e. surface imaging and modification) in a wide range from micron down to subnanometer, when both electron beams are utilized for imaging and modification. SEM/STM combinations have been attempted only by the use of commercial SEMs with low vacuum chambers [9, 10] or a UHV chamber [11]. Design optimization of the STM chamber, the SEM column, and the electron source for in-situ nanofabrication including both surface imaging and modification has not been made till now.

In this study, an UHV SEM column connected to a chamber with a STM has been designed and constructed to solve difficulties arising from nanofabrication using STM tips. The focusing performance of the SEM column for surface monitoring (i.e. high resolution mode) and modification (i.e. high current mode) has been simulated.

ELECTRON BEAM SYSTEM DESIGN

STM Chamber Design

Figure 2 shows the schematic of the UHV STM/SEM system having a load-lock chamber for sample change. The STM is mounted on the stage in the UHV chamber made of iron and coated with nickel. Iron is used to suppress the influence of stray magnetic field on both SEM and STM. Surface coating of nickel is employed for low outgassing and for corrosion protection during nanofabrication using reactive gases. The whole system is suspended by coil springs to damp vibrations from the floor.

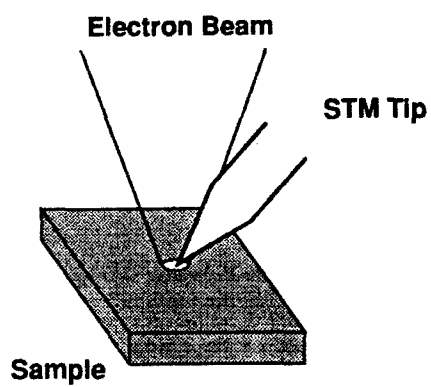


Fig. 1 Schematic of STM/SEM combination covering a wide range of field.

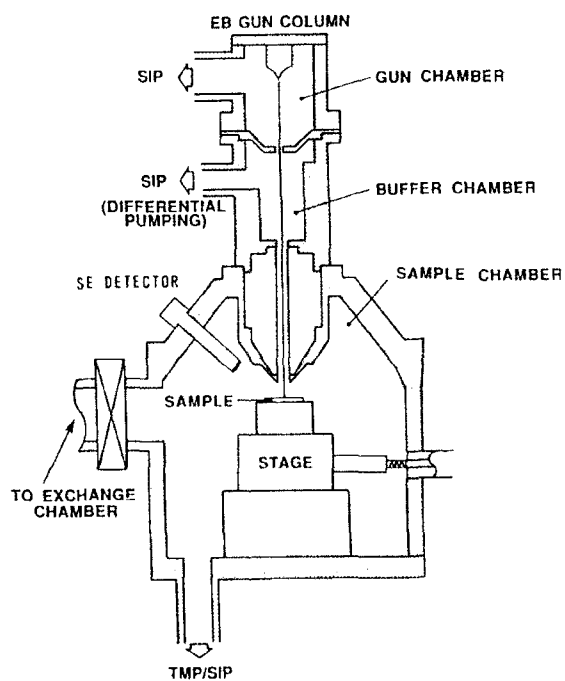


Fig. 2 Schematic of a UHV STM/SEM system having a load-lock chamber for sample change.

Table I A comparison of electron emission source characteristics between field emission (FE) and Schottky emission (SE). ΔV : energy spread, $dI/d\Omega$: angular current density, ∂ : source size.

	FE	SE (ZrO/W(100))
ΔV (eV)	0.3	0.5 ~ 1.5
$dI/d\Omega$ ($\mu A/sr$)	10^4	$10^2 \sim 10^3$
∂ (nm)	5	15
vacuum (Torr)	$\sim 10^{-10}$	$\sim 10^{-9}$
curr. stability	bad	good

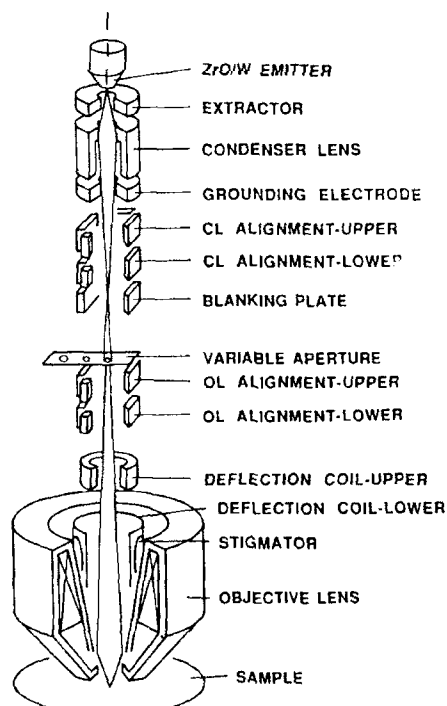


Fig. 3 Schematic of beam optics.

Electron Gun

Electron guns usually used for finely focused electron beams are field emission (FE) and Schottky emission (SE) electron sources. The FE electron source has smaller energy spread and source size than the SE as shown in table I. However, the angular current density of the FE source is much lower than that of the SE source. The current stability of the FE source is also worse than that of the SE source. Therefore, a SE electron source with ZrO/W(100) is employed as an electron gun.

Acceleration Column

Figure 3 shows the schematic of the acceleration column mounted with a ZrO/W SE source. The column consists of an electrostatic condenser lens and a magnetic objective lens. The important point for modification application using a STM is a working distance between the sample and the bottom of the objective lens, the value of which is settled at 20 mm.

BEAM OPTICS SIMULATION

Aberrations of the focusing lens system shown in Fig. 3 can be calculated by a finite element method [12]. Figure 4 shows the spherical and chromatic aberrations, cross-over point distance, and magnification as a function of voltage ratio (V_{CL}/V_{ACC}) under a condition of $V_{EX}/V_{ACC} = 0.3$. These parameters (Csi, Cci, Zi, and M) drastically change as the voltage ratio between the condenser lens and acceleration voltages changes. Both aberration coefficients are minimized at a lowest magnification, in which a finest beam can be obtained (i.e. high resolution mode).

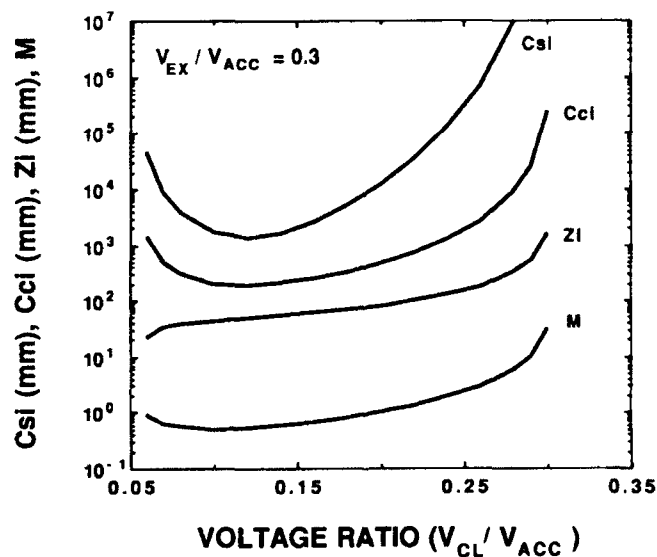


Fig. 4 Condenser lens aberrations (Csi: spherical, Cci: chromatic), cross-over point distance (Zi), and magnification (M) as a function of voltage ratio (V_{CL}/V_{ACC}) under a condition of $V_{EX}/V_{ACC} = 0.3$.

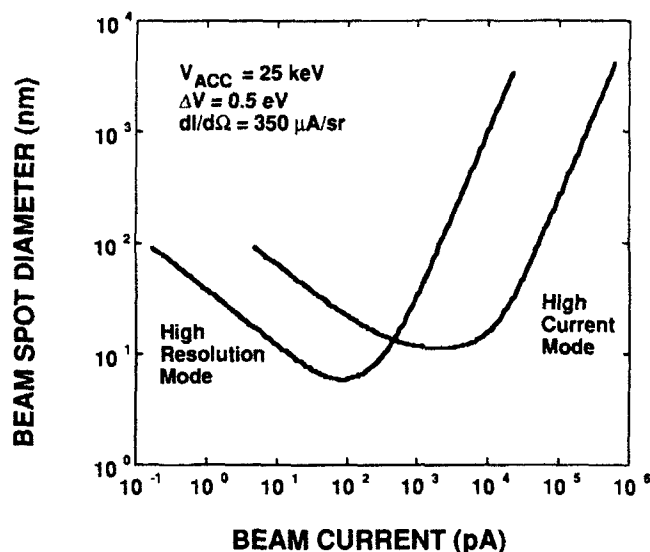


Fig. 5 Beam spot diameter as a function of current for 25 keV electron beams with two different modes.

Focusing characteristics can be further estimated using calculated aberrations and electron source specifications [13]. Figure 5 shows the calculated beam spot diameter for the designed electron beam column as a function of current for high resolution (SEM) and high current (fabrication) modes. In case of high resolution mode, a minimum beam spot diameter of 6 nm with a current of 100 pA can be obtained under a condition of $M=0.52$ in Fig. 4, while that of 12 nm with a current of about 4 nA is estimated for high current (fabrication) mode under a condition of $M=2.1$. Thus this electron beam system provides two operation modes for monitoring and fabrication ranging from 6 nm to 1 μm .

SUMMARY

The design concept of the UHV SEM/STM system and additional problems arising from the combination of the UHV SEM and STM such as the influence of stray magnetic field and vibration have been discussed. A ZrO/W thermal emitter in a Schottky mode has been used for an electron gun to obtain a low energy spread with a high angular current density. Minimum beam spot diameters of 6 and 12 nm with currents of 100 pA and 4 nA are estimated by optical property calculation for high resolution (SEM) and current (fabrication) modes, respectively.

ACKNOWLEDGMENTS

The authors are indebted to K. Haramura and K. Mino for their help during experiment.

REFERENCES

1. G.Binnig, H.Rohrer, Ch.Gerber and E.Weibel: Phys. Rev. Lett. **49**, 57 (1982)
2. S.-T.Yau, D.Saltz, A.Wriekat and M.H.Nayferh: J. Appl. Phys. **69**, 2970 (1991)
3. J.A.Dagata, J.Schneir, H.H.Harary, J.Bennett and W.Tseng: J. Vac. Sci. Technol. **B9**, 1384 (1991)
4. I.-W.Lyo and P.Avouris: Science **253**, 173 (1991)
5. W.Mizutani, J.Inukai and M.Ono: Jpn. J. Appl. Phys. **29**, L815 (1990)
6. D.M.Eigler and E.K.Schweizer: Nature **344**, 524 (1990)

7. N. Yokoi, S. Ueda, S. Namba, and M. Takai, Jpn. J. Appl. Phys. (1993) in press
8. N. Yokoi, S. Namba, and M. Takai, Advanced Materials for Optics and Electronics (1993) in press
9. Ch. Gerber, G. Binnig, H. Fuchs, O. Marti, and H. Rohrer, Rev. Sci. Instrum. **57**, 221 (1986)
10. L. Vazquez, A. Bartolome, R. Garcia, A. Buendia, and A.M. Baro, Rev. Sci. Instrum. **59**, 1286 (1988)
11. E.E. Ehrichs, W.F. Smith, and A.L. de Lozanne, J. Vac. Sci. Technol. **B9**, 1380 (1991)
12. E. Munro, PhD Thesis, University of Cambridge, 1972
13. O.C. Wells, *Scanning Electron Microscopy* (McGraw-Hill, New York, 1974)

SCANNING TUNNELING MICROSCOPY PERSPECTIVE OF STRUCTURES ON REDUCED $\text{SrTiO}_3(001)$ SURFACES

YONG LIANG AND DAWN A. BONNELL

Department of Materials Science and Engineering, University of Pennsylvania, Philadelphia, PA 19104-6272

Abstract

Scanning tunneling microscopy has been used in ultra high vacuum to provide atomic scale structural information on reduced $\text{SrTiO}_3(001)$ surfaces. Our tunneling images exhibit row-like features with 12 Å and 20 Å periodicities on the reduced surface. A local 2x1 reconstruction was also revealed on some regions of the surface. The experimental results are discussed in terms of the different sublimation rates of surface constituents and formation of lamella structures of $\text{Sr}_{n+1}\text{Ti}_n\text{O}_{3n+1}$.

Introduction

The surface structure of SrTiO_3 has attracted considerable attention over the years due to many interesting properties, which include surface relaxation and related ferroelectric properties, photo-catalysis, and structural relationship with novel high- T_c superconductor. A good understanding of these properties, is closely related to the understanding of surface structures and defect formation. Although many surface analytical-techniques have been used to provide insight into surface electronic structure and symmetry, little is known about the geometric structure and the composition of the surface at an atomic scale.

There are two possible terminations for a perovskite $\text{SrTiO}_3(001)$ surface; the surface can either terminate at a SrO plane or at a TiO_2 plane. Fig.1 shows a plausible configuration of a surface with two terminations separated by a single height step. The left terrace consists of only oxygen and strontium atoms, i.e., a SrO termination; the right terrace is a TiO_2 termination with only oxygen and titanium atoms. The population of the two terminations on a (001) surface is determined by a number of factors, and since the symmetry is the same for both terminations, four-fold symmetry and a square surface-unit-cell is anticipated for an ideal perovskite (001) surface as shown in Fig.1. In contrast to many transition-metal oxides, SrTiO_3 is able to support both oxygen and titanium deficiencies through formation of variant structures such as the intergrowths of lamellae (Ruddlesden-Popper phases) [1,2]. This type of structure can be formulated as $\text{Sr}_{n+1}\text{Ti}_n\text{O}_{3n+1}$. The structure is related to ideal perovskite by a shear for every n perovskite layers and reduction of coordination of a fraction of Sr atoms from 12-fold to 9-fold.

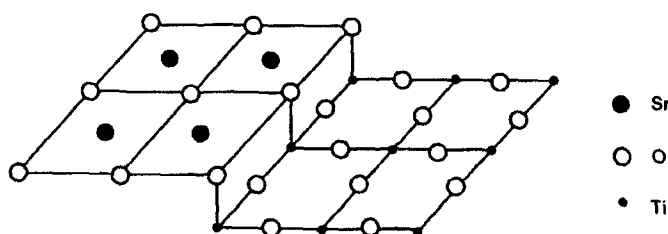


Fig.1 The $\text{SrTiO}_3(001)$ surface illustrating SrO termination and TiO_2 termination separated by an atomic height step.

Although scanning tunneling microscope (STM) has been widely used to study the metal and semiconductor surfaces, STM on wide-gap, dielectric ceramic surfaces are, with a few exceptions [3], very limited due to the specialty of those surfaces. For example: (1) The high density of surface states and associated band bending could "pinch off" the tunneling [4]. (2) The capacitive coupling between tunneling tip and surface may hamper the STM resolution [5]. We reduce these effects by increasing the carrier concentration of the crystal via reduction, and obtained STM images which resolve atomic features on the reduced surface. In this paper we focus on atomic structures of the surface annealed under ultra high vacuum (UHV). A detail discussion of change of surface morphology and surface ordering with respect to different annealing conditions was discussed elsewhere [6].

Experimental Procedures

A 10mm x 5mm x 1.5mm single crystal SrTiO_3 (Commercial Crystal Lab, FL) was cut to within $\pm 0.5^\circ$ of the (001) face, as determined by x-ray diffraction. The surface was polished with progressively finer alumina paste down to $0.03\mu\text{m}$ and then was chemically etched in order to eliminate mechanical damage. Samples were reduced under 10^{-7} Torr vacuum at 1000°C for two hours and quickly introduced into an UHV chamber for a further annealing at vacuum of 5×10^{-10} Torr, 600°C for 35 min. The reduction yielded a crystal with a green-yellow color and a resistivity on the order of $10^3 \Omega\text{cm}$. The high temperature reduction was achieved through a resistive heater made of tantalum foil that was firmly attached to the back side of the crystal.

Experiments were performed under UHV with a base pressure of 2×10^{-10} Torr. Surfaces are imaged using two STM's; One built in-house and described earlier [7], was modified with spring suspension and tube scanner, and the other is a commercial STM (WA Technologies, UK). Pt-Ir tips were mechanically formed and were further *in-situ* cleaned and sharpened via field emission with an emission current of $1 \mu\text{A}$ for two minutes. All images were acquired in constant current mode with a typical tunneling current of 0.5 nA . Auger electron spectroscopy (AES) was used to verify the surface cleanliness.

Results and Discussion

Annealing in UHV at elevated temperature for 35 min produced a surface with the row-like structures shown in Fig. 2. Clearly, distinct row features run across the surface along the [100] direction. The typical spacings between two rows are 12 \AA and 20 \AA . Fig. 2a shows features with periodicity of 12 \AA . In which detailed atomic structures are evident in some regions. The vertical corrugation of the rows is approximately 2 \AA . Fig. 2b shows features with periodicities of both 12 \AA and 20 \AA , observed at another area of the surface. Both images demonstrate that the surface consists of intergrowths of rows with different spacings. The width of the intergrowths with 20 \AA periodicity appears to be larger than that of intergrowths with 12 \AA spacing. In addition to row features, we occasionally observed a local 2×1 structure as shown in Fig. 3. The size of the unit cell is about $4 \text{ \AA} \times 8 \text{ \AA}$ with the large dimension along the [010] direction. This result agrees with the LEED observation by Cord *et al.* [8] in which a 2×1 reconstruction was observed on the surface annealed in UHV. Most of the surface structures appear to be insensitive to the sample bias; as we vary the bias and change the polarity, no essential changes in the images are observed. This implies that our images are likely dominated by topographic structure instead of electronic effects [9]. In any event the observations are clearly different from an ideal bulk-truncated surface structure, on which a square unit cell with 4-fold symmetry is expected. Our results show directional features which introduce a prime direction [100] on the surface and lower the surface symmetry from 4-fold to 2-fold.

One direct consequence of annealing is a change of stoichiometry of the crystal. Due to the lower coordination, reduction on the surface may be different from that in the bulk. Consequent surface structural changes that are consistent with our experimental observation could occur through two possible processes: The first requires formation of new phases on the surface upon reduction. This involves changes of both surface geometry and surface composition. The second is based solely on the oxygen vacancy distribution with the basic surface structure remaining unchanged. It is assumed that oxygen vacancies created by reduction form an appropriate pattern that gives rise to an observed structure.



Fig.2 Constant current STM image of an annealed surface showing row-like structures with spacing of 12 Å and 20 Å. (a) a 370 Å x 300 Å image with black-to-white scale of 11 Å. (b) 130 Å x 105 Å image with a black-to-white scale of 6 Å.



Fig.3 Constant current STM image showing a local 2x1 structure on the $\text{SrTiO}_3(001)$ surface.

We first discuss how the UHV annealing could affect the surface composition, leading to new phases. When heating the crystal at elevated temperature, the surface adsorbates are expected to desorb and, if the temperature is sufficiently high, some host surface atoms will also leave the surface by sublimation. The sublimation rate generally depends upon the bonding strength, coordination of each atom, concentration of constituents on the surface, and partial pressure of constituents in the vacuum. Oxygen is known to have a high sublimation rate, partially due to its high concentration. In our experiment the typical vacuum pressure is 5×10^{-10} Torr during annealing, and the partial pressure of Sr, Ti, and O is at least on the order of 10^{-12} Torr, but is likely to be lower. The bonding strength of Sr-O is about two thirds that of Ti-O [10]. On the other hand, Sr has 12-fold coordination in the bulk and 8-fold coordination at the surface, which is nearly twice as large as that of Ti, which has 6-fold coordination in bulk and 5-fold coordination at the surface. Taking into account these two factors, Ti is expected to have a higher sublimation rate than Sr in SrTiO_3 . In fact, Brooks *et al.* found that sputtering $\text{SrTiO}_3(001)$ followed by an UHV annealing at temperature of 760 °C produced a surface with concentration of Sr as high as 85%, and Ti only 15% [11]. In contrast, Henrich *et al.* concluded that sputtering alone yielded a Ti rich $\text{SrTiO}_3(001)$ surface [12]. The difference between the two results suggests that UHV annealing does increase the surface Sr-to-Ti ratio. From these considerations, we believe that UHV annealing can change the surface stoichiometry as described by $\text{SrTi}_{1-x}\text{O}_{3-y}$. If we parameterize x and y in terms of an integer n :

$$\begin{aligned} x &= 1/(n+1) \\ y &= 2/(n+1) \quad \text{where } n=0, 1, 2, \dots, \infty, \end{aligned}$$

then the surface composition can be formulated as $\text{Sr}_{n+1}\text{Ti}_n\text{O}_{3n+1}$. This corresponds to the lamella structure, a variant of SrTiO_3 which is known to be stable at several different orders, i.e., different n [13-15]. $\text{Sr}_{n+1}\text{Ti}_n\text{O}_{3n+1}$ exhibits two interesting features: First, in accommodating the O and Ti deficiency, those Sr atoms which are located in and next to the shear layers change their coordination from 12-fold to 9-fold. Second, one section of each unit cell is displaced by an amount of $a/2$ and $b/2$, i.e., half of the unit cell (2 Å) along both [100] and [010] directions. This structure has two-fold symmetry along a and b axes rather than the 4-fold symmetry of the perovskite structure. Fig.4 shows two lamellae with $n=1$ for Sr_2TiO_4 , and $n=2$ for $\text{Sr}_3\text{Ti}_2\text{O}_7$. The sizes of the unit cells are 12 Å along c direction for Sr_2TiO_4 and 20 Å along c direction for $\text{Sr}_3\text{Ti}_2\text{O}_7$, respectively.

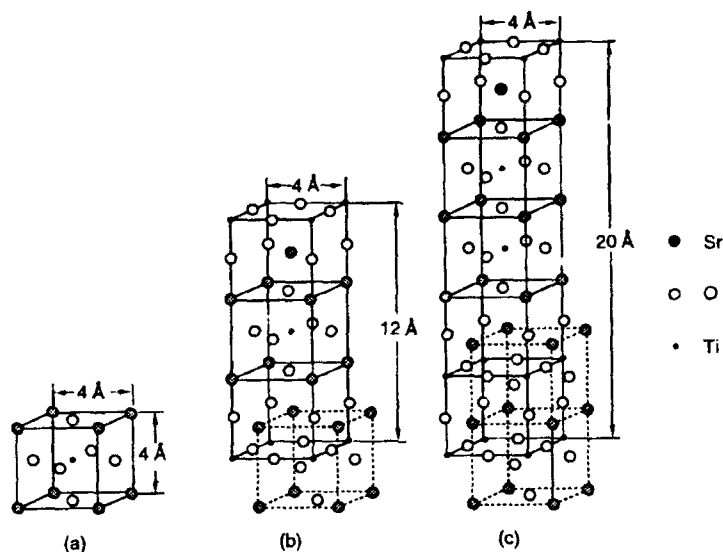


Fig. 4 Schematic drawing illustrating the relationship between ideal perovskite SrTiO_3 (a) and two lamella structures of Sr_2TiO_4 (b) and $\text{Sr}_3\text{Ti}_2\text{O}_7$ (c).

From the previous discussion, it is clear that annealing in UHV results in a surface deficient in oxygen and titanium. To accommodate the deficiencies, some Sr atoms change their coordination from original 12-fold to 9-fold and surface forms phases of $\text{Sr}_{n+1}\text{Ti}_n\text{O}_{3n+1}$ with different order depending upon the local degree of deficiency. If the UHV reduction is sufficiently long, lamella phases merge and form intergrowths which reduce the surface symmetry to two-fold and give rise to the row-like structures. The images in Fig. 2 are consistent with formation of lamella phases with spacing of 12 Å for Sr_2TiO_4 and 20 Å for $\text{Sr}_3\text{Ti}_2\text{O}_7$. The displacement described in Fig. 4 results in a protrusion with a height of 2 Å as our STM images show. At present we are not able to determine how deep the lamellae extend.

The second mechanism which could partially explain our results is the oxygen vacancy model. This model assumes that the basic surface structure is unchanged, but that the concentration of oxygen vacancies and the ordering of oxygen vacancies varies with annealing. Differing concentration and ordering would naturally lead to different surface morphology. However, this model is deficient in that it can not explain the change of surface symmetry. In addition, one must assume that the oxygen vacancies arrange themselves in such a pattern as to produce the observed periodicities. This is difficult to reconcile without involving further surface structural transformation. Furthermore, this model is based solely on oxygen vacancy formation which essentially assumes that the sublimation rates of Sr and Ti are equal. This is difficult to justify based on the above discussion.

In conclusion, reduced $\text{SrTiO}_3(001)$ surface has been characterized using STM to provide atomic scale structural information. Our topographic images revealed row-like structures with spacings of 12 Å and 20 Å. A local 2x1 structure was also observed at some regions of the surface. The row-like structures are consistent with lamellae of Sr_2TiO_4 and $\text{Sr}_3\text{Ti}_2\text{O}_7$. The experimental results could be explained in terms of the formation of reduced phases that result from different sublimation rates of Sr, Ti, and O.

Acknowledgments

This work was supported by the National Science Foundation under the Presidential Young Investigator's Program grand #DMR-90-58557 (DAB) and under the MRL Program grand #DMR91-20668. The authors thank P. Davies for extensive discussion regarding chemistry of titanates.

References

1. J. S. Anderson and R. J. D. Tilley, in Surface and Defect Properties of Solids, edited by M. W. Roberts and J. M. Thomas (The Chemical Society London, 3, 1974) pp. 1-56.
2. S. N. Ruddlesden and P. Popper, Acta Cryst. 11, 54 (1958).
3. see, for example, G. S. Rohrer, V. E. Henrich, and D. A. Bonnell, Science, 250, 1239 (1990).
4. R. M. Feenstra and J. A. Stroscio, J. Vac. Sci. Technol. B5, 923 (1987).
5. D. A. Bonnell, Characterization Tech. 5, 315 (1989).
6. Y. Liang and D. A. Bonnell, Sur. Sci. Lett. submitted.
7. D. A. Bonnell and D. R. Clarke, J. Am. Ceram. Soc. 71, 629 (1988).
8. B. Cord and R. Courths, Surf. Sci. 162, 34 (1985).
9. N. D. Lang, Phys. Rev. Lett. 56, 1164 (1986).
10. L. H. Dubois and J. L. Gole, J. Chem. Phys. 66, 779 (1977).
11. F. Engelke, R. K. Sander, and R. N. Zare, J. Chem. Phys. 65, 1146 (1976).
12. N. B. Brookes, F. M. Quinn, and G. Thornton, Vacuum, 38, 405 (1988).
13. V. E. Henrich, G. Dresselhaus, and H. J. Zeiger, Phys. Rev. B17, 4908 (1978).
14. R. J. D. Tilley, J. Solid State Chem. 21, 293 (1977).
15. G. Burns, F. H. Dacol, G. Kliche, W. Konig, and M. W. Shafer, Phys. Rev. B37, 3381 (1988).
16. N. J. Cockroft, S. H. Lee, and J. C. Wright, Phys. Rev. B44, 4117 (1991).

SURFACE STRUCTURE AND ELECTRONIC PROPERTY OF REDUCED $\text{SrTiO}_3(100)$ SURFACE OBSERVED BY STM/STS

TAKUYA MATSUMOTO, HIROYUKI TANAKA, TOMOJI KAWAI, AND
 SHICHIO KAWAI
 The Institute of Scientific and Industrial Research,
 Osaka University, Mihogaoka, Ibaraki, Osaka 567, Japan.

ABSTRACT

We have obtained STM images and STS data with atomic-scale resolution for $\text{SrTiO}_3(100)$ surface annealed in UHV at 1200 °C. A $\sqrt{5} \times \sqrt{5}$ -R26.6° surface superstructure indicating oxygen vacancy ordering has been observed. The STS data provide evidence for a localized surface state arising from oxygen vacancies at 1.35 eV below the Fermi level. STM images of the $\sqrt{5} \times \sqrt{5}$ structure correspond to the surface orbital of the ordered Ti-oxygen vacancy complex.

1. INTRODUCTION

The surface of metal oxides with a perovskite structure (ABO_3 , where A is a group I or II ion and B is a transition-metal) plays an important role in surface photocatalysis [1] and as a substrate for thin film deposition [2]. Surface defects in these materials are especially important as centers of chemical reaction [3] and for the nucleation of crystal growth. The surface of strontium titanate (SrTiO_3) is interesting from the viewpoint of not only a typical perovskite but also typical dielectric material. For these reasons, there have been many surface science studies on SrTiO_3 . With low energy electron diffraction (LEED), a 2×2 superstructure has been reported after annealing in ultra high vacuum (UHV). Photoelectron spectroscopic (PES) studies indicate a superstructure model consisting of ordered surface defects, where the defects are \square -Ti³⁺-O (\square : oxygen vacancy) complexes forming a state inside the band gap [4,5]. Moreover, the surface electronic states related with oxygen vacancies have been calculated [6,7]. In spite of these studies, the relationship between reconstructed surface and electronic energy structure have not been well understood. In order to characterize such a surface, scanning tunneling microscope (STM) and scanning tunneling spectroscopy (STS) are powerful tools. However, STM-images for metal oxide with atomic-scale resolution are scarcely reported except for cuprate superconductor and TiO_2 so far.

In this paper, we report STM and STS data for a SrTiO_3 surface with atomic resolution after annealing in UHV. We will show high resolution images of a $\sqrt{5} \times \sqrt{5}$ -R26.6° superstructure indicating the existence of localized surface states arising from oxygen vacancy ordering on the reduced surface.

2. EXPERIMENTAL

The STM and STS measurements were performed with a USM-301 (UNISOKU, Japan). Current-versus-voltage (I-V) spectra were

acquired during imaging. The experiments were conducted in an UHV chamber with a base pressure of 8×10^{-11} Torr. Both mechanically formed Pt-Ir and electrochemically etched W tips were used. We calibrated the XYZ-scale by imaging a well-known Si(111)- 7×7 surface. The STM chamber was equipped with a preparation chamber for sample heating and various surface treatments. Reflection high-energy electron diffraction (RHEED) experiments were conducted in the preparation chamber using the 25-kV beam from a RHG-1000 (PHYSITEC, Japan) electron gun.

Polished and (100) oriented, plate-shaped crystals of SrTiO_3 were purchased from Earth-Jewelry Co. (Japan). The SrTiO_3 crystal was clamped on a Si heater mounted on a holder made of Ta and Mo. The sample was pre-heated for degassing in the preparation chamber and annealed at high temperature in the STM chamber. The sample temperature was measured with an optical pyrometer. The chamber pressure during annealing did not exceed 1×10^{-9} Torr. After annealing, the sample was transferred to the STM head. It was possible to obtain STM images with atomic-resolution within 3 hours after the annealing.

3. RESULT AND DISCUSSION

3.1 RHEED Measurements of Reduced SrTiO_3 (100) Surface

The sample was annealed in UHV at 1200°C for 2min. Fig.1 (a) and (b) show RHEED patterns from the reduced SrTiO_3 (100) surface with the electron beam incident along the [010] and [021] azimuth, respectively. Pattern (a) consists of the zero order main streaks and split streaks located on the first order Laue circle, with sharp line width and high contrast to back ground. The spacing of the main streaks is corresponding to a lattice spacing of $d_{\langle 100 \rangle} = 0.39$. This value suggests that the square lattice has the same periodicity as that of bulk unit cell. This surface, however, is quite different from the 1×1 surface. The splitting of the streaks lying on the first Laue circle indicates a twin-like structure. On the other hand, pattern (b) taken with the electron beam incident along the [021] azimuth shows also symmetrical streaks. The angle between the [021] and [010] azimuths is 26.6° . The streaks in pattern (b) have very sharp line width and intensity

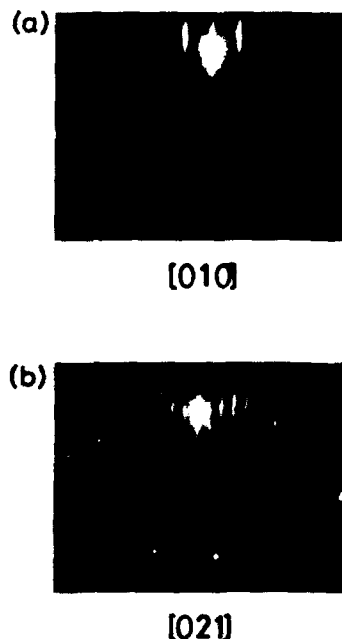


Fig.1
RHEED patterns from the reduced SrTiO_3 (100) surface annealed at 1200°C in UHV for 2min, observed with the electron beam incident in (a): [010] azimuth and (b) [021] azimuth.

maxima lying on a zero order Laue circle, indicating a very flat surface. This pattern consists of three main streaks and 1/5-order streaks. The spacing between the main streaks corresponds to a lattice spacing of $d_{012} = 0.174$ nm. The 1/5-order streaks indicate a reconstruction with $5d_{012} = 0.87$ nm in the $[021]$ direction.

3.2 Topographic Structure of Reduced $\text{SrTiO}_3(100)$ Surface

Reduced SrTiO_3 has sufficient conductivity for STM measurements. This conductivity arises from the oxygen defects introduced during annealing. The Ti-oxygen vacancy complexes induce a defect band inside the band gap without changing the main electronic structure below the Fermi surface.

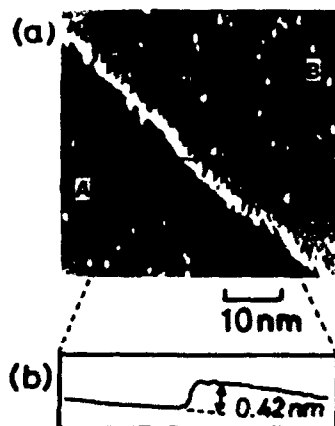


Fig.2
(a): A current image of 50 nm by 50 nm region of the reduced $\text{SrTiO}_3(100)$ surface. (b): A cross section obtained with constant-current scan along the line indicated in (a).

A current image presenting a surface step is shown in Fig.2 (a). Fig.2 (b) shows a cross section taken with constant current along the line indicated in Fig.2 (a). Atomically flat terraces and a clear step are observed. SrTiO_3 has a perovskite structure and different surface terminations with either SrO or TiO_2 are possible. The observed height of the step is 0.42 nm, similar to the unit cell dimension for bulk SrTiO_3 . Sub-unit cell steps were not observed in any of the images. Moreover, the surface image of terrace (A) is the same as that of terrace (B). Accordingly, the top layer of the surface is always of one kind, either SrO or TiO_2 .

Fig.3 show STM images of reduced $\text{SrTiO}_3(100)$ surface with atomic scale resolution. Many atomic size particles are observed on the surface. These particles are not due to contamination from background gases, because the number of particles does not change with time, even after exposure for two days. Moreover the particles are always located at a lattice point of the square structure. The number of particles on the clean surface decreases after longer annealing. However, long time annealing cannot remove the particles at surface boundary. Evidently these particles are attracted by the disordered boundary. These results suggest that the as-polished surface of SrTiO_3 is strongly damaged and that the damaged layer can be removed and/or rearranged by annealing in UHV at 1200 °C for few minutes.

The surface shown in Fig.3 can be divided into three domains (A) and (B) by surface boundaries. The axis of the square lattice in domain (A) is rotated compared to that in domain (B). A similar rotation is also in all other samples. The axes of these square lattices are rotated by about 26 degrees from the $\langle 100 \rangle$ symmetry direction of the bulk crystal. This rotation angle is in good agreement with RHEED measurement. Another type of boundary is observed between domain (A) and (C). The square

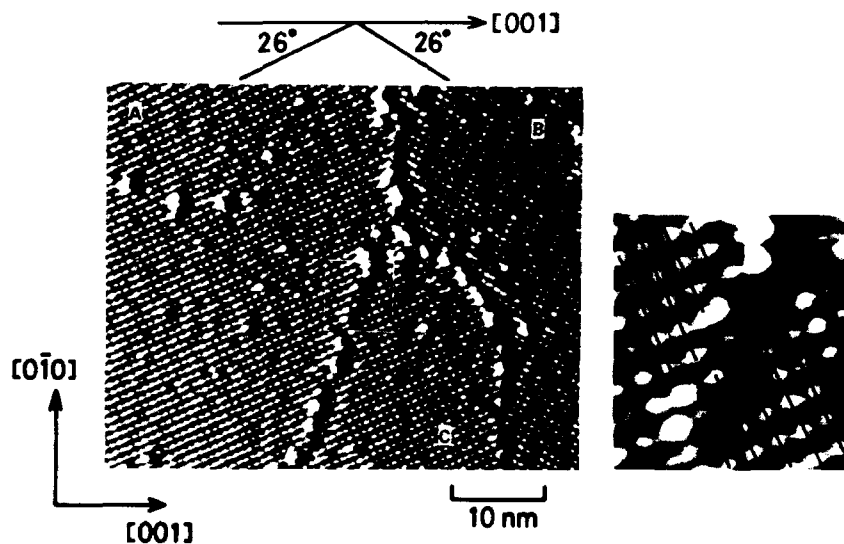


Fig.3
An atomic-scale resolution current-image of 40 nm by 40 nm region of the reduced $\text{SrTiO}_3(100)$ surface taken with a tip bias of 0.6 V and a tunneling current of 400 pA. The axis of square lattice rotate by about 26° from the axis of bulk crystal. The rotational boundary between domain (A) and (B) is observed. The extended image of a phase shift between domain (A) and (C) is shown.

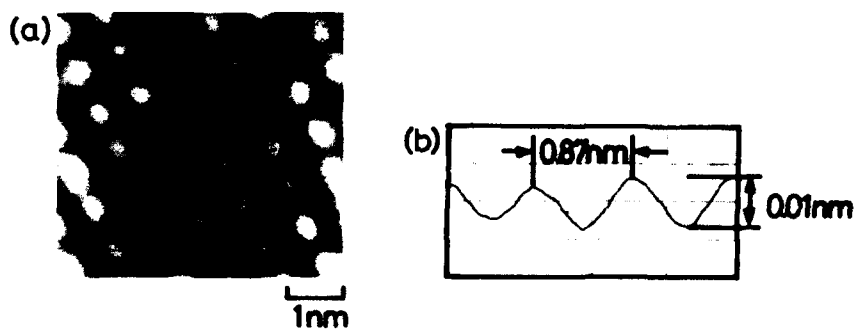


Fig.4
(a): A constant current image of 5.5 nm by 5.0 nm region of the reduced $\text{SrTiO}_3(100)$ surface taken with a tip bias of 3.0 V and a tunneling current of 300 pA. (b): A cross section of the surface indicated in (a).

lattice of domain (A) slides against that of domain (C) as illustrated in the expanded image. This phase shift suggests that the observed square lattice does not correspond to the actual unit cell, but instead corresponds to a superstructure. To examine the details of the square superstructure, the high-resolution constant-current image have been observed as shown in Fig.4. The spacing of square lattice is 0.87 nm which is in good agreements with the STM measurements. Therefore, the RHEED and STM results indicate that the surface annealed at 1200 °C is reconstructed in $\sqrt{5}\times\sqrt{5}$ -R26.6° superstructure.

3.3 Electronic Structure of Reduced $\text{SrTiO}_3(100)$ Surface

In order to study the origin of the $\sqrt{5}\times\sqrt{5}$ surface structure, we examine the differences in the electronic structure of the dark and bright regions in the STM image. The STS data shown in Fig.5 were averaged for the bright and dark regions respectively. The spectrum of the dark region (dotted line) has a band gap energy of about 3 eV which agrees with the value for stoichiometric SrTiO_3 . This suggests that the dark region has a similar electronic structure as the stoichiometric SrTiO_3 surface. On the other hand, in the bright region, we found a band around -1.35 eV below the Fermi level (solid line). This value agrees well with the result of PES data. Cord and Courths reported a surface defect state ($E=-1.3$ eV) induced by oxygen vacancies [5]. Therefore, the contrast in the STM image corresponds to an oxygen defect band.

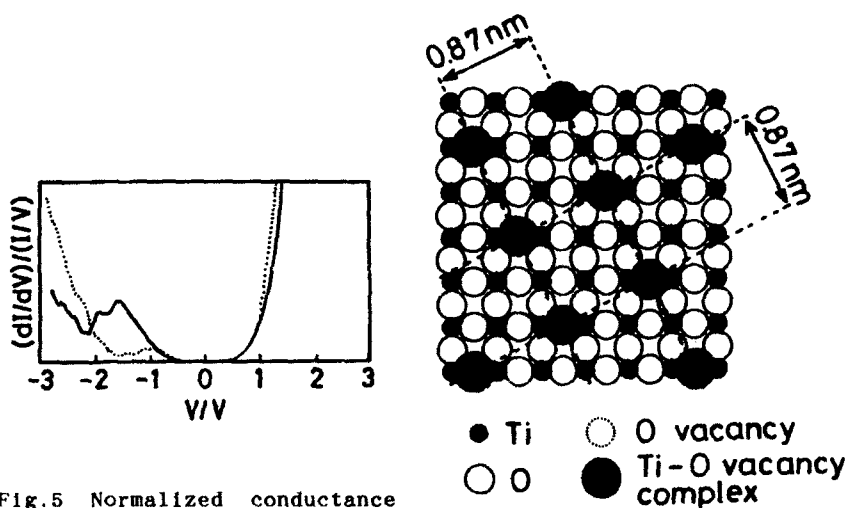


Fig.5 Normalized conductance of the reduced $\text{SrTiO}_3(100)$ surface. The solid and dotted lines represent the spectra averaged over 6 spectra at bright and dark regions of STM image (a) respectively. These spectra were obtained during imaging of (a).

Fig.6 A possible model of $\sqrt{5}\times\sqrt{5}$ reconstruction of $\text{SrTiO}_3(100)$ surface. Oxygen defects is ordered along $\langle 012 \rangle$ azimuth in the TiO_2 top layer.

The Sr level is too deep to be observed by STM/STS. Accordingly we can not determine whether the top most surface layer is SrO or TiO_2 . However, the STM/STS data are consistent with the assumption of a TiO_2 layer as the topmost surface. Tsukada et al. has calculated the surface electronic structure of SrTiO_3 with oxygen defects by the DV-X α cluster method. In the absence of defect, SrTiO_3 has no state near the Fermi level. Upon introduction of oxygen vacancies in the TiO_2 surface, defect states appear near the Fermi surface. The highest occupied molecular orbital (HOMO) induced by oxygen defects shows a broad maximum around the Ti atoms and swells toward the vacuum side [7]. Based on this theoretical result, we propose a structure model that oxygen defects ordered along $\langle 012 \rangle$ azimuth in the TiO_2 top layer as shown in Fig.6. In the STM measurement, the tunneling current flows from this surface defect state to the tip. Therefore the STM image reflects the topology of this state. Consequently, the bright region of the STM image may correspond to the periodicity of the $\square\text{-Ti}^{3+}\text{-O}$ vacancy complex.

4. CONCLUSION

We have performed STM/STS measurements of $\text{SrTiO}_3(100)$ surfaces with atomic-scale resolution. A $\sqrt{5} \times \sqrt{5}$ -R26.6° surface superstructure indicating oxygen vacancy ordering in the TiO_2 top layer has been observed using STM and RHEED. The STS data provide evidence for a localized surface state induced by oxygen vacancies. From these results, a model is proposed in which the STM image is assumed to result from the surface orbital of the $\square\text{-Ti}$ -oxygen vacancy complex. Such direct observation of oxygen vacancy and electronic structure in real-space is important to reveal the mechanism of surface reaction and initial stage of crystal growth on SrTiO_3 .

References

- [1] J.G.Mavroides, J.A.Kafalas and D.F.Kolisar: Appl.Phys.Lett. 28 (1976) 241.
- [2] P.Chaudhari, R.H.Koch, R.B.Laibowitz, T.R.McGuire and R.J.Gambino: Phys.Rev.Lett, 58, (1987) 2687.
- [3] S.Ferrer and G.A.Somorjai: Surface Sci. 94 (1980) 41.
- [4] V.E.Henrich, G.Dresselhaus and H.J.Zeiger: Phys.Rev. B17 (1978) 4908.
- [5] B.Cord and R.Courths: Surface Sci. 162 (1985) 34.
- [6] M.Tsukada, C.Satoko and H.Adachi: J.Phys.Soc.Jpn. 48 (1980) 200.
- [7] M.Tsukada, H.Adachi and C.Satoko: Prog.Surface.Sci. 14 (1983) 113.

METASTABLE STRUCTURAL SURFACE EXCITATIONS AND CONCERTED ADATOM MOTIONS: A STM STUDY OF ATOMIC MOTIONS WITHIN A SEMICONDUCTOR SURFACE

JENE GOLOVCHENKO*, ING-SHOUH HWANG*, ERIC GANZ**, & SILVA K. THEISS*

*Department of Physics and Division of Applied Sciences, Harvard University, Cambridge, MA 02138

**Department of Physics and Astronomy, University of Minnesota, 116 Church Street S.E., Minneapolis, MN 55455

ABSTRACT

Knowledge about atomic scale motions is essential to the understanding of dynamical phenomena on surfaces, such as diffusion, phase transitions, and epitaxial growth. We demonstrate that the addition of a very small number of Pb atoms to a Ge(111) surface reduces the energy barrier for activated processes, thus allowing one to observe concerted atomic motions and metastable structures on this surface near room temperature using a tunneling microscope. The activation energy for surface diffusion of isolated substitutional Pb atoms in Ge(111)-c(2x8) was measured by observing individual atomic interchanges from 24°C to 79°C. We also observed the formation and annihilation of metastable structural surface excitations, which are associated with large numbers of germanium surface atoms in one row of the c(2x8) reconstruction shifting along that row like beads on an abacus. The effect provides a new mechanism for atomic transport on semiconductor surfaces and can explain a number of other observed phenomena associated with Ge(111) surfaces, including the surface diffusion of Pb atoms.

INTRODUCTION

Dynamical phenomena on surfaces, such as diffusion, phase transitions, and epitaxy, are of fundamental importance in condensed matter physics. Experimental studies of the detailed atomic motions associated with these dynamical processes clearly require atom-resolved microscopy. However, direct observation of these atomic motions has been elusive. We introduce a remarkable system for atomic-scale study of dynamical processes: Pb/Ge(111)-c(2x8). A very small amount of Pb lowers the activation energy for motion within the surface reconstruction so that atomic diffusion and metastable structures occur near room temperature and can be observed with atomic resolution. This provides us with an unprecedented opportunity for *in situ* observations of atomic processes.

Diffusion on metal surfaces has been measured using the field-ion microscope (FIM), and detailed mechanisms such as concerted atomic exchange have been documented[1]. The FIM studies, along with the calculations they motivated, have greatly improved our understanding of atomic dynamics on metal surfaces. The scanning tunneling microscope (STM) is just beginning to fulfill some of its promise as a tool to study atomic dynamics. It has recently been used in studies which are very promising for furthering our understanding of diffusion and epitaxy in systems of direct technological interest[2]. Additionally, phase transitions on Si(111)-7x7[3] and on Ge(111)-c(2x8)[4] surfaces have been observed using hot STM. In all of these cases, however, the motions of individual atoms have not been directly measured.

Pb/Ge(111)-c(2x8) is a favorable system for the atomic scale study of dynamics on reconstructed semiconductor surfaces for several reasons. First, unlike Si atoms for example, the Pb atoms are readily distinguished from the Ge adatoms by the STM. Thus it is clear when they move, and they can be used as markers which allow the registry and motion of the Ge atoms to be determined. Second, bulk Pb and Ge do not intermix and Pb atoms do not evaporate from the surface below 300°C, so we can be sure that any Pb atom which disappears from our field of view in the STM has gone to another surface site. Finally, the pure Ge(111)-c(2x8) surface is a "soft" reconstruction that undergoes a phase transition near 300°C. This is a low transition temperature compared with that of Si(111)-7x7 (which is around 860°C) and

suggests a relatively weak bonding of Ge adatoms to the substrate. As a result, Ge adatoms are mobile at room temperature on the Pb doped surface[5,6].

LEAD DIFFUSION

Activation energy

Details of sample preparation and STM operation have been presented elsewhere[5]. Diffusion data were taken at two different coverages of Pb: one at which the Pb atoms constitute about 6% of the total adatoms in the $c(2 \times 8)$ reconstruction and one at which they constitute about 4% of the total. The diffusion temperature was varied between room temperature and about 80°C by passing direct current through the sample. The data were analyzed by comparing the positions of Pb atoms in one image to those in the previous image. If a Pb atom appeared in a given position in one image but not in the following image, the motion was counted. Only departures (atoms which move away from sites they previously occupied) were counted, not arrivals (atoms which move in to sites they did not previously occupy). This avoids double-counting, since each individual migration event consists of both an arrival and a departure. By analyzing a large number of images, we can thus measure the diffusion of the adatoms one atomic motion at a time.

Fig. 1 shows four STM images taken on the high coverage sample at 48°C at two and four minute intervals. The Pb adatoms are clearly visible as white spots, and occupy substitutional adatom sites in the $\text{Ge}(111)\text{-}c(2 \times 8)$ reconstructed layer (presented schematically in Fig. 2). For

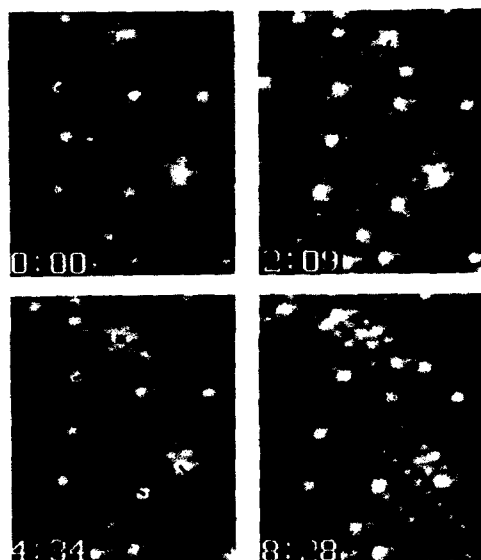


Fig. 1 Four successive $100 \times 115 \text{ \AA}$ STM images of Pb adatoms in substitutional sites on the high coverage sample. Elapsed time in [minutes:seconds] is indicated at the bottom of each image. The black arrows indicate the direction and length of eight single interchanges. Four atoms which do not appear at the same position or near-neighbor positions in the subsequent frame are marked with black stars. These are discussed in the text as long jumps.

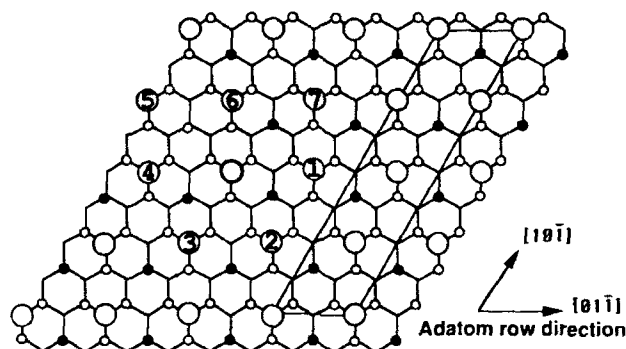


Fig. 2 Schematic diagram of the Ge(111)-c(2x8) surface. Small circles represent top layer bulk Ge atoms, large circles are Ge adatoms (shaded) and a Pb adatom (open). Seven near neighbors are identified. We find that the diffusion by single interchanges occurs primarily along the indicated adatom row direction.

the high coverage sample, 171 images containing 1001 motions from a total of 9901 atoms were analyzed. For the low coverage sample, 248 images containing 1187 motions from a total of 5530 atoms were analyzed. (The proportion of data at high temperatures was greater on the low coverage sample, so a greater fraction of the atoms under observation moved.) In Fig. 1, we observe eight single (near neighbor) interchanges. For these eight interchanges we have placed a black arrow showing the position of the adatom in the next image. We also identify four long jumps with black stars. In our analysis, a long jump is counted when an atom is present in one image and is not present either at its old site or at a neighboring one in the next image.

The average atomic movement rate R and deviation σ at a particular temperature are given by $R = \Sigma m_i / \Sigma t_i a_i$ and $\sigma = (\Sigma m_i)^{1/2} / \Sigma t_i a_i$, where m_i is the number of movements that occur among a field of a_i Pb adatoms in the i^{th} time interval t_i [5]. If the motion is thermally activated, then R varies with absolute temperature T as $R = \nu \exp(-E_D/kT)$, where ν is an effective attempt frequency and E_D is the activation energy. Log R versus $1000/T$ for the high coverage sample is plotted in Fig. 3. Note that a straight line fits the data quite well, and yields $E_D = 0.54 \pm 0.03$ eV and $\nu \approx 7 \times 10^5 \text{ s}^{-1}$. In Fig. 4 we plot the same thing for the low coverage sample. Again, a straight line fits the data quite well, although it yields $E_D = 0.73 \pm 0.03$ eV and $\nu \approx 4 \times 10^8 \text{ s}^{-1}$. The ratio of single interchanges to long jumps remains constant over our temperature range for both samples; log R versus $1000/T$ of the single interchanges yielded the same value of E_D (with a larger uncertainty.) Either the single interchanges and the long jumps occur by the same process or they occur by processes with very similar activation energies, and we consider the data together.

The strong dependence of the diffusion parameters on Pb concentration suggests that complicated processes are at work. Activation energies in the range of 0.5 to 0.7 eV are not surprising. Effective attempt frequencies as low as 10^5 to 10^8 s^{-1} are. (Attempt frequencies are usually expected to be about the Debye frequency, $\approx 10^{13} \text{ s}^{-1}$.) Such small prefactors suggest that there is a relatively small phase space associated with the atomic motions involved in the transport of Pb atoms from one substitutional site to another. That is, recalling that the effective attempt frequency contains an entropy term as well as atomic vibration frequency terms, these results show that the entropy associated with the diffusion mechanism is small. As we shall see

in the next sections, this is not unreasonable because even simple near neighbor interchanges of Pb and Ge atoms are accompanied by extensive atomic motions far from the site of the exchange.

We carefully examined the influence of the scanning process on the adatom movement rate, and found two strong indications that it has negligible effect. First, at each temperature we made a few images at intervals two to five times as long as the rest in that data set. By analyzing the dependence of movement rate on imaging frequency, we can measure the number of interchanges induced by scanning. We find 0.01 ± 0.015 interchanges/adatom for each

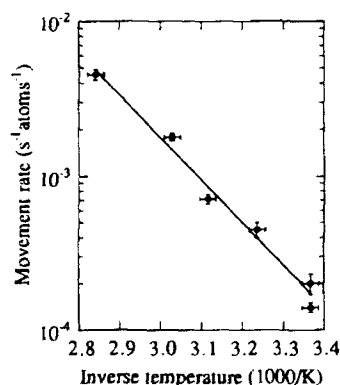


Fig. 3 Arrhenius plot of the observed movement rate for Pb adatoms on the high coverage sample at temperatures from 24°C to 79°C. Vertical error bars come from the expression for σ in the text, horizontal error bars reflect $\pm 2^\circ\text{C}$.

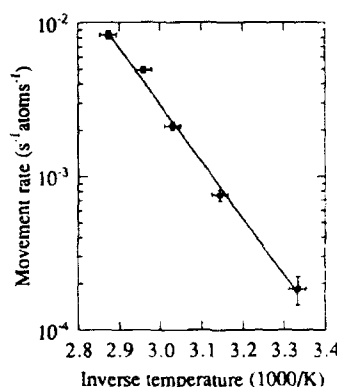


Fig. 4 Arrhenius plot of the observed movement rate for Pb on the low coverage sample at temperatures from 27°C to 75°C.

image scanned. Second, since we expect any scan-induced effects would be independent of temperature, the fact that the movement rate increases as a function of the temperature according to the Arrhenius relation indicates that the scanning process does not contribute to the movement rate. Therefore we conclude that our means of measurement does not alter the measured activation energy.

Anisotropy

Since in the Pb/Ge(111)-c(2×8) system the surface reconstruction breaks the symmetry of the bulk, the anisotropy of the diffusion in this system was analyzed. For the high coverage sample, we examined the relative frequency of interchanges with the seven near neighbors shown in Fig. 2. Compiling 285 single interchanges and referring to Fig. 2, we find that 56% are to positions 1 or 4, 31% to positions 2 or 3, 7% to position 5 or 7, and 6% to position 6. Thus diffusion perpendicular to the direction indicated in Fig. 2 is constrained; the ratio between the diffusion rate for single interchanges along the indicated direction to that perpendicular to it was found by a Monte Carlo simulation to be 2.6[7]. (Note that the existence of three differently oriented c(2×8) domains on the surface will generally mask the role of this anisotropic diffusion in macroscopic measurements.) We observe no correlation between the diffusion and the direction of the current flowing through the sample.

The anisotropy in the long junctions turns out to be even more striking. On the low coverage sample, because of the lower concentration of Pb adatoms, it was possible to study the fate of

many of the long jumps. We assumed that the atoms made the shortest jumps consistent with the data. Temperature did not seem to affect either the length or the fraction of jumps along the row, so the data at all temperatures were taken together. Of the 183 movements which could be definitely identified as being to one of the fourteen second-nearest neighbors (i.e., two single interchange spacings away), 81 were to positions on the same row. That is, 44% of the two-spacing interchanges were to 14% of the possible two-spacing-distant sites. Further, 43% of the identifiable three-spacing interchanges and 42% the four-spacing interchanges were to sites on the same row. Same-row sites constitute only 10% and 7% respectively of the possible sites at that distance. If our assumption that all jumps were of the shortest possible distance is not accurate, this fraction might actually go up somewhat.

ROW SHIFTS: THE ABACUS EFFECT

Metastable structures and the diffusion mechanism

Subsequent to the diffusion studies discussed above, a third sample was prepared with intermediate coverage to enable us to study the detailed mechanism of Pb diffusion. Fig. 5

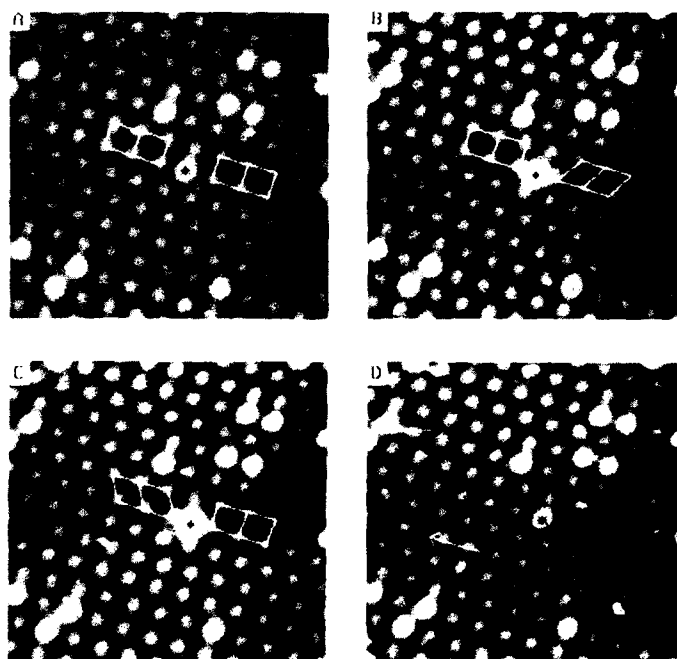


Fig. 5(A)-(D) show four consecutive STM images taken at 45°C, separated by 65 seconds each. (B) and (C) show metastable states with Pb atom \bullet sitting on two different H_3 sites. Notice the Ge adatom structure change on both sides of the Pb atom \bullet . The 2×2 and $c(4 \times 2)$ structures transform into each other through an adatom row shift. (D) shows that the metastable state relaxes, and it also shows adatom row shifts occurring on an adatom row during data acquisition (indicated by an arrow).

shows four consecutive images of $90 \times 90 \text{ \AA}$ taken at 45°C , separated by 65 seconds each. Fig. 5a shows a $c(2 \times 8)$ surface. All Pb atoms replace Ge adatoms in the $c(2 \times 8)$ reconstruction, as observed in Fig. 1. We call these substitutional Pb atoms. They, like all the Ge adatoms, sit on T_4 sites. (See Fig. 6a.) However, in Fig. 5b, a Pb atom (marked with an asterisk) shifts left to an H_3 site. Also, on the same row and to the right of the Pb atom, a string of Ge adatoms concertedly shifts left by one primitive vector to the next T_4 sites. Notice that 2×2 and $c(4 \times 2)$ rows of subunit cells transform into each other by this atomic row shift, as indicated in the figure. A model of this concerted motion is shown in Fig. 6b. Fig. 5c shows the same Pb atom shifted right to another H_3 site accompanied by another adatom row shift (presumably

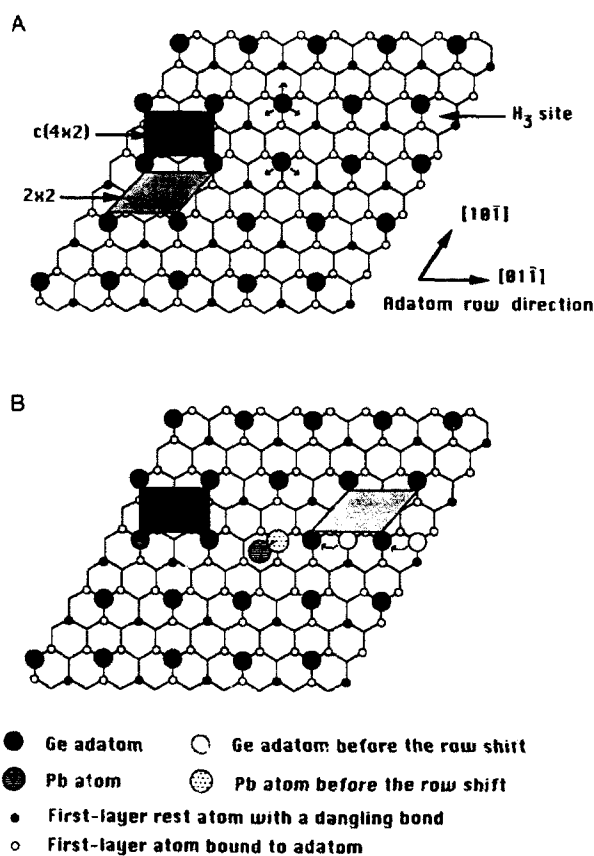


Fig. 6 (A) is a simple adatom model of $\text{Ge}(111)\text{-}c(2 \times 8)$. Subunits of 2×2 and $c(4 \times 2)$ are indicated by shaded areas. Note that there are two inequivalent adatom sites. A substitutional Pb atom on adatom site 1 can hop to three adjoining H_3 sites, whereas it can hop to only two on adatom site 2, because of the availability of rest atom dangling bonds. (B) shows a model for a metastable surface structural excitation. The Pb atom moves from a T_4 site to an adjoining H_3 site, accompanied by a cascade of Ge atom transitions along the adatom row.

after the structure relaxed back to that in Fig.5a). The structure finally relaxes back to the original structure in Fig.5d. This case demonstrates that there are at least two possible neighboring H_3 sites to which the Pb atom can hop. However, we usually see only individual excitations either like Fig.5b or like Fig.5c, then the structure relaxes. Both structures in Fig.5b and 5c are metastable: they can last minutes at low temperatures before relaxation. We call this phenomenon a metastable structural surface excitation. Surprisingly, it involves the motion of very many adatoms. The length of an adatom row shift usually extends beyond our scan area. Occasionally it terminates at a pre-existing defect or a domain boundary. We have never observed the creation of a vacancy which might be expected from a partial row shift. The Ge atoms appear to move as concertedly as the beads on an abacus: when one is pushed, they all slide together. The longest row shift we observed involves 21 Ge adatoms moving (corresponding to 168\AA), and the end is still beyond our scan area.

The concerted motion of Ge adatoms may provide a clue to the mechanism of Pb diffusion and the basis for its anisotropy. The single interchanges may occur by a concerted exchange mechanism similar to that suggested by Parley for bulk Si [8]. Since the exchanging atoms must move in concert, it is not surprising that the effective attempt frequency we observe is orders of magnitude smaller than the attempt frequency that would be expected for a one atom process (usually taken to be about the Debye frequency). The long jumps may also occur by a concerted exchange mechanism involving larger numbers of atoms. Clearly, the row direction is an easy pathway for Pb atom diffusion, and the adatom row shift can provide a mechanism which can explain the large anisotropy of the long jumps. The vacancy which a substitutional Pb atom leaves behind can propagate through a partial adatom row shift until it recombines with the Pb atom. Likewise, as we have observed, a Pb atom trapped on an H_3 site can make a long jump along the row direction, and land on a different H_3 site through an adatom row shift[6]. A model is drawn in Fig.7.

Other processes involving row shifts

The phenomenon of row shifts may also play an important role in the phase transition of $\text{Ge}(111)\text{-c}(2\times 8)$ observed between 200 and 300°C . A recent hot STM study of this phase transition observed fuzzy rows, which were ascribed to the hopping motion of the adatoms

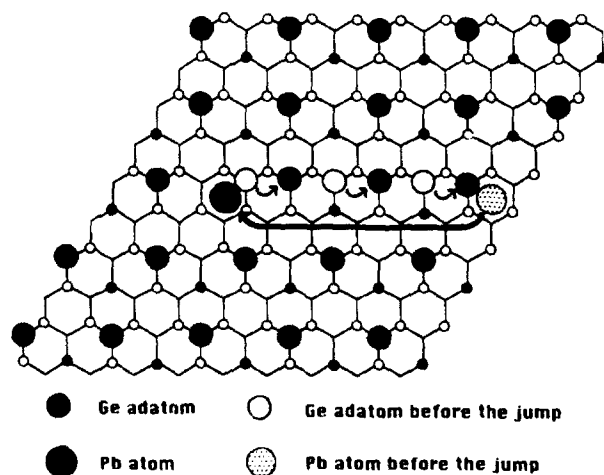


Fig.7 Model for a long jump of an H_3 -site Pb atom along an adatom row.

during the imaging process[4]. We believe those are the adatom row shifts we report here. We do not observe this motion on the clean Ge(111) surface at temperatures between 24°C and 80°C. However, the weak Pb-Ge bonding reduces the activation energy of this process so that we can observe the atomic motions at low temperatures. On a clean Ge(111) surface, Ge adatom row shifts can also occur at high temperatures, for Ge adatoms then have a good chance to hop to H₃ sites by themselves. We believe Ge adatoms form rows upon cooling from the transition temperature of c(2x8), and through appropriate row shifts the c(2x8) reconstruction forms with occasional occurrence of three or more adatom rows in 2x2 or c(4x2) local arrangement. This adatom row shift also represents a previously unrecognized mechanism for atomic transport on crystal surfaces, and may explain the roughness of the steps in STM images of this surface. Additionally, the accommodation of Pb atoms into substitutional sites after deposition may be accomplished by this concerted shifting of Ge adatom rows toward domain boundaries.

CONCLUSION

We are still in the early stages of developing an understanding of the fundamental dynamical processes responsible for phase transformations, growth, and diffusion on semiconductor surfaces. The Pb/Ge(111)-c(2x8) surface has proven to be a practical system for direct, atomic-scale study of these processes. We hope our diffusion studies, identification of structural excited states, and observation of the formation and annihilation of these excited states will stimulate further experimental and theoretical study of these phenomena and their role in surface dynamics.

Acknowledgements

We are particularly grateful to Prof. Efthimios Kaxiras, Harvard University, for the Monte Carlo simulation of the anisotropy of single interchanges. This research was supported by the Office of Naval Research (contract #N00014-90-J-1234), the Materials Research Laboratory at Harvard University (contract #NSF-DMR-8920490), and the Joint Services Electronics Program (contract #N00014-89-J-1023).

References

1. G. Ehrlich and F.G. Hudda, *J. Chem. Phys.* **44**, 1039 (1966); G. Ehrlich, *J. Chem. Phys.* **44**, 1050 (1966); G.L. Kellogg, T.T. Tsong, and P. Cowan, *Surf. Sci.* **70**, 485 (1978); T. Tsong, *Rep. Prog. Phys.* **51**, 759 (1988); G.L. Kellogg and P.J. Feibelman, *Phys. Rev. Lett.* **64**, 3143 (1990); G.L. Kellogg, *Phys. Rev. Lett.* **67**, 216 (1991); T.T. Tsong and C. Chen, *Phys. Rev. B* **43**, 2007 (1991).
2. M.G. Lagally, Y.-W. Mo, R. Kariotis, B.S. Swartzentruber, and M.B. Webb, in *Kinetics of Ordering and Growth at Surfaces* edited by M.G. Lagally (Plenum, New York, 1990) p.145; H. B. Elswijk, A.J. Hoeven, E.J. van Loenen, and D. Dijkamp, *J. Vac. Sci. Tech. B* **9**, 451 (1991); R.M. Feenstra and M. A. Lutz, *Surf. Sci.* **243**, 151 (1991); Y.-W. Mo, J. Kleiner, M.B. Webb, and M.G. Lagally, *Phys. Rev. Lett.* **66**, 1998 (1991).
3. S. Kitamura, T. Sato, and M. Iwatsuki, *Nature* **351**, 215 (1991).
4. R. M. Feenstra, A.J. Slavin, G.A. Held, and M.A. Lutz, *Phys. Rev. Lett.* **66**, 3257 (1991).
5. E. Ganz, S.K. Theiss, I.-S. Hwang, J. Golovchenko, *Phys. Rev. Lett.* **68**, 1567 (1992).
6. I.-S. Hwang and J. Golovchenko, *Science* **258**, 1119 (1992).
7. E. Kaxiras (private communication).
8. K.C. Pandey, *Phys. Rev. Lett.* **57**, 2287 (1986); K.C. Pandey and E. Kaxiras, *Phys. Rev. Lett.* **66**, 915 (1991).

MECHANISMS AND ENERGETICS OF SURFACE ATOMIC PROCESSES, AN ATOM-PROBE FIELD ION MICROSCOPE STUDY

Tien T. Tsong
Institute of Physics, Academia Sinica
Taipei, Taiwan, ROC

ABSTRACT

Atom-probe field ion microscopy is capable of imaging solid surfaces with atomic resolution, and at the same time chemically analyzing atoms selected by the observer from the atomic image. The samples are restricted to those having a tip shape, but in many cases this is no longer a drawback since structures in high-tech materials are reducing in size to that comparable to or smaller than the field ion emitter tip. This technique is finding many applications in different areas. Our recent applications of this technique to the study of the dynamical behavior of surfaces and surface atoms and their mechanisms and energetics, and the atomic scale chemical and composition analysis will be briefly described.

INTRODUCTION

It is well known that using the field ion microscope (FIM) the atomic structures of solid surfaces can be imaged. Using the atom-probe FIM, not only the structures of the surfaces can be seen, the chemical species of these atoms can be identified by time-of-flight mass spectrometry also, or the composition of the surface layers can be analyzed.¹ Some of the most ardent applications of field ion microscopy are now in materials science.² The subjects studied include defect structures, radiation damages, precipitate structures and composition variations, grain and phase boundary structures and impurity segregations to these boundaries, oxidation and compound formation, etc. Here I discuss our recent atom-probe field ion microscope studies of the dynamical behavior of solid surfaces and their mechanisms and energetics, and the chemical analysis of solid surfaces at the true atomic scale.

ATOMIC STRUCTURES OF SOLID SURFACES

Early field ion microscope observations of surfaces prepared by low temperature field evaporation did not detect any surface reconstruction as concluded from studies with macroscopic techniques such as LEED and ion scattering experiments; FIM images were therefore viewed by some surface scientists to be somewhat in suspect. The suspicion is compounded by the fact that we need to apply a field of ~ 4.5 V/Å to image the surface. Only in the 1980's, the difference between a low temperature field evaporated surface and a thermally annealed surface was recognized. The atomic structure of a low temperature field evaporated surface reflects the details of how atoms are field evaporated. For metals, field penetration depth is less than 0.2 to 0.5 Å, or much less than the layer separation. Atoms are removed from lattice steps one by one. Thus the structure of the surface so prepared should be identical to that of the bulk, or they should have the (1×1) structure. This is what has been

observed in the FIM. For semiconductors, the field penetration depth is very much greater than the layer separation. Atoms can be field evaporated from almost anywhere at the surface. Thus the structure of a surface prepared by low temperature field evaporation should be disordered. However, if the emitter surface prepared by low temperature field evaporation is further annealed to reach the thermodynamic equilibrium structure, then the structures are found to be mostly consistent with those derived by other techniques. In fact, FIM result was able to help establishing the missing row (1x2) reconstruction of the Pt and Ir {110} surfaces as well as the quasi-hexagonal atomic arrangement of the (1x5) reconstructed Ir {001} surface.^{3,4} For semiconductors, atomic structures of the reconstructed high index surfaces of Si can be observed,⁵ but it is still very difficult to observe atomic structures of low index surfaces with the FIM.

The size of the facets available on a field ion emitter is very small. In addition, the image distortion produced by the atomic and lattice step structures of the field emitter surface is non-linear, or it is very difficult to correct. Thus even though the FIM can give the atomic images of solid surfaces and in fact it has been successfully used to help solving surface reconstructions of a few metal surfaces, it is in general not considered a convenient microscope for studying the atomic structures of solid surfaces, at least not for studying the atomic and step structures of large surfaces. On the other hand, structures in high-tech materials are getting smaller and smaller every day. They are now comparable in size to or smaller than the size of typical field ion emitters. As the size of these structures gets smaller, the surface atom to bulk atom ratio also gets larger. The stability of these surfaces and the dynamical behavior of the surfaces as well as surface atoms will become an important issue. It is for studying these problems that the FIM finds its utmost usefulness.

SURFACE ATOMIC PROCESSES AND DYNAMICS OF SURFACES

The temperature of the sample in an FIM can be easily and accurately adjusted. The surface on which an experiment can be carried out can be prepared by either low temperature field evaporation or by thermal annealing. The number of adatoms deposited on a facet for an experiment can be specified according to the design of the experiment and then be implemented by repeated deposition and controlled field evaporation. It is with these capabilities that the FIM finds its great advantages in the study of the dynamical behavior of surface atoms and surfaces. Early studies focused on surface diffusion and atomic interactions.⁶ In surface diffusion, these studies already establish that most adatoms diffuse on metal surfaces by atomic hopping. The activation energies are sensitive to the chemistry of the systems but the pre-exponential factors are not. On some fcc {110} surfaces, which have a channel atomic row structure, atomic exchanges by diffusing adatoms with channel wall atoms can occur. Descending lattice steps can be reflective or non-reflective to adatom diffusion depending on the chemistry of the system. When it is reflective, the extra height of the potential barrier is only about 0.1 to 0.2 eV. In adatom-adatom interactions, the

interactions are very weak of only about one-tenth of a chemical bond for many systems.⁸ They are long-range and usually show small oscillatory tails of a few meV. The existence of a repulsive region in the adatom-adatom interaction can explain why an adlayer superstructure can be formed.

Recent FIM studies reveal that on the fairly smooth fcc {001} surfaces such as those of Ir and Pt, self-adatom-diffusion can also occur by atomic exchanges. The adatom moves with a substrate atom in concerted motion. For heterosystems, atomic exchange process was considered earlier to be a mechanism for adatom diffusion. However, we now recognize that this is not the case.¹⁰ A foreign adatom, once substituting itself into the surface layer, can no longer migrate at the adatom diffusion temperature. Thus for these systems, the atomic exchange will induce a surface self diffusion instead of the diffusion of the foreign adatom. A system exhibiting interesting behavior is Re/Ir{001}. When the surface is heated to 220 K to 260 K with a Re atom deposited on the Ir{001} surface, a diatomic cluster is formed as shown in Fig. 1. A surface vacancy can be found near the dimer when the top surface layer is gradually field evaporated. However if the surface is further heated to over 280 K, the dimer will dissociate. The Re adatom is incorporated into the substrate layer. This Re atom gives a slightly brighter image than other substrate atoms when the substrate atomic layer is reduced in size by field evaporation. Based on these observations, it was concluded that the dimer was a Re-Ir which sits on the vacancy formed. Our more recent theoretical analysis using the embedded atom method and an atom-probe mass analysis, however, find that the dimer is in fact an Ir₂,¹¹ not Re-Ir. The relative positions of these atoms and the vacancy is still under investigation.

Concerted atomic motion is not restricted to the atomic-exchange process. One of our studies indicates that in the (1x1) to (1x2) surface reconstruction of the fcc Pt and Ir {110} surfaces, several atoms of the <110> atomic rows tend to "jump" together in concerted atomic motion.¹² Or the atom transport in this surface reconstruction is accomplished by breaking of the <110> atomic rows into small fragments of several atoms and by spreading of these atomic row fragments. Atoms in these row fragments jump in concerted motion either by hopping along the <110> directions or by atomic exchanges with atomic rows of the underneath layer in the <001> directions as illustrated in Fig. 2.

A subject of our current interest is the two-dimensional analog of the equilibrium crystal shape, surface roughening, sublimation, and energetics involved in all these processes.¹³ Although this work is only preliminary, we already find that the equilibrium crystal shape of an Ir {001} surface layer is a perfect square with its four sides parallel to the <110> directions of the closely packed atomic rows. Above 420 K, atoms will start to dissociate from the step of the layer. Dissociation is not orderly, or atoms can dissociate from edge sites, kink sites, ledge sites, and recessed sites, etc. with comparable probabilities. In other words, the binding energies are not pairwise additive. Thus the lattice steps are roughened above this temperature. From the dissociation times as functions of the temperature, we are able to derive the

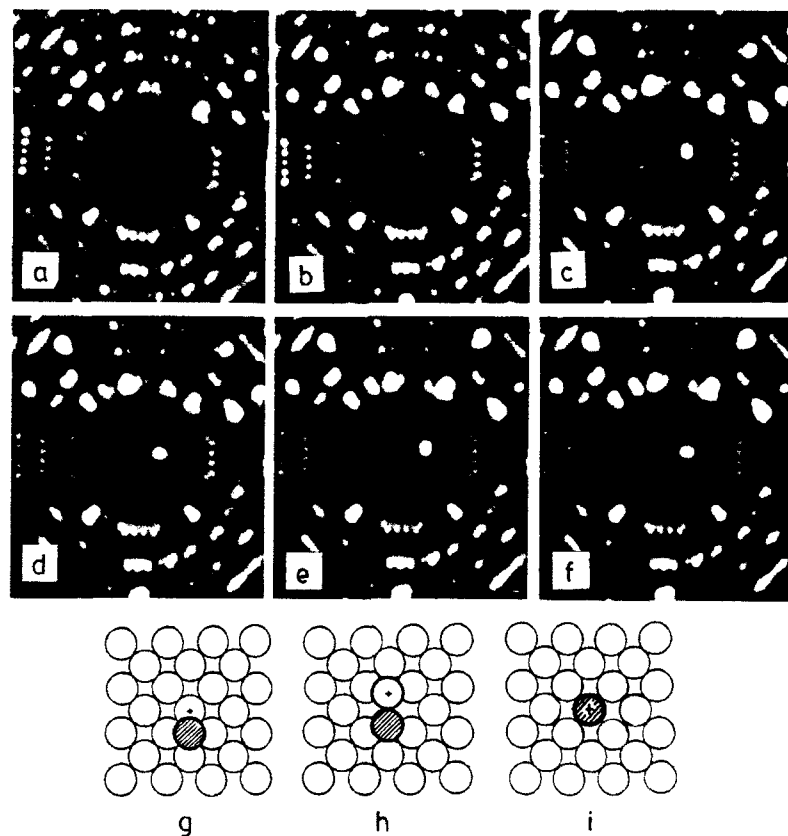


Fig. 1. (a) shows an FIM image of a nearly circular Ir (001) surface. In (b), a Re adatom is deposited on it. By heating the surface to 240 K for 30 s, a dimer is formed as seen in (c). From (c) to (f), the dimer changes orientation by 90 degrees each time it is heated to about the same temperature. If one field evaporates the dimer and the top surface layer gradually, a vacancy can be seen at the position near the original Re adatom. If one heats the surface above 280 K, the dimer will dissociate. Upon gradual field evaporation of the top surface layer, a brighter atom is found to be substituted in the layer. From these observations we conclude that a Re-Ir dimer-vacancy complex is formed at 240 K and above 280 K, when the dimer dissociates, the Re atom is incorporated into the substrate, ((g) to (i)).

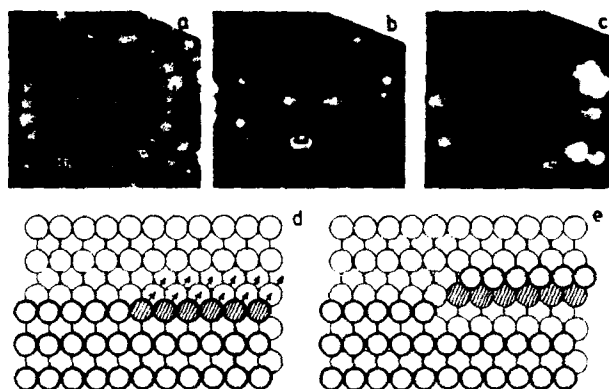


Fig. 2. (a) is a (1x1) surface layer of a Pt (001) surface. Between two images was a pulsed heating of the surface to ~400 K by the action of a 5 ns width laser pulse. Note that atoms in a small atomic row jump together. By spreading of the <110> atomic rows over the terrace, the small (1x1) surface is transformed into the missing row (1x2) structure. (d) and (e) illustrate how atoms in the shaded part of an atomic row at the edge of the top surface layer "jump" to the neighbor surface channel by exchanging with atoms in the layer below.

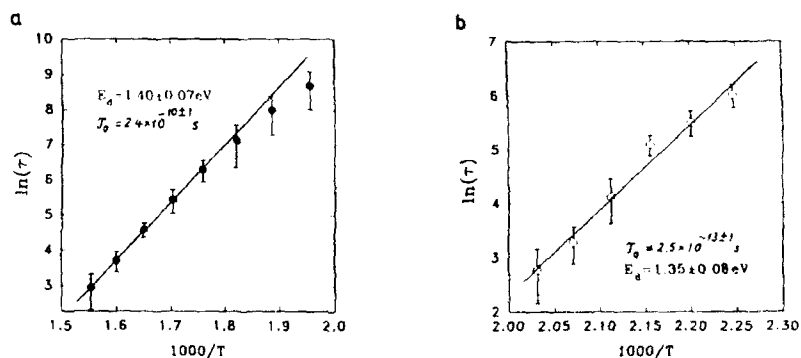


Fig. 3 (a) Lattice step atoms of the Ir {001} can dissociate into terrace sites upon heating over 500 K. The average dissociation energy is determined from a measurement of the temperature dependence of the dissolution time of the {001} layers. It is found to be $1.35 \pm 0.07 \text{ eV}$. (b) A similar measurement for edge (or corner) atoms of the square-shape thermodynamics equilibrated Ir {001} layers. Their dissociation energy is found to be $1.35 \pm 0.08 \text{ eV}$.

dissociation energies of some of these atoms as shown in Fig. 3. As a consequence of this non-additivity of pair energies, hollow clusters can be formed as shown in Fig. 4.

SURFACE CHEMICAL ANALYSIS

Atom-probe can be used to identify the chemical species of surface atoms with single atom detection sensitivity as well as to analyze the composition of surface layers with true atomic layer depth resolution. As just mentioned, originally from the images we naturally arrive at the conclusion that in the atomic replacement of Re/Ir(001), the dimer formed is a Re-Ir which sits on a vacancy. Our recent atom-probe analysis, however, finds that the dimer is in fact an Ir_2 . The Re adatom already goes into the substrate layer between 240 to 280 K when the dimer is formed. Again, at the present moment we do not know the relative positions of the Ir_2 -dimer, the substitutional Re atom and the vacancy formed.

Using the atomic layer composition analysis capability of the atom-probe, we have established the atomic layer by atomic layer oscillatory composition variation of the near surface layers of Pt-Rh alloys in a surface segregation and cosegregation study.¹⁴ The oscillation is found to go as deep as the 10th atomic layer as shown in Fig. 5. An indirect method based on a LEED intensity analysis was able to establish such oscillation down to the depth of only three atomic layers.¹⁵ Recent theoretical studies conclude that for stoichiometric ordered alloys such as Cu_3Au or CuAu , atomic layer by atomic layer oscillatory surface segregation can occur.¹⁶ The oscillation is believed to be associated with order-disorder phase transformation. As Pt-Rh alloys are random solid solutions, and neither of the alloys we studied are stoichiometric, the atomic layer by atomic layer oscillation we have found appears to be an effect of the surface segregation alone rather than linked in any way to order-disorder phase transformation.

HIGH FIELD EFFECTS AND THEIR APPLICATIONS

In field ion microscopy, image formation requires a positive field of a few $\text{V}/\text{\AA}$. Under such a high electric field, novel effects of the atoms can occur. These high electric field effects include field ionization, field evaporation and field desorption, field adsorption, field dissociation, field association or field induced polymerization, and field gradient induced surface diffusion, etc. Studies of these effects are not only needed to properly operate the FIM and the atom-probe, they are needed also to help provide valid interpretations of FIM and atom-probe FIM data. There are interesting sciences in these effects also. In addition, some of these effects have now been successfully applied to develop new technologies such as liquid metal ion sources, single atom or point ion and electron sources, and field emission tip array image display panels, etc.

Some of the effects now being used for atomic and molecular manipulations with the STM¹⁷ have already been studied in detail in field ion microscopy earlier although in changing from the FIM configuration to the close-double-electrode configuration of

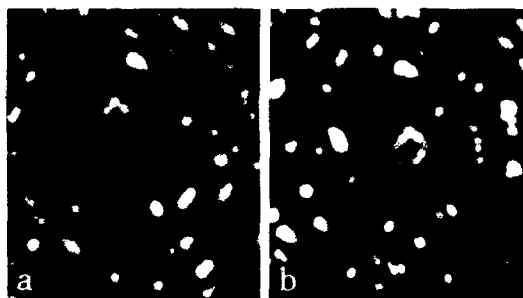


Fig. 4. (a) A hollow 8-atom cluster is formed when an Ir (001) layer is gradually dissolved by heating to ~ 560 K. (b) A hollow 10-atom cluster.

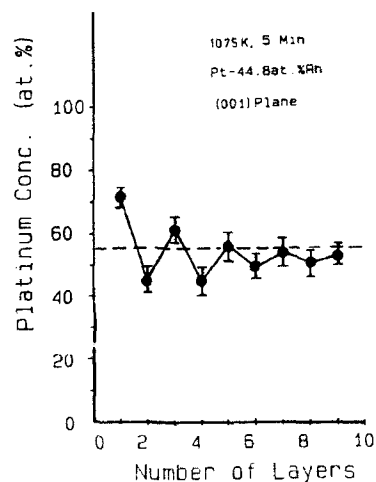


Fig. 5. When a Pt-Rh alloy is in thermodynamics equilibrium, the composition of the near surface layers will vary with their depth. Using the atom-probe FIM, we find the composition to oscillate from one atomic layer to the next to a depth beyond the 10th atomic layer. The top surface layer is enriched with Pt.

the STM, some modifications of the theories are often needed. Our recent calculations using the charge-exchange model and realistic potentials indicate that in the STM, field evaporation of silicon and gold will occur at a field of $\sim 1 \text{ V/\AA}$ as $(2-)$ ions if the tip to sample separation is greater than say $\sim 6 \text{ \AA}$, or greater than the range of direct atomic interactions.¹⁸ The much lower critical fields needed in the STM is consistent with recent STM observations although at the present moment the polarity favored is not consistent among different STM experiments.¹⁹ In atomic manipulations with the STM, field evaporation is used to deposit tip atoms to the sample surface, to create holes or vacancies in the sample surface, and to transport atoms from one location to another. In FIM, it is used for cleaning the surface, for mass analysis, and for reaching into the bulk of the solids. As the applied field in the STM can reach a value required for field evaporating a material, in principle it is also possible to utilize this effect to remove surface layers of the sample one by one by applying a biasing voltage between the scanning tip and the sample in a way similar to that in field ion microscopy. The field evaporation probably can be more easily initiated from a lattice step as in field ion microscopy. In this way one should be able to reach into the deep surface layers or an interface to study their atomic arrangements and defects, etc.

FIM experiments find that a field gradient at the surface can induce the directional motion of surface atoms.²⁰ Such atomic motion can also be induced in the STM and this effect has been used for atomic manipulations.²¹ As shown in Fig. 6(a), because of the field variation produced by a lattice step of the emitter surface, the polarization binding is smaller when the adatom is located near the center of the facet than when it is near the edge of the facet. Thus the originally horizontal surface potential is inclined toward the edge of the facet; or the adatom will drift from the center of the facet directly toward the edge as seen in Fig. 6(b). In the STM configuration, because of the geometrical asymmetry of the tip and the sample, the field strength at a spot directly below the tip is much higher than those spots away from the tip. The surface potential as seen by an atom on the sample surface is now inclined toward the center, or the adatom will drift directly toward the spot below the tip as has been observed in an STM experiment.

In this short paper, I have explained some of the limitations as well as the advantages of the atom-probe FIM technique, and describe a few of our recent studies to illustrate these points. While the atom-probe FIM is unlikely to become a microscopy of choice for routine sample examinations, it is a powerful and useful tool for basic research in surface and materials sciences especially at the atomic scale.

The author would like to acknowledge many of his coworkers, especially C.L. Chen and D.M. Ren for their contributions to the work reported in this paper.

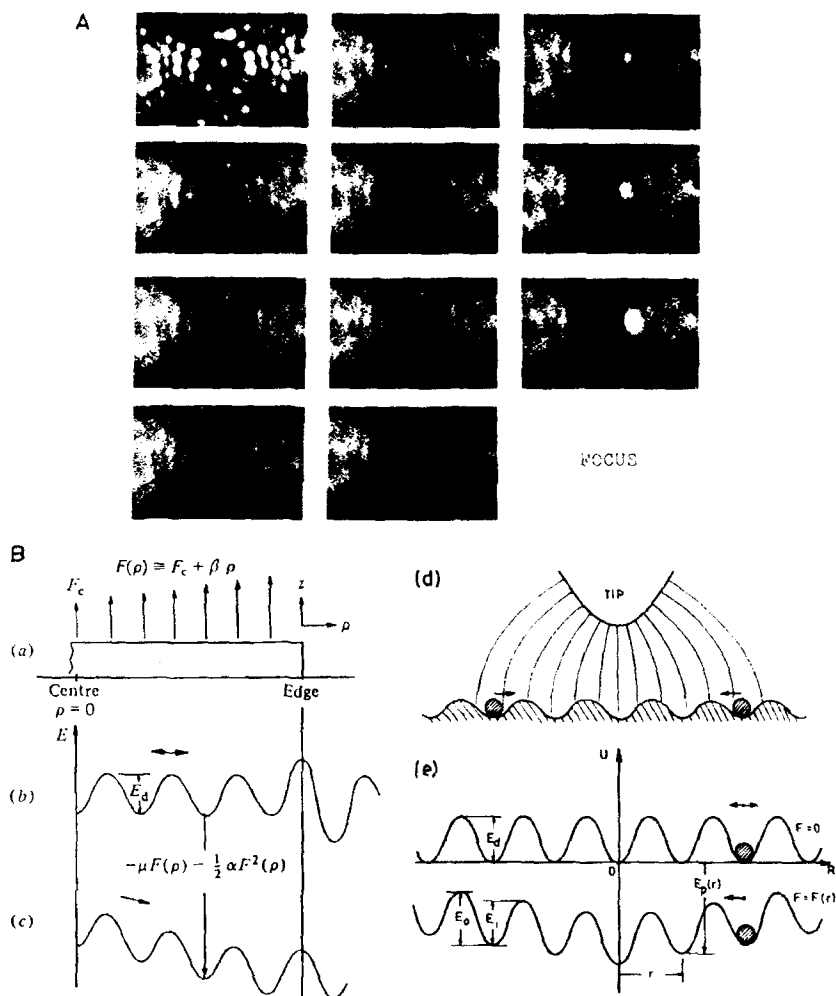


Fig. 6. A: A W adatom is deposited on a W (112) surface. The first image is taken at 78 K while the rests are taken at ~270 K. Note that at ~270 K in an image field of about 4.2 V/Å, the adatom performs random walk near the center of the surface (2 to 5). Once it moves out of the central region, it drifts continuously toward the edge of the surface because of a field gradient produced by the lattice step as explained in (a) to (c) of B. This directional walk by a field gradient can also occur in the STM as illustrated in (d) and (e) of B. The field gradient arises from the geometrical asymmetry of the STM.

REFERENCES

1. T.T. Tsong, "Atom-Probe Field Ion Microscopy," Cambridge Univ. Press, Cambridge (1990).
2. M.K. Miller and G.D.W. Smith, "Atom-Probe Microanalysis: Principles and Applications to Materials Problems," Mat. Res. Soc. Pittsburgh (1989); T. Sakurai, S. Sakai and H. Pickering, "Atom-Probe Field Ion Microscopy and Its Applications," Academic Press, N.Y. (1989).
3. Q.J. Gao and T.T. Tsong, Phys. Rev. Lett. 54, 452 (1986).
4. G.L. Kellogg, Phys. Rev. Lett. 55, 2168 (1985).
5. H.M. Liu, T.T. Tsong, and Y. Liou, Phys. Rev. Lett. 58, 1535 (1987).
6. (a). G. Ehrlich and K. Stoltz, Ann. Rev. Phys. Chem. 31, 603 (1980).
(b). T.T. Tsong, Rep. Prog. Phys. 51, 759 (1988).
7. D.W. Bassett and P.R. Weber, Surface Sci. 70, 520 (1978); J.D. Wrigley and G. Ehrlich, Phys. Rev. Lett. 44, 661 (1980).
8. T.T. Tsong and R. Casanova, Phys. Rev. B24, 3063 (1981).
9. G.L. Kellogg and P.J. Feibelman, Phys. Rev. Lett. 64, 3143 (1990); C.L. Chen and T.T. Tsong, Phys. Rev. Lett. 64, 3147 (1990); P.J. Feibelman, Phys. Rev. Lett. 65, 729 (1990).
10. T.T. Tsong and C.L. Chen, Nature, 355, 328 (1992).
11. S.P. Chen, C.M. Wei, D.M. Ren, C.L. Chen, and T.T. Tsong, to be published.
12. T.T. Tsong and Q.J. Gao, Surface Sci. 182, L257 (1987).
13. C.L. Chen and T.T. Tsong, to be published.
14. M. Ahmad, and T.T. Tsong, J. Chem Phys. 83, 388 (1985); D.M. Ren, J.H. Qin, J.B. Wang, and T.T. Tsong, to be published in Phys. Rev. B.
15. Y. Gauthier, R. Baudoing, M. Lundberg, and J. Rundgren, Phys. Rev. B35, 7867 (1987), and references therein.
16. J. Tersoff, Phys. Rev. B42, 10965 (1990).
17. J. Stroscio and D.M. Eigler, Science 254, 1319 (1991).
18. N.M. Miskovsky and T.T. Tsong, Phys. Rev. B46, 2640 (1992); N.M. Miskovsky, C.M. Wei, and T.T. Tsong, Phys. Rev. Lett. 69, 2427 (1992).
19. H.J. Mamin, P.H. Guethner, and D. Rugar, Phys. Rev. Lett. 65, (1990); I.W. Lyo and A. Avouries, Science 253, 173 (1991); A. Kobayashi, F. Grey, S. Williams, and M. Aono, to be published.
20. T.T. Tsong and G.L. Kellogg, Phys. Rev. B12, 1343 (1975); S.C. Wang and T.T. Tsong, Phys. Rev. B26, 6470 (1982).
21. L.J. Whitman, J.A. Stroscio, R.A. Dragoset, and R.J. Celotta, Science 251, 1206 (1991).

ATOMIC ARRANGEMENT OF Al NEAR THE PHASE BOUNDARIES BETWEEN $\sqrt{3}\times\sqrt{3}$ -Al AND 7×7 STRUCTURES ON Si(111) SURFACES

Katsuya TAKAOKA*, Masamichi YOSHIMURA*, Takafumi YAO*,
 Tomoshige SATO**, Takashi SUEYOSHI** and Masashi IWATSUKI**

*Department of Electrical Engineering, Hiroshima University, Higashi-hiroshima 724, Japan

**JEOL Ltd., Akishima, Tokyo 196, Japan

ABSTRACT

Scanning tunneling microscopy (STM) is used to study the structure of $\text{Al-}\sqrt{3}\times\sqrt{3}$ domains on the $\text{Si(111)-}7\times 7$ surface and the atomic arrangement near the domain boundary. $\text{Al-}\sqrt{3}\times\sqrt{3}$ domains grow from the lower side of the $\langle 1\bar{1}2 \rangle$ step and extend over the $\text{Si-}7\times 7$ terrace. The phase transition is observed to occur in units of the 7×7 size. Detailed investigation at around the boundary reveals that faulted halves of the 7×7 unit are adjacent to the boundary on the $\text{Si-}7\times 7$ side, while on the $\text{Al-}\sqrt{3}\times\sqrt{3}$ side, Al adatoms occupy the T_4 sites except for the rows adjacent to the phase boundaries where Al atoms occupy the Si adatom sites. The latter Al atoms play an important role to retain the dimer structure at the boundary.

Introduction

The atomic and electronic structure of metal overlayers on semiconductor surfaces have been widely studied to understand metal-semiconductor interfaces. Among the ordered-metal-overlayer systems observed, the most well known is the $\text{Si(111)-}\sqrt{3}\times\sqrt{3}\text{R}30^\circ$ reconstruction appearing at $1/3$ monolayer coverage.¹⁻⁴ Al is typical of those which induce the $\sqrt{3}\times\sqrt{3}$ reconstruction. With respect to the adsorption site, two different types of symmetrical sites on Si(111) can be considered; one is the H_3 site where Al atoms adsorb above the Si atoms in the fourth layer and the other is the T_4 site located above the second layer Si atoms. Northrup examined these two adatom models using the first-principles pseudopotential calculation of the total energy and of the surface states dispersion,⁵ and concluded that the T_4 model was more favorable. Qualitative support to this assignment was later given by means of angle-resolved ultraviolet photoelectron spectroscopy (ARUPS),⁶ low-energy electron diffraction (LEED),⁷ k-resolved inverse-photoemission spectroscopy (KRIPES).⁸ Recently, Hamers et al. reported that the tunneling spectroscopy measurement on the $\text{Al-}\sqrt{3}\times\sqrt{3}$ structure prefers assignment to the T_4 site over the H_3 site.^{9,10} However, the local atomic structure at the phase boundary between the $\text{Si-}7\times 7$ and $\text{Al-}\sqrt{3}\times\sqrt{3}$ domains at low Al coverage has not been yet understood.

In this paper, we report STM results on coexisting areas of $\text{Si-}7\times 7$ and $\text{Al-}\sqrt{3}\times\sqrt{3}$ and discuss the local atomic structure at the phase boundary. It is found that the $\text{Si-}7\times 7$ structure holds a dominant position on the upside of $\langle 1\bar{1}2 \rangle$ step edges and $\text{Al-}\sqrt{3}\times\sqrt{3}$ structure on the downside. This result indicates that the $\text{Al-}\sqrt{3}\times\sqrt{3}$ domains grow from the step and extend over the terrace, which is confirmed by the real time observation of the phase transition from $\text{Si-}7\times 7$ to $\text{Al-}\sqrt{3}\times\sqrt{3}$. The phase transition occurs in unit of the 7×7 size. Detailed investigation on the phase boundary confirms that the faulted halves of the 7×7 unit cells are faced to the boundary, on the other side, Al atoms occupy the T_4 sites except adjacent rows to the boundary where they occupy the Si adatom positions. The important role of the latter Al adatoms at the Si adatom positions is discussed.

Experimental

The STM used in this study is a commercial UHV-STM (JEOL JSTM-4000XV) capable of high temperature operation which enables us to observe the phase transition in real time. N-type, P-doped Si(111) with resistivity of $1\text{--}10\Omega\text{cm}$ was used as a substrate. After introduction into the STM chamber, the base pressure of which is below $1.8\times 10^{-8}\text{Pa}$, the substrate was outgassed overnight. The surface was cleaned by repetitive thermal annealing at 1200°C for a few seconds, which yielded a large flat area of 7×7 reconstruction. In order to obtain coexisting areas of 7×7 and $\text{Al-}\sqrt{3}\times\sqrt{3}$, Al of less than $1/3$ monolayer coverage was deposited onto the substrate at room temperature followed by annealing at 500°C . Alternatively,

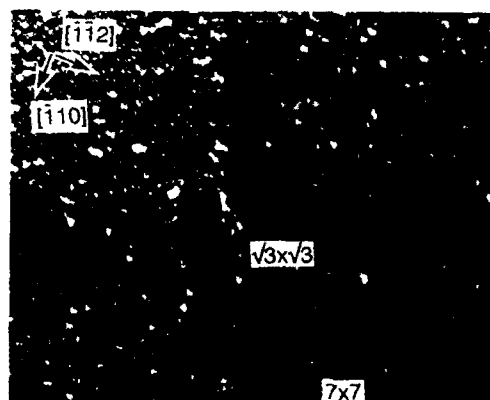


Fig. 1. STM image showing coexisting areas of 7×7 and $\text{Al-}\sqrt{3}\times\sqrt{3}$ structures at room temperature ($V_s = 1.72$ V, $I_{av} = 0.4$ nA, 80×100 nm 2). The 7×7 structure holds a dominant position on the upside of step edges and the $\sqrt{3}\times\sqrt{3}$ structure on the downside.

Al was deposited onto the heated substrate at 550°C . In order to observe the phase transition, Al was deposited onto the heated substrate at 622°C . STM measurements were performed after cooling the sample down to room temperature or during heating the sample. An electrolytically polished tungsten tip was used to probe tunneling current.

Results and Discussion

Figure 1 shows a $80\times 100\text{nm}^2$ image taken after annealing at 580°C . The sample bias is 1.72 V and the average tunneling current (I_{av}) is 0.4 nA. Si- 7×7 and Al- $\sqrt{3}\times\sqrt{3}$ domains coexist on each terrace with atomic steps along the $\langle 110 \rangle$ direction. It is noted that the 7×7 domain is situated on the upside of the step edges and the $\sqrt{3}\times\sqrt{3}$ domain on the downside. The $\sqrt{3}\times\sqrt{3}$ domain does not exist as islands on the terrace but contacts step edges.

The same spatial distribution of the $\sqrt{3}\times\sqrt{3}$ and 7×7 domains was observed not only on the surface prepared by depositing Al of less than $1/3$ ML onto a heated substrate, but on the surface deposited by a few monolayers of Al onto the substrate followed by annealing. In the latter case the coexisted area is considered to be formed by desorption of Al atoms from the Al- $\sqrt{3}\times\sqrt{3}$ surface. These facts indicate that the step sites play an important role to form the $\sqrt{3}\times\sqrt{3}$ domain on the 7×7 surfaces or vice versa. The Al- $\sqrt{3}\times\sqrt{3}$ domain grows from the downside sites of steps to take over the 7×7 terrace and Al atoms desorb from the upside sites of steps.

To confirm the above speculation real time observation of phase transition (PT) is performed. Figure 2 shows sequential STM images at 622°C . The elapsed time from the first step of Fig.2(a) is indicated in each STM image. It takes 9 seconds to obtain one picture. One recognizes that Al- $\sqrt{3}\times\sqrt{3}$ domain expands over the Si- 7×7 domain, and eventually the 7×7 domain disappears after 183 seconds. A closer investigation reveals that: (1) PT occurs in unit of the 7×7 size. (2) PT initiates at the position far away from the step edge ("P"), and expands towards the step edge as clearly seen in Fig.2(a)-(c). In Fig 2(d) one row of the 7×7 unit cell disappears perfectly. (3) Fluctuation between the two phases is observed on the position "P" in Fig.(e)-(f). Figure 3 shows the number of the 7×7 unit cell untransformed into $\sqrt{3}\times\sqrt{3}$ domain as a function of pass time. The number decreased almost linearly, and the transition rate is estimated to be 0.47 unit cell/second, independent of the size of the 7×7 domain. A further analysis is underway.



Fig 2 STM images at a phase transition at 622°C ($V_s = -0.18$ V, $I_{av} = 0.5$ nA, 13×17 nm²). Elapsed time is (a) 0s, (b) 9s, (c) 17s, (d) 28s, (e) 52s, (f) 60s, (g) 165s, and (h) 183s.

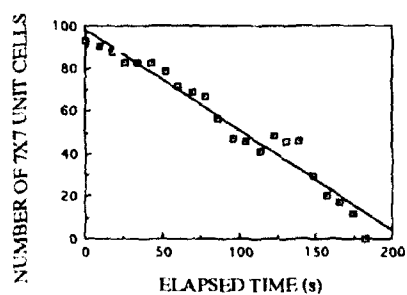


Fig 3. Variation in the number of the 7x7 unit cells as a function of elapsed time.

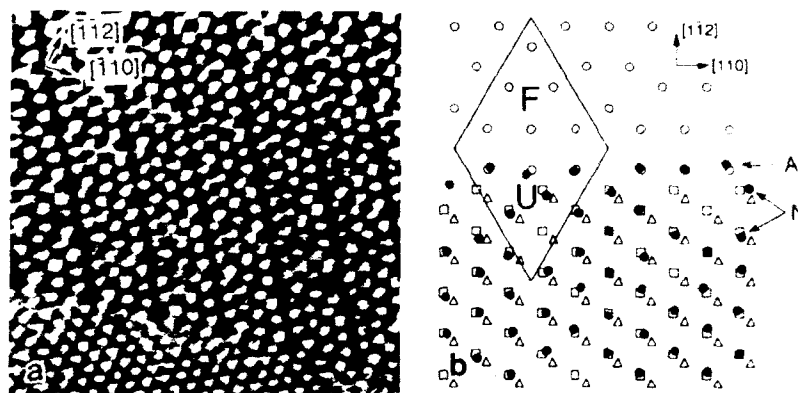


Fig 4 (a) STM image at around the domain boundary between the Si-7x7 and Al- $\sqrt{3}\times\sqrt{3}$ taken at 600°C, ($V_s = -0.18$ V, $I_{av} = 0.5$ nA, 16×16 nm 2) (b) A schematic representation of Fig 3(a) superimposed on possible models (\square T_4 site, Δ H_3 site, \circ Si adatom site, \bullet experiment)

Figure 4(a) shows a high-temperature (600°C) STM image of a phase boundary between the Si-7x7 and Al- $\sqrt{3}\times\sqrt{3}$. The upper and lower parts of the figure represent the 7x7 and Al- $\sqrt{3}\times\sqrt{3}$ domains, respectively. Figure 4(b) shows a schematic view of atomic positions observed in a part of Fig 4(a), in which Al positions based on the T_4 (indicated by triangle) and H_3 (square) models are superimposed. On the Si-7x7 side, the faulted sites are observed to face the boundary. This is due to the fact that more energy is necessary to form the $\sqrt{3}\times\sqrt{3}$ atomic arrangement on the faulted site which contains the stacking fault layer than on the unfaulted site, since in order to form the $\sqrt{3}\times\sqrt{3}$ atomic arrangement, the stacking fault should be rearranged. The observed Al adsorption sites, indicated by closed circles, are in good agreement with the T_4 sites except for those adjacent to the boundary. The Al adatoms adjacent to the boundary are found to occupy not the T_4 sites but the Si adatom positions of the 7x7 unit cell. The former and the latter Al atoms are referred to "N" and "A" atoms hereafter. In order to understand why the "A" atoms appear at the boundary, a comparison is carried out between the boundary structure based on the atomic arrangement observed experimentally (model a) and the reference structure where all Al atoms adsorb on the T_4 sites (model b). Figure 5 shows schematics of bonding configurations of model a and b. The 7x7 unfaulted half site and the $\sqrt{3}\times\sqrt{3}$ unit cell are drawn by the solid lines for reference. In the model a, three bonds from "A" atom (hatched circle) are completed by bonding three Si atoms underneath for simplicity. In the 21 times periodicity along the $\langle 110 \rangle$ direction indicated by dashed line, the number of dangling bonds of Si and Al in the model a is 10 and 6, while in the model b that is 12 and 2, respectively. Judging from the total number of the dangling bond, the model a seems energetically less favorable. Therefore, the difference in the configuration of Al dangling bonds should be taken into account. Al dangling bonds appear at the nearest sites of the "A" atoms in the model a, while they are located at the boundary in the model b. In the model a the Al dangling bond of "N" can be shared with the nearest Si atom which bonds to an "A" atom, while in the model b it would be implausible because available Si atoms are located at the next nearest positions. In addition, the more Si dangling bonds are situated at the boundary, the less stable the dimer structure at the boundary becomes. Therefore, Al adatoms favor the Si adatom positions at the boundary. When the dimer row is broken and the stacking fault layer is rearranged, the Al domain can extend over the unfaulted site and pass easily on an adjacent unfaulted site until it reaches a phase boundary with a faulted site. Thus, the "A" atoms should exist at the domain boundary to stabilize the Si domain.

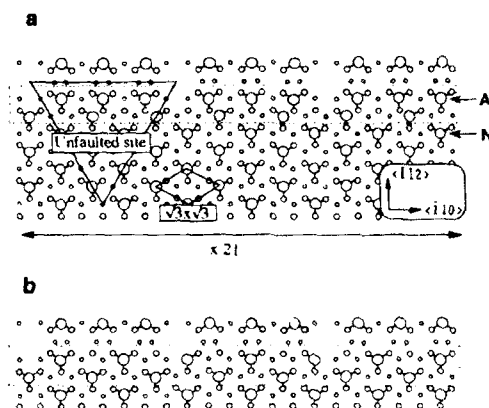


Fig. 5. Possible structural models of the domain boundary between the 7×7 and $\sqrt{3}\times\sqrt{3}$ phases. Model **a** is based on the experimental results. Al atoms adsorb on the T_4 sites ("N" atoms) except the adjacent rows where they adsorb on the Si adatom sites of 7×7 reconstruction ("A" atoms). Model **b** all Al adatoms adsorb on the T_4 sites.

Conclusions

The high-temperature STM observation of the domain distribution of the $\text{Al-}\sqrt{3}\times\sqrt{3}$ structure on $\text{Si}(111)\text{-}7\times 7$ after adsorption or desorption of Al demonstrates that the $\sqrt{3}\times\sqrt{3}$ domains forms at the downside of step edges and extend over the 7×7 terrace, and desorbs at the upside of the step edges to form $\text{Si-}7\times 7$. The real time observation of the phase transition reveals that the transition from $\text{Al-}\sqrt{3}\times\sqrt{3}$ to $\text{Si-}7\times 7$ occurs towards the step edge in units of the 7×7 size. Close STM images at around the domain boundary between the $\text{Si-}7\times 7$ and $\text{Al-}\sqrt{3}\times\sqrt{3}$ reveal that the faulted sites of the 7×7 unit cells are faced to the boundary and that Al adatoms are found to occupy the T_4 site except for those adjacent to the boundary, when Al adatoms are situated on the Si adatom positions of the 7×7 unit cell. The latter Al atoms have an important role to preserve dimer rows to stabilize keeping the domain boundary.

The authors are grateful to A. Kawazu and H. Sakama of the University of Tokyo for valuable comments.

References

- ¹J J Lander and J Morrison, *Surf. Sci.* **2**, 553 (1964)
- ²G Margaritondo, J E Rowe, and S B Christman, *Phys. Rev.* **B14**, 5396 (1976)
- ³G V Hansson, R Z Bachrach, R S Bauer, and P Chiaradia, *Phys. Rev. Lett.* **46**, 1033 (1981)
- ⁴H Nagayoshi, *Solid State Sci.* **59**, 167 (1985)
- ⁵J E Northrup, *Phys. Rev. Lett.* **53**, 683 (1984)
- ⁶R I G Uhrberg, G V Hasson, J M Nicholls, and P E S Persson, *Phys. Rev.* **B31**, 3805 (1985)
- ⁷H Huang, S Y Tong, W S Yang, H D Shih, and F Jona, *Phys. Rev.* **B42**, 7483 (1990)
- ⁸J M Nicholls, B Reihl, and J E Northrup, *Phys. Rev.* **B35**, 4137 (1987)
- ⁹R J Hamers and J E Demuth, *J. Vac. Sci. Technol.* **A6**, 512 (1988)
- ¹⁰R J Hamers, *Phys. Rev.* **B40**, 1657 (1989)

GROWTH AND SURFACE MORPHOLOGY OF THIN SILICON FILMS USING AN ATOMIC FORCE MICROSCOPE

RAMA I. HEGDE, MARK A. CHONKO AND PHILIP J. TOBIN
Advanced Products Research and Development Laboratory,
Motorola, Inc., Austin, Texas 78721

ABSTRACT

The growth and surface morphology of thin LPCVD silicon films were investigated with an atomic force microscope (AFM). Silicon films of 30 nm thicknesses were deposited on SiO₂ using SiH₄ at four different temperatures between 550 °C and 625 °C. These AFM results permitted visualization of silicon surface granularity, roughness, and the transition with temperature from amorphous to crystalline structure between 550 °C and 580 °C. The surface of the amorphous film deposited at 550 °C is very smooth and the film is continuous physically, while the film formed at 580 °C appears crystalline, rough and porous. At 600 °C and 625 °C the films are fully crystalline. For these higher temperature films surface roughness and the average grain size decreased significantly compared to 580 °C film. Crystallinity and film continuity were further examined by x-ray diffraction (XRD) and cross-sectional TEM measurements.

INTRODUCTION

Silicon films are used in semiconductor technology for MOS gates, bipolar emitter and base contacts, trench refill, elevated source/drain structures, solid diffusion sources for shallow junction formation, and the active material for thin film transistors [1 - 6]. A very thin (\approx 50 nm) Si film called "Poly A" is used as the bottom layer of a split gate to protect the gate oxide during implantation prior to the top layer, "Poly B" deposition. Of key importance in the production of thin silicon films are thickness uniformity, continuity, surface topography and grain size distribution. Several studies of the structure, morphology, and electrical properties of LPCVD silicon films have been reported [1 - 6]. Here we report the application of an atomic force microscope (AFM) to study growth and surface morphology of thin LPCVD Si layers.

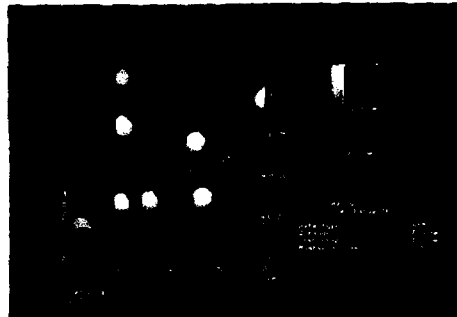
EXPERIMENTS

Silicon films of \approx 30 nm thicknesses were deposited on SiO₂ by LPCVD using SiH₄ at 550 °C, 580 °C, 600 °C and 625 °C. The deposition pressure was between 200 and 250 mTorr. The morphology of these thin silicon films were investigated with an atomic force microscope (AFM). X-ray diffraction (XRD) and cross-sectional TEM were employed to evaluate the crystallinity, micro structure and continuity.

RESULTS AND DISCUSSION

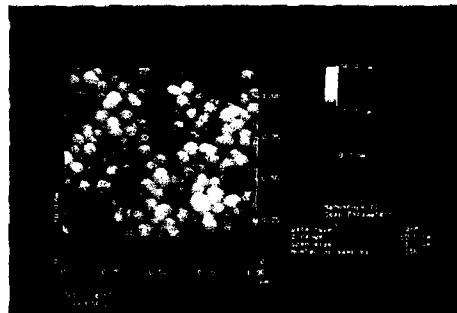
Three dimensional AFM images of 30 nm silicon films formed at 550 °C, 580 °C, 600 °C and 625 °C are shown in Figures 1A - 1D. The AFM tip scanned an area of 1 μ m X 1 μ m in each case. The silicon film deposited at 550 °C is amorphous. However, a few isolated grains are seen on the amorphous Si film which are difficult to identify by methods such as TEM or

1A



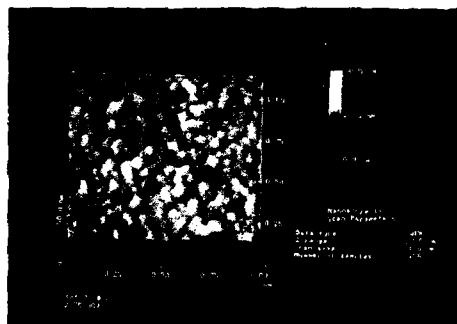
550 °C

1B



580 °C

1C



600 °C

1D



625 °C

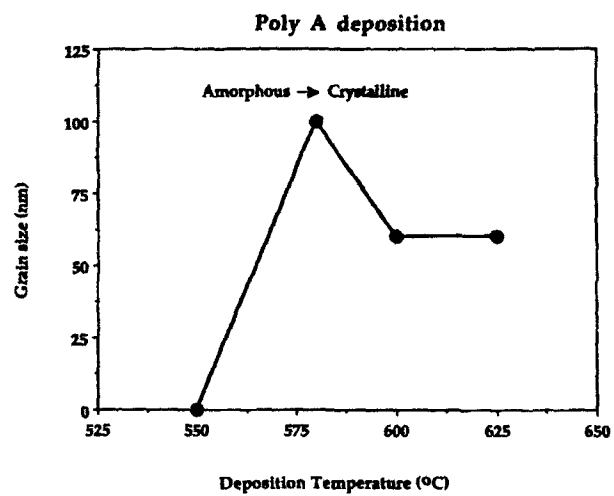


Figure 2

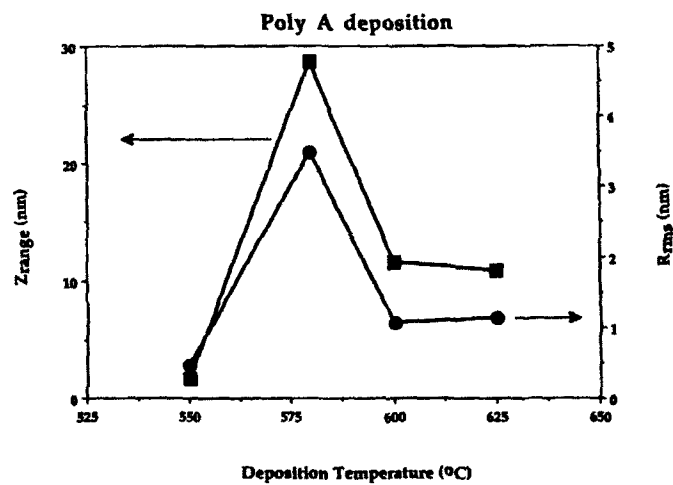


Figure 3

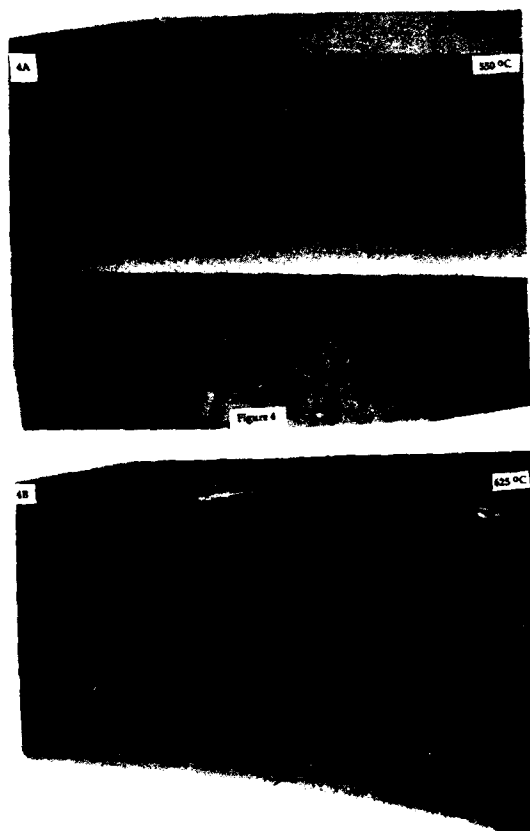
XRD (see below). At 580 °C the film appears crystalline with a bimodal grain size distribution, while the films deposited at 600 °C and 625 °C films are fully crystalline with more uniform grains. The 580 °C film exhibited an average grain size of 100 nm for the larger grains, while the 600 °C and 625 °C films have an average grain size of 60 nm. These data are shown in Figure 2.

The R_{rms} (root mean square) surface roughness as a function of deposition temperature is shown in Figure 3. The R_{rms} roughness of the amorphous film is < 0.5 nm. For the crystalline films deposited at 600 °C and 625 °C, the R_{rms} roughness is 1.1 nm which is less than 4% of the total film thickness. The roughest surface occurs for the 580 °C film where the R_{rms} value is about 12% of the thickness. Figure 3 also shows Z_{range} (peak-to-valley) surface roughness of the silicon films as a function of deposition temperature. The Z_{range} surface roughness of the amorphous Si film was < 2 nm while the value was 29 nm for the crystalline Si film deposited at 580 °C. The latter value is about 100% of the total film thickness. The Z_{range} value for the 600 °C film decreased substantially from 29 nm to 12 nm. For the crystalline Si film deposited at 625 °C the Z_{range} value was 11 nm which is about 40% of the total film thickness. This led us to question the accuracy of the optical thickness. Film uniformity and continuity of the deposited Si films was therefore further investigated by cross-sectional TEM.

The cross-sectional TEM images of the silicon films deposited at 550 °C and 625 °C are shown in Figures 4A and 4B, respectively. The film deposited at 550 °C presented no evidence of crystallinity. On the other hand, the film deposited at 625 °C exhibited a polycrystalline columnar structure. The average grain dimension by TEM is in the range of \approx 40 nm for the film deposited at 625 °C. Both silicon films look continuous and the thickness of both films is similar and in agreement with the optical thickness. The surface of the polycrystalline Si film is rougher than the amorphous film in agreement with the AFM data. The Z_{range} surface roughness obtained from Figure 4B is about 13% of the total film thickness compared with the AFM value of 40%. We believe this difference is due to the smaller scanned area in the TEM case.

The crystallinity and orientation of the films were further examined by XRD measurements as well. The XRD patterns of silicon films deposited at 550 °C and 625 °C are shown in Figures 5A and 5B, respectively. The film deposited at 550 °C is amorphous as evident from no XRD line intensities. However, at 625 °C the film is polycrystalline with all three prominent reflections from the (111), (220) and (311) planes observed. Note the fact that the few grains observed by AFM on the amorphous film deposited at 550 °C do not give sufficient diffracted intensity to be detected. No preferred orientation was apparent from the XRD data for the film deposited at 625 °C.

Poly A films in production must have good thickness uniformity, continuity, smooth surface topography and uniform grain size so that quality of these thin silicon films will be improved to guarantee device performance and reliability as well as production yield. At first, it is important to realize that the quality of these thin films is reflected in their surface topography as shown in Figures 1A - 1D. At 550 °C the deposition rate is higher than the crystallization rate which results in the amorphous film. At temperatures of 580 °C, 600 °C and 625 °C the films grow crystalline. Furthermore, a large grain size can be obtained when the nucleation rate is low and the growth rate is high [4]. The higher deposition temperature gives rise to an increased nucleation rate which explains the smaller grain size for 600 °C and 625 °C films compared to



W-44X
7 nm

Figure 4

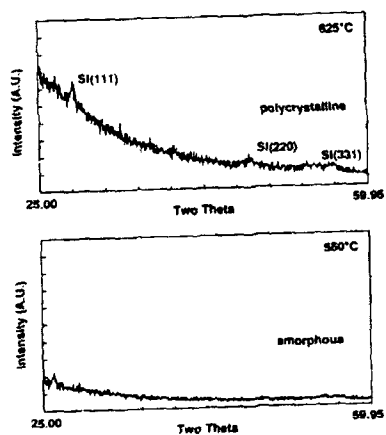


Figure 5

580 °C. As shown in Figure 2, the average Si grains are much larger than the film thickness and grains will grow perpendicular to the surface forming two dimensional columnar grain growth.

The surface of the amorphous film is very smooth and the film is continuous physically. The Z_{range} (peak-to-valley) surface roughness of the crystalline film deposited at 580 °C is about 100 % of the total film thickness. This indicates that the film is porous, due to coarser nucleation, which is readily apparent in Figure 1B. The porous silicon film consists of numerous micro voids on the surface while still maintaining a crystalline structure. The porous silicon may provide a direct path for cleaning solutions to the underlying gate oxide and hence can short capacitors fabricated using 580 °C Si films [3]. The amorphous films form uniformly, there is no pathway for the etching exists and the gate oxide is protected. For these higher temperature films the surface roughness values (both R_{rms} and Z_{range}) decreased significantly. This indicates that higher temperatures (600 °C and 625 °C) Si films are much smoother allowing the micro voids to be filled. The AFM images have shown that the average grain size of Si decreases with increasing deposition temperatures. This may be a potential explanation for the smooth surface morphology of the films deposited at higher temperatures. However, the 580 °C film has bimodal grain size distribution without columnar growth. Thus the surface morphology of 580 °C film can not be explained on the basis of grain size theory alone.

CONCLUSIONS

The growth and surface morphology of thin silicon films used as "Poly A" in MOS capacitors were investigated with an AFM. Silicon films of 30 nm thicknesses were deposited on SiO₂ by LPCVD using SiH₄ at four different temperatures between 550 °C and 625 °C. These AFM results permitted direct visualization of grain size, surface roughness, and the transition from the amorphous to the crystalline form with temperature. The transition deposition temperature from amorphous to polycrystalline silicon is between 550 °C to 580 °C. The silicon film deposited at 550 °C is amorphous, very smooth and the film is continuous physically. The films deposited at 580 °C and above are crystalline. The 580 °C film has the largest grains and is the roughest and porous.

ACKNOWLEDGMENTS

We would like to thank Lou Parrillo and Joe Mogab for their support. Special thanks to Vidya Kaushik for doing TEM analysis.

REFERENCES

- 1 T. Kamins, "Polycrystalline silicon for integrated circuit applications," Kluwer, Academic Publishers, (1988).
- 2 A. Kermani, K. E. Johnsgard, F. Wong, *Solid State Technology* (1991) 71.
- 3 R. I. Hegde, M. A. Chonko and P. J. Tobin, *Spring ECS*, 1993 (submitted).
- 4 R. B. Iverson and R. Reif, *J. Appl. Phys.* **62**, (1987) 1675.
- 5 M. Chonko, D. Vandenberg and D. Keitz, *Second International Symposium on Physics and Chemistry of SiO₂ and Si/SiO₂ Interface*, Spring ECS, 92-1 (1992) 390.
- 6 R. I. Hegde and P. J. Tobin, *Surface Science*, **261**, (1992) 1.

SOLVING INTERFACE STRUCTURES BY COMBINED ELECTRON MICROSCOPY AND X-RAY DIFFRACTION

A. BOURRET and G. FEUILLET

Département de Recherche Fondamentale sur la Matière Condensée
Centre d'Etudes Nucléaires de Grenoble - 85 X - 38041 GRENOBLE Cedex, FRANCE

ABSTRACT

By a combination of high resolution imaging (HREM) and grazing incidence X-ray scattering (GIXS), periodic interfaces with large unit cell can be solved at an atomic scale. The advantage of recording information in the real space is that phases are directly encoded in the image. On the other hand the X-ray diffraction gives quantitative information at a resolution level better than with HREM. This combined analysis is illustrated on GaAs (001)-CdTe (111) and on GaAs(001)-GaSb(001) interfaces. In both cases the structure at the interface is obtained and some mechanisms for the strain relaxation at heterostructures with large misfit are proposed.

INTRODUCTION

Solving the interface structure in heterostructures is a very important issue for technological reasons as well as for a better understanding of the relaxation phenomena at interfaces with large misfit. The desire to grow heterostructures with large lattice parameter mismatch (Ge on Si or GaAs on Si) for use in high-performance optoelectronic devices has recently driven much attention to the creation mechanism of dislocations in order to produce good performance devices [1]. Two ways are clearly possible for producing defect free epilayers : either inhibiting the dislocation nucleation and/or propagation, or creating a well defined dislocation lattice confined to the interface. The second approach could produce completely relaxed structures and is the only possible way for very large misfit ($> 7\%$) [2-3] or for very slow growth. In this case the classical Van der Merwe approach [4] would imply a critical thickness for the formation of an incoherent interface of the order of one or two monolayers. Therefore dislocations have to be formed at the interface at a very early stage if the growth mechanism is purely two dimensional. In fact most of these systems grow through the formation of islands as shown for medium range misfit (4 %) as for the Ge-Si (100) and GaAs-Si (001) systems [5-6]. The Stranski-Krastanov mechanism involving an intermediate 2D-layer has been proposed as a possible transition between the 2D and the 3D growth. However it is difficult to understand i) the atomic mechanism which enables to introduce more or less regularly spaced interfacial dislocations even with an intermediate layer and ii) what is the real structure of this intermediate layer.

On a different class of material, potential applications of II-VI compounds in optoelectronics have also driven an extensive and generally successful effort to grow CdTe, CdMnTe, ZnTe, ZnSe, ZnS [7] on various substrates including GaAs (001). In most cases strong chemical bonding is likely to occur between the substrate and the epilayer inducing an epitaxial growth. The lattice mismatch should be small and the crystallographic symmetry should be preserved for a coherent growth. However none of these two conditions are satisfied in several cases known to grow pseudo-epitaxially. A typical case is the growth of (111) oriented CdTe on GaAs (001) substrate [8]. CdTe (111) has a 0.7 % misfit along $\langle 110 \rangle$ direction and 14.6 % along $\langle 1-10 \rangle$. The physical reasons for this pseudo-epitaxy are not well understood. Several ideas have been suggested : the formation of an ordered precursor when selected absorption sites are occupied during the initial growth [9], or the formation of an intermediate layer with intermixed species [10], or the formation of a definite compound [11]. Testing experimentally these different models is not straightforward. Most of the surface techniques which describe the precursors at submonolayer level are not applicable to buried interfaces except with high energy particles by diffraction or imaging. Among these, high energy electrons and hard X-rays are the most promising. The high resolution electron microscopy (HREM) technique has

already been extensively employed at interfaces and its characteristics are now well established. On the other hand the grazing incidence X-ray scattering (GIXS) has been applied to a limited number of cases for interfaces but is now a well established technique for surfaces [12].

The complementary character of the imaging and diffraction techniques can be appreciated by considering the advantages and limiting factors of both.

THE HREM TECHNIQUE

Foremost about the HREM technique is its ability to give direct measurements of the respective atomic position and registry across the interface. The "phase" lost in any diffraction experiment is encoded in the image intensity. From a quantitative comparison between experimental and simulated images, the atomic position of individual atomic columns is directly deduced [13] with a resolution limit around 2 Å when atomic columns are individually resolved. In addition periodicities and the existence of variants could be checked and moreover the HREM technique is not limited to periodic objects. The rigid body translation (RBT) between the two structures across an hetero-interface is directly measurable: the resolution is then one order of magnitude better than the resolution limit. Finally the recently developed chemical analysis enables to determine the chemical content of individual atomic column when the atomic species are already known [14].

These progresses in the quantitative interpretation of the image intensity have given to the HREM the ability to resolve crystallographic structures in specific cases.

On the other hand HREM suffers from several drawbacks: i) very few zone axes are available for imaging all individual columns. In particular along the commonly used $\langle 110 \rangle$ and $\langle 112 \rangle$ zone axes in semiconductors only atomic column pairs are resolved, ii) a 3D object is reduced to a 2D image by a complex non linear transformation which can be reduced to a projection only for weak phase object iii) as a consequence of the "projection", the relaxation strain field should be independent of the position along the observation axis. As a consequence the interface has to be observed in a cross sectional view and at least two viewing axes are necessary in order to extract 2D information at the interface (figure 1). The condition iii) is not fulfilled for a 2D dislocation array resulting from a lattice mismatch in more than one direction at an interface.

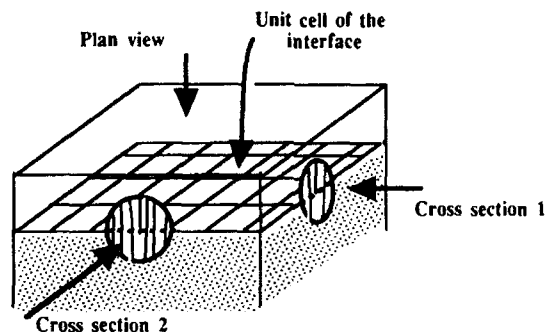


Figure 1 : Scheme of the geometry employed for preparing thin foil for electron microscopy. The interface can be viewed either in plan view or in cross sections

THE GIXS TECHNIQUE

If the atomic relaxation is periodic the GIXS method is available and has great advantages. By contrast to the HREM the GIXS technique has a much better resolution. In the case of a reconstructed buried interface four kinds of reflections are present coming respectively from the substrate, the epilayer, the truncation rods and from the interface reconstruction. Those

later reflections are specific to the interfacial structure and easily measured in the in-plane diffraction geometry. Information down to better than 0.5 \AA is often available, and gives the projected structure of the relaxation on the interface plane. This information is easily quantified with appropriate detectors. Above all, the interaction of X-rays with the thin layer associated with the interface is kinematic. As a consequence, structures can be refined using quantitative criteria to approach the real structure. Out-of-plane measurements along the superlattice rods give the relaxation perpendicular to the interface but could be often limited in resolution for experimental reasons (due to the limited exit angle of X-ray scattering at beryllium windows). Moreover the number of observable superlattice reflections is limited due to their small intensity compared to the background. As a consequence the choice of the initial structure to start the refinement calculation is of prime importance and is often very difficult when the number of atoms contained in the interface unit cell is large.

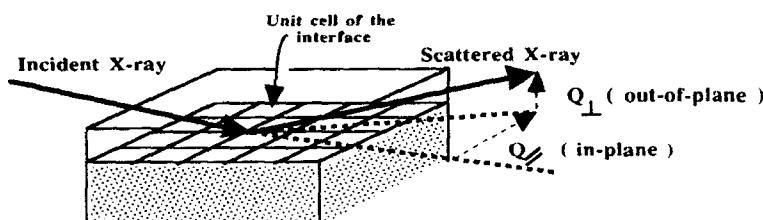


Figure 2 : Scheme of the geometry employed in the grazing incidence X-ray scattering technique in order to study buried interface. Scattering by an interface supercell gives extra peaks or satellites in addition to the substrate or epilayer peaks.

Experiments are performed on beam-line X-16 A at the NSLS using GIXS with a specially designed ultrahigh vacuum chamber mounted on a five-circle goniometer stage [15]. The specimens prepared in the same conditions as for HREM, are vertically positioned so that the scattering vector is in the vertical plane. Most of the scans are measured at fixed incident angle, 0.25 to 0.3° , which corresponds to 1 to 1.2 times the critical angle. Integrated intensities of the individual peaks as measured during a rocking θ -scan are corrected for the variation of the area seen by the detector and for the Lorentz factor. No polarization corrections are necessary for in-plane diffraction in our specific geometry. The in-plane diffraction intensities are recorded on several samples and averaged on several symmetry equivalent reflections. In-plane as well as out-of-plane (figure 2) intensities are measured at each individual diffraction peaks.

HOW TO COMBINE HREM AND GIXS

The previous comparison suggests a practical route to solve the interface structure. Electron microscopy provides the defect content at the interfaces, the periodic or non periodic character of the relaxation, and atomic images from which the defect character is generally deduced. Therefore in favorable cases, HREM provides, from two cross sectional views, a first trial structure with a resolution limited to 2 \AA in 3D space. In particular, it defines the number of layers involved in the relaxation at the interface and gives the rigid body translation (RBT) components in each cross sectional view. In addition it provides the number of atom concerned in each layer, a parameter which is difficult to find in large unit cells by diffraction experiment. We then refine the projected structure using the in-plane X-ray diffraction data with several combinations of atom types compatible with some *a-priori* information or other experimental techniques. The Rutherford back-scattering gives for instance the crystal polarity of the heterostructure in polar crystals. Depending on the collected data we can either test different models suggested by electron microscopy or, after selecting among the different

trial structures, the refinement process can start. The residual factor (R-factor) or the chi-square value is minimized as a function of the atomic coordinates and eventually the Debye-Waller factors. As a final step, we computer simulate HREM images and adjust the relaxation perpendicular to the interface until a good fit is obtained with the experimental images. This gives, in principle, a 3D description of the interface structure.

THE LONG RANGE STRAIN FIELD NEAR AN INTERFACE

We have shown in previous reports that GIXS from GaSb-GaAs (001) interfaces (7.8 % misfit) gives support to an intermediate layer but in a new sense : the interface is slightly corrugated. [10]. Briefly summarized the experiment was as follows :

The epitaxial layer of (001) GaSb (miscut angle $< 1^\circ 5'$) is grown ex-situ at 470 °C by molecular-beam epitaxy (MBE) on (001) GaAs substrate. In-plane transmission electron microscopy reveals the presence of an island growth mode with a well ordered square array of pure edge dislocations (Lomer type) along the two $\langle 110 \rangle$ at the substrate-island interface [3]. The unit cell is square with a 50 Å periodicity as demonstrated in plan view (figure 3). HREM was also performed on cross sections of the same systems by Ichinose [16] along the $\langle 110 \rangle$ axes and confirmed the presence of Lomer dislocations. These images were matched to the calculated dislocation strain field [17] and gave a crude agreement to the experimental atomic positions at long distances from the dislocation core. In fact the first set of dislocations is observed end-on but is blurred by the second set of dislocations running parallel to the thin foil, although a bending of the interface seems present. Indeed the relaxation is not limited along the observation axis and any quantitative interpretation is not justified. This is where the X-ray scattering measurements could help.

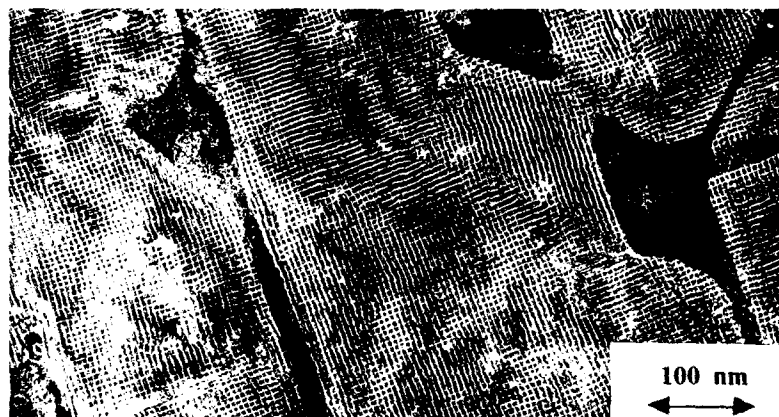


Figure 3 : Electron micrograph of the interface between GaAs(100) and GaSb(100) obtained in plane view (220 dark field) Nominal thickness 240 Å. Note the periodic array of dislocations at the interface along $\langle 110 \rangle$ directions. (courtesy A. Rocher)

In the vicinity of the main peaks of the substrate and of the epilayers several regularly spaced satellites are present. We deduce that i) the epitaxy is perfect within $\pm 0.02^\circ$ and the residual strain of the epilayer is limited to about 0.3 %, therefore most of the misfit is accommodated through dislocations, ii) the satellites are present around any substrate and epilayer peak and are coming from the diffraction on a periodic square array of dislocations with a four-fold symmetry. The dislocation spacing measured using transmission electron microscopy agrees with the distance between satellites and to the calculated distance between Lomer dislocations, d , as given by $d = 0.5 a_1 a_2 / (a_1 - a_2)$ where a_1 is the lattice parameter of the epilayer (GaSb) and a_2 the lattice parameter of the substrate (GaAs).

This distance is $58 \pm 2 \text{ \AA}$ and corresponds to a quasi-periodic interface structure which could be approximated by a mixture of $\sqrt{2}$ (14×14) and $\sqrt{2}$ (15×15) super-cell. At each satellite, the out-of-plane scattering along the rods perpendicular to the interface describes the atomic relaxation on each side of the interface (figure 4). The diffraction by an interfacial dislocation grid is complex : the entire strain field produced by the interfacial defects extends at distances of the order of the supercell period and extracting the entire atomic structure is not possible with so few satellites. As a consequence the data analysis is limited to the determination of few overall but relevant parameters : the exact location of the interface relative to the dislocation core and the presence of a non-planar interface.

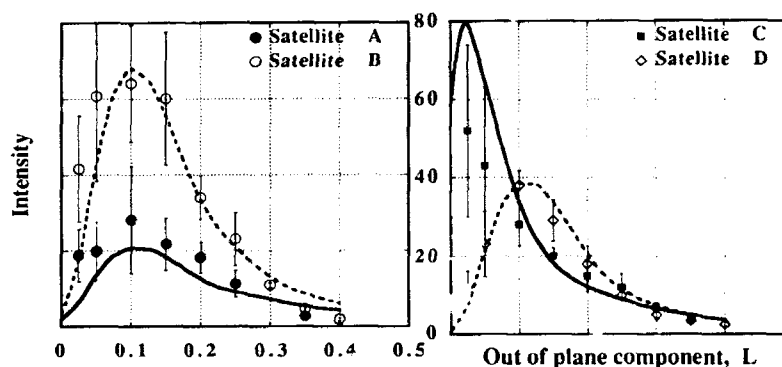


Figure 4 : Comparison between measured (GIXS) and calculated intensity at satellites due to the periodic relaxation at the GaAs-GaSb interface. The four satellites were measured around the 440 peak of the substrate B, C D being located between the GaAs and GaSb peaks. Modelling is performed with a corrugated interface and three layers of GaAs protruding in the GaSb epilayer.

The rational choice of trial structures is the major step and has been carried out in two ways. The first non-parameterized approach is to calculate the atomic displacements due to a 2D periodic array of dislocations through elasticity theory. The elastic displacement field at an incoherent interface has been calculated by Van der Merwe [18] and with more appropriate boundary conditions by Bonnet [19]. Analytical expressions are available for periodic dislocation networks in the isotropic case with the dislocation at the interface plane. The second approach is to computer relax a given structure by energy minimization using an appropriate interatomic potential. In view of the large number of atoms involved (15,000), the simplest empirical potential has been chosen : the Keating potential. Among the large variety of interface shape and chemical profile we select three classes : i) those containing a planar abrupt interface located at a variable distance from the dislocation core, ii) a uniform interdiffused interface with Sb and As atom exchanges and an error function profile, iii) a corrugated interface defined by h and w respectively the height and width of the corrugation. As the Keating potential reflects the strain energy but not the chemical or electronic rearrangement at the interface, the minimum energy criterion has to be taken with caution in comparing trial models. Consequently any model having an interfacial energy differing up to 30 % from the lowest energy configuration has been considered as a possible trial structure. This is the best way to rationalize the choice.

The intensity of the four satellites A-D around the 440 peaks, $I^2(L)$, was calculated and fitted simultaneously to the four experimental curves using the chi-square minimum criterion

(figure 4). We conclude that i) the corrugated structures in particular those containing 2 to 4 atomic layers of GaAs protruding in the GaSb epilayer give a good fit with a low chi-square value, ii) all planar configurations give higher chi-square values (3 or more), iii) uniform interdiffusion does not improve the fit. It is worthwhile to note that the corrugated configuration giving the best fit (figure 5) have strain energies comparable to the lowest energy found for planar structures with dislocation core at two atomic planes from the interface.

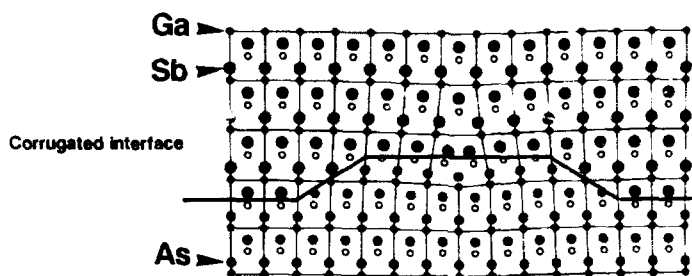


Figure 5 : The relaxed interfacial structure of GaAs-GaSb(001) as calculated for a corrugated interface by energy minimization using a Keating potential. A section of one unit cell of the interface is drawn at equal distance from two dislocations.

In this example the complementary nature of HREM and GIXS has been exploited. In particular one of the main limitation of the HREM in the case of a 2D array of defects has been overcome. Unfortunately the unit cell size is so large that all atomic coordinates are not available. This is not the case in the following example.

ATOMIC RESOLUTION AT AN INCOHERENT INTERFACE

Few interfaces exhibit superstructures with large unit cells in only one direction. This limits the number of atoms involved and the structure is more tractable with X-ray diffraction. This is the case for the GaAs(001)-CdTe(111) interface. GaAs (001) surface is stabilized in Ga-rich conditions forming a $c(8 \times 2)$ structure which is known to be one of the precursor of CdTe (111) growth [8]. A nominal 10 Å layer of CdTe is grown on this surface by molecular beam epitaxy at 520 °C. This layer is protected by evaporation of a Te cap layer deposited at room temperature. We first describe the results obtained by HREM (figure 6). In the $[1-10]$ cross section (figure 6b) the interface appears planar and mostly coherent with no apparent supercell visible, the RBT in the $[110]$ direction is measured to be close to zero, and most of the relaxation should occur along the observation axis as the image appears very regular and undisturbed at the interface. In contrast on a $[110]$ cross section (figure 6a), the interface is incoherent with a periodic arrangement involving four and five GaAs unit cells, the relaxation is directly visible at the interface with grouping of white dots by pairs. Perpendicular to the interface, it is clear that approximately four atomic layers are involved in the relaxation : two layers are slightly relaxed away from the CdTe (111) atomic sites and two layers are close to the GaAs (001) sites. At this point we cannot distinguish the chemical species. However the stacking sequence imaged by HREM combined with the crystal polarity measured by Rutherford Back Scattering [20], gives the following sequence for the four layers : 1/ Ga in 001 sites, 2/ As on 001 sites, 3/ Cd in 111 sites, 4/ Te in 111 sites. It is not excluded that layer 2/ or 3/ be replaced by another chemical species provided they are respectively close to 001 and 111 sites and with the same number of atoms, respectively 18 and 16 per unit cell for 001 and 111 sites.

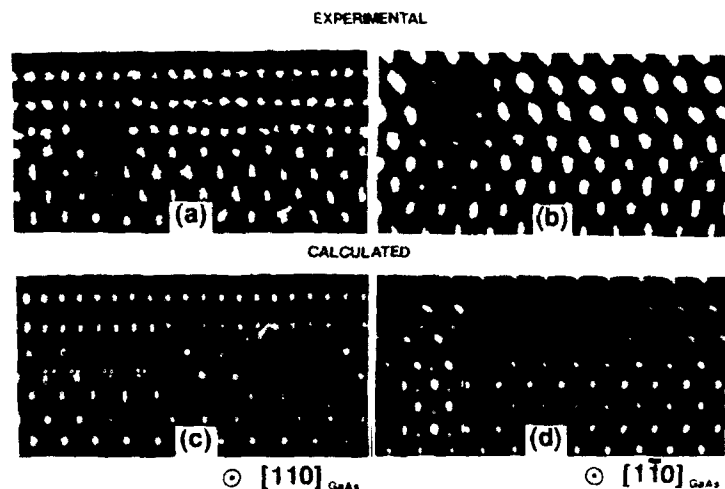


Figure 6 : Lattice image of a GaAs(001)-CdTe(111) interface along two perpendicular viewing axes. The atomic column pairs are encoded in white dots in a) and black dots in b). Calculated images c) and d) are computer simulated and compared to the experimental images using the atomic positions deduced from GIXS.

The results obtained by X-ray diffraction are as follows (figure 7). The bulk reflections from the epilayer show that a residual strain of 2 % in the $[1-10]$ direction is still present. In addition the in-plane diffraction pattern contains superlattice reflections clearly coming from the buried GaAs-CdTe interface. We observe them independently of the surface state (with or without the cap layer) and the integrated intensities along the superlattice rods decrease with the out-of-plane component, L . This decrease is compatible with a relaxation of three to four atomic layers at the interface but not with a truncation rod. These two observations point at an interfacial supercell and not to a purely surface reconstruction. All observed superlattice reflections belong to a $\sqrt{2}(2 \times 9)$ unit cell. The nine units along $[1-10]$ direction are compatible with the HREM images. The two units along $[110]$ are not evidenced by HREM from which we deduce that the cell has a glide symmetry element along the observation axis ie. $[110]$. Among the 312 superlattice reflections which were looked for and measured, only 20 independent reflections give well defined and measurable peaks with a dynamic of 70:1. All others are below the background intensity which originates mostly from the amorphous cap layer. However the measured background is used to evaluate an upper limit of the structure factor, F_H , at this reflection. This value is incorporated in the calculation of the residual factor, R defined as :

$$R = \sum_G \left| F_G^* - F_G^{\text{calc}} \right| / \sum_H F_H^{\text{obs}}$$

where $F_G^* = F_G^{\text{obs}}$ at the 20 measurable superlattice reflections, H , and $F_G^* = F_H$ at all other reflections of the $\sqrt{2}(2 \times 9)$ superlattice. F_G^{calc} and F_G^{obs} are respectively the calculated and observed structure factors at the superlattice reflection G .

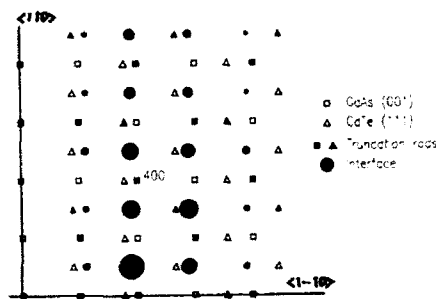


Figure 7 : In-plane diffraction pattern obtained by GIXS. The diameter of each individual superlattice reflection is proportional to its amplitude.

We first start with trial combinations of three unrelaxed layers with atoms at (001) sites and/or (111) sites assuming a RBT along [110] equal to zero. The R-factor ranges from 2 to 4 and the best combination involves three layers respectively 2/ As in (001) sites, 3/ Ga or Cd in 111 sites and 4/ Te in 111 sites. No improvement is obtained by the addition of other layers on either side of the interface. The R-factor is drastically reduced to 0.33 by moving the As atoms off their perfect crystal position in order to form dimers with alternate translation along [1-10] at $y=0$ and $y=0.5$. This creates the apparent pairing observed by HREM. The atom type of layer 3/ is then adjusted and found to be Ga ($R=0.33$) rather than Cd ($R=0.63$). Further refinement is made with the conjugate gradient method with the x and y coordinates of each atom as parameters, down to $R=6.6\%$. Although the number of parameters greatly exceeds the number of measured peaks, the R-factor definition incorporates the additional information on the upper value obtained for the smallest reflections.

Two tests give us confidence on the reliability of the procedure : i) atomic relaxations along [110] remain negligible as observed by HREM, and ii) the refinement procedure, applied to other structures, gives always a larger R-factor, for instance $R=10.4\%$ if Ga is replaced by Cd. Going back to the direct space image we refine the structure perpendicular to the interface (z direction). We obtain a good fit between the experimental and simulated images (figure 6) for the following z values : layer 2/, 3/ and 4/ are respectively at $z=0, 1.4\text{\AA}, 2.33\text{\AA}$. The final coordinates of each atom are employed in the perspective view of figure 8. From the data it is easy to deduce the first nearest neighbor distances and the local atomic coordination.

The main features of this interface structure are as follows : i) The last layer related to the original GaAs (001) planes is an arsenic layer with relaxation along [1-10] and formation of a zig-zag chain. Every 4 or 5 unit cells those chains are in antiphase position with local formation of dimers, ii) The last substrate layer contains Ga atoms close to the CdTe 111 sites, iii) The interface is composed of large regions with relatively uniform structural units separated by two "dislocations" lines per period associated with the As dimers. Successive dislocation core structure along [1-10] are shifted by half a period, iv) Most of the Ga atoms in layer 3/ are five-fold coordinated.

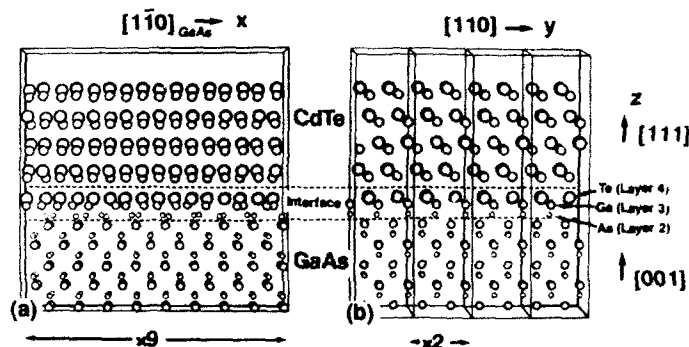


Figure 8 : Two perspective views at right angle of the GaAs(001)-CdTe(111) interface as determined after refinement with the X-ray data. The supercell is $7.99 \text{ \AA} \times 35.9 \text{ \AA}$

IMPLICATIONS ON THE GROWTH PROCESS

Two different ways of relaxing the strains at large misfit interfaces have been evidenced : producing a periodic square array of dislocations and forming a reconstructed large unit cell.

In the first case the existence of a non-planar and periodic interface has several implications. The misfit dislocations which are associated with a protrusion (2 or 3 monolayers) of GaAs should be involved in the formation process of the corrugated interface. However a purely diffusive phenomenon occurring after the interface formation seems unlikely. First the pseudo-binary alloy GaAs/GaSb is a peritectic alloy with a miscibility gap with low solubility of As (in GaSb rich alloy) or Sb (in GaAs rich alloy) at 470 C. As a consequence large interdiffusion is not thermodynamically driven in bulk materials. In addition the growth temperature is too low to allow for significant atomic mobility. Elastically driven diffusion with small atoms (Ga) attracted in compressive core region is therefore unlikely to take place once the incoherent islands are formed. For the same reasons, dislocation climb necessary for a sessile configuration to move is not possible and dislocations cannot be produced at the island surface once it is far from the interface. We conclude that both the dislocation formation and the Ga atom movement are essentially surface or near surface phenomena. Two mechanisms can be invoked based on near surface mobility and driven by the size effect. The first is a stress induced mechanism at the triple point while the island is laterally growing. The shear stress, σ , created as long as the epilayer is coherent with the substrate could reach a critical value, σ_c , necessary to nucleate a Lomer dislocation. Simultaneously the compressive strain field produced in the GaAs substrate could induce the upward migration of smaller Ga atoms in the top layers. This process is solely governed by the distance between the triple point and the last created dislocation. Therefore it explains well why the dislocation grid is so periodic : dislocations are nucleated in position and no further climb is necessary. In addition this process creates a corrugated interface with the same periodicity as the dislocation distance. The second mechanism, which at this stage cannot be ruled out, is the formation prior to the island growth of an intermediate layer : it is a generalized Stranski-Krastanov mechanism. This layer, two or three monolayers high, could

contain an ordered structure with square tiles of GaSb connected by joint of GaAs (figure 5). This arrangement lowers the interfacial energy compared to a continuous GaSb film by a factor roughly proportional to the surface of the GaSb tiles as compared to the total surface.

In the second case the formation of the supercell could be induced by an initial reconstructed surface. In fact the initial Ga-rich surface known to induce the CdTe (111) growth is still reflected in the interface structure. The Te atoms as shown by Tatarenko et al. [8] are the first adsorbed species and XPS shows numerous Ga-Te bonds, a tendency which is even more systematic when the epilayer has fully grown. Therefore some general trends observed during the CdTe initial growth are preserved after completion of a 3D epitaxial layer. However, when analyzed in more detail, the initial adsorption sites are strongly modified. The buried interface has no Te-As bonds as opposed to the one detected by XPS on the (* x3) surface and no Te-Te bonds detected on the (6x1) 111 surface, another precursor of the (111) CdTe growth. Therefore the Cohen-Solal model [21] with two Te-Ga bonds and one Te-As at each Te adsorbed atom could only be a transient structure. The reason why the Ga atoms are in the Cd sites can be understood as follows : it is the only arrangement which is compatible with no net charge at the interface. We note that for Te, Ga, As with respective 6, 3, 5 s and p electrons and 4, 5, 4 coordination numbers, there are two electrons per bond at any atom. In the framework of the bond orbital model these electron pairs provide the dominant energy term in the cohesion energy through the filled bonding states. The sp^3 hybrid involved in the Te and As bonds are therefore still present. Although pairing is still ensured for Ga, the hybridisation should be modified in order to include d orbitals. Further, bond structure calculations should give more insight to the respective degree of covalent and ionic binding. Nevertheless, the observed structure is compatible with a high cohesive energy and, as a consequence, a relatively stable interface. We also note that no intermediate compound, for instance the stable Ga_2Te_3 is observed. This is in contrast with ZnSe (001) on GaAs (001) : an intermediate layer of Ga_2Se_3 is formed with a (2x2) supercell at the interface [22].

CONCLUSION

More generally the implications of our work are as follows. First we have demonstrated the advantages of combining information on the same structure in real space and in reciprocal space to solve quasi 2D-structures. Thus our approach can be generalized to any reconstructed interface and should be particularly attractive for incoherent interfaces in heterostructures. Second, the ability to obtain local atomic positions in an interface between multicomponent constituents should stimulate energy calculations. The stable structure similar to the one found in the system GaAs(001)-CdTe(111) is difficult to predict even with extensive calculations. The present experimental determination opens the way to feasible electronic structure ab-initio calculations. The electron transfer and local charge induced at the interface are particular points of interest which should now be studied. Finally we have shown that the final configuration of an interface cannot be extrapolated from the knowledge of the initial growth of the first adsorbed species. This points to the need of detailed structural studies on interfaces per-se, in addition to the whole body of theoretical and experimental work performed at surfaces.

Acknowledgements

We acknowledge S. Tatarenko who prepared the CdTe specimens, A. Rocher who provided us with the GaSb specimens and P. Fuoss for his help in the GIXS technique and numerous fruitful discussions.

References

- [1] R. Hull, J.C. Bean, D.J. Werder and R.E. Leibenguth, Phys. Rev. B **40**, 1681 (1989)
- [2] C.J. Kiely, J.I. Chyi, A. Rockett and H. Morkoç, Philos. Mag. A **60**, 321 (1989)
- [3] A. Rocher, F. W. O. Da Silva and C. Raisin, Revue Phys. Appl. **25**, 957 (1990)
- [4] J.H. Van der Merwe, J. Appl. Phys. **41**, 4725 (1970)

- [5] D.B. Fenner, D.K. Biegelsen, B.S. Krusor, F.A. Ponce and J.C. Tramontana, in Atomic scale structure of interfaces, edited by R.D. Bringans, R.M. Feenstra and J.M. Gibson (Mater. Res. Soc. Proc. **159**, Pittsburgh 1990) pp. 15-20
- [6] M. Asai, H. Veber and C. Tatauyama, J. Appl. Phys. **58**, 2577 (1985)
- [7] For a review see for instance in II-VI Compounds 1991 Edited by S. Fujita, T. Vishino, T. Taguchi - North Holland 1992 - Elsevier Publ.
- [8] S. Tatarenko, J. Cibert, Y. Gobil, G. Feuillet, K. Saminadayar, A.C. Chami and E. Ligeon, Appl. Surface Science **41/42**, 470 (1989).
- [9] P. Faurie, C. Hsu, S. Sivanathan and X. Chu, Surface Science **168**, 473 (1986)
- [10] A. Bourret and P.H. Fuoss, Appl. Phys. Lett. **61**, (9) 1034 (1992)
- [11] M. Kolodziejski, T. Filz, A. Krotz, W. Richter and D.R.T Zahn, J. Cryst. Growth **117**, 549 (1992)
- [12] I. K. Robinson, E. Vlieg and S. Ferrer, Phys. Rev. B **42**, 6954 (1990)
- [13] A. Bourret, J. L. Rouviere and J. M. Penisson, Acta. Cryst. A **44**, 838 (1988)
- [14] A. Ourmazd, D.W. Taylor, M. Bode and Y. Kim, Science **246**, 1751 (1989)
- [15] P.H. Fuoss and I.K. Robinson, Nucl. Instrum. and Methods A **222**, 164 (1984)
- [16] Y. Ichinose, private communication
- [17] M. Loubradou Thesis, Université de Grenoble, France (1990)
- [18] J.H. Van der Merwe, J. Appl. Phys. **34**, 123 (1963)
- [19] R. Bonnet, Philos. Mag. A. **43**, 1165 (1981)
- [20] A. C. Chami, E. Ligeon, R. Danielou and J. Fontenille, Appl. Phys. Lett. **52**, 1502 (1988)
- [21] G. Cohen-Solal, F. Bailly and M. Barbe, Appl. Phys. Lett. **49**, 1519 (1986)
- [22] D. Li, Y. Nakamura, N. Otsuka, J. Quiu, M. Kobayashi and R.L. Gunshor, J. Vac. Sci. Technol. **B9**, 2167 (1991)

QUANTITATIVE HREM STUDY OF THE ATOMIC STRUCTURE
OF THE $\Sigma(310)/[001]$ SYMMETRIC TILT GRAIN BOUNDARY IN Nb

WAYNE E. KING AND GEOFFREY H. CAMPBELL

Chemistry and Materials Science Department, University of California, Lawrence Livermore
National Laboratory, Livermore, CA 94550

ABSTRACT

We have used a non-linear least squares optimization method to deduce a model for the atomic structure of the $\Sigma(310)/[001]$ symmetric tilt grain boundary in Nb from high resolution electron micrographs (HREM) of a bicrystal prepared by diffusion bonding. The resultant model is similar to, but differs in detail from a theoretical prediction based on interatomic potentials which included angular forces thought to be important in the prediction of defect structures in body centered cubic metals. Results validate this approach as a step towards making HREM a quantitative technique.

INTRODUCTION

The atomic structure of the symmetric 36.9° tilt grain boundary with $[001]$ tilt axis forming a twin about (310) in Nb has been predicted in a related work by atomistic simulation,^{1,2} using interatomic interactions derived from the Embedded Atom Method (EAM)^{3,4} and the Model Generalized Pseudopotential Theory (MGPT).⁵ These models differ primarily by the absence or inclusion of angular dependent interactions. EAM potentials are of the pair functional type⁶ [Carlsson, 1990 #51] and incorporate the trend that higher coordination implies longer, weaker bonds. These potentials include no angular dependence of the atomic interactions. In contrast, the MGPT potentials incorporate angular-dependent 3- and 4-body interactions based on a model treatment of canonical d-bands.⁵

The $\Sigma(310)/[001]$ boundary in Nb is a case where the two models predict distinctly different interface structures.² The EAM predicts two possible structures, both with relative shifts of the adjacent crystals which break mirror symmetry on the atomic scale. In particular, EAM predicted, for both structures, a relative shift of the crystals along the tilt axis. In contrast, the MGPT predicts a fully mirror symmetric structure. The experimental observation by HREM along $[1\bar{3}0]$ revealed no relative shift of the lattices along the tilt axis.^{1,2} Further inspection of the images along $[001]$ indicate that the boundary atomic structure is mirror symmetric, which agrees with the prediction of the MGPT.^{1,2} The complex relationship that exists between the atomic structure of a grain boundary and the resultant HREM image has made it impossible to unfold the experimental images directly to obtain the atomic structure of the grain boundary. The conclusion that the experimental image is in agreement with the MGPT prediction was based on visual comparisons of experimental images with simulated images based on model structures.

In this report, we test the above conclusion by carrying out a refinement of the atomic structure of the $\Sigma(310)/[001]$ symmetric tilt grain boundary in Nb viewed by HREM along the tilt axis. We have used a method that is commonly employed in structure refinement by x-ray diffraction and in the analysis of γ -ray and x-ray spectra, namely unconstrained, non-linear, least-squares optimization.

BACKGROUND

It is the goal of a least-squares problem to fit a model, $f_i^{calc}(x)$, to experimental data, f_i^{obs} , and thus to minimize the residuals, $f_i(x)$

$$f_i(x) = \frac{f_i^{obs} - f_i^{calc}(x)}{W_i}, \quad (1)$$

where f_i^{obs} is the intensity value of the i th pixel in the experimental image, $f_i^{calc}(x)$ is the intensity value of the i th pixel in the simulated image based on the image model x , and W_i is the image which represents the uncertainty associated with measurement of the intensity of each pixel in the experimental image, that is,

$$\min \left[\sum_{i=1}^k f_i(x)^2 \right]. \quad (2)$$

In this context, x refers to the parameters governing the image simulation such as the location of the atomic columns projected along the viewing direction or the electron-optical imaging parameters and k is the number of pixels in the image.

This problem has been addressed in the current work using the MINPACK-1 unconstrained, non-linear, least-squares optimization code⁷ coupled with the EMS image simulation code.⁸ MINPACK-1 employs the Levenberg-Marquardt algorithm to solve the non-linear, least-squares problem.⁹ The algorithm relies on the calculation of the Jacobian matrix

$$\left(\frac{\partial f_i(x)}{\partial x_j} \right), 1 \leq i \leq k, 1 \leq j \leq s \quad (3)$$

which is used to correct the initial guess, x_o . Functionally, MINPACK-1 calculates $f(x_o)$ then uses the forward-difference approximation to calculate the Jacobian matrix. The algorithm then estimates a correction p to x_o such that

$$\|F(x_*)\| < \|F(x_o)\|, \quad (4)$$

where $x_* = x_o + p$ and $\|F(x_*)\|$ is the Euclidean norm of F

$$\|F(x_*)\| = \left(\sum_{i=1}^k f_i(x_*)^2 \right)^{1/2}. \quad (5)$$

This procedure is iterated with x_* replacing x until specific convergence criteria are met.⁷ In this work $s = 84$ (atom positions) and $k = 65,536$, which corresponds to a 512×128 pixel image. The EMS computational cell was 4.16×1.04 nm². Optimization required ~16 iterations corresponding to >1300 multislice calculations. Optimizations were run on a Silicon Graphics Personal IRIS 4D-35 and a Sun SPARCstation IPX.

PROCEDURE

High resolution images of a section of a $\Sigma 5(310)/[001]$ symmetric tilt grain boundary in Nb were acquired along the common $[001]$ zone axis under two different focus conditions which gave strong contrast of the $\{110\}$ fringes in the bulk crystals. The micrographs, shown in Figure 1, were acquired at an electron-optical magnification of 8×10^5 in a JEOL-4000EX high resolution electron microscope using Kodak SO-163 electron-image film. Negatives were developed in Kodak D-19 developer diluted 1:2 with water for 4.5 minutes at 20°C . Negatives were digitized using a $1024 \times 1024 \times 14$ bit Photometrics CCD array camera coupled with a Questar telescope. Using this configuration, digital images were acquired from the negatives at a resolution of 190 pixels/nm which is comparable with the resolution of image simulation. Digitized images, I , were corrected for pixel-to-pixel gain differences by normalizing the images to the so-called flat-field image, I_0 . Dark-current images were subtracted from both the experimental image and the flat-field image prior to making the flat-field correction.

Flat-field corrected images were corrected for nonlinearities in film response as described previously.¹⁰ Linearized images were normalized by the incident electron beam intensity measured from the unobstructed beam on the exposed negative. The resultant normalized images are dimensionally the same as those simulated using the EMS image simulation package.

Average, f_i^{obs} , and standard deviation images, σ_i^{obs} , of the unit cell of the $\Sigma 5(310)/[001]$ symmetric tilt grain boundary were calculated from eight unit cells extracted from the normalized images. Average and standard deviation images of the Nb unit cell viewed along $[001]$ were extracted from the f_i^{obs} and σ_i^{obs} grain boundary unit-cell images. Using this procedure, the random contribution to the image contrast due to the amorphous phase always present on the upper and lower surfaces of the sample resulted in the average image contrast being superimposed on a constant background. The background is included in the analysis by a modification of Equation 1

$$f_i(x) = \frac{f_i^{obs} - (f_i^{calc}(x) + b_i^{fit})}{W_i} \quad (6)$$

where b_i^{fit} is the fitted background. The overall effect of the background is to decrease the intensity



Figure 1. HREM images acquired from the same section of a symmetric tilt grain boundary in Nb produced by diffusion bonding at two defoci. Both images were acquired under "black-atom" contrast conditions.

of the electrons contributing to the image. Including uncertainties in linearizing the images, W_i was calculated as

$$W_i = \sigma_i^{obs} + 0.05 f_i^{obs}. \quad (7)$$

Optimizations were carried out to determine the critical imaging parameters, such as thickness and defocus, as described previously¹⁰ with the exception that in this work, experimental images were normalized by the incident beam intensity to bring the experimental and simulated images into dimensional consistency and the effect of background was taken into account.

Once the imaging parameters were established, the optimization of the atomic structure of the grain boundary was carried out. The starting "guess" for the atomic structure of the grain boundary was the coincidence-site-lattice model (CSL) construction which is illustrated in Figure 2 and described above (see also Ref. 2). Also shown in Figure 2 is the relaxed MGPT prediction.

RESULTS AND DISCUSSION

Results of the optimization of thickness and defocus are shown in Table I. f_i^{obs} , $f_i^{calc}(x)$, and $f_i(x)$ for the three images in Table I are shown in Figure 3. Figure 3a and Figure 3b were derived from opposite sides of the grain boundary in Figure 1a. Figure 3c was derived from the lower half of the image in Figure 1b. For an ideal fit, the values in the $f_i(x)$ image would be randomly distributed between -1 and +1. Deviations from a random distribution indicates a systematic deviation of the model from the experiment, which we believe in this case to be associated with specimen drift during the exposure. The background values are consistent with what we expect based on analysis of the contrast from the amorphous phase at the edge of the sample. The agreement between the results from Figure 3a and 3b is an important test for internal consistency of this work. In this analysis, we also optimized the parameters associated with crystal tilt and beam tilt. The results of the optimization indicated that there was a small difference in the alignment of the crystals on either side of the interface relative to the electron beam, a situation which is not unexpected. This difference was ignored in the grain boundary structure optimization since the simulation method employed was unable to easily include this complication. The values of thickness, defocus, and background shown in Table I along with the other parameters shown in Table II were applied in the structure optimization.

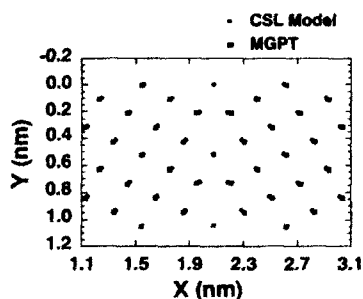


Figure 2. Comparison between the atom positions predicted by the MGPT and by the CSL model.

Figure 4a shows f_i^{obs} , $f_i^{calc}(x)$ based on the structure predicted by the CSL, and the resultant $f_i(x)$. The $f_i(x)$ images in Figure 4c indicate that the fit between experiment and simulation is acceptable. The region of interest comprises the 42 atomic columns surrounding the interface. It is evident from detailed comparison of the experimental image with the simulation that while these images are qualitatively in agreement (e.g. both exhibit mirror symmetry), they differ in the details of the contrast near the interface. Specifically, a four-sided contrast feature is ob-

Table 1. Optimized values for thickness, defocus, and background for the three images shown in Figure 3.

	Figure 3a	Figure 3b	Figure 3c
Thickness (nm)	5.9	5.9	5.9
Δf (nm)	34	32	-35
Background (normalized electron intensity)	-0.08	-0.11	-0.07

Table II. Image simulation parameters used for optimization of imaging parameters and boundary atomic structure.

Parameter	Value
Accelerating voltage (keV)	400
Debye-Waller Factor (nm^2)	0.0046
C_s (nm)	1.00
Defocus spread (nm)	8.5
absorption constant	0.03
lattice parameter (nm)	0.3361
convergence semi-angle (mrad)	0.7

served at the interface in the experimental image whereas the same feature comprises five sides in the simulated image. Therefore, we expect that there is a difference between the CSL and actual atom column positions.

The interface atomic structure was optimized using the f_i^{obs} data obtained from the image in Figure 1a. Positions of the 42 atomic columns in the center of the computational cell were optimized. Since the position of each column has two degrees of freedom, this gives rise to 84 free parameters. Figure 4b shows the f_i^{obs} , the $f_i^{\text{calc}}(x)$ based on the best-fit structure calculated using the non-linear least squares optimization, and the corresponding $f_i(x)$ image. The marked improvement in goodness-of-fit between Figure 4a and Figure 4b is evidenced by the reduction in absolute magnitude of $f_i(x)$ in the vicinity of the interface compared with Figure 3. The best-fit atom positions, superimposed on the $f_i^{\text{calc}}(x)$ image in Figure 4b show that there is a significant difference between the best fit atomic column positions and those of the CSL and

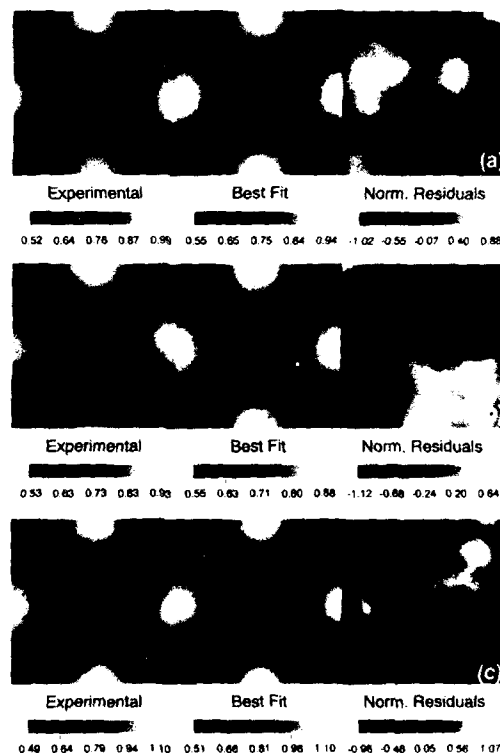


Figure 3. f_i^{obs} , $f_i^{\text{calc}}(x)$, and $f_i(x)$ for the three images in Table I.

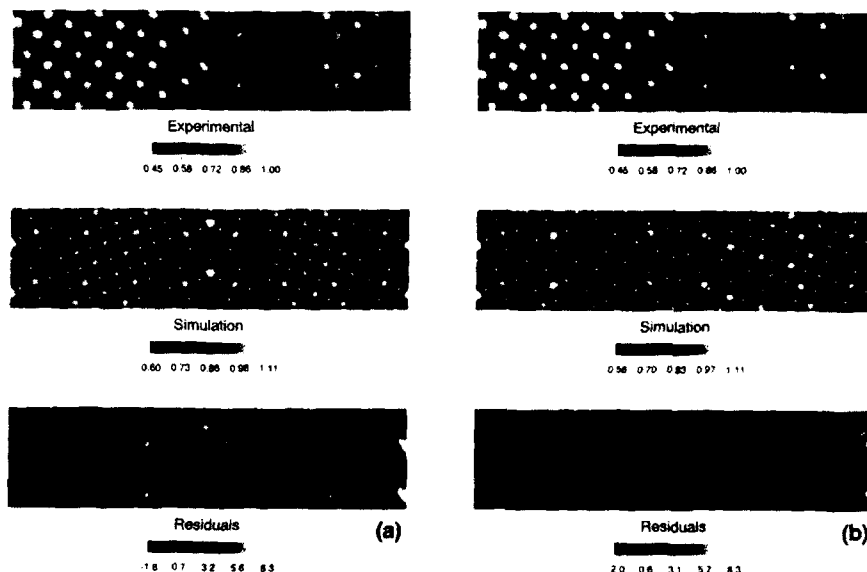


Figure 4. Results from the images shown in Figure 1a. (a) f_i^{obs} , $f_i^{calc}(x)$ based on the structure predicted by the CSL, and the resultant $f_i(x)$. (b) f_i^{obs} , $f_i^{calc}(x)$ based on the best-fit optimized structure, and the resultant $f_i(x)$.

MGPT. Specifically, there are sizable reduction in the (310) interplanar spacing in the immediate vicinity of the interface (one or two planes). Second, some atomic columns surrounding the interface break the mirror symmetry observed in the CSL and MGPT model. While the structure does not exhibit strict mirror symmetry, the contrast of the simulated image is in close agreement with the experimental image.

A second defocus value was investigated (Figure 1b). Figure 5 is analogous to Figure 4 except that the defocus for this image is 34 nm. Looking at the atom positions in the $f_i^{calc}(x)$ image, it is evident that similar, although not equal relaxations of the atomic columns are observed in the vicinity of the interface. The mirror symmetry predicted by the MGPT and evident in the experimental image, is broken immediately in the vicinity of this interface in the same way as in Figure 4, i.e. the atomic columns have moved in the same directions from the MGPT prediction. An atomic structure based on the weighted average positions from Figure 4 and 5 is shown in Figure 6. Also plotted in Figure 6 are the atomic column positions predicted by the MGPT.

CONCLUSIONS

Is the structure shown in Figure 6 the "real" atomic structure of the $\Sigma 5(310)/[001]$ symmetric tilt grain boundary in Nb? The results of our structural refinement indicate that in absence of error in estimation of thickness or defocus, the MGPT qualitatively predicts the structure of the grain

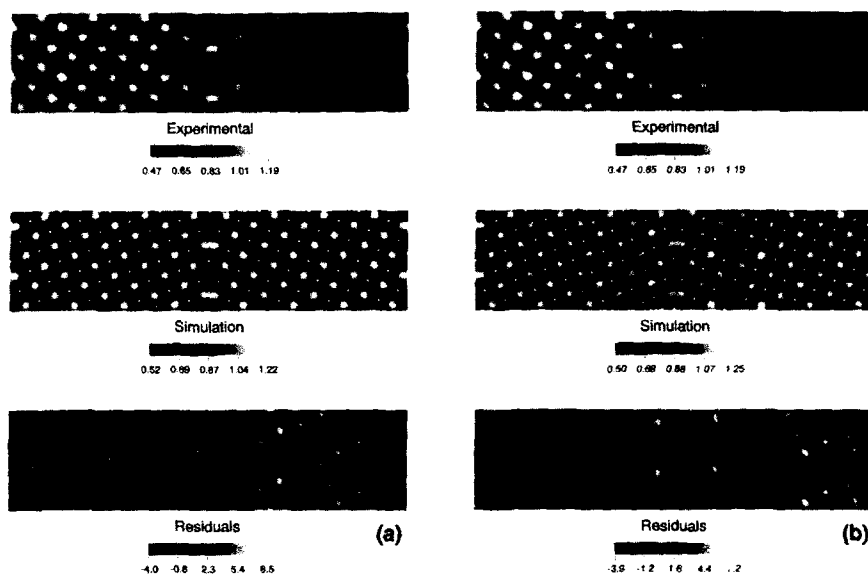


Figure 5. Results from the images shown in Figure 1b. (a) f_i^{obs} , $f_i^{calc}(x)$ based on the structure predicted by the CSL, and the resultant $f_i(x)$. (b) f_i^{obs} , $f_i^{calc}(x)$ based on the best-fit optimized structure, and the resultant $f_i(x)$.

boundary but is in error in the details. Specifically, the atomic column spacings nearest to the interface in the best-fit structure are smaller than that predicted from the MGPT. Currently, we believe the optimized model to be physically reasonable, i.e. there is no obvious reason why this structure may not exist. We have already noted in a previous work that the repulsive part of the MGPT potential is likely to be too stiff which could affect the boundary relaxations in the manner observed.¹¹ Verification of the validity of this new model requires additional structural refinements from HREM images of the same interface acquired at different defoci and calculation of the total energy of this interface using electronic structure methods and comparing that energy with that of the MGPT structure.

ACKNOWLEDGMENTS

The authors acknowledge useful discussions with Prof. W. M. Stobbs and Dr. M. J. Mills. This work performed under the auspices of the Division of Materials Science of the Office of Basic Energy Sciences, U. S. Department of Energy, and the Lawrence Livermore National Laboratory under contract No. W-7405-Eng-48.

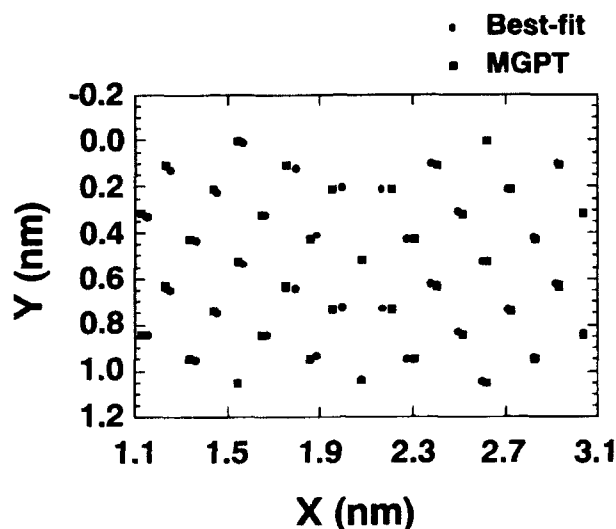


Figure 6. Comparison between the atom positions predicted by the MGPT and the best-fit positions resulting from the optimization.

REFERENCES

1. G. H. Campbell, S. M. Foiles, P. Gumbsch, M. Rühle and W. E. King. Phys. Rev. Lett., (1992); Submitted.
2. G. H. Campbell, W. E. King, S. M. Foiles, P. Gumbsch and M. Rühle in Atomic Scale Imaging of Surfaces and Interfaces, edited by B. K. Biegelson, D. S. Y. Tong and D. J. Smith (Mater. Res. Soc. Symp. Proc. 295, Pittsburgh, PA 1992).
3. M. S. Daw and M. I. Baskes, Physical Review Letters, **50** (17), 1285 - 1288, (1983).
4. M. S. Daw and M. I. Baskes, Physical Review B, **29** (12), 6443 - 6453, (1984).
5. J. A. Moriarty in Many - Atom Interactions in Solids, edited by R. N. Nieminen, M. J. Puska and M. J. Manninen (Berlin 1990) pp. 158 - 167.
6. A. E. Carlsson in Advances in Research and Applications, edited by H. Ehrenreich and D. Turnbull (Solid State Physics 43, New York 1990) pp. 1 - 91.
7. J. J. Moré, B. S. Garbow and K. E. Hillstom, User Guide for MINPACK-1, Argonne National Laboratory, ANL-80-74, 1980.
8. P. Stadelmann, Ultramicroscopy, **21** 131-146, (1987).
9. J. J. Moré in Lecture Notes in Mathematics, edited by G. A. Watson (Numerical Analysis 630, Berlin 1977) pp. 116.
10. W. E. King and G. H. Campbell, Ultramicroscopy, (1992); Accepted.
11. G. H. Campbell, S. M. Foiles, W. E. King, M. Rühle and W. Wien in Structure/Property Relationships for Metal/Metal Interfaces, edited by A. D. Romig Jr., D. E. Fowler and P. D. Bristowe (Mater. Res. Soc. Symp. Proc. 229, Pittsburgh, PA 1991) pp. 191 - 195.

HRTEM OBSERVATIONS OF A $\Sigma=3$ {112} BICRYSTAL BOUNDARY IN ALUMINUM

D.L. MEDLIN*, M.J. MILLS *, W.M. STOBBS**, M.S. DAW*, AND F. COSANDEY***

*Sandia National Laboratories, Livermore CA 94551, USA

**Department of Materials Science and Metallurgy, Cambridge University, Cambridge CB2 3QZ, UK

***F. Cosandey, Department of Mechanical and Materials Science, Rutgers University, Piscataway NJ 08854, USA

ABSTRACT

We present here a study of the $\Sigma=3$ {112} incoherent twin boundary in aluminum. Atomistic studies of this boundary indicate that several high energy boundary structures may exist, with the lowest energy structure exhibiting a small rigid body shift parallel to the boundary. The observations presented here indicate that the rigid body shift does in fact occur and that its magnitude, as well as the local grain boundary structure, is well predicted by atomistic calculations using the Embedded Atom Method. The low energy boundary configuration is much narrower than the equivalent boundaries that have been observed in the lower stacking fault energy FCC metals.

INTRODUCTION

Recent work has recognized that in gold [1], silver [2], and copper [3], the $\Sigma=3$ {112} incoherent twin boundary is dissociated, and can be thought of as a slab of 9R stacked material, roughly 10 Å thick, between two blocks of FCC material. The 9R stacking serves as an intermediate stacking arrangement to reverse the ABC stacking to CBA and is equivalent to an FCC stacking of {111} planes with an intrinsic stacking fault at every third plane [2]. Thus, it is likely that this dissociated structure is stabilized because of the low stacking fault energies of these materials (Au: 32 mJ/m²; Cu: 45 mJ/m²; Ag: 16 mJ/m²) [4]. By this explanation, the same boundary in a high stacking fault energy material, such as aluminum (Al: 166 mJ/m²), would be expected to be much narrower with little resemblance to the 9R packing. Indeed, atomistic calculations of the aluminum boundary using both the Embedded Atom Method (EAM) and pair potentials predict that the lowest energy boundary structure is quite narrow.

Such calculations also predict that the lowest energy structure should exhibit a small rigid body shift parallel to the boundary, the magnitude of which depends on the particular potential that is used. Interestingly, a recent HRTEM study of the $\Sigma=3$ {112} boundary, observed within an internally twinned grain of a polycrystalline aluminum film, found not the low energy, shifted structure, but instead, a mirror symmetric boundary that matched well with a higher energy calculated structure [5]. In this previous work it was noted that because the observations were made near a junction with the coherent twin, the boundary may have been physically constrained from relaxing to the shifted configuration. In order to resolve this issue, we present here a study of an aluminum bicrystal possessing only the $\Sigma=3$ {112} interface. Because the coherent twin boundary is absent, the physical constraints on translation present in the earlier study are eliminated, and the observed boundary should represent the fully relaxed state.

ATOMISTIC CALCULATIONS

Relaxed boundary structures were obtained from molecular statics calculations using the Embedded Atom Method (EAM) [6,7] with the Voter and Clein aluminum potential [8]. Starting configurations were generated both by varying the initial displacement of atoms on one side of the boundary from their CSL positions and by removing atoms from sites on the boundary. In order to allow for density changing relaxations perpendicular to the boundary, two types of starting cells were constructed. The first cell type was constructed with free surfaces, parallel to the {112} planes, with 40 Å thick slabs on either side of the boundary. The second cell type was periodically continued in the [112] direction (x) by truncating the structure at a proper lattice position such that an equivalent, but inverted, coherent twin

boundary was formed at the ends of the cell. The x dimension of the periodic cells was allowed to vary dynamically during the relaxation. Several different slab lengths were tested with equivalent results. In the directions parallel to the boundary, both cell types were periodically continued with fixed boundary lengths. The free surface cells were constructed with three periods in $[11\bar{1}]$ (y) and two in $[1\bar{1}0]$ (z), whereas the periodic cells had two periods in y and one in z.

As is summarized in figure 1 and table 1, three minimum energy configurations, consisting of one mirror symmetric structure (A) and two shifted structures (B and C), were obtained from these calculations. The mirror symmetric structure resulted only from the free surface cell, relaxed from its symmetric CSL position, whereas the two shifted structures were obtained for both cell types relaxed from several different initial states. The mirror symmetric structure has been shown previously to correspond to the structure observed near junctions with the $\{111\}$ coherent twin [5]. In contrast, structures B and C exhibit rigid body shifts, Δy , of differing magnitude parallel to the boundary: structure B is displaced by greater than half a $\{111\}$ spacing, whereas structure C is displaced by less than a third of a $\{111\}$ spacing. Consistent with the calculations of D. Wolf [9] for copper and gold, the calculated grain boundary energies scale roughly with the excess volume displacement perpendicular to the boundary, Δx , with structure C having both the lowest grain boundary energy and excess volume.

The core region of structure B is fairly wide with severe bending of the common $\{111\}$ planes as they pass through the boundary. Such bending is similar, though to a lesser degree, to what is both calculated and observed for the low SFE metals. Indeed, the boundary packing for structure B may be generated from the packing in the relaxed silver $\Sigma=3$ $\{112\}$ boundary, which consists of a slab of 9R a single unit cell wide [2], by the removal of one $\{112\}$ plane of atoms within the boundary.

The small shift structure (C) is similar to that published previously by Pond and Vitek [10] using a pair potential derived from pseudopotential theory. Δx and Δy in this structure are slightly larger (0.45 Å and 0.79 Å, respectively) than predicted by the EAM calculation. Interestingly, their alpha fringe measurements indicated a Δx of 0.21 Å, which is closer to the EAM calculation, and a Δy of 0.82 Å, which is closer to the pair potential calculation. In

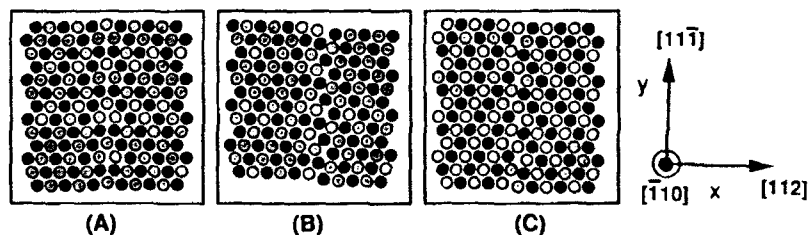


Figure 1. Boundary structures calculated using EAM for the aluminum $\Sigma=3$ $\{112\}$ $\langle 110 \rangle$ boundary.

Table 1. Calculated grain boundary energy and rigid body shifts (Δx is the excess volume displacement in the $[112]$ direction, Δy is in the $[11\bar{1}]$ direction parallel to the boundary).

	GB Energy (mJ/m ²)	Δx (Å)	Δy (Å)
Mirror Sym. (A)	327	0.40	0.00
Large Shift (B)	316	0.38	1.26
Small Shift (C)	223	0.33	0.68

analogy to the relationship between boundary B and the 9R structure, the boundary packing of structure C may be generated from the large shift structure by the removal of yet one more (112) plane, and thus is fully removed from the 9R structure which has been calculated for the lower SFE metals.

EXPERIMENTAL

Observations and Comparisons with image simulations.

The $\Sigma=3$ {112} $\langle 110 \rangle$ aluminum bicrystals, grown using a horizontal zone melting technique, were provided by C. Goux and M. Biscondi of the École Nationale Supérieure des Mines, St. Etienne, France. Thin foils were prepared by electrical discharge machining sections that were then electropolished in a solution of 70% methanol - 30% nitric acid. All observations were made on a JEOL 4000 EX electron microscope operated at 400 keV. Images were obtained from region of material within the first extinction contour indicating that the specimen thickness was less than 11 nm. Defocus values were measured from the peak and minimum positions in optical diffractograms. Images, digitized either from prints using a flatbed scanner or directly from negatives using a densitometer, were analyzed using the Semper 6 Image Analysis Software from Synoptics. Images from three defocus conditions are illustrated in figure 2. These images show clearly a shift of the common (111) fringes across the boundary. Image A is an overfocus condition corresponding to a focus of +30 nm, image B is at -30 nm defocus, and image C is at -70 nm defocus, which is near the first broad band.

Image simulations for the three structures predicted by the EAM were performed using the EMS package of simulation software [11] implemented on a Silicon Graphics workstation. The following were used as image simulation parameters: C_s : 1.0 mm; objective aperture diameter: 22.5 nm^{-1} ; spread of focus: 10 nm; semiconvergence angle: 0.9 milliradians; and specimen thickness: 5.7 nm.

Measurement of Boundary Displacements

In order to make a precise measurement of the shifts parallel and perpendicular to the boundary we have used a regression technique [12] that allows one to accurately track the mean position of a block of fringes on both sides of the boundary. Variations of this technique have been applied previously to a number of gold boundaries and found to have a precision on the order of 0.1 Å [13] although possible variations with defocus were not stated.

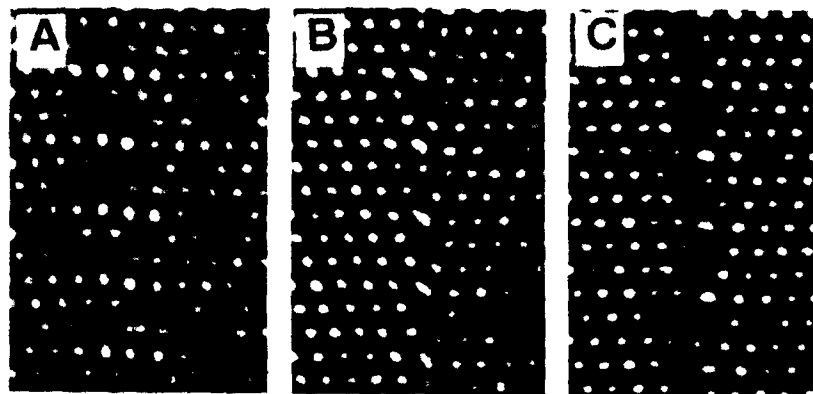


Figure 2. Experimental Images. (A) +30 nm, (B) -30 nm, (C) -70 nm defocus.

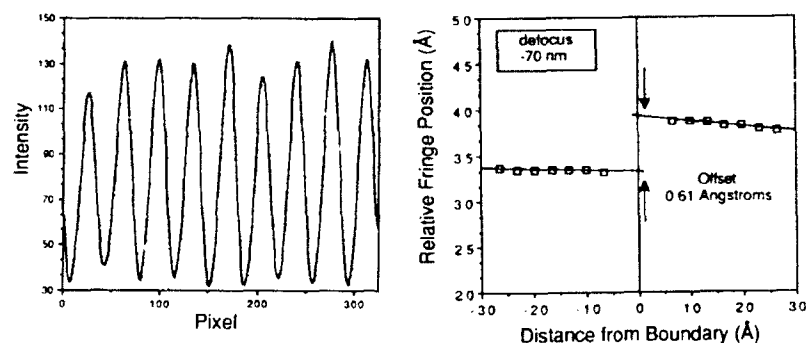


Figure 3. (a) (111) fringe intensities projected in the [112] direction for -70 nm defocus condition. (b) Trace of the relative (111) fringe positions extrapolated to the boundary plane.

Δy is measured by digitizing a small block of the image, in this case $7 \times 20 \text{ \AA}$, and averaging the intensities, in the x direction, of the common (111) fringes. As illustrated in figure 3a, this produces an averaged line profile of the fringe intensity. A peak search, refined by a local center of mass calculation, is used to locate the midpoints of each of the peaks which are then assigned an index number in order of occurrence. Plotting the peak position as a function of peak index produces a straight line whose slope is equal to the number of pixels per fringe, thus giving an internal calibration of the magnification. The intercept, or for greater statistical confidence, the value of the regression function evaluated at the mean peak index, provides a reference position for the block of fringes. By performing this analysis along a series of positions on both sides of the boundary, the relative position of the fringes within the block is accurately tracked. The rigid body shift is obtained by extrapolating the traces of the relative fringe position to the boundary (see figure 3b).

The excess volume shift perpendicular to the boundary is obtained by a similar procedure. However, in this case the image intensity is averaged in the y direction, and the regression analysis identifies a "best" position for two parallel (224) fringes based on the positions of the surrounding fringes. To avoid overlapping peaks, the averaging is over every third (111) fringe. Δx may be determined from the relative phase shift between the mean fringe locations from:

$$\Delta x = D \text{ modulo } d_{224} \quad (1)$$

where D is the distance between the fringe positions identified on both sides of the boundary by the regression procedure and d_{224} is the spacing between (224) planes (0.8266 \AA). However, in order to unambiguously determine Δx , the number of atomic planes between the two sites must be counted, in which case the displacement is given by:

$$\Delta x = D - n_p d_{224} \quad (2)$$

where n_p is the number of planes identified between the measured fringe locations.

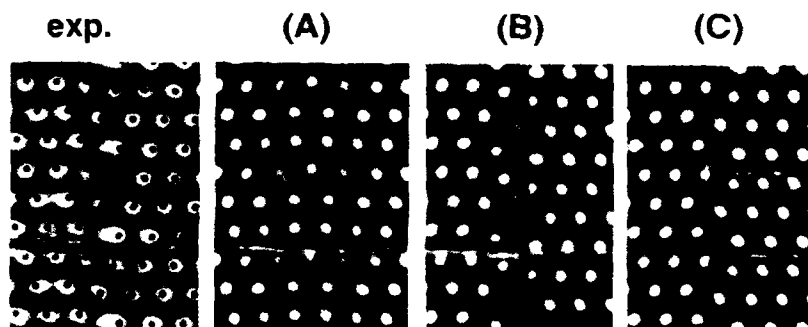


Figure 4. Experimental image compared with the simulated images for EAM structures A, B, and C ($C_s=1.0$ nm; objective aperture diameter: 22.5 nm^{-1} ; spread of focus: 10 nm ; semiconvergence angle: 0.9 milliradians; thickness : 5.7 nm). Peak positions from the low energy structure (C) are overlaid on the experimental image.

RESULTS AND DISCUSSION

A comparison of the -70 nm defocus image with images simulated for the three EAM boundary structures is shown in figure 4. Intensity peak positions from the simulated image for structure C (the lowest energy structure) are overlaid on the experimental image demonstrating that the local boundary structure, as well as the shift of the $(11\bar{1})$ planes, appears to be well predicted. These results are supported by the fringe shift measurements for Δy (see table 2) which indicate a displacement of $0.66 \pm 0.07 \text{ \AA}$, averaged over the three focus conditions. This displacement is much closer to the EAM calculation for structure C than for structure B.

The measurements of the excess volume displacement are somewhat more problematic. Although the Δx measurements for the $+30$ and -70 nm focus settings indicate an expansion 0.07 \AA larger than that predicted by the EAM, the values measured from the -30 nm defocus condition consistently gave a physically unlikely contraction relative to the bulk density. A possible cause for this effect is the presence of astigmatism which is sufficiently severe ($C_a = 15 \text{ nm}^{-1}$) that at this defocus the unshared $\{111\}$ fringes are imaged asymmetrically. Indeed, this result underscores the importance of good imaging conditions (namely, precise beam and specimen tilt, and proper astigmatism correction). The sensitivity of the particular measurement to these effects is only clear when the analysis is performed on images obtained at different defoci.

Table 2. Measured displacements perpendicular (Δx) and parallel (Δy) to the boundary and standard deviations of measurements.

Focus relative to Gaussian (nm)	Δx (\AA)	$\sigma_{\Delta x}$ (\AA)	Δy (\AA)	$\sigma_{\Delta y}$ (\AA)
+30 nm	0.42	0.05	0.64	0.05
-30 nm	-0.17	0.04	0.77	0.01
-70 nm	0.38	0.01	0.59	0.02
		Pooled Values :	0.66	0.07

SUMMARY

In conclusion, we have observed a rigid body shift parallel to the $\Sigma=3$ {112} boundary in an aluminum bicrystal. This result supports the hypothesis that the previously observed mirror symmetric structure was stabilized by its close proximity to a junction with the coherent {111} twin. The features of the local region compare well with image simulations for the lowest energy structure predicted by the EAM, and from precise measurements of Δy we can clearly discriminate between the two shifted structures, although the value of the excess volume displacement is not yet clear. The low energy structure is much narrower and localized than that for the same boundary in gold, silver, and copper, which is most likely due to the much higher stacking fault energy of aluminum.

ACKNOWLEDGEMENTS

The authors would like to thank Geoffrey Campbell of Lawrence Livermore National Laboratory for kindly making the densitometer measurements. This research is supported by the U.S. Department of Energy, BES-Materials Sciences, under contract DE-AC04-76DP00789.

REFERENCES

1. U. Wolf *et al.* Colloque de Physique (1) **51** C1:359-366 (1990).
2. F. Ernst *et al.* Phys. Rev. Lett. **69** (4) 620-623 (1992).
3. U. Wolf *et al.* Philosophical Magazine (to be published).
4. Hirth and Lothe, *Theory of Dislocations* 2nd ed. (Wiley, New York, 1982) p. 839.
5. J.M. Penisson, U. Dahmen and M.J. Mills, Phil. Mag. Lett. **64** (5), 277-283 (1991).
6. M.S. Daw and M.I. Baskes, Phys. Rev. Lett. **50**, 1285 (1983).
7. M.S. Daw and M.I. Baskes, Phys. Rev. B **29**, 6443 (1984).
8. A.F. Voter and S.P. Chen in *Characterization of Defects in Materials* (Mater. Res. Soc. Proc. 82, Pittsburg, PA, 1987) pp. 175-180.
9. D. Wolf, Scripta Metallurgica **23**, (1989) 1913-1918.
10. R.C. Pond and V. Vitek, Proc. Royal Society London B **357**, 453-470 (1977).
11. P. Stadelman, Ultramicroscopy **21**, 131 (1987).
12. W.M. Stobbs, G.J. Wood, and D.J. Smith, Ultramicroscopy **14**, 145-154 (1984).
13. K.L. Merkle, Ultramicroscopy **40**, 281-290 (1992).

ATOMIC STRUCTURE OF THE (310) TWIN IN NIOBIUM: THEORETICAL PREDICTIONS AND COMPARISON WITH EXPERIMENTAL OBSERVATION

GEOFFREY H. CAMPBELL,* S.M. FOILES,[†] M. RÜHLE,[§] AND W.E. KING*

*Lawrence Livermore National Laboratory, Livermore, CA, 94550, USA

[†]Sandia National Laboratories, Livermore, CA 94551, USA

[§]Max-Planck-Institut für Metallforschung, Institut für Werkstoffwissenschaft, Seestr. 92, 7000 Stuttgart 1, FRG

ABSTRACT

High - resolution transmission electron microscopy (HREM) has been used to characterize the atomic structure of the symmetric 36.9° tilt grain boundary with [001] tilt axes forming a twin about (310) in Nb. The projected structure was imaged along two different directions in the plane of the boundary and was compared to model structures through high - resolution image simulation. The atomic structure of this $\Sigma 5$ boundary was predicted with atomistic simulations using interatomic potentials derived from the Embedded Atom Method (EAM), Finnis-Sinclair (FS), and the Model Generalized Pseudopotential Theory (MGPT). The EAM and FS predicted structures with translations of the adjacent crystals which break mirror symmetry. The MGPT predicted one stable structure with mirror symmetry. The atomic structure of the (310) twin in Nb was found by HREM to be mirror symmetric. These findings indicate that the angular dependent interactions modeled in the MGPT are important for determining the grain boundary structures of bcc transition metals.

INTRODUCTION

Atomistic simulations which can model the interactions of many tens of thousands of atoms are increasingly used as a predictive tool in materials science and have the potential to play an important role in the overall understanding of the properties of materials,¹ such as the atomic structure of defects,² segregation,³ and fracture.⁴ The present investigation seeks to distinguish among several models of the interatomic interactions used in these types of calculations by comparing their predictions to experimental data. In particular, the interest is to assess the differences among the Embedded Atom Method (EAM),^{5,6} Finnis - Sinclair (FS),⁷ and the Model Generalized Pseudopotential Theory (MGPT)⁸ for predicting the atomic structure of defects in body centered cubic (bcc) transition metals. The predictive power of the EAM and FS for face - centered cubic (fcc) noble metals is well established (e.g. see references 2 and 9). Defect structures in bcc transition metals may be less easily predicted as compared to fcc metals owing to the partial filling of the d-bands which is expected to add an angular dependence to the interactions.¹⁰ Early work on bcc metals, however, proposed that the similar importance of the first and second nearest neighbor interactions was the dominant feature in stabilizing the bcc structure and determining the atomic structure of defects.¹¹

The grain-boundary simulations studied here differ primarily by the absence or inclusion of angular dependent interactions between the atoms in the theoretical model used to derive the potentials. The EAM and FS potentials are both of the pair functional type.¹⁰ They incorporate the trend that higher coordination implies longer, weaker bonds. However, they include no angular dependence of the atomic interactions. In contrast, the MGPT potentials incorporate 3- and 4-body interactions based on a model

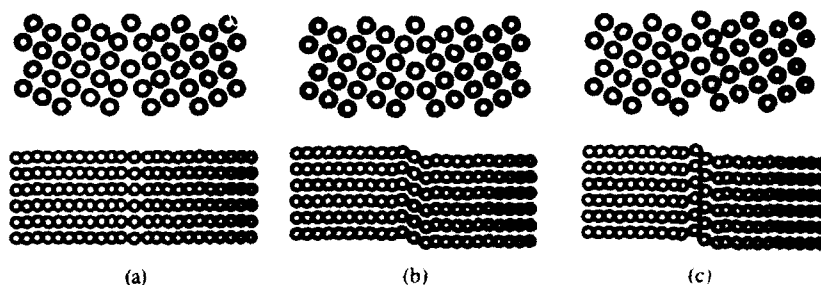


Figure 1: Model atomic structures of the (310) twin in Nb predicted by various interatomic potentials: (a) MGPT, (b) "Model 1" predicted by EAM and FS, and (c) "Model 2" predicted by EAM and FS. The model structures are shown in two orientations: The top row has a viewing direction parallel to the tilt axis, [001], while the bottom row is viewed perpendicular to the tilt axis, along $[1\bar{3}0]$.

treatment of canonical d - bands.⁸ Potentials which incorporate angular dependencies have been shown to correctly predict the reconstruction of Mo and W (100) surfaces.^{12, 13} Similar success has not been observed with pair - functional methods.¹⁴ Grain boundaries are more similar to bulk material than surfaces, possessing comparable coordination, but with different atomic arrangements. They should provide additional information on the importance of angular dependent interactions due to the presence of interatomic angles not present in the bulk. At present, little experimental data exist for grain boundary atomic structures in bcc transition metals.^{15, 16}

ATOMISTIC SIMULATIONS

The atomic structure of the symmetric 36.9° tilt grain boundary with [001] tilt axes forming a twin about (310) has been calculated using EAM,¹⁷ FS,¹⁸ and MGPT¹⁹ potentials for Nb. The size of the simulation cell was chosen corresponding to the expected periodicity of the grain boundary ($\Sigma 5$ within the Coincident Site Lattice²⁰ model). To explore the formation of different metastable grain boundary structures, many different translational states of the adjacent crystals were used as initial conditions for the energy-minimization calculation.

The simulations predict three model structures, shown in Fig. 1. The MGPT potential predicts a structure which exhibits mirror symmetry across the interface and is very close to a $\Sigma 5[001]/(310)$ unrelaxed structure. Within the MGPT, this structure was the only one found to be stable. As expected from the similarity of the methods, the use of the EAM and FS potentials lead to nearly identical results. They predicted several metastable structures. The two shown in Figs. 1(b) and 1(c) exhibited the lowest energies. There exist translational shifts between the adjacent crystals which differentiate "Model 1" and "Model 2" from the MGPT prediction. In Model 1 there is a relative shift in the crystal positions by a translation of 0.078 nm in the [001] direction, corresponding to half a (002) lattice plane spacing. Model 2 includes a crystal translation of 0.083 nm in the [001] direction as well as a translation of 0.052 nm in the $[1\bar{3}0]$ direction, which lies in the plane of the boundary. The mirror symmetric structure predicted by the MGPT is stable when simulated using EAM potentials, but the energy of the structure, 1.20 J/m², is significantly

greater than that of the two other structures, 1.03 J/m^2 for Model 1 and 0.98 J/m^2 for Model 2. Additionally, when Model 1 and Model 2 are used as the initial configurations for the MGPT calculation they are unstable and relax to the MGPT structure shown.

EXPERIMENT

High-resolution transmission electron microscopy (HREM) is a useful tool for characterizing the atomic structure of certain high symmetry grain boundaries.^{21,22} Likewise, theory is limited to studying "special" grain boundaries which are periodic in the plane of the boundary. Due to these limitations, the comparison between theoretically predicted grain boundary structures and experimentally characterized structures requires the fabrication of model grain boundaries which was done in this study by diffusion bonding of single crystals. Diffusion bonding allows complete freedom in the selection of the orientation of a bicrystal. HREM reveals atomic structure via comparison of experimental images with images simulated using a model atomic structure as the input.²³ The comparison of simulated with experimental images then allows the choice of the model which best fits the data.

Grain boundaries forming (310) twins in Nb were prepared by diffusion bonding two precisely oriented, to within $\pm 0.1^\circ$, Nb single crystals with flat - polished (310) surfaces which were misoriented by 180° about [310] relative to the perfect crystal.²⁴ Two projections are required for a complete HREM investigation. For this case [001] and [130], which lie in the interface, were chosen. Image simulation²⁵ was performed using the multi-slice formalism.²⁶

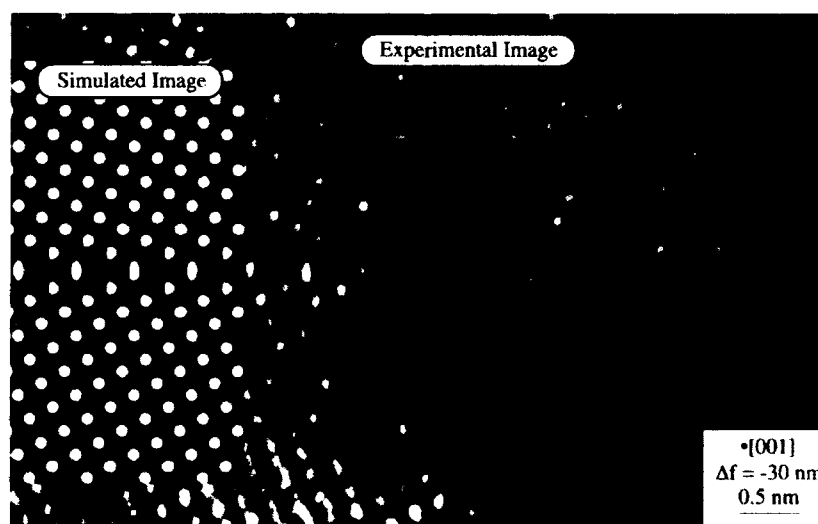


Figure 2: Comparison of an experimental image with a simulated image for the (310) twin in Nb as viewed along [001]. The simulated image uses the MGPT model atomic structure from Fig. 1, but the result would be identical if EAM and FS Model 1 were used. The positions of the atomic columns are indicated by white crosses.

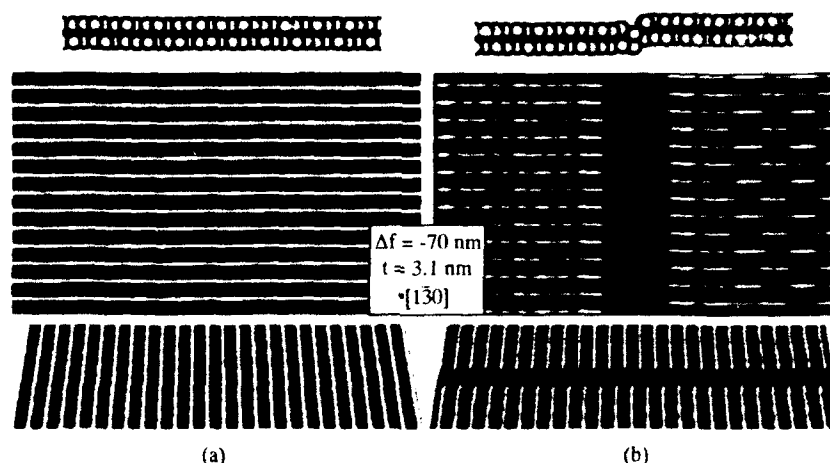


Figure 3: Simulated high resolution images using the remaining model (310) twin structures as viewed along $[1\bar{3}0]$ for (a) MGPT and (b) EAM and FS Model 1. The lattice fringe image arises from (002) planes with spacing of 0.165 nm. The bottom row of images are glancing angle, perspective views of the same images as in the row above to emphasize the displacement of the lattice fringes at the boundary for Model 1.

RESULTS AND DISCUSSION

Previous work has established the mirror symmetry of this boundary when viewed along $[001]$.²⁷ A HREM image is shown in Fig. 2 with a simulated image from the MGPT model shown as an insert. The symmetry of the boundary was confirmed by also comparing experimental and simulated images for other focus values as well.²⁷ Model 2 is thus inconsistent with experimental observation.

The $[1\bar{3}0]$ direction, orthogonal to the first viewing direction, is most suitable for the second projection of the grain boundary structure. This direction is shown in the second row of model structures in Fig. 1. The largest spaced atomic planes of Nb parallel to $[1\bar{3}0]$ are (002) and (310), with interplanar spacings of 0.165 nm and 0.104 nm, respectively. The spacing of the (310) are below the information limit of the microscope, which is approximately 0.14 nm. The (002) reflections will be the only ones contributing to the phase contrast image resulting in a lattice fringe image (Fig. 3). The (002) planes are perpendicular to the (310) twin plane and a relative shift of the adjacent crystals in $[001]$ (Model 1 and Model 2) should result in a discontinuity of the (002) lattice fringes at the interface (Fig. 3). Conversely, for the MGPT model, where no shift exists between the crystals, the (002) fringes are continuous across the interface. The experimental high - resolution image corresponding to this viewing direction is shown in Fig. 4. The (002) fringes run vertically and are seen, especially easily in the glancing - angle perspective view, to be continuous across the grain boundary. Thus, the results of the high - resolution microscopy indicate that the boundary atomic structure is mirror symmetric, which agrees with the prediction of the MGPT.

One limitation for all HREM studies is that the area of grain boundary probed is very small. For example, the area imaged in Fig. 2 is approximately 6 nm thick and 5 nm long.

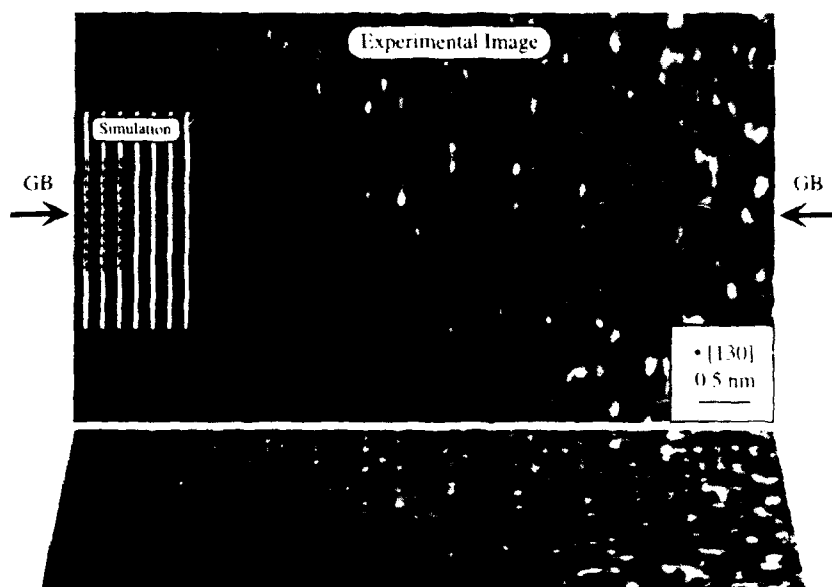


Figure 4: A high resolution image of the (310) twin in Nb as viewed along [130]. A simulated image based on the MGPT structure is shown as an insert, with the positions of the atomic columns indicated by black crosses. The boundary runs horizontally between the arrows. The bottom image is a glancing angle, perspective view of the same image to emphasize that the (200) lattice fringes run straight across the boundary without any displacements due to relative shifts of the crystals.

This sampling cannot rule out the possibility of grain - boundary structural multiplicity.²⁸ But the extensive facetting to the (310) plane at the diffusion bonding process temperature of 1500C indicates that the observed structure is of a relatively low energy compared to boundaries with small deviations in tilt angle from the exact $\Sigma 5$ (310) geometry. The facetting also suggests that the two high resolution images shown, although not from the same sample, came from boundaries having the same structure.

CONCLUSIONS

The success of the MGPT in predicting the atomic structure of the (310) twin in Nb is due to the incorporation of multibody interactions in the model. Partial filling of the d - bands in Nb imparts a directionality to the bonding, suggesting that these bond - angle effects may also be important for other central transition metals. The similar results obtained by the EAM and FS potentials indicate that their failure results from an inadequacy of pair - functional methods rather than from possible problems associated with the practical implementation of these potentials. These results indicate that multibody interaction models, such as the MGPT, which incorporate angular dependent interactions are required to predict defect structures in Nb and probably the other central transition metals as well.

ACKNOWLEDGEMENTS

This work performed under the auspices of the Division of Materials Science of the Office of Basic Energy Sciences, U. S. Department of Energy, and LLNL under contract No. W-7405-Eng-48. Part of this work performed while G. H. Campbell was at the Max-Planck-Institut für Metallforschung, Stuttgart, and was supported by the Alexander von Humboldt Foundation. We would like to thank Mr. W. Wien for his careful preparation of the Nb crystals, Mr. D. Korn for his assistance with the UHV diffusion bonding machine, Dr. J. A. Moriarty for providing the MGIT potential for Nb prior to publication and Dr. P. Gumbsch for the FS calculations.

REFERENCES

1. Atomistic Simulation of Materials, ed. V. Vitek and D. J. Srolovitz (Plenum Press, New York, 1989).
2. M. I. Baskes, S. M. Foiles and M. S. Daw, *Mater. Sci. Forum* **46**, 187 (1989).
3. S. M. Foiles, in *Surface Segregation Phenomena*, edited by P. A. Dowben and A. Miller (CRC Press, Boca Raton, FL, 1990) p. 79.
4. S. Kohlhoff, P. Gumbsch and H. F. Fischmeister, *Philos. Mag. A* **64** (4), 851 (1991).
5. M. S. Daw and M. I. Baskes, *Phys. Rev. Lett.* **50** (17), 1285 (1983).
6. M. S. Daw and M. I. Baskes, *Phys. Rev. B* **29** (12), 6443 (1984).
7. M. W. Finnis and J. E. Sinclair, *Philos. Mag. A* **50** (1), 45 (1984).
8. J. A. Moriarty, *Phys. Rev. B* **42** (3), 1609 (1990).
9. U. Dahmen, C. J. Hetherington, M. A. O'Keefe, K. H. Westmacott, M. J. Mills, M. S. Daw and V. Vitek, *Philos. Mag. Lett.* **62** (5), 327 (1990).
10. A. E. Carlsson, in *Advances in Research and Applications*, edited by H. Ehrenreich and D. Turnbull (Academic Press, Solid State Physics 43, New York, 1990) p. 1.
11. V. Vitek, D. A. Smith and R. C. Pond, *Philos. Mag. A* **41** (5), 649 (1980).
12. J. A. Moriarty and R. B. Phillips, *Phys. Rev. Lett.* **66** (23), 3036 (1991).
13. A. E. Carlsson, *Phys. Rev. B* **44** (13), 6590 (1991).
14. G. J. Ackland and M. W. Finnis, *Philos. Mag. A* **54** (2), 301 (1986).
15. J. M. Penisson, R. Gronsky and J. B. Brosse, *Scripta Metall.* **16**, 1239 (1982).
16. J. A. Moriarty, T. Nowicki and M. Biscondi, *Philos. Mag. A* **58** (6), 947 (1988).
17. R. A. Johnson and D. J. Oh, *J. Mater. Res.* **4** (5), 1195 (1989).
18. G. J. Ackland and R. Thetford, *Philos. Mag. A* **56** (1), 15 (1987).
19. J. A. Moriarty, in *Many-Atom Interactions in Solids*, edited by R. N. Nieminen, M. J. Puska and M. J. Manninen (Springer-Verlag, Berlin, 1990) p. 158.
20. W. Bollmann, *Crystal Defects and Crystalline Interfaces* (Springer Verlag, Berlin, 1970).
21. K. L. Merkle and D. Wolf, *Bull. Mater. Res. Soc.* **15** (9), 42 (1990).
22. P. Pirouz and F. Ernst, in *Metal-Ceramic Interfaces*, edited by M. Ruhle, A. G. Evans, J. P. Hirth and M. F. Ashby (Pergamon Press, New York, 1990) p. 199.
23. J. C. Barry, in *Computer Simulations of Electron Microscope Diffraction and Images*, edited by W. Krakow and M. O'Keefe (The Minerals, Metals, and Materials Society, Warrendale, PA, 1989) p. 57.
24. W. F. King, G. H. Campbell, A. Coombs, M. J. Mills and M. Ruhle, in *Defects in Materials*, edited by P. D. Bristowe, J. E. Epperson, J. E. Griffith and Z. Liliental-Weber (Mat. Res. Soc. Symp. Proc. 209, Pittsburgh, PA, 1991) p. 39.
25. P. A. Stadelmann, *Ultramicroscopy* **21**, 131 (1987).
26. J. M. Cowley and A. F. Moodie, *Acta Cryst.* **10**, 609 (1957).
27. G. H. Campbell, W. E. King, S. M. Foiles, P. Gumbsch and M. Ruhle, in *Structure and Properties of Interfaces in Materials*, edited by W. A. T. Clark, U. Dahmen and C. L. Briant (Mat. Res. Soc. Symp. Proc. 238, Pittsburgh, PA, 1992) p. 163.
28. K. L. Merkle and D. J. Smith, *Phys. Rev. Lett.* **59** (25), 2887 (1987).

QUANTITATIVE HIGH-RESOLUTION ELECTRON MICROSCOPY OF GRAIN BOUNDARIES IN α - Al_2O_3

T. HÖCHEL, P.R. KENWAY, H. J. KLEEBE and M. RÜHLE

Max-Planck-Institut für Metallforschung, Institut für Werkstoffwissenschaft, Seestr. 92,
D-W 7000 Stuttgart 1, F.R.Germany

ABSTRACT

Detailed structural characterization of a near $\Sigma 11$ grain boundary in ultra-pure α - Al_2O_3 bicrystals was performed by means of high-resolution transmission electron microscopy (HRTEM). High-resolution imaging revealed a characteristic periodic pattern along the grain boundary. In addition to HRTEM studies, atomistic simulations based on an ionic model were used to calculate three-dimensional structure models that were compared with the experimentally obtained images of the grain boundary. The comparison between the simulated and experimental HRTEM images showed good agreement for the theoretically proposed grain-boundary structure with the lowest grain boundary energy of 1.8 Jm^{-2} .

INTRODUCTION

The atomistic structure and distribution of internal defects such as grain boundaries are known to strongly influence the macroscopic properties of polycrystalline ceramic materials [1-5]. In order to control relevant material properties it is therefore important to characterize grain boundaries and to investigate how processing conditions can change their structures and consequently grain-boundary properties. However, commercially available polycrystalline materials with statistically distributed grain orientations and equiaxed, rounded grains are difficult to investigate using high-resolution transmission electron microscopy (HRTEM) owing to overlapping matrix grains and tilted grain boundaries.

In view of these difficulties and in order to study the atomistic structure of a grain boundary, a well defined interface in an ultra-pure α - Al_2O_3 bicrystal was investigated by HRTEM. The grain boundary discussed in this paper is a near $\Sigma 11$ grain boundary in which the two crystal halves terminate with (0111) and (0 $\bar{1}\bar{1}\bar{1}$) planes and which has a tilt of 35.2 degrees about the $[2\bar{1}\bar{1}0]$ -axis. We chose ultra-pure bicrystals because impurities will segregate to the boundary and complicate the determination of the atomistic interface structure.

These experimental investigations were correlated with theoretical studies on the grain-boundary structure. Such a comparison enables us to unambiguously define the three-dimensional environment of the atoms in the boundary, which is a prerequisite for further calculations on defect and impurity segregation and on the electronic structure of the grain boundary.

EXPERIMENTAL

$\text{Al}(\text{OH})_3$ powder was calcined using a CO_2 laser heat source until complete transformation into α - Al_2O_3 was confirmed by x-ray powder diffraction. Pellets were isopressed and fired using the laser-heating system. Growth and zone refinement (x2) of the feed rods were performed in an Ar-atmosphere. After single crystal growth, two seed-crystals were cut in defined directions and put together to form the bicrystal seed. The bicrystals were grown in an Ar-atmosphere using the seed composed of two times zone passed feed rods. Chemical analysis showed a total impurity content of less than 59 ppm [6]. TEM foils were prepared in the usual way with an edge on cross section of the grain boundary, i.e. the $[2\bar{1}\bar{1}0]$ -direction of each crystal was parallel to the foil normal.

HRTEM was performed using a JEOL 4000EX microscope operating at 400 kV acceleration voltage with a point-to-point resolution of 0.17 nm. In addition, electron-diffraction and Kikuchi patterns were analysed to verify bicrystal misorientation and parallel alignment of the $[2\bar{1}10]$ -zone axes.

The atomistic lattice simulations were performed using the MIDAS program [7] to calculate the grain-boundary and adhesion energy. HRTEM-image simulations were calculated using the EMS-package [8]. The IMSL/IDL program was used for comparing experimentally obtained and subsequently digitized images with the simulated images of theoretically suggested structure models. Noise reduction in the micrographs was achieved with a program for adaptive Fourier filtering of internal interfaces [9].

RESULTS AND DISCUSSION

The near $\Sigma 11$ (the Σ value referred to in this paper is a planar coincidence ratio $\Sigma_p(10)$) grain boundary investigated shows the expected tilt misorientation about the $[2\bar{1}10]$ -direction as shown in the electron diffraction pattern in Fig. 2. The corresponding tilt angle was determined to be 35.2 ± 0.2 degrees. However, analysis of Kikuchi patterns taken from thicker regions of the bicrystal revealed a slight misorientation of the $[2\bar{1}10]$ -axes of the two crystals on either side of the boundary. The Kikuchi patterns are rotated with respect to each other and additionally shifted.

After compensating for the intrinsic rotation owing to the tilt character of the grain boundary, the distance between equivalent points in both patterns was analysed. This distance corresponds to a tilt misalignment of both $[2\bar{1}10]$ -axes of less than 0.7 degree. The trace of the direction of this tilt projected parallel to the electron beam was determined to be 80 degrees inclined with respect to the normal of the common boundary plane of both crystals. As shown in Fig. 1 the grain boundary appeared to be atomically flat with adjoining planes $(0\bar{1}11)$ and $(01\bar{1}1)$. Very few facets of the $(0\bar{1}11) // (01\bar{1}4)$ type were observed, each having a step height of about a nanometer.

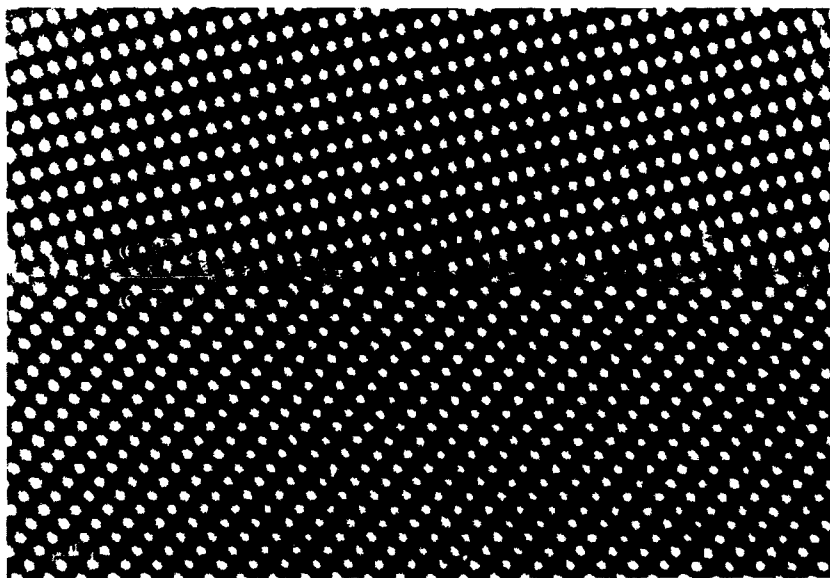


Figure 1: The near $\Sigma 11$ grain boundary in the α - Al_2O_3 bicrystal

It is important to note that TEM foils were prepared from two bicrystals grown with slightly different seed preorientation. Despite these minor deviations in starting orientations, the grain-boundary structure was found to be identical in both samples. The appearance of an identical grain-boundary structure in two bicrystals, grown under slightly different preorientations of the crystal seeds, seemingly suggests that the observed interface is of low energy configuration. This experimental observation is supported by theoretical arguments discussed later. The observed interface structure shows a periodicity of 1.363nm. This distance corresponds with the diagonal of the α - Al_2O_3 elementary cell projected along the $[2\bar{1}10]$ -direction. HRTEM-images of the edge-on interface could be obtained using the Fresnel fringe technique (symmetric Fresnel fringes at strong underfocus conditions) to align the specimen in the microscope.

The HRTEM images do not reveal the atomistic structure of the grain boundary directly. The atomistic structure of the interface is obtained by comparing a simulated HRTEM image of a model structure with the experimental HRTEM image. The model structure is then modified by various criteria until the simulated and observed images match.

The atomistic interface structure of the grain boundary was generated by constructing two separate crystal slabs with surfaces terminating with $(0\bar{1}11)$ - and $(01\bar{1}\bar{1})$ -planes and putting them together. These two planes are not mirror related in the α - Al_2O_3 structure, because the stacking sequence of the aluminium atoms along the $[0001]$ -direction has no mirror plane. Consequently, the stacking sequences of the atomic planes perpendicular to the $(0\bar{1}11)$ - and the $(01\bar{1}\bar{1})$ -planes are different and are: OAIOAIO and AIOOOAIO, respectively. The two slabs comprising the bicrystal can each terminate in different planes which have different compositions and atomistic environments. For example, at the $(0\bar{1}11)$ surface, there are five possible terminations: three different oxygen terminations and two different aluminium terminations. The combination of the two slabs to form the bicrystal leads to 25 possible boundary combinations. As unreconstructed pure boundaries which have dipolar stacking sequences perpendicular to the interface plane are unstable, the number of these boundary combinations that needs to be considered are greatly reduced. In fact, only one of these boundary structures is non-dipolar. This model structure was refined until the agreement between the simulated image and the observed image of the grain boundary was maximised. This was achieved by using atomistic lattice simulation. In this approach, a potential is used to calculate the energy and forces acting on the atoms. The potential used is based on the Born Model [11] of solids and includes a long-range-attractive-Coulombic interaction and a short-range-repulsive interaction. Ion polarisability is also included via the Shell Model [12]. The grain-boundary-core structure was then embedded between two pure crystals terminating with $(0\bar{1}11)$ - and $(01\bar{1}\bar{1})$ -planes and the atoms within the grain-boundary core were relaxed until

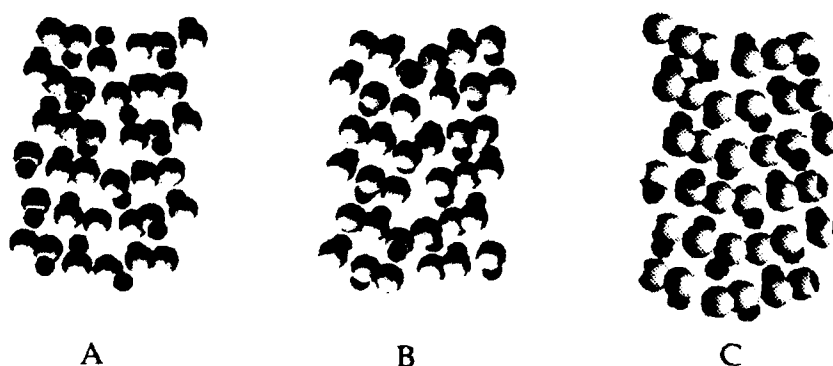


Figure 2: Three different starting structures resulting in different relaxed configurations (larger balls indicate oxygen atoms, smaller balls are aluminium atoms)

there were no net forces acting on them (mechanical equilibrium). The crystal blocks were also allowed to rigidly translate perpendicular and parallel to the boundary and the size of the grain boundary core was increased so that the grain boundary energy had converged. This approach is encoded in the MIDAS computer program [7]. It was found that different relaxed configurations of the grain boundary could be obtained by using starting configurations which differed in the relative displacements of the two crystal blocks. For comparison, the structures of three relaxed boundaries are given in Figure 2 and their energies and excess volumes are given in Table 1. The boundary with the lowest energy of 1.8 Jm^{-2} (see boundary C in Figure 1), has the highest density of atoms in the boundary (smallest excess volume). The structure of the present boundary is such that the repulsive short range and Coulombic interactions have been minimised, and the attractive Coulombic interactions maximised.

structure	relaxed energy (Jm^{-2})	adhesion energy (Jm^{-2})
A	7.9	1.5
B	2.5	-4.0
C	1.8	-4.7

Table 1: Grain-boundary and adhesion energy of the 3 structures depicted in Figure 2

In order to analyse the complicated interface structures, image simulations of the bulk material must first be matched with experimentally imaged regions of the bulk material. This was done automatically by comparing experimental images of the bulk region with the simulated HRTEM images of structure C using image processing routines. Digitized images of both the bulk region and the interface were Fourier filtered using a program for noise reduction in images of internal interfaces. Losses due to Fourier filtering were excluded by calculating the difference picture of the filtered and unfiltered micrograph and by analysing it with respect to changes of the image of the interface as an effect of the filtering procedure. The relative translation of the two crystals forming the grain boundary was determined by measuring the angles between corresponding points. To get the accuracy of relative rigid-body translation the two crystal halves were shifted with respect to each other in the computer parallel and perpendicular to the grain boundary. The simulated HRTEM images of the shifted structure C indicate that the translational deviation parallel and perpendicular to the interface is reproduced to better than 0.02nm .

The atomistic simulations described previously provide calculated atomistic grain-boundary structures. These models have the shape of supercells containing the grain boundary and are periodic in two directions parallel to the interface. For each of the theoretically calculated model structures the resulting HRTEM image was simulated using optimum thickness and defocus values. The comparison of the experimental and the calculated image was done by subtracting the intensity-normalised experimental image and the shift-optimised and intensity-normalised simulated image (compare Fig. 4). The sum of the pixel intensities was used as a measure of similarity. The simulated image that showed best fit with the experimentally obtained micrograph is depicted in Fig. 3 (boundary C). As outlined by the kites, all white spots that are observed in the experimental image are reproduced in the simulated image. Some minor features of the HRTEM image - especially the interconnections between white spots - are not reproduced by the simulated image of structure C. To see if these features were introduced by relaxations of the atoms in the boundary when setting up structure C, the simulated image of the unrelaxed structure of C was generated. The simulated images are compared in Fig. 4 (i and ii) and it can be seen that the relaxation is not the source of the minor differences between theory and experiment.

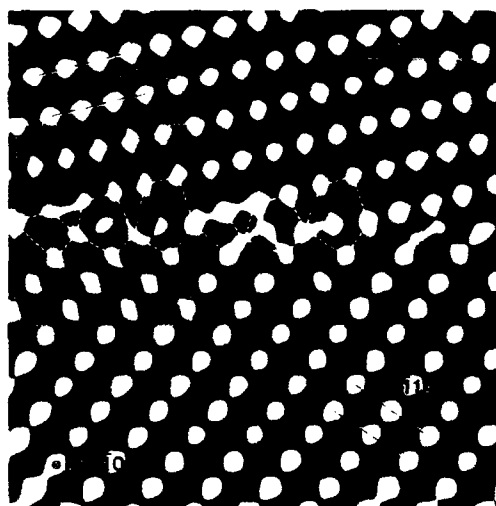


Figure 3: Fourier filtered experimental images of the near $\Sigma 11$ grain boundary in an α - Al_2O_3 bicrystal, inset: simulated image resulting from structure C in Fig. 2 at Scherzer defocus (50nm), specimen thickness $\approx 40 \text{ \AA}$

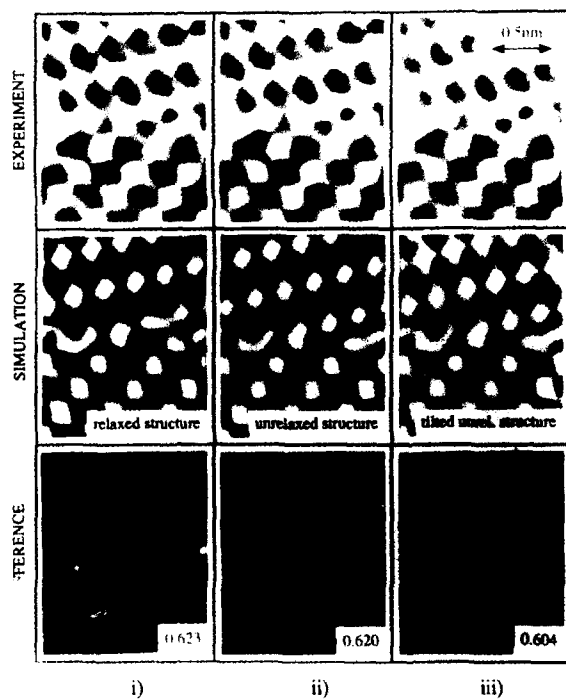


Figure 4: Comparison of experimentally observed (upper row) and simulated HRTEM images (middle row) by calculating the difference picture (lower row); the numbers in the lower right corner of the difference pictures indicate the sum of the pixel intensities contained in the picture, i.e. a lower number indicates a better agreement than a high number:
column (i): relaxed structure C; column (ii): structure C before relaxation; column (iii): unrelaxed structure tilted in the way described in the text

As mentioned above, Kikuchi patterns recorded on both sides of the boundary revealed a slight misorientation of the two crystals of 0.7 degree. To analyse whether the effect of such a misalignment of the zone axes on the image contrast is important, a supercell containing the α - Al_2O_3 interface was multiplied by 8 in the z-direction. This huge cell was cut along the interface and afterwards symmetrically tilted about 0.7 degree (0.35 degree each side) in 80 degree trace inclination to the grain-boundary normal. The contents of the wedge arising from this procedure was not altered, i.e. it consists of vacuum. New slices perpendicular to the former z-axis were cut and fed into the multislice program yielding the exit-face wave function of the tilted structure. The resulting images of the untilted and the tilted model are depicted in Fig. 4. The only minor effect of tilting on the image contrast is mainly due to the thinness of the investigated specimen of $\sim 5\text{nm}$. The importance of this part of the study is, that the degree of similarity measured in the above mentioned manner slightly increased (3%) with respect to the unrelaxed, untilted model. This means that the explanation of the minor deviations is presumably based on this small misalignment in tilt. At present, it is not possible to incorporate the tilt into the atomistic lattice simulation of model C because the necessary supercell is too large for the available computer resources.

SUMMARY

The application of HRTEM to α - Al_2O_3 bicrystals in conjunction with atomistic calculations of the corresponding grain-boundary structure is described. A near $\Sigma 11$ 35.2° tilt grain boundary with the $(0\bar{1}11) // (01\bar{1}1)$ interface was studied. Good agreement between experimentally observed and theoretically calculated HRTEM images was obtained for the most stable structure (grain boundary energy of 1.8 Jm^{-2}) that was considered. Rigid-body translations parallel and perpendicular to the interface were reproduced to better than 0.02nm .

ACKNOWLEDGEMENTS

P.R.K. acknowledges the financial support of an Alexander-von-Humboldt fellowship. The authors thank P.A. Morris, currently working at Du Pont, Wilmington, Delaware, U.S.A., who prepared the ultra-pure bicrystals.

REFERENCES

1. R.M. Cannon, W.H. Rhodes and A.H. Heuer, *J. Am. Ceram. Soc.* **63**, 46 (1980).
2. L. Priester and S. Lartigue, *J. Europ. Ceram. Soc.* **8**, 47 (1991).
3. E. Moya and F. Moya, in Non-stoichiometric Compounds, Surfaces, Grain Boundaries and Structural Defects, edited by J. Nowotny and W. Weppner (Kluwer Academic Press, Rottach-Egern, 1988), p.363
4. M. L. Kronberg, *Acta Met.* **5**, 507 (1957).
5. I.-W. Chan, and L.A. Xue, *J. Am. Ceram. Soc.* **73**, 2585 (1990).
6. P.A. Morris, PhD thesis, M.I.T. Cambridge, MA, 1986.
7. J.H. Harding, Report No. R 13127, AERE Harwell Laboratory, 1988.
8. P.A. Stadelmann, *Ultramicroscopy* **21**, 131 (1987).
9. G. Möbus, G. Necker, and M. Rühle, *Ultramicroscopy* (in press).
10. R.P. Fortunée, M.S. thesis, Case Western Reserve University, 1981.
11. M. Born and K. Huang, Dynamical Theory of Crystal Lattices, (Oxford University Press, Oxford, 1954).
12. B.G. Dick and A.W. Overhauser, *Phys. Rev.*, **90**, 112, (1958).

COMPARISONS OF OBSERVED AND SIMULATED ATOMIC STRUCTURES OF Pd/NiO HETEROPHASE INTERFACES

M. I. BUCKETT, J. P. SHAFFER, AND KARL L. MERKLE

Materials Science Division, Argonne National Laboratory, Argonne, IL 60439

ABSTRACT

High-resolution electron microscopy (HREM) and image simulations using the multislice algorithm have been used to study the atomic structure of a Pd/NiO (111) interface in an internally oxidized sample. Samples prepared in this way result in cube-on-cube oriented or twin-related precipitates whose (111) interfaces exhibit a contrast modulation along the boundary plane in HREM images. Previous studies have reported that the observed structural period of this modulation corresponds qualitatively to the expected spacing if the boundary was composed of a network of misfit dislocations. In this study, rigid models of the (111) interface as viewed from the [110] direction were simulated using the EMS suite of programs. The questions we address are: (1) whether the terminating plane on the oxide side is made up of a Ni or an O layer, and (2) whether a rigid body translation normal to the interface exists. Finally, the results of the simulations are compared and contrasted to through-focal experimental images to investigate the origin of the contrast modulations and their possible relation to the extent of the misfit localization in these systems.

INTRODUCTION

Metal/ceramic interfaces are playing an increasingly important role in the development of high performance materials for new and existing technologies. Despite the wide range of interest, very little is presently known about the atomic structure and interactions which fundamentally control the interfacial properties of these systems. Recent high resolution electron microscopy studies of simple fcc metal/metal-oxides have provided some insight into the question of atomic structure of heterophase interfaces [1-4]. These types of boundaries are readily prepared for HREM by internal oxidation of an alloy with very low (< a few atomic percent) solute concentration. When annealed in an appropriate partial pressure of oxygen, precipitation of the solute-oxide phase occurs such that the low energy interfaces make up the precipitate faces. A low-index cube-on-cube or twin orientation relation generally develops between the precipitate and matrix, thus making HREM studies feasible. Metal/metal-oxide interfaces which have been prepared in this way and studied by HREM include Pd/NiO [1], Cu/NiO [1], Ag/CdO [2], Pd/MgO [3], Cu/MgO [3], Cu/Al₂O₃ [4] and Nb/Al₂O₃ [5]. Other than in our own studies [6], HREM image simulations of fcc metal/metal-oxide systems have been performed only for Ag/CdO and Cu/MgO. For the Ag/CdO case, it was concluded that the (111) interface was incoherent. For the Cu/MgO case, it was concluded that the (111) interface was partially coherent, being made up of a network of misfit dislocations. Both studies, however, provided only limited qualitative comparison of *experimental* to *simulated* images to support their conclusions.

The objective of the present study is to provide detailed comparisons of experimental to simulated HREM images of the (111) cube-on-cube interface in Pd/NiO viewed along the [110] beam direction in order to evaluate the local atomic arrangements as well as the local defect structure, specifically addressing the question of coherence across the interface. The questions of whether the boundary plane on the oxide side is terminated with an oxygen or a nickel layer and whether a rigid body translation exists normal to the boundary (volume expansion) are addressed. HREM simulations for a number of cases were performed: (1) rigid model with an oxygen plane as the terminating layer on the oxide side and no expansion normal to the interface; (2) rigid model with a nickel plane as the terminating layer on the oxide side and no expansion normal to the interface; (3) rigid models with an oxygen termination layer on the oxide side and with 0%, 5%, and 10% expansions of the (111) plane spacing at the interface. For comparison, simulations of rigid models (oxygen terminated, no relaxations) of the higher misfit Cu/NiO and Cu/MgO (111) interfaces were also performed.

EXPERIMENTAL

A Pd-0.03Ni (at%) alloy was heat-treated in air at 1273 K for 3 hr to produce NiO pre-

cipitates sufficiently large for HREM investigation. Additionally, the samples were equilibrated in an Ar-0.02% O₂ atmosphere for 17-24 hr and slow-cooled to room temperature to minimize the residual strains. HREM was performed on a JEM4000EX microscope operating at 400 keV.

Image simulations were performed using the multislice routines in the EMS suite of programs [7]. A diagram illustrating the periodic supercell used for the simulations is shown in Fig. 1(a), with the dimensions of the supercell being given in Table I. The supercell was built up by stacking 28 (220) planes on the NiO side and 30 (220) planes on the Pd side. A total of 12,456 atoms were included in the simulation. The parameter dx represents the width separating the two halves of the supercell. To produce simulations which include volume expansion, this width was varied by some fractional amount. It was also determined that by allowing a vacuum fraction equal to one quarter of the total supercell length normal to the interface plane, the problem of aliasing was sufficiently avoided. Instrumental parameters were as follows: $C_s = 1.0$ mm, rms focal spread = 8 nm, semi-convergence angle = 0.5 mR, and objective aperture radius = 6 nm⁻¹. Debye-Waller factors of 0.005 nm for oxygen and 0.003 nm for both Ni and Pd were used. No absorption corrections were included.

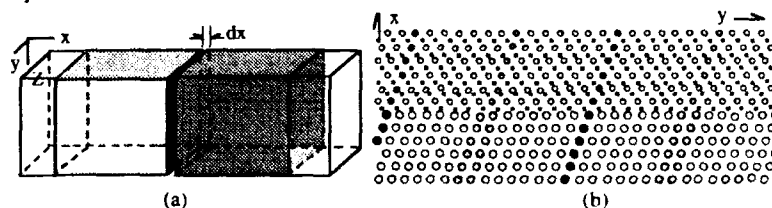


Fig. 1 a) Supercell used for the multislice calculations. b) Graphic representation of the projected atom positions at the Pd/NiO interface. Large circles = Pd; small circles = Ni; squares = O. Shaded regions show where projected planes are in minimum (light) and maximum (dark) coincidence. x = dimension perpendicular to interface; y = dimension parallel to interface.

The problem of sufficient sampling was considered in detail. A comparison of the sampling parameters used in the present study to those for the previous work on Ag/CdO and Cu/MgO is shown in Table I. In each case it was found that to faithfully reproduce the contrast effects in the boundary, sampling resolution of at least 0.1 Å was necessary. To obtain quantitative information on the volume expansion, an even finer sampling resolution would be desirable. To achieve these values, the EMS routines were modified to allow a maximum array size of 2048 x 1024.

TABLE I

System	Supercell Dimensions (Å)		Array Size	Real Space Sampling (Å)	
	x	y		x	y
Pd/NiO	77.56	71.60	1024 x 1024	0.08	0.07
Cu/NiO	71.37	30.07	1024 x 1024	0.07	0.03
Cu/MgO	71.94	30.95	1024 x 512	0.07	0.06
Cu/MgO[3]	64.0	15.5	512 x 128	0.12/0.19	0.12/0.18
Ag/CdO[2]	46.74	40.25	512 x 512	0.14	0.12

RESULTS AND DISCUSSION

The (111) interface on the oxide side is composed of alternating O²⁻ and Ni²⁺ planes. The question of whether multislice simulations could determine the identity of the terminating plane at the interface was explored by simulating both types of structures as outlined in the previous section. For the oxygen termination, the interatomic distance between the Pd and O atoms in PdO (0.201 nm) was used to calculate dx (0.108 nm). For the nickel termination, an average lattice parameter for the Pd-Ni alloy was used to calculate dx (0.214 nm). Typical results from the simulations are shown in Figure 2. In each of the through-focal (-10 nm to -140 nm) and through-thickness (4.1 nm, 5.9 nm, 7.4 nm, and 8.3 nm) conditions, a clear distinction between the O-terminated and Ni-terminated interface could be determined. A characteristic feature of the O-terminated structure is the periodic contrast modulation along the boundary. Using the NiO (112) projected plane spacings as a guide (0.256 nm), the periodicity is seen to be broken up into regions approximately 9 spacings and 5 spacings in length. The result is a strong periodic

contrast modulation along the interface, which is consistent with the experimental observations. The Ni-terminated structure gave rise to either a very weak modulation or no modulation in contrast along the interface. Using quantitative measurement techniques as outlined in reference [8], we found that the O-terminated structure perpendicular to the interface also gave a statistically better match to the through-focal experimental images than the Ni-terminated structure. A more detailed description of this comparison is given in the next section.

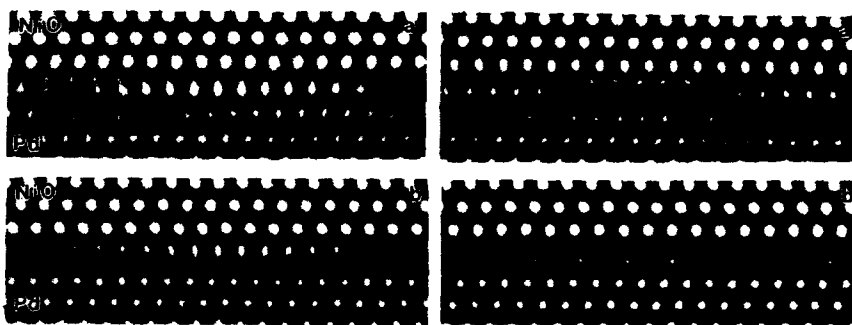


Fig. 2 Comparisons of O-terminated (left) to Ni-terminated (right) Pd/NiO [110]/(111) interface simulations. Thickness = 8.3 nm. a) -12 nm; b) -64 nm. NiO is above interface. Pd is below.

The presence of a rigid body translation normal to the boundary (volume expansion) was explored by incorporating 5% and 10% expansions in the dx value of the O-terminated structure described previously. An example comparison of the experimental observation to the 0% and 10% cases is shown in Figure 3. The volume expansion in each case was determined by using a linear least-squares fit to the centers of gravity of a set of peak positions ('white dot') or valley positions ('black dot') on both sides of the boundary. This procedure was repeated for multiple images within the through-focal series. For the example in Fig. 3 (thickness = 8.3 nm), a volume expansion of 0.001 ± 0.007 nm was derived for the experimental images. It should be noted that the measurement technique could easily distinguish statistical differences between the 0%, 5%, and 10% simulations. These results indicate that essentially zero volume expansion is associated with this interface when account is taken of the statistical errors of the measurement itself coupled with the sampling resolution of the simulations. It also illustrates the importance of sampling to better than 0.1 Å for interfacial simulations.

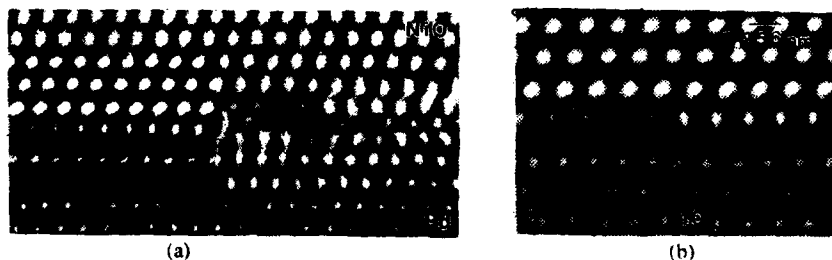


Fig. 3 (a) Experimental image with 0% volume expansion simulation inset. (b) Comparison of the 0% simulation to the 10% simulation.

Based simply on geometric considerations [9], pure misfit boundaries such as the (111) interface in the fcc metal/metal-oxides are predicted to form a network of misfit dislocations with Burgers vectors of the type $\mathbf{b} = a/2[110]$ and line vectors along $\langle 112 \rangle$ directions. This is illustrated in Fig. 4 for a hexagonal type of network. For two lattices of spacings a_1 and a_2 , the network spacing (D) is given by $D = |b|/|\partial|$, where $\partial = (a_2 - a_1)/a_1$. In the Pd/NiO system, D is approximately 4 nm.

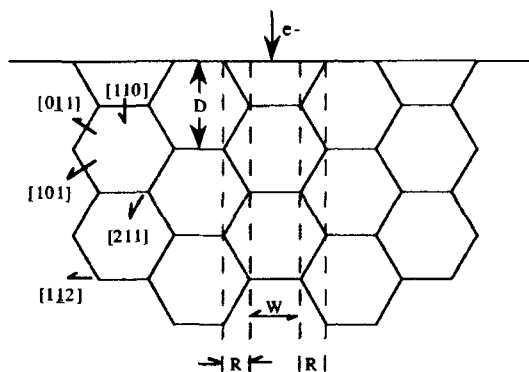


Fig. 4 Misfit dislocation model based on geometric considerations.

Although HREM and weak-beam dark-field microscopy are standard techniques used for the general study of misfit dislocation networks, there are inherent difficulties associated with both in imaging of the (111) interface of pure misfit fcc metal/metal-oxide systems. Even though weak-beam dark-field imaging will not be addressed in this paper, it should be noted that there are complications in interpretation which arise when the dislocation spacing is of the same order as possible moiré fringe spacings [10]. Also, the dislocation network spacings in many of these high misfit systems are below the resolution limit of the technique. The difficulties in the HREM case arise because the atomic positions in the defect structure are not always projected along atomic columns parallel to the beam when viewed along [110] (the 'structure image' direction). This can be clearly seen in Fig. 4. In region R, two sets of misfit dislocations ($b = a/2[0\bar{1}1]$ and $a/2[10\bar{1}]$) are present which are inclined to the beam by 30° . Atomic columns are significantly disrupted perpendicular to the beam. In the region marked W, the misfit dislocations ($b = a/2[110]$) are parallel (or anti-parallel) to the beam and atomic columns are disrupted only along the beam direction. If the misfit is highly localized, atomic column resolution should be relatively unaffected in region W, but quite complex within the region R. At the other extreme, if the interface is completely incoherent, then the contrast along the boundary would again vary due to the relative positioning of the atoms. Now, however, the variation would be completely delocalized along the entire period since only 2 out of 28 projected (111) planes are in alignment as they cross the interface (See Fig. 1(b)). Consequently, a strict periodicity of length 3.58 nm should result for this case.

A typical HREM micrograph of the [110]/(111) Pd/NiO interface is shown in Fig. 5. One characteristic feature is the 9-plane/5-plane periodic contrast modulation along the boundary. A number of experimental images we have analyzed show this feature - which agrees quite well with the simulations. Therefore, qualitatively, the rigid model image simulations alone can predict contrast modulations of this type. Similar types of contrast modulations were also reproduced in simulations for Cu/NiO (a 4-plane/2-plane modulation of the projected NiO(112) spacings along the boundary) and for Cu/MgO (also a 4-plane/2-plane modulation of MgO). This is in agreement with the experimental observations of Lu and Cosandey [3] but in contrast to their simulations (where half the true period along the interface was investigated) and apparently no contrast modulations were visible until relaxations were put into the structure.

A more detailed comparison was made of the contrast modulations by evaluating an experimental versus simulated through-focal series, as shown in Fig. 6. A series of five images was analyzed, although only three are shown. Diagonal arrows on the images locate equivalent positions. The thickness of this sample was determined to be approximately 8.3 nm. First, it can be seen that the atomic column contrast is strongly affected in the vicinity of the interface. Strain contrast is clearly observed on the Pd side of the interface (which is perhaps more evident in Fig. 5). Closer inspections of the 9/5 periodicity reveal that it is not strictly adhered to in the experimental images. The features along the interface in the experimental images is also more localized in comparison, with regions of confusion separated by regions where features are sharp and well-defined, as would be expected from the misfit dislocation model outlined in the previous

section. In addition, certain contrast features which are continuous in the simulations appear to be broken up in the experimental images (see, e.g., Fig. 6(c)). These observations indicate that a certain degree of misfit localization must exist, and thus we conclude that the interface cannot be incoherent.

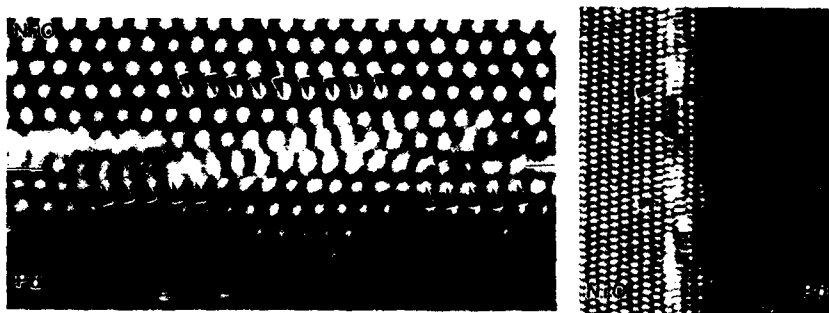


Fig. 5 (Left) Contrast modulations showing the 9/5 grouping. (Right) Same image digitally compressed. Diagonal arrows mark an entire period. Note strain contrast features and bending of the lattice planes on the Pd side.

CONCLUSIONS

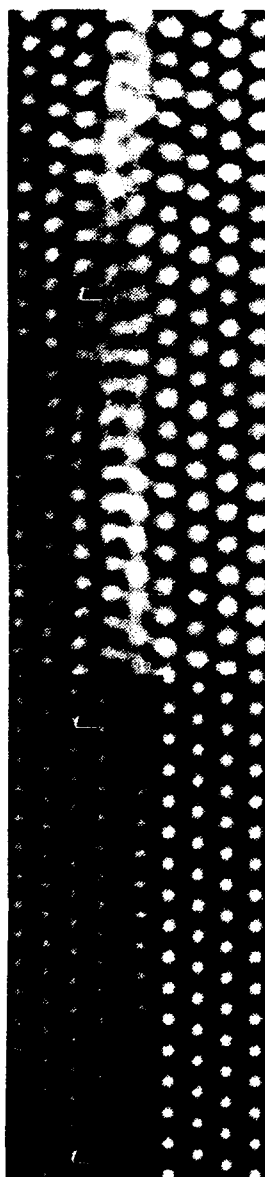
Detailed comparisons of experimental observations and image simulations of the Pd/NiO (111) interface have been performed. In contrast to earlier work, the rigid model atomic structure simulations could account for the periodic contrast modulations along the interface, making the observation of this type of interface contrast an insufficient criterion for determining whether it is incoherent or not. The observation of strain contrast as well as subtle differences in the images in addition to the contrast modulations lead us to conclude that the interface is partially coherent. This work also shows that although rigid model simulations can lead to some important insights into the nature of heterophase interfaces, they fail to give quantitative information on the extent of the misfit localization. This area must still be developed - most logically beginning with atomistic calculations of relaxed interfaces. The metal/metal-oxide systems await the development of appropriate atomic potentials. Calculations of relaxed interfaces between dissimilar metals (where the potentials are known) have already been applied successfully [11], revealing extremely subtle, but quantifiable, effects due to misfit localization.

The authors wish to thank D. Ricker and A. Huen for their assistance. This work was funded by the U. S. Department of Energy, Basic Energy Sciences under contract W-31-109-ENG-38.

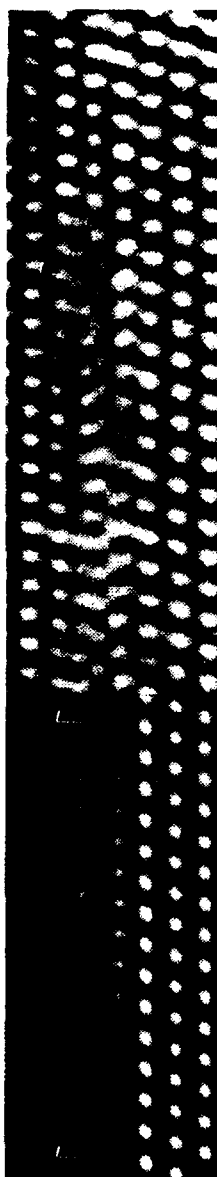
REFERENCES

1. K.L. Merkle, in *Metal-Ceramic Interfaces*, Ed.: M. Ruhle, A. Evans, M. Ashby and J. Hirth, (Acta-Scripta Metall. Proc. Ser. 4) 242 (1990).
2. G. Necker and W. Mader, *Phil. Mag. Lett.* 58, 205 (1988).
3. P. Lu and F. Cosandey, *Ultramicroscopy* 40, 271 (1992).
4. F. Ernst, P. Pirouz and A.H. Heuer, *Phil. Mag. A* 63, 259 (1991).
5. W. Mader and G. Necker, in "Metal-Ceramic Interfaces", Ed.: M. Ruhle, A. Evans, M. Ashby and J. Hirth, (Acta-Scripta Metall. Proc. Ser. 4) 222 (1990).
6. K.L. Merkle, M.I. Buckett, and Y. Gao, *Acta Met.* 40, S249 (1992).
7. P. Stadelmann, *Ultramicroscopy* 21, 131 (1987).
8. Karl L. Merkle, *Ultramicroscopy* 40, 281 (1992).
9. W. Bollman, *Crystal Defects and Crystalline Interfaces* (Springer Verlag, New York, 1970).
10. A. R. Tholen, *Phys. Stat. Sol. (a)* 2, 537 (1970).
11. Y. Gao and Karl L. Merkle, *J. Mater. Res.* 5(9), 1995 (1990).

(a) defocus = -64 nm



(b) defocus = -72 nm



(c) defocus = -88 nm

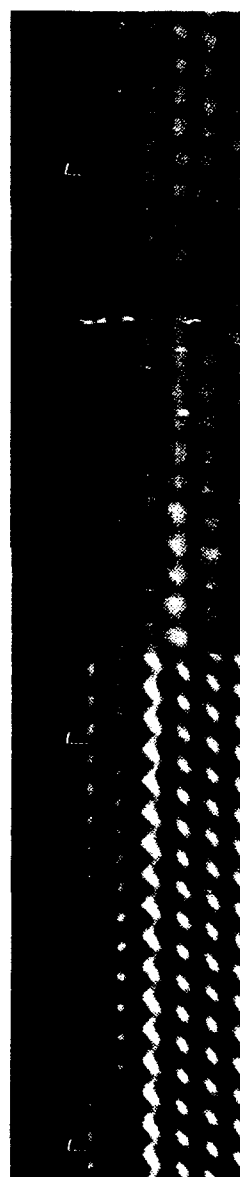


Fig. 6 Through-focal series of the Pd/NiO [110]/(111) interface. Comparison is between experimental images and oxygen-terminated, 0% volume expansion simulations. Thickness is 8.3 nm. Pd is to the right of the interface, NiO is to the left.

ATOMIC STRUCTURE OF $\Sigma = 5$ (130) SYMMETRICAL TILT BOUNDARY IN STRONTIUM TITANATE

V. RAVIKUMAR AND VINAYAK P. DRAVID

Department of Materials Science and Engineering, and Materials Research Center,
Northwestern University, Evanston, IL 60208.

ABSTRACT

The atomic structure of a pristine (undoped) boundary in strontium titanate has been investigated using transmission electron microscopy techniques. Results of electron diffraction studies indicate a pure tilt boundary with a common $[001]$ tilt axis, and a tilt angle of 36.8° , which corresponds to a $\Sigma = 5$ grain boundary in the Coincidence Site Lattice (CSL) notation. High Resolution Transmission Electron Microscopy (HRTEM) indicates a symmetric tilt grain boundary with a (130) type grain boundary plane. No cation non-stoichiometry or impurity segregants could be detected at the interface, within the limits of the Energy Dispersive X-ray microanalysis technique used. The grain boundary has a compact core, with negligible plane-normal rigid body translation (RBT). An in-plane RBT of $(1/2)d_{130}$ ($\approx 0.62 \text{ \AA}$) was identified from the high resolution electron micrographs. An empirical model of the relaxed atomic structure of the grain boundary is proposed.

INTRODUCTION

It is important to understand the structure-property relationships for grain boundaries in materials to be able to tailor grain boundaries to specific needs. The first step towards correlating the grain boundary structure to properties is to determine the detailed atomic structure of the boundary. Considerable work has been done on the determination of the atomic structure of grain boundaries in metals [1]. However, there is a paucity of similar studies in oxides. The atomic structure of grain boundaries in oxides is expected to be different from metals due to complications that arise due to ionicity, presence of electrostatic potential at the boundary and associated space charge in the vicinity of the interface. Due to the processing conditions, quite often there is the presence of a glassy phase at the boundary [2], which makes analysis of the grain boundary structure difficult. Grain boundaries in many binary oxides, notably NiO [3], MgO [4] and Al_2O_3 [5] have been studied in detail. For example, Merkle et. al. have shown that for tilt boundaries in NiO, the free volume at the interface core is much less than predicted by lattice static calculations [6]. They also found that the atomic density at the interface was lower due to the introduction of vacancies, but that there was not much lattice expansion associated with the interface. Similarly, studies of low energy interfaces in directionally solidified eutectic oxide systems including NiO-ZrO₂ and NiO-Y₂O₃ have also shown that there is negligible lattice expansion adjacent to the interfaces, and that the interface cores are compact [7]. There is a scarcity of similar studies in ternary oxides. In this contribution, we present our TEM investigation of the atomic structure of a symmetrical tilt grain boundary in SrTiO_3 .

Strontium titanate is an important electroceramic material which, under appropriate processing and dopant additions exhibits both varistor and Grain Boundary Layer Capacitor (GBLC) behavior [8-11]. The presence of electrically active grain boundaries is essential for these properties to be observed. We have employed bicrystals of Strontium Titanate for this study. The atomic structure of a pure undoped ("pristine") grain boundary has been investigated using a variety of transmission electron microscopy techniques. This provides the basic reference structure, changes to which can be studied as a function of doping and/or processing parameters, and correlated to electrical and dielectric properties.

EXPERIMENTAL PROCEDURE

3mm discs were ultrasonically drilled out of a bicrystal of SrTiO_3 . TEM samples were made from these discs by the conventional sample preparation route - mechanical thinning to 100 μm , dimpling to less than 10 μm , and ion beam thinning at liquid nitrogen temperature to perforation. HRTEM was performed using a Hitachi H-9000 300 kV dedicated high resolution electron microscope. Microanalysis was performed using a Hitachi HF-2000, a 200 kV cold field emission TEM equipped with a Link ultra-thin window Energy Dispersive Spectroscopy (EDS) detector. The sample was cooled down to liquid nitrogen temperature while performing the microanalysis to reduce contamination. Multislice calculations to simulate high resolution images were performed using NUMIS[®] [12] on an Hewlett Packard (HP-700) workstation.

RESULTS AND DISCUSSION

Selected area electron diffraction pattern (SAED) analysis showed the bicrystal to be of a pure tilt type, with a common [001] tilt axis and a tilt angle of 36.8° . This corresponds to a $\Sigma = 5$ grain boundary in the CSL notation. Figure 1 shows a schematic of the misorientation between the grains and the SAED pattern obtained from the bicrystal.

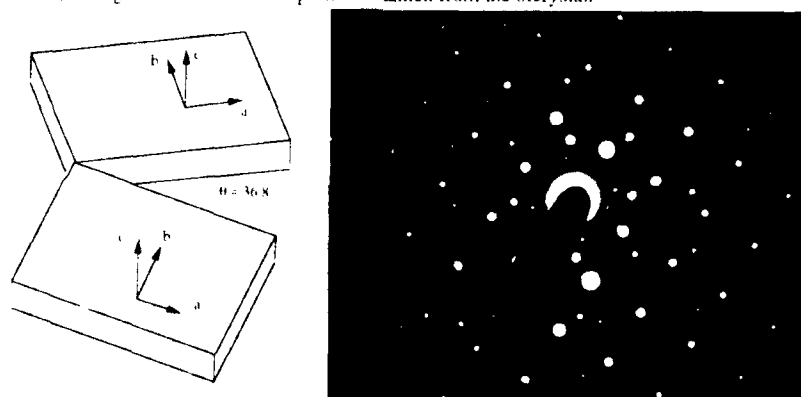


Fig. 1: Schematic representation of the misorientation between the grains and SAED pattern from a $\Sigma=5$ boundary in SrTiO_3

Figure 2 is an HRTEM of a typical grain boundary region in the sample. As can be seen from the figure, the boundary is relatively flat over large distances, with occasional steps (indicated by arrows). In between the steps, the boundary is straight and has a compact core with a periodic repeating structural unit. One such region is indicated by a box, and is shown at higher magnification in Figure 3. There are no glassy phases present at the boundary. From the arrangement of the lattice fringes, it can be seen that this is a symmetrical tilt boundary. The grain boundary plane can be determined to be of (130) type.

Before determining the atomic arrangement of the interface, it was necessary to determine whether there were any chemical inhomogeneities at the interface. The composition profile across the grain boundary was determined at high spatial resolution ($< 5 \text{ nm}$) by EDS using a fine probe ($\approx 2 \text{ nm}$). The probe was positioned in steps of 5 nm across the interface. The integrated intensities under the $\text{TiK}\alpha$ and the SrL peaks were calculated and Figure 4 shows the Ti:Sr peak intensity ratio as a function of distance across the interface. The vertical bars on each data point indicate the error due to experimental limitations like counting statistics. As is clear from Figure 4, there does not seem to be any appreciable cation non-stoichiometry at this pristine boundary, within the limits of this experimental technique. Also, there is no indication

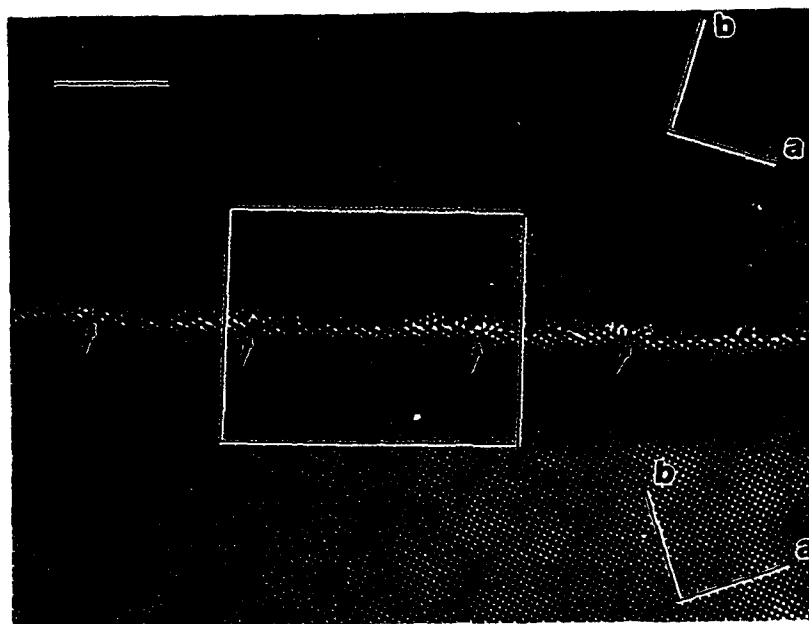


Fig. 2: A representative high resolution micrograph of the $\Sigma=5$ boundary in SrTiO_3 . Arrows indicate steps along the interface

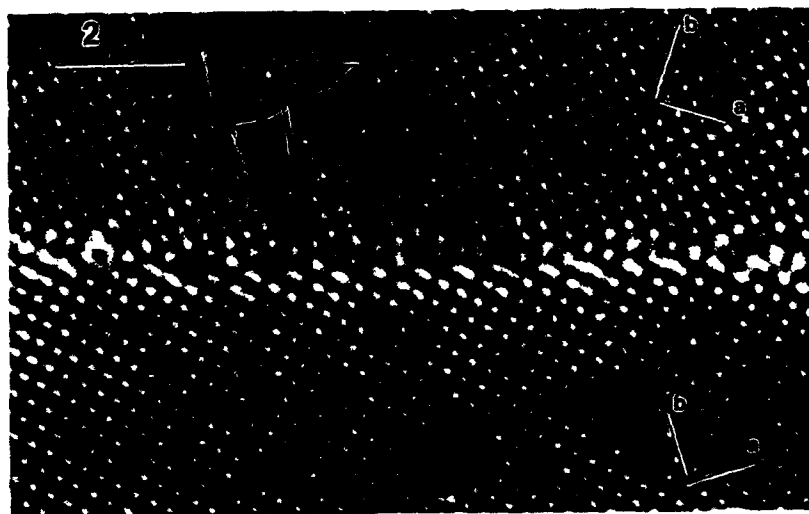


Fig. 3: A higher magnification view of the boxed region in Figure 2. The interface is devoid of any second phase, and is composed of repeating structural units

of any impurity segregation to the boundary. Hence the atomic structure of the boundary can be expected to be representative of a pristine undoped boundary.

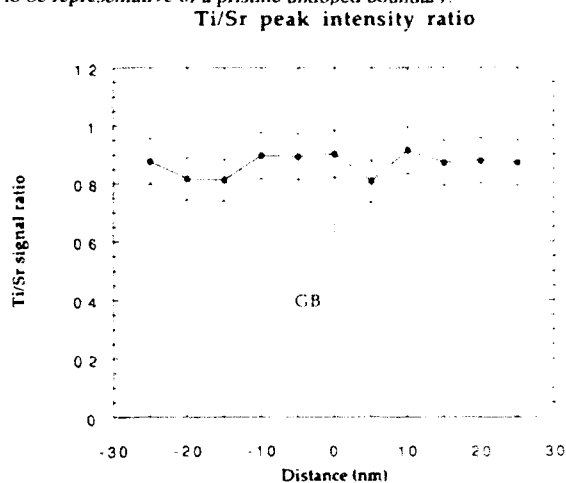


Fig. 4: Ratio of the $\text{TiK}\alpha$ to SrL x-ray peak intensity as a function of distance across the boundary

By analyzing the high resolution micrographs, an in-plane RBT of $(1/2)d_{130}$ was identified. It should be noted that this is just the projected in-plane RBT perpendicular to the beam direction, and the component of the in-plane RBT parallel to the electron beam cannot be determined in this geometry. No appreciable plane-normal RBT (lattice expansion) could be observed. Based on these observations, an empirical model has been proposed, and is shown in Figure 5 (the sizes of the ions are not drawn to scale). This model incorporates the RBT

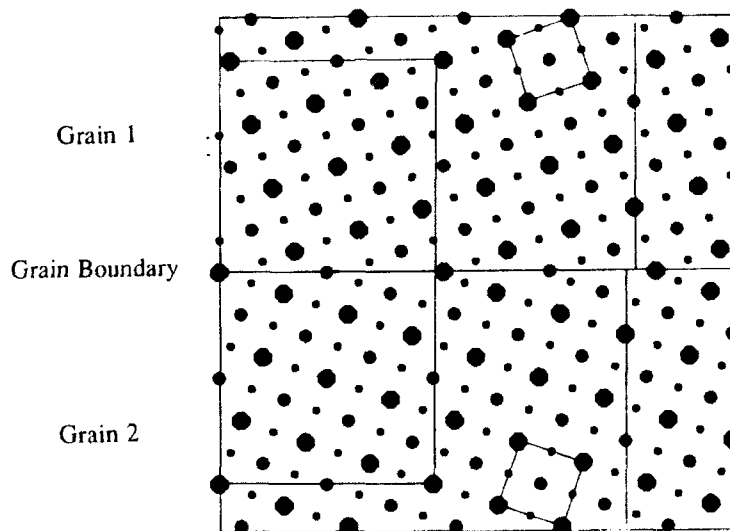


Fig. 5: Proposed semi-empirical model of the $\Sigma=5$ boundary in SrTiO_3

determined from the HRTEM images. Ions of Sr, Ti and O were removed in stoichiometric amounts (to ensure no residual charges at the boundary) to reduce the crowding at the interface, using crystal chemistry principles. The unit cells of both the grains (drawn as small squares) as well as the repeat unit of the boundary (drawn as the large rectangle) are shown in the figure. The in-plane RBT incorporated into the model is shown as an offset of the solid line at the interface.

Multislice calculations were performed to simulate high resolution micrographs using the empirical model for different thicknesses and defocus conditions, and a reasonable agreement was found between the experimental and simulated images for a thickness of about 100 Å. One such comparison between the experimental image and the simulated image is shown in Figure 6. The arrowheads point to similar features in the two images. There are subtle, yet important differences between the two images, and this is probably due to the fact

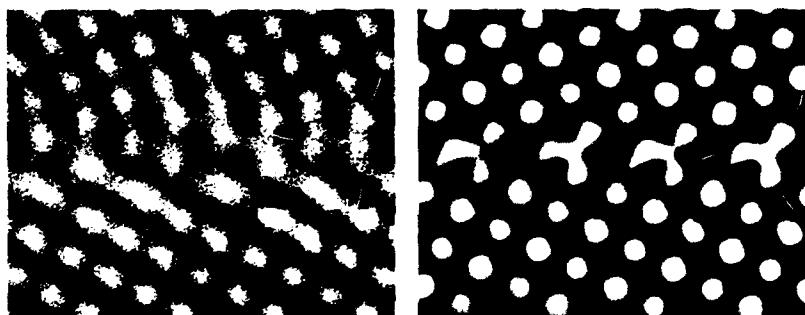


Fig. 6: Comparison between the experimental (left) and simulated (right) images. The arrows point to equivalent features in the two images.

that local individual atomic relaxations have not been incorporated into the model. Currently, these atomic relaxations are being incorporated using crystal chemistry principles to obtain a better fit between the simulated and experimental images. Theoretical calculations using static lattice energy minimization schemes will also be performed to determine the relaxed atomic structure of this boundary. We expect that this will provide more information regarding the detailed atomic arrangement at the boundary.

CONCLUSIONS

The atomic structure of $\Sigma = 5$ (130) symmetrical tilt boundary in SrTiO_3 has been investigated for the first time using TEM. No appreciable changes in cation stoichiometry could be observed within the limits of X-ray microanalysis using EDS. HRTEM image analysis indicates a compact boundary core, with an in-plane RBT of $(1/2)\langle 130 \rangle$, and negligible plane-normal RBT. An empirical model of the atomic arrangement at the interface has been proposed which fits reasonably well with the experimental observations. Subtle, yet important differences between the simulated and experimental images are believed to be due to local individual atomic relaxation, which was not included in the model. Work is currently underway to incorporate these relaxations, and also to calculate the relaxed atomic structure of this interface using theoretical lattice static calculations.

ACKNOWLEDGEMENTS

This research is supported through a seed grant by the MRL program of the National Science Foundation, at the Materials Research Center of Northwestern University, under award no. DMR-9120521, and the U. S. Department of Energy - Basic Energy Sciences, Grant No. DE-FG02-92ER45475.

REFERENCES

1. See, for example, *Interface Science and Engineering '87: An International Conference on the Structure and Properties of Internal Interfaces*, J. de Physique **49** (1988)
2. C. B. Carter, in *Surfaces and Interfaces of Ceramic Materials*, edited by Louis-C. Dufour, Claude Monty and Georgette Peiot-Ervas (Kluwer Academic Publishers, Boston, 1988), p. 29
3. K. L. Merkle and D. J. Smith, Phys. Rev. Lett. **59** [25], 2887 (1987); Ultramicroscopy **22**, 57 (1987)
4. C. P. Sun and R. W. Balluffi, Phil. Mag. A **46**, 49 (1982)
5. K. J. Morrissey and C. B. Carter, J. Am. Ceram. Soc. **67** [4], 292 (1984)
6. D. M. Duffy and P. W. Tasker, Phil. Mag. A **48** [1], 155 (1983); J. de Physique **46**, 185 (1985)
7. Vinayak P. Dravid et. al., Met. Trans. A **21A**, 2309 (1990)
8. N. Yamaoka and T. Matsui in *Grain Boundary Phenomena in Electroceramics*, edited by L. M. Levinson and D. C. Hill (Advances in Ceramics Vol 1, ACerS Publishers, Columbus, OH, 1986) p.232
9. H. D. Park and D. A. Payne in *Grain Boundary Phenomena in Electroceramics*, edited by L. M. Levinson and D. C. Hill (Advances in Ceramics Vol 1, ACerS Publishers, Columbus, OH, 1986) p. 242
10. M. Fujimoto and W. D. Kingery, J. Am. Ceram. Soc **68** [4], 169 (1985)
11. N. Yamaoka et. al., Am. Ceram. Soc. Bull **62** [6], 698 (1983)
12. NUMIS[®], High Resolution Image Simulation Program, Northwestern University

ASSESSMENT OF GaInAs/GaInAsP INTERDIFFUSION PROFILES OBTAINED USING STEM-EDX AND HREM

R E MALLARD, N J LONG, G R BOOKER, E J THRUSH* AND K SCARROTT*
Department of Materials, University of Oxford, Parks Road, Oxford, OX1 3PH, UK
BNR Europe Limited, London Road, Harlow, CM17 9NA, UK.

ABSTRACT

We report on an investigation into the interfacial structure of undoped GaInAs/GaInAsP multiple quantum wells grown by metalorganic chemical vapour deposition (MOCVD), which exhibit a pronounced blue shift in luminescence output upon in-situ thermal annealing at 750°C. Using a recently developed composition mapping technique based on the scanning transmission electron microscope (STEM) in conjunction with energy dispersive X-ray (EDX) analysis, the constituent element concentration profiles across the interdiffused multilayer interfaces are measured with a spatial resolution of less than 2nm and a precision of better than 2-3%. The accuracy of the analysis is significantly improved by employing stoichiometric normalisation factors which compensate for systematic errors due to electron channelling. The results showed that the interdiffusion follows a highly non-linear path due to the relatively fast diffusion of the group V species compared to that of the group III species. This implies an increase in the coherency strain in the multilayer, a result which is supported by five-crystal X-ray diffraction analysis of the layers. The samples have also been examined by high resolution electron microscopy (HREM) under chemically sensitive imaging conditions. The analysis of the interfacial chemical profile using HREM must be performed under analysis conditions for which a known and unique relationship between image contrast and composition occurs. This condition may not be satisfied in cases in which more than two chemical constituents interdiffuse and the diffusivities of these elements are not equal, as a range of similar lattice fringe motifs across the interface, representing different "diffusion paths", could occur. The complementary nature of information provided by HREM and STEM provides a means of resolving this ambiguity.

INTRODUCTION

The ability to independently vary the bandgap, lattice parameter and individual layer thickness of multiple quantum wells (MQW) is important, because it enables one to optimise the performance of devices reliant on the physics of low dimensional structures. GaInAs/GaInAsP is an attractive materials combination for use in the fabrication of mid-infrared optical devices, because of the inherent flexibility of quaternary alloys with regard varying the aforementioned parameters, due to the increased number of compositional degrees of freedom compared to ternary or binary alloys.

The compositional abruptness of the interfaces between the well and barrier layers, and the thermal stability of those interfaces during multistage epitaxial growth, are important factors in the production of devices such as integrated MQW lasers and optical modulators. Photoluminescence (PL) and High Resolution Electron Microscopy (HREM) have been important tools in the analysis of the structure of semiconductor MQWs because of their high sensitivity to the presence of interfacial imperfections. However, difficulties arise in the interpretation of the raw data from these techniques, which are more severe for structures employing GaInAsP barriers than for those using InP layers for confinement. We have previously shown (1) that the luminescence wavelength of GaInAs/GaInAsP MQWs may be shifted by thermal annealing at temperatures as low as 650°C, and furthermore, that the direction in which this shift occurs is sensitive to the relative amounts of group III or group V

interdiffusion. As a result, photoluminescence itself cannot be used as a reliable means of measuring the interdiffusion coefficients of the elements in the MQW. Likewise, an ambiguity can arise in the interpretation of HREM images of interfaces in the system. We have recently developed a Scanning Transmission Electron Microscope-Energy Dispersive X-ray (STEM-EDX) technique for the determination of the compositional profiles of compound semiconductor interfaces which circumvents these problems. In this paper, we demonstrate the application of the technique to the study of GaInAs/GaInAsP MQWs, whereby the contrast ambiguity in HREM images has been resolved by providing a complementary analysis of the definitive path along which interdiffusion proceeds.

EXPERIMENTAL

A GaInAs/GaInAsP MQW laser structure, consisting of a $1\mu\text{m}$ layer of InP, followed by $0.2\mu\text{m}$ of $\text{Ga}_{21}\text{In}_{79}\text{As}_{45}\text{P}_{55}$, a 6 period undoped MQW of 7nm of $\text{Ga}_{47}\text{In}_{53}\text{As}$ wells confined by 11nm $\text{Ga}_{21}\text{In}_{79}\text{As}_{45}\text{P}_{55}$ barriers, a further $0.2\mu\text{m}$ of $\text{Ga}_{21}\text{In}_{79}\text{As}_{45}\text{P}_{55}$, and a $0.1\mu\text{m}$ InP capping layer, was grown on (100) S-doped InP by metalorganic chemical vapour deposition (MOCVD) at a temperature of 650°C . The entire structure was nominally lattice-matched to InP. Half of the wafer was then subjected to a second growth stage, during which a further $1\mu\text{m}$ of InP was deposited and the sample annealed in the reactor under a PH_3 ambient at 750°C for 1 hour.

The structure of these samples was assessed by a variety of analytical techniques, including room temperature PL, electron microscopy, five crystal X-ray diffraction in the Philips HR1 diffractometer, and STEM-EDX. Cross sectional HREM was performed in the JEOL 4000EX microscope with an information limit of approximately 0.13nm , and image simulations in support of this analysis were carried out using EMS (2). The STEM analysis was performed in a VG HB501 instrument equipped with a high brightness field emission source, using a 1.5nm convergent probe, as described elsewhere (3). Briefly, the technique consists of the acquisition of spatially resolved EDX compositional maps of the X-ray emission from a cross section of the MQW. The electron beam is moved across the MQW region of the sample in a stepwise fashion along successive lines, to build up a rectangular analysis region, with a dwell time per analysis point of 100ms . The simultaneously measured X-ray intensity, characteristic of each of the elements present in the sample, at each analysis point, is processed using a quantitative analysis routine, by which the X-ray intensity maps are converted to elemental concentration maps, with a spatial resolution determined by the electron probe size. Average compositional linescans across the MQW interfaces are derived by integrating, along the direction parallel to the interfaces, the signal from successive scans.

RESULTS

The photoluminescence wavelength of the MQW was measured before and after the overgrowth and annealing schedule. This analysis showed that the thermal treatment induced a blue shift in luminescence of 131nm , which implies that significant amounts of layer interdiffusion in the quantum well region had occurred. This hypothesis was confirmed by cross sectional Transmission Electron Microscopy (TEM) of the samples. In the TEM, the $\{200\}$ scattered intensity is approximately five times greater in the GaInAsP layers than in the GaInAs layers for a specimen thickness of approximately 18nm . The HREM image contrast of the MQW before and after annealing, shown in fig 1, is therefore characterised by a $\{200\}$ square fringe motif in the quaternary barriers, and diagonal $\{220\}$ fringes in the ternary wells. The position of the interface is distinguished as the line along which the image contrast changes between these two characteristic motifs. It is evident in the case of the as-grown material, in fig 1a, that this transition occurs abruptly across a single monolayer, indicating a high degree of

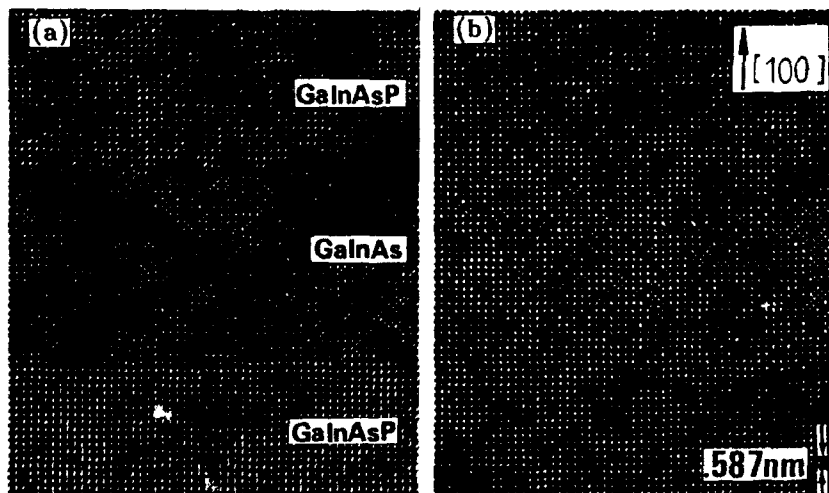


Fig 1: [001] HREM images of (a) as-grown and (b) overgrown and annealed GaInAs/GaInAsP MQWs, at a specimen thickness of approximately 18nm and at extended Scherzer defocus

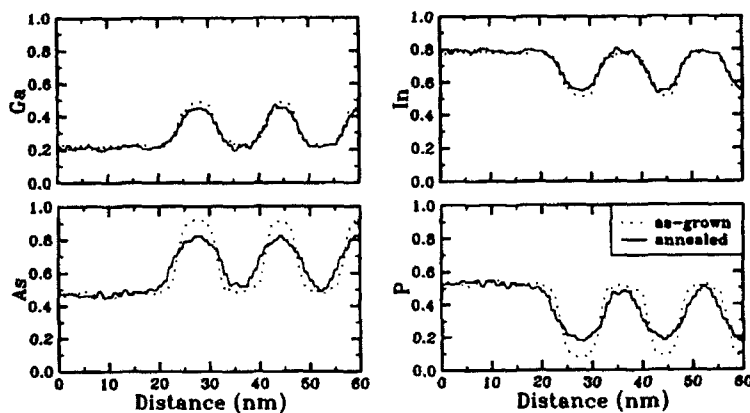


Fig 2: Concentration variations across two periods of the as-grown and annealed MQW.

interfacial chemical abruptness. The {220} fringes characteristic of the GaInAs are much less distinct in the annealed case in fig 1b, and the distance across the interface over which change between the two motifs occurs is approximately 10 monolayers, giving a first order measurement of the degree of layer interdiffusion induced by the annealing procedure. Conventional (200) dark field TEM analysis of the samples yields a similar result, in which the as-grown interfaces are chemically abrupt to within the resolution of the technique, of approximately 0.5nm, and the annealed interfaces have a width of approximately 3nm.

Compositional linescans across the interfaces of the as-grown and annealed samples are shown in fig. 2. The data have been normalised by setting the sum of the concentrations of the elements residing on each of the FCC sublattices to one, which we term the stoichiometric normalisation. This procedure is used to compensate for systematic errors in the analysis due

to the wide variations in relative X-ray yield between chemical groups of elements residing on different sublattices, which occur as a result of the phenomenon of electron beam channelling during the STEM analysis (4). The interfacial width, measured as the distance over which the concentration change is 20% to 80% of the total concentration change at the interface, is 2nm in the case of each of the elements in the as-grown sample. This value is large in comparison to the interfacial width measured by TEM because of the finite STEM electron probe size, and because of beam broadening effects in the specimen. The annealed interfaces are much more diffuse: the Ga and In interfacial widths are equal to 3nm and those of the group V elements, equal to 4nm. Similar values are obtained if the measurement of the interfacial widths is made directly from the measured X-ray intensity variations across the interfaces, rather than from the normalised concentrations. This result demonstrates that the diffusion of the group V species proceeds more rapidly than that of the group III species, which is in agreement with previous studies of undoped GaInAs/GaInAsP multilayers (5,6). In both the as-grown and annealed sample average linescan analyses, the measured non-normalised elemental concentrations in the quaternary material away from the interdiffused regions are accurate to within 5 atomic percent of the nominal values. The agreement between nominal and measured values is improved to 2% after employing the stoichiometric normalisation, with a precision of the order of 2%.

DISCUSSION

In an interdiffused GaInAs/GaInAsP heterostructure, preservation of the group III/group V stoichiometry (ignoring changes in the vacancy and interstitial concentrations, and noting that no precipitates were observed by TEM) requires that elements within each FCC sublattice diffuse at the same rate, as indeed has been observed. In addition, the unique interdiffusion path along which there is no deviation in lattice matching is that in which *all* of the constituent elements have the same diffusion constant, since the "parent" binary compounds comprising the layers have different individual lattice parameters. In our analysis, group V interdiffusion which is faster than that of the group III elements therefore results in an increase in coherency strain in the MQW. Conversion of the quantitative STEM concentration measurements in fig 2 to lattice parameter, using Vegard's law as in fig 3, indicates that the as-grown MQW is indeed close to lattice matched, and that in the annealed sample there is a tensile misfit in the well layers of approximately 0.4%, and a compressive misfit in the barrier layers of approximately 0.2%. This observation is supported by X-ray diffraction analysis of the MQWs, in which the satellite peak intensities of X-ray rocking curves increase as a result of the annealing procedure.

Ourmazd et al (7) have demonstrated the application of a lattice fringe pattern recognition algorithm to the chemical mapping of $\text{Ga}_{1-x}\text{Al}_x\text{As}/\text{GaAs}$ and CdTe/HgTe interfaces. It was reported that the change in character of the lattice fringes could be linearly related to a single compositional variable, that is, to x in $\text{Ga}_{1-x}\text{Al}_x\text{As}$, in the former case, and to the Cd/Hg ratio in the latter case. The legitimacy of such an analysis is critically dependent on the accuracy with which the local lattice fringe periodicity and intensity can be related back to the absolute composition. In the present experiment, the STEM data clearly indicates that the extents of the group III and group V interdiffusion are not identical. This result shows that the assumption that the interdiffusion proceeds along a lattice matched path, which would be required to reduce the problem of the modelling of the interdiffusion profiles to a single diffusion coefficient, is not valid.

Simulated HREM images of abrupt and diffuse GaInAs/GaInAsP interfaces, corresponding to the experimental conditions used in obtaining fig 1, are shown in fig 4. The group V elements occur at the corner FCC sublattice positions of the model unit cells (and the group III atoms at positions displaced from the group V sites by 1/4 of a unit cell body diagonal). Under these analysis conditions, GaInAsP has an anion-type contrast (bright spots centred on columns of group V atoms), whereas bright spots are centred on columns of both group III and group V

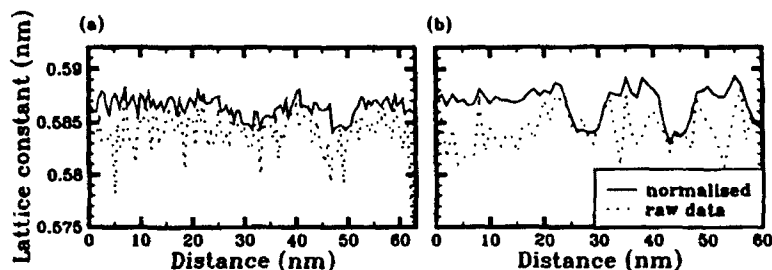


Fig 3: Variation of deduced relaxed lattice parameter with distance across as-grown and annealed MQWs. The lattice parameter variation with and without a normalisation of the data to correct for electron channelling effects in the microscope is shown, and demonstrates a remarkable improvement in the precision of the analysis using the stoichiometric normalisation.

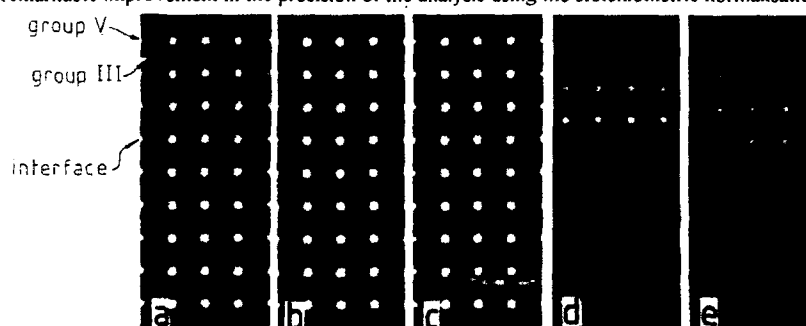


Fig 4: Simulated HREM images of GaInAs/GaInAsP MQWs, all corresponding to a specimen thickness of 18nm and a microscope defocus of -50nm. The ternary material is at the top of the simulated images, and the quaternary, at the bottom. (a) theoretical atomically abrupt interface. (b) simulation based on the experimental STEM data from the analysis described in fig 2, neglecting atom displacements due to coherency stresses. (c) simulation based on identical error function diffusion profiles for all elements and an equivalent amount of interdiffusion as that observed for the group V constituents in (b). (d) difference between simulations (a) and (b), with enhanced contrast. (e) difference between simulation (c) and one in which the tetragonal displacements are included in the model interdiffused multilayer.

atoms in the GaInAs regions. In the case of a perfectly abrupt interface, fig 4a, we observe a sharp transition between these contrast motifs, as observed in the experimental image of fig 1a. Fig 4b is a simulated image using the concentration variations across the interfaces derived from the experimental STEM data of the annealed sample shown in fig 2 (but with a reduced distance scale across the interface, and for the moment neglecting the displacement of the atomic planes in the annealed sample due to diffusion along the non-lattice matched path). Fig 4c is a simulation of a diffuse interface having error function shaped concentration profiles, in which case the interdiffusion coefficient is identical for all four elements, and equal to that determined for the group V elements in fig 4b. Both simulations exhibit a gradual transition from {200} to {220} contrast across the interfaces, again in qualitative agreement with the experimental results. The calculated difference between the abrupt simulation in fig 4a and fig 4b, shown in fig 4d, demonstrates that the change in motif is due to variations in intensity of the image contrast centred on the group III atom columns. However, the difference between the two diffuse simulations, representing different "compositional paths", is virtually negligible, and

can only be observed when the image contrast is expanded beyond the range which would be observed in an experimental image due to noise restrictions.

One manifestation of the observed unequal diffusion rates between atoms of different sublattices, as fig 3 shows, is the introduction of a varying degree of tetragonal distortion along the growth direction of the MQW. Including the displacement of the atoms in the MQW due to the lattice parameter modulation in our image simulation of the annealed MQW, produces a corresponding displacement of the lattice fringes in the image. This is evident in fig 4e, which shows the difference between simulated images based on compositional changes only, as in fig 4b, and the same data including lattice strain. In principle it may thus be possible to determine the degree of the departure from the lattice matched diffusion path by the extent of the displacement of the lattice fringes from their expected (i.e. lattice matched) positions. The integration of this information with that obtained using an HREM pattern recognition algorithm might then be used to more fully describe the interdiffusion behaviour of multilayer systems with more than one compositional variable. It should however be pointed out that such an analysis necessitates the consideration of the effects of the relaxation of the coherency strains at the thinned specimen surfaces, which would lead to another superposed displacement of the atoms in the samples and lattice fringes in the image (8).

CONCLUSIONS

We have demonstrated the application of high resolution energy dispersive X-ray analysis in the STEM to the problem of measuring chemical interdiffusion profiles in undoped GaInAs/GaInAsP MQWs. This analysis has shown that the extent of the interdiffusion in MQWs annealed at 750°C is greater for the group V elements than for the group III elements, and that this difference results in the incorporation of increased coherency strain in the material. This behaviour is consistent with the observation of a blue shift in luminescence output upon annealing. The implication of this result for HREM analysis of interfaces is that the image contrast cannot unambiguously be related to a particular composition in the interfacial region, without prior knowledge of the relative group III/group V diffusion rates.

ACKNOWLEDGEMENTS

This work was partially funded by the SERC and DTI LINK program. We wish to acknowledge the help of E M Allen with the photoluminescence analysis.

REFERENCES

- (1) R E Mallard, E J Thrush, R W Martin, S L Wong, R J Nicholas, R E Pritchard, B Hamilton, N J Long, S A Galloway, A Chew, D E Sykes, J Thompson, K Scarrott, J M Jowett, K Satzke, A G Norman, and G R Booker, *Semicond Sci Tech*, (1992), in press
- (2) P A Stadelmann, *Ultramicroscopy*, **21**, 131 (1987)
- (3) N J Long, A G Norman, A K Petford-Long, B R Butler, C G Cureton, G R Booker, and E J Thrush, *Proc Oxford Conf Micros Semicon Mater*, IOPCS 117, 69 (1991)
- (4) N J Long and R W Glaisher, *Proc EMAG*, IOPCS 98, 277 (1989)
- (5) K Nakashima, Y Kawaguchi, Y Kawamura, Y Imamura, and H Asahi, *Jpn J Appl Phys*, **26**, L1620 (1988)
- (6) M Razeghi, O Acher and F Launay, *Semicon Sci Tech*, **2**, 793 (1987)
- (7) A Ourmazd, F H Baumann, M Bode, and Y Kim, *Ultramicroscopy*, **34**, 237 (1990)
- (8) R E Mallard, G Feuillet, P-H Jouneau, *Proc Oxford Conf Micros Semicon Mater*, IOPCS 117, 17 (1991)

ELECTRON MICROSCOPY CHARACTERIZATION OF EPITAXIAL GROWTH OF Ag DEPOSITED ON MgO MICROCUBES.

J. LIU*, M. PAN* AND G. E. SPINNLER**

* Center for Solid State Science, Arizona State University, Tempe, AZ 85287, USA

**Shell Development Company, Westhollow Research Center, P. O. Box 1380
Houston, TX 72871, USA

ABSTRACT

The crystalline structure, the morphology and the chemistry of small Ag particles vacuum-deposited on preheated MgO microcubes were characterized by *in situ* and *ex situ* electron microscopy and surface analysis techniques. Observations were made of the nucleation and growth of Ag clusters on MgO surfaces and along surface steps. It is found that Ag particles deposited onto clean MgO crystals have an epitaxial orientation relationship of $(100)_{\text{Ag}} \parallel (100)_{\text{MgO}}$ with $[100]_{\text{Ag}} \parallel [100]_{\text{MgO}}$. Prior to air exposure Ag particles are stable under the electron beam but they become unstable upon exposure to air. During electron irradiation on air-exposed samples terraces are formed on the surfaces of MgO cubes, preferentially near Ag particles and at their interfaces with the substrate. The stability of vacuum-deposited Ag particles and the growth of the terraces on MgO microcubes seem to depend on air exposure of the sample.

INTRODUCTION

Metal particles and surfaces are significant to heterogeneous catalysis. It is therefore important to establish their local structure, surface rearrangements and interactions with the substrate. Model catalysts consisting of small metallic particles vacuum-deposited onto oxide supports have been of interest recently [1, 2]. The growth mechanisms and the morphology of small metallic particles as well as their crystallographic relationships with respect to the oxide support have recently been investigated by electron microscopy techniques [1, 2].

Silver particles are well known to exhibit catalytic properties and are extensively used as catalysts in several oxidation reactions [3]. Epitaxial growth of Ag on vacuum-cleaved MgO (100) surfaces has been reported [4]. Silver evaporated onto untreated MgO smoke crystals, however, showed no epitaxial growth instead surface reactions were observed [5]. The epitaxial growth, being intrinsically a surface phenomenon, is significantly influenced by the state of substrate surfaces and other deposition parameters. In this paper we employ both *in situ* and *ex situ* electron microscopy and surface analysis techniques to characterize the epitaxial growth of Ag clusters deposited, *in situ*, onto preheated MgO microcubes.

EXPERIMENTAL METHODS

MgO microcubes were produced by burning a pre-cleaned Mg ribbon in air and collected on a molybdenum microscope grid covered by a holey carbon film. The sample was then introduced into the UHV specimen preparation chamber attached to the UHV STEM. The samples were annealed at 700° C for 5 hours in the UHV chamber. At the end of the annealing the chamber vacuum pressure was less than 3×10^{-10} torr. Silver deposition was performed *in situ* by condensing an atomic beam ($\sim 7 \times 10^{11}$ atoms/cm²s⁻¹) generated by a water cooled Knudsen cell. During deposition the chamber vacuum pressure was kept below 4×10^{-10} torr. A total deposit of 8×10^{14} Ag atoms/cm² was evaporated onto MgO microcubes.

In situ characterization was performed in the Vacuum Generators HB501S UHV STEM, codenamed MIDAS (Microscope for Imaging, Diffraction and Analysis of Surfaces). Detailed descriptions of the MIDAS system were published elsewhere [6].

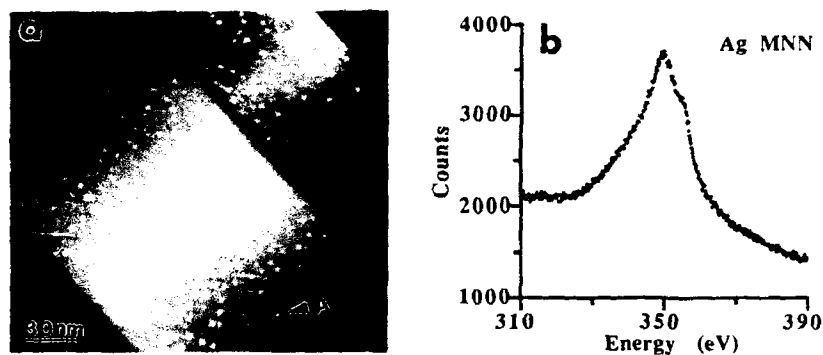


Fig. 1. (a) HAADF image of Ag particles *in situ* deposited onto MgO microcubes and (b) Ag MNN Auger electron spectrum obtained from the MgO cube shown in Fig. 1a

Secondary electron imaging and high-angle annular dark-field (HAADF) imaging techniques were used to examine the distribution and the morphology of small Ag particles. The nanodiffraction technique was used to identify the orientations of Ag particles and their crystallographic relationships with MgO supports. High spatial resolution Auger electron spectroscopy and microscopy techniques [7] were also used to analyze the surface properties of the Ag/MgO model catalyst. All images and Auger spectra were acquired digitally. After *in situ* characterization the samples were taken out of the UHV chamber for *ex situ* HREM characterization in a JEM 4000 EX electron microscope, operating at 400 kV with an image resolution of 0.17 nm.

RESULTS AND DISCUSSION

In Situ Characterization

Figure 1a shows a HAADF image of Ag particles deposited on preheated MgO microcubes at room temperature. It can be seen that small Ag particles are uniformly distributed on the MgO surface with sizes in the range of 1-5 nm in diameter. Figure 1b shows a Ag MNN Auger electron spectrum obtained from the MgO cube shown in Figure 1a. It took about 5 minutes to collect this spectrum. Because of the high probe energy and relatively thin sample the peak to background ratio is extremely high. Oxygen KLL and magnesium KLL Auger spectra were also obtained with high peak to background ratio. The high quality of Ag, O and Mg Auger spectra and the fact that no observable carbon Auger peak was detected from this MgO cube, indicate that clean surfaces of MgO microcubes have been obtained with heat treatment (700°C for 5 hours) of the sample in the UHV chamber.

The crystallographic orientations of these deposited silver particles were examined by obtaining nanodiffraction patterns from Ag/MgO cubes with a probe size about 1-1.5 nm in diameter. Figure 2a shows such a nanodiffraction pattern obtained from a small Ag particle indicated by A in Figure 1a. One can see that the MgO cube is in the [110] orientation. The diffraction spots originating from Ag particles overlap those of MgO support for low order reflections since the difference in lattice constants between MgO and Ag is only about 3%. The determination of lattice constants by the nanodiffraction method is accurate only to within about 6% because of the finite spot size, due to the convergent beam illumination, the uneven intensity distribution within a spot caused by coherent illumination and distortion of the pattern introduced by the recording system. The intensity of the diffraction spots, however, changed when the electron probe was positioned on/off the Ag particle.

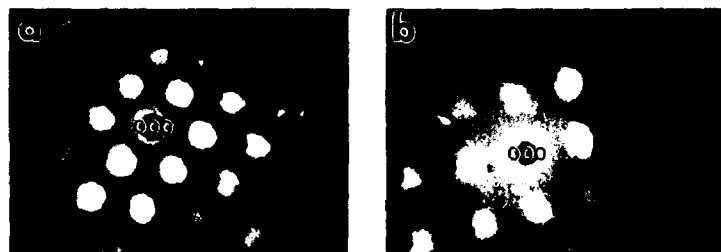


Fig. 2. Nanodiffraction patterns showing the epitaxial growth of Ag particles *in situ* deposited onto preheated MgO cubes: (a) [110] zone axis and (b) [100] zone axis.

This indicates that the Ag particle is in epitaxy with the MgO cube. Nanodiffraction patterns obtained from other Ag particles by scanning the probe over the whole MgO cube were similar to that shown in Figure 2a, suggesting that all the Ag particles have the same orientation and they are all in epitaxy with the MgO substrate. Figure 2b shows another nanodiffraction pattern obtained from a small Ag particle on a MgO cube oriented to the [100] zone axis. Again this nanodiffraction pattern shows that the Ag particle is in epitaxy with the MgO support. After examining many nanodiffraction patterns we concluded that Ag particles vacuum-deposited onto clean MgO microcubes have an epitaxial orientation relationship of $(100)_{\text{Ag}} \parallel (100)_{\text{MgO}}$ with $[100]_{\text{Ag}} \parallel [100]_{\text{MgO}}$.

Spectroscopic images are formed by collecting energy-selected Auger electron signals. Figure 3 shows a Ag MNN Auger peak (nominally 350 eV) image of Ag particles supported on a big MgO cube. Ag particles as small as 2 nm in diameter are clearly resolved. With the use of an intensity ratio method Ag clusters containing as few as 15 atoms have been detected [7]. These nanometer resolution Auger electron images have proven very powerful for yielding information about the distributions of surface species. No silver oxides were detected by nanodiffraction and Auger imaging techniques. The Ag growth on clean MgO seems to follow the Volmer-Weber or 'island growth' mode.

Figure 4a shows a secondary electron image of Ag deposited on a big MgO cube at a substrate temperature $T_s = 373$ K. The Ag particles seem to be randomly nucleated on the MgO free surface (lower part of Figure 4a) with particle sizes ranging from 2-6 nm in diameter. MgO surface steps are, however, decorated with

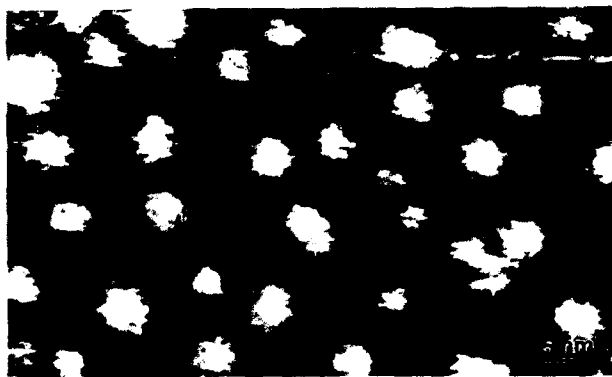


Fig. 3. Ag MNN Auger peak image of small Ag particles supported on a big MgO cube.

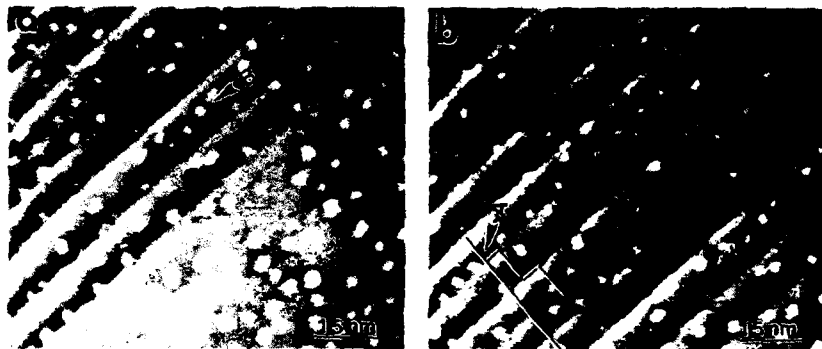


Fig. 4. SE images of Ag particles *in situ* deposited onto MgO cubes at $T_s = 373$ K revealing random nucleation of Ag on free surfaces (a) and preferential nucleation at the lower part of MgO surface steps (b).

Ag particles as shown more clearly in Figure 4b. Therefore, silver preferentially nucleated at MgO surface steps when deposited at $T_s = 373$ K. Several unique features should be noted. First, Ag particles are preferentially formed at the lower part of MgO surface steps (indicated by A in Figure 4b) and a denuded zone exists near the steps. This is a result of the competition between nucleation on terraces and capture by the nearest nuclei and surface steps. Nucleation is depressed in denuded zones. The width of the denuded zone (L_c) was estimated to be about 8.5 nm. For terraces with a width $L > L_c$ Ag particles were formed on the flat terraces as shown clearly in Figure 4a (indicated by B). Secondly, the size and spatial distribution of Ag particles formed at surface steps are different from these formed on free surfaces. This phenomenon is related to the nucleation and growth mechanisms of Ag at surface steps and on MgO free surfaces. A related consequence of this nucleation and growth process is the quasi-periodic spatial distribution of Ag clusters along surface steps (Figure 4b) as opposed to the random spatial distribution of Ag particles on free surfaces (bottom part of Figure 4a). Detailed discussions of the nucleation and growth processes of Ag on MgO will be reported elsewhere.

It should be mentioned that Ag particles epitaxially grown on clean MgO surfaces were stable under electron beam irradiation prior to air exposure. After the sample was exposed to air for a few hours, however, the Ag particles were no longer stable in the UHV STEM and they were even evaporated under electron beam irradiation.

Ex Situ Characterization By HREM

The Ag/MgO sample was exposed to air for about 48 hours before HREM observation. Figure 5a shows a profile view of Ag particles on the edge of a MgO cube oriented to the [001] zone axis. Small Ag particles are clearly in epitaxy with the MgO support with the (200) fringes parallel to the corresponding MgO fringes. It should be noted that the Ag particles are separated from the original flat interface by terraces with fringe spacings and orientations exactly like these of the MgO cube. Figure 5b shows another HREM profile image of two Ag particles on the edge of a MgO cube tilted to the [110] zone axis. Again the Ag particles are in perfect epitaxy with the MgO support and terraces are formed underneath the particles. The profile of the Ag particles consists of two {111} and two {100} faces. Based on the above observations it is concluded that the Ag particles have a half cubo-octahedral shape.

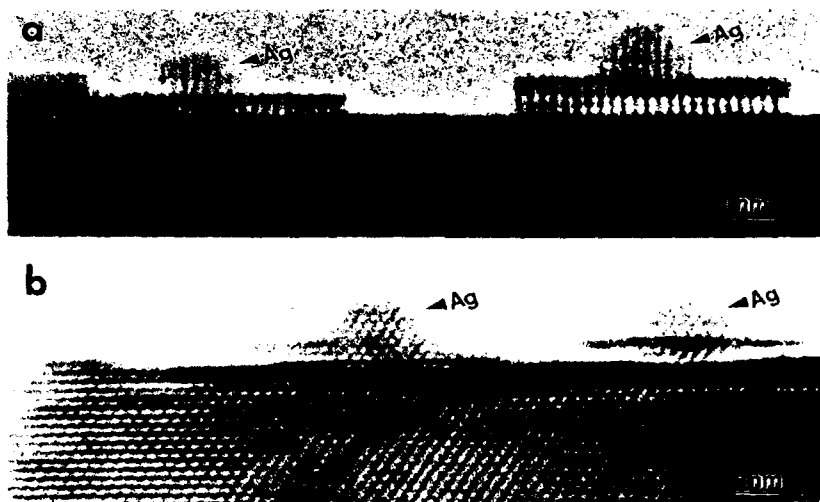


Fig. 5. HREM profile images show epitaxial growth of Ag particles on clean MgO cubes: (a) [001] zone axis and (b) [110] zone axis.

in the (100) epitaxial orientation.

From Figures 5a and 5b one can deduce that the terraces separating Ag particles and MgO cubes may have a square-like shape. In order to investigate the origin of these terraces HREM images of the sample exposed to air for different periods of time were obtained. Figure 6 shows a pair of HREM profile images of Ag particles on the edge of a MgO cube with incident beam aligned in the [001] direction. This is the same sample as that shown in Figure 5 except the sample had been exposed to air for about 3 months before observation. Figure 6a shows small Ag particles sitting on terraces which are connected to the MgO cube. The terrace widths are much broader than these shown in Figure 5. Furthermore, the small Ag particles were not stable and they disappeared under electron irradiation as shown in Figure 6b, a HREM image of the same area as that shown in Figure 6a recorded about 20 minutes later. Not only have the Ag particles disappeared but also the terraces have grown much wider. By analyzing many HREM profile images of MgO cubes exposed to air for different periods of time it is found that the stability of vacuum-deposited Ag particles decreases with air exposure and that the growth rate and the total growth of terraces near and underneath Ag particles increase with air exposure. It should be noted that the lattice fringes of the terraces are in perfect alignment with these of the MgO cube and that the fringe spacings of these terraces are exactly the same as these of the MgO within experimental error. A similar type of terrace growth under electron beam has been observed on Au/MgO system [8]. It is suggested that the formation of the terraces results from the decomposition of $\text{Mg}(\text{OH})_2$ formed during air exposure of MgO surfaces. Our results reported here also indicate that MgO surfaces are modified upon exposure to air. It appears that Ag particles enhance the nucleation and growth of MgO terraces under electron beam irradiation, probably due to a catalytic effect.

In summary, Ag epitaxially grown on clean MgO microcubes were characterized by both *in situ* and *ex situ* electron microscopy techniques. Vacuum-deposited Ag particles have a half cubo-octahedral shape with an epitaxial orientation relationship of $(100)_{\text{Ag}} \parallel (100)_{\text{MgO}}$ with $[100]_{\text{Ag}} \parallel [100]_{\text{MgO}}$. Preferential nucleation of Ag particles along MgO surface steps was observed. Vacuum-deposited, epitaxially grown Ag particles are stable in the UHV STEM. Upon exposure to air, however, Ag particles

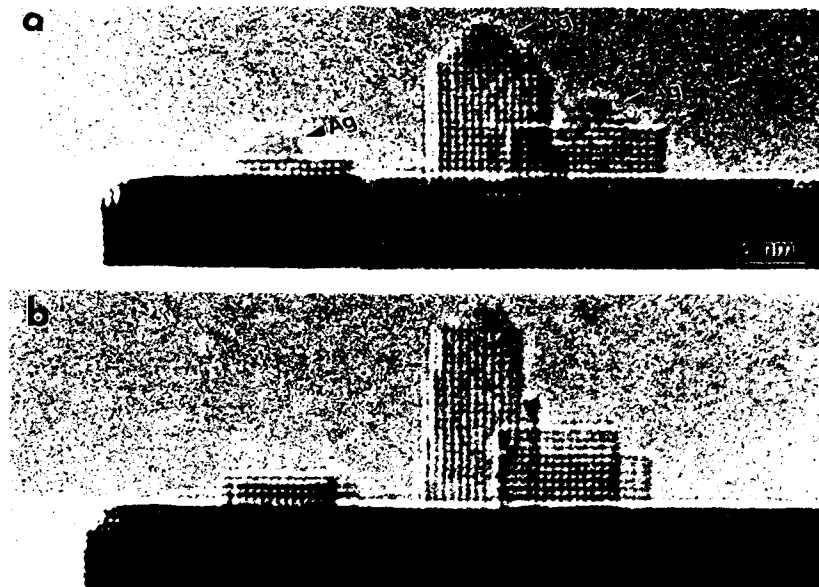


Fig. 6. HREM images show the growth of terraces on a MgO cube and the disappearing of Ag particles under electron beam irradiation.

become unstable under electron beam irradiation and MgO terraces are formed near and underneath Ag particles. Further experimental results are needed to explain the effects of small metallic particles on the formation of the MgO terraces and their interactions with the MgO support.

ACKNOWLEDGEMENTS

This research was supported by Shell Development Company and by the CHREM IAP Program and was conducted at CHREM at ASU, supported by the National Science Foundation under grant No. DMR-9115680.

REFERENCES

- [1] S. Ladas, H. Poppa and M. Boudart, *Surf. Sci.* **102**, 151 (1981); C. R. Henry and H. Poppa, *J. Vac. Sci. Technol.* **A6**, 1113 (1988).
- [2] C. R. Henry, C. Chapon, C. Duriez and S. Giorgio, *Surf. Sci.* **253**, 177 (1991).
- [3] C. N. Satterfield, *Heterogeneous Catalysis In Industrial Practice*, (McGraw-Hill, New York, 1991).
- [4] A. K. Green, J. Dancy and E. Bauer, *J. Vacuum Sci. Technol.* **7**, 159 (1970).
- [5] E. A. Lodge and J. M. Cowley, *Ultramicroscopy* **13**, 215 (1984).
- [6] G. G. Hembree, P. A. Crozier, J. S. Drucker, M. Krishnamurthy, J. A. Venables and J. M. Cowley, *Ultramicroscopy* **31**, 111 (1989).
- [7] J. Liu, G. G. Hembree, G. E. Spinnler and J. A. Venables, *Surf. Sci.* **262**, L111 (1992); *Catalysis Lett.* **15**, 133 (1992).
- [8] S. Giorgio, C. R. Henry, C. Chapon, G. Nihoul and J. M. Penisson, *Ultramicroscopy* **38**, 1 (1991).

REAL-TIME VIEWING OF DYNAMIC PROCESSES ON CdTe SURFACES AT ELEVATED TEMPERATURE

DAVID J. SMITH, R. VOGL AND PING LU*

Center for Solid State Science & Dept. of Physics, Arizona State University, Tempe, AZ 85287

*Present address: Dept. of Mechanical and Materials Science, Rutgers University, Piscataway, NJ 08855

ABSTRACT

Online video recording with a high-resolution electron microscope has been used to study real-time atomic events occurring at cadmium telluride surfaces over a range of temperatures from 27°C to 500°C. Using the profile imaging mode of observation, different types of surface activity have been documented on (001), (111) and (110) surfaces. For example, the (001) surfaces displayed reversible phase transformations between 2x1 and 3x1 reconstructions at a transition temperature of about 200°C. The (111) surfaces exhibited sublimation by a ledge mechanism that depended upon the terminating surface: layer-by-layer removal invariably occurred for (110) surface terminations whereas bilayer removal was usually seen for terminations by (100) surfaces. Finally, the (110) surface rearranged by a hopping mechanism, but no substantial loss of material was observed.

INTRODUCTION

Dynamic surface processes can be observed on the atomic scale with the high-resolution electron microscope (HREM) operated in the surface profile imaging geometry [1]. Early work in the field relied on the imaging beam to activate the crystal surface [2, 3] but a considerable drawback of the method was the lack of temperature control. It was also possible that the beam altered the surface and near-surface structure by other means, which could include desorption, dissociation and sublimation. In the absence of well-defined surface preparation methods and a well-controlled local environment, reproducibility of results was also considered to be a problem. By using a heating holder to regulate the sample temperature, those processes that are genuine thermal effects can be differentiated from those that are beam-induced artifacts.

Dynamic viewing and online image recording has been successfully used in recent studies of interfacial reactions in semiconductors [4]. However, unlike these interface studies, in order to study genuine surface processes, special steps must be taken to ensure that the surface of the sample is free of contamination or oxide layers. This condition can be met by cleaning the sample in situ within an ultrahigh-vacuum (UHV) environment. It is well-known that, under such conditions, semiconductor surfaces are liable to reconstruct to equilibrium configurations as a result of dangling bonds and surface free energy [5]. In the particular case of the CdTe (001) surface, we have previously observed a reversible phase transition between (2x1) and (3x1) reconstructions [6].

In this study, we have concentrated upon dynamic processes occurring on clean CdTe surfaces under controlled temperature conditions. With assistance from online video recordings, we have observed and documented surface processes at different temperatures using a specially modified UHV HREM [7]. We describe here in some detail the different mechanisms that occur on low-index CdTe surfaces and the dependence of these mechanisms on temperature. A brief account of some of this work has been previously published [8].

EXPERIMENTAL DETAILS

A single crystal of CdTe in the [110] orientation was mechanically thinned to a thickness of about 20 microns, and then ion-milled to perforation using argon ions with energies of ~4keV at an incident angle of about 15°. Observations were made with a Philips-Gatan 430ST HREM that had an interpretable resolution of slightly better than 2.0Å at an operating voltage of 300kV [7]. The microscope was modified to provide a vacuum of ~2-3x10⁻⁹ torr at the specimen level

after column bake-out by using a completely novel specimen chamber and adding considerably to the pumping capacity. The single-tilt specimen heating holder could provide temperatures to beyond 1200°C , although 500°C was the maximum used for these particular studies of CdTe. Typical electron-optical magnifications were 750,000 or 900,000 times, with a Gatan 622 TV camera available for additional image viewing and recording of dynamic surface events. Video-recordings were edited by surface, enabling the prevailing mechanism(s) to be followed as a function of temperature. Unless noted, the images shown here were all taken directly from the videotape recordings.

RESULTS

The clean CdTe surfaces displayed several different rearrangement processes: it had been observed previously that the frequency of these rearrangements was related to temperature but no detailed study had been made [8]. Our major objective in this study was to systematically classify the different surface motions. It was found that these could be conveniently categorized according to surface.

A. Ledge sublimation on the (111) surface.

The (111) surface was observed to rearrange by a ledge sublimation mechanism. Layer-by-layer sublimation was observed starting from the (110) surface, with atomic columns being removed by rows. At a temperature of 380°C , the atomic columns were desorbing rapidly, with one entire row of columns being removed from the field of view in approximately two seconds. Figs. 1(a)-(c), recorded at 380°C over a time interval of approximately 5 seconds, show examples of this sublimation originating from the (110) surface at the bottom right of the field of view. At 230°C , the atomic columns were removed at much slower rates with one row typically being removed in approximately ten seconds. It was interesting that, once the process of desorption was initiated, the rest of the row was removed very rapidly.

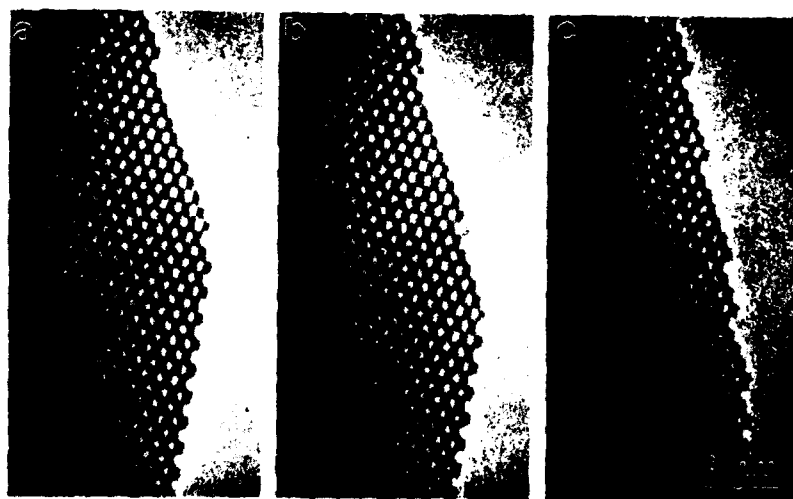


Fig. 1. Profile images showing removal of the (111) surface, layer-by-layer, in a process initiated from the (110) surface at bottom right. Images recorded at a temperature of 380°C over a time interval of approximately 5 seconds.

When the (111) surface row was instead terminated by a reconstructed (001) surface, bilayer sublimation was invariably observed with two layers of atomic columns being removed at a time. At 380°C, the layers of atomic columns on the (111) surface were clearly desorbing at a much slower rate than those observed originating from (110) surfaces. The rate observed was approximately two atomic pairs per second whereas, at 230°C, the rate of removal was slowed down to approximately one atom pair every second. Figure 2, which shows a series of four images recorded at 230°C over a time interval of approximately 15 seconds, represents a good example of this bilayer sublimation process.

Finally, it should be mentioned that no examples have been documented where the process of sublimation of the (111) surfaces was not initiated from either the (110) or (001) terminating end of the surface.

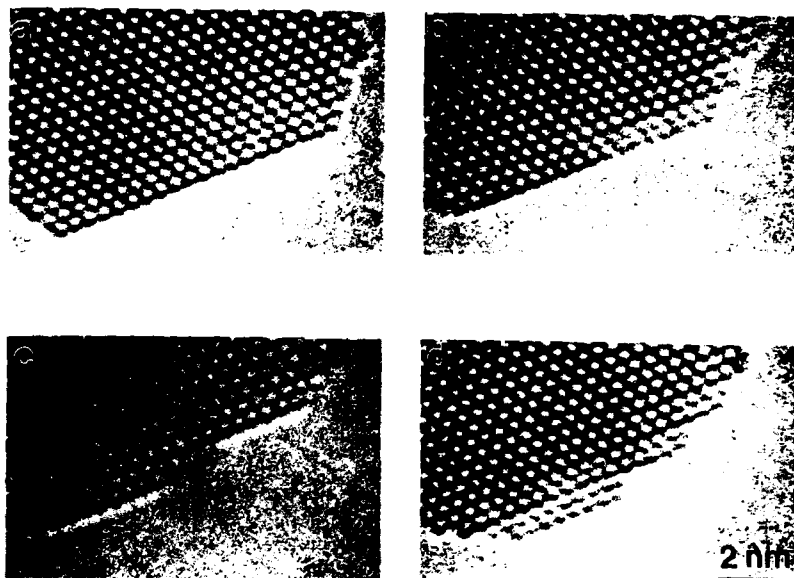


Fig. 2. Profile images from videotape showing bilayer removal of atomic columns from the (111) surface when the ledge sublimation process is initiated from the reconstructed (001) surface. Images were recorded over a time interval of approximately 15 seconds with the sample at a temperature of 230°C.

B. Surface hopping on (110) surfaces.

The (110) surface was observed to rearrange primarily by a hopping mechanism. This motion was very rapid at higher temperatures: at 380°C, and rows of atomic columns were being displaced at approximately three second intervals. The profile images in Fig. 3, recorded over a period of about ten seconds at 380°C, show examples of this (110) surface hopping. In comparison, when the crystal temperature was reduced to 140°C, there was effectively no residual surface motion.

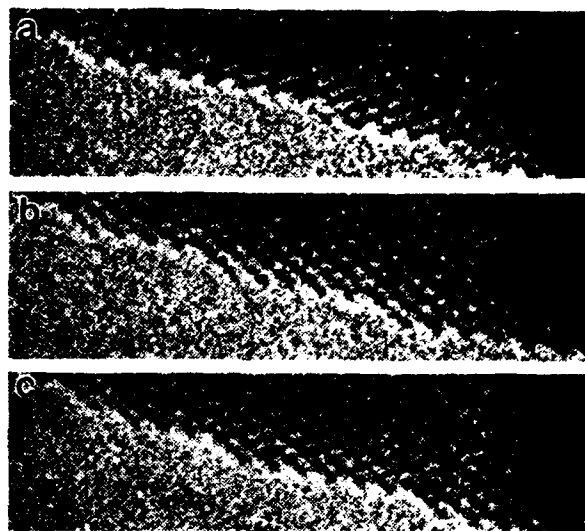


Fig. 3. Profile images of the (110) surface, recorded at 380°C over a time interval of about ten seconds, showing examples of the prevailing phenomenon of surface hopping.

C. Reconstructions on the (001) surface.

The (001) surface reconstructed to either a (2x1) or a (3x1) surface depending upon the sample temperature [6]. At 380°C, motion occurred very rapidly, atomic columns were being rearranged at the rate of 2 or 3 times per second, and no long-term or stable reconstructions were observed. At 230°C, the surface was less active, with atomic columns being rearranged at approximately one second intervals. Fig. 4(a) shows an example of the (001) surface at 230°C. The (3x1) reconstruction was predominantly visible at this temperature, although the (2x1) configuration could also be seen in some places. For comparison, Fig. 4(b) shows the (001) surface at 140°C: it obviously consists primarily of (2x1) reconstructions. It was observed that some limited motion still occurred at this temperature. At 33°C, the (2x1) surface reconstruction was predominant, the surface was stable, and no motion was seen.

DISCUSSION

The objective of this study has been to characterize the dynamic processes occurring on clean CdTe surfaces at elevated temperatures under UHV conditions. With careful control of the sample temperature, we have observed three distinct mechanisms by which low-index CdTe surfaces rearrange: a) ledge sublimation on (111) surfaces; b) surface hopping on the (110) surface; and c) (2x1) and (3x1) reconstruction on the (001) surface.

The ledge sublimation process on the (111) surfaces occurred in two different ways. When the reaction started from the (110) surface, material was removed layer-by-layer from the surface. In contrast, a bilayer sublimation occurred when the reaction originated at the (001) surface. This latter process was presumably related to the lowering of the surface free energy associated with the dimer reconstruction of the (001) surface. It was significant that no examples were observed where sublimation was initiated from the middle of an extended (111) surface. It was also interesting that the hopping processes that occurred on the (110) surfaces did not result in any significant long-term change in the morphology of the (110) surface. Material moved around considerably, especially at higher temperatures, but very little sublimation of material was observed.

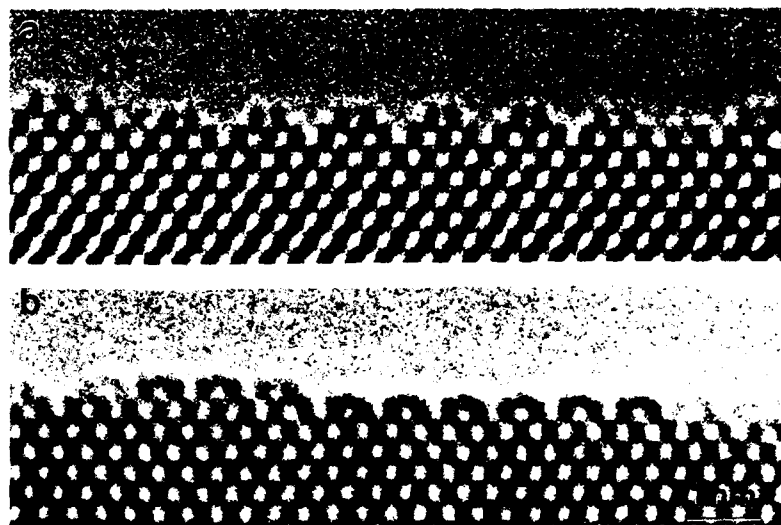


Fig. 4. Profile images, not from videotape, showing reconstruction of the (001) surface:
(a) (3x1) reconstruction recorded at 230°C; (b) (2x1) reconstruction recorded at 140°C.

The frequency at which these various processes occurred increased substantially with temperature in all cases. The images recorded at 380°C showed motion that was much more rapid than that seen at lower temperature. Indeed, at room temperature, virtually no motion was observed across the surfaces of the sample, despite the addition of energy to the sample by the imaging beam of electrons, i.e., an important conclusion of this work was that the electron beam was not the major cause of the surface motion, since the surfaces were stable at lower temperatures under the same conditions used for imaging.

Finally, it is clear that surface profile imaging represents a useful method for observations and studies of surface processes in the particular case of CdTe. However, this type of surface microscopy does have some shortcomings: The possibility of surface modification by the imaging beam means that the number of materials that can be studied in this fashion is somewhat limited. For example, transition metal oxides are known to suffer from electron-stimulated-desorption of oxygen from near-surface regions, even under UHV conditions [9]. Moreover, the edge of the sample must be thin in order to produce a high quality profile image, and it is quite possible that such a thin edge may not behave in a manner that is sufficiently representative of the bulk material.

CONCLUSIONS

Rearrangements of clean CdTe crystal surfaces at elevated temperatures have been observed using the technique of surface profile imaging with the HREM. By using video equipment to record the various types of surface activity facilitates their documentation and study in real-time, thereby eliminating the gaps in time that must otherwise occur when relying upon conventional, sequential recording of electron micrographs. It is clear that utilization of the surface profile imaging has been productive for these atomic resolution studies of edge sublimation, surface hopping, and reconstruction processes occurring at CdTe crystal surfaces.

ACKNOWLEDGEMENTS

This work was conducted at the Center for High Resolution Electron Microscopy at Arizona State University supported by NSF Grants DMR-89-13384 and 91-15680. Partial support from NSF grant DMR 85-14583 (PL), and the ASU-NSF Physics REU Program (RV) is gratefully acknowledged. We thank Professors L.Eyring and I. Tsong for access to their video editing equipment.

REFERENCES

- [1] D.J. Smith, J. Vac. Sci. Technol., B3, 1563 (1985).
- [2] R. Sinclair, T. Yamashita and F.A. Ponce, Nature, **290**, 386 (1981).
- [3] D.J. Smith and L.D. Marks, Mater. Res. Soc. Symp. Proc., **41**, 129 (1985).
- [4] R. Sinclair, M.A. Parker and K.B. Kim, Ultramicroscopy, **23**, 383 (1987).
- [5] A. Kahn, Surf. Sci. Reports **3**, 193 (1983).
- [6] P. Lu and D.J. Smith, Surface Sci., **254**, 119 (1991).
- [7] D.J. Smith, J. Podbrdsky, P.R. Swann and J.S. Jones, Mater. Res. Soc. Symp. Proc., **139**, 289 (1989).
- [8] P. Lu and D.J. Smith, in Proc. XIIth. Int. Cong. for E.M., Vol. 1, 310 (1990).
- [9] M.R. McCartney and D.J. Smith, Surface Sci., **250**, 169 (1991).

AFM IMAGING OF THE CRYSTALLINE-TO-AMORPHOUS TRANSITION ON THE SURFACE OF ION-IMPLANTED MICA

RAY K. EBY* GRANT S. HENDERSON* FRED J. WICKS** AND GEORGE W. ARNOLD***

*Dept of Geology, Univ of Toronto, 22 Russell St, Toronto, Ontario, Canada M5S 3B1

**Mineralogy Dept, Royal Ontario Museum, 100 Queens Park, Toronto, Ont M5S 2C6

***Dept 1111, Sandia National Laboratories, Albuquerque, New Mexico, USA 87185

ABSTRACT

Scanning microscopy is the only technique available for directly imaging the short-range structural features of the crystalline-to-amorphous (C-A) transition. Cleaved sheets of muscovite were implanted with 600 keV argon ions in order to induce radiation damage; thus producing the C-A transition. AFM images of Ar-implanted muscovite show the surface structural features of the C-A transition. Low-resolution images show a progressive increase in the surface roughness of muscovite with increasing ion dose, as seen by the development of hummocky microtopography, whose individual hummocks are 25 nm across. High-resolution AFM images of unimplanted muscovite reveal a highly crystalline structure, as shown by the hexagonal arrangement of the (SiO₄)-tetrahedral layers. By scraping through the uppermost surface layer of the implanted samples, using a cantilever forces of 50 - 100 nN, the C-A transition is recognized by a decrease in the long-range order of the tetrahedral layers. Accordingly, crystal defects and highly disordered regions increase in frequency and size with Ar-dose. At the highest Ar-dose, disordered regions dominate the structure, lending complications to AFM image interpretation. Surface hardness decreases with higher radiation doses, as evidenced by the greater ease of scraping through atomic layers in the more damaged samples.

INTRODUCTION

Although many uses for the AFM¹ are still relatively novel, this instrument is rapidly becoming a mainstream tool for studying a wide variety of problems at the atomic/molecular scale, such as showing structural details at the surface of inorganic crystals^{2,3}, or examining adsorbed species on solid substrates^{4,5}. The scanning tunneling microscope (STM), a cousin to the AFM, was first used to study radiation damage features produced on the surface of ion-bombarded silicon⁶ and graphite^{7,8}. More recently, the AFM was used to study the microtopography of single ion tracks on ion-bombarded mica⁹. These scanning microscopy studies showed that the surfaces of radiation-damaged solids can develop large hillocks^{6,7}, linear ridges, localized disordered regions⁸, and cylindrical amorphous features⁹, the presence of which depend on the accelerated ion's energy, and mass, and the ion dose; however, these previous studies did not obtain atomic-scale resolution of the disordered regions.

The structural characteristics of the C-A transition are important, and any direct images are useful for understanding the amorphous state in general. Here, we used moderate cantilever tracking forces to scrape through the irregular relief that is produced in the upper surface layers of ion-bombarded material in order to image the partly amorphous state in layers below. In addition, we were able to reproduce images of the hummocky topography using lower tracking forces. The

fine-scale details of the C-A transition are not fully understood, although previous studies of naturally damaged and ion-bombarded minerals have provided much knowledge on the general characteristics of this phenomenon^{10,11}. Most of the techniques used to characterize non-crystalline solids must inherently examine the bulk-structure (e.g., X-ray diffraction); thus, the short-range topological features of non-periodic solids are averaged. Conversely, the AFM is a good candidate for studying disordered solids, because it can distinguish individual atoms, thus revealing structural topology. However, examination of fully amorphous materials with the AFM is problematic, as is the case for STM⁸. Image interpretation of disordered solids is limited by how well the scanning probe tip can respond to non-periodically arranged atoms and produce a meaningful, recognizable, signal-to-noise ratio. Layer silicates routinely yield atomic-scale images when in the crystalline state^{2,3,12,13}; thus, these materials hold the greatest potential for studying the partly amorphous state with the AFM. We therefore chose to study the C-A transition using AFM imaging of ion-implanted muscovite, a mica (i.e., layer silicate) with composition $\text{KAl}_2(\text{Si}_3\text{AlO}_{10})(\text{OH})_2$.

EXPERIMENTAL METHODS

The muscovite samples were implanted with 600 keV Ar at doses of 5.0×10^{12} , 2.5×10^{13} , 5.0×10^{13} and 1.0×10^{14} Ar/cm². The highest dose does not represent completion of the C-A transition, but is close to the critical amorphization dose¹⁴ of muscovite. The methods used for ion implantation are described elsewhere¹⁵.

The AFM used is a Digital Instruments Nanoscope III equipped with a 0.7 μ scan head and operated in height mode (i.e., constant force). A 200 μ wide-legged cantilever (Au-coated, Si_3N_4) was used for low-resolution imaging of larger-scale topographic features. The low spring constant of this cantilever provided a lower tracking force (< 20 nN), which prevented removal of the fragile surface features on radiation damaged samples. A 100 μ wide-legged cantilever was used for high-resolution imaging of the radiation-damaged structures. Rather than trying to image the atomic-scale features of the C-A transition at the original, uppermost surface, the structure was examined in layers below. In order to do this, the upper layer was scraped away using cantilever forces of 50 - 100 nN. Radiation softening of the implanted samples allowed us to use tracking forces much lower than those needed for scraping away layers of highly crystalline muscovite (> 200 nN).

Given the difficulty of imaging disordered structures at the atomic scale, using scanning microscopy, the following procedures should be made routine. Images were first collected on an unimplanted muscovite sample for comparison with the radiation-damaged samples. The unimplanted muscovite serves as an external standard for ensuring that the AFM is operating at optimum conditions. As such, the muscovite standard was scanned before and after scans of each implanted sample. If the image quality of the standard was similar before and after scanning the implanted sample, then images of the implanted sample were considered to be of interpretable quality. Furthermore, all samples were scanned using the same instrumental parameters, except for the tracking force. The tracking force was set lower with the more damaged samples (due to radiation softening) in order to avoid continually scraping away the layers. With this routine, one achieves a greater degree of confidence that the AFM images accurately represent the implanted surfaces, as opposed to representing merely electronic noise. Such a distinction between noise and disordered structure is not otherwise readily apparent. A consistent methodology for filtering the AFM images, using the same

filtering specifications for all images, was also used in order to avoid introducing a bias when showing the differences in crystallinity between samples with different Ar-doses and the unimplanted standard.

RESULTS & DISCUSSION

Low-Resolution AFM Images

The surface effects of argon implantation on muscovite are seen in Figure 1. As the radiation dose increases so does the roughness of the samples. Table I shows a quantitative estimate of the increase in surface roughness, as caused by radiation damage. The surface produced with the highest dose has a hummocky topography similar to that observed in earlier studies. Figure 1f shows several depressions amidst the hummocky surface. The size of these features (25 nm across) is much larger than those proposed as single ion-tracks by other workers⁹, and the size of our hummocks vary from 15-35 nm. Furthermore, their appearance does not change with scan direction, unlike in previous work. The processes resulting in these features are not the same as the high energy tracks, the latter of which are caused by high-density electronic spikes⁹. Lower energy damage from Ar-implantation is probably the result of atomic collision cascades¹⁴.

Table I: Radiation Doses & Roughness Measurements of Ar-Implanted Muscovite

Radiation Dose	Surface Roughness* (R_a , R_q)	Corresponding Figures
unimplanted	0.042, 0.053	1a, 2a
2.5×10^{13} Ar/cm ²	0.064, 0.080	1b, 2b
5×10^{13} Ar/cm ²	0.085, 0.121	1c, 2c, 2e
1×10^{14} Ar/cm ²	0.114, 0.144	1d, 2d

* R_a = mean roughness; R_q = rms std. dev.; calculations from software of Digital Instruments

High-Resolution AFM Images

A representative AFM image of the unimplanted muscovite standard is seen in Fig. 2a. The hexagonal pattern of the (SiO₄)-tetrahedral sheet is evident at a point-to-point resolution of 3 Å. For comparison, a model of muscovite's tetrahedral sheet is overlain and shows the hexagonally arranged tetrahedral rings¹⁶. The holes within the rings are 4 Å in diameter and are similar in size, and arrangement, to the areas of lowest relief in the AFM image (i.e., the dark areas in Fig. 2a). Most of the AFM images of the muscovite standard contain a few defects. However, the overall appearance of the tetrahedral sheet is quite regular compared to AFM images of the implanted samples.

AFM images of muscovite given a low Ar-dose (5×10^{12} Ar/cm²) do not display any significant disorder compared to the muscovite standard; thus, this sample is not shown. At a higher Ar-dose (see Table I for specific doses), the symmetry of the tetrahedral sheet is significantly reduced (Fig. 2b). The tetrahedral sheets should remain intact at this dose, because the spatial density of Ar collision cascades is not sufficient enough for overlap (assuming a cascade radius of 25 Å). Several features observed are: (i) a frequent "pinching out" between adjacent rows of tetrahedra within the sheet, i.e., dislocation defects; (ii) the appearance of small partly disordered regions. At yet a higher dose, the amount of disorder in the structure noticeably increases (Fig. 2c). Fragments of the tetrahedral sheets are still resolved

amidst the high density of dislocations and large disordered areas. At the highest dose, the original structure is unrecognizable (Fig. 2d). Several features are vaguely

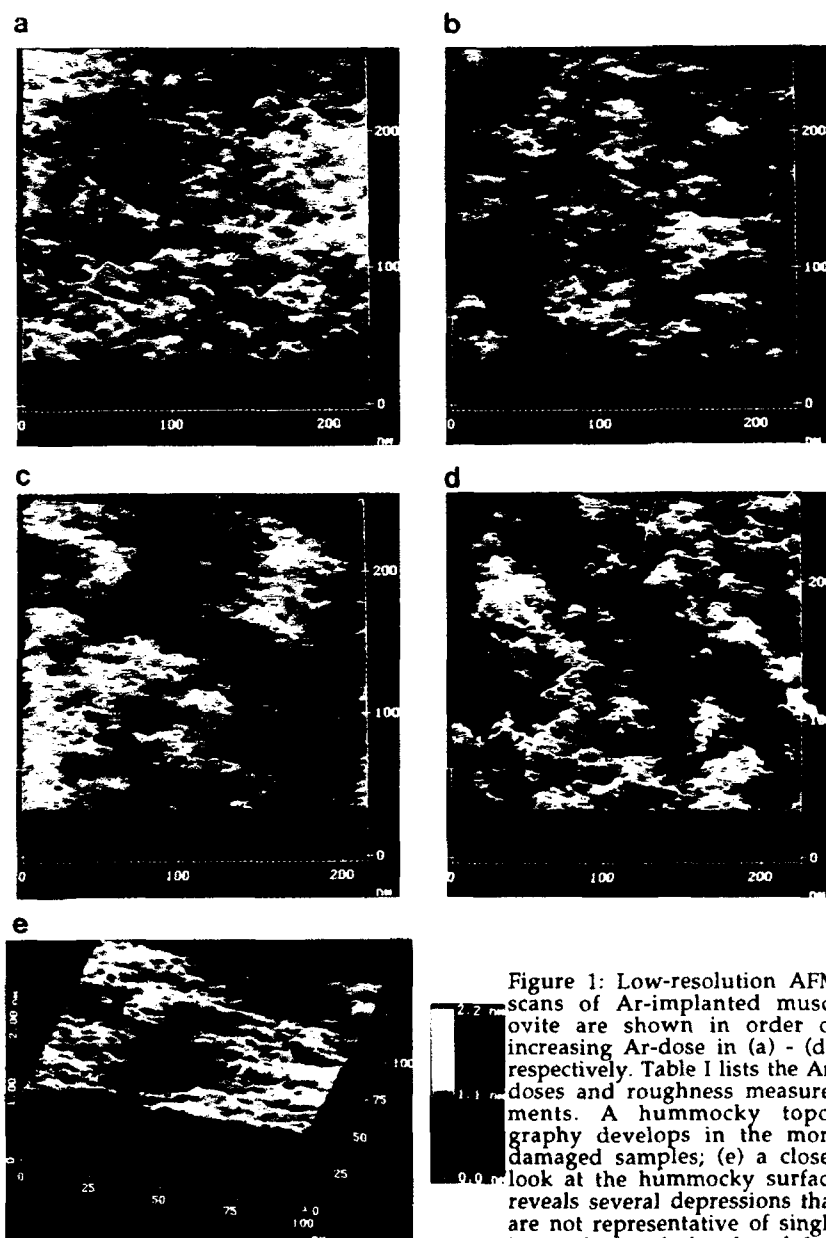


Figure 1: Low-resolution AFM scans of Ar-implanted muscovite are shown in order of increasing Ar-dose in (a) - (d), respectively. Table I lists the Ar-doses and roughness measurements. A hummocky topography develops in the more damaged samples; (e) a closer look at the hummocky surface reveals several depressions that are not representative of single ion tracks. Vertical scale at left.

interpretable as small fragments of the tetrahedral sheets, but most of the image is unresolvable because we have nearly completed the C-A transition.

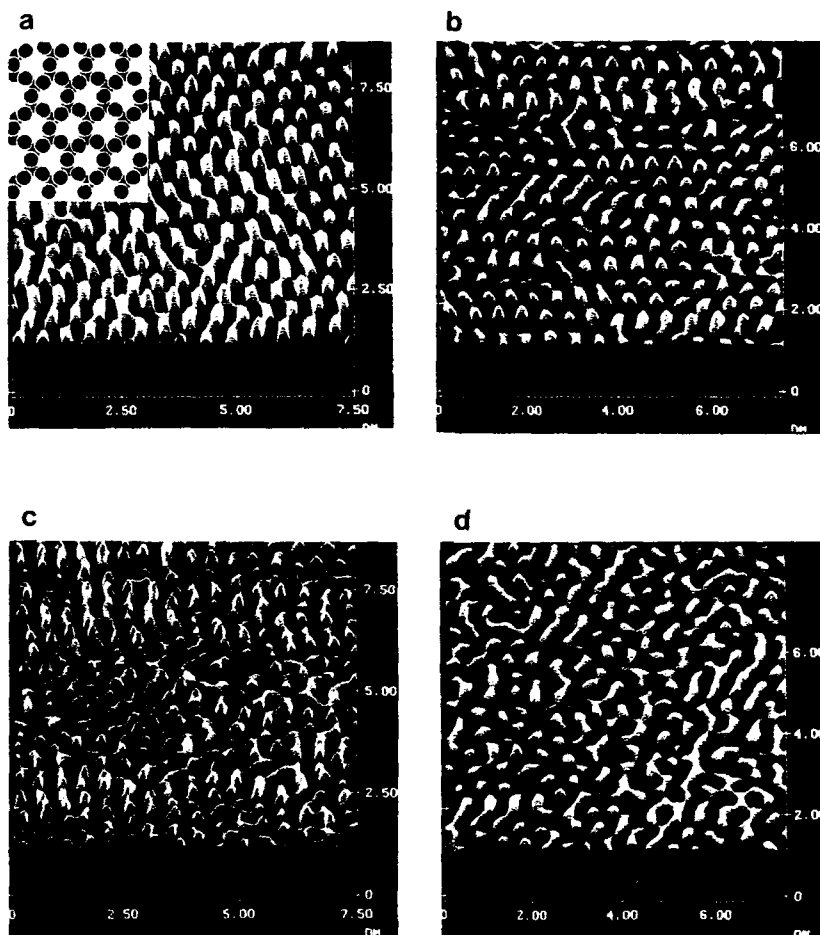


Figure 2: Filtered (2D fast Fourier transformed) AFM images of Ar-implanted muscovite (Ar-doses used are given in Table I). (a) the unimplanted standard shows the regular structure of the tetrahedral sheet. Inserted is the structural model of oxygen atoms within muscovite's tetrahedral sheet. The dark regions in the image correspond in size and symmetry to the holes in the tetrahedral rings; (b) the lowest dose - there is no noticeable radiation damage; (c) a higher dose - the long-range order of the tetrahedral sheet is reduced; (d) with increasing dose - the only fragments of the tetrahedral sheets remain. It is difficult to interpret the image since it has no long-range order; (e) the highest ion dose - image interpretation is tenuous. Vertical scale at left.

Individual Ar-tracks were not resolved with the AFM in the samples of lower dose (i.e., doses in which Ar collision cascades do not overlap). Apparently then, the density of atomic collisions in individual Ar-tracks is not high enough to result in a significant volume of amorphous material. Thus, amorphization can only result by multiple track overlap. At the highest Ar-dose observed with the AFM, collision cascades overlap several times. Previous work has shown that multiple overlap of Ar collision cascades is necessary in order to attain the amorphous state¹⁷. The observations of this study support that earlier conclusion.

CONCLUSIONS

The surface structure of the partly amorphous state can be examined in detail with the AFM. Ion-implanted muscovite is an ideal material for such a study, as this layer silicate is readily imaged at the atomic scale. With increasing ion dose, muscovite undergoes the C-A transition, which is observed as a progressive loss of long-range order in the (SiO₄)-tetrahedral sheets. Dislocations and disordered regions are resolved within AFM images until nearing completion of the C-A transition. Our observations indicate that multiple overlap of Ar collision cascades is necessary to produce the amorphous state in muscovite.

ACKNOWLEDGEMENTS

This project was funded by NSERC of Canada in the form of operating and equipment grants to FJW and GSH and with a PDF award to RKE. We thank Ken Minor of Sandia National Laboratories (SNL) for his efforts with the ion-beam instrumentation. Work at SNL was supported by DOE under contract DE-AC04-76-DP00789.

REFERENCES

1. G. Binning, C.F. Quate and C. Gerber, *Phys. Rev. Lett.* **56**, 930 (1986).
2. H. Hartman et al., *Clays and Clay Minerals* **38**, 337 (1990).
3. F.J. Wicks, K. Kjoller and G.S. Henderson, *Canad. Mineral.* **30**, 83 (1992).
4. B. Drake et al., *Scienc.* **243**, 1586 (1989).
5. P.E. Hillner, A.J. Gratz, S. Manne and P.K. Hansma, *Geology* **20**, 359 (1992).
6. R.M. Feenstra and G.S. Oehrlein, *Appl. Phys. Lett.* **47**, 97 (1985).
7. L. Porte, M. Phaner, C.H. de Villeneuve, N. Moncoffre and J. Tousset, *Nucl. Instr. Meth. Phys. Res.* **B44**, 116 (1989).
8. Coratger, A. Claverie, F. Ajustron and J. Beauvillain, *Surf. Sci.* **227**, 7 (1990).
9. F. Thibaudau, J. Cousty, E. Balanzat and S. Bouffard, *Phys. Rev. Lett.* **67**, 1582 (1991).
10. R.C. Ewing, B.C. Chakoumakos, L.R. Lumpkin and T. Murakami, *MRS Bull.* May/June, 58 (1987).
11. L.M. Wang, and R.C. Ewing, *MRS Bull.* **XVII/5**, 38 (1992).
12. J.N. Israelachvili, J.N. *Intermolecular and Surface Forces with Applications to Colloidal and Biological Systems* (Academic Press, New York, 1985).
13. H. Lindgreen et al., *Amer. Mineral.* **76**, 1218 (1991).
14. R.K. Eby, and R.C. Ewing, *Journ. Mater. Res.* **7(11)**, 3080 (1992).
15. *Ion Implantation - Science & Technology*, ed. J.F. Ziegler (Academic Press, NY, 1984).
16. S.W. Bailey, in *Micas, Reviews in Mineralogy* **13**, ed. S.W. Bailey (BookCrafters, Inc., Michigan, 1984), pp. 13-60.
17. W.J. Weber, *Journ. Mater. Res.* **5**, 2687 (1990).

AFM IMAGINGS OF FERRITIN MOLECULES BOUND TO LB FILMS OF POLY-1-BENZYL-L-HISTIDINE

Imaging the ordered arrays of water-soluble protein ferritin with the atomic force microscope

SATOMI OHNISHI*, MASAHICO HARA†, TAJI FURUNO‡,
WOLFGANG KNOLL‡ & HIROYUKI SASABE*‡

* Saitama University, Urawa, Saitama 338, Japan.

‡ Institute of Physical & Chemical Research (RIKEN),
Frontier Research Program, Wako, Saitama 351-01, Japan.

ABSTRACT

A water-soluble protein, ferritin, on a silicon surface has been imaged in pure water at room temperature with the atomic force microscope (AFM). The samples were prepared by binding ferritin molecules electrostatically to a charged polypeptide layer of poly-1-benzyl-L-histidine (PBLH). The hexagonal arrangement of ferritin molecules was imaged with high reproducibility, since the force between tip and the sample surface could be kept sufficiently lower than 10^{-10} N. The applied force can be stabilized and weakened mainly due to a "self-screening effect" of the surface charges of the ferritin-PBLH layer. We demonstrate that the electrostatic-binding sample preparation is one of the suitable methods for soft biological specimens to achieve the nondestructive low-force AFM imagings.

INTRODUCTION

The AFM [1] has been increasingly drawing our attention as an entirely new approach in the study of the surface topography of biological specimens. In our previous paper [2], we reported the AFM images of ordered arrays of ferritin molecules. The relationship between the pH condition during the sample preparation and the AFM imagings has also been investigated. From these results, we concluded that controlling of the binding condition of biological specimens to the substrate is one of the crucial factors in getting reliable AFM images, and the PBLH film can be useful for AFM imagings as a general substrate for fixing water-soluble protein molecules without denaturation. From these points of view, an investigation on the properties of PBLH is necessary for obtaining unambiguous AFM images of biological molecules. The structure and properties of LB films of PBLH have already been studied by x-ray analysis and π -A isotherms [3]. In order to obtain more informations on the properties of PBLH films, we have studied the pH dependency of the forces between tip and surface of PBLH film, in addition to the AFM imagings of ferritin molecules bound to PBLH films.

EXPERIMENTAL

Ordered arrays of ferritin monolayers

Horse spleen ferritin (Sigma Chemical, St. Louis, MO, USA) was dissolved in pure water and fractionated by ultracentrifugation several times at 200,000g for 40 minutes. The heavier fractions were diluted with a solution of sodium chloride (10 mM) to a final concentration of 100 mg/ml. The ferritin solution was diluted with phosphate buffer (5 mM, pH 5.0–5.3) and prepared to a concentration of 30 µg/ml. The micro Langmuir trough (20 mm in width, 35 mm in length, and 2 mm in depth) was filled with the ferritin solution until the air-water interface became slightly convex. PBLH (Sigma Chemical) with an average degree of polymerization of 100 was dissolved in chloroform containing dichloroacetic acid (0.68 µl to 1 mg of PBLH) to a concentration of 0.54 mg/ml. An appropriate amount (3 µl) of PBLH was spread over the ferritin solution and incubated for three hours at room temperature so as to allow condensed ferritin molecules to form monolayers at a ferritin-PBLH interface.

We used silicon wafer (n-type, (100)) as a substrate because the two-dimensional ordered arrays of ferritin molecules have been observed previously with high-resolution SEM on this substrate prepared without staining or metal shadowing [4]. Before transferring ferritin-PBLH film, the silicon wafers were irradiated with UV light from a low pressure mercury lamp to obtain hydrophilic surfaces, placed in a glass desiccator filled with hexamethyldisilazane vapor, and then heated to 60 °C for one hour to bind hexamethyldisilazanes covalently to the surface, thus forming alkylated hydrophobic surface. The interfacial film (hetero-bilayer of ferritin-PBLH) on the trough was transferred onto such an alkylated silicon wafer by a horizontal transfer method [4]. The ferritin-PBLH film transferred on a silicon wafer was rinsed with pure water. The wafer glued to a steel disc was placed on an electrically grounded magnetic disc on top of a piezoelectric translator in an AFM system without drying. The film was imaged using a fluid cell in pure water.

AFM imagings

The AFM system used in this study was a commercially available NanoScope II (Digital Instruments, Inc., Santa Barbara, CA, USA). After slowly circulating pure water around the sample in a fluid cell, a Si₃N₄ cantilever, which is V-shaped and 200 µm long with a spring constant of 0.12 N/m (reported by Digital Instruments, Inc.), was positioned and scanned over

the sample in pure water at room temperature. AFM images (400 x 400 pixels) were obtained using the "height mode", which kept the force constant. The software provided with the AFM from the manufacture was used to measure force-versus-distance curves.

RESULTS AND DISCUSSION

pH dependency of the forces between tip and the surface of PBLH layer

Horse spleen ferritin has an isoelectric point of about 4.5 and is negatively charged in a solution of phosphate buffer of pH 5 or above [5]. The imidazole ring of PBLH, on the other hand, should be positively charged when PBLH is spread on a subphase at pH lower than the pKa of the histidyl residue (in the range of 6-7). Therefore, it is expected that ferritin in the subphase would bind electrostatically to a PBLH film at a slightly acidic pH range of 4.5-6.5 and form only a monolayer, even if there exist excess ferritin molecules near the interface. In this case, electrostatic charges at the ferritin-PBLH interface are cancelled, thereby forming a more efficient screening of the surface charges of ferritin monolayers, which we called the "self-screening effect" in our previous paper [2].

To elucidate the surface properties of PBLH films in the buffer solution, we investigated the forces of the tip interacting with a PBLH surface at various pH conditions. Figure 1 shows a series of force-versus-distance curves between the Si₃N₄ tip and the PBLH surfaces in different pH solutions. We used 10mM Tris-HCl buffer for pH 8.0, 7.5 and 7.0, and 10mM phosphate buffer for pH 7.0, 6.5, 6.0 and 5.0.

At pH 8.0, a repulsive force was observed upon approach and withdrawal of the AFM tip from the sample. When lowering the pH, the repulsive force decreased upon approach of tip, while an attractive force increased upon withdrawal. Since there is no large difference between the force curves at pH 7.0 in Tris buffer and phosphate buffer (data is not shown), the attractive force is independent on the species of electrolyte. From pH 6.5, as the pH value decreased, attractive forces increased upon approach and withdrawal of tip. Actually, we could not get any unambiguous images of the PBLH layers, owing to these repulsion and attraction.

This variation of the forces with changing a pH condition can be explained by electrostatic and hydrophobic interactions. The attractive force can be attributed mainly to hydrophobic interaction, since the PBLH film on the silicon substrate has a hydrophobic surface. Moreover, the surface of the tip is negatively charged, because silicon nitride bears a slight negative surface

charge in water. Therefore the interaction between negatively charged tip surface and positively charged PBLH may also enhance the electrostatic attraction below pH 6.5. Above pH 7.0, a repulsive force is expected because both surfaces bear negative charges. From these results, it is clear that the applied forces between tip and PBLH film in the solution are controllable by changing the pH. In addition, these results support our previous data with regard to the effect of pH of the buffer on the stability of the biological sample and the AFM imagings [2]. In this system, the PBLH film plays a critical role as an electrostatically charged substrate to fix ferritin molecules.

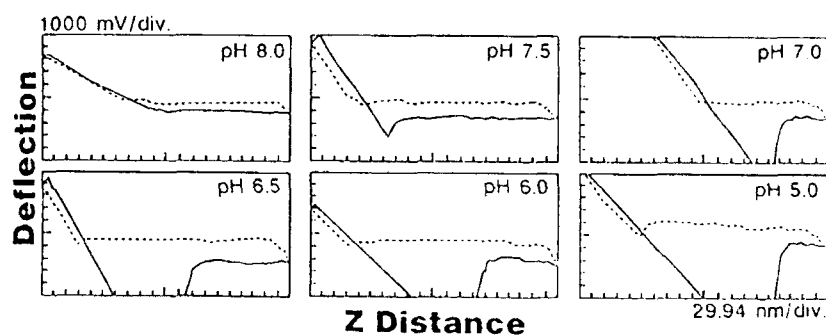


Fig. 1 A series of force-vs-distance curves between the Si_3N_4 tip and the PBLH surfaces in different pH solutions. The dashed and solid curves are for approach and withdrawal of the tip, respectively. (pH 8.0, 7.5, 7.0 ; 10mM Tris-HCl buffer; pH 6.5, 6.0, 5.5 ; 10mM phosphate buffer)

AFM imagings of ferritin molecules

Figure 2-a shows an AFM image of the ferritin sample on a silicon surface, which was prepared following the "self-screening effect" with the charged PBLH layer. Small spheres covering over the surface can be observed in an area of at least $738 \times 738 \text{ nm}^2$, approaching the limiting scanning area of this AFM. In Fig. 2-b, we show the typical unfiltered AFM image of the molecular packing of ferritin on a silicon surface taken in pure water at room temperature. Individually distinguishable spherical patterns and regular alignment are observed.

Figure 2-c shows an AFM image in a small scanning area. It is evident that seven spheres form a hexagonally packed arrangement. The hexagonally packed structure is in good agreement with the two-dimensional array of ferritin molecules observed by high resolution SEM, as we reported previously [4]. In addition, the spacing between these spheres in this pattern is about 14 nm with a

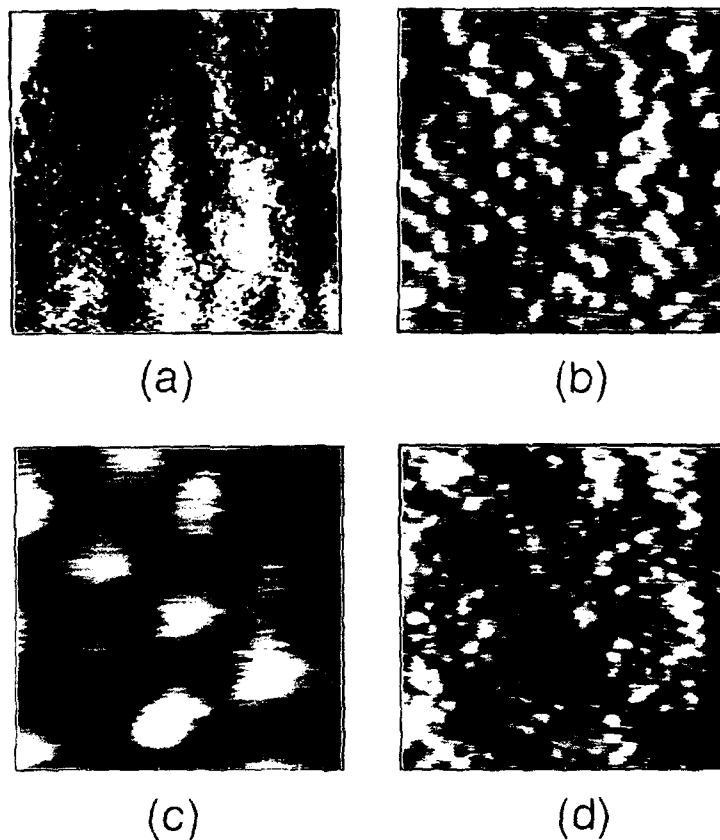


Fig. 2 Unfiltered AFM images of ferritin samples prepared at pH : (a-c) 5.3; and (d) 5.0. The image area is : (a) $738 \times 738 \text{ nm}^2$; (b) $200 \times 200 \text{ nm}^2$; (c) $45 \times 45 \text{ nm}^2$; and (d) $200 \times 200 \text{ nm}^2$. The imaging was carried out in pure water.

diameter of about 12 nm, which agrees well with that of a ferritin crystal deduced from x-ray analysis [6]. From these results, each spherical image obtained with AFM is identified as an individual ferritin molecule. These imagings were carried out for the ferritin monolayers prepared with phosphate buffer at pH 5.3. The applied forces operated in these images were estimated from the force curves to be 10^{-10} ~ 10^{-11} N. We have discussed in our previous paper [2] about the suitable pH condition for the AFM imagings during the sample preparation.

In the AFM image of the sample prepared at the pH value of around 5.0, we observed some domains in which ferritin molecules were bound to PBLH film in ordered arrays (Fig. 2-d). Ferritin molecules is likely to form some domains at pH 5.0, because the negative charge density of ferritin molecule becomes smaller as the pH increases.

From these results, we conclude that the sample preparation with electrostatic binding is one of the suitable methods to achieve the nondestructive low-force AFM imagings for biomacromolecules. In addition, controlling of the binding condition of protein molecules is also an important factor to get unambiguous AFM imagings.

REFERENCES

1. G. Binnig, C. F. Quate, and Ch. Gerber, *Phys. Rev. Lett.* **56**, 930 (1986).
2. S. Ohnishi, M. Hara, T. Furuno, and H. Sasabe, *Biophys. J.* **63**, 1425 (1992).
3. T. Furuno, H. Sasabe, R. Nagata, and T. Akaike, *Thin Solid Films.* **133**, 141 (1985).
4. T. Furuno, H. Sasabe, and M. Ulmer, *Thin Solid Films.* **180**, 23 (1989).
5. J. P. Arbutnott and J. A. Beeley. *Isoelectric Focusing*. 125pp (Butterworths, London 1975).
6. P. M. Harrison, *J. Mol. Biol.* **6**, 404 (1963).

ARTIFACTS IN ATOMIC FORCE MICROSCOPY OF NANOPOROUS AND MESOPOROUS FIDUCIAL SAMPLES

H. W. DECKMAN and R. J. PLANO

Corporate Research, Exxon Research & Engineering Co., Annandale, N.J.

ABSTRACT

Artifacts dominate atomic force microscope (AFM) images of nanoporous and mesoporous inorganic oxide materials taken under ambient atmospheric conditions with currently available tips. Artifacts in these AFM images are attributed to tip-sample interactions and the sharpness of tips on currently available cantilevers. We show that by modifying currently available AFM tips with carbonaceous materials, many image artifacts are eliminated. To characterize image artifacts, a variety of fiducial samples with feature sizes between ~ 100 Å and $2,000$ Å are used. One of the most useful fiducial samples is a close packed array of holes in a commercially available alumina membrane and we suggest that it be adopted as a standard fiducial sample.

Introduction

We have been examining the ability of atomic force microscopy (AFM) to probe the structure of inorganic nanoporous and mesoporous oxide materials. These materials¹⁻³ contain physical pores with sizes ranging from ~ 25 Å to $\sim 2,000$ Å and are often made from α -alumina, γ -alumina, silica, zirconia and composite structures such as of zeolites held in a porous α -alumina matrix. They are used in almost all heterogeneous catalysts as either a support⁴ for a dispersed catalytic material (such as Pt clusters) or as the active catalytic⁵ material (such as the composite zeolite / α -alumina matrix used in catalytic cracking). Nanoporous and mesoporous oxide materials are also used in inorganic microfiltration membranes⁶ and ultrafiltration⁶ membranes. To maximize mass transfer, materials used in catalysts and membranes are fabricated with a high density of pores which can comprise 10-50% of any exposed surface. We have scanned ~ 20 types of these inorganic nanoporous and mesoporous materials with the AFM under ambient atmospheric conditions. Although the AFM readily produces an image when these materials are scanned, a general correspondence between the image and the physical morphology of the sample surface is often lacking. We believe that the reasons for this are somewhat different from the multiple tip effects which give rise to Moiré patterns⁷ in atomic resolution images of materials such as graphite. We propose that for these classes of porous materials, image artifacts are generated both by the morphology (tip radius) and solid state surface chemistry of currently used AFM tips.

To image pores exposed at the surface, the tip radius must be small enough to fall into the pore mouth and must be able to lift out of the pore without sticking or deforming. Under ambient atmospheric conditions, the surface of an oxide pore structure contains species which may chemically and physically interact with an AFM tip. To change this interaction we have developed techniques to modify existing AFM tips structures with carbonaceous materials. Artifacts produced by these different tip modifications were characterized using a standard set of fiducial samples which have surface topography representative of the porous oxide materials. These fiducial samples will be described first.

Fiducial Samples

Two different classes of fiducial samples have been used to represent structures found on nanoporous and mesoporous inorganic oxide materials. The first has high spatial frequencies created by sharp edges around uniform sized pores in an alumina filtration membrane. The second has lower spatial frequencies formed by smoother spherical and prolate protrusions fabricated on a flat surface.

Easily obtainable ten micron thick alumina filtration membranes produced by Anotec Separations Ltd. were used as high spatial frequency fiducial samples. The membranes were made by controlled anodic oxidation of aluminum⁸ and different pore sizes can be created by controlling an electrochemical overpotential. Membranes made with 2,000 Å pores have a rough and smooth side and the morphology of the hole structure on the smoothest side of one of these alumina membranes is shown in Figure 1 below. Membranes with a smaller 200 Å pore structure formed asymmetrically at the surface of a ~2,000 Å pore structure are also available and Figure 2 shows their surface structure.

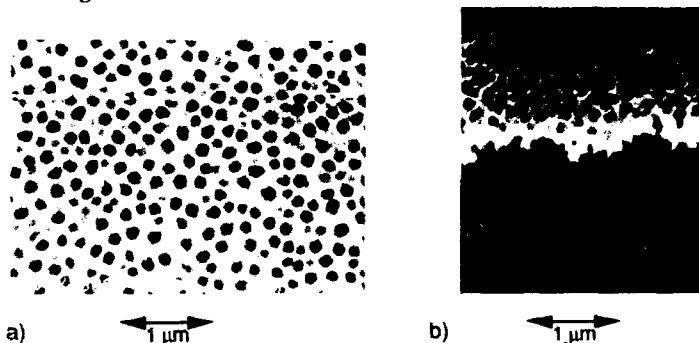


Fig. 1 a (Left) Electron micrograph showing a regular ~2,000 Å pore structure at the surface of an alumina filtration membrane made by Anotec Ltd.
Fig. 1 b (Right) Electron micrograph showing a cross section of the pore structure.

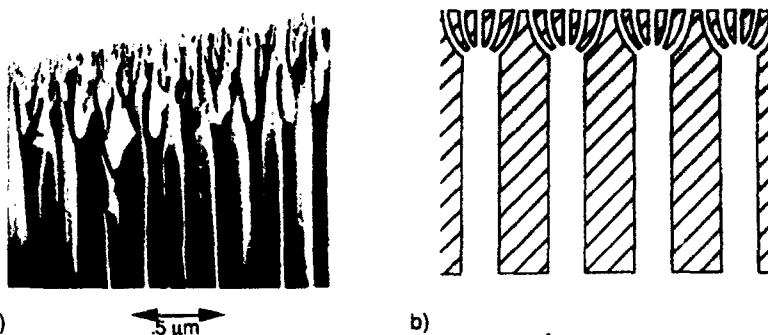


Fig. 2 a (Left) Electron micrograph of asymmetric ~200 Å pore structure formed on 2,000 Å pores. b (Right) Schematic diagram of pore structure.

Samples with lower spatial frequencies were prepared from monolayer coatings of polyballs on flat silicon substrates. Polyball coatings⁹ were either used directly as a fiducial or as a lithographic mask from which posts were fabricated⁹. Fig. 3a shows the hemispherical surface presented by a polyball monolayer coated onto a silicon wafer and Fig. 3b shows the morphology of a smooth prolate post structure created by using a coating of $\sim 5000 \text{ \AA}$ polyballs as a lithographic etch mask.

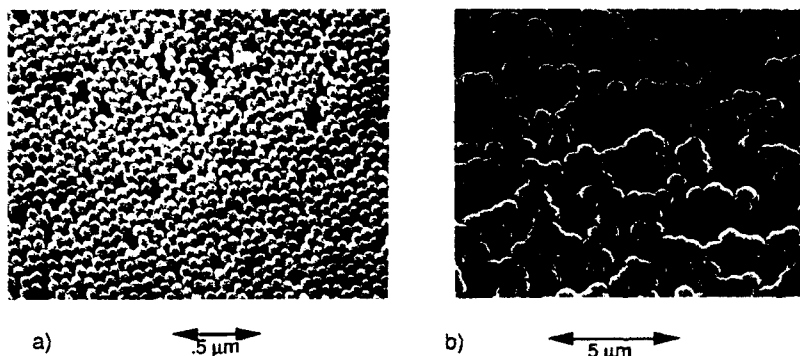


Fig. 3 a (Left) Electron micrograph showing monolayer thick coating of $\sim 2,000 \text{ \AA}$ polyballs on a silicon wafer.
 Fig. 3 b (Right) Electron micrograph showing $\sim 5,000 \text{ \AA}$ post structures formed by using a polyball monolayer as a mask in an ion beam etching process.

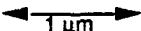
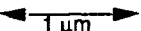
Scanning Of Fiducial Samples With Conventional AFM Tips

Fiducial samples were scanned under ambient atmospheric conditions with a Digital Instruments Nanoscope III using cantilevers obtained from two different suppliers. Cantilevers with silicon nitride tips having a $\sim 1,200 \text{ \AA}$ radius of curvature were obtained from Digital Instruments and cantilevers with silicon tips having a $\sim 250 \text{ \AA}$ radius of curvature were obtained from Nanoprobe (Germany). Although the tip radii were almost an order of magnitude different, they gave remarkably similar images of the fiducial samples. The reason for this may be that the sharper tips are blunted during the scanning process. Figure 4 shows the profile of a Nanoprobe silicon cantilever tip before and after scanning an alumina membrane with $\sim 2,000 \text{ \AA}$ pores. It is seen that the radius of the tip on the cantilever has changed from $\sim 250 \text{ \AA}$ to $\sim 1,000 \text{ \AA}$ during the course of the scan. This blunting during scanning did not seem to happen with the coarser silicon nitride tips. Figure 5 shows that the $\sim 1,200 \text{ \AA}$ radius of a silicon nitride tip on cantilevers supplied by Digital Instruments is not significantly changed after scanning fiducial samples.

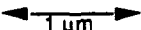
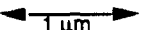
Images of lower spatial frequency fiducial samples (polyballs and posts) often showed significant distortions, however, individual elements in the fiducial pattern were clearly recognizable. Profiles of the $\sim 2,000 \text{ \AA}$ polyball samples were usually hemispherical with some distortion in the profile occurring at the lim of the sphere. With some tips, the polyball structure was asymmetrically distorted. Profiles across the $\sim 5,000 \text{ \AA}$ lithographically formed posts were significantly more distorted with most of the distortion occurring near the edge of the post. The sharper Nanoprobe silicon cantilever tips tended to give a somewhat better image than the Digital Instruments silicon nitride cantilevers.

Images of higher spatial frequency fiducial samples (alumina membranes with 200 Å and ~2,000 Å pores) were completely unrecognizable. Individual pore mouths could not be located within the images and Figure 6 shows typical examples of images produced. In principle both of these tips have radii small enough to image ~2,000 Å pores. The inability to image a ~2,000 Å pore structure could be due to a strong interaction of the tip with certain pores or features on the sample, causing it to stick at certain sites.



a)  b) 
 Fig. 4 a (Left) Electron micrograph of pristine ~250 Å radius silicon tip.
 Fig. 4 b (Right) Electron micrograph taken after scanning an alumina membrane fiducial with tip in Fig 4a. Tip radius has changed from ~250 Å to ~1,000 Å.



a)  b) 
 Fig. 5 a (Left) Electron micrograph of pristine 1,200 Å radius silicon nitride tip.
 Fig. 5 b (Right) Electron micrograph taken after scanning shows no change.

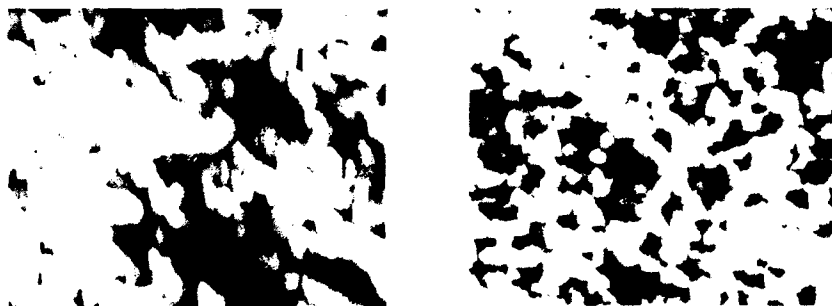


Fig. 6 AFM scans of 2,000 Å pores in alumina membrane shown in Fig. 1a. The features seen do not correspond with the sample's pore structure.
 a) Scan with silicon nitride tip b) Scan with silicon tip.

Modification Of Tips With Carbonaceous Deposits

The inability of conventional AFM tips to image $\sim 2,000 \text{ \AA}$ pores in alumina membranes may be due to tip-sample interactions. To change this interaction, we have coated the surface of conventional AFM tips with carbonaceous materials. Two different methods have been used to produce coatings. The first used contamination lithography¹⁰ to polymerize hydrocarbon vapors introduced into a scanning electron microscope. The electron beam grew a single whisker at the apex of the cantilever tip. A whisker ($\sim 800 \text{ \AA}$ radius end) grown on a cantilever using a 10 keV electron beam is shown in Figure 7a. A second method produced a coating of filamentous carbon¹¹ over the entire cantilever by catalytically decomposing propane at 700°C . Part of a filamentous carbon coating on a silicon nitride cantilever is shown in Figure 7b below. Tips with these types of carbonaceous coatings tended to produce sharper images of fiducial samples and one of the tips coated with filamentous carbon produced an image in which $\sim 2,000 \text{ \AA}$ pores in alumina membranes were identifiable (Figure 8).

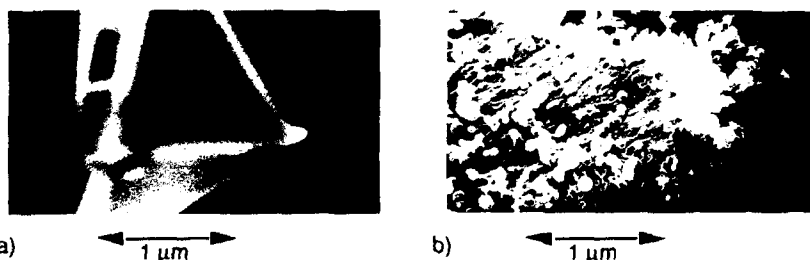


Fig. 7 a (Left) Electron micrograph of showing carbonaceous filament grown selectively at the apex of a cantilever tip using contamination lithography.
Fig. 7 b (Right) Electron micrograph showing filamentous carbon deposit on tip.



Fig. 8 AFM scans of $2,000 \text{ \AA}$ pores in alumina membrane shown in Fig. 1a. The features seen tend to correspond with the sample's pore structure.

Summary

The inability of conventional tips to image $\sim 2,000 \text{ \AA}$ pores in alumina could be due to strong interactions with surface absorbates and chemical groups terminating porous oxide surfaces. These interactions could potentially even produce a capillary force, pulling the tip into a pore. Carbon coatings that produced images of $\sim 2,000 \text{ \AA}$ pores are expected to have relatively nonpolar surfaces which would reduce interactions with species present on oxide surfaces.

References

1. C. N. Statter: ed, Heterogeneous Catalysis In Industrial Practice, 2nd ed. (McGraw-Hill Inc., New York, 1991), pp. 87-172.
2. D. Vaughn in Zeolites: Facts, Figures, Future edited by P. A. Jacobs and R. A. van Santen (Studies In Surface Science And Catalysis 49, Elsevier, Amsterdam, 1989) pp. 95-119.
3. C. J. Brinker and G. W. Scheer, Sol-Gel Science, (Academic Press, Boston, 1990), pp. 1-21.
4. J. H. Sinfelt, Bimetallic Catalysts, (John Wiley & Sons, New York, 1983), pp. 131-155.
5. C. E. Jahnig, D. L. Campbell, and H. Z. Martin in Proceedings Of International Fluidization Conference, edited by J. R. Grace and J. M. Matsen (Engineering Foundation, Plenum Press, New York, 1980). pp. 51-98.
6. A. F. Leenaars, K. Keizer, and A. J. Burgraff, J. Mater. Sci. **19**, 1077 (1984).
7. P. Rasch, W. M. Heckl, H. W. Deckman, and W. Haberlee in Synthesis/Characterization and Novel Applications Of Molecular Sieve Materials, edited by R. L. Bedard, T. Bein, M. Davis, J. Garces, V. Maroni, and G. Stuckey (Mater. Res. Soc. Proc. 233, Pittsburgh PA, 1991) pp. 287-293.
8. R. C. Furneaux, W. R. Rigby, A. P. Davidson, Nature **377**, 147 (1989).
9. H. W. Deckman and J. H. Dunsmuir, J. Vac. Sci. Technol. **B1**, 1109 (1983).
10. H. W. P. Koops, R. Weiel, and D. P. Kern, J. Vac. Sci. Technol. **B6**, 477 (1988).
11. R. T. K. Baker, Carbon **27**, 315 (1989).

Acknowledgments

The authors gratefully acknowledge technical assistance provided by J. McHenry and F. Lai.

Al INDUCED RECONSTRUCTIONS ON THE Si(111) SURFACES STUDIED BY SCANNING TUNNELING MICROSCOPY

Masamichi YOSHIMURA*, Katsuya TAKAOKA*, Takafumi YAO*,
Tomoshige SATO**, Takashi SUEYOSHI** and Masashi IWATSUKI**

*Department of Electrical Engineering, Hiroshima University, Higashi-hiroshima 724, Japan

**JEOL Ltd., Akishima, Tokyo 196, Japan

Abstract

The atomic arrangements of the α -7x7 phase and incommensurate phases of Al adsorbed Si(111) surface are investigated respectively by scanning tunneling microscopy (STM). STM images of α -7x7 surface reveal that characteristic triangular structures consisting of three Al adatoms situated on the center part of each half unit cell. The three Al adatoms form a triangular cluster and are bonded to the center adatoms. In this situation, the dangling bond of the center adatom is saturated, which would modify its electronic structure into non-metallic. The incommensurate phase consists of approximately 9x9 structures, which are separated each other with misfit dislocations. In the "9x9" structure, individual Al atom is visible arranged in threefold symmetry.

Introduction

Among the metal adsorbed Si(111) systems Al induced reconstruction has been one of the most attractive because of various structural phases. Investigations by low-energy electron diffraction (LEED)[1,2], angle-resolved ultraviolet photoelectron spectroscopy (ARUPS)[3] and electron energy loss spectroscopy (EELS)[4] etc. have been reported on their atomic or electronic structure. Hamers et al. studied the $\sqrt{3} \times \sqrt{3}$, $\sqrt{7} \times \sqrt{7}$ and Al-7x7 reconstructions, which appear at around 600°C with a coverage of less than 1 ML, with STM and scanning tunneling spectroscopy (STS). According to the recent LEED and RHEED studies[2], the Al-7x7 phase, which was denoted in earlier LEED work as " γ -7x7 phase" by Lander and Morrison[1], is not correct by name, since it does not have 7 but approximately 9 times periodicity. Hence this phase is referred to as "incommensurate phase". In contrast to the extensive studies of the above phases, few attention has been paid to α -7x7 reconstruction appearing at low temperature and low coverage. LEED pattern of this phase has a 7x7 periodicity but is different from that of clean Si(111) 7x7 surface[2]. The atomic structure of this phase has not been determined because the number of atoms in a unit cell is too large for dynamical LEED calculation, in addition to the lack of appropriate structural models.

In this paper we report the first STM observation of the α -7x7 and incommensurate phases on an atomic scale. The STM image over the α -7x7 surface reveals that a characteristic triangular cluster consisting of three Al atoms adsorbs on the center part of each half unit cell. The cluster affects the electronic structure of center adatoms while none of corner adatoms. High resolution images over the incommensurate phases demonstrate that individual Al atoms are clearly resolved and the periodicity of the surface observed is not 7x7 but almost 9 x 9, which is contrary to the STM work reported earlier by Hamers [5] but is consistent with recent LEED study[2].

Experimental

The STM used is a commercial one (JEOL JSTM-4000XV) which is designed for high temperature operation in ultra-high vacuum. The sample used as substrate is 1-10 Ω cm, B-doped Si(111) wafer. Before being loaded into the STM chamber (2×10^{-8} Pa) the sample is ultrasonically cleaned in acetone. It was then outgassed in the STM chamber for 12 hours and finally flashed repetitively at 1200°C to obtain a large flat area of the clean 7x7 surface. A tungsten wire is electrochemically etched for use of the probing tip. No thermal drift correction is made on STM images.

Results and Discussion

(a) α -7x7 phase

Figure 1 shows the α -7x7 surface after deposition of a few monolayer Al at 412°C obtained with the sample bias of -0.12V in the constant height mode. The 7x7 periodicity is clearly observed but definitely different from that of the clean surface. Only corner adatoms are visible, indicating that Al atoms react preferentially to center adatoms. With increase of the bias voltage (-2.0V), a bright triangular protrusion appears in the center of the half unit cell, as is shown in Fig 2. A 7x7 unit cell is drawn for reference. In consideration of their size and shape, they are likely to be clusters consisting of three Al atoms.

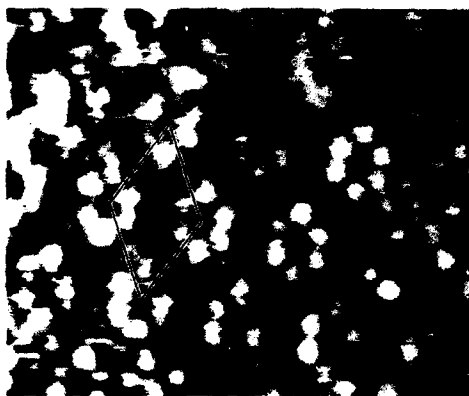


Fig. 1. STM image of α -7x7 surface at 412°C obtained at the sample voltage of -0.12V in a constant height mode. Only center adatoms are visible. The size is 13 x 10 nm².



Fig. 2. The α -7x7 surface obtained at the sample voltage of -2.0V in the constant current mode. Bright triangular protrusions correspond to Al clusters which locate at the center part of the half unit cells. The size is 13 x 12 nm².

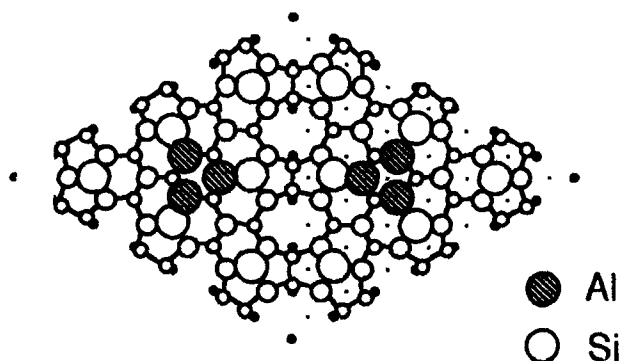


Fig. 3 A proposed structural model for α -7x7 surface. Three Al atoms form a cluster sitting on the center part of a half unit cell.



Fig. 4 Coexisted surface with 3x3, 7x7 and incommensurate structures (γ). The sample voltage is 1.47 V with an average current of 0.30 nA. The size is 16.5 x 19.5 nm².

Figure 3 shows a proposed structural model for α -7x7 structure. Al atoms form clusters by bonding each other and adsorb over the center adatoms. As a result, the number of dangling bond per half unit cell is reduced by three with a saturation of dangling bonds of the center adatoms. The saturation of dangling bonds causes the reduction of surface density of states near the Fermi energy, resulting in no protrusions as seen in Fig.1. Almost similar result was reported by St.Tosch et al. for Cu/Si(111) [6].

(b) Incommensurate phase

Incommensurate phase appears at about 600°C with a coverage of about 1 ML. This phase had long been mistaken for showing 7x7 periodicity. According to the recent LEED experiment [2] it shows mostly approximate 9x9 incommensurate structure together with a faint feature of 5x5 periodicity. The same structure was also reported by REM study [7].

A few monolayer of Al is deposited onto the clean 7x7 surface. Figure 4 shows an STM image of the surface after annealing at 600°C for 10 seconds. The sample voltage is 1.47V



Fig. 5 High-resolution image of the incommensurate structure. Individual Al atom is resolved on the triangles with 9x9 or 5x5 times reconstruction. Each triangle is separated by dark lines, misfit dislocations. The size is $16 \times 7.6 \text{ nm}^2$.

taken in a constant height mode. The variety of structures, 3×3 , 7×7 and incommensurate phases, are observed to coexist on the surface. The 7×7 structure consists of Al trimers in consistent with the earlier STM work by Hamers [5]. The incommensurate phase consists of characteristic triangles. Figure 5 shows a closer image of the incommensurate structure. The size of the triangle is about 8.94 times as that of bulk Si, the value of which is very close to that reported by LEED study [2]. Smaller triangles with 5×5 structure are also observed in a few cases. Each triangle is separated by dark lines which is considered to be misfit dislocations. On the terrace of the triangles is observed individual Al atom arranged in threefold symmetry.

Summary

We have observed the α - 7×7 and incommensurate phases in a Al/Si(111) system by scanning tunneling microscopy. The α - 7×7 surface has a 7×7 periodicity based on the ideal 7×7 structure. Al atoms adsorb in the form of clusters on the center part of half unit cells, which would affect the electronic structure of center adatoms by saturation of their dangling bonds. High-resolution images of the incommensurate surface reveal that characteristic triangles with about 9 and 5 times (in a few case) periodicity covers over the surface, each of which is separated by misfit dislocations. Individual Al atom is arranged with threefold symmetry on the terrace of the triangles.

Acknowledgement

We very appreciate Prof. A. Kawazu and Dr. H. Sakama of the University of Tokyo and Dr. Nishikata of the Furukawa Electric Co., Ltd for useful comments.

References

- [1] J. J. Lander and J. Morrison, *Surf. Sci.* 2, 553 (1964)
- [2] K. Nishikata, K. Murakami, M. Yoshimura and A. Kawazu, *Surf. Sci.* 269/270, 995 (1992)
- [3] T. Kinoshita, S. Kono and T. Sagawa, *Phys. Rev. B* 32, 2714 (1985)
- [4] M. K. Kelly, G. Margantondo, L. Papagno and G. J. Lapeyre, *Phys. Rev. B* 34, 6011 (1986)
- [5] R. J. Hamers, *Phys. Rev. B* 40, 1657 (1989)
- [6] St. Tosch and H. Neddermeyer, *Surf. Sci.* 211/212, 133 (1989)
- [7] K. Takayanagi, Y. Tanishiro, T. Ishitsuka and K. Akiyama, *Appl. Surf. Sci.* 41/42, 337 (1989)

STRUCTURE OF THE $\Sigma=3$ (111) GRAIN BOUNDARY IN Cu-1.5%Sb

RICHARD W. FONDA AND DAVID E. LUZZI

Laboratory for Research on the Structure of Matter and Department of Materials Science and Engineering, University of Pennsylvania, Philadelphia, PA 19104-6272

ABSTRACT

Grain boundaries in quenched and aged Cu-1.5%Sb were examined with Auger electron microscopy, transmission electron microscopy, and high resolution electron microscopy. The $\Sigma=3$ grain boundaries are strongly faceted, with the facets lying primarily along the coincident (111) planes of the two grains. The grain boundaries are enriched in antimony, as demonstrated by both AES and HREM. HREM images of the $\Sigma=3$ (111) \parallel (111) grain boundary differ from those of the Cu-Bi $\Sigma=3$ (111) \parallel (111) grain boundary in the lack of a significant grain boundary expansion to accommodate the excess solute at the boundary. A preliminary investigation of the atomic structure of the $\Sigma=3$ (111) \parallel (111) facet by HREM and multislice calculations is presented.

INTRODUCTION

Many alloys of copper exhibit segregation of solute to the grain boundaries. In Cu-Bi, Ference and Baluffi [1] have demonstrated that segregation of bismuth to the grain boundary induces a faceting transformation of that boundary. This faceting is common, occurring on a variety of crystallographic planes, but grain boundaries between grains with the $\Sigma=3$ misorientation exhibit a strong tendency for faceting. For example, after 24 h at 600°C, approximately 30% of the total grain boundary area consists of faceted $\Sigma=3$ grain boundaries [2]. The abundance of faceted boundaries in this alloy, as well as the increase in grain boundary area necessary to facet a boundary, attests to a low interfacial energy of these facets. The atomic structure of the primary facet orientation of grain boundaries in Cu-Bi, the $\Sigma=3$ (111) \parallel (111) facet, has recently been solved by HREM and atomistic calculations [3]. This structure contains a very large expansion of the grain boundary, with a close-packed plane of large bismuth atoms positioned above periodic vacancies in the (111) copper grain boundary plane.

Antimony is also known to embrittle copper, although not as severely as bismuth [4]. Since the chemistry of antimony and bismuth in copper should be similar, the most important difference is in the atomic sizes. The atomic radius of antimony is much smaller than bismuth but still significantly larger than copper. Therefore, it is of interest to explore the different structures which can form on grain boundaries with the same misorientation and boundary plane. In this paper we present preliminary results of a study of the $\Sigma=3$ (111) \parallel (111) grain boundary in Cu-1.5%Sb.

EXPERIMENTAL

Samples of Cu-1.5%Sb were prepared following the procedure used in the preparation of Cu-Bi samples [2]. The Cu-Sb alloy was cast into a 12 mm diameter mold. The cast structure was removed by annealing this sample, which had been

encapsulated with excess antimony, for 24 h at 650°C. The annealed sample was then swaged to a final diameter of 3 mm with one intermediate anneal. Isothermal heat treatments were conducted on lengths of this swaged rod, which were encapsulated with turnings of the same alloy to reduce antimony loss from the sample. Heat treatments were performed at 600°C for 3 h, 6 h, and 24 h. This treatment resulted in embrittlement of the grain boundaries. TEM samples were prepared by mechanically thinning slices of the heat treated rods to 110 μm , followed by electrochemical etching with 30% nitric acid in methanol at 100 V and electropolishing with the same solution at -60°C and 130 mA (13 V) to perforation. These samples were analyzed on a Philips 400T and JEOL 4000EX. Auger spectroscopy was conducted on a Perkin Elmer PHI-600 scanning Auger microprobe equipped with an in-situ fracture mechanism.

RESULTS AND DISCUSSION

The $\Sigma=3$ orientation relationship is defined for fcc metals as a 70.52° rotation of one crystal about a common [110] zone axis. This rotation produces superposition of all of the atomic sites on every third (111) plane. Therefore, if there are no rigid body displacements at the interface, the structure of a $\Sigma=3$ (111) || (111) grain boundary is crystallographically identical to that of the $\Sigma=3$ (111) || (111) twin boundary. Both of these interfaces would therefore be indistinguishable. However, in alloys which exhibit grain boundary segregation, the accumulation of solute at the grain boundary is likely to increase the interfacial energy of the $\Sigma=3$ grain boundaries while decreasing the total energy of the material. This difference is reflected in the contact angle of a high angle grain boundary which is intersected by the $\Sigma=3$ boundary. If the $\Sigma=3$ boundary were a twin boundary, the low interfacial energy would produce a very small inflection of the intersected grain boundary. However, if this were a $\Sigma=3$ grain boundary with segregated solute, the higher interfacial energy would produce a significant inflection of the intersected grain boundary. This criterion was used to determine the nature of $\Sigma=3$ boundaries in this study, and only $\Sigma=3$ boundaries which could be definitively defined as $\Sigma=3$ grain boundaries were used in the analyses.



Figure 1. Typical morphology of the $\Sigma=3$ grain boundary. The grain boundary plane is strongly faceted along (111) || (111). The diffraction pattern shows the $\Sigma=3$ misorientation with coincident reflections from the (111) planes.

Whereas faceted $\Sigma=3$ grain boundaries comprise up to 30% of the grain boundaries in Cu-Bi, there were only about 4% of these boundaries in the samples of Cu-Sb examined. The large driving force for their formation which is present in Cu-Bi is apparently not present in the Cu-1.5%Sb. However, the $\Sigma=3$ grain boundaries in Cu-1.5%Sb were all observed to be strongly faceted. These boundaries were almost exclusively faceted in the $(111)\parallel(111)$ orientation (Figure 1). Presumably, as in the case of Cu-Bi, the formation of a large number of $(111)\parallel(111)$ facets is a result of the pressure of segregant at the boundary; the driving force for segregation to a twin boundary is quite small in fcc alloys. The diffraction pattern of the boundary in Figure 1 demonstrates the $\Sigma=3$ orientation relationship, with coincident $[110]$ zone axes and superposition of the (111) reflections. Small steps on different facet planes were occasionally observed (Figure 2). In this image, the intersection of the two small steps with the foil surface show them to be faceted in different orientations. This indicates that the energy of these two facet orientations is similar. There is therefore no preferred facet orientation other than $(111)\parallel(111)$, as would be predicted from the predominance of this facet.



Figure 2. Image of a stepped $\Sigma=3$ grain boundary with three different facet planes. This boundary shows the predominance of the $(111)\parallel(111)$ facet orientation.

The segregation of antimony to the grain boundaries was measured by Auger electron spectroscopy. A notched 3 mm rod which had been heat treated at 600°C for 6 h was fractured in-situ at -190°C to ensure intergranular fracture with minimal deformation. The distribution of antimony on different grain boundary faces was very similar. A typical spectrum is shown in Figure 3. Semi-quantitative analysis of this

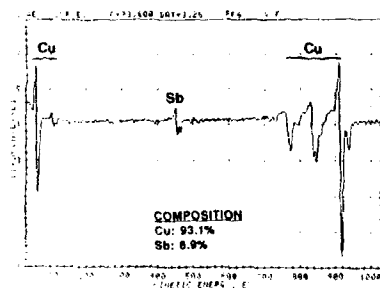


Figure 3. Auger electron spectroscopy of an in-situ intergranular fracture surface of Cu-Sb.

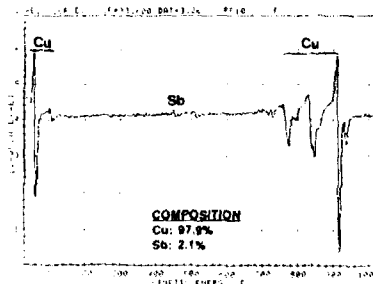


Figure 4. Auger electron spectroscopy of the same sample after removal of the grain boundary layer.

spectrum revealed an antimony concentration of about 7% at the grain boundary. In order to directly compare this result with the composition of the grain interiors, the intergranular fracture surface was sputtered with 3 keV argon for 10 min followed by chemical analyses of the exposed surface. Analyses of these grain interiors (Figure 4) revealed an antimony content which was less than one-third of what was observed at the grain boundaries, demonstrating that there is significant segregation of antimony to the copper grain boundaries.

High resolution images of the $\Sigma=3$ (111) || (111) grain boundary (Figure 5) are very similar to images of a twin boundary. However, images of the grain boundary typically exhibit a higher brightness of the boundary plane; images of a twin boundary show a uniform contrast across the boundary. This grain boundary contrast is even more evident at other defoci. Figure 5 also demonstrates a slight asymmetry in the interface. While the grain boundary atoms are perfectly aligned with the atomic sites of one grain, the other grain is slightly displaced parallel to the grain boundary. This displacement causes the grain boundary sites to be displaced from the atomic planes of that grain. Both the increased grain boundary intensity and this slight displacement parallel to the boundary are further evidence of segregation to this boundary.

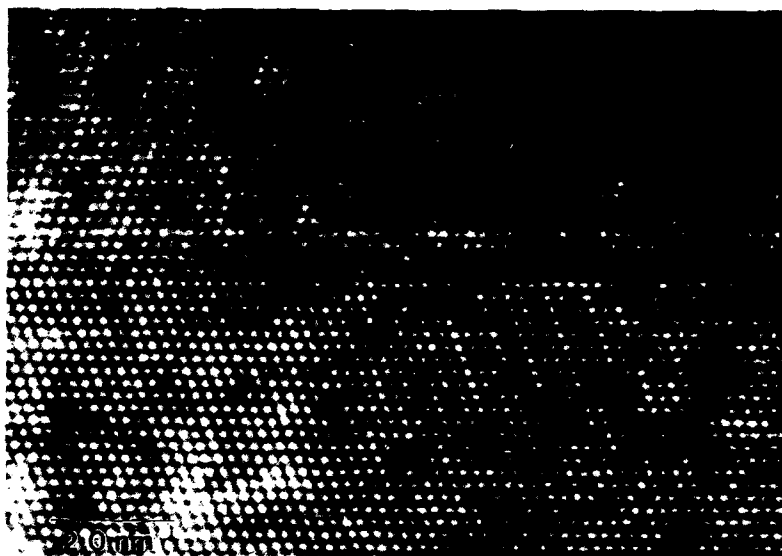


Figure 5. High resolution image of the $\Sigma=3$ (111) || (111) grain boundary. Note the bright contrast at the grain boundary plane.

Multislice image simulations were used to investigate possible structures of this segregated $\Sigma=3$ grain boundary. Replacing one-quarter of the grain boundary sites with antimony will reproduce a similar environment at the grain boundary to the low temperature copper-rich equilibrium phase, Cu_4Sb , which has a DO_{19} structure [5]. The distribution of solute atoms within the grain boundary plane and the simulated image of this structure are shown in Figure 6. The periodic grain boundary contrast displayed in

this image is not experimentally observed even though it is preserved for many other thicknesses and defocus conditions. A better match with the experimental images is produced for the grain boundary structure analogous to the Cu-Bi $\Sigma=3$ grain boundary structure but which contains no rigid body expansion. This structure has solute located at second-nearest neighbor positions within the grain boundary plane. The solute distribution and simulated image of this structure are shown in Figure 7. The major improvement in this image over Figure 6 is that the periodicity of the contrast within the boundary plane is reproduced. The overall grain boundary contrast is decreased with respect to the experimental image and some blurring has occurred. This structure contains a $1/3$ occupancy of antimony on the boundary lattice sites which is consistent with the Auger determination of 7% antimony at the boundary. This value of 7% is obtained by assuming that the antimony is strongly segregated to the grain boundary, that the escape depth of a low energy copper Auger electron is three atomic layers, and that one-half of the antimony is present on each face of the fracture surface.

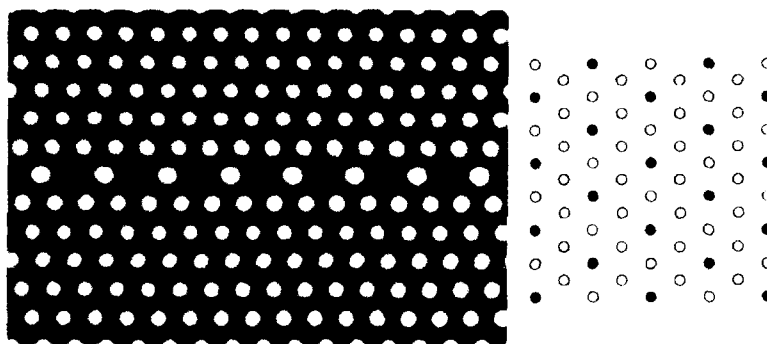


Figure 6. Schematic of solute distribution on the grain boundary plane for a $D0_{19}$ -like structure and simulated image of this structure. The grain boundary in this structure is $1/4$ antimony.

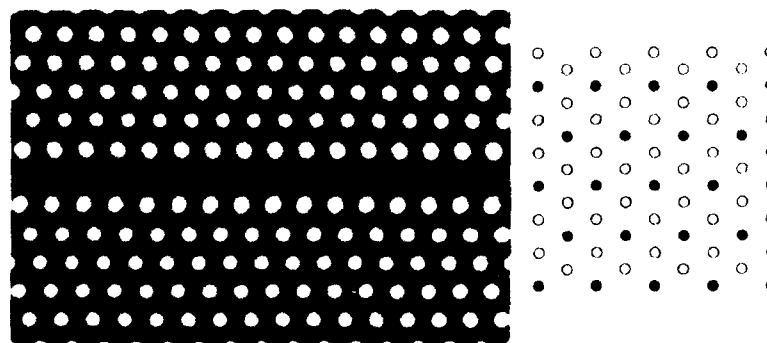


Figure 7. Schematic of solute distribution on the grain boundary plane for a structure similar to the Cu-Bi $\Sigma=3$ $(111)\parallel(111)$ grain boundary and simulated image of this structure. The grain boundary in this structure is $1/3$ antimony.

It is clear from simulations that the presence of antimony at the grain boundary can induce significant changes in local contrast. It is expected that this contrast will be a strong function of specimen thickness, defocus, the arrangement of antimony on the boundary lattice sites, and the compositions of antimony, copper, and point defects. Work is now in progress to vary the last two parameters within the constraints of the observed periodicities, the rigid body displacements at the boundary, and the Auger data in order to reproduce boundary images as a function of defocus and thickness.

SUMMARY

Electron microscopy was used to examine the grain boundaries in Cu-1.5%Sb. The segregation of antimony to grain boundaries was observed by Auger electron microscopy. The concentration of antimony at the grain boundary was more than three times the concentration within the grain. Grain boundaries with the $\Sigma=3$ orientation are strongly faceted, and the facet plane of these boundaries is predominantly $(111)\parallel(111)$. HREM images of this facet orientation exhibit a high intensity of the grain boundary plane, and a slight displacement of one grain parallel to the boundary, which are not present in the image of a twin boundary. However, the large grain boundary expansion which was observed in Cu-Bi was not present in this alloy. In addition, the high concentration of $\Sigma=3$ grain boundaries in Cu-Bi is also not paralleled in Cu-Sb. Only about 4% of the grain boundaries in Cu-Sb exhibit this misorientation.

ACKNOWLEDGEMENTS

The authors would like to acknowledge support of this project by the National Science Foundation under grants 91-11775 and 91-20668 and support for central facilities through the Penn-MRL. They would also like to thank Ms. D. Ricketts-Foot for the maintenance of the microscopes.

REFERENCES

1. T. G. FERENCE and R. W. BALUFFI, *Scripta Metall.*, **22**, 1929 (1989).
2. E. C. Urdaneta, D. E. Luzzi, and C. J. McMahon, Jr. in Structure and Properties of Interfaces in Materials, edited by A. T. Clark, U. Dahmen, and C. L. Briant (Mater. Res. Soc. Proc. **238**, Pittsburgh, PA 1992) pp. 201-205.
3. D.E. Luzzi, Min Yan, M. Šob and V. Vitek, *Phys. Rev. Lett.*, **67**, 1894 (1992).
4. Ye. E. Glikman, Yu. V. Goryunov, Yu. V. Piguzov, I. Ya. Rzhetskaya, and B. Ya. Tokarev, *Fiz. metal. metalloved.*, **41**(3), 553 (1976).
5. W. B. Pearson, A Handbook of Lattice Spacings and Structures of Metals and Alloys, Vol. 2, (Pergamon Press, Oxford, 1967), p. 884.

HIGH RESOLUTION ELECTRON MICROSCOPY OF $\Sigma=3$ NiSi₂ ($\bar{1}11$)/($\bar{1}\bar{1}5$) Si AND NiSi₂($2\bar{2}1$)/(001)Si INTERFACES

Wen-Jauh Chen* and Fu-Rong Chen**

* Department of Mechanical Materials Engineering, National Yun-Lin Institute of Technology,
Yun-Lin, Taiwan, R.O.C.

** HRTEM LAB, Materials Science Center, National Tsing-Hua University, Hsinchu, Taiwan,
R.O.C.

ABSTRACT

High resolution imaging technique is applied to systematically study the $\Sigma=3$ NiSi₂ ($\bar{1}11$)/($\bar{1}\bar{1}5$) Si and NiSi₂($2\bar{2}1$)/(001)Si interfaces. The long-period boundaries of $\Sigma=3$ NiSi₂ ($\bar{1}11$)/($\bar{1}\bar{1}5$) Si and NiSi₂($2\bar{2}1$)/(001)Si have been shown to decompose into short period of symmetrical NiSi₂($\bar{1}\bar{1}1$)/($\bar{1}\bar{1}1$)Si and NiSi₂($\bar{1}\bar{1}2$)/($\bar{1}\bar{1}2$)Si atomic facets which are similar to the case of asymmetrical twin boundaries in NiSi₂ crystal. This result is consistent with the computer simulation in grain boundary case that asymmetrical tilt boundaries which are generally of longer periods may facet on an atomic scale into short period symmetrical boundaries.

The domain-related atomic faceting interfaces have been found in both of $\Sigma=3$ NiSi₂ ($\bar{1}11$)/($\bar{1}\bar{1}5$) Si and NiSi₂($2\bar{2}1$)/(001)Si interfaces. The coexistence of two domain-related atomic faceting interfaces in the $\Sigma=3$ NiSi₂ ($\bar{1}11$)/($\bar{1}\bar{1}5$) Si has also been observed in different area of an interface which are separated by a $1/4\langle 111 \rangle$ type of dislocation associated with a 'demi-step'. The Burgers vector and step of a dislocation required to separate two domain structures in the $\Sigma=3$ NiSi₂/Si interface can be derived from the C CSL model.

INTRODUCTION

Usually, there are two observed orientations for epitaxial NiSi₂ and CoSi₂ on Si, known as type A and type B orientations. Both NiSi₂ and CoSi₂ have the CaF₂ structure which have lattice mismatch 0.4% and 1.2% with the substrate Si, respectively. Type A silicides have the same crystallographic orientation as the substrate, while type B silicide shares the substrate [111] axis, but is rotated 180° about this axis. Applying the idea of Constrained-Coincidence-Site-Lattice (CCSL) model [1, 2] $\Sigma=1$ and $\Sigma=3$ CCSL unit cells for type A and type B NiSi₂/Si can be obtained by constraining 0.4% in $\langle 100 \rangle$ direction of Si crystal, respectively.

In the previous high resolution electron microscopy studies of the NiSi₂/Si and CoSi₂/Si interface [3-12], particular attention was given to the coordination of the interfacial metal atoms at $\Sigma=1$ NiSi₂/(001)Si, $\Sigma=1$ NiSi₂/(111)Si and $\Sigma=3$ NiSi₂/(111)Si interfaces.

In this paper, we report a systematically HRTEM investigation on the long-period boundaries of $\Sigma=3$ NiSi₂($2\bar{2}1$)/(001)Si and $\Sigma=3$ NiSi₂ ($\bar{1}11$)/($\bar{1}\bar{1}5$) Si. All possible domain-structures of $\Sigma=3$ NiSi₂($2\bar{2}1$)/(001)Si and $\Sigma=3$ NiSi₂ ($\bar{1}11$)/($\bar{1}\bar{1}5$) Si interfaces and their associated dislocation can be deduced from the Constrained-Coincidence-Site-Lattice model.

EXPERIMENTAL PROCEDURES

The epitaxial NiSi₂ thin film were grown by depositing 30nm metal nickel on phosphorus doped (001) oriented silicon wafer followed by isothermal annealing in a three zone furnace at 800°C in N₂ ambient for 20 min. A standard method of processing metal silicide thin films was described in detail elsewhere [13]. High resolution imaging was carried out in a JEOL 4000EX microscope with C_s=1.0mm, focus spread $\Delta=15$ nm and beam divergence $\alpha=0.55$ mrad. The 'optimum underfocus', $-1.2(C_s\lambda)^{1/2}$ of the JEOL 4000EX is near -50 nm. However, the high resolution image contrast behaviors of Si as well as NiSi₂ crystal within the underfocus values of -32 nm and -50 nm are not much different. The bright spots in the high resolution images of NiSi₂ and Si viewed along a common [110] direction

correspond to the positions of empty channels in these two structures for the underfocus values of -32 nm and -50 nm, except bright dots are elongated along $[1\bar{1}0]$ in the high resolution image of NiSi₂ for a underfocus value of -50 nm. Except mentioned specially, all the high resolution images shown in this paper were taken at a underfocus value -32 nm. The underfocus value is estimated from the minimum contrast of the amorphous region in the edge of specimen. Program "CrystalKit" written by Kilaas [14] was used as an aid to model the complex atomic structure of the symmetrical and the asymmetrical boundaries. Computer image simulation was carried out using a program "MacTempas" also developed by Kilaas [14].

RESULTS

CCSL Model of NiSi₂/Si interfaces

The lattice constant of NiSi₂ is 0.504 nm and the unit cell of NiSi₂ is composed of three interpenetrated f.c.c. cells whose origins located at Ni (0,0,0), Si (1/4,1/4,1/4) and Si (3/4,3/4,3/4), respectively. Each Ni atom in NiSi₂ is surrounded by eight equidistant Si atoms whereas each Si atom is surrounded by four equidistant Ni atoms. The bonding length of Si-Ni bonds in NiSi₂ is the same as Si-Si bonds in Si given by 0.234 nm. The CCSL dichromatic patterns can be generated by selecting different Si atoms in NiSi₂ and Si crystals as the origins and subsequently it yields four possible CCSL dichromatic patterns formed by NiSi₂ and Si crystals for $\Sigma=3$. The CCSL unit cells of $\Sigma=3$ are shown in the figure 1. The CCSL patterns in (b), (c) and (d) can be obtained from that in (a) by shifting the Si crystal a vector **b**, **c** and **d**, respectively, indicated in figure 2 for $\Sigma=3$. The vectors **b** and **c** are the $1/4\langle 111 \rangle$ type of vectors. However, these two vectors are different. The **b** type of vectors join two Si atoms in Si crystal, while **c** type of vectors are not the vectors joining two Si atoms. The **d** vectors are $1/2\langle 010 \rangle$ type. An interfacial dislocation of Burgers vector **b**, **c**, or **d** is needed to separate two coexisting interfacial domain structures created from two different CCSL dichromatic patterns [15-17].

The procedures of constructing possible unrelaxed geometric models for an interface were given by Pond [15,16]. The (C)CSL dichromatic patterns of two crystals can first be constructed. Possible unrelaxed geometric models of a bicrystal are then created from placing a chosen orientation of interfacial plane in the (C)CSL dichromatic patterns, and subsequently locating atoms of crystal 1 in one side of interface and atoms of crystal 2 in the other side of interface. Further relaxation such as relative displacement of the adjacent crystals, migration of the interfaces, local relaxation of individual atoms, or removal or addition of atoms in the interface core may be involved to achieve the final low energy interface structures.

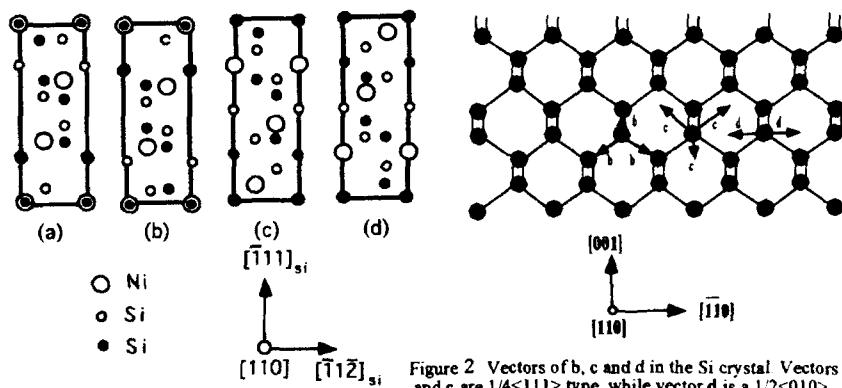


Figure 2 Vectors of **b**, **c** and **d** in the Si crystal. Vectors **b** and **c** are $1/4\langle 111 \rangle$ type, while vector **d** is a $1/2\langle 010 \rangle$

Fig. 1 The CCSL unit cells of $\Sigma=3$.

- is the coincidence sites of Ni and Si atoms
- is the coincidence sites of Si and Si atoms

Interface structure of $\Sigma=3$ NiSi₂(2 $\bar{2}$ 1)/(001)Si and NiSi₂($\bar{1}$ 11)/(1 $\bar{1}$ 5)Si

Since the boundary plane of NiSi₂ and Si are crystallographically different for $\Sigma=3$ NiSi₂(2 $\bar{2}$ 1)/(001)Si and NiSi₂($\bar{1}$ 11)/(1 $\bar{1}$ 5)Si interfaces, we refer these two interfaces to be asymmetrical 'hetero-twin' boundaries. These asymmetrical 'hetero-twin' boundaries have been shown to form symmetrical atomic facets of ($\bar{1}\bar{1}\bar{1}$)NiSi₂/($\bar{1}\bar{1}\bar{1}$)Si and ($\bar{1}\bar{1}2$)NiSi₂/(1 $\bar{1}2$)Si [18] which is similar to the case of asymmetrical twin boundaries in NiSi₂ crystal [19]. This result is consistent with the computer simulation in grain boundary case that asymmetrical tilt boundaries which are generally of longer periods may facet on an atomic scale into short period symmetrical boundaries [20-21].

Four possible models of atomic facets for $\Sigma=3$ NiSi₂(2 $\bar{2}$ 1)/(001)Si interface can be deduced from the CCSL dichromatic patterns by the procedures given in last section and are depicted in the figure 3 (a) to (d). The symmetrical atomic facets of ($\bar{1}\bar{1}\bar{1}$)NiSi₂/($\bar{1}\bar{1}\bar{1}$)Si and ($\bar{1}\bar{1}2$)NiSi₂/(1 $\bar{1}2$)Si facets are shown by dashed lines. The ($\bar{1}\bar{1}\bar{1}$)NiSi₂/($\bar{1}\bar{1}\bar{1}$)Si facet contains 6-atom ring and the ($\bar{1}\bar{1}2$)NiSi₂/(1 $\bar{1}2$)Si facet contains 5- and 7-atom rings. In the models 3(a) and (b), the bond length of Ni-Si and Si-Si are everywhere preserved as those in the bulk, however, the Ni-Si and Si-Si bonds of 5-atom, 6-atom and 7-atom rings for the structure models 3(c) and (d) are slightly distorted. The simulated images of these four models for a underfocus value -32nm and thickness 4nm are depicted in figures 4(a) to (d). As we can see, the common {111} lattice planes of both crystals in the simulated image of figure 4(b) continuously across the interface, while those of figures 3(a), (c) and (d) are slightly shifted.

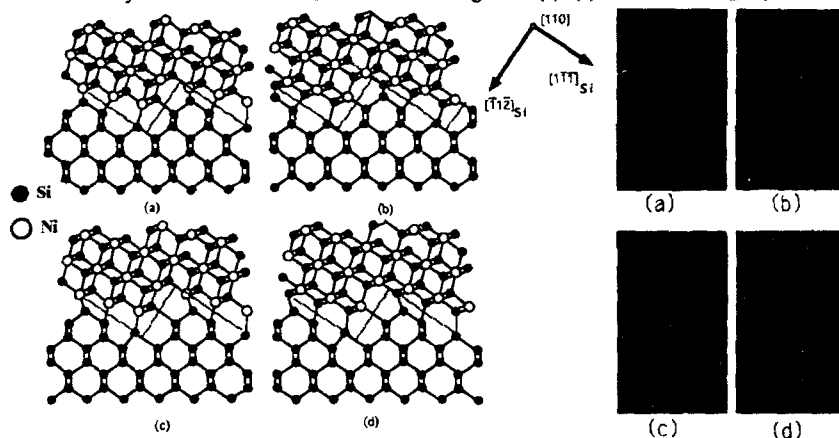


Figure 3. Four possible models of atomic facets for $\Sigma=3$ NiSi₂(2 $\bar{2}$ 1)/(001)Si interface deduced from the $\Sigma=3$ CCSL dichromatic patterns

Figure 4 The simulated images of four models in figure 16 for a underfocus value -32nm and thickness 4nm

Figure 5(a) shows a high resolution image of $\Sigma=3$ NiSi₂(2 $\bar{2}$ 1)/(001)Si interface. The model of this image can be constructed independently from the reference of positions of bright dots and is same as that given in the figure 3(b). The simulated image in figure 4(b) is shown as an inset in figure 5(a) and good match between the simulated image and experimental image is obtained.

Figure 5(b) is the other high resolution image of $\Sigma=3$ NiSi₂(2 $\bar{2}$ 1)/(001)Si interface. Carefully comparing the difference between figure 5(a) and (b), the common {111} lattice planes continuously cross the boundary which are shown as a continuous dark line in the figure 5(a), however, the common {111} lattice planes of both crystals are shifted across the boundary and are shown as a broken solid line in figure 5(b). In addition, the contrast of bright dots in this interface seems to suggest that the structural unit rings are distorted compared with

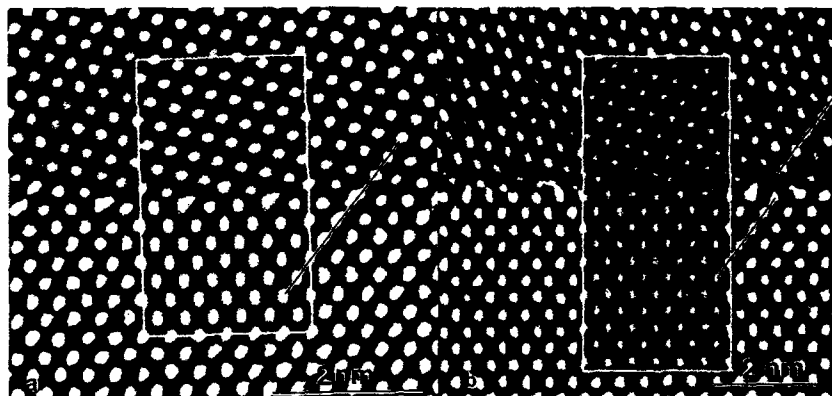


Figure 5 (a) and (b) are two different contrast of high resolution images of $\Sigma=3$ $\text{NiSi}_2(221)/(001)\text{Si}$ interface. The top crystal is NiSi_2 and the lower crystal is Si .

that in the interface of figure 5(a). Examining the simulated images in figures 4(a) to (d), the simulated image of interface model in figure 4(d) which shows periodic arc contrast in the interface matches superior to the others. This simulated image is shown as an inset in the figure 5(b) for comparison. A d-type of $1/4\langle 111 \rangle$ type of interfacial dislocation is required for the coexistence of these two domain-related atomic faceting interfaces.

The coexistence of two domain-related atomic faceting interface is found in a $\Sigma=3$ $\text{NiSi}_2(\bar{1}11)/(\bar{1}\bar{1}5)\text{Si}$ interface and is shown in the figure 6(a). These two faceting structures are separated by a dislocation which is shown as a symbol \perp in the figure 6(a). It can be seen that a set of common $\{111\}$ lattice plane shown as a dark line continuously passes through the boundary in the right hand side of dislocation, while the $\{111\}$ lattice planes in the left hand side of dislocation are shifted slightly which is shown by the broken dark line. The structure model of figure 6(a) is depicted in figure 6(b). This structural model is constructed with the reference of the positions of the bright dots in the figure 6(a).

Again, similar to the case of the $\Sigma=3$ $\text{NiSi}_2(221)/(001)\text{Si}$ interface, there are four possible structural models for $\Sigma=3$ $\text{NiSi}_2(\bar{1}11)/(\bar{1}\bar{1}5)\text{Si}$ interface which can be deduced from the CSSL dichromatic patterns. They are depicted in figures 7(a) to (d) and their simulated image for a underfocus value -32nm and thickness 4nm are shown in figures 8(a) to (d). The Burgers vector of the dislocation in the figure 6 is, therefore, a b-type of $1/4\langle 111 \rangle$, since it separates two domain-related atomic faceting interfaces which can be deduced from the CSSL patterns in figure 1(a) and (b). This b-type of $1/4\langle 111 \rangle$ dislocation is associated with a demi-step which separates two different terminating lattice planes of NiSi_2 in the interface [17]. This $1/4\langle 111 \rangle$ dislocation may be responsible for the accommodating the misfit and migration of the $\Sigma=3$ $\text{NiSi}_2(\bar{1}11)/(\bar{1}\bar{1}5)\text{Si}$ interface by a process similar to diffusion induce grain boundary migration (DIGM).

As it can readily be seen, the simulated image of structural model in figure 8(a) shown as an inset matches with the experimental image in the left hand side of dislocation, while that in figure 8(b) matches with the experimental image in the right hand side of dislocation. The $\Sigma=3$ $\text{NiSi}_2(\bar{1}11)/(\bar{1}\bar{1}5)\text{Si}$ interface of structural models (c) and (d) were not found in our experiment. However, they may also exist in different parts of interface.

DISCUSSION AND CONCLUSIONS

The possible geometrical structure models of NiSi_2/Si interface can be completely derived from the CSSL dichromatic patterns. The long period of asymmetrical $\Sigma=3$ $\text{NiSi}_2(221)/(001)\text{Si}$ and $\text{NiSi}_2(\bar{1}11)/(\bar{1}\bar{1}5)\text{Si}$ interfaces form symmetrical $(\bar{1}\bar{1}\bar{1})\text{NiSi}_2/(\bar{1}\bar{1}\bar{1})\text{Si}$

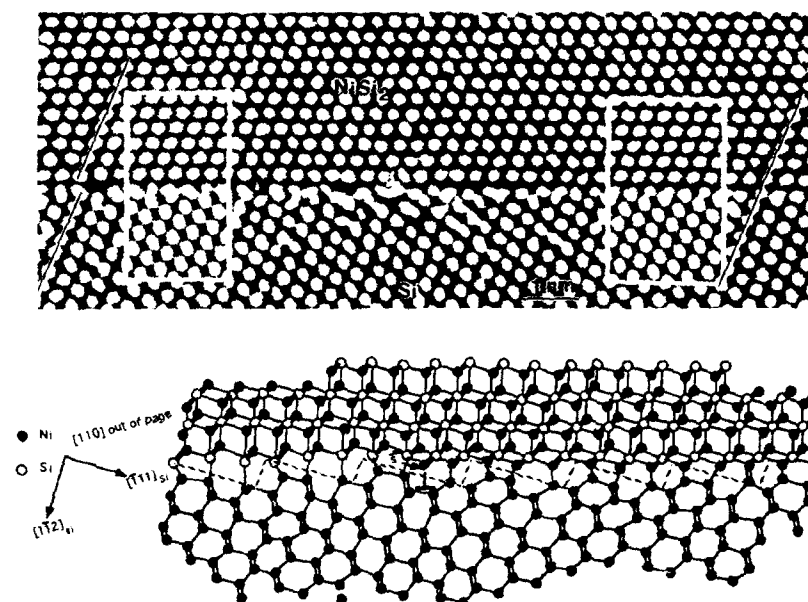


Figure 6 (a) shows the coexistence of two domain-related atomic faceting interface in a $\Sigma=3$ $\text{NiSi}_2(111)/(115)\text{Si}$ interface. These two faceting structures are separated by a $1/4\langle 111 \rangle$ dislocation which is shown as a symbol \perp . (b) The structure model of figure 6(a).

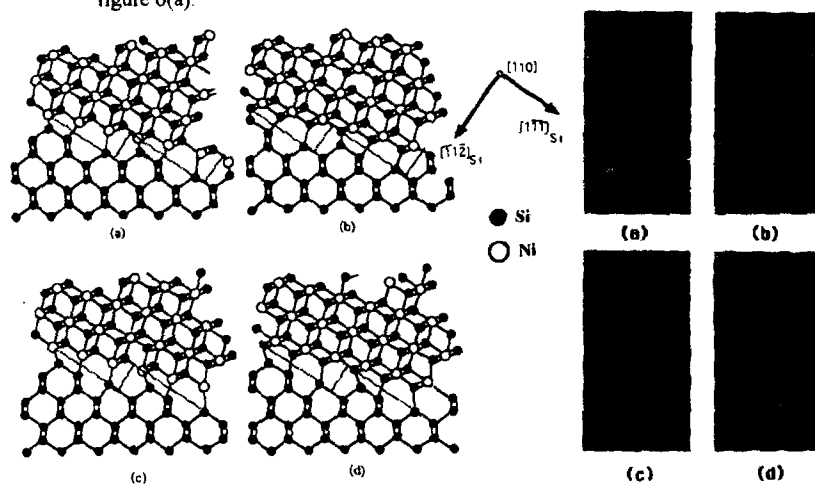


Figure 7 Four possible structural models for $\Sigma=3$ $\text{NiSi}_2(111)/(115)\text{Si}$ interface which can be deduced from the $\Sigma=3$ CCSL dichromatic patterns.

Figure 8 The simulated images of the interface models in figure 7 for a underfocus value -32nm and thickness 4nm .

and $(\bar{1}12)_{\text{NiSi}_2}/(1\bar{1}2)_{\text{Si}}$ facets in atomic scale which is similar to the case of asymmetrical tilt grain boundary. The domain-related structure were found in the atomic faceting $\Sigma = 3$ $\text{NiSi}_2(2\bar{2}1)/(001)_{\text{Si}}$ and $\text{NiSi}_2(\bar{1}11)/(1\bar{1}5)_{\text{Si}}$ interfaces. Two domain-related interfaces are separated by a $1/4\langle 111 \rangle$ type dislocation which is associated with a demi-step. The $1/4\langle 111 \rangle$ dislocations may be responsible for accommodating the 0.4% lattice misfit and for migration of the interface by a diffusive flux of Ni or Si atoms which is a process similar to the diffusion induced grain boundary migration (DIGM) in grain boundary case [22, 23].

Qualitatively, the interfacial energy is dependent on the number of distorted bonds, dangling bonds in the boundary core [24] and the coordination number of Ni atoms [25-27]. The interfacial energy of the domain structure in the $\Sigma = 3$ $\text{NiSi}_2(2\bar{2}1)/(001)_{\text{Si}}$ interface of figure 5 (b) may be higher than that in the figure 5(a), since the length and angle of Ni-Si bonds of the 5-, 7- and 6- atom rings in figure 5(b) are stretched and distorted compared with those in the interface of figure 5(a). The interfacial energy of two domains in the $\text{NiSi}_2(\bar{1}11)/(1\bar{1}5)_{\text{Si}}$ interface may be also different, since interfacial Ni atoms are 5-fold coordinated left hand side of dislocation and are 6-fold coordinated the right hand side of dislocation. Calculation of interfacial energy is not attempted in this research. However, the existence of different domain structures in the atomic faceting $\Sigma = 3$ $\text{NiSi}_2(2\bar{2}1)/(001)_{\text{Si}}$ and $\text{NiSi}_2(\bar{1}11)/(1\bar{1}5)_{\text{Si}}$ interfaces may suggest that they are metastable structures which could transform to each other by gliding or climbing a $1/4\langle 111 \rangle$ dislocation.

ACKNOWLEDGMENTS

The authors would like to thank the support from Materials Science Center, National Tsing Hua University and the support from the Republic of China National Science council. Thanks to Professor L. J. Chen for accessing E-gun. The support for maintaining JEOL 4000EX by Ms. L. J. Yang is also appreciated.

REFERENCES

1. R. Bonnet and F. Durand, *Phil. Mag.*, **32**, 997 (1975)
2. F.-R. Chen and A. H. King, *Phil. Mag.*, **57**, 431 (1988)
3. D. Cherns, G. R. Anstis, J. L. Hutchison and J. C. H. Spence, *Philos. Mag.* **A46**, 849 (1982)
4. D. Cherns, C. D. J. Hetherington and C. J. Humphrey, *Philos. Mag.* **A 42**, 165 (1984)
5. A. E. White, K. T. Short, R. C. Dynes, J. P. Garro and J. M. Gibson, *Appl. Phys. Lett.*, **50**, 95 (1987)
6. A. F. De Jong and C. W. T. Bulle-Lieuwma, *Phil. Mag.* **62**, 183 (1990)
7. C. W. T. Bulle-Lieuwma, A. H. Van Ommen, D. E. W. Vandenhoult, J. J. M. Ottenheim and A. F. De Jong, *J. Appl. Phys.* **70**, 3093 (1991)
8. C. W. T. Bulle-Lieuwma, A. F. De Jong and D. E. W. Vandenhoult, *Phil. Mag.* **64**, 255 (1991)
9. J. M. Gibson, J. C. Bean, J. M. Poate and R. T. Tung, *Appl. Phys. Lett.*, **41**, 818 (1982)
10. D. Loretto, J. M. Gibson and S. M. Yalisove, *Phys. Rev. Lett.*, **63**(3), 298 (1989)
11. A. Catana, M. Heintze and P. E. Schmid and P. Stadelmann *Mat. Res. Soc. Symp. Proc.*, **159**, 147 (1990)
12. C. D'Anterroches Meneau and P. Perret, *Phil. Mag.* **63**, 1221 (1991)
13. W. J. Chen, F.-R. Chen and L. J. Chen, *Appl. Phys. Lett.*, **60**, 2201 (1992a)
14. R. Kilaas, *Proceedings of 49th EMISA Meeting*, San Fransisco, CA USA, (1991) 528
15. R. C. Pond, *Phil. Mag.* **A47**, L49 (1983 a)
16. R. C. Pond, *Inst. Phys. Conf. ser.* **67**, 59 (1983 b)
17. R. C. Pond and D. Cherns, *Surf. Sci.*, **152/3**, 1197 (1985)
18. W. J. Chen and F.-R. Chen, accepted by *Ultramicroscopy* (1992)
19. W. J. Chen, F.-R. Chen and L. J. Chen, accepted by *Phil. Mag.* (1992b)
20. A. P. Sutton and V. Vitek, *Phil. Trans. Roy. Soc. London*, **A309**, 1,37,55 (1983)
21. A. Brokman, P. D. Bristowe and R. W. Balluffi, *Script Met.*, **15**, 201 (1981)
22. A. H. King and D. A. Smith, *Acta Crystallogr.*, **A36**, 335 (1980)
23. R. W. Balluffi, A. Brokman and A. H. King, *Phil. Mag.*, **30**, 1453 (1982)
24. H. J. Möller, *Phil. Mag.*, **A43**, 1045 (1981)
25. D. R. Hamann, *Phys. Rev. Lett.*, **60**, 313 (1988)
26. P. J. Van Den Koek, W. Ravenek and E. J. Baerends, *Surf. Sci.*, **205**, 549 (1988)
27. Y. Xu, K. Zhang and X. Xie, *Phys. Rev. (b)*, **33**, 8602 (1996)

IMAGE SIMULATIONS OF Ge TWIN BOUNDARIES.

STUART MCKERNAN AND C. BARRY CARTER.

Department of Chemical Engineering and Materials Science, University of Minnesota, Minneapolis, MN 55455.

ABSTRACT

General high-angle tilt grain boundaries may be described by an arrangement of repeating structural units. Some grain-boundary defects may also be modeled by the incorporation of structural units of related boundary structures into the boundary. The simulation of these structures requires the use of prohibitively large unit cells. The possibility of modeling these boundaries by the superposition of image simulations of the individual structural units is investigated.

INTRODUCTION

The modeling of general tilt grain-boundaries in terms of repeating structural units with varying separation is now well documented. High-resolution electron microscope (HREM) images obtained from different tilt grain-boundaries in many materials display a remarkable similarity in the configuration of the image contrast at the grain boundary, implying a similarity in the boundary structures. In general there will be different structural units (or different spacings between the structural units) along a boundary, according to the local orientation of the grain-boundary plane. Defects may be introduced into the grain boundary; for example by deviations of the boundary plane away from the perfect tilt orientation. These crystallographic defects result in the appearance of defects in the repeating structural-unit configuration. If they have a regular and well defined structure, these defects may be viewed simply as a more complex type of structural unit.

These structural units have traditionally been examined by high-resolution electron microscopy. Images obtained in this way are particularly sensitive to the presence of defects, such as dislocations or steps in the boundary plane, which occur throughout the thickness of the foil parallel to the electron beam. This is because the HREM images are determined primarily by the projected structure of the boundary and not by the full three dimensional structure. Typically areas of the boundary selected for detailed analysis are those which appear to be in perfect alignment, and devoid of defects. This strategy minimizes the variation in the different variables - such as specimen misorientation, boundary misorientation, thickness variation across the boundary etc., which must be used in generating simulated images to compare with the experimental image. The number of such boundaries which may be analyzed is rather small. For tilt grain-boundaries with simple structural units, the "supercell" required to generate a simulated image of the boundary is relatively small; maybe 2nm by 100nm. For the case of more complex structural unit repeats, or defects in the structural unit repeat, much larger "supercells" are required, with a concomitantly larger amount of computer time to generate the results.

The $\Sigma 27$ $\langle 110 \rangle$ symmetrical tilt grain-boundary segment in Ge has a fairly complex repeating structural unit configuration, and can occur in different configurations [1-4]. Defects in the ordering of the structural units are also observed [3], as well as defects in the grain boundary structure itself [4]. It thus represents a boundary which may be fruitfully investigated using simulated images of individual structural units.

EXPERIMENTAL

Czochralski grown incoherent $\Sigma = 3$ Ge bicrystals have been produced previously [5]. The $\Sigma = 3$ boundary dissociated into a $\Sigma = 27$, third order twin boundary and several coherent $\Sigma = 3$ first order twin boundaries. TEM samples were prepared from the $\Sigma = 27$ boundary and examined in a high-resolution TEM.

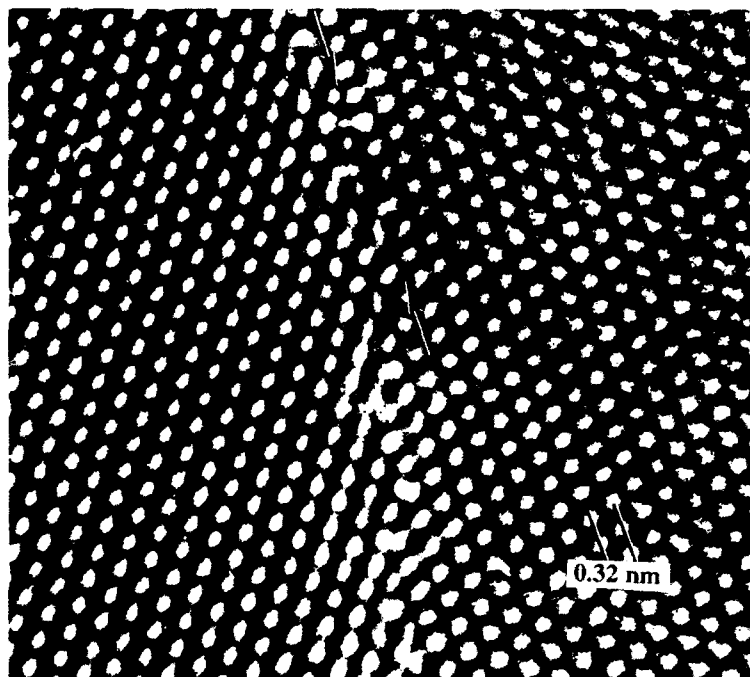


Figure 1. High-resolution lattice image of a defect (interface step) on the symmetric $\Sigma = 27$ tilt grain boundary in Ge

Multislice image simulations were performed on several different structural-unit models. The structural-unit "unit cell" was created using CrystalKit [6] software on a Macintosh Quadra computer. The width of the unit cell was taken as the repeat distance in the (552) interface plane - 2.94 nm. The length of the unit cell was varied to insure adequate separation of the boundary from the image boundary necessary for the periodic boundary conditions imposed by the multislice program. Different arrangements of the atoms at the boundary plane were obtained by creating the boundary in different locations within the bicrystal, and adjusting the positions of the atoms at the interface to get the appropriate model structure. The simulations were performed by MacTempas [6] and by EMS [7] - both using the atomic positions generated by CrystalKit. Images were simulated for a crystal 10nm thick, imaged at 300kV with a convergence angle of 0.5 mrad and a focus spread of 9 nm.

The image in figure 1 shows a portion of the symmetric $\Sigma = 27$ tilt grain boundary in germanium, containing a defect. It is obviously not possible at present to create model structures, carry out the simulations, and attempt to match the images for such an extensive defect structure within a reasonable time. However, the pattern of intensity at the boundary shows some regularity of features. The simulation and matching of individual structural units can, however, be attempted with current computer hardware. A first order model for the defect structure may be obtained by matching the individual intensity patterns at the boundary with simulations of the different structural units of the boundary, and those of related boundaries.

RESULTS

The images in figure 2 show the results of simulations (using EMS) performed with a short unit cell (left) and the central region of a simulation performed using a long unit cell (right). The

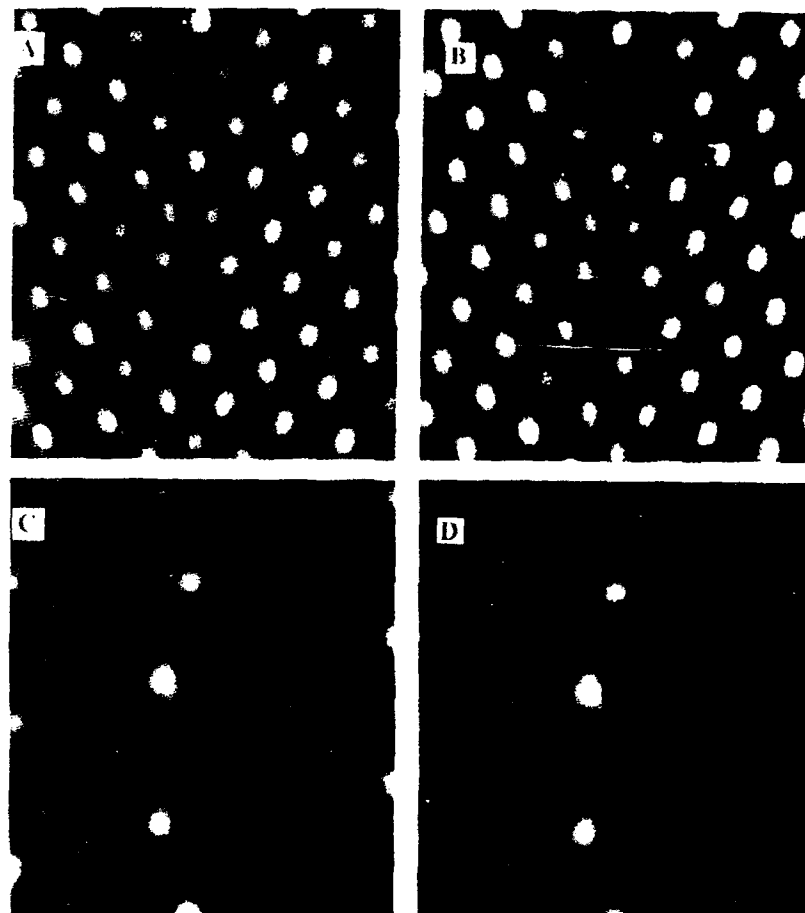


Figure 2. Image simulations of the $\Sigma = 27$ symmetric tilt grain-boundary using 5 nm (a,b) and 10 nm (c,d) long unit cells for defocus values of 30 nm (a,c) and 90 nm (b,d). Note the presence of contrast at the edge of the shorter unit cell because of the image grain-boundary.

lengths used were 2.5 nm and 5.0 nm respectively. It is evident that the contrast at the boundary is largely independent of the unit-cell size, although some slight differences do exist. In the short unit cell simulation there is not much undistorted Ge lattice visible between the distorted, boundary region and the distorted region at the edge of the unit cell. The images are displayed for two different values of defocus; -30 nm (top) giving "black atom" and -90 nm (bottom) giving "white atom" contrast. Under these conditions the image contrast is relatively high, and the differences between the images are hard to see. Simulations calculated for defocus values giving very low contrast images tend to be more sensitive to precise details of the unit cell configuration, probably because the Fourier "ringing" associated with the boundaries is not swamped by the high contrast of the periodic component of the image.

The images in Figure 3, part of a through-focus, through-thickness series, show the extreme sensitivity of the contrast at the grain boundary to the particular imaging conditions used. The simulations were performed for a foil thickness of 10 nm and defocus values of 30 nm (a) and

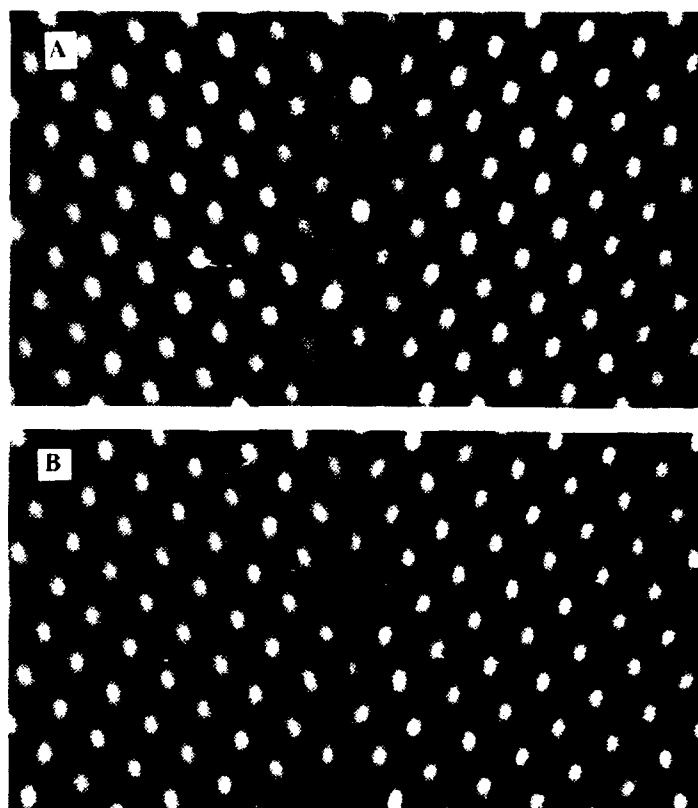


Figure 3. Part of a through-focus, through-thickness series for one model of the $\Sigma = 27$ symmetric tilt grain-boundary of thickness 10 nm and defocus a) 30nm and b) 90nm.

90nm (b). The contrast of the bulk material in both grains is reversed in the two images as in Fig. 1. The prominent "white dots" which mark the position of the boundary in Fig 3a are much less visible than the corresponding features in Fig. 3b. This effect is seen in experimental images, where the visibility of the boundary contrast can change much more dramatically than is illustrated here.

The images in Figure 4 show simulations performed for a foil thickness of 10nm and defocus values of 30nm for three different models of the atomic arrangement at the grain boundary. The models used here were simply different orderings of the 5- and 7-fold coordinated rings, and should thus give large differences in the observed intensity pattern along the boundary, which indeed they do. No attempt has been made at this stage to relax the boundary to a more energetically favorable configuration, or to adjust the rigid body translation between the two grains.

DISCUSSION

Grain-boundary structural units have traditionally been examined by high-resolution electron microscopy. It is possible, by inspection, to check that the grains on either side of the boundary

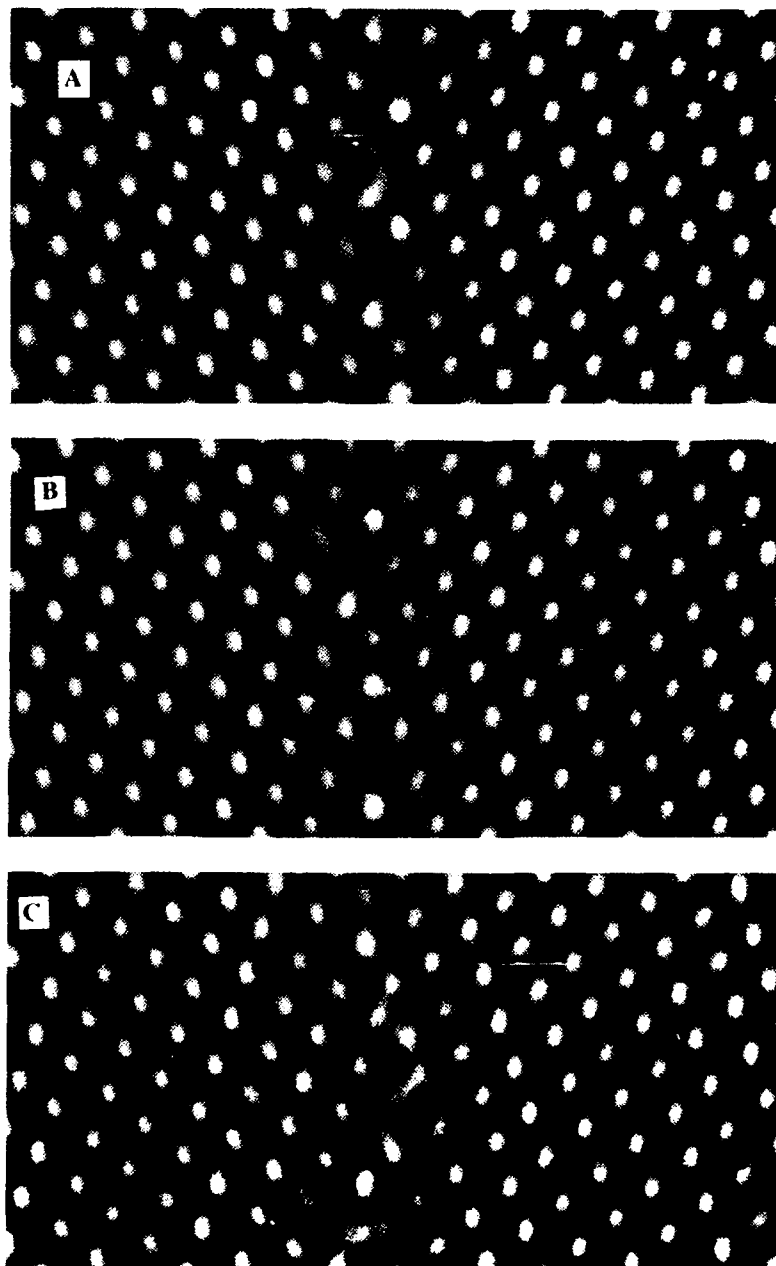


Figure 4. Image simulations for three different models for the $\Sigma = 27$ tilt grain-boundary imaged for a thickness of 10 nm and defocus of 30nm.

are adequately aligned, so that the image contrast is relatively easily interpretable. However, when there are defects present in the grain-boundary, it may not be possible to correctly orient both grains simultaneously. Even when the two grains appear to be well aligned, the insidious effects of screw dislocations parallel to the electron beam cannot be ignored. The images are also affected by defects, such as dislocations and steps in the boundary plane, which give rise to inclined interfaces within the foil thickness. In analyzing the structure of grain-boundaries these extrinsic boundary defects must be taken into account. Typically a complementary technique - such as weak-beam imaging - can be used to determine the presence of these extrinsic boundary defects. The difference in the appearance of the different structures in Figure 4 suggests that some progress can be made in correlating intensity patterns at the boundary with different structural unit configurations.

Simulation artifacts appear to be well taken care of by the computer programs, provided that sensible values are input for all the calculation parameters, and that the unit cell size is chosen to be sufficiently large to avoid interference problems. The output from the two different programs generally agreed with each other, although there were some differences in the details of the image contrast.

Through-focus, through-thickness series such as these can be used to determine the thickness and misorientation of the bulk crystals. By combining the information from all the micrographs in the series, the requirements for any particular structural model to match the image contrast become more stringent. A degree of sensitivity to structure along the electron beam direction is also acquired. By varying the defocus over a larger range than is common for bulk material, additional information about the grain boundary structure may be obtained. At relatively large defocus values, Fresnel fringes are obtained which have previously been used to investigate various average grain boundary properties.

CONCLUSIONS

High-resolution lattice images have been simulated for several possible structural units of the $\Sigma \approx 27$ tilt grain-boundary in Ge. The resulting images clearly show differences in the image contrast at the grain-boundary, which should make it possible to differentiate between different model structures. The qualitative agreement between the simulated and experimental images is very good; particularly in the relative intensity of the boundary plane features with respect to those in the bulk. A detailed comparison of the simulated and experimental images is still in progress.

Some of the simulation parameters have been investigated. It was found to be necessary to create structural unit "unit cells" which were larger than 2.5 nm perpendicular to the grain-boundary to avoid interference between the computed grain boundary and the image grain boundary.

ACKNOWLEDGMENTS

This research is supported, in part, by DoE under grant # DE-FG02-92ER45465.

REFERENCES

1. Z. Elgat; PhD Thesis, Cornell University, (1985)
2. Z. Elgat, and C.B. Carter; Ultramicroscopy, **18**, 313, (1985)
3. D.A. Smith, Z. Elgat, W. Krakow, A.A. Levi and C.B. Carter; Ultramicroscopy, **30**, 8, (1989)
4. S. McKernan, C.B. Carter, and Z. Elgat; Mat. Res. Soc. Symp. Proc. **209**, 637-642 (1991)
5. W. Skrotzki, H. Wendt, C.B. Carter; and D.L. Kohlstedt; Mat. Res. Soc. Symp. Proc. **25**, 341, (1984)
6. Total Resolution, 20 Florida Ave., Berkeley, CA 94707
7. P. Stadelman; Ultramicroscopy, **21**, 131, (1987)
8. D. R. Rasmussen, S. McKernan, and C. B. Carter; Proc. **47th** EMSA, 130, (1989).

SURFACE STRUCTURE OF OXIDE CATALYST MICROCRYSTALS: HIGH RESOLUTION ELECTRON MICROSCOPY STUDY

G.N.KRYUKOVA, A.L.CHUVILIN, V.A.SADYKOV
Boreskov Institute of Catalysis of Russia Academy of Sciences,
prospekt Lavrentieva 5, Novosibirsk, Russia 630090

ABSTRACT

The surface structure of α -alumina and α -ferrous catalyst microcrystals was studied using high resolution electron microscopy. For "pure" oxides as well as the same materials after promotion by alkali metals, models of the oxide surface based on results of image simulation procedure have been proposed. The surface structure reconstruction of the catalysts upon electron beam irradiation was also observed. For the specimens under investigation surface steps and kinks were shown to be essential for strong interaction between oxides and supported Pt particles preventing their migration and suppressing the sintering process.

INTRODUCTION

Many supported catalysts facilitate chemical conversion at active sites on their exterior surface following adsorption of reactant gases. Examples of this kind of catalysts are platinum group metals supported on oxides, such as alumina, or carbon for the catalytic oxidation of carbon monoxide to carbon dioxide [1]. Question about the arrangement of the support surface as well as that of active particles arises because the catalysts work under high pressure or at elevated temperatures. Moreover, reactant molecules are predisposed to undergo surface rearrangement leading to catalysis. Profile image technique for high resolution electron microscopy (HREM) offers a direct observation of the surface arrangement in oxide catalyst materials. This paper describes some results of HREM investigation of the surface structure of Al and Fe oxides used as catalyst supports.

EXPERIMENTAL

Oxide materials have been prepared by spraying parent solutions in arc plasma: details of the preparation procedure are given elsewhere [2]. The obtained materials are fine powders with specific surface area above 10 sq. meters per g according to BET measurements. Their phase composition were found to be pure (ca.98%) α -alumina and α -ferrous oxides in accordance with X-ray powder diffraction data. HREM samples were prepared by ultrasonically mixing the powders in ethanol followed by placing a drop of suspension on holey carbon film supported on copper grid. HREM experiments were carried out using JEM-4000EX machine (0.18 nm resolution limit). Image simulations were performed with multislice routine modified by one of us [3].

RESULTS AND DISCUSSION

Plasmochemical preparation procedure leads to the formation of α -alumina and α -ferrous microcrystals with different grain morphology. α -alumina particles possess many crystal orientations (i.e.(0001), (1120), (2201) etc.) whereas α -ferrous material is crystallized in the form of platelets with (0001) as the most developed plane.

Fig.1 shows a structure image of α -alumina particle viewed along [0111] direction. On the micrograph one can see a smooth surface. It is interesting

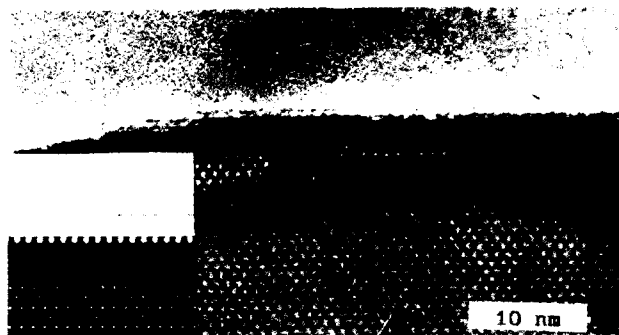


Fig.1. Structure image of α -alumina crystal viewed along [0111]

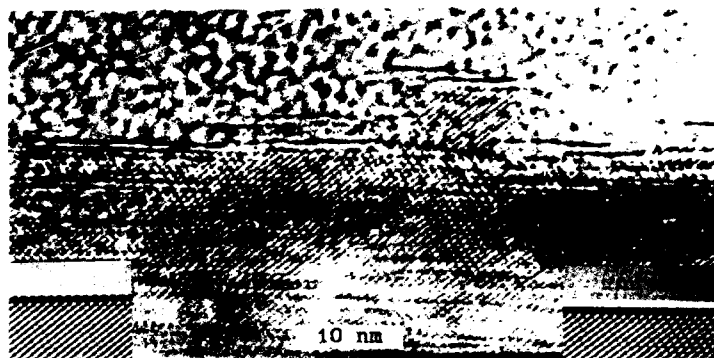


Fig.2. Extensive facetting observed for α -alumina crystal aligned into $\langle 11\bar{2}0 \rangle$. Simulated images inserted into the figure are calculated on the base of different structure models: left - oxygen layer, right - cation layer on (0001) surface (crystal thickness = 20 nm, $\Delta f = -97$ nm).

to note that, upon electron beam irradiation at 300 kV voltage and in high vacuum, facets extensively form on the $[11\bar{2}0](0001)$ habits of alumina during specimen observation (see Fig.2). This phenomenon is consistent with results reported by Bursill and Lin [4]. Such facetting was ascribed by these authors to a monolayer of a spinel phase.

We tried to examine the arrangement of these facets. For calculations, two models based on the structure arrangement with one kind of atomic termination have been used. Results of the simulations are inserted into Fig.2. It is evident that the calculated images do not fit very well with experimental image. Simulations involving a model of spinel monolayer on the surface of α -alumina are in progress at our laboratory.

Bonevich and Marks [5] also observed facet formation due to surface reaction which, in their opinion, is catalyzed by molecular oxygen and residual hydrocarbons of ambient vacuum environment in the microscope. From this point of view, observed facetting is significant because such a situation (i.e., phase transformation occurring in the surface or subsurface layers of catalysts) might take place during catalyst treatment in reaction media. Promotion of α -alumina by small (ca.200 ppm) amount of K or Rb leads to

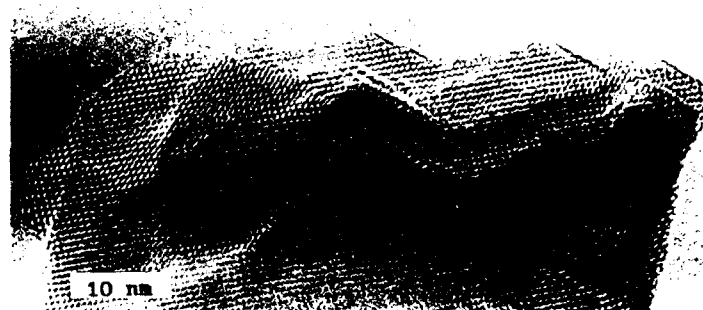


Fig.3. Surface roughening of α -alumina crystal oriented into $\langle 2\bar{2}01 \rangle$.



Fig.4. HREM image of α -ferrous microcrystal viewed along $[0001]$.

roughening of the crystal surface. Such surface erosion has been observed for almost all crystal orientations: see, for example, HREM image of alumina crystal viewed along $[2\bar{2}01]$ (Fig.3).

Fig.4 demonstrates HREM image of α -ferrous microcrystal viewed in $\langle 0001 \rangle$ projection. As evident from micrograph the surface of α -Fe oxide particle is smooth without facetting. One can only see small surface steps. It should be noted that a noticeable rearrangement of steps or ledges did not take place during observation of this material. There is also no evidence for surface transformation of α -ferrous particles after alkali metal donation in contrast to strong facetting being observed for promoted α -alumina crystals. Previous study [6] of the surface of α -Fe oxide (0001) natural growth face after Ar ion bombardment indicated the formation of disordered surface layers. For our α -ferrous sample with (0001) most developed plane facet formation could not be detected because facets may develop in the plane of view, i.e. perpendicular to the incident electron beam.

It seems likely that a promotion of oxide microcrystals by alkali metals plays a significant role in stabilizing active particles on the surface of oxide supports thus preventing particle migration process. In the field of catalysis



Fig.5. HREM image of Pt particle supported on alumina. Defects in the structure of metal particle are arrowed.

the well-known "size effect" [7] results in decrease of the number of surface active sites due to the sintering of active particles after catalyst treatment in reaction media at elevated temperatures. The latter leads to diminishing catalyst reactivity. Therefore, support surface should be designed in such a way as to provide strong interaction between support and metal particles. Fig.5 shows a micrograph of Pt particle supported on promoted γ -alumina. Steps on oxide surface are easily visible. One can also see that Pt particle attaches strongly to the alumina surface. After specimen treatment in the electron microscope column at 673K in vacuum for 20 min, neither an oxide surface reconstruction nor a change of metal particle position have been observed. The main difference between initial and annealed samples lies in the fact of rearrangement of the defects (arrowed in Fig.5) in the bulk structure of supported active particle.

SUMMARY

Our results indicate the difference in the surface arrangement of microcrystals of γ -Al and γ -Fe oxides prepared by plasmachemical method. For γ -alumina electron irradiation may accelerate surface roughening along certain orientations whereas surface erosion after alkali metal promotion of the oxide does not demonstrate a strong orientation dependence. Disordered surface layers of alumina oxide offer a strong interaction between support and active particles. "Stable" surface arrangement of γ -ferrous microcrystals is associated with their morphological peculiarity ((0001) well-developed faces).

REFERENCES

- 1.C.L.Thomas, *Catalytic Processes and Proven Catalysts*, 1st ed. (Academic Press, New York, 1970), p.14.
- 2.V.A.Sadykov, S.F.Tikhov, G.N.Kryukova, *Proceed. 10th Intern. Cong. "CHISA-90"* (Prague, Czechoslovakia, 1990), p.21.
- 3.A.L.Chuvilin, B.L.Moroz, V.A.Likholobov (submitted to *Catalysis Letters*).
- 4.L.A.Bursill, P.J.Lin, *Phil.Mag.*A60, 807(1989).
- 5.J.E.Bonevich and L.D.Marks, *Ultramicroscopy* 35, 161(1991).
- 6.R.J.Lad and V.E.Henrich, *Surf.Sci.* 193, 81(1989).
- 7.M.Che and C.O.Bennette, in *Advances in Catalysis*, edited by D.D.Eley, H.Pines, P.B.Weisz (Academic Press, London, New York, Tokyo, 1989), p.55.

A MICROSTRUCTURAL STUDY OF REACTION-BONDED SILICON CARBIDE

K. DAS CHOWDHURY,* R. W. CARPENTER* AND W. BRAUE,**

*Center for Solid State Science, Arizona State University, Tempe, AZ

**German Aerospace Research Establishment, D5000, Cologne, Germany.

ABSTRACT

Interfaces in Reaction Bonded Silicon Carbide (RBSC) have been characterized by Analytical and High Resolution Electron Microscopy. Both Si/SiC and SiC/SiC interfaces were free of any oxygen impurity segregation, but contained metallic impurity precipitates. Oxygen was detected in the second phase particles in the SiC grains. A model is presented to explain the evolution of these second phase particles in the SiC grains.

INTRODUCTION

The high resistance of RBSC to thermal stress and thermal shock and its good corrosion resistance in high temperature oxidizing atmospheres have made RBSC a potential material for use in high temperature applications. RBSC is formed by reacting liquid Si with C in porous green compact of primary α -SiC and organic resin to form secondary β -SiC. Organic resin is used as a precursor for carbon. The β -SiC bonds the original α -SiC together to form a dense compact of RBSC. The structure and chemistry of Si/SiC and SiC/SiC interfaces in RBSC play an important role in the fracture behavior of RBSC. Studies on fracture behavior of RBSC indicate that the Si/SiC interfaces are strength limiting, compared to SiC/SiC interfaces [1,2].

This paper describes microstructural characterization of Si/SiC and SiC/SiC interfaces in RBSC by high spatial resolution EELS, EDS and high resolution imaging electron microscopy. It will be shown that the interfaces were free of oxygen impurity segregation but contained metallic impurity precipitates. Impurity oxygen present in the surface oxide layers of Si and SiC powder and in organic resins used as precursors for C were detected in the second phase inclusions in SiC grains. A brief account of the mechanism of the incorporation of impurity oxygen in these inclusions is given.

EXPERIMENTAL DETAILS

Planar TEM specimens of a commercially available RBSC were made by conventional technique. The HREM of interfaces was examined in a JEOL 4000EX microscope. High resolution electron micrographs were recorded at Scherzer defocus with a point resolution of 0.17 nm.

EELS and EDX were used to determine the chemistry of the interfaces. The nanospectroscopy was done with a Philips400ST TEM fitted with a field emission gun, coupled to a PEELS detector. A liquid nitrogen cooled specimen holder was used to eliminate specimen borne contamination. The field emission gun was operated at 100KeV, with an approximately 3nm diameter probe with a current density of the order of 10^8 A/m^2 at the specimen level and a beam convergence half angle of 5mrad. All the experiments were carried out in the diffraction mode with the entrance aperture for the parallel EELS detector centered around the transmitted beam. The acceptance half angle for the parallel EELS detector was 10mrad.

RESULTS

Figure 1 shows a BF image of a RBSC material. The residual Si appears in between two large SiC grains. Small second phase inclusions marked by arrows were observed in the SiC grains. It was not obvious that the Si/SiC interfaces in the boxed area of figure 1 contained any interfacial impurity layer. Note that the interfaces are curved, indicating that they were mobile at the processing temperature. Figure 2 is an HREM image of a Si/SiC interface in the boxed region of figure 1.

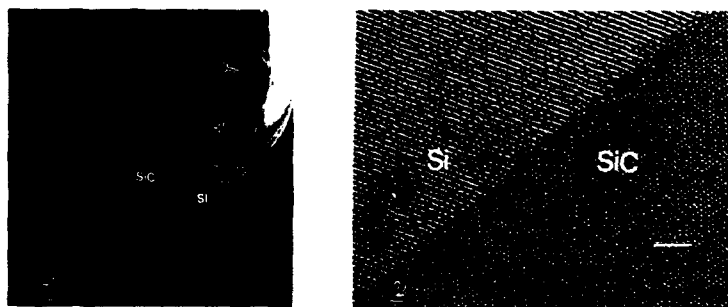


Fig.1 Low magnification BF image of Reaction Bonded SiC

Fig.2 HREM image of Si/SiC boundary indicating no interfacial layer.

This interface did not show any resolvable amorphous or impurity phase layer. The α -SiC was in $\langle 3-1-1 \rangle$ orientation and Si was in $g=\langle 111 \rangle$ two beam condition. Good planar matching between the Si and SiC grain with periodic misfit was observed. Since three Si{111} interplanar spacings are approximately equal to four SiC {103} interplanar spacings, every third Si{111} fringes matched with every fourth {103} α -SiC fringes. Therefore the interface is considered atomically flat with periodic array of edge dislocations. It also showed small $\sim 1\text{nm}$ ledges, not associated with the dislocations. This good matching indicates that

the residual Si nucleated on the SiC grains. Position Resolved EELS analysis showed that there was no sharp increase in oxygen concentration at the Si/SiC interface. But in some areas along these interfaces, precipitates containing Ni, Cr, Cu, Fe, were detected. No amorphous layer was visible at SiC/SiC grain boundaries. Position-resolved EELS analysis confirmed that there was no sharp rise in

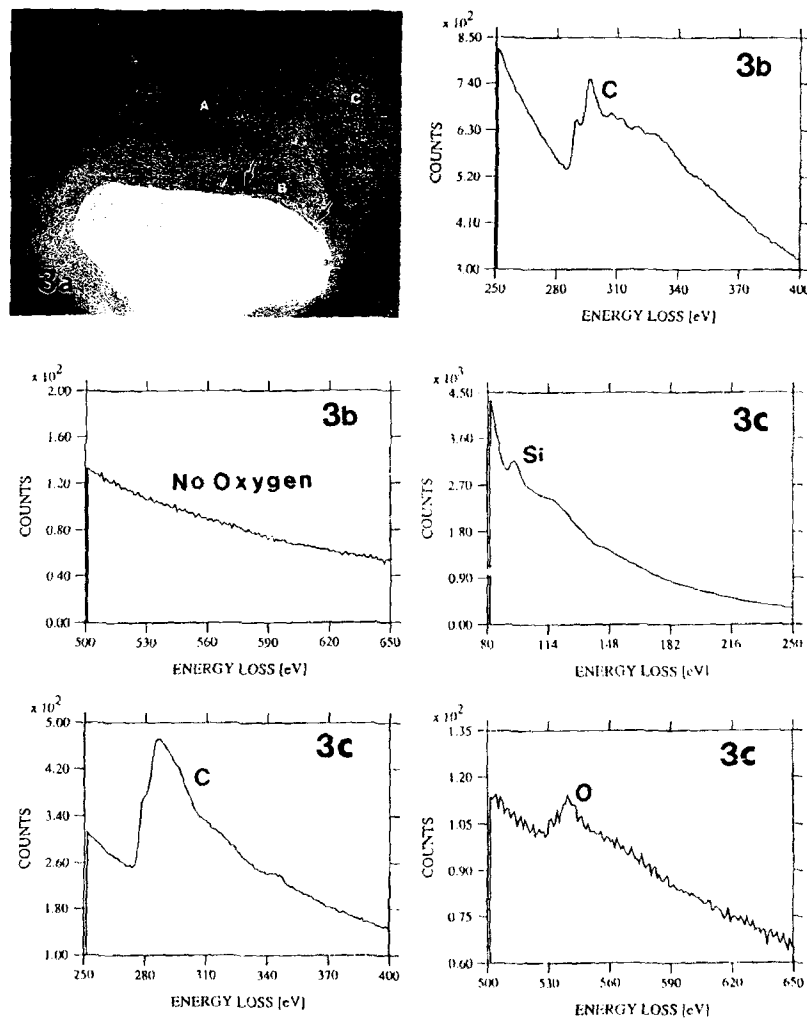


Fig.3 Second phase inclusion in α -SiC (a) TEM image (b) EELS spectrum taken from the region A in (a) (c) EELS spectrum taken from region B in (a)

oxygen concentration at the grain boundaries either. Precipitates were observed at some regions of the SiC/SiC grain boundaries. EDX analysis showed that these precipitates contained mainly Fe, Cu, Mn. Hence it can be concluded that the Si/SiC interfaces and SiC/SiC grain boundaries were free of any light element impurity (mainly oxygen) segregation but exhibited metallic impurity precipitation.

Bulk chemical composition analysis of RBSC showed that it contained 0.29 wt% oxygen. Hence, HREM and AEM analyses were performed on the small second phase intragranular inclusions to determine the impurity oxygen distribution in the material. Figure 3a shows an HREM image of a second phase inclusion in a SiC grain. The inclusion consisted of two characteristic areas namely, a graphitic region showing 0.34nm (002) fringes marked A and an amorphous region, marked B. The hole near the middle of the inclusion was due to preferential ion milling of the amorphous region. EELS analyses from region A and B are shown in figures 3b and 3c. As evident in figure 3b, region A contained graphite with no detectable oxygen but did contain a small amount of Si (not shown in the figure). EELS spectrum from region B (figure 3c) indicated that the amorphous region contained Si, C and O and a small amount of Ca. EELS spectrum taken from the region marked C in the HREM image showed no Si but did contain C and some O (not shown here).

DISCUSSION

To understand the evolution of these second phase inclusions and subsequently the incorporation of oxygen in these inclusions, the formation of RBSC must be explained briefly.

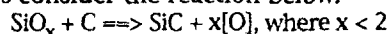
The formation of RBSC microstructure involves the solution of C in liquid Si and subsequent nucleation and growth of secondary β -SiC on the original α -SiC and the eventual transformation of β -SiC to α -SiC [3]. It is well known that the dissolution of C in Si(l) is an exothermic reaction with a heat of solution at 2200°C of approximately 250KJ/mol [4] and the heat of formation of SiC of 120KJ/mol [5]. Therefore deposition of SiC during densification is an endothermic reaction. Therefore there will be a rise in temperature at the dissolution site due to the exothermic nature of dissolution of C in Si(l) which will cause further dissolution of C in Si(l). Due to the endothermic nature of deposition of β -SiC on existing α -SiC particle surfaces, a drop in temperature at the deposition site of β -SiC will occur. A temperature gradient will develop between the dissolution and deposition sites. This temperature gradient will result in a gradient in the activity of C between the two sites, the activity of C being higher in the high temperature region [1].

There may be two competing processes at this stage namely, the diffusion of C in Si(l) and the diminution of temperature difference

between the two sites. Calculations showed that the diffusion of C will be much faster than the diminution of temperature difference. Hence diffusion of C to the low temperature deposition site will induce a supersaturation of C at the deposition site. It is generally believed that C transports as C-Si pairs or CSi_4 tetrahedra in Si(l) [1]. Consequently SiC will be deposited on the α -SiC surface.

As mentioned earlier impurity oxygen was present as an oxide layer on the surface of Si and SiC powder particles and also in the organic precursors for C. As Si melted this oxygen went into solution with Si(l). The solubility limit of oxygen in Si(s) and SiC(s) and that of carbon in Si(s) [6] are very low on the order of 10^{18} atoms/cc.

Let us consider the reaction below:



This reaction may not reach equilibrium because the available oxygen concentration is limited and for kinetic reasons. The equilibrium constant for this reaction is

$K = a_{\text{SiC}} [a_{\text{O}}]^x / a_{\text{SiO}_2} a_{\text{C}} = [a_{\text{O}}]_{\text{eq}}^x$, assuming $a_{\text{SiC}}, a_{\text{SiO}_2}, a_{\text{C}} = 1$ for the chosen standard state

At points along the SiC(s)/Si(l) interface, where β -SiC nucleates and grows the local oxygen activity in the liquid solution will increase beyond the equilibrium oxygen concentration, $[a_{\text{O}}]_{\text{eq}}$. And since $\Delta G_{\text{SiO}_2} < \Delta G_{\text{SiC}}$ [8], the above reaction should proceed to the left. This means that SiO_x and C would form and deposit on the growing β -SiC surface. During further grain growth of SiC, the deposits of SiO_x and C would be entrapped by mobile SiC(s)/Si(l) interface forming second phase inclusions in SiC grain. Since the processing temperature was $\sim 2000^\circ\text{C}$, the free C will only partially graphitize. Careful background subtraction [9] of Si-L and O-K edges in the EELS spectra collected from the amorphous region B (figure 3b) and subsequent edge integration over a window of 100eV indicated that the concentration ratio of O to Si is 0.7. However, upon careful inspection of the amorphous region in the HREM image (figure 3a) tiny microcrystals of the order of 3nm in diameter (marked by arrows in the figure) were detectable. Lattice fringe measurements of these microcrystals indicated that they were Si and SiC. When the electron probe was placed in the amorphous region to acquire an EELS spectrum, the probe encompassed the microcrystals as well. Hence an average O/Si ratio of 0.7 was reflected on the EELS spectra collected from the region containing the amorphous region and the microcrystals.

CONCLUSIONS

Interfaces were free of any amorphous layer within the resolution limit of the HREM microscope (0.17nm) and oxygen impurity atoms within the detectable limit (1 at%) of the PEELS spectrometer. Metallic impurity precipitation was detected at the interfaces and grain

boundaries. Oxygen was detected in the second phase intragranular inclusions in SiC. The inclusions contained partially graphitized C, and an amorphous phase containing Si, O and residual C. With the growth of SiC, the O concentration in Si(l) at the precipitation sites will increase beyond the equilibrium concentration. The graphite and SiO_x will deposit at the SiC-deposition sites and will be entrapped by the mobile SiC surfaces. EELS analysis of the amorphous region in the second phase inclusions showed that the O/Si ratio was 0.7. Tiny microcrystals of Si and SiC, approximately 3nm in diameter, were observed in the amorphous region. The EELS spectrum from the amorphous region was acquired from a region containing these microcrystals and SiO_x phase. Therefore the spectrum produced an average O/Si ratio of 0.7 in the amorphous region.

ACKNOWLEDGMENTS

This research was supported by a grant from US DOE Basic Energy Sciences, DE-FG02-87ER-45305, and was performed at the Facility for HREM, ASU.

REFERENCES

- [1] J. N. Ness and T. F. Page, J. Mat. Sci., 21, 1377, (1986)
- [2] G. R. Sawyer and T. F. Page, in Tailoring Multiphase and Composite Ceramic; Proc. of the 21st. Univ. Conf. on Ceramic Science, (Plenum Press, NY, 1986), pg. 347.
- [3] D. R. Clarke, J. Am. Cer. Soc., 60(11-12), 539 (1977).
- [4] R. I. Scace and G. A. Slack, J. Chem. Phys., 30(6), 1551, (1959).
- [5] D. H. Kirkwood and J. Chipman, J. Phys. Chem., 65, 1082, (1961).
- [6] T. Nozaki, Y. Yatsurugi, and N. Akiyama, J. Electrochem. Soc., 117(12), 1566, (1970).
- [7] R. Chaim and A. H. Heuer, J. Am. Cer. Soc., 74(7), 1663, (1991).
- [8] JANAF Thermochemical Data, Army-Navy-Air Force Thermochemical Panel, The Dow Chemical Co. Midland, MI, 1962-63.
- [9] M. Skiff, R. W. Carpenter and S. H. Lin, J. Appl. Phys., 62, 2439, (1987).

COMPOSITIONAL ANALYSIS AND HIGH RESOLUTION IMAGING OF GRAIN BOUNDARIES IN Pr-DOPED ZnO CERAMICS

I. G. SOLORZANO, J. B. VANDER SANDE, K. K. BAEK, AND H. L. TULLER
Center for Materials Science and Engineering, MIT, Cambridge, MA 02139, USA

ABSTRACT

An electron microscopy investigation has been conducted in ZnO:Pr:Co varistor structures prepared by a new in-diffusion method. It has been shown that some boundaries host intergranular precipitates of a Pr_xO_y -based phase. All observations lead to the conclusion that grain boundaries exhibit Pr segregation, while Co is homogeneously distributed in the ZnO matrix. No continuous intermediate layer is present at the ZnO/ZnO boundary nor at the $\text{Pr}_2\text{O}_3/\text{ZnO}$ interfaces. This is consistent with a barrier model based solely on a space charge depletion region(s).

INTRODUCTION

Metal oxide varistors are multijunction materials whose highly nonlinear current-voltage characteristics derive from the electrical activity of their grain boundary regions. To obtain high degree of nonlinearity in polycrystalline ZnO it has been found to be necessary to add a minimum of two types of cation dopants in sufficient concentrations (~0.5 - 1.0 mol%) and to follow sintering with an oxidative anneal at ~600°C [1]. The common dopants include transition metals, such as Co and Mn which have ionic radii similar to that of Zn and therefore have high solubilities and low grain boundary segregation coefficients, and dopants with large ionic radii, such as Bi and Pr, which segregate at grain boundaries and usually form intergranular phases [2-4]. Empirically, these dopants act synergistically, resulting in enhancement in varistor electrical properties which is greater than the sum of individual contributions. While the microstructures of Bi doped varistors have been extensively studied, the specific role of each additive remains unclear.

The present investigation was undertaken with the objective of clarifying the role of dopants in an electrically active Pr and Co doped ZnO ceramic varistor by studying the structure and chemistry of individual grain boundaries through high resolution and analytical electron microscopy and correlating these results with electrical and spectroscopic measurements [5].

EXPERIMENTAL

Specimen Preparation

In order to simplify the structure of such devices single or a limited number of grain boundaries were activated by an in-diffusion specimen preparation procedure. This procedure consists of the application of aqueous nitrate solutions of Pr:Co onto undoped ZnO polycrystalline discs which are subsequently covered by a second, similar disc to form a sandwich structure. The structures are subsequently fired in air at 1400°C for 36h in ZnO powder to minimize volatilization. Upon heating, the metal nitrates are calcined to metal oxides which are subsequently incorporated at the interface and into the adjacent bulk region by solid state diffusion. Specimens were given an oxidative anneal in air at 650°C for 3h to further enhance their electrical activity. Due to the high firing temperature, the in-diffusion process was accompanied by grain growth which yielded a large grain size, 300 μm average. This procedure proved to be effective in attaining well-defined varistor-like characteristics at one or more electrically active boundaries [5]. For comparison, bulk specimens containing 1 mol% Pr and 1 mol% Co were prepared by conventional sintering.

Microstructural Characterization

Cross-sectional electron-transparent samples from the in-diffusion product were prepared by dimpling followed by Argon ion beam milling under liquid nitrogen conditions. Conventional TEM observations were carried out with a JEOL 200 CX microscope while high resolution images of selected grain boundaries were obtained with a TOPCON 002B microscope, both working at 200 kV. For analytical microscopy a 100 kV field-emission-source STEM, manufactured VG HB5, was used. In all cases, the grain boundaries analyzed in this study were oriented parallel to incident electron beam and the 10A diameter electron probe followed, step-by-step, a direction either along, or perpendicular to, the boundary.

RESULTS AND DISCUSSION

General

Observations by conventional TEM of the in-diffused sample microstructures clearly indicated that a precipitate phase had been formed at several grain boundaries. Electron diffraction and dark field imaging show that this phase is crystalline contrary to some observations by Clack [3] in Bi-doped ZnO varistors. The elongated morphology of the precipitate shown in Fig.1 suggests that this phase wets the ZnO grains at the firing temperature (1400°C) and that, in some boundaries, the grain orientation and the interface energy balance maintains this morphology even after annealing at 650°C. However most of the intergranular precipitates, upon anneal at 650°C, recede to accommodate themselves into a morphology with a higher dihedral angle and thus equilibrate the interfacial energy with the neighboring grains, as illustrated in Fig.2.



Fig.1 TEM micrograph on intergranular precipitate with low dihedral angle



Fig.2 TEM micrograph of grain boundary precipitate with high dihedral angle morphology

The majority of grain boundaries were found to be free of intergranular precipitates. In order to clarify whether a continuous intergranular layer is present at precipitate-free boundaries, as has been demonstrated to occur in Bi containing ZnO varistors [3, 6], and also to determine the structure and compositional nature of the formed interfaces, STEM and HREM techniques have been combined.

Precipitate-free Boundaries

All grain boundaries analyzed by EDS spectroscopy exhibited Pr segregation. There was no significant presence of Pr in the ZnO matrix. Co, on the other hand, is homogeneously distributed in the matrix, with no detectable enrichment at the grain boundaries. These observations were consistent in all boundaries analyzed, independent of the degree of misorientation between neighboring grains.

A typical image of an edge-on oriented grain boundary in the STEM is shown in Fig.3a. Fig.3c displays the EDS spectrum obtained from the boundary superimposed on a corresponding spectrum obtained from the ZnO matrix 10 nm away from the boundary. The same grain boundary in a TEM image is shown in Fig.3b. The localized contrast change at some points neighboring the boundary could be interpreted as due to strain fields. High resolution imaging shows that such boundaries are also free of any intergranular layer since the lattice plane fringes of adjacent ZnO grains were seen to be continuous right up to the plane of the boundary. Careful examination of the boundary also reveals terminating fringes that accommodate the mismatch between the planes in the two grains, suggesting that they are grain boundary dislocations. This supports the conclusion that no intergranular film is present at the boundary.

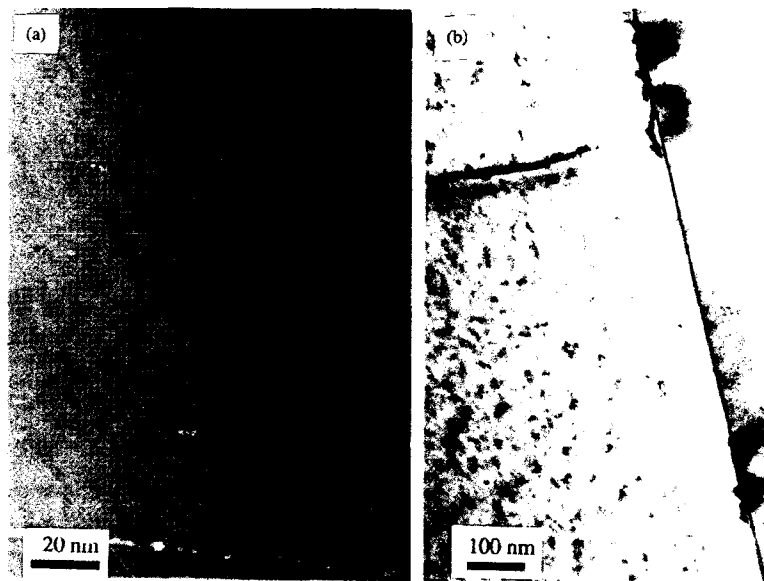


Fig. 3 A precipitate-free grain boundary : (a) Bright field STEM image; (b) Bright field TEM image of the same boundary showing localized strain fields; (c) EDS spectrum from the boundary (solid line), and from the neighboring ZnO matrix (dotted line).

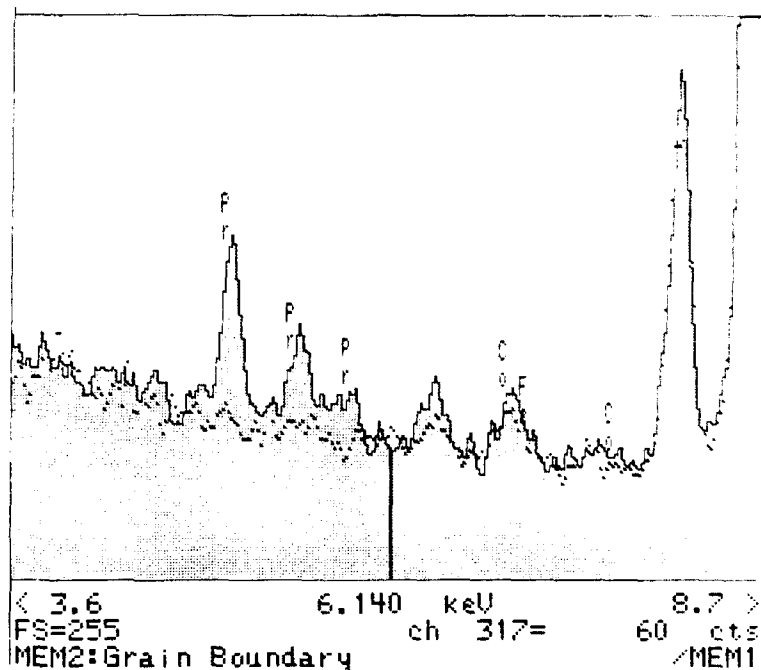


Fig. 3 (Cont.)

Grain Boundary Precipitate

Point to point STEM compositional analyses across grain boundary precipitates were accomplished with a minimum spacing of 5 nm. Although no quantitative determination has been attempted, the EDS spectra from the precipitates reveal only Pr and O peaks with a constant ratio. This could indicate that the precipitate constitutes the Pr_2O_3 hexagonal phase as proposed by Mukae [7]. Fig.4 exemplifies a typical grain boundary precipitate region which has been studied by STEM and HREM. Fig.4a gives the precipitate scale and morphology. Fig.4 b-d represent typical EDS spectra for which Fig.4b corresponds to the precipitate phase, Fig.4c to the matrix in front of the precipitate, and Fig.4d to the grain boundary 50 nm away from the precipitate. The same observations indicated in the previous section are valid here. Furthermore, no variation in the concentration of these elements is measurable in the ZnO matrix in front of the precipitates. This finding is in agreement with the argument that the grain boundary precipitate results from the recessing at lower temperatures of the Pr-rich intergranular phase as has been discussed with respect to the Bi-rich intergranular phase in Bi-Co-ZnO varistors [8]. Fig.4e gives a lattice image of the precipitate/matrix interfaces. The absence of any amorphous layer separating these two phases should be noted as this is contrary to some observations in Bi-doped varistors [9].

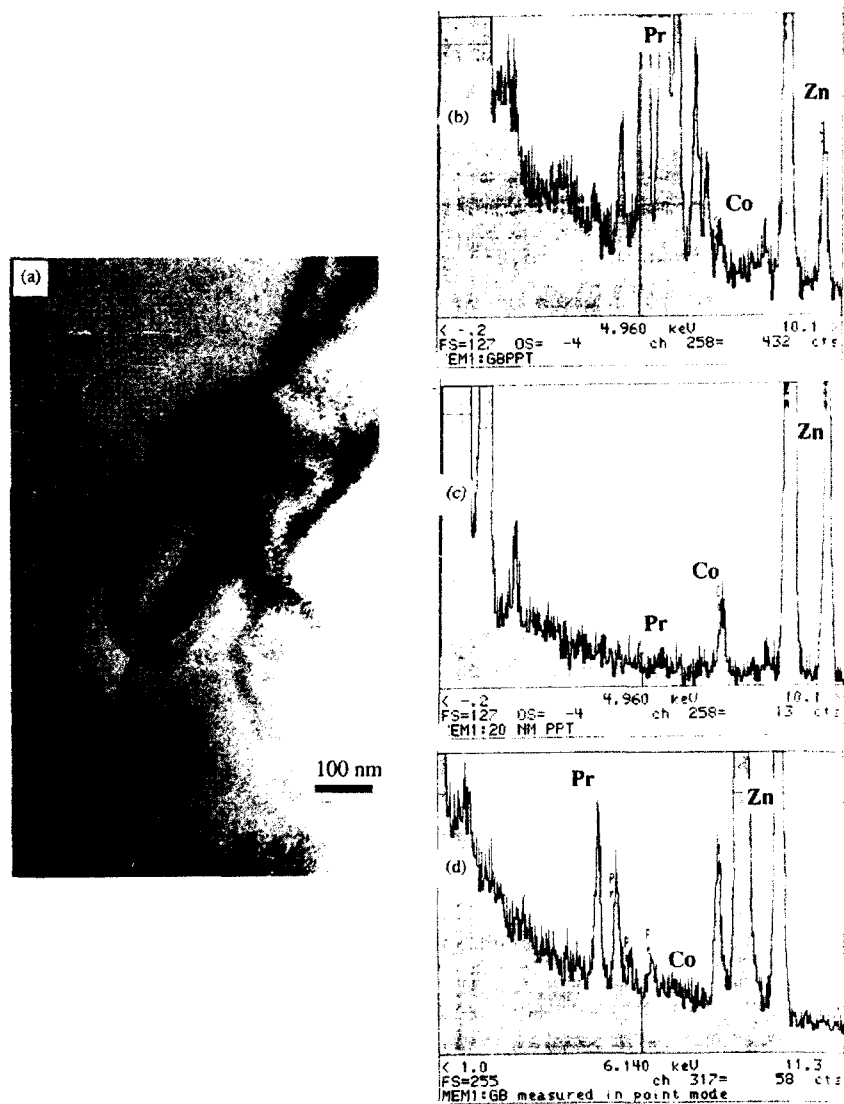


Fig. 4 Analysis of a grain boundary precipitate (a) TEM image; (b) EDS spectrum from the precipitate; (c) from the ZnO matrix; (d) from the grain boundary; (e) HREM image of the precipitate/matrix interface(next page).



Fig. 4 (Cont.)

CONCLUSION

An electron microscopy investigation has been conducted in ZnO:Pr:Co varistor structures prepared by a new in-diffusion method. It has been shown that some boundaries host intergranular precipitates of a Pr_xO_y -based phase. All observations lead to the conclusion that grain boundaries exhibit Pr segregation, while Co is homogeneously distributed in the ZnO matrix. No continuous intermediate layer is present at the ZnO/ZnO boundary nor at the $\text{Pr}_2\text{O}_3/\text{ZnO}$ interfaces. This is consistent with a barrier model based solely on a space charge depletion region(s). Current work is being done to establish a correlation between structural and compositional properties of the grain boundary including precipitation/segregation effects and the generation of interface traps and related electrical barriers.

Acknowledgements

The authors thank the Center for Materials Science and Engineering at MIT for supporting this work under the Contract NSF-MRL DMR-9022933.

REFERENCES

- [1] M. Matsuoka, Jpn. J. Appl. Phys., **10**, 736 (1971)
- [2] W. G. Moris, J. Vac. Sci. Technol., **13**, 925 (1976)
- [3] D. R. Clark, J. Appl. Phys., **50**, 6829 (1979)
- [4] W. D. Kingery, J. B. VanDer Sande and T. Matamura, J. Am. Ceram. Soc., **62**, 221 (1979)
- [5] K. K. Baek, A. Broniatowski and H. L. Tuller, in proc. 6th Intl. Conf. Intergranular and Interphase Boundaries in Materials, Greece, June 1992
- [6] J. Wong, P. Rao and E. F. Koch, J. Appl. Phys., **46**, 1827 (1975)
- [7] K. Mukae, Cer. Bull., **66**, 1239 (1987)
- [8] J. P. Gambino, W. D. Kingery, G. E. Pike, L. M. Levinson and H. R. Phillipp, J. Am. Ceram. Soc., **72**, 642 (1989)
- [9] H. Kanai, M. Imai and T. Takahashi, J. Mat. Sci., **20**, 3975 (1985)

ATOMIC STRUCTURES AND DEFECTS OF AS-GROWN $\text{Nb}_{1+x}\text{S}_2$ PLATELETS ON Nb SUBSTRATES

CHUXIN ZHOU¹ AND L. W. HOBBS

Department of Materials Science & Engineering, MIT, Cambridge, MA

ABSTRACT

The interlocking of $\text{Nb}_{1+x}\text{S}_2$ platelets developed during sulfidation of Nb results in formation of a compact scale. The atomic structure and defects of these platelets were investigated using HREM. The resulting microstructure is very different from conventional microstructure consisting of polygonal grains and polyhedral grain boundaries because of the anisotropy of the crystal structure. The principal phase was identified as $3\text{R-Nb}_{1+x}\text{S}_2$ intergrown with $2\text{H-Nb}_{1+x}\text{S}_2$, or with some other arrangement of S-Nb-S slabs. The $-\text{S}_6-$ octahedral sites between two S-Nb-S slabs provide accommodation for extra Nb or foreign atoms and the large non-stoichiometry of $\text{Nb}_{1+x}\text{S}_2$. Stacking faults along the c axis account for the high density of planar defect structures observed within almost every platelet. Axial lattice fringe images and streaking in the diffraction pattern indicate that the planar defects are normal to the c direction.

INTRODUCTION

The present work aims at a thorough study of the sulfidation products of niobium using TEM and HREM. The special interest in Nb sulfides derives from the observation that Nb, in sulfidizing environments, behaves in its corrosion kinetics similar to Cr, Cr- and Al-bearing alloys in oxidizing environments. Just as Cr_2O_3 and Al_2O_3 are stable and protective in oxidizing atmospheres, $\text{Nb}_{1+x}\text{S}_2$ provides very good protection for Nb in sulfidizing atmospheres. The growth rate of $\text{Nb}_{1+x}\text{S}_2$ formed on Nb is of the same order of magnitude as that of Cr_2O_3 on Cr at 900°C (1173K) [1, 2]. A possible mechanism is discussed for the large deviation of $\text{Nb}_{1+x}\text{S}_2$ from its stoichiometry in terms of our TEM and HREM results and why the large observed derivations do not lead to rapid sulfidation as they do in Fe_{1-x}O and in Fe_{1-x}S .

Our TEM and HREM foils were prepared directly from polycrystalline $\text{Nb}_{1+x}\text{S}_2$ scales produced by reacting Nb metal with either sulfur vapor ($P_{\text{S}_2} = 10^{-1}\text{atm}$) or $\text{H}_2 - \text{H}_2\text{S}$ gas mixtures ($P_{\text{S}_2} = 10^{-4.62} \sim 10^{-9}\text{atm}$). Three-mm discs were cut ultrasonically from the surface of the as-sulfidized Nb specimens. The depth of the cut was 100–200 μm . The other side of the specimen was abraded and polished until the 3-mm discs were parted from the bulk sample. Instead of using jet-polishing, the 3-mm discs (50–100 μm thick) were mechanically dimpled from the metal side to 20 μm or less thickness at the center with a VCR Dimpler, then thinned to electron transparency by ion milling with the metal side facing one ion gun and the sulfide side facing the second gun (turned off in this case) and shielded by a stainless steel cylinder.

The TEM and HREM observations were performed on a JEOL 200CX instrument operating at 200KV or an Akashi EM-002B(UHR/HTS) instrument operating at 200KV.

¹Present Address: Radiation Monitoring Devices, Inc., 44 Hunt St., Watertown, MA 02172



Figure 1: (a) TEM BF image at the middle portion of NbS_2 scale formed on polycrystalline Nb in $\text{H}_2 - \text{H}_2\text{S}$ gas mixtures ($P_{\text{S}_2} = 10^{-4.62} \text{ atm}$) at 900°C (1173K) for 190 min, showing scale compactness and interlocking of NbS_2 platelets.

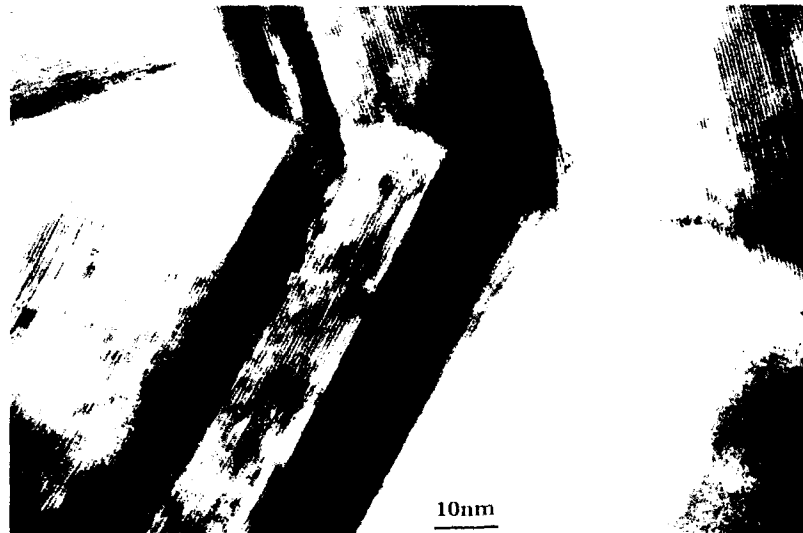


Figure 1(b) HREM bright-field 3-beam axial lattice fringe image shows the growth of two platelets with large misorientation angle to form a compact junction or grain boundary.

TEM AND HREM STUDY OF NbS_2 SCALES

The microstructures of $\text{Nb}_{1+x}\text{S}_2$ sulfide scales were similar to each other for all samples sulfidized in $\text{H}_2\text{-H}_2\text{S}$ from $P_{\text{S}_2} = 10^{-9}\text{atm}$ to $P_{\text{S}_2} = 10^{-4.62}\text{atm}$ under both SEM and TEM observations. Resulting TEM images observed from the middle portion of the scale confirmed that the sulfide grains were arrayed in a more compact layer and also retained a platelet structure which was very similar to that revealed by SEM examination of the scale surface structure[2,3]. The formation of these platelets is attributable to either (1) outward diffusion of Nb, with the sulfidation reaction taking place principally at the gas/solid interface or (2) inward diffusion of S, with the reaction taking place principally at the scale/metal interface. The TEM examinations revealed an interior scale microstructure which had a similar morphology to that of the external scale surface, but it could not be concluded whether the former had evolved from the latter or vice versa.

Figure 1a shows the bright field image from a middle portion of a sulfidation scale. The niobium sample was sulfidized in $\text{H}_2\text{-H}_2\text{S}$ ($P_{\text{S}_2} = 10^{-4.62}\text{atm}$) at 1173K for 100 min. The interlocking of the $\text{Nb}_{1+x}\text{S}_2$ platelets results in formation of a compact scale. These images are very different from conventional microstructures of polygonal grains and of polyhedral grain boundaries. Stacking faults along the c axis can account for the high density of planar defect structures observed within almost every platelet. From observation of the lattice fringes and analysis of streaking in the diffraction patterns, we understand that the planar defects are normal to the c direction.

The growth of the $\text{Nb}_{1+x}\text{S}_2$ platelets appears to favor the basal plane, as illustrated in Figure 2. The growth of the $\text{Nb}_{1+x}\text{S}_2$ grains stops when two or more neighboring $\text{Nb}_{1+x}\text{S}_2$ platelets grow together at large angles by forming a junction, as shown in Figure 1b. Bending of the lattice planes was also observed at the junction area. The compactness and protection provided by the $\text{Nb}_{1+x}\text{S}_2$ sulfidation scale are related to the complete interpenetration of two or more platelets at large angle grain boundaries which are very different from classical grain boundaries.

Figure 3 shows a high resolution image of a platelet from the middle portion of the $\text{Nb}_{1+x}\text{S}_2$ scale shown in Figure 1a. A thin lamellar heterogeneity (about 5nm in thickness) is observed. From X-ray diffraction results[3], we have shown that $\text{Nb}_{1+x}\text{S}_2$ scale is principally of rhombohedral structure, but 2H NbS_2 can result locally due to stacking faults, because the only difference between these 2H and 3R phases is a variation in the stacking sequence along the c axis. If we use capital letters A, B and C to represent the sulfur layer, and lower case letters a, b and c refer to Nb layers, the stacking sequence of 2H phase is AbACbCA, which has a period of 1.2nm along the c axis; the stacking sequence of 3R phase is AbABcBCaCA to form a period of 1.8nm along the c axis. Intergrowth of these two phases can take place at stacking faults or by a shear in the basal plane normal to the c axis.

Faulting of these stacking sequences is relatively easy because of the weak bonding between S-S layers and the weak communication between neighboring Nb layers which are separated by two sulfur layers. In addition to the continued stacking of 3R structure, AbABcBCaC|AbA, three other stacking faults may be created, for example AbABcBCaC|AcA corresponds to a simple fault, AbABcBCaC|BaB to the intergrowth of 2H structure (CaCBaB), and AbABcBCaC|bcB to a twin (BcBCaC|BcB). If additional stacking of the trigonal prismatic S-Nb-S slabs is considered, a combination of these faults may form very complicated structures as discussed in detail

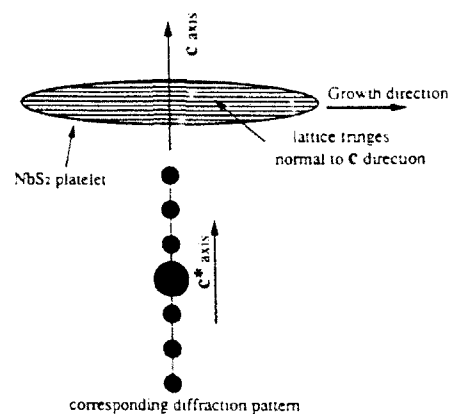


Figure 2: Schematic diagram illustrating the orientation relationship between platelet, lattice fringes and diffraction pattern.

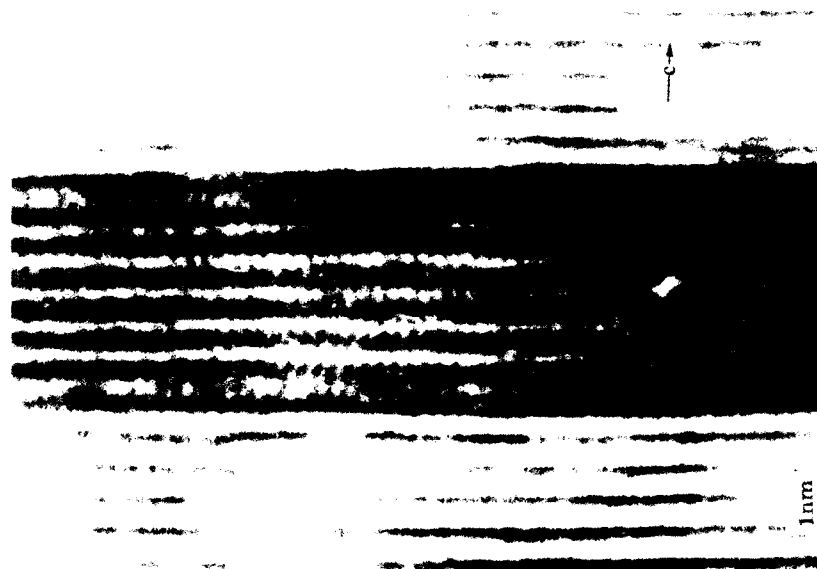


Figure 3: (a) HREM image of a platelet from Figure 1 shows a lamellar heterogeneity of 5nm width. The average lattice spacing of adjacent 3P₂ material is $d=0.597-0.605\text{nm}$ with a maximum value $d=0.635\text{nm}$. The resolved atomic spacing of the secondary lattice fringes, which form an $86-88^\circ$ angle with the c axis, is 0.284nm .

elsewhere[3, 4].

At least two crossed lattice-fringe images are resolved from the lamellar heterogeneity in Figure 3; one set corresponds to lattice planes normal to the c axis and the others are nearly parallel to the c axis, the two sets of planes forming an angle of $86-88^\circ$. The interplanar angle does not match any lattice planes in either sulfide and may be an interference anomaly without direct correspondence to a real lattice plane. By recalling the weak bonding and simple shearing between two S-Nb-S slabs, we expect such an angular deviation as observed from sample to sample. The average resolved atomic spacing between their planes is 2.84\AA , which is closer to that for $\{01\bar{1}0\}$ in $2\text{H-Nb}_{1+\alpha}\text{S}_2$ than in $3\text{R-Nb}_{1+\alpha}\text{S}_2$. The adjacent area was identified as 3R phase where no crossing fringes are observed.

For perfect crystals of either 2H- or $3\text{R-Nb}_{1+\alpha}\text{S}_2$, $\{10\bar{1}0\}$ planes are normal to $(000l)$ where $l=2$ for 2H and $l=3$ for 3R structures, respectively. Experimental measurements indicate that the crossing angle is less than 90° . This may be attributed to a shearing between adjacent the $(000l)$. This sheared structure (and also bending of the lattice planes as shown in Figure 1) is a common phenomenon within all $\text{Nb}_{1+\alpha}\text{S}_2$ platelets from the middle portion of the scale observed in the present study. Figure 3b shows both effects in a multi-beam axial lattice fringe image.

NON-STOICHIOMETRY AND POINT DEFECTS IN NbS_2

Using the electron probe microanalyzer, the range of non-stoichiometry of $\text{Nb}_{1+\alpha}\text{S}_2$ sulfidation scales was determined[2, 3]. The maximum deviation from stoichiometry of NbS_2 is an approximately 30% Nb extra.

The extra diffuse peak in X-ray diffraction and the appearance of kinematically forbidden spots in electron diffraction experiments indicate the formation of ordered defects[3]. This defect ordering has been reported for other system[5, 6].

If we consider the non-stoichiometry in $\text{Nb}_{1+\alpha}\text{S}_2$ as described elsewhere[8, 9], with the sulfidation rate depending on the non-stoichiometry, catastrophic sulfidation of Nb is predicted. For example, if we assume a stoichiometric deviation parameter $\alpha = 0.3$, which was determined from our experiments, and that all interstitials are mobile, then the concentration of Nb interstitial $[\text{Nb}_i] = x = 0.3$, and the corresponding self-diffusivity of Nb through the $\text{Nb}_{1+\alpha}\text{S}_2$ scale can be estimated as

$$D = \gamma a^2 \nu_o \exp\left(\frac{\Delta S_m}{R}\right) \exp\left(-\frac{\Delta H_m}{RT}\right)$$

where $\gamma \approx 1$ is a geometrical factor, $a \approx 2.5 \times 10^{-8}$ is the average distance for an atom to jump and $\nu_o \approx 3kT/2h \approx 3.67 \times 10^{13} \text{ Hz}$ is the thermal vibration frequency of atoms in free state, $\Delta S_m/R \approx 3-5$ and $\Delta H_m \approx 80-150 \text{ kJ/mol}$ at about $0.5-0.8T_m$. The estimated diffusion coefficient of Nb is $D = 3 \times 10^{-8} - 3 \times 10^{-4} \text{ cm}^2/\text{s}$. Consequently, if the niobium interstitials are predominantly mobile point defects, we would expect a parabolic scaling rate of the order of $K_p \approx 10^{-8} - 10^{-4} \text{ cm}^2/\text{s}$ which is 4 to 8 orders of magnitude greater than the parabolic sulfidation rate constant of Nb at 1173K we have determined experimentally.

The measured diffusivity of sulfur in the niobium sulfide scale is

$$D_S = 1 \times 10^{-6} \exp\left(-\frac{120 \text{ kJ/mol}}{RT}\right)$$

At 1173K, $D = 4.5 \times 10^{-12} \text{ cm}^2/\text{s}$, and the corresponding sulfur vacancy concentration is $\{V_S^{+2}\} \approx 10^{-6}$. This is a reasonable estimate in comparison to the defect concentration in Cr_2O_3 as discussed by Greskovich[10], e.g., $\text{Cr}_{2-\alpha}\text{O}_3$ with $\alpha = 9 \times 10^{-5}$ at 1373K.

By considering both the appreciable non-stoichiometry and diffusion-barrier transport properties in NbS_2 , we conclude that the extra Nb atoms responsible for the observed nonstoichiometry must be identified with well-bonded $-S_6-$ octahedral sites within the sulfide. The marker experiments as well as kinetic measurements are consistent with the possible importance of sulfur vacancies[2,7]. We may thus write the general form of $\text{Nb}_{1+\alpha}\text{S}_2$ as $\text{Nb}_{1+x}\text{S}_{2-y}$, with $x \gg y$, ($x \approx 0.1 - 0.3$, $y \approx 10^{-6}$). Structurally, interstitial Nb atoms (for the octahedral $-S_6-$ coordination) form ordered structures, and the Nb atoms have a strong interaction with their neighboring atoms and defects; consequently, they will not significantly contribute to the transport properties or other dynamic properties. On the other hand, the minority sulfur vacancies of sulfur on the sulfur sublattice are free to move, and we suggest they are the dominant mobile defects for the growth of $\text{Nb}_{1+\alpha}\text{S}_2$ scale. This interpretation is consistent with our experimental observations.

REFERENCES

- [1] K. N. Strafford and J.R. Bird, *J. Less-Common Metals* (1979) **68**, 223.
- [2] C. Zhou and L. W. Hobbs, *Heat-Resistant Materials*, ed. K. Natesan (ASM, 1991) p.225.
- [3] C. Zhou, *Growth, Structure and Properties of Cr_2O_3 and NbS_2 Corrosion Scales*, Sc.D thesis, MIT, Cambridge, MA(1991).
- [4] C. Zhou and L. W. Hobbs, *Proc. 50th Annual Meeting of EMSA*, ed. G. W. Bailey, J. Bentley and J. A. Small, (San Francisco Press, 1992) p.38.
- [5] C. N. R. Rao and J. Gopalakrishnan, *New Directions in Solid State Chemistry*, (Cambridge University Press, 1986) p. 208, and p. 421.
- [6] J. S. Anderson, *Intercalation Chemistry*, (Academic Press, 1982) p. 503.
- [7] C. Zhou and L. W. Hobbs, "Growth Mechanism of $\text{Nb}_{1+\alpha}\text{S}_2$ Film on Nb Using Marker Experiments", *MRS Proceedings*, **222** (1991) 321.
- [8] P. Kofstad, *High Temperature Corrosion*, (Elsevier, London, 1988) p. 436.
- [9] S. Mrowec and K. Przybylski, *High Temperature Materials and Process*, **6** (1984)1-79.
- [10] C. Greskovich, *J. Am. Ceram. Soc.* **67**(1984) C111.
- [11] C. Lebreton and L. W. Hobbs, "Defect Structure of Fe_{1-x}O ", *Radiation Effects* **74**(1983)227.

A COMPACT NUCLEAR MICROPROBE WITH A LIQUID METAL ION SOURCE AND A TOROIDAL ANALYZER

Mikio Takai*, Ryou Mimura**, Hiroshi Sawaragi**, and Ryuso Aihara**

*Faculty of Engineering Science and Research Center for Extreme Materials,
Osaka University, Toyonaka, 560 Osaka, Japan.

**EIKO Engineering Co., Ltd., 50 Yamazaki, Nakaminato, Ibaraki 311-12, Japan.

ABSTRACT

A nondestructive three-dimensional RBS/channeling analysis system with an atomic resolution has been designed and is being constructed in Osaka University for analysis of nanostructured surfaces and interfaces. An ultra high-vacuum sample-chamber with a three-axis goniometer and a toroidal electrostatic analyzer for medium energy ion scattering (MEIS) was combined with a short acceleration column for a focused ion beam. A liquid metal ion source (LMIS) for light metal ions such as Li^+ or Be^+ was mounted on the short column.

A minimum beam spot-size of about 10 nm with a current of 10 pA is estimated by optical property calculation for 200 keV Li^+ LMIS. An energy resolution of 4×10^{-3} ($\Delta E/E$) for the toroidal analyzer gives rise to atomic resolution in RBS spectra for Si and GaAs. This system seems feasible for atomic level analysis of localized crystalline/disorder structures and surfaces.

INTRODUCTION

Nuclear microprobes have successfully been applied to elemental mapping using PIXE in the field of biology, geology, and mineralogy [1 - 3]. In the meantime, increasing demands in microelectronics for localized image mapping of designed structures enforced to apply microprobe techniques with Rutherford backscattering (RBS) to semiconductor process developments [4, 5], in which a lateral resolution of 1 micron or less with a depth resolution of a few ten nanometers is required. However, the minimum feature size of integrated circuits (ICs) continues to shrink from a micron down to submicron. Nanofabrication using electron beams and scanning tunneling microscope (STM) tips facilitates further miniaturization in fabrication. Under such a circumstance, structural and/or atomic imaging of modified structures are of great importance for process control. A nuclear microprobe with a probe spot-size of several ten nanometers, combined with a high resolution analyzer, can provide not only structural images but also cross-sectional atomic images (i.e., in-depth imaging) without sample sectioning.

In this study, a compact nuclear microprobe with a liquid metal ion source (LMIS) and a toroidal analyzer has been designed and is being constructed in Osaka University. The compact nuclear microprobe system has a size of conventional scanning electron microscopes and provides a beam spot-size of about ten nanometers with a current of 10 pA. Such a system can meet the requirement of future nanofabrication with a feature size of several hundreds nanometers or less.

RBS MAPPING AND TOMOGRAPHY

Figure 1 shows the concept of total quantitative recording of RBS spectra for each of the scanning positions of a nuclear microprobe, the resulting RBS mapping at a certain depth and RBS tomography at a certain cross-sectional plane [4, 5]. The microprobe is raster-scanned over a sample surface. Each of the RBS spectra is stored in computer memory as a data block for a certain scanning position. The stored data blocks can be displayed or analyzed with appropriate software windows afterwards to produce both RBS mapping (at a certain depth or at a given species) and RBS tomography (at a certain cross-sectional plane). All the data necessary for analysis can be obtained by a single measurement, which drastically reduces measuring time and, hence, radiation damage in a sample.

The lateral resolution of RBS mapping is determined by the probe diameter, while the in-depth resolution is determined by an energy loss factor and an energy resolution of detecting systems. Therefore, the lateral resolution ranges from 5 to 1000 nm, depending on the beam

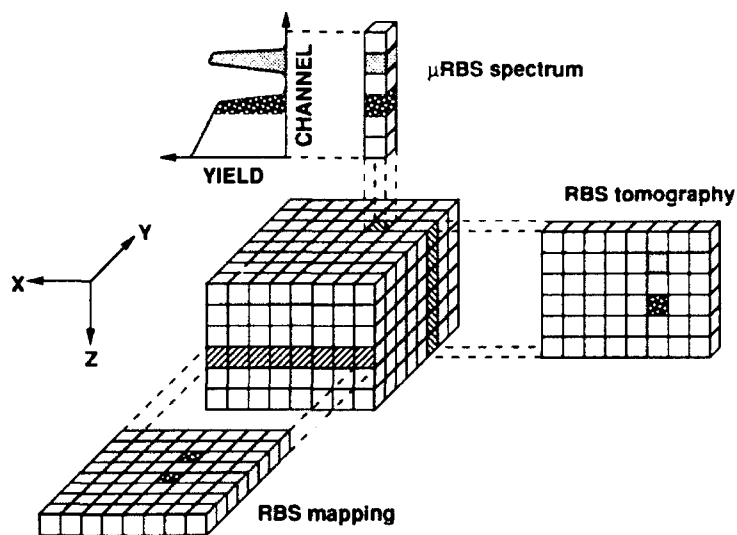


Fig. 1 Schematic of RBS mapping and tomography with a scanning microbeam.

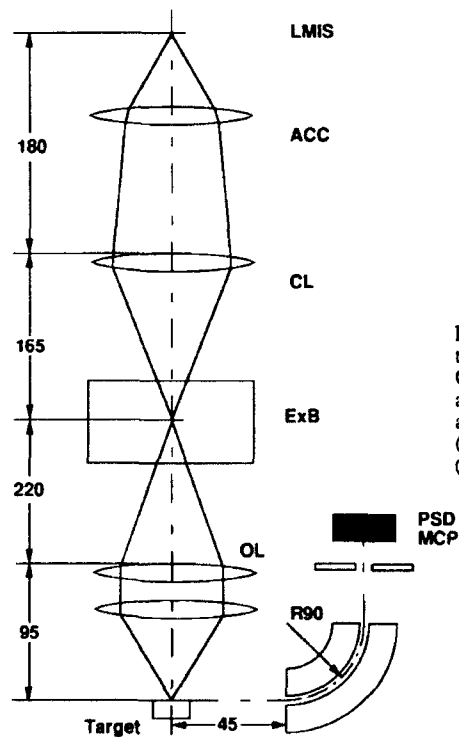


Fig. 2 Schematic of beam optics including three stage lenses (ACC: Acceleration Lens, CL: Condenser Lens, OL: Object Lens) with an analyzing magnet (ExB) and a toroidal analyzer coupled with a multichannel plate (MCP) and a position sensitive detector (PSD). Sizes are given in millimeters.

current, the values of which are not yet feasible for lateral atomic scale imaging. However, a depth resolution of subnanometer can be obtained by the use of a toroidal static energy analyzer used in this study, in which atomic level analysis or imaging in depth is possible.

MICROPROBE SYSTEM DESIGN

Figure 2 shows the schematic illustration of a compact nuclear microprobe system with a LMIS. The system consists of three stages of lenses: an accelerator lens, a condenser lens, and an objective lens with an ExB mass filter. A maximum acceleration voltage of the column is designed to be 200 kV. Therefore, a maximum accelerating energy of 400 keV is achieved when doubly-charged ions (e.g. Be^{++}) are used. A target chamber with a vacuum of 5×10^{-10} Torr has a sample holder mounted on a goniometer for channeling. A solid state detector and an electrostatic toroidal analyzer with a microchannel plate (MCP) are used for RBS measurement.

Lithium and/or beryllium LMISs will be used because of the simplicity in operation. 100 keV Li^+ or Be^+ probe ions yield a factor of 900 - 1600 larger scattering cross section in Si than for 2 MeV He^+ , though radiation damage due to probe beams should be carefully investigated. Thus, the compact system can provide higher RBS scattering yield with good energy resolution (i.e. depth resolution) when an electrostatic energy analyzer (a toroidal analyzer) with an energy resolution of 4×10^{-3} ($\Delta E/E$) is combined to a medium energy ion scattering (MEIS). The energy resolution of 4×10^{-3} ($\Delta E/E$) corresponds to depth resolutions of 0.21, 0.29, and 0.32 nm for Au, GaAs, and Si, provided that a Li^+ probe at 100 keV and a scattering angle of 90° are used.

BEAM OPTICS SIMULATION

Aberrations of the focusing lens system shown in Fig. 2 can be calculated by a finite element method [6]. Table I shows the spherical and chromatic aberration coefficients for accelerator, condenser, and objective lenses. Focusing characteristics can be further estimated using calculated aberrations and ion source specifications [7].

Figure 3 shows the calculated beam spot diameter as a function of beam current for a Be^+ and Be^{++} LMISs. The source size, the angular current density, and the energy spread of the Be^+ and Be^{++} LMISs are obtained from published data [8] and are 25 nm, 6 $\mu\text{A}/\text{sr}$, and 10 eV, and 25 nm, 15 $\mu\text{A}/\text{sr}$, and 8 eV, respectively. Singly-charged beryllium ion-beams provide a current of 100 pA with a beam spot-size of 600 and 1600 nm at 200 and 100 keV, respectively, while doubly-charged beryllium ion-beams provide smaller beam spot-sizes because of the higher angular current density and lower energy spread. Be^{++} microprobes with a beam spot-size of about 100 nm with a current of 40 - 80 pA are estimated at 200 - 400 keV. A minimum beam spot-size of 10 nm with a beam current of 2 pA is estimated for 200 keV Be^{++} beams.

Table I Optical coefficients of the focusing column. Cs: Spherical aberration coefficient, Cc: Chromatic aberration coefficient, M: Magnification

	Cs (mm)	Cc (mm)	M
Accelerator Lens	39506	3085	-1.087
Condenser Lens	2110681	759.4	0.494
Objective Lens	113689	243.5	0.351

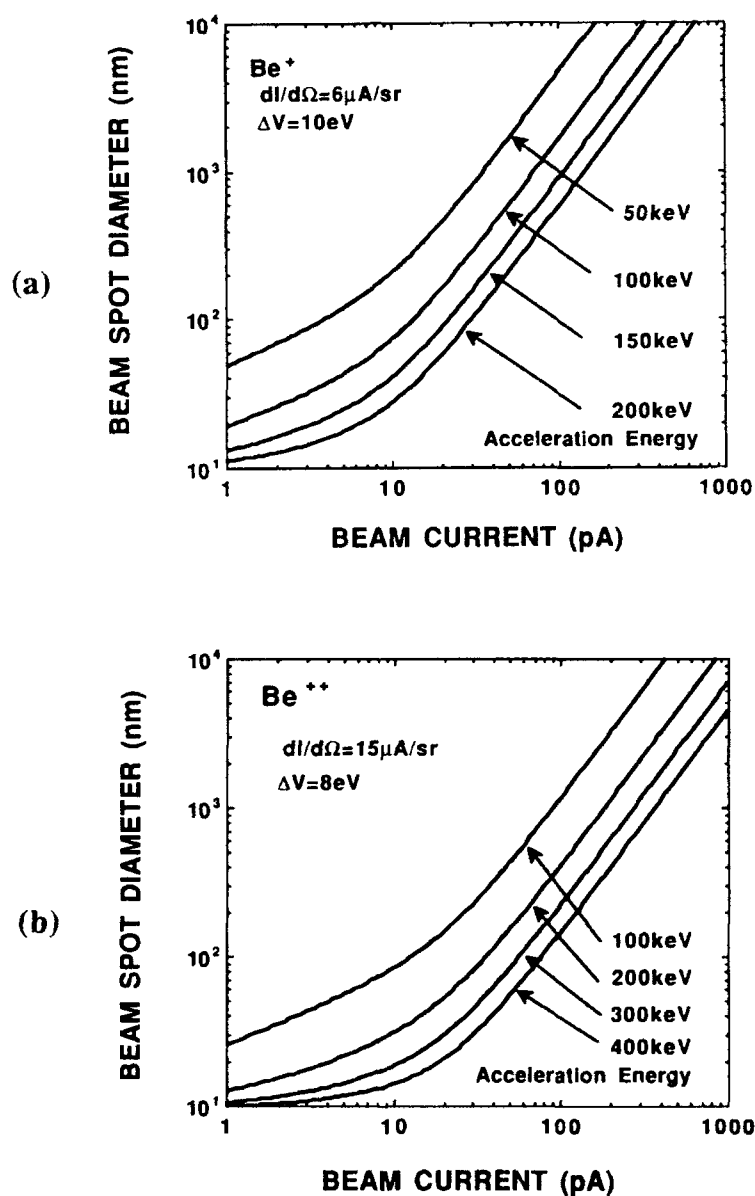


Fig. 3 Beam spot diameter as a function of current for 100 keV and 200 keV Be^+ (a) and 200 keV and 400 keV Be^{++} (b) LMISs obtained using calculated aberrations.

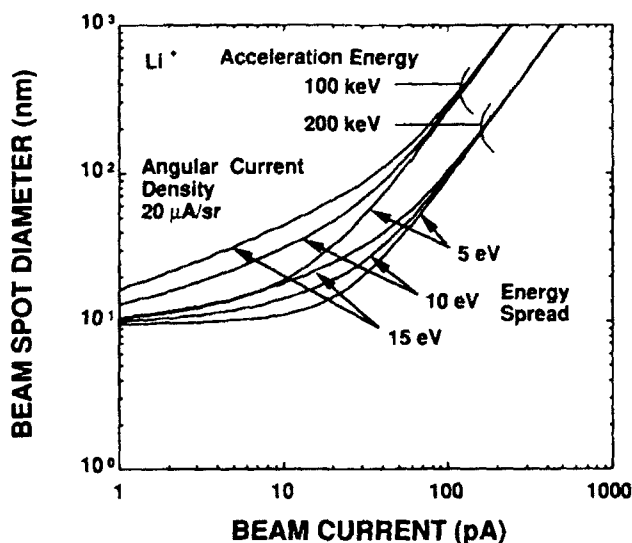


Fig. 4 Beam spot diameter as a function of current for 100 keV and 200 keV Li^+ LMISs obtained using calculated aberrations.

Figure 4 shows the calculated beam spot diameter as a function of beam current for a Li^+ LMIS, provided that the source size, the angular current density, and the energy spread of the Li^+ LMIS are 25 nm, $20 \mu\text{A}/\text{sr}$, and 5 - 15 eV. Microprobes with a beam spot-size of about 100 nm with a current of 100 pA can be obtained at 200 keV. A minimum beam spot-size of 10 nm with a current of 10 pA is estimated for 200 keV Li^+ beams. Therefore, the lithium LMIS is more suitable for obtaining smaller spot-size with high current. This probe beam characteristics can not meet the requirement of the atomic surface imaging. However, structural image mapping, combined with micro RBS and channeling contrast techniques, with lateral and in-depth resolutions of 10 and 0.2 nm, respectively, would provide indispensable information for future nanofabrication process development.

SUMMARY

A compact microprobe system with a LMIS for surface and/or interface analysis has been designed and is being constructed. The system size is almost comparable with a conventional SEM system and can be easily installed in a clean room for semiconductor processing. A beam spot diameter of 10 - 50 nm with a current of 10 - 50 pA is estimated by optical property calculation for 200 keV Li^+ LMIS. The estimated lateral and in-depth resolutions of 10 and 0.2 nm, respectively, are feasible for atomic level analysis and structural mapping of localized crystalline/disorder structures and surfaces.

ACKNOWLEDGMENTS

This work was supported by the System of Joint Research with Industry in 1992 (the Ministry of Education, Science and Culture and EIKO Engineering Co., Ltd.).

REFERENCES

- [1] F.Watt and G.W. Grime, *Principles and Applications of High Energy Ion Microbeams* (Adam Hilger, Bristol, 1987)
- [2] G.W. Grime and F. Watt, *Nuclear Microprobe Technology and Applications* (North-Holland, Amsterdam, 1988): Nucl. Instr. and Methods **B30** (1988) 227 - 506
- [3] G.J.F. Legge and D.N. Jamieson, *Nuclear Microprobe Technology and Applications* (North-Holland, Amsterdam, 1991): Nucl. Instr. and Methods **B54** (1991) 1 - 446
- [4] M. Takai, *Scanning Microscopy* **6** (1992) 174
- [5] M. Takai, *Intern. J. PIXE* **2** (1992) 107
- [6] E. Munro, PhD Thesis, University of Cambridge, 1972
- [7] O.C. Wells, *Scanning Electron Microscopy* (McGraw-Hill, New York, 1974)
- [8] H. Arimoto, E. Miyauchi, and H. Hashimoto, *Japan. J. Appl. Phys.* **24** (1985) L288

IN-PLANE ASYMMETRIES ON THE Ge(111)-c(2×8) SURFACE MAPPED WITH THE SCANNING TUNNELING MICROSCOPE

P. Molinàs-Mata,¹ J. Zegenhagen,¹ M. Böhrringer,¹ N. Takeuchi,² and A. Selloni^{2,3}

¹ Max-Planck Institut für Festkörperforschung, Heisenbergstr. 1, D-7000 Stuttgart 80, FRG

² Scuola Internazionale Superiore di Studi Avanzati, via Beirut 4, I-34014 Trieste, Italy

³ Department of Physical Chemistry, University of Geneva, Geneva, Switzerland

ABSTRACT

We report on new experimental studies of the Ge(111)-c(2×8) reconstruction performed with low-energy electron diffraction (LEED) and scanning tunneling microscopy (STM). Weak quarter-order reflections are present in the c(2×8) LEED pattern in agreement with previous observations and results of *ab initio* calculations. In order to gain insight into the predicted splitting of dangling bond states, we compare constant current topographs (CCT's) performed at high-tunneling currents (40.nA) with first-principles calculations of the local density of states (LDOS) 1 Å above the surface adatoms and obtain good qualitative agreement. We finally discuss to what extent the STM CCT's at high tunneling currents (small sample-tip distances (STD)) are sensitive to surface states outside the $\bar{\Gamma}$ point.

INTRODUCTION

The Ge(111)-c(2×8) reconstruction has been extensively studied with a variety of probes and still attracts much attention. Recent *ab initio* calculations,[1] e.g. indicate a reduction of the structural symmetry of the c(2×8) reconstruction in comparison with what has been previously accepted. Due to the small departure from mirror plane symmetry, the reconstruction displays the lowest possible symmetry, i.e. only translational invariance. Therefore six instead of 3 c(2×8) domains should cover an annealed Ge(111) surface, as suggested rather early.[2] The result of the calculation may not be all that unexpected because the c(2×8) structure even with mirror planes breaks the 3-fold symmetry of the underlying bulk structure, in contrast to what occurs in Si(111)-(7×7), where the symmetry of the unreconstructed surface is preserved.

In this paper we present LEED and STM experimental results, which represent a continuation of a work already presented,[3] and new first-principles calculations. In typical STM CCT's atomic positions or high density of states appear as bright *spots*. Frequently one spot is attributed to the position of a single atom which is not generally the case, as it will be shown in this study. We observe more spots than there are (top layer = adatoms + rest atoms) surface atoms. There may be several explanations for the observation of multiple spots. We could, e.g. observe second layer atoms or, as in the present case, the LDOS (or atomic orbitals) exhibits more than one density maximum in a plane above the surface. This effect, which could be called spot splitting, is predicted for the LDOS 1 Å above the adatoms in the case of filled states (see Fig. 4(a) of [1]). In the present work, we compare theory with STM CCT's for unfilled states performed at high tunneling currents.

The outline of the paper is as follows. We will first offer an incomplete overview (only centered on symmetry considerations) of previous work on the c(2×8) reconstruction. Afterwards we shall present the LEED and STM results. In the following section, the

observation of the quarter-order spots in the LEED pattern as well as the features of our CCT's for high tunneling currents will be discussed and compared with calculated LDOS pictures. The last section is devoted to the conclusions and to comment on the limitations of CCT measurements, mostly with high tunneling currents, in proving structural asymmetries. This is due to the fact that the surface electronic states at $k_{\parallel} \neq 0$ may influence the contrast in the tunnelling images.

THE Ge(111)-c(2×8) RECONSTRUCTION AND ITS PREDICTED ASYMMETRY

Yang and Jona proposed a c(2×8) structure (shown schematically in Fig.1) with mirror plane symmetry[4] in order to justify why the quarter-order spots of the c(2×8) were not observed in the LEED pattern. By contrast, Phaneuf and Webb observed the quarter-order reflections,[5] though with an intensity 1000-, 100-, and 10-times weaker than that of the integer-, half-, and eighth-order reflections, respectively. A detailed study of the quarter-order reflections as a function of the angle of incidence[5] showed that they do not result from surface wave enhancement of eighth-order beams in a double scattering process, as assumed by Ichikawa and Ino[6]. Therefore some small distortion from the structure suggested by Yang *et al* should exist, although atomic displacements should be really small considering the fact that they were neither detected with surface x-ray diffraction,[7] nor in the earliest STM investigations.[8]

Table I. Calculated structural shift of the atomic *in-plane* positions of adatoms and rest atoms, with respect to those of the unrelaxed c(2×8) structure. Displacements along the axes shown in Fig.1 are given in *tenths* of Å. Atomic labels correspond to those of Fig.1.

Atom	x	y
A ₄	0.31	0.06
A ₃	-0.17	-0.06
R ₃	0.17	0.02
R ₄	1.14	-1.34

Ab initio calculations of the surface structure and electronic properties of the Ge(111)-c(2×8) showed a small buckling between the two rest atoms, in agreement with previous STM observations.[9] With respect to the small predicted asymmetry, type-R₄ rest atoms show the largest displacement (0.18Å) from the expected symmetrical position (see Table I and Fig. 1). The weak LEED intensities for the fourth-order reflections were calculated[1] in agreement with the results of Phaneuf *et al.* Moreover, the calculations showed that the violation of the symmetry is more pronounced in the electronic density of states at the surface, which has been corroborated by recent STM measurements.[3] Another result of the calculations concerned the LDOS of the adatom dangling-bond states. Filled states (0.5 eV below the Fermi level) appeared split in real space, i.e. a single state exhibits two maxima in a plane 1Å above the surface.

Spot splitting for unfilled states (1.1 eV sample bias) was observed with the STM in the CCT mode, for relatively high tunneling currents (≈ 40 nA); i.e., when the sample-tip distance (STD) was small. From the experiment the location of these anomalous brightness maxima with respect to the c(2×8) unit cell could not be determined and the correspondence between maxima in brightness and surface states of particular atoms remained unclear.[3]

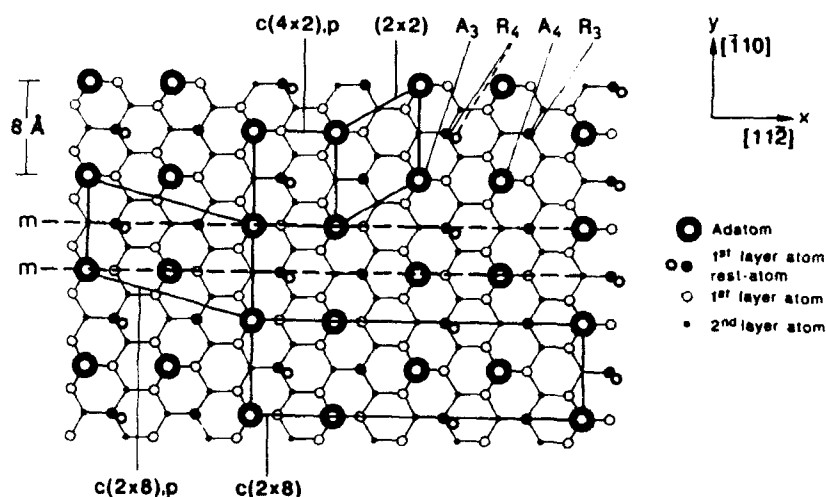


Figure 1: Top view of the Ge(111)-c(2x8) reconstruction. Large open circles correspond to adatoms. Medium sized filled and open circles represent 1st layer unsaturated atoms (rest atoms), and 1st layer saturated atoms, respectively. The calculated shift of type R₄ rest atoms (see Table I), enlarged for the sake of clarity, is indicated by open circles with a circumference thicker than that for the 1st layer saturated atoms. Small filled circles correspond to 2nd layer atoms. The previously assumed mirror planes are indicated by dashed lines.

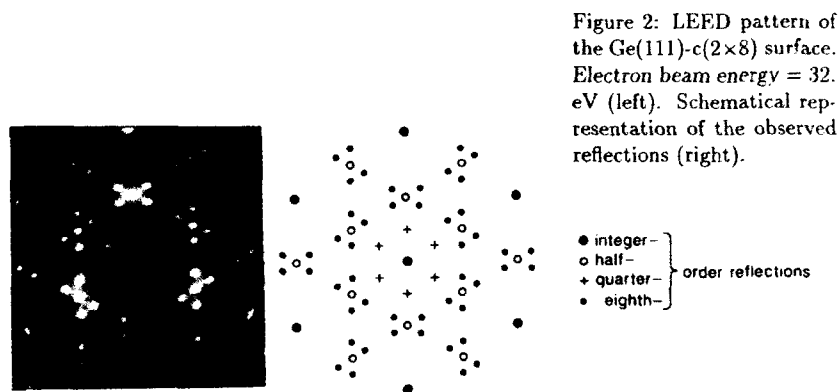
LEED AND STM RESULTS

The quarter-order reflections in the LEED pattern

Although, to the best of our ability, we prepared all samples in the same way, quarter-order reflections could only be identified for roughly one fourth of the specimens. There is, however, a relation between the size of the (rotationally equivalent) single c(2x8) domains and the appearance of the quarter-order spots. From our observations it is obvious that the quarter-order spots are indicative of large domains. Thus, it is clear that minute differences in the sample preparation procedure affect the strength of the quarter-order reflections, which represents an explanation for the old controversy whether these LEED spots are present or not. A typical LEED picture and a schematical reproduction of this pattern is shown in Fig. 2.

High-current STM CCTs: the spot splitting

The STD decreases with increasing tunneling current. Therefore, we establish a comparison between a CCT performed at high tunneling current (small STD) and a calculated LDOS only 1 Å above the adatoms. In particular, we would like to obtain some information about the physical origin of the spot splitting. We found stable tunneling conditions leading to CCT's where spot splitting can be observed when probing empty



states (positive sample bias). In Fig.3(top) we show a CCT obtained at a sample bias value of + 0.8 V and high tunneling current, and in Fig.3(bottom) the LDOS for states at the \bar{M}_2 point (see Fig.4) at a significantly higher energy level (+1.6 eV) above the Fermi level.[1] In spite of large energy difference, there is a qualitatively good agreement between these pictures as far as the density of spots is concerned, which is higher than the number of dangling bonds. Note, however, that the spot located at A_4 does not split in the CCT like in the LDOS. Intensities and shapes do not match exactly. Calculated spots, i.e. LDOS, originate mainly from back-bond states. For details about the calculation the reader is referred to Ref.[1].

DISCUSSION

As previously mentioned, there is a significant difference between the sample-bias value in the STM image of Fig.3(top) and the energy for which the LDOS was calculated. Assignment of absolute energy levels, however, is a notorious difficulty of these type of calculations. We also note that we do not sample the LDOS at one particular \vec{k} -point when performing a CCT, but integrate over the whole reciprocal space. This integration may become more important the closer we get to the surface. The reason for that arises from the decrease of the decay length of the electronic wave function with the increase of the in-plane component of \vec{k} (k_{\parallel}) for the states involved in the tunneling.[10] For large STD's only those states of small in-plane \vec{k} component will tunnel, whereas for smaller distances even states outside the center of the Brillouin zone will have a non negligible contribution to the tunneling current. In particular, in case no states at the $\bar{\Gamma}$ point were available, the tunneling current would be dominated by states with larger k_{\parallel} .

Furthermore, if the tunneling tip approaches the surface closely, tip-atom-surface-atom interactions may become significant. This may lead to an energy shift of states or may even introduce new states. Last but not least, even if we are tunneling with a one-atomic tip, the symmetry of the electronic states of the sampling tip atom could introduce features in the image such that simple surface atoms give rise to multiple protrusions.[11] However, in the present study this is most likely not the case since obviously not every surface atom gives rise to multiple protrusions.

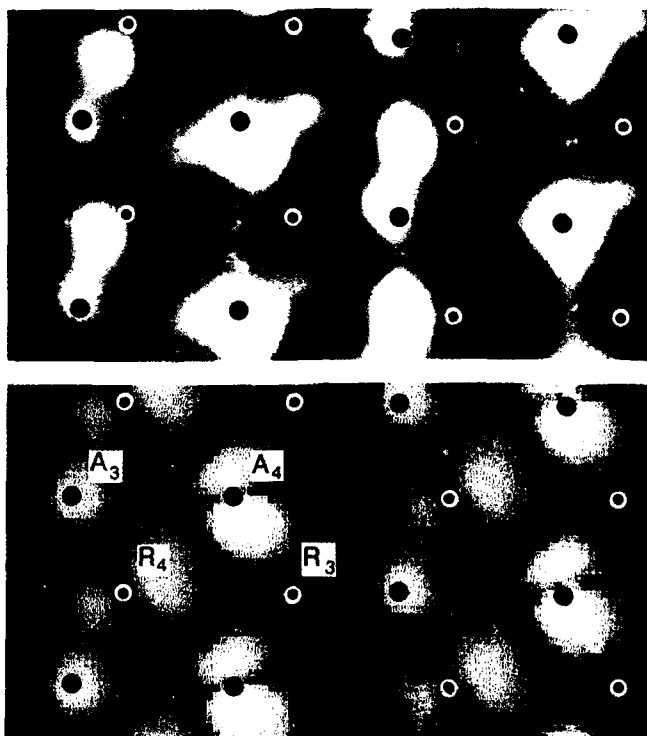


Figure 3: STM CCT image of Ge(111)-c(2 \times 8) obtained with + 0.8 V sample bias and a tunneling current of 39.7 nA (top). Calculated LDOS 1 Å above the c(2 \times 8) surface top for states + 1.6 eV above the Fermi level (bottom).

CONCLUSIONS

We have observed the quarter-order reflections in the LEED pattern of the c(2 \times 8) reconstruction, which agree with previous detailed observations of these spots as well as with theoretical calculations. CCT's at high tunneling currents appear to be quite sensitive to states at $k_{\parallel} \neq 0$ if no states of the same energy exist at the center of the Brillouin zone.[10] Therefore, the high sensibility of the STM to electronic states, which is responsible for its unmatched resolution in real space, may become a drawback, when trying to prove properties of the geometrical structure.

ACKNOWLEDGMENTS

Valuable discussions with M. Cardona and D. Leach are acknowledged. We would like to thank W. Stiepany and G. Schneider for the technical support provided throughout this project. One of us, P.M.M., acknowledges the financial support of the Directorate-General for Science, Research, and Development (EC).

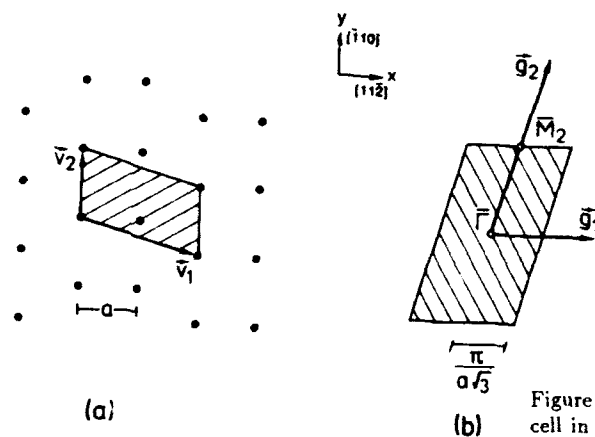


Figure 4: Primitive unit cell in real space (left) and Brillouin zone (right) of the $c(2 \times 8)$ reconstruction. a equals 4\AA .

REFERENCES

1. N. Takeuchi, A. Selloni, and E. Tosatti, *Phys. Rev. Lett.* **69**, 648 (1992).
2. No mirror planes were assumed in the buckled model for the $\text{Ge}(111)\text{-}c(2 \times 8)$ reconstruction. D.J. Chadi and C. Chiang, *Phys. Rev. B* **23**, 1843 (1981).
3. P. Molinäs-Mata and J. Zegenhagen, *Solid State Commun.* **84**, 393 (1992).
4. W.S. Yang and F. Jona, *Phys. Rev. B* **29**, 899 (1984).
5. R.J. Phaneuf and M.B. Webb, *Surf. Sci.* **164**, 167 (1985).
6. T. Ichikawa and S. Ino, *Surf. Sci.* **85**, 221 (1979).
7. R. Feidenhans'l, J.S. Pedersen, J. Bohr, M. Nielsen, F. Grey, and R.L. Johnson, *Phys. Rev. B* **38**, 9715 (1988).
8. R.S. Becker, B.S. Swartzentruber, J.S. Vickers, and T. Klistner, *Phys. Rev. B* **39**, 1633 (1989) and references therein.
9. E.S. Hirschorn, D.S. Liu, F.M. Leibsle, A. Samsavar, and T.C. Chiang, *Phys. Rev. B* **44**, 1403 (1991).
10. J.A. Kubby, J.E. Griffith, R.S. Becker, and J.S. Vickers, *Phys. Rev. B* **36**, 6079 (1987).
11. C.J. Chen, *J. Vac. Sci. Technol. A*, **6**(2), 319 (1988).

Experimental Optimization for Imaging with Photoelectron Diffraction

J.G. TOBIN*, G.D. WADDILL*, HUA LI**, and S.Y. TONG**

*Chemistry and Materials Science Department, Lawrence Livermore National Laboratory,
Livermore, CA 94550 • USA

**University of Wisconsin, Laboratory for Surface Studies and Department of Physics, Milwaukee,
WI 53201 • USA

PACS #79.60 Dp, 61.10 Lx, 68.55 Jk

ABSTRACT

The experimental apparatus and its optimization for holographic imaging with energy dependent photoelectron diffraction are described. A substantial improvement in data taking efficiency has resulted, allowing total data collection time to be reduced to about twelve hours for a single image-map.

DISCUSSION

Extraction of structural information from diffraction data is predicated upon conversion of measured variations in angular or energy space into real space dependences. A time-honored and highly precise method is to use trial and error comparison of model dependent calculations of scattering cross sections to fit measured data. A different approach is to Fourier transform (FT) normalized diffraction curves, either energy or angular variations. But for an FT to be meaningful, an accurate theory which condenses down into a simple sinusoidal dependence is required. Recently, there has been great interest in use of the single-energy, many-angle variant of photoelectron diffraction, often referred to as photoelectron holography¹, to generate real space images of surfaces and interfaces. Alternatively, one can pursue the FT of the energy variation. Early work^{2,3}, done on a fairly empirical basis, suggested that there was some validity to this method for determining scalar distances with normal emission. Subsequent attempts at improvement used energy variations along a few high symmetry directions⁴. We have developed a new method which involves inverting energy variations at a number of angular positions. The theoretical framework⁵, which permits the FT of the data, has been presented earlier. This direct method, based upon the intersection of contour arcs associated with each measurement direction, can provide three-dimensional vectorial atomic positions with atomic scale resolution. Here will be described an experimental arrangement which has been optimized for rapid data collection, to provide the large phase-space information base that is necessary for image generation with energy dependent photoelectron diffraction. These experiments were performed at the Stanford Synchrotron Radiation Laboratory, using the University of California/National Laboratories Participating Research Team facilities, on the spherical grating monochromator (SGM) beamline⁶, Beamline 8-2. A schematic of the beamline layout is shown in Figure 1. Both Beamline 8-2 [Ref. 7] and Beamline 8-1 [Ref. 8], a toroidal grating monochromator, have been demonstrated to be very high resolution instrumentation. Beamline 8-2 has also been used as a source of circularly-polarized x-rays⁹. The data was collected in a three-tiered, two-chamber photoelectron spectrometer¹⁰, shown in Figure 2, equipped for photoemission with full energy and angular ($\pm 3^\circ$) resolution and multi-channel detection.

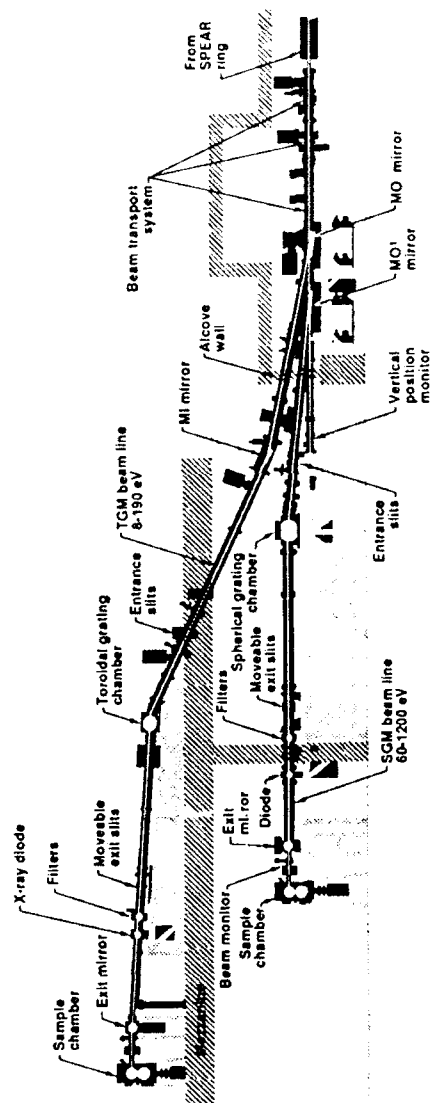


Figure 1. Elevation view of the Beamline VIII facility at SSRL showing a spherical grating monochromator branch on the ground floor and the toroidal grating monochromator branch with a mezzanine end station [6].

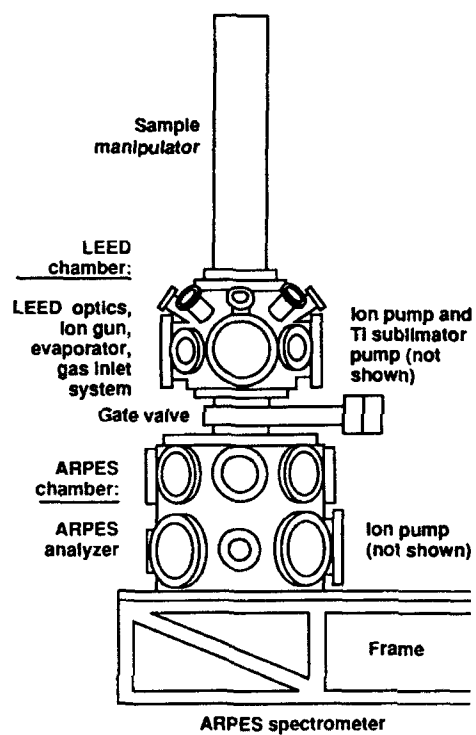


Figure 2. Schematic of the angle-resolved photoelectron spectrometer (ARPES) [10].

An example of data is shown in Figure 3. Here, energy distribution curves (EDC) at a series of photon energies demonstrates the strength of the Au feature in this photon energy range.

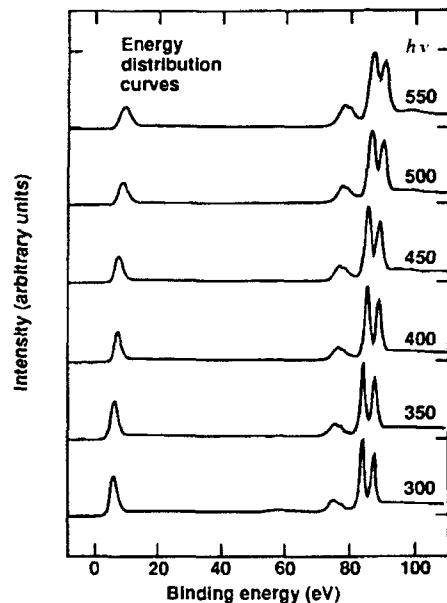


Figure 3. Energy distribution curves of 1.5 ML Au/Cu(001). For each photon energy, the analyzer voltages are scanned to select a range of kinetic energies. From this, plots of spectral intensity versus binding energy are obtained. The zero in binding energy corresponds to the Fermi energy. There are three major sets of features here: The valence bands (VB) immediately adjacent to the Fermi energy, the Cu3p doublet at binding energies of 75 and 77 eV, and the Au4f_{7/2} and Au4f_{5/2} peaks at binding energies of 84 eV and 88 eV, respectively. These spectra were normalized to the largest feature in each.

We have utilized an alternative method of data collection for our photoelectron diffraction imaging experiment. It is a constant initial state (CIS) mode, scanning the photon energy and kinetic energy of the analyzer together, so that emission from specific core lines, in this case the Au4f_{7/2} and Au4f_{5/2} of c(2x2) Au/Cu(001), could be directly monitored. The success of this operation could be confirmed by direct visual observation of the channel plate response, using a display scope. The position-sensitive amplification of the channel plate assembly, plus the double-focusing capabilities of the hemisphere can produce a real-time energy-dispersion spectrum on the hemisphere exit plane. Using 80 eV pass energy, the window is about 10 eV wide, encompassing both the Au4f_{7/2} ($B^F = 84$ eV) and Au4f_{5/2} ($B^F = 88$ eV) peaks but excluding the Cu3p ($B^F = 75, 77$ eV). Here B^F is the binding energy with respect to the Fermi energy. The channel plate output at each photon energy was integrated and then normalized to

photon flux by dividing by the output of a gold grid, placed upstream. The middle energy grating was used in this experiment and the Au photoyield for the grating is shown in Figure 4. In this experiment and over the photon energy range of interest (~ 300 eV to ~ 500 eV), the Au photoyield is dominated by the Au4f photoemission¹¹, so that dividing by the Au photoyield also takes out the atomic cross structure variations from the photoelectron intensity, leaving the modulations associated with the photoelectron diffraction imaging¹².

These modulations ride on a monotonically decreasing background, which reflects the $1/KE$ transmission function of this lens and analyzer system^{2,4,10}. Simply put, because the electrons are decelerated to a pass energy of 80 eV, the outside acceptance angle scales as $1/KE$. This effect can easily be taken into account and corrected in the data analysis.

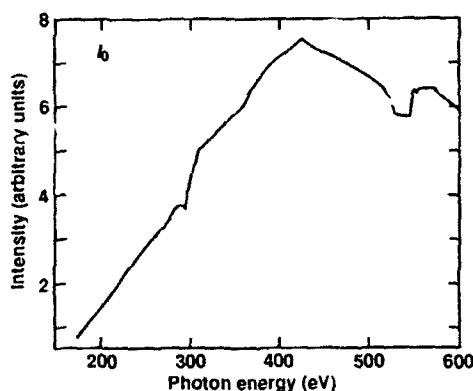


Figure 4. The Au grid photoyield of the middle grating (500l/mm) versus photon energy.

We have found that this method of data collection reduces our data taking time by an order of magnitude or more, over the previous mode^{10,13} of collecting an energy distribution curve (EDC) at each photon energy. Although the EDC method produces oscillations of 25–50% and this procedure has modulations of about 3%, the diffraction effects are still easily observable. In the case of imaging, the trade of oscillation size for a larger angular database is well worthwhile. The results of our study of Au/Cu(001) will be presented elsewhere¹² and clearly demonstrate imaging of surface structure with energy-dependent photoelectron diffraction.

ACKNOWLEDGMENTS

Work performed under the auspices of the US Department of Energy by Lawrence Livermore National Laboratory under contract number W-7405-ENG-48. This work was supported in part by ONR grant No. N00014-90-J1749. We also wish to thank Stanford Synchrotron Radiation Laboratory and its staff. Karen Clark provided clerical support for this work at LLNL.

REFERENCES

1. L.J. Terminello and J.J. Barton, *Science*, **251**, 1218 (1991).
2. J.G. Tobin, L.E. Klebanoff, D.H. Rosenblatt, R.F. Davis, Y. Huang, W.M. Kang, and S.Y. Tong, *Phys. Rev. B.*, **26**, 7076 (1982).
3. S.Y. Tong, W.M. Kang, D.H. Rosenblatt, J.G. Tobin, and D.A. Shirley, *Phys. Rev. B.*, **27**, 4632 (1983).
4. C.C. Bahr, J.J. Barton, Z. Hussain, S.W. Robey, J.G. Tobin, and D.A. Shirley, *Phys. Rev. B.*, **35**, 3773 (1987).
5. S.Y. Tong, H. Huang, and C.M. Wei, *Phys. Rev. B.*, **46**, 2452 (1992).
6. K.G. Tirsell and V.P. Karpenko, *Nucl. Inst. Meth.*, **A291**, 511 (1990).
7. L.J. Terminello, G.D. Waddill, and J.G. Tobin, *Nucl. Instrum. Meth.*, **A319**, 271 (1992).
8. Z. Hussain, et. al., Private communication, 1992.
9. G.D. Waddill, J.G. Tobin, and D.P. Pappas, *Phys. Rev. B.*, **46**, 552 (1992); J.G. Tobin, G.D. Waddill, and D.P. Pappas, *Phys. Rev. Lett.*, **68**, 3642 (1992).
10. J.C. Hansen, M.K. Wagner, and J.G. Tobin, *Solid State Comm.*, **72**, 319 (1989); J.C. Hansen, Ph.D. Thesis, University of Wisconsin-Madison (1989); J.A. Benson, Masters Thesis, University of Wisconsin Madison (1986); B.J. Knapp, J.C. Hansen, M.K. Wagner, W.D. Clendening, and J.G. Tobin, *Phys. Rev. B.*, **40**, 2814 (1989).
11. J.J. Yeh and I. Lindau, *Atomic Data and Nuclear Data Tables*, **32**, 1 (1985).
12. J.G. Tobin, G.D. Waddill, Hua Li, and S.Y. Tong, in preparation.
13. J.G. Tobin, J.C. Hansen, and M.K. Wagner, *J. Vac. Sci. Tech.*, **A8**, 2494 (1990).

LOW ENERGY PHOTOELECTRON HOLOGRAPHY ON GAAS

R. DENECKE*, R. ECKSTEIN*, L. LEY*, A. BOCQUET**, J. RILEY**, R. LECKEY**

*Universität Erlangen-Nürnberg, Institut für Technische Physik II, Erwin-Rommel-Str. 1, W-8520 Erlangen, Germany

**La Trobe University, Department of Physics, Bundoora Vic., Australia 3083

ABSTRACT

For GaAs (001) and ($\bar{1}\bar{1}\bar{1}$) we have measured the photoelectron diffraction patterns at a kinetic energy of 86 eV. We applied an extended Fourier-transform algorithm to the (001) data to obtain real space images. The origin of structures in these images not representing atomic positions is investigated with the help of single scattering calculations.

INTRODUCTION

In the past few years there has been a renewed interest in photoelectron diffraction. Since A. Szöke suggested in 1986 that a diffraction pattern caused by photoelectron emission from a core level can be interpreted as a hologram [1] there have been increasing numbers of publications dealing with this so-called photoelectron holography. Most of the studies so far have dealt with single crystals of metals which have been investigated using photoelectrons with rather high kinetic energy. The main reason for the use of high kinetic energies is the better spatial resolution that can be achieved with decreasing electron wavelength.

By comparison, very little has been done in the low kinetic energy regime and for semiconductor materials. Low kinetic energies provide some interesting advantages. First there is the small escape depth of the photoelectrons which leads to higher surface sensitivity and to a better determination of the location of the emitter atoms. Secondly a more isotropic distribution of the scattering amplitude should in principle aid the reconstruction process. Yet it remains to be seen whether these advantages outweigh the disadvantages like the worse spatial resolution caused by the increased wavelength and the increasing probability of multiple scattering.

The step from metal to semiconductor crystals is accompanied by a change from relatively simple to more complex structures. In the case of GaAs there is the additional problem of two different types of atoms with different scattering factors. On the other hand this is an advantage when it comes to identify the two basis atoms of the zincblende structure as would be the case in Silicon [2].

EXPERIMENTAL RESULTS

Photoelectron intensity distributions were obtained using a toroidal energy analyser (TEA) [3]. As a light source we used the synchrotron radiation facility BESSY in Berlin, Germany, in conjunction with a toroidal grating monochromator providing photons in the energy range from 10 to 120 eV.

The TEA is particularly suited to acquire the required intensity distributions quite quickly. The design is such that it allows to register electrons emitted into a full 180° arc of polar angles with an angular resolution of 1° . The azimuthal angle is changed by rotating the sample around its surface normal in steps of 2° . The combined energy resolution of the monochromator and the analyser has been determined to be about 0.2 eV. Light was incident parallel to the surface normal.

Here we present data obtained for the As-terminated (001) and ($\bar{1}\bar{1}\bar{1}$) surfaces of GaAs. Both samples were grown by molecular beam epitaxy (MBE) and had been capped by a thick layer of amorphous As to protect them from oxidation. By heating the samples to above 300°C the As cap sublimates and leaves an As-stabilized surface. From the observed

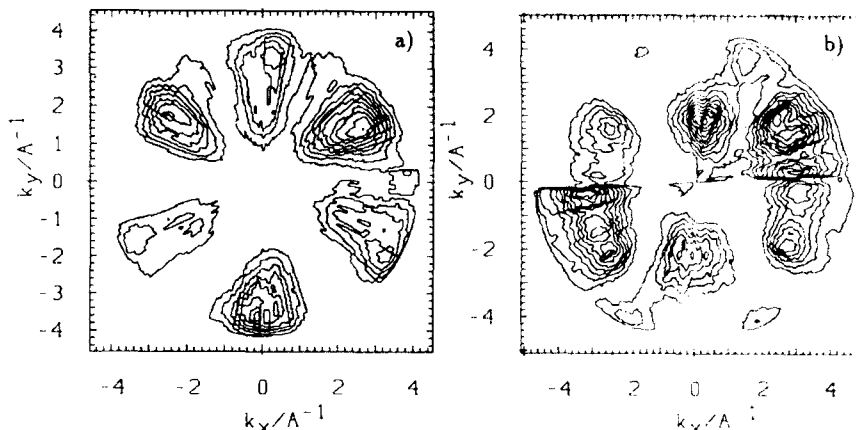


Figure 1: Measured diffraction patterns for the Ga 3d core level emission from a) GaAs($\bar{1}\bar{1}\bar{1}$) and b) (001) at a kinetic energy of 86 eV.

LEED patterns we deduced a (1x1) reconstruction for the GaAs(001) surface and a (2x2) reconstruction for GaAs($\bar{1}\bar{1}\bar{1}$).

Figure 1a) and 1b) show the intensity distribution in contour form of the Ga 3d emission from the ($\bar{1}\bar{1}\bar{1}$) and the (001) surfaces of GaAs, respectively. The original data have been transformed from $I(\theta, \phi)$ to $I(k_x, k_y)$, where k_x and k_y are the components of electron wave vector parallel to the surface. The measured intensity distributions have been corrected for background emission and have been normalized to the photon flux. The data of the ($\bar{1}\bar{1}\bar{1}$) surface exhibit the expected threefold symmetry quite clearly whereas the twofold symmetry of the (001) surface is less obvious in the diffraction pattern.

IMAGE RECONSTRUCTION

In order to get real space images from the measured diffraction patterns we have to reconstruct the data. First the data $I(\mathbf{k})$ as shown in Figure 1 are normalized in order to suppress isotropic contributions:

$$\chi(\mathbf{k}) = I(\mathbf{k}) - \frac{1}{2\pi} \int d\Omega_{\mathbf{k}} I(\mathbf{k}) \quad (1)$$

The anisotropy function $\chi(\mathbf{k})$ is then transformed using the extension of Barton's phased Fourier-transform [5] by Hardcastle et al. [6] to yield the real space image function $\Phi(\mathbf{r})$:

$$\Phi(\mathbf{r}) = \int d\Omega_{\mathbf{k}} \frac{1}{\mathcal{F}(\mathbf{k}, \mathbf{r})} \chi(\mathbf{k}) e^{-i\mathbf{k} \cdot \mathbf{r}}, \quad (2)$$

where $\mathcal{F}(\mathbf{k}, \mathbf{r})$ is the phase-only part of the complex conjugate of the scattering factor. In Figure 2a) and 2b) we show the result of the reconstruction. Figure 2a) is a contour plot of the image function in an x - y -plane 2.8\AA above the plane containing the emitter, i.e. the plane at $z=2.8\text{\AA}$ in Figure 2b). The latter represents the image function in a vertical (100) plane. Both cuts are chosen to contain only Ga atoms, so that the function $\mathcal{F}(\mathbf{k}, \mathbf{r})$ in equation (2) applies to Ga scatterers. The appropriate scattering factor is taken from [4]. The crystallographic positions of the atoms are marked by crosses. Local maxima in the image function may be seen within 0.5\AA of the expected locations, which is consistent with the wavelength of the electrons of 1.3\AA . However, there is even stronger structure in unphysical locations closer to the origin. This is particularly evident in the vertical cut.

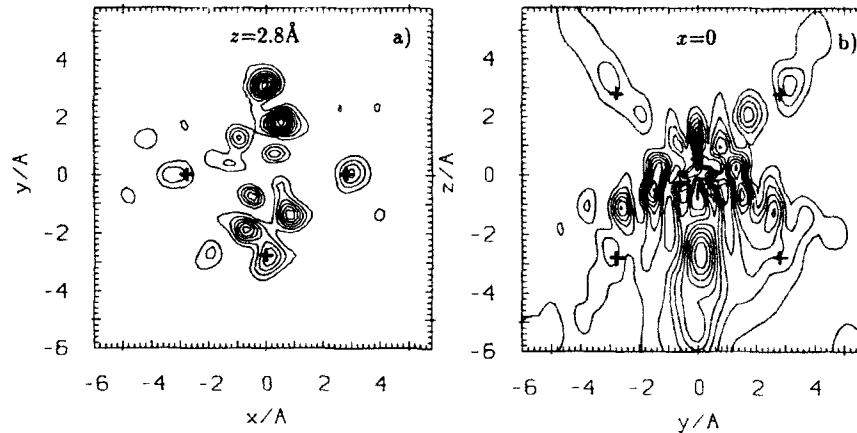


Figure 2: Real space images of the GaAs(001) sample reconstructed using eq. (2). The crosses mark the crystallographic positions of the atoms.

In order to obtain some insight into the origin of these extraneous structures we performed the following simulations. We consider a cluster of 30 atoms on a zincblende lattice involving six layers. We have calculated the diffraction pattern due to a single s-wave emitter placed in the fourth layer, 4.2 Å below the surface, using a single scattering formalism:

$$I(\mathbf{k}) \propto 1 + \sum_j \left[\frac{|f_j|^2}{r_j^2} + 2 \frac{|f_j|}{r_j} \cos(kr_j - \mathbf{k} \cdot \mathbf{r}_j + \delta_j) \right] + 2 \sum_{j < j'} \frac{|f_j| |f_{j'}|}{r_j r_{j'}} \cos[k(r_{j'} - r_j) - \mathbf{k} \cdot (\mathbf{r}_{j'} - \mathbf{r}_j) + (\delta_{j'} - \delta_j)], \quad (3)$$

where j and j' sum over all scatterers. $f_j = |f_j|e^{i\delta_j} = f_j(\mathbf{k} \cdot \mathbf{r})$ is the scattering factor for the j th atom and \mathbf{r}_j is the vector pointing from the emitter to the j th scatterer. To maximize the similarity between this simulation and optical holography we first assume isotropic scattering factors. The resulting diffraction pattern is then transformed using Barton's phased Fourier-transform [5]:

$$\Phi(\mathbf{r}) = \int d^3\mathbf{k} \chi(\mathbf{k}) e^{-i\mathbf{k} \cdot \mathbf{r}} \quad (4)$$

The result presented in Figure 3 for the two cuts discussed previously shows indeed good agreement with the known atomic positions. When the scattering factors are changed from isotropic to realistic ones for Ga and As [4], the resulting real space images are as shown in Figure 4. Although weak structure is observed at the correct positions the image function is now dominated by spurious peaks which are particularly strong near the origin.

As a next step we tried to improve the reconstruction procedure by using the method described by Hardcastle et al. [6]. By using the full scattering factor for $\mathcal{F}(\mathbf{k}, \mathbf{r})$ in equation (2) we found that the image quality was significantly degraded whereas using the phase of the scattering factor only yields results shown Figure 5. By comparing Figures 4 and 5 it is evident that the main effect is a significant enhancement of the true structures relative to the artifacts even though the latter remain prominent. As expected from Hardcastle's algorithm the twin images of the atoms at $z = +2.8$ Å in Figure 5 are no longer superimposed on the true atom positions at $z = -2.8$ Å.

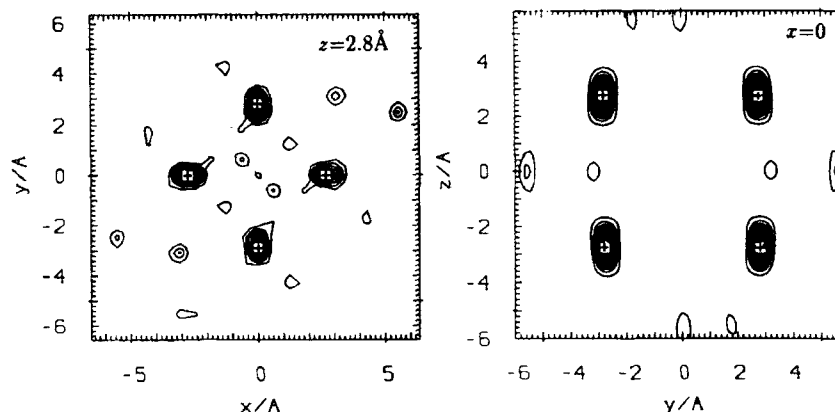


Figure 3: Reconstruction of a calculated diffraction pattern (see text) according to eq. (4) for the x - y plane at $z=2.8\text{\AA}$ and the y - z plane at $x=0$.

We now return to the consideration of the transformed experimental data shown in Figure 2. As previously stated we have used the phase only form of Hardcastle's algorithm in reconstructing the experimental diffraction patterns. In the light of the above simulation exercises it is clear that significant artifacts are to be expected; these have their origin in the non-isotropic nature of electron scattering from Ga or As atoms. The remaining strength of the artifacts is such as to make the determination of an unknown structure unlikely at the present stage of the development of this technique.

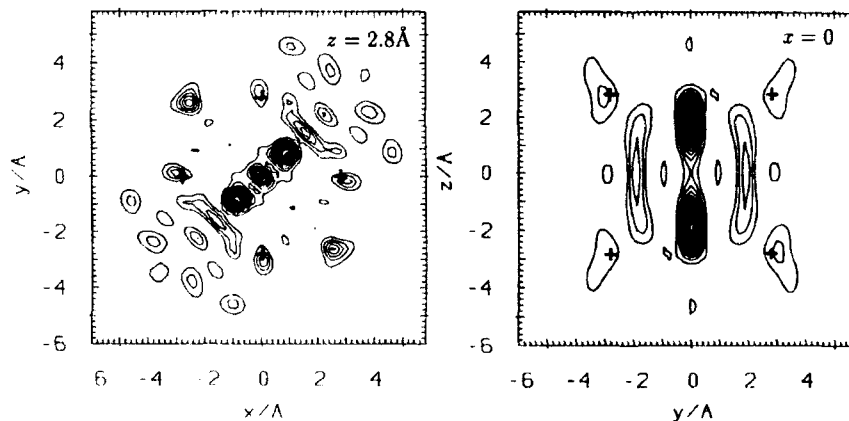


Figure 4: Real space images for simulations with realistic Ga and As scattering factors reconstructed with Barton's formula (4).

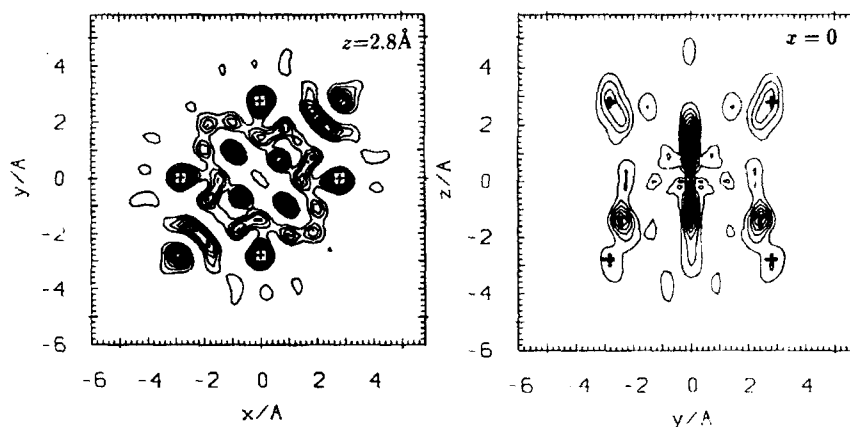


Figure 5: Real space images for simulations with realistic Ga and As scattering factors reconstructed using eq. (2) with the phase of the scattering factor only. Crosses mark the positions of the atoms, the twin images are marked by the letter T.

The authors would like to thank J. Faul and G. Neuhold for help with the experiments and the staff of BESSY for support during the measurements. This work is supported by the Bundesminister für Forschung und Technologie under contract number 05 5WEDA B 3.

REFERENCES

- [1] A. Szöke in Short Wavelength Coherent Radiation: Generation and Applications, AIP Conference Proceedings No. 147 (American Institute of Physics, New York, 1986)
- [2] G. S. Herman, S. Thevuthasan, T. T. Tran, Y. J. Kim and C. S. Fadley, *Phys. Rev. Lett.* **68**, 650 (1992)
- [3] R. Leckey, J. D. Riley, *Appl. Surf. Sci.* **22/23**, 196 (1985)
F. Toffoletto, R. Leckey and J. D. Riley, *Nucl. Instrum. Meths.* **B12**, 282 (1985)
- [4] M. Fink, J. Ingram, *At. Data* **4**, 129 (1972)
- [5] J. J. Barton, *Phys. Rev. Lett.* **61**, 1356 (1988)
- [6] S. Hardcastle, Z. -L. Han, G. R. Harp, J. Zhang, B. L. Chen,
D. K. Saldin and B. P. Tonner, *Surf. Sci. Lett.* **245**, L190 (1991)

EFFECT OF THE ANGULAR MOMENTUM AND MAGNETIC QUANTUM NUMBERS ON AUGER AND PHOTOELECTRON SCATTERING

D.E. RAMAKER^{*,**}, H. YANG^{*}, AND Y.U. IDZERDA^{**}

^{*}Dept. of Chemistry, George Washington Univ., Wash., DC 20052

^{**}Naval Research Laboratory, Washington, DC 20375

ABSTRACT

Angle-resolved electron intensity distributions for Auger and photo- electrons are calculated using a curved-wave electron scattering formalism and compared with experiment. The distributions are found to depend significantly on both the l and m_l quantum numbers of the scattered electron. We consider the simple metals Ir and Al. Although l intensity patterns depend strongly on the l quantum number at relatively low energy, even at high energies (around 1500 eV), a significant l effect remains, which we find arises from nearest neighbor single scattering and from the multiple scattering or defocussing effect. The relative contribution of each l and m_l partial wave is determined not only by the quantum mechanical matrix elements, but also by the energy, polarization, and direction of the excitation beam.

INTRODUCTION

Angle-resolved electron intensity distributions have been successfully used in recent years for structural characterization of single crystal films, overlayers and surfaces [1]. In spite of these successes, quantitative understanding of the intensity patterns are often lacking; even after utilization of sophisticated quantum mechanical electron scattering theories. However, a more detailed understanding is required if we are to utilize these intensity patterns to generate electron holograms [2], examine magnetic materials, or in some instances even to reliably obtain the correct structural information [3].

Recently, we and others have significantly extended the understanding of the l quantum number effect on the intensity patterns, particularly at low energies [4,5]. Specifically, it has been found that at high energies and low l (usually found in x-ray photoelectron scattering), the forward-scattering mechanism is dominant, but at lower energies and high l (usually found in low energy Auger scattering), a shadowing or "back-lighting" effect is dominant [6] along with stronger diffraction effects. We have intuitively explained this effect in terms of an effective potential on the scatterers which consists of an attractive screened Coulomb potential plus a repulsive centrifugal potential. For electrons with large angular momentum, the combined effective potential has a repulsive barrier outside the attractive well so low energy electrons traversing the outer regions of the atomic potential are repelled by the barrier. At higher energies the electrons penetrate the outer barrier and are forward focussed by the inner attractive well. The centrifugal barrier may also generate an additional phase shift for the scattered wave which

can result in destructive interferences and change the intensity patterns.

These studies above involved Cu, Ag, and AuCu₃. However, recently Klebanoff and van Campen [7] published experimental high energy photoelectron scattering results for Ir which still showed a significant l dependence, although less dramatic than distributions at lower energy. Also recently, Greber et al [8] reported low energy Auger electron scattering results for Al and compared them with results from electron scattering calculations. Fitting the theoretical contributions for the different l to the experimental data gave relative l ratios which are very different from those indicated by quantum mechanical Auger matrix elements. In this work, we will present details of our spherical-wave single-scattering cluster results for Ir, and briefly summarize our results for Al. These results provide further insight into the variation of the intensity patterns with l and m_l , and reveal the importance of the energy, polarization, and direction of the excitation beam.

THEORY

We utilize the single-scattering cluster (SSC) code of Fadley et al for these calculations [1,9]. This code includes the scattering-matrix formulation of the curved wave theory developed by Rehr and Albers [10]. The code has been slightly modified to allow for the different l and m_l components to be determined separately, and allow for the different experimental incident beam and polarization settings utilized in the Ir and Al results. A 4x8x8 unit cell metal atom cluster (1444 atoms) was utilized for Ir and a 3x6x6 cluster (592 atoms) for Al. Broadening due to the analyzer aperture and Debye-Waller factors were not included. The ratio of radial matrix elements $R(l-1)/R(l+1)$ at the required energies were obtained from Goldberg et al [11] for Ir, although variation in these ratios do not significantly alter the results. These calculations were conveniently performed on a standard 486-50 PC computer requiring about 20 hours for the full 2π distributions utilized in the Al calculations, and about 10 minutes for the single azimuthal angle results shown here for Ir.

HIGH ENERGY SCATTERING IN Ir

Figure 1 summarizes the experimental photoelectron scattering results obtained by Klebanoff and van Campen [7] from the (001) surface of Ir. In these experiments, the sample is rotated about an axis in the photon beam-detector axis plane with the angle θ equal to zero when the [001] surface normal is in this plane. Therefore at $\theta = 0$, the electron direction corresponds to [001] so that $\theta = 45^\circ$ corresponds to [011]. In Fig. 1, x equals $(I-I_0)/I_0$, where I_0 is obtained by angle averaging the (001) data in both theory and experiment. This experimental data very clearly shows the expected forward scattering (zeroth order diffraction) maxima at 0° and 45° , with minor peaks at 18° and 32° arising probably more from first-order diffraction effects. Most significant is the regular decrease (i.e. $s \rightarrow d \rightarrow f$) in the forward scattering peak intensities at 45° with l .

Comparison of the experimental results with our SSC results (Fig. 1b), where we have estimated the inelastic mean free path from the typical "universal" curve (i.e. $\lambda > 10 \text{ \AA}$), reveals similar peaks, but with the range of x much larger than that

found in the experimental data. This clearly shows that too much forward scattering is present in these single-scattering calculations, a conclusion commonly reported previously [12,13]. Note, that the differences in the shape and position of the 13° and 32° features for the $4s \rightarrow kp$ spectrum is reproduced in the theory, but very small l effects are visible in the intensity of the forward scattering peaks, and it varies in the wrong order (i.e. now $f > s > p > d$) from experiment.

Full inclusion of the multiple-scattering (MS) or defocussing effects has been performed on simple linear chains such as Cu, Al and Ni [12,13]; and on representative clusters of Cu [14]. These calculations reveal that multiple scattering dramatically reduces the forward scattering peaks. Furthermore, calculations show that by substantially decreasing the inelastic mean free path, one can mimic the defocussing effects; indeed in some cases results obtained with a decreased λ agree better with experiment than the full MS results [15]. For Cu it has been found that λ must be reduced by a factor of two (i.e.

Fig. 1

Expt.) Experimental polar angle x-ray photoelectron diffraction data from Ir(001) as reported in ref. [7] for the

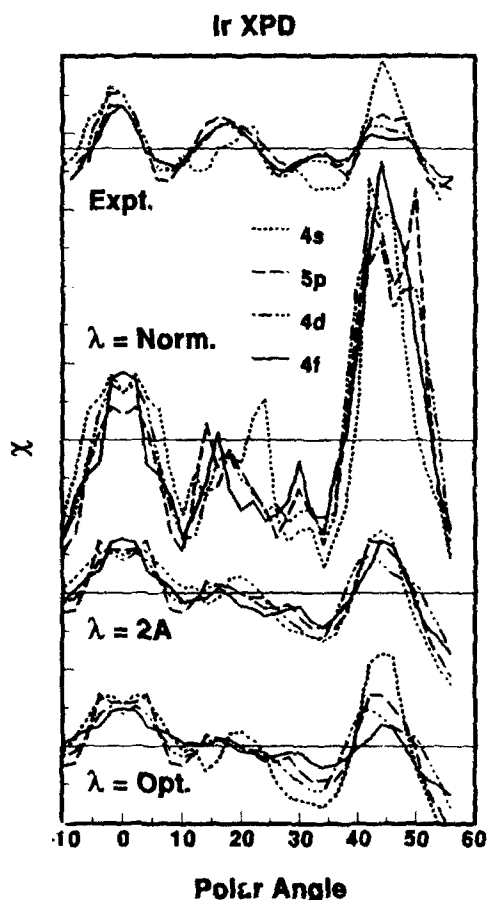
$4s \rightarrow p$ (795 eV),
 $5p \rightarrow d,s$ (1438 eV),
 $4d \rightarrow f,p$ (992 eV), and
 $4f \rightarrow g,d$ (1426 eV)

transitions, where the dominant l contribution of the scattered electron is indicated first and the electron kinetic energies are given in parentheses. The horizontal lines are at the zero point for each case, and each tick for $\chi \approx (I-I_0)/I_0$ is separated by 0.5. The polar angle (in degrees) is from the normal.

$\lambda \approx \text{Norm.}$) Polar angle distributions obtained from our SSC calculations utilizing the appropriate inelastic mean free path (i.e. $\lambda > 10 \text{ \AA}^0$) at each energy.

$\lambda \approx 2\text{ \AA}^0$) Same as above but using $\lambda \approx 2 \text{ \AA}^0$.

$\lambda \approx \text{Opt.}$) Same as above but using optimal λ 's as follows $4s \approx 2.5 \text{ \AA}^0$, $5p$ and $4d \approx 2.0 \text{ \AA}^0$, $4f \approx 1.5 \text{ \AA}^0$.



from 10 to 5 \AA^0 [15], although this may not be true in all crystallographic directions [14]; in Al, MS effects are also important (but perhaps less so [16,17]) consistent with results discussed below.

Fig. 1 shows theoretical results obtained with $\lambda = 2 \text{\AA}^0$ for all spectra, where the value 2\AA^0 was chosen to reproduce the experimental range of x from -0.5 to 0.5. Small l effects are still revealed in the theoretical results but now the 45° forward scattering intensity varies in more reasonable agreement with the experiment (i.e. now $s > p > f > d$). We attribute these l effects to the following phenomena. With the dramatically reduced λ , only nearest-neighbor scattering at the surface is significant. The curved wave character (as opposed to the plane wave character) is more significant for close-in scattering, thus emphasizing the l dependence [10]. The very strong reduction in λ required for Ir (i.e. from ≈ 10 to 2\AA^0), suggests that the MS effect increases as the number of core electrons increase as one might expect [17]. Thus for Ir, the very strong defocussing effect apparently increases the importance of nearest-neighboring single scattering, so that an l effect occurs even at large electron energies.

Fig. 1 also shows results where λ was chosen to provide optimal agreement with experiment for each l . The decrease in λ with l suggests that the magnitude of the defocussing effect also increases with l . We note that the agreement with experiment utilizing this single parameter is now surprisingly good. Except for the varying width of the 45° peak, the relative intensity of the four features and the decreasing width with l of the peak at 0° are in excellent agreement with experiment.

LOW ENERGY SCATTERING IN Al

Recently Greber et al [8] reported experimental full 2π is photoelectron and Al $L_{23}VV$ normal and $L_{23}^2-L_{23}VV$ satellite Auger electron distributions for Al(001). The notation here indicates that two L_{23} holes exist in the initial state and an L_{23} hole and two valence holes exist in the satellite final state. Because Greber et al excited the Auger spectra utilizing an experimental setup which had the incoming photons coming at an oblique angle with respect to the plane defined by the surface normal and the detector, they observed a mirror-symmetry breaking in the angular distribution of the is XPS. Surprisingly a significant symmetry breaking was still present in the $L_{23}^2-L_{23}VV$ case, although nearly negligible in the $L_{23}VV$ case. Using similar SSC theoretical results, they obtained reasonable agreement with experiment by least squares fitting their theoretical results for individual l contributions including $l = s, p$, and d . For the $L_{23}VV$ Auger emission at 70 eV, they found the $s:p:d$ ratio to be 0.24:0.26:0.50 and for the $L_{23}^2-L_{23}VV$ satellite emission at 85 eV to be 0.08:0.67:0.25.

We believe the $L_{23}VV$ Auger electrons are largely excited by back-scattered secondary electrons since the 1250-1740 eV photons (Mg and Si K_α) can excite many secondary electrons above the 2p Al binding energy around 80 eV [18]. This essentially eliminates the mirror symmetry breaking since the secondary electrons do not "remember" the incoming photon direction.

The $L_{23}^2-L_{23}VV$ satellite results from two processes; namely a cascade process $K \rightarrow L_{23}L_{23} \rightarrow L_{23}VV$ and a shakeoff process $L_{23}^2 \rightarrow L_{23}VV$. The former requires high energy primary electrons to ionize the 1s electrons, and the spherical nature of the 1s

orbital eliminates the mirror symmetry breaking. The shakeoff process in the sudden approximation [19] also requires high energy photons, and now the incoming photon direction will unequally populate the p_x, p_y ($p_x, p_y \propto p_1 \pm p_{-1}$) levels, which will be reflected in the Auger electron yield breaking the mirror symmetry.

An examination of the Auger matrix elements indicates that little d character should be emitted for Al. Performing our own SSC calculations, we find that we can obtain reasonable agreement with the experimental angular distributions without the inclusion of d character, but with nonstatistical populations of the m_l levels; namely with $s:p_z:p_{xy}$ equal to 0:40:60 for the $L_{23}VV$ and 20:40:40 for the $L_{23}^2-L_{23}VV$ patterns, provided we again decrease the λ by a factor of ≈ 2 ; indeed, we believe the inclusion of d contributions by Greber et al was necessary because they did not account for the defocussing effect and the possibility for non-statistical m_l populations. The negligible s contribution for the $L_{23}VV$ case is consistent with the known final-state shakeoff process which nearly eliminates the ss and sp contributions and hence the s contribution in the scattered electron yield for Al and Si [20,21]. (The contributions can be denoted as ss[p], sp[s], and pp[p], where the notation indicates the orbital location of the final state holes and the predominant character of the emitted electron in brackets). This shakeoff process is substantially reduced in the $L_{23}^2-L_{23}VV$ satellite because now the initial and final states have a common core hole.

The unequal magnitude of the p_z ($p_z = p_0$) and p_x, p_y contributions for the $L_{23}VV$ distribution suggests the importance of the backscattered secondary electrons. Previous experimental and theoretical calculations reveal that the $2p_z:2p_{x,y}$ ionization cross-section ratio for the 2p levels increases at lower beam energy; where in this case the z axis is assumed to be along the beam direction [22]. In our case, the maximum backscattered electron intensity is along the surface normal, also our z axis (the backscattered electrons have a $\cos\theta$ distribution where θ is relative to the surface normal [23]). Furthermore, the secondary electron energy distribution is largest just above the Al 2p threshold around 80 eV. Thus the $2p_z:2p_{x,y}$ ionization ratio may be significantly larger than one, so that the Auger electrons may have a corresponding nonisotropic distribution (i.e. $2p_{x,y}:2p_z > 1$).

SUMMARY AND CONCLUSIONS

Previous work has shown the important effect of the l quantum number on the extent of forward scattering vs. blocking at low energies. In this work we show that a significant l effect remains at high energies due to both single scattering and a defocussing effect. We also find that the angular distributions depend strongly on the m_l quantum numbers at low energies. This suggests the possibility of gaining information on the orbital component of the magnetization in magnetic materials. We further note that the changes with m_l introduce anisotropies in the angular distributions arising from the direction and polarization of the exciting beam. The beam energy can also alter the relative sizes of the different l contributions. Obviously, much further work needs to be done to sort out these important dynamical Auger effects before we can utilize these data to obtain electron holograms [24,25] or study magnetic materials.

ACKNOWLEDGEMENTS Support from GWU Enhancement Funds (HY) and the Office of Naval Research (DER and YUI) are gratefully acknowledged.

REFERENCES

1. C.S. Fadley, *Prog. Surf. Sci.* 16, 275 (1984); *Synchrotron Radiation Research: Advances in Surface Science*, ed. R.Z. Bachrach (Plenum, NY, 1990); S.A. Chambers, *Surf. Sci. Reports*, 16, 261 (1992).
2. J.J. Barton, *Phys. Rev. Lett.* 61, 1356 (1988); 67, 3106 (1991).
3. A.T. Hubbard, D.G. Frank, O.M.R. Chyan, and T. Golden, *J. Vac. Sci. Tech. B8*, 1329 (1990).
4. Y.U. Idzerda and D.E. Ramaker, *Phys. Rev. Lett.* 69, 1943 (1992).
5. T. Greber, J. Osterwalder, D. Naumovic', A. Stuck, S. Hufner, and L. Schlapbach, *Phys. Rev. Lett.* 69, 1947 (1992).
6. D.G. Frank, N. Batina, T. Golden, T. Lu, and A.T. Hubbard, *Science* 247, 182 (1990); *Langmuir* 5, 1141 (1989).
7. L.E. Klebanoff and D.G. Van Campen, *Phys. Rev. Lett.* 69, 196 (1992).
8. T. Greber, J. Osterwalder, S. Hufner, and L. Schlapbach, *Phys. Rev. B45*, 4540 (1992).
9. D.J. Friedman and C.S. Fadley, *J. Elect. Spectrosc. Related Phenom.* 51, 689 (1990).
10. J.J. Rehr and R.C. Albers, *Phys. Rev.* 41, 8139 (1990).
11. S.M. Goldberg, S. Kono, and C.S. Fadley, *J. Electron. Spectrosc. Related Phenom.* 21, 285 (1980).
12. M.L. Xu and M.A. Van Hove, *Surf. Sci.* 207 215 (1989).
13. J. Osterwalder, A. Stuck, D.J. Friedman, A. Kaduwela, C.S. Fadley, J. Mustre de Leon, and J.J. Rehr, *Phys. Scripta*, 41, 990 (1990).
14. S.Y. Tong, H.C. Poon and D.R. Snider, *Phys. Rev. B32*, 2096 (1985); S.Y. Tong, Y. Chen, H. Li, and C.M. Wei, "Surface Physics", ed. by X. Li, Z. Qiu, D. Shen, and D. Wang, (Gordon and Breach, London, 1991), p. 75.
15. A.P. Kaduwela, G.S. Herman, D.J. Friedman, C.S. Fadley, and J.J. Rehr, *Phys. Scripta*, 41, 948 (1990).
16. H.A. Aebischer et al., *Surf. Sci.* 239, 261 (1990).
17. G.S. Herman and C.S. Fadley, *Phys. Rev. B43*, 6792 (1991); J. Osterwalder, T. Greber, S. Hufner, and L. Schlapbach, *Phys. Rev. B41*, 12495 (1990).
18. A. Jablonski, *Surf. Sci.* 87, 539 (1979).
19. J. Stohr, R. Jaeger, and J.J. Rehr, *Phys. Rev. Lett.* 51, 821 (1983); T.D. Thomas, *Phys. Rev. Lett.* 52, 417, (1984).
20. D.E. Ramaker, F.L. Hutson, N.H. Turner, W.N. Mei, *Phys. Rev. B33*, 2574 (1986).
21. E.J. McGuire, SS-RR-710075 Research Report, Sandia Laboratories.
22. B. Cleff and W. Mehlhorn, *Phys. Lett.* 37A, 3 (1971); W. Mehlhorn, *Phys. Lett.*, 26A, 166 (1969); S.C. McFarlane, *J. Phys. B* 5, 1906 (1972).
23. S. Schneider, W.C. Werner and G. Nolte, *Nucl. Instr. Meth.* 194, 345 (1982); K. Saiki and S. Tanaka, Japan, *J. Appl. Phys.* 21, L529 (1982).
24. A. Stuck, D. Naumovic', H.A. Aebischer, T. Greber, J. Osterwalder, and L. Schlapbach, *Surf. Sci.* 264, 380 (1992).
25. P. Hu and D.A. King, *Nature*, 353, 831 (1991).

IMAGING OF METAL/SEMICONDUCTOR INTERFACE BY BALLISTIC-ELECTRON-EMISSION MICROSCOPY (BEEM)

E. Y. LEE*, B. R. TURNER*, J. R. JIMENEZ**, and L. J. SCHOWALTER*

*Physics Department and Center for Integrated Electronics, Rensselaer Polytechnic Institute, Troy, NY 12180

**Electro-optics Technology Center, Tufts University, Medford, MA 02155

ABSTRACT

Studies in ballistic-electron-emission spectroscopy (BEES) have enabled precise energy measurements of Schottky barrier heights with excellent spatial resolution and, more recently, it was shown that even scattering at the metal/semiconductor interface affects the BEES spectrum [1]. Monte Carlo simulations have been done to predict the spatial resolution of ballistic-electron-emission microscopy (BEEM) [2]. In this paper, we will discuss the experimental spatial resolution of BEEM, and we will also give some of our BEES results for Au/Si and for Au/PtSi/Si. Our experimental BEEM studies indicate that, for Au/Si, hot electron transport is diffusive rather than ballistic, because the inelastic mean free path length (~ 100 nm) is much larger than the elastic mean free path length (~ 10 nm). This is in agreement with existing theories and with the literature on the internal photoemission method of studying the transport. Even in this diffusive regime, the spatial resolution of BEEM is still expected to be very good, being on the order of 10 nm [2]. Our preliminary work on PtSi shows that it has an attenuation length of 4 nm, which differs significantly from that of Au.

INTRODUCTION

In ballistic-electron-emission microscopy (BEEM) and in ballistic-electron-emission spectroscopy (BEES), the scanning-tunneling microscope (STM) tip functions as an emitter of electrons, and the electrons tunnel across a vacuum energy barrier into a base region consisting of a thin metal overlayer on a collector region consisting of a semiconductor. By injecting electrons over a local base region and changing the STM tip-to-sample bias, one does BEES, and by holding the bias voltage the same and scanning the STM tip over the metal base, one does BEEM [3]. By using BEES, one can study the energy dependence of carrier transport within the metal base and across the metal/semiconductor (m/s) interface. By using BEEM, one can study the spatial variation of the Schottky barrier height and of transport across the metal base and across the m/s interface. The superior spatial resolution of STM suggests that the spatial resolution of BEEM may be excellent. This important issue has not yet been settled, and it is a purpose of this paper to address this issue and to show that the spatial resolution of BEEM is on the order of 10 nm instead of 1 nm because of elastic scattering in the metal base region. We will also discuss what energy levels can be probed via BEES together with BEEM.

SPATIAL RESOLUTION OF BEEM

There are many probes, most of which involve photoexcitation, that can be used to measure the Schottky barrier height and the quantum yield. The first study in BEEM promised a superior spatial resolution of 1-2 nm by BEEM for a 50 Å thick metal overlayer [3]. This spatial resolution requires that the injected electron beam remains ballistic in the metal base, i.e. no elastic scattering occurs and all inelastic scattering take away enough energy to thermalize the electrons. This requirement contradicts the finding from experiments using internal photoemission that discovered inelastic mean free path to be much longer than the elastic mean free path length in many metals including Au [4]. It also contradicts the theoretical estimates on the inelastic mean free path of electrons [5]. If, as the theory predicts, the inelastic mean free path length is approximately 1000 Å for an electron 1 eV above the Au Fermi level, then an electron injected into a 50 Å thick metal base will scatter elastically many times before it thermalizes, and the spatial

resolution of BEEM will be on the order of 10 nm.

It is important, however, to distinguish between the experimentally observed spatial resolution and the spatial resolution for the ideal cases. If there are strongly scattering defects such as a domain boundary, then sharp contrasts may be seen in the BEEM images, e.g. across grain boundaries, even though the intensity within each grain may be uniform. This effect may have been observed by Niedermann [6]. It is important to realize that the spatial resolution of BEEM is not the same everywhere, that the ideal case in which the metal overlayer is a single crystal has limited applications because defects such as grain boundaries are not included.

A test of the claim that the electron transport is ballistic in the metal overlayer is the evidence for or the lack of the "search-light effect." This effect arises because the tunneling electron distribution from the STM tip is sharply peaked about the surface normal of the metal base. If the metal surface is tilted with respect to the semiconductor substrate, then the injected electrons will have to travel longer than the thickness of the metal overlayer to reach the m/s interface, the distance being greater if the tilt angle is greater. In the ballistic regime where there is no elastic scattering, this effect should be noticeable, whereas, in the diffusive regime, this effect should not be seen except for a very thin metal overlayer. Fig. 1 shows the calculated attenuation of the BEEM current as a function of the surface tilt angle of the metal base, and Fig. 2 shows a typical experimentally measured BEEM current as a function of the surface tilt angle for Au/Si. We used the planar tunneling model (based on WKB approximation for a trapezoidal barrier) as is commonly done, and we feel justified in using it since a more sophisticated s-wave model by Tersoff gives nearly the same momentum distribution of the tunneling electrons [7]. The absence of the search-light effect supports our earlier Monte Carlo simulation [2] in presuming that the electron transport in Au base is diffusive.

The data in Fig. 2 were calculated from a single line scan from a BEEM image consisting of 128×128 data points. Other line scans also show the absence of the search-light effect. As in Fig. 2, there are occasional sharp features in the BEEM current correlated to steps on the Au surface and these may be caused by strong scattering by defects near the steps, but no evidence for the search-light effect was observed.

Our experimental finding is consistent with the first BEEM study of Au/Si by Kaiser and Bell [3] in which they found that the BEEM images of the Au/Si interface were very uniform even though surface roughness was present; however, no attempt was made then to study this quantitatively nor was the significance of this question realized. More recently, Prietsch and Ludeke [8] realized the significance of the search-light effect and

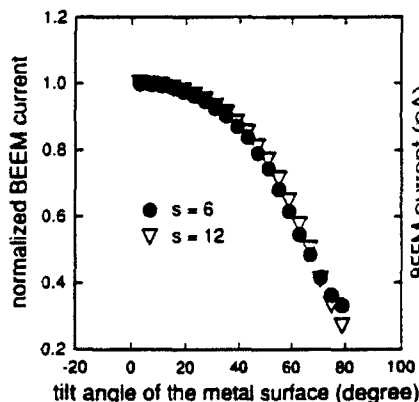


Fig. 1. BEEM current was calculated as a function of the tilt angle of the metal surface. The parameter s is the tip-to-sample separation in Å.

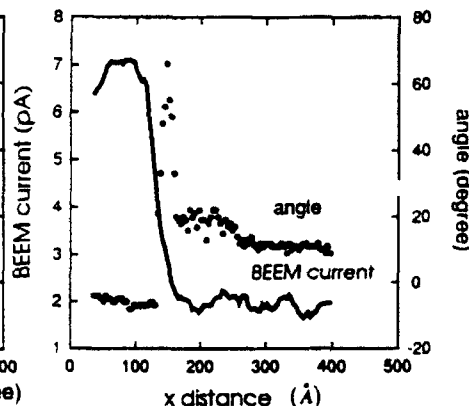


Fig. 2. A typical experimentally measured surface tilt angle and BEEM current are shown.

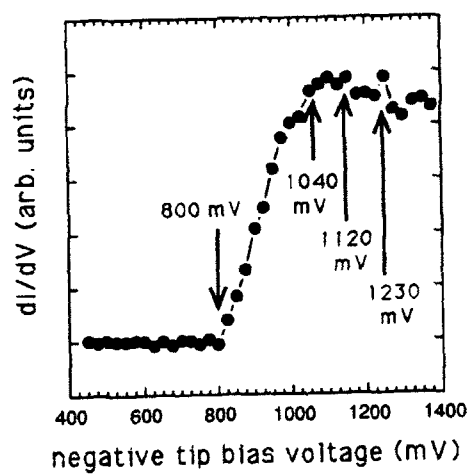


Fig. 3. An ac BEES spectrum for Au/Si(001) n-type is shown.

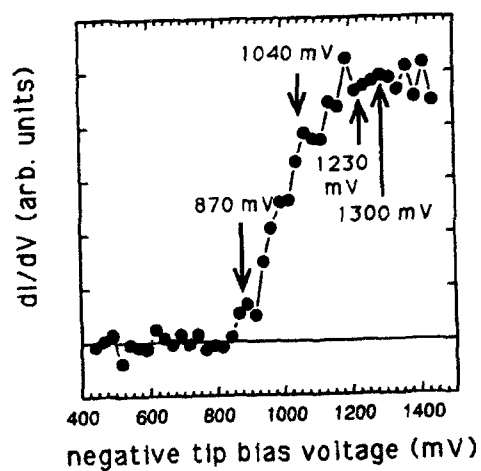


Fig. 4. An ac BEES spectrum for Au/PtSi/Si(001) n-type is shown.

reported its apparent manifestation for the metal/GaP system. It is entirely possible that the interface of metal/GaP behaves very differently from that of Au/Si, although alternative explanations are possible for their observation.

Another study of interest was done by Fernandez *et al.* [9] who found that, on some Au/impurity/Si samples, they could modify the interface under certain BEEM conditions (high current and voltage). The modified interfaces can be imaged with an apparent spatial resolution of 1-2 nm. Lastly, there was a recent report of excellent spatial resolution for Au/(patterned SiO₂)/Si by Manion *et al.* [10]. However, their Au thickness was 150 Å so that, as they noted, the observed spatial resolution of 1-2 nm was too good for any realistic angular distribution of electrons from the STM tip.

It should be clear from the discussion of the effective inelastic mean free path length that, if the Au layer could be modified in such a way as to significantly reduce the inelastic mean free path with respect to the elastic mean free path length, then the spatial resolution would improve. In addition, macroscopic defects in the metal layer (cracks, grain boundaries, steps, etc.) may present barriers to the hot electrons which would appear to improve the interface resolution artificially. It is significant that none of these studies reported finding the search-light effect for Au/Si, and we have argued that this is a strong evidence that the electron transport in Au is diffusive rather than ballistic.

ENERGY RESOLUTION OF BEES

We have done BEES on Au/Si and on Au/PtSi/Si, and our data shows that the energy resolution of BEES is excellent. Fig. 3 shows our ac BEES spectrum for Au/Si, and in it the Schottky barrier height, the 1040 meV threshold for phonon assisted electron-hole pair creation at the m/s interface [1], the band gap energy of Si, and a mysterious peak at 1230 mV are seen. (The ac BEES spectrum is exactly the same as a numerical derivative of a dc BEES spectrum.) The ac BEEM threshold is obviously linear, and this allows precise measurement of the Schottky barrier height by linear interpolation. The data was taken at 25 meV intervals, and it is seen that the limit of energy resolution of BEES at room temperature is thermal broadening of the tunneling electron distribution.

Fig. 4 shows our ac BEES spectrum for Au/PtSi/Si. The signal was weaker in this case due to the scattering at the Au/PtSi boundary and within the PtSi. The spectrum is a spatial average and this may explain why the Schottky barrier threshold is not as sharp as for Au/Si; it has been found that most epitaxial silicides have different Schottky barrier heights depending on the relative orientation of the silicide and the silicon substrates [11].

ACKNOWLEDGEMENT

This work was supported in part by ONR contract N0014-92-J-1277 and by Air Force Contract F19628-91-K-0030 through Rome Laboratory at Hanscom Field.

REFERENCES

- [1] E. Y. Lee and L. J. Schowalter, Phys. Rev. B15, 45, 6325(1992).
- [2] L. J. Schowalter and E. Y. Lee, Phys. Rev. B15, 43, 9308(1991).
- [3] W. J. Kaiser and L. D. Bell, Phys. Rev. Lett. 60, 1406(1988).
- [4] R. N. Stuart, F. Wooten, and W. E. Spicer, Phys. Rev. Lett. 10, 7(1963).
- [5] J. J. Quinn, Phys. Rev. 126, 1453(1962); J. J. Quinn, Appl. Phys. Lett. 2, 167(1963).
- [6] P. Niedermann, L. Quattropani, K. Solt, A. D. Kent, O. Fischer, J. Vac. Sci. Tech. B 10, 580(1992).
- [7] J. Tersoff (unpublished).
- [8] M. Prietsch and R. Ludeke, Phys. Rev. Lett. 66, 2511(1991).
- [9] A. Fernandez, H. D. Hallen, T. Huang, R. A. Buhrman, and J. Silcox, Appl. Phys. Lett. 57, 2826(1990).
- [10] S. J. Manion, A. M. Milliken, L. D. Bell, M. H. Hecht, W. J. Kaiser, Bull. Am. Phys. Society 37, 618(1992).
- [11] R. T. Tung, A. F. Levi, J. P. Sullivan, and F. Shrey, Phys. Rev. Lett. 66, 72(1991).

LOW ENERGY POINT SOURCE ELECTRON MICROSCOPY

H.J. Kreuzer
Department of Physics, Dalhousie University, Halifax, N.S. B3H 3J5,
Canada

ABSTRACT

The theory of the point source low energy electron microscope is reviewed. Images are calculated for a carbon fibre, a small cluster of MgO and a double helix of carbon atoms. A Kirchhoff-Helmholtz transform is used for reconstruction. The importance of image size is stressed and the chemical specificity of the method is demonstrated.

INTRODUCTION

More than 40 years ago, D. Gabor [1] proposed a new principle of microscopy to overcome the limitations of lenses. Using a coherent ensemble of particles with wave nature, the fraction of the beam elastically scattered by an object is made to interfere with a coherent reference wave at some two-dimensional detector creating a hologram that contains information on both the amplitude and the phase of the scattered wave. The laser provides such a coherent source of photons for light holography. Only recently has electron holography been demonstrated in electron microscopy [2,3], in photoemission electron holography [4], and in lensless low energy point source electron microscopy [5-8].

In the lensless low-energy point source electron microscope an ultrathin metal tip with one or a few atoms at its apex serves as a "point" source for electrons which, after acceleration to energies in the range of 20 - 200 eV, scatter off the atoms of an object film a distance of 0.1 - 1 μm away. On a screen some 10 cm away an image is formed by the unscattered and the scattered electrons. If the object film only blocks a small fraction of the incoming electron beam, most electrons arrive on the screen unscattered and we have the typical situation of an in-line hologram, as demonstrated explicitly with the images of carbon fibres. On the other hand, if the object film is extended, images are obtained with structures of length scales that correspond to the lattice of the object film. These structures are, however, not geometric shadow images but interference patterns.

In the point source electron microscope lenses to produce a reduced image of the beam source have been made obsolete by the fact that an atomic size metal tip generates an aberration-free, virtual source whose dimensions can be estimated to be less than 0.5 \AA . Because it is the point-like character of the electron source that distinguishes this microscope from others we propose to name it the kendoroscope from the greek kendoron meaning sharp tip or spine. Imaging with the kendoroscope we will refer to as kendoroscopy, and the images we will call kendorograms. We will show below that kendorograms are composed of two contributions, a modified hologram or holographic diffraction pattern and a classical diffraction pattern.

The theory of the kendoroscope has been developed recently [9] that allows the simulation of kendorograms to aid in the interpretation of

experimental images. A modified Fourier transform of the Kirchhoff-Helmholtz type was also advanced that allows to reconstruct the spatial structure of the object film from the image or kentrogram. Further work on the theory of the kentroscope has been published by Spence *et al.* [10-11]

In this paper we will report on some new developments since the submission of the theory paper. We will show some interesting kentrograms, e.g. of a double helix structure for which we also do the reconstruction. Doing the latter for a small MgO cluster we will see that element-specific information can be obtained.

SCATTERING THEORY

The theory of the kentroscope uses a scattering approach based on the Lippmann-Schwinger equation. One models the electron source as emitting a wave of mostly spherical symmetry by writing (for large distances from the source, i.e. $kr \gg 1$)

$$\psi^{(in)}(\mathbf{r}) = \langle \mathbf{r} | \psi^{(in)} \rangle = r^{-1} \exp(ikr) \left[1 + \sum_{l=1}^{\infty} \sum_{m=-l}^l c_{lm} (-i)^l Y_l^m(\mathbf{r}/r) \right] \quad (1)$$

For the object film this represents the incoming electron beam (which in LEED is a plane wave). The deviations of the incoming wave from perfect spherical symmetry can be intrinsic to the source itself or might arise from the accelerating electric field between the source and the object. To account for the energy spread in the incoming electron beam, we can sum the final result over different wave numbers k due to the linearity of the Schrödinger equation.

The scattered wave emanating from the object film is given by

$$| \psi^{(+)} \rangle = | \psi^{(in)} \rangle + G^{(+)} T | \psi^{(in)} \rangle \quad (2)$$

where $G^{(+)}$ is the free Green's function, and the T -matrix satisfies the Lippmann-Schwinger equation

$$T = V + V G^{(+)} T \quad (3)$$

Next we assume that the scattering potential of the object film can be written as a constant inner potential, V_0 , and a sum of pseudo-potentials centered at the positions, \mathbf{r}_i , of the atoms or ions of the object, i.e.

$$V(\mathbf{r}) = V_0 + \sum_i V(\mathbf{r}-\mathbf{r}_i) \quad (4)$$

Expressing the full T -matrix in terms of the T -matrices, T_i , of single atoms, one eventually finds for the scattering solution for a cluster of identical atoms

$$\psi^{(+)}(\mathbf{r}) = \frac{\exp(i\mathbf{k}\mathbf{r})}{r} \left[1 + \sum_{\ell=1}^{\infty} \sum_{m=-\ell}^{\ell} c_{\ell m} (-i)^{\ell} Y_{\ell}^m(\mathbf{r}/r) \right] + \sum_{ilm} \frac{\exp(ik\rho_i)}{\rho_i} \tau_{\ell} Y_{\ell}^m(\hat{\rho}_i) F_{\ell}^m(\mathbf{r}_i) \quad (5)$$

where $\rho_i = |\mathbf{r} - \mathbf{r}_i|$ and

$$\tau_{\ell} = k^{-1} \sin \delta_{\ell} \exp(i\delta_{\ell}) \quad (6)$$

contains the scattering phase shifts δ_{ℓ} . We also defined a structure factor

$$F_{\ell}^m(\mathbf{r}_i) = \Phi_{\ell}^m(\mathbf{r}_i) + \sum_{j \ell' m'} M(\mathbf{r}_j - \mathbf{r}_i; \ell, m, \ell', m') \Phi_{\ell'}^{m'}(\mathbf{r}_j) + \sum_{j \ell m' j' \ell' m'} M(\mathbf{r}_j - \mathbf{r}_i; \ell, m, \ell', m') M(\mathbf{r}_j' - \mathbf{r}_j; \ell', m', \ell'', m'') \Phi_{\ell''}^{m''}(\mathbf{r}_j') + \dots \quad (7)$$

with

$$\Phi_{\ell}^m(\mathbf{r}) = 4\pi Y_{\ell}^m(\hat{\mathbf{r}}) r^{-\ell} \exp(i\mathbf{k}\mathbf{r}) \left[1 + \sum_{\ell=1}^{\infty} \sum_{m=-\ell}^{\ell} c_{\ell m} (-i)^{\ell} Y_{\ell}^m(\mathbf{r}/r) \right] \quad (8)$$

$$M(\mathbf{a}_n; \ell, m, \ell', m') = 4\pi Y_{\ell}^m(\hat{\mathbf{a}}_n) \tau_{\ell'} Y_{\ell'}^{m'}(\hat{\mathbf{a}}_n) \exp(ika_n)/a_n \quad (9)$$

Factoring out a spherical wave

$$\psi^{(+)}(\mathbf{r}) = \frac{\exp(i\mathbf{k}\mathbf{r})}{r} \left[1 + \sum_{\ell=1}^{\infty} \sum_{m=-\ell}^{\ell} c_{\ell m} (-i)^{\ell} Y_{\ell}^m(\mathbf{r}/r) + \bar{\psi}_e^{(+)}(\mathbf{r}) \right] \quad (10)$$

one gets for the contrast image on a screen

$$I(\mathbf{r}) = \hat{I}(\mathbf{r}) - \frac{L}{\rho^3} = \frac{L}{\rho^3} [2\text{Re}\bar{\psi}_s^{(+)}(\mathbf{r}) + |\bar{\psi}_s^{(+)}(\mathbf{r})|^2] \quad (11)$$

We will refer to the first term as the "holographic diffraction pattern" because it arises from the superposition of the interference terms between the reference wave and the scattered wave from any one of the atoms. The second term in (11) contains the interference between the scattered waves. We will refer to it as the "classical diffraction pattern". Neither term, holographic or classical diffraction, is meant to be exclusive but simply is coined to refer to the terms in (11) linear and quadratic in the scattered waves. Because both holographic and classical diffraction are present to a larger or lesser degree, we feel that a new name, namely a kendrogram, is appropriate for these images.

Holographic diffraction dominates the kendrograms for thin objects that are semi-transparent to electrons; examples are carbon fibres, C_{60} and similar carbon clusters and thin metal clusters of a few atomic layers. As the scattered wave function grows due to multiple scattering in thicker films, classical diffraction becomes more important. When it eventually dominates the image, we are in the regime of classical wave optics. At this stage objects become opaque and information about the atomic structure of the object is lost. Image formation can then be described as diffraction around macroscopic objects.

In our discussion so far we have not dealt with inelastic electron scattering. In the experimental setup inelastically scattered electrons are prevented from reaching the detector by applying the negative of the accelerating voltage (between the tip and the object) to the detector. Thus at a given energy the effect of inelastic scattering is to reduce the flux of detected electrons. This implies that in our theory we can restrict ourselves to elastic scattering as well. The overall reduction of the scattered signal as a function of energy can then be adjusted by multiplying the calculated flux with an overall damping factor involving the mean free path. For energies between 30 and 200 eV the latter varies from 5 to 10 Å for most metals. This suggests that kendroscopy is possible on metallic films of thicknesses of the order of a few atomic layers.

In Fig.1 we show an example of a calculated kendrogram, namely for a carbon fibre of 5x51 atoms.

THEORY OF RECONSTRUCTION

The r -dependence in the scattering wave function (5) suggests that reconstruction of the object from the kendrograms can be achieved via a Kirchhoff-Helmholtz transform

$$K(\mathbf{r}) = \frac{1}{4\pi} \int_S d\xi I(\xi) \exp(ik\xi \cdot \mathbf{r}/\xi) \quad (12)$$

where the integration extends over the 2-dimensional surface S of the

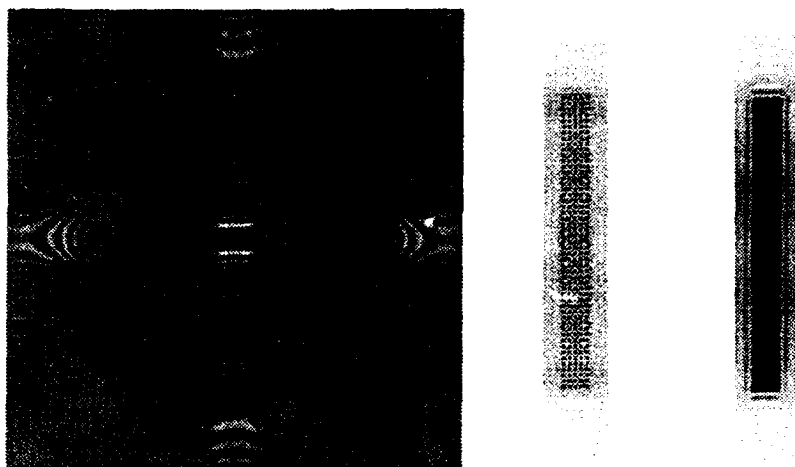


Fig.1: Left panel: Kendrogram of a carbon fibre consisting of 5×51 carbon atoms arranged on a square lattice with $a=2.5\text{\AA}$, at an electron energy of 95eV and a source to atom distance $d=1000\text{\AA}$; the image covers an angular opening of $\pm 35^\circ$. Center panel: Reconstruction from the left image showing atomic resolution. Right panel: Reconstruction from a smaller image that covers an angular opening of only $\pm 15^\circ$, showing only the outline of the fibre.

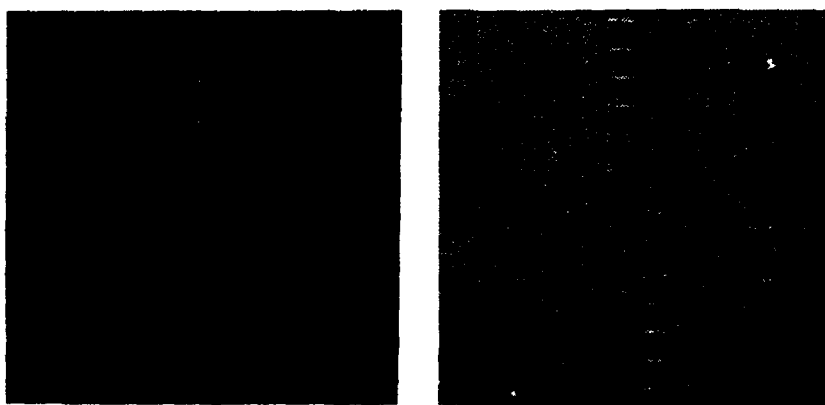


Fig.2: Kendrogram of a double helix of carbon atoms at an electron energy of 95eV and a source to atom distance $d=1000\text{\AA}$. Diameter of the double helix is 60\AA ; its pitch is 40\AA per turn. The images cover an angular opening of $\pm 35^\circ$ (left) and $\pm 15^\circ$ (right), respectively.

screen with coordinates $\xi=(X,Y,L)$, a distance L from the source. Such a transform has also been used in photoemission electron holography [4]. The applicability of this transform to kendroscopy has been demon-

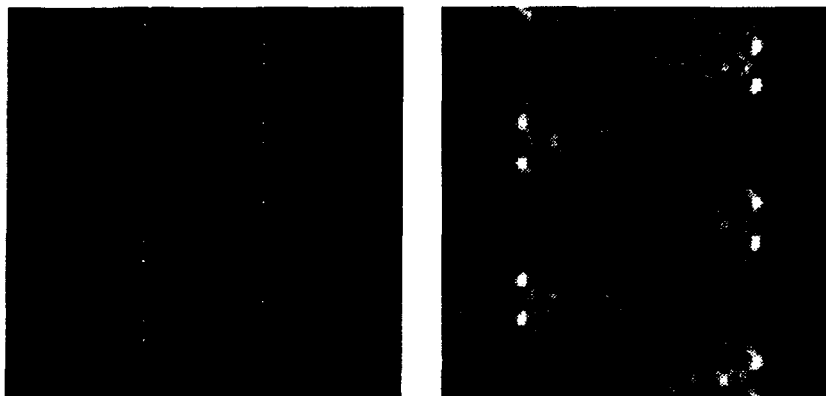


Fig.3: Reconstruction from the kendrograms of a double helix, Fig.2.

strated in detail by inverting theoretical kendrograms. As an example we show the reconstruction from the kendrogram of a single layer carbon fibre, Fig.1. To obtain atomic resolution in the reconstruction, center panel, we need an image with an angular opening of $\pm 35^\circ$, i.e. large enough to contain information about the first Bragg peaks. If the latter information is excluded by choosing a smaller screen to record the kendrogram, only the outline of the carbon fibre can be obtained. As a further demonstration we have calculated, in the single scattering approximation, the kendrogram of a double helix of carbon atoms, as a rather crude model for a DNA molecule, shown in Fig.2 on a screen larger than the shadow projection of the object (left panel). The right panel of Fig.2 shows an enlargement of the central section. The respective reconstructions are shown in Fig.3. With the full image, left panel of Fig.2, as input, atomic resolution can again be achieved in the reconstruction including depth resolution (left panel of Fig.3). However, the limited information contained in the right image in Fig.2 is only sufficient to indicate the secondary structure of the double helix without atomic resolution, see the right panel in Fig.3. Depth resolution is equally reduced in this case.

The question arises whether reconstruction with atomic resolution can yield information as to the chemical composition of the object. To demonstrate that this is possible we have used the theoretical kendrogram of a small MgO cluster, taken at an electron energy of 95eV over a half angle of 35° , and reconstructed the object. We find, see Fig.4, that the Mg spots in the reconstruction have about twice the intensity of the O spots. Thus although one cannot readily identify the chemical nature of a particular spot in the reconstruction, one can still differentiate between different atomic species.

It has been suggested, both for kendroscopy and for photoemission electron holography, that lateral and, more importantly depth resolution can be improved if images obtained at several electron energies are used in the reconstruction.[9,12-16] Because spurious structures in the reconstruction are strongly energy dependent, one hopes that a superposition of reconstructed pictures for several energies will enhance the real atomic structures and smear out the spurious ones. Still one cannot circumvent limiting factors of apertured optical systems [17]. We have tried energy averaging, both without and with prem-

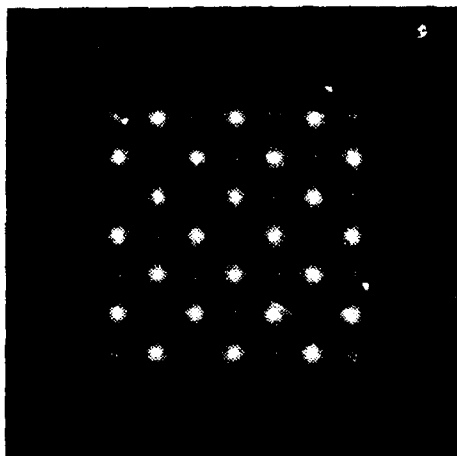


Fig.4: Reconstruction from a kentrogram of a 7x7 MgO cluster at an electron energy of 95eV and a source to atom distance $d=1000\text{\AA}$, showing the chemical specificity of the method: bright dots are Mg and dull spots are O.

ultiplying the images with a phase factor $\exp(ikr)$, and found that averaging helps in locating the atoms (more so without the phase factor), but the procedure still needs some new ideas.

OUTLOOK

In this paper we have reviewed the theory to calculate electron kentrograms for the point source electron microscope. Holographic diffraction and single scattering are dominant for small carbon clusters and carbon fibres. Multiple scattering becomes appreciable for large metal films for which classical diffraction also starts to play a role and eventually becomes dominant for films of more than a few atomic layers.

A Fourier-like transform can be used for the reconstruction of the object. To obtain atomic resolution in the reconstruction, the image screen must be large enough to record zero and first order Bragg diffraction. Taking images at various electron energies or at different tilt angles of the object can enhance the resolution in reconstruction.

The reconstruction formula has now been applied to experimental data. First results for carbon fibres and DNA are very encouraging.

ACKNOWLEDGEMENT

This work was supported by a Joint Research Agreement between Dalhousie University and the IBM Zurich Research Laboratory. Funding was also provided by the Network of Centres of Excellence in Molecular and Interfacial Dynamics, one of the fifteen Networks of Centres of Excellence supported by the Government of Canada.

REFERENCES

- [1] D. Gabor, *Nature (London)* **161**, 777 (1948).
- [2] H. Lichte, *Ultramicroscopy* **20**, 293 (1986).
- [3] A. Tonomura, *Rev. Mod. Phys.* **59**, 639 (1987).
- [4] J.J. Barton, *Phys. Rev. Lett.* **61**, 1356 (1988).
- [5] H.-W. Fink, *Phys. Scripta* **38**, 260 (1988).
- [6] W. Stocker, H.-W. Fink, and R. Morin, *Ultramicroscopy* **31**, 379 (1989).
- [7] H.-W. Fink, W. Stocker, and H. Schmid, *Phys. Rev. Lett.* **65**, 1204 (1990).
- [8] H.-W. Fink, H. Schmid, H.J. Kreuzer, and A. Wierzbicki, *Phys. Rev. Lett.* **67**, 1543 (1991).
- [9] H.J. Kreuzer, K. Nakamura, A. Wierzbicki, H.-W. Fink, H. Schmid, *Ultramicroscopy* (in press).
- [10] J.C.H. Spence and W. Quian, *Phys. Rev. B* (in press).
- [11] W. Quian, J.C.H. Spence and J.M. Zuo, *Acta Cryst.* (in press).
- [12] G.R. Harp, D.K. Saldin, and B.P. Tonner, *Phys. Rev. Lett.* **65**, 1012 (1990).
- [13] C.M. Wei, T.C. Zhao, and S.Y. Tong, *Phys. Rev. Lett.* **65**, 2278 (1990).
- [14] S.Y. Tong, Hua Li, and H. Huang, *Phys. Rev. Lett.* **67**, 3102 (1991).
- [15] J.J. Barton, *Phys. Rev. Lett.* **67**, 3106 (1991).
- [16] D.K. Saldin, G.R. Harp, B.L. Chen, and B.P. Tonner, *Phys. Rev. B* **44**, 2480 (1991).
- [17] J.J. Barton, *J. El. Spectr. Related Phen.* **51** (1990) 37.

Atomic Force Microscopic Imaging of Biologically Important Materials

Lorraine M. Siperko* and William J. Landis**

*IBM Technology Laboratory, Endicott, NY 13760

**Harvard Medical School and Children's Hospital, Boston, MA 02115

ABSTRACT

Atomic force microscopy (AFM) has been used to image the surface atomic structure of hydroxyapatite [$\text{Ca}_{10}(\text{PO}_4)_6(\text{OH})_2$], HA, and brushite [$\text{CaHPO}_4 \cdot 2\text{H}_2\text{O}$], DCPD. Compared to HA, the surface of DCPD was found to be much less complex. Identification has been made of one crystal plane of DCPD that has atoms commensurate with those of one of the observed crystal planes of HA.

INTRODUCTION

The development of AFM, since its invention in 1986¹, has led to the use of this instrumentation in the atomic scale imaging of both conductors and non-conductors. Scanning the sample under a probe tip (mounted on a deflecting cantilever) by means of a piezoelectric drive generates deflections which are indicative of surface topography or structure. One

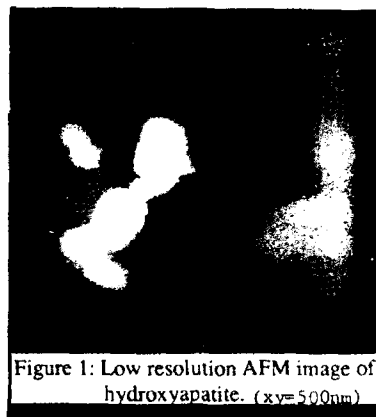


Figure 1: Low resolution AFM image of hydroxyapatite. (xy=500nm)

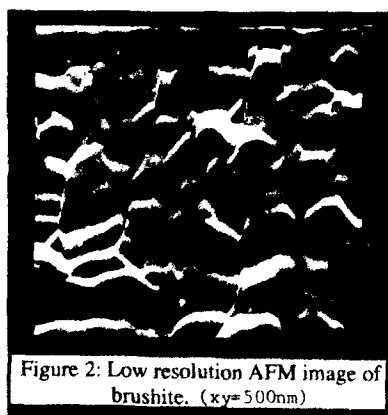


Figure 2: Low resolution AFM image of brushite. (xy=500nm)

interesting aspect of this technique is the capacity to image the surface of materials in a variety of environments (air, liquid, vacuum). It is the flexibility of the instrument which accounts for its use in many fields, including biochemistry.²⁻⁵

The structure and chemical nature of the minerals hydroxyapatite and brushite have been studied extensively in biological research.⁶⁻¹⁰ HA is found naturally in hard tissues such as bones and teeth. Certain structural features of brushite have

suggested it may be a precursor for the formation of HA,¹¹ a consideration which is important in understanding the mineralization of biological tissues. The initial results of the investigations presented here will demonstrate the feasibility of studying the surface atomic structure of these minerals. Such work with HA and DCPD surfaces could be used to gain insight into their possible interaction.

EXPERIMENTAL

HA and DCPD samples were prepared by suspending the mineral powders in absolute ethanol (1 mg/ml) and depositing an aliquot of the suspension onto a glass slide.¹² The samples were allowed to dry in air. A Digital Instruments NanoScope II AFM with silicon nitride integrated tips, operated in air, was used to acquire data. Atomic scale images were obtained in the force mode and the data subjected to low-pass filtering. The cantilever tip was in contact with the surface of the sample, which moved under the tip by means of piezoelectric drives.



Figure 3: Atomic resolution AFM image (1.2nm x 1.2nm) of HA (top) and DCPD (bottom).

RESULTS AND DISCUSSION

HA samples prepared in the manner described above tend to form well isolated crystal clusters, as shown in Figure 1. In contrast, DCPD forms flat, thin crystal platelets (Figure 2). Present studies have shown that the atomic structure of HA is more complex than that of DCPD. At least six different surface structural AFM patterns have been detected for the HA crystal surface, but only one for DCPD. Atomic top scale images of HA and DCPD with similar atomic spacings are shown in Figure 3. Of the different atomic configurations, the HA structure shown is most often observed during imaging and may represent the largest expressed face of the mineral. Measurements taken on this surface of the HA sample show spacings of $3.5\text{\AA} \pm 0.2\text{\AA}$ in a slightly distorted square configuration. Distance across the farthest corners of the (distorted) square

measures 6.5\AA . Measurements taken on the DCPD sample yield atomic spacings of $4.4\text{\AA} \pm 0.2\text{\AA}$. The diagonal distance measures 5.6\AA . The corresponding HA and DCPD line traces are shown in Figure 4. The measurements show that the HA and DCPD surface structures observed in this study are comparable in size.

When they are superposed graphically as shown in Figure 5, the respective crystal planes are geometrically similar at the atomic perspective. Both the HA and DCPD configurations are drawn to scale from data taken from the images in Figures 2 and 3. From

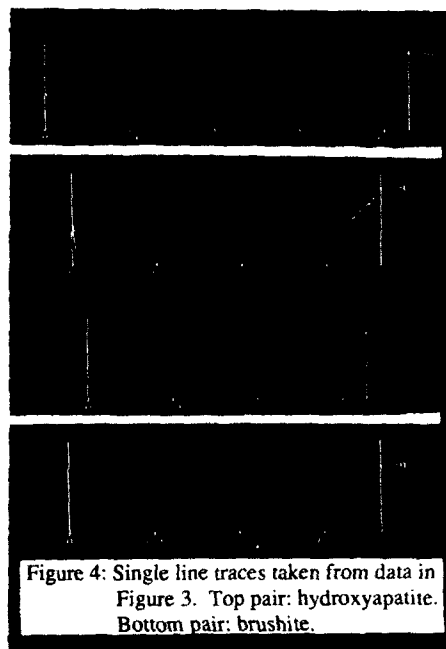


Figure 4: Single line traces taken from data in Figure 3. Top pair: hydroxyapatite. Bottom pair: brushite.

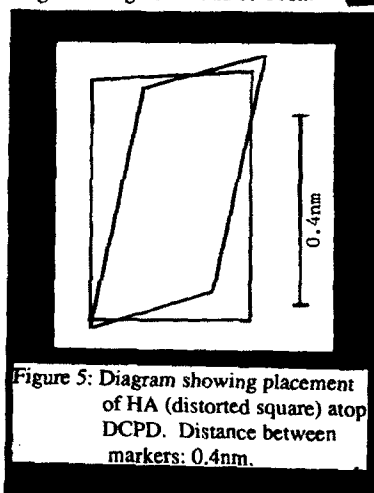


Figure 5: Diagram showing placement of HA (distorted square) atop DCPD. Distance between markers: 0.4nm .

the model, it can be seen that the atoms at the vertices of the HA and DCPD surface structure are positioned to within 0.9\AA of each other. The close atomic distance correspondence determined by AFM may be consistent with the concept that DCPD may serve as a template for the deposition of HA.¹¹ Further observations by AFM characterizing the surface atomic structure of these two biological materials are vital to understanding potential HA-DCPD interactions.

REFERENCES

1. G. Binnig, H. Rohrer, C. Gerber, and E. Weibel, *Phys. Rev. Lett.* **50**, 120 (1986).
2. D. Ruger and P. Hansma, *Phys. Today* **43** (10), 23-30 (1990).

3. O. Marti, B. Drake and P.K. Hansma, *App. Phys. Lett.* **51**, 484 (1987).
4. R. E. Marchant, A. S. Lea, J. D. Andrade and P. Bockenstedt, *J. Colloid Interface Sci.* **148**, 261 (1992).
5. S. M. Lindsay, N. J. Tao, J. A. DeRose, P. I. Oden, Yu. L. Lyubchenko, R. E. Harrington and L. Shlyakhtenko, *Biophys. J.* **61**, 1570 (1992).
6. M. I. Kay, R. A. Young and A. S. Posner, *Nature* **204**, 1050 (1964).
7. W. J. Landis and M. J. Glimcher, *J. Ultrastruct. Res.* **63**, 188 (1978).
8. H. Ji and P. M. Marquis, *J. Mater. Sci. Lett.* **10**, 132 (1991).
9. N. A. Curry and D. W. Jones, *Z. Kristallogr.* **181**, 205 (1987).
10. R. H. Plovnick, *J. Cryst. Growth* **114**, 22 (1991).
11. M. D. Francis and N. C. Webb, *Calc. Tiss. Res.* **6**, 335 (1971).
12. L. M. Siperko and W. J. Landis, *J. Mater. Sci. Lett.* (accepted.).

CHARACTERIZATION OF INTERNAL INTERFACES BY ATOM PROBE FIELD ION MICROSCOPY

M. K. MILLER AND RAMAN JAYARAM

Metals and Ceramics Division, Oak Ridge National Laboratory, Oak Ridge, TN 37831-6376.

ABSTRACT

The near atomic spatial resolution of the atom probe field ion microscope permits the elemental characterization of internal interfaces, grain boundaries and surfaces to be performed in a wide variety of materials. Information such as the orientation relationship between grains, topology of the interface, and the coherency of small precipitates with the surrounding matrix may be obtained from field ion microscopy. Details of the solute segregation may be obtained at the plane of the interface and as a function of distance from the interface for all elements simultaneously from atom probe compositional analysis. The capabilities and limitations of the atom probe technique in the characterization of internal interfaces is illustrated with examples of grain boundaries and interphase interfaces in a wide range of materials including intermetallics, model alloys, and commercial steels.

INTRODUCTION

The characterization of grain boundaries and other interfaces requires a technique with elemental mass resolution and high spatial resolution. The energy-compensated atom probe field ion microscope (APFIM) is well suited to this type of characterization due to its near atomic spatial resolution and its ability to identify and quantify solute segregation for all elements present in the material [1]. These abilities permit the acquisition of data on a local scale that is not possible by other analytical techniques such as transmission electron microscopy or Auger spectroscopy. For example, the field ion micrographs shown in Fig. 1 reveal that the boron segregation was significantly higher at a small facet on the grain boundary in an Ni₃Al intermetallic as indicated by the brightly-imaging boron atoms [2] and that a grain boundary in a Soviet type VVER 440 pressure vessel steel was decorated by ultrafine brightly-imaging molybdenum carbo-nitride precipitates. In addition, atom probe analysis of the VVER 440 steel revealed that there was a significant (>50x) enrichment of phosphorus at the grain boundary. These observations have important implications on the mechanical properties of the materials: in the Ni₃Al case, the boron segregation is linked to a significant improvement in the ductility of the material, and in the pressure vessel steel case, the high phosphorus level indicates that the material is susceptible to temper embrittlement.

One of the limitations of the atom probe technique is the relatively small volume of material that may be analyzed in a specimen. However, modern methods of specimen preparation that involve examination and preselection in the transmission electron microscope, together with micropolishing and precision ion milling techniques, enable the efficient study of features present in low number densities such as grain boundaries in materials with grain sizes several orders of magnitude larger than the size of the analyzable apex region of a field ion specimen [1].

ANALYSIS OF BOUNDARIES

The atom probe field ion microscope may be used to determine several parameters of a grain boundary. For example, a field ion micrograph of a grain boundary in an Fe-45% Cr alloy aged for 500 h at 500°C is shown in Fig. 2. This field ion micrograph indicates that the grain boundary is decorated with a darkly-imaging ~15 nm thick film [3]. Analysis of the crystallographic relationship [4] between the two grains revealed that this boundary was consistent with a Σ9 orientation. Atom probe analysis revealed that the darkly-imaging film was chromium nitride and there was a 5 to 10 nm thick region adjacent to this chromium nitride film that was depleted in chromium to ~15% Cr. The micrograph also reveals that the interior of the grain was decomposed into a complex interconnected mixture of brightly-imaging iron-rich α and darkly-imaging chromium-enriched α' phases and there was no

change in scale of this two phase microstructure with respect to position away from the boundary. It should be noted that this decomposition is difficult to resolve by other analytical techniques such as transmission electron microscopy. This two phase microstructure was not present in the chromium-depleted zone. In addition, a darkly-imaging 5 nm thick chromium nitride precipitate is evident protruding from the boundary.

The compositional analysis of grain boundaries or interfaces in the atom probe requires careful selection of the experimental parameters, such as the effective size and position of the probe aperture used to define the region analyzed. Since the analysis is performed by collecting the atoms that originate in a small cylinder of analysis, the three dimensional geometry of the boundary and the orientation of the cylinder of analysis must be taken into account in the selection of the optimum location for the probe aperture. The axis of the cylinder of analysis is determined by the taper angle of the specimen, $\alpha/2$, and the position of the probe aperture as shown in Fig. 3. A composition profile along the plane of the grain boundary is shown in Fig. 4. The periodic peaks of iron and dips in chromium and nitrogen indicates that the chromium nitride film was not continuous. In order to maintain the correct analysis conditions, frequent realignment of the position of the probe aperture is generally required for this type of analysis.

The composition of the volume defined by the cylinder of analysis is determined by simply counting the number of atoms of each type in that volume. However, the result is an average composition over the entire volume. Although the lateral extent of this cylinder is generally selected to be only a few atom diameters wide, it does not necessarily reflect the true levels of solutes at a grain boundary in cases where the width of segregation is narrower than the effective extent of the probe aperture such as in the boron-doped NiAl specimen shown in Fig. 5 [5]. A more appropriate concentration may be determined by considering the relative contributions from the boundary region and the surrounding matrix included in the cylinder of analysis as shown in Fig. 6. The relationship between the true concentration at the boundary, C_b , the average measured concentration, C , and the measured concentration of the matrix, C_m , is given by [6]

$$C_b = \frac{\pi r}{r(\pi - 2\theta) + w \sin\theta} (C - C_m) + C_m \quad (1)$$

where $\theta = \cos^{-1}(w/2r)$, and r is the effective radius of the probe aperture. In order to perform this correction, a width of the boundary region, w , is assumed. The variation of the enrichment factor is a function of this width, as shown in Fig. 7 for the boron enrichment at a grain boundary in boron-doped NiAl [5,6]. Although it is difficult to assign a value to the width of the boundary region, a sensible choice is the interplanar spacing of the closest packed plane, e.g. d_{110} . It is evident that the true enrichment is significantly higher than the measured value. However, it should be noted that this volumetric approach assumes that the composition may be treated as a continuum and that there are no variations in density on a local scale: these assumptions may not be correct or even appropriate at the atomic level.

INTERFACE MORPHOLOGY

The three dimensional morphology of interfaces and precipitates may be accurately determined with the atom probe. Since the technique of field evaporation [1] enables small amounts of material to be carefully and precisely removed from the specimen, the morphology of the feature may be reconstructed from its extent in a sequence of field ion micrographs or field evaporation micrographs [7]. Until recently, this technique has mainly been used to determine the shape of small precipitates. However, the introduction of the new generation of three dimensional atom probes (3DAP) has enabled more elaborate types of visualization and parameterization of complex microstructures. However, it should be emphasized that it is the more powerful computer capabilities rather than the new types of position-sensitive detectors that have permitted these types of visualizations.

An example of the complex microstructures that may be visualized at the atomic level is the two phase microstructure that is formed by spinodal decomposition within the low temperature miscibility gap in the Fe-Cr system, as indicated in interior of the grains in Fig. 2. A three dimensional set of data may be obtained by field evaporating the Fe-45% Cr specimen and recording in a digital format the sequence of field evaporation micrographs that

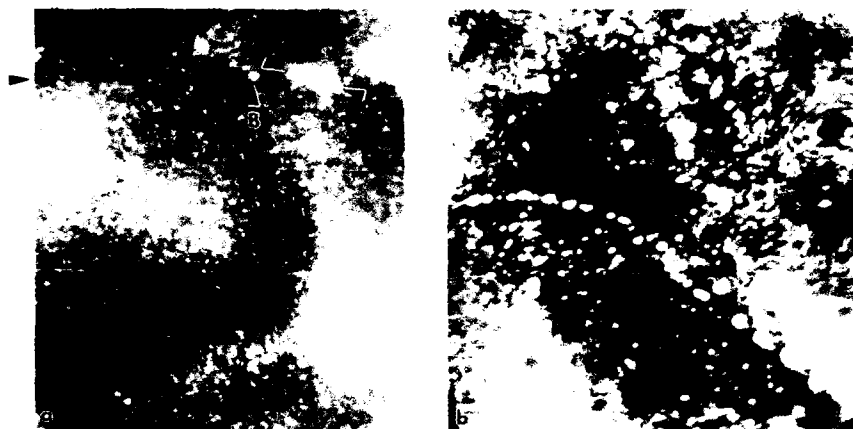


Fig. 1. a) Field ion micrograph of a grain boundary in boron-doped Ni_3Al showing brightly-imaging boron atoms decorating a small facet (arrowed). (b) Boundary in a Soviet type VVER 440 pressure vessel steel showing ultrafine brightly-imaging molybdenum carbonitride precipitates. Atom probe analysis also revealed that there was a significant enrichment of phosphorus at this boundary.



Fig. 2. Field ion micrograph of a $\Sigma 9$ grain boundary in Fe-45% Cr aged for 500h at 500°C exhibiting a darkly-imaging chromium nitride film. A chromium nitride precipitate is also evident protruding from the boundary.

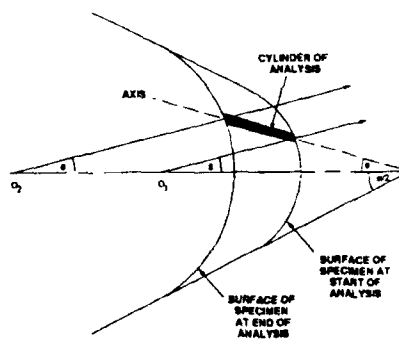


Fig. 3. Schematic diagram of the orientation of the cylinder of analysis in the atom probe. The axis of the cylinder makes an angle ϕ with respect to the axis of the specimen.

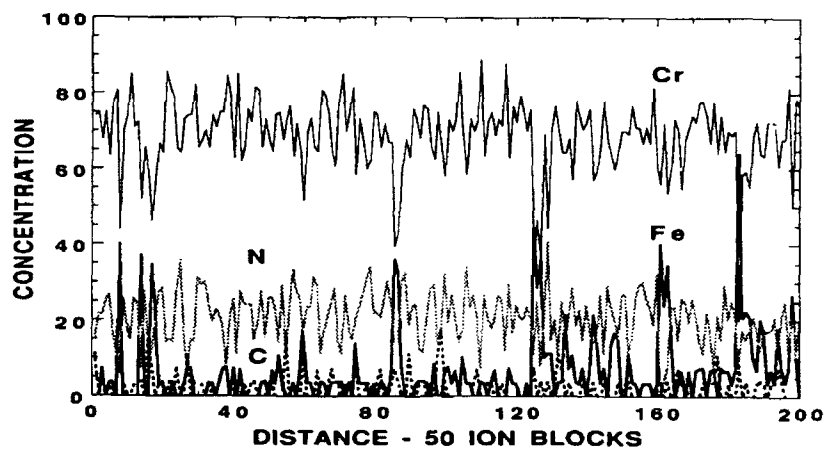


Fig. 4. Atom probe composition profile along the $\Sigma 9$ grain boundary in the Fe-45% Cr model alloy shown in Fig. 2. The periodic iron peaks indicate that the chromium nitride film of precipitates is not continuous.



Fig. 5. Field ion micrograph of a boron decorated grain boundary in boron-doped NiAl. The boron enrichment is confined to the plane of the boundary.

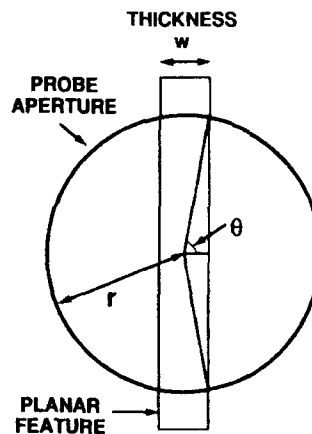


Fig. 6. Schematic diagram of the intersection of a planar feature of width w , with the circular probe aperture of effective radius r .

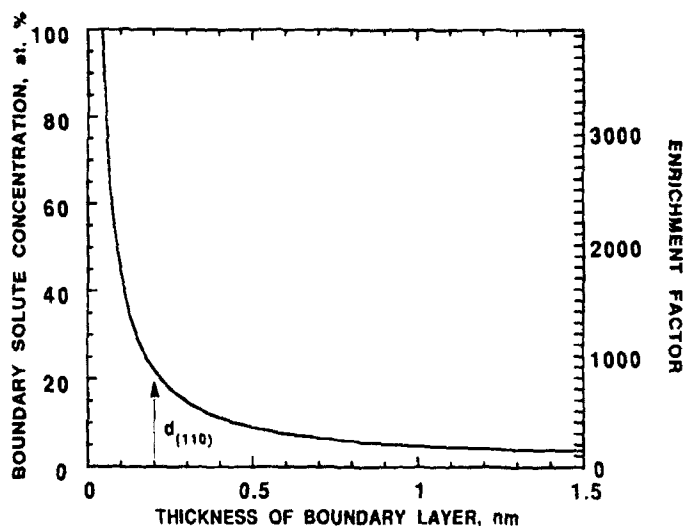


Fig. 7. The enrichment of boron as a function of grain boundary width, w , based on equation 1 for the NiAl grain boundary shown in Fig. 5. A sensible choice for the width of the boundary is the interplanar spacing of the close packed (110) plane, i.e. d_{110} .



Fig. 8. A three dimensional reconstruction of the isosurface between the iron-rich α phase and the chromium-enriched α' phase obtained from a sequence of field evaporation micrographs in the optical atom probe. The material was an Fe-45% Cr alloy aged for 192 h at 540°C. This volume is a cube of side 21 nm.

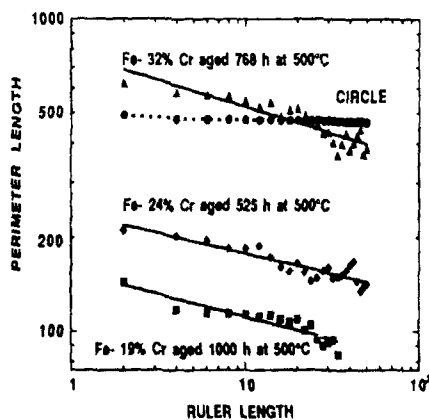


Fig. 9. Plot of the perimeter length as a function of the ruler length obtained from field evaporation micrographs of Fe-19, 24 and 32% Cr alloys aged at 500°C and a reference circle. The fractal dimension of the interface was found to vary between ~ 1.1 and 1.5 which indicates that the interface is fractal.

appear on the position-sensitive detector of the optical atom probe (OAP) [8,9]. One of the most effective representations of the morphology of this complex interconnected microstructure is to calculate the isosurface between the two phases. An example of an isosurface in an Fe-45% Cr alloy aged for 192 h at 540°C is shown in Fig. 8. This set of data corresponds to a cube that is approximately 21 nm on each side. The complex interconnected nature of this two phase microstructure is clearly evident. Similar isosurfaces have also been determined for this material from three dimensional composition maps [10].

The three dimensional data may also be subjected to other types of analyses. For example, examination of the length of the perimeter of the interface as a function of the ruler length of similar sets of field evaporation sequences in Fe-19, 24, and 32% Cr alloys aged at 500°C has indicated that the interphase interface has fractal properties, as shown in Fig. 9 [11]. Some other types of fractal and topological analyses have also been performed on these model Fe-Cr alloys [10]. These types of analyses provide means for comparing different aging conditions.

CONCLUSIONS

The examples given in this paper have illustrated some of the types of information that may be obtained with the atom probe field ion microscope in the characterization of internal interfaces. The high spatial resolution and serial sectioning capabilities of the field ion microscope enables the three dimensional morphology of the interface to be visualized and the mass spectrometer section of the atom probe enables compositional variations and segregation behaviour to be accurately determined.

ACKNOWLEDGMENTS

The authors would like to thank K.F. Russell and J.A. Horton for their technical assistance. This research was sponsored by the Division of Materials Sciences, U.S. Department of Energy, under contract DE-AC05-84OR21400 with Martin Marietta Energy Systems, Inc. and through the Postgraduate Research Program administered by Oak Ridge Institute for Science and Education.

REFERENCES

1. M.K. Miller and G.D.W. Smith, *Atom Probe Microanalysis: Principles and Applications to Materials Problems*, (Material Research Society, Pittsburgh Pa, 1989).
2. M.K. Miller and J.A. Horton, *Scripta Metall.*, **20** 789 (1992).
3. M.K. Miller and R. Jayaram, *Appl. Surf. Sci.* in press.
4. K.M. Bowkett and D.A. Smith, *Field Ion Microscopy*, (North Holland, Amsterdam, 1970)
5. R. Jayaram and M.K. Miller, *Surf. Sci.*, **266** (1992).
6. M.K. Miller, R. Jayaram and P.P. Camus, *Scripta Metall.*, **26** 679 (1992).
7. A. Cerezo, M.G. Hetherington, J.M. Hyde, M.K. Miller, G.D.W. Smith and J.S. Underkoffler, *Surf. Sci.*, **266** 471 (1992).
8. M.K. Miller, *Surf. Sci.*, **246** 434 (1991).
9. M.K. Miller, *Surf. Sci.*, **266** 494 (1992).
10. J.M. Hyde, A. Cerezo, M.G. Hetherington, M.K. Miller and G.D.W. Smith, *Surf. Sci.*, **266** 370 (1992).
11. M.K. Miller and K.F. Russell, *Surf. Sci.*, **266** 232 (1992).

THE ORIGINS OF HIGH SPATIAL RESOLUTION SECONDARY ELECTRON MICROSCOPY

M.R. Scheinfein^{*,#}, J.S. Drucker[#], J. Liu[#], J.K. Weiss[#], G.G. Hembree^{*}, J.M. Cowley^{*,#}

^{*}Department of Physics and Astronomy, Arizona State University, Tempe, AZ 85287-1504

[#]Center for Solid State Science, Arizona State University, Tempe, AZ 85287-1704

ABSTRACT

The secondary electron generation process is studied in an ultra-high vacuum scanning transmission electron microscope using electron coincidence spectroscopy. Production pathways for secondary electrons are determined by analyzing coincidences between secondary electrons and individual excitation events. The ultimate spatial resolution available in scanning electron microscopy is limited by the delocalization of the secondary electron generation process. This delocalization is studied using momentum resolved coincidence electron spectroscopy. The fraction of secondary electrons resulting from localized excitations can explain the high spatial resolution observed in secondary electron microscopy images.

INTRODUCTION

The high spatial resolution structural determination of surfaces, overlayers and monolayer thin films often utilizes the secondary electron (SE) signal produced by a focused probe of fast electrons, e.g. imaging surface steps on Si(111) [1], Si(100) [2], GaAs(110) [3], Cu(100) [4], NiO, MgO and Pt [5,6]. The production of SE by focused, fast electron beams is a multistage process which includes excitation of target electrons by the energetic incident beam, subsequent decay yielding hot SE, transport to the surface, and transmission over the surface potential barrier [7]. Although the excitation process for inelastic scattering of fast electrons in thin films is well described by the Bethe theory [8] pioneered over 50 years ago, detailed theoretical treatments of SE production and transport [7] have yet to be verified. The ultimate spatial resolution of a SE image formed by scanning a well focussed probe across a surface is limited by the spatial delocalization of the specific excitation event which leads to the production or generation of SE. This delocalization can be related to the transverse momentum transferred to the specimen during the excitation process through the Heisenberg uncertainty principle. Theoretically, Ritchie et. al. [9] concluded that high spatial resolution SE images result from localized scattering from valence excitations, in accordance with the experimental results of Bleloch et. al. [4]. Liu and Cowley [5] maintain that it is the higher-angle inelastic scattering that gives rise to the observed high spatial resolution, and that these events are likely due to single electron excitation processes. Even the role of the delocalized plasmon excitation and subsequent decay into SE [10] in free electron metals, which has received considerable theoretical attention, remains controversial and awaits experimental characterization [11].

The accepted model for SE production [7] is not well characterized since it is extremely difficult to separate experimentally the generation, transport and transmission processes during a given SE creation event. Here, we examine the SE generation pathway by correlating SE of a given energy produced by an initial inelastic excitation using time coincidence detection [12-14]. This technique can be used, for example, to isolate the role of plasmon decay [10,11] in the SE generation process.

EXPERIMENTAL RESULTS

The experiments were performed in a Vacuum Generators HB501-S UHV scanning transmission electron microscope (STEM), operating at a base pressure of 5×10^{-11} torr. The microscope which forms sub-nanometer focused 100 keV probes [15] is equipped with a second order corrected magnetic sector spectrometer for microanalysis using transmission electron energy loss spectroscopy (EELS). The spectrometer has 0.5 eV resolution at 100 keV beam energies at spectrometer acceptance semi-angles up to 5 milliradians (mr). Electrons scattered by 100 mr at the sample can be focused into the spectrometer by post specimen electron optics. Surface microanalysis using SE or Auger electron (AE) spectroscopy is performed within the magnetic field of the objective lens using the parallelizer principle [15,16]. The collection efficiency is

100% at SE energies, and degrades to 40% at intermediate AE energies (300-400 eV). Collected electrons are deflected by an astigmatic Wein filter, and energy analyzed by a 100 mm radius, 180° spherical electrostatic energy analyzer operated at a fixed retard ratio of 5. Microstructural analysis is performed in situ using standard electron diffraction and/or microscopy techniques. Excellent EELS momentum resolution (0.01 mrad) can readily be obtained in STEM by employing small incident beam convergence angles and appropriately exciting post-specimen lenses.

High-angle-annular-dark-field (HAADF) and SE images of in-situ deposited Ag islands on a < 5 nm thick amorphous carbon substrate are shown in Figs. 1a and 1b respectively. These images were acquired simultaneously, and hence are absolutely registered. The HAADF imaging mode in STEM is capable of atomic point-resolution. Contrast in HAADF images can be most simply envisioned as a convolution of the atomic scattering function of the object under observation with the beam intensity profile (incoherent imaging). The secondary electron image, upon visual inspection shows (nearly) identical features and resolution. Line scan profiles extracted from identical regions of the HAADF and SE of Figs. 1a and 1b are shown in Fig. 1c. The striking similarity between these profiles indicates that the resolution in each image is identical, and is limited by the probe diameter in this instrument to roughly 1 nm. Why is the secondary electron image resolution so great? In order to investigate this question, we correlate the production of a SE of a given energy with an inelastic excitation (of the incident high energy electrons) using time coincidence detection [12-14]. In the coincidence detection experiment, individual electrons which have been inelastically scattered are detected with an electron energy loss spectrometer (EELS) and correlated in time with those secondary electrons which are detected by the 180° electrostatic analyzer.

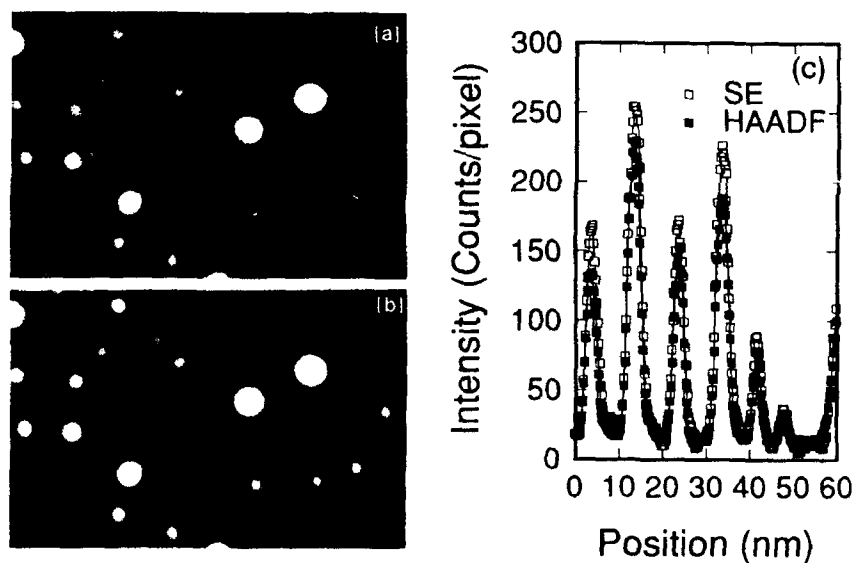


Fig. 1 : (a) High angle annular dark field (HAADF) and (b) entrance face secondary electron (SE) micrographs of in-situ evaporated Ag islands on < 50 nm thick amorphous carbon film. The micrographs are 75 nm across and in exact registration. (c) Line scan profiles across Ag islands illustrating that similar resolution is obtained in HAADF and SE images.

Specifically, EELS electrons are detected by a single-crystal Ce-doped yttrium-aluminum-garnet (YAG) scintillator, selected for its resistance to radiation damage under bombardment by 100 keV electrons and its suitability for UHV. The SE channel employs a channeltron electron multiplier. Pulses resulting from single electron events can be counted at rates up to 1 MHz. In the coincidence experiments, time correlation spectra (TCS) are formed by starting the timing electronics with EELS pulses, and using the delayed SE pulses to gate the stop. The EEL spectrometer pass energy is ramped while the SE spectrometer remains fixed at a particular energy with a 1 eV energy window. A time correlation spectrum is acquired at each EEL energy, and the true and false coincidence signals, which are integrals under the TCS peak and background [17], are extracted and stored.

Timing resolution and counting rates are limited by intrinsic processes such as plasmon decay (< 1 ps), and instrumental factors such as transit time spreads in the parallelizer field (< 10 ns) and electrostatic energy analyzer (< 30 ns), and, any delays introduced by electron conversion electronics. Our system is limited by the fluorescent decay times of the Ce:YAG scintillator which is between 80 and 100 ns. Coincidence spectra acquired at high starting and/or stopping count rates are dead-time corrected [17]. These corrections are verified by analyzing the false coincidence spectrum, the EELS spectrum and the secondary count rate [17].

Electronic Structure

EELS, coincidence and generation probability spectra for p-type ($n_h = 10^{15} \text{ cm}^{-3}$) Si<111> are shown in Figs. 2a and 2b. The SE generation probability spectrum is defined as the ratio between the coincidence and EELS spectra [12-14,18], and is a measure of SE generation efficiency for a particular inelastic excitation. The plasmon excitation visible at 17.7 eV is the dominant peak in the EELS spectrum (Fig. 2a). The excitation energy of the planar surface plasmon [19] ($\omega_s = \omega_p / (1 + \epsilon_s)^{1/2}$, where ϵ_s is the real part of the dielectric constant for the medium adjacent to the surface) can be used to gauge the surface cleanliness. A monolayer of absorbed contamination can shift this peak. The Si coincidence (Fig. 2a) and generation probability (Fig. 2b) spectra are each shifted for visibility. The role of plasmon decay in SE production remains controversial. These excitations have large cross sections and the accompanying planar surface plasmons [19] are localized within an SE escape depth of the surface. A number of authors have suggested that plasmons may be a major production pathway for SE in metals [10,14] while Massignon, et. al. [11], in direct contradiction to theoretical predictions, suggested that plasmons were not responsible for SE production in Al. We observe that the peak, and in fact, most of the generation probability for SE creation, lies at excitation energies above the volume plasmon excitation energy (Fig. 2), suggesting that SE production resulting from the decay of plasmons is not the primary production mechanism in p-type Si<111>.

The data of Fig. 2 provide evidence that interband valence excitations play a major role in the production of SE. Peaks in the Si coincidence spectra (Fig. 2a) move linearly with the kinetic energy of the detected secondary electrons. For example, examining the peaks in the 7.5 eV SE coincidence spectrum at 20.0 and 24 eV, and subtracting the SE kinetic energy and the work function from the peak energies, we see that these events originated 8 and 11.7 volts below E_F in the valence band. There are large densities of states (along L) at -7.24 and -10.17 eV [20] ($E_F = 0$ in this highly doped p-type Si). The correspondence between the peaks in the generation spectra and the large density of states along the incident momentum vector suggests that the decay of ionizations from deep in the valence band play a significant role for SE production in Si(111).

SE production in amorphous (glassy) carbon films has been investigated by Voreades [12] Mulleijans [13] and Piiper and Kruit [14]. We have also investigated the secondary electron generation process in carbon films [18]. Since the band structure of amorphous carbon is not well defined, there are no peaks in the coincidence spectra which can be linked to any particular electronic states. However, when the generation probability spectrum is divided by the EELS energy, the resulting normalized generation probability spectrum [18] has zero slope ($\pm 4\%$) between 25 eV and 100 eV energy loss. This suggests that secondary electron production resulting from higher loss energies than valence band excitations result from simple energy deposition local to the surface mediated by the escape depth of the SE. This is consistent with the Sternglass theory [21] for secondary electron production, where the secondary yield is proportional to the stopping power of the film [7,22].

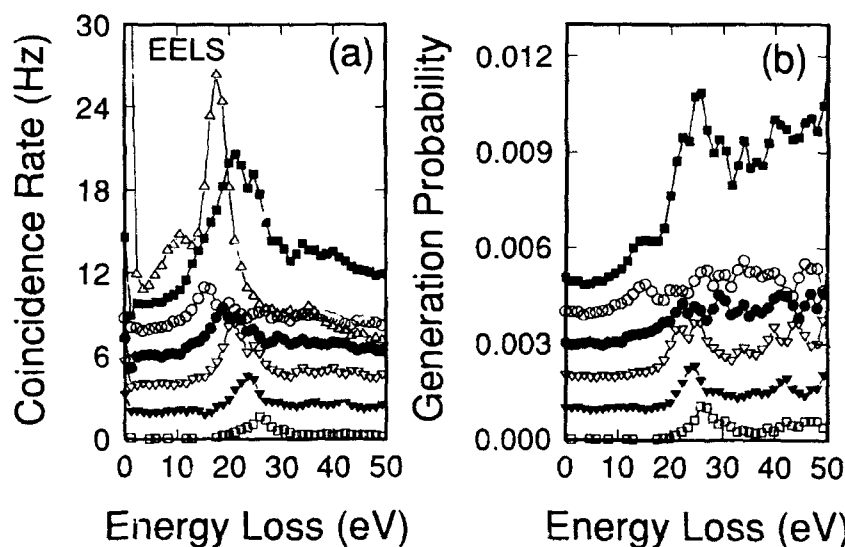


Fig 2: (a) The EELS (open upfacing triangles) and coincidence spectra for p-type Si $\langle 111 \rangle$. The coincidence spectra are between inelastic events and 2.5 eV (open circles), 5.0 eV (filled circles), 7.5 eV (open downfacing triangles), 10.0 eV (solid downfacing triangles), 12.5 eV (open squares) and the total SE (filled squares) signals. (b) The generation probability derived from (a) which reflects the efficiency by which SE electrons of given energy (as above) are created for each inelastic scattering event of given energy.

Spatial Resolution

In this section, we present data from a momentum-resolved electron coincidence spectroscopy study of the SE generation process in thin Si(111) crystals. This data shows that SE more probably result from the decay of valence excitations produced by large momentum transfer inelastic scattering events. This data shows that the fraction of SE resulting from sufficiently localized scattering can explain the observed high spatial resolution in secondary electron microscopy (SEM) images; the SE generation process becomes more efficient as the initial inelastic excitation event transfers more transverse momentum to the sample.

Coincidence electron spectra were accumulated between 2.5 eV SE and primary inelastically scattered electrons at discrete energies, 17 eV (the plasmon energy in Si), 34 eV and 51 eV. In each case, three effective angular apertures were defined with the post specimen lens optics such that electron energy loss excitations with perpendicular momentum transfer wave vectors up to 1.00 \AA^{-1} , 0.18 \AA^{-1} and 0.15 \AA^{-1} were accepted into the spectrometer. The ratios of the number of SE produced by primary electrons which have scattered through a certain angle can be obtained by fitting this data (not shown). With the 1.00 \AA^{-1} (the cut-off wave vector for plasmon excitations in Si [19] is 1.1 \AA^{-1}) transverse momentum data used for the normalization, 44% of all SE produced in thin Si(111) crystals result from primary electrons which have scattered through at least 0.18 \AA^{-1} , and 87% are the result of scattering by at least 0.15 \AA^{-1} .

The spatial resolution of an image can be estimated from the degree of delocalization from the inelastic scattering distribution and the Heisenberg uncertainty principle. Since the EEL spectrometer integrates over all scattering angles up to the angle subtended by the collection aperture at the sample, θ_0 , the angularly resolved coincidence data are proportional to

$\int_0^{\theta_0} d^2\sigma(E, \theta)/d\theta dE \sin\theta d\theta$, where $d^2\sigma(E, \theta)/d\theta dE$ is the differential cross section for scattering from excitations of energy E through an angle θ [23]. The average scattering angle, $\langle\theta\rangle$, is found by integrating $\theta d^2\sigma(E, \theta)/d\theta dE$ first over the collection aperture [24] and then over the energy distribution of the inelastic scattering products, $N(E)$. For estimating the delocalization in a SE image, $N(E)$ is just the coincidence spectrum. By contrast, when estimating the delocalization in an inelastic image, $N(E)$ is EEL spectrum. The average transverse wavevector for an inelastic scattering event is $\langle q_{\perp} \rangle = k_0 \langle\theta\rangle$, where $k_0 = 170 \text{ \AA}^{-1}$, is the incident wavevector. The average scattering angle $\langle\theta\rangle$ can be related to the spatial resolution (delocalization) in an image through the Heisenberg uncertainty relation as, $\Delta x \sim 1/\langle q_{\perp} \rangle = 1/(k_0 \langle\theta\rangle)$. Following this procedure for the angularly resolved coincidence data, and the EEL spectra which produced these SE, we estimate the spatial delocalization which is shown in table 1. The calculated spatial resolution is greater for images formed with (all of the) SE than for images formed with the (small-angle) inelastically scattered electrons (0-50 eV).

Table 1

$\Delta q (\text{\AA}^{-1})$	SE	$\Delta x (\text{\AA})$	EEL
1.00	3.5		4.0
0.18	13.1		14.3
0.15	15.9		16.7

Table 1: The delocalization expected in an image formed with 2.5 eV secondary electrons (SE) and inelastic electrons (EELS) estimated from the Heisenberg uncertainty relation due to scattering of given average wavevector.

The reason for the higher spatial resolution in the SE images is made apparent in Fig. 3 which illustrates the SE production efficiency initiated by an inelastic event of a given energy for all momenta collected by the EEL spectrometer, the angle resolved generation probability. SE are more probably produced by the decay of valence excitations resulting from high momentum transfer inelastic scattering in thin Si(111) crystals. High spatial resolution SE images obtained by normally incident beams on a planar surfaces report 20% - 80% edge resolutions of around 1 nm using sub-nm diameter probes [25]. Our data can explain this observed spatial resolution. A 1.0 nm delocalized excitation event (a weighted sum of the data of Table 1) when convolved with a 0.5 nm diameter probe yields a SE 20% - 80% edge resolution of about 1.2 nm. Higher spatial resolution SE images have been obtained using either glancing incidence (aloof illumination) or imaging asperities on a planar surface [5]. The spatial resolution of some of these images approaches 0.5 nm. Either a more localized generation process or one with increased weighting towards high momentum transfer must be responsible for this observed high spatial resolution.

Simple geometric arguments based on classical kinematic scattering can be used to show how ultra-high spatial resolution SE images may be obtained at glancing incidence. For primary electrons normally incident on a surface, momentum conservation causes the excitations resulting from large angle, highly localized scattering to travel more nearly parallel to the surface than those excitations resulting from low angle scattering. Thus, the subsequent decay of these localized excitations into hot SE are more likely to escape than those SE resulting from delocalized excitations. The preferential emission of SE produced by the decay of excitations resulting from high angle scattering may be enhanced for glancing incidence. Those excitations produced by high angle scattering travel nearly perpendicular to the beam. Those traveling toward the surface can decay into SE which escape and contribute to the high resolution image. Production in proximity to the surface may be further enhanced by surface enhanced damping of valence excitations [26]. As the beam moves away from the surface (edge), less of these high

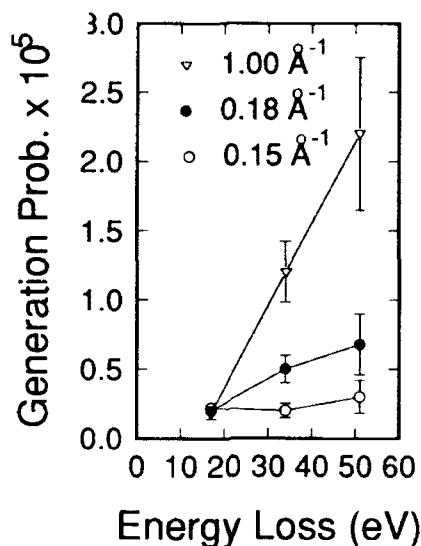


Fig. 3: SE production efficiency initiated by an inelastic event of a given energy for all momenta collected (indicated) by the EEL spectrometer.

resolution SE escape since the distance the excitation travels before decay is limited by its group velocity multiplied by its lifetime to about a nanometer. The SE subsequently produced are further attenuated by their inelastic mean free path. Excitations resulting from low angle scattering events travel more nearly parallel to the surface than do those resulting from more localized high angle scattering. The subsequent decay of these delocalized excitations yield hot SE which contribute low spatial resolution Fourier components to the image.

CONCLUSIONS

We have employed coincidence electron spectroscopy as a means of studying the SE generation process. We determined that SE production in thin Si crystals is unlikely to originate in plasmon or surface plasmon decay. In the energy loss region above the valence band excitations and below the final core loss energy, the probability of SE production is proportional to the energy deposited in the film as predicted by the Sternglass model. Momentum resolved electron coincidence spectroscopy results suggest that SE are more probably produced by the decay of valence excitations resulting from large momentum transfer inelastic scattering in thin Si(111) crystals. Quantitative analysis of this data shows that SE images will have higher spatial resolution than images formed with those inelastically scattered electrons from which the SE result. Our data can explain the spatial resolution of SE images obtained with primary beams normally incident on planar surfaces. Higher spatial resolution images obtained at glancing incidence (aloof illumination) or of asperities on a surface may be the result of enhanced preferential emission of SE produced by the decay of highly localized inelastic scattering.

ACKNOWLEDGEMENTS

We would like to acknowledge the technical assistance of A. Higgs. We acknowledge M. Isaacson, P. Rez, J.C.H. Spence, and J.M. Zuo for useful discussions. This work was performed at the NSF supported Center for High Resolution Electron Microscopy at Arizona State University, Grant No. DMR-91-15680.

REFERENCES

1. Y. Homma, M. Tomita, T. Hayashi, *Surf. Sci.* **258**, 147 (1991).
2. J. S. Drucker, M. Krishnamurthy, G.G. Hembree, *Ultramicrosc.* **35**, 323 (1991); J. S. Drucker, *J. Appl. Phys.*, **70**, 2806 (1991).
3. R.H. Milne, *Ultramicrosc.* **27**, 433 (1989).
4. A.L. Bleloch, A. Howie, R.H. Milne, *Ultramicrosc.* **31**, 99 (1989).
5. J. Liu, J.M. Cowley, *Scanning Microsc.* vol. **2**, 65 (1988); J. Lui, J.M. Cowley, *Scanning Microsc.* vol. **2**, 1957 (1988).
6. Y. Uchida, G. Weinberg, G. Lempfuhr, *Micr. Res. Tech.* **20**, 406 (1992).
7. D.M. Suszcynsky, J.E. Borovsky, *Phys. Rev.* **A45**(9), 6424 (1992); M. Rosler, W. Brauer, *phys. stat. sol. (b)* **104**, 161 (1981); M. Rosler, W. Brauer, *phys. stat. sol. (b)* **104**, 575 (1981); M. Rosler, W. Brauer, *phys. stat. sol. (b)* **148**, 213 (1988); J. Schou, *Scanning Microsc.* **2**, 607 (1988); R. Bindi, H. Lateri, P. Rostaing, *Scanning Microsc.* **1**, 1475 (1987); V.E. Henrich, *Phys. Rev.* **B7**, 3512 (1973); R. Willis et. al, *Phys. Rev.* **B9**, 1926 (1974).
8. H. Bethe, *Z. Phys.* **76**, 293 (1930); H. Bethe, in *Handbuch der Physik*, edited by H. Geiger and K. Scheel (Springer, Berlin, 1933), Vol. 24/1, p. 273; M. Inokuti, *Rev. Mod. Phys.* **43**(3), 297 (1971).
9. R.H. Ritchie, A. Howie, P.P. Echique, G.J. Basbas, T.L. Ferrell, J.C. Ashley, *Scanning Microsc. Suppl.* **4**, 45 (1990).
10. T.E. Everhart, M.S. Chung, *J. Appl. Phys.* **43**(9), 3707 (1972); M.S. Chung, T.E. Everhart, *Phys. Rev.* **B15**(10), 4699 (1977); J.P. Ganachaud, M. Cailler, *Surf. Sci.* **83**, 498 (1979); J.P. Ganachaud, M. Cailler, *Surf. Sci.* **83**, 519 (1979).
11. D. Massignon, F. Pellerin, J.M. Fontaine, C. LeGressus, T. Ichinokawa, *J. Appl. Phys.* **51**(1), 808 (1980).
12. D. Voreades, *Surf. Science*, **60**, 325 (1976).
13. H. Mulleijans, A.L. Bleloch, A. Howie, C. McMullan, *Inst. Phys. Conf., Ser. No.* **119**(3), 117 (1991); H. Mulleijans, Ph. D. Thesis, University of Cambridge, 1992.
14. P. Kruit, H. Shuman, A.P. Somlyo, *Ultramicrosc.* **13**, 205 (1984); F.J. Pijper, P. Kruit, *Phys. Rev.* **B44**(17), 9192 (1991).
15. G.G. Hembree, P.A. Crozier, J.S. Drucker, M. Krishnamurthy, J.A. Venables, J.M. Cowley, *Ultramicrosc.* **31**, 111 (1989).
16. A.J. Blecker, Ph. D. Thesis Technische Universiteit Delft., (1991); A. Blecker, P. Kruit, *Nucl. Instr. Meth.* **A298**, 269 (1990); P. Kruit, J. A. Venables, *Ultramicrosc.* **25**, 183 (1988);
17. T. Akimoto, I. Murai, M. Nakata, Y. Ogawa, *Nucl. Instr. Meth.* **184**, 525 (1981); H. Jeremie, *Nucl. Instr. Meth.* **A244**, 587 (1986); G.F. Knoll, **Radiation Detection and Measurement**, 2nd Ed. (John Wiley and Sons, New York, New York, 1988) chaps. 4 and 17.
18. M.R. Scheinfein and Jeff Drucker, *Phys. Rev. B* (in press).
19. H. Raether, **Plasmons and Intraband Electronic Transitions**, Springer Tracts in Modern Physics, vol. **88** (Springer Verlag, Berlin, 1982).
20. J.R. Chelikowsky, M.L. Cohen, *Phys. Rev.* **B14**(2), 556 (1976).
21. J. Sternglass, *Phys. Rev.* **108**, 1 (1957).
22. M. Cailler, J.-P. Ganachaud, *Scanning Microsc. Suppl.* **4**, 57 (1990); M. Cailler, J.-P. Ganachaud, *Scanning Microsc. Suppl.* **4**, 81 (1990).
23. R.A. Ferrell, *Phys. Rev.* **101**, 554 (1956).
24. R.H. Ritchie, A. Howie, *Philos. Mag.* **A58**(5), 753 (1988); D. Ugarte, C. Colliex, P. Trebbia, *Phys. Rev.* **B45**(8), 4332 (1992); M.R. Scheinfein, *Scanning Microsc. Suppl.* **1**, 161 (1987).
25. D. Imeson, R.H. Milne, S.D. Berger and D. McMullan, *Ultramicroscopy* **17**, 243 (1985); A. Howie and R.H. Milne, *Ultramicroscopy* **18**, 427 (1985); M. Issacson, J. P. Langmore and H. Rose, *Optik* **41**, 92 (1974).
26. C. Kunz, *Z. Phys.* **167**, 53 (1962).

REM AND RHEED STUDIES OF Pb ADSORPTION ON Si(111)

YASUMASA TANISHIRO, MASAHICO FUKUYAMA AND KATSUMICHI YAGI
Department of Physics, Tokyo Institute of Technology,
Oh-okayama, Meguro-ku, Tokyo 152, JAPAN

ABSTRACT

Structure changes of Si(111)-Pb surfaces due to deposition and heat treatment are studied by REM-RHEED. Surface structures observed are summarized as a phase diagram. Formation of an incommensurate layer(α) and a phase transition between incommensurate structures of α and α' is described.

INTRODUCTION

Growth of metal on semiconductor surfaces and structure changes due to heat treatment are of great interest in surface physics and semiconductor device technology. Lead adsorption on Si(111)7x7 surface has attracted much attention, because of the report that the Schottky barrier height for Pb/Si(111) contacts depends strongly on the interface structure[1]. This system has been studied by LEED[2-4], RHEED[5], ion-scattering spectroscopy[3] and ellipsometry[6], and various kinds of $\sqrt{3}\times\sqrt{3}$ (abbreviated to $\sqrt{3}$ hereafter), "1x1" structures and a two-dimensional(2D-) Pb(111) layer have been reported. The structures, and the phase transitions between them, however, have not yet been clarified.

X-ray diffraction has been used to study the structures near 1 ML coverage[7]. The 2D-Pb(111) layer formed by deposition at room temperature and the structure formed by subsequent annealing have been analyzed. It was found that the latter is an incommensurate structure, although it was identified to be the $\sqrt{3}$ structure and labeled $\sqrt{3}$ -II[2], $\sqrt{3}$ - α [3,5] and $\sqrt{3}_1$ [4] in previous papers. The present authors have studied the structure changes resulting from the deposition of lead at various substrate temperatures and by heat treatment using reflection electron microscopy and diffraction(REM-RHEED), and found a 2D-contracted Pb(111) layer, "1x1", two kinds of $\sqrt{3}$ structures and incommensurate layers α and α' [8,9] as described below. We have also found that the α layer is not the $\sqrt{3}$ but an incommensurate structure and further found that a phase transition from the α to α' occurs by heating[8].

The STM, ion scattering and LEED have been used to study structures and coverages of the various phases[10]. Two kinds of the $\sqrt{3}$ structures named mosaic phase($\theta=1/6$) and standard phase($\theta=1/3$), 1x1 overlayer and the rotated incommensurate phases were observed on annealed samples.

In the present paper, a REM-RHEED study of the adsorbate structures formed by the deposition of lead and heat treatment is summarized and a "phase diagram" will be given. The formation of the incommensurate layer α and the phase transition between the α and α' are fully described. Since the formation and phase transitions of the other structures have been described in the previous paper[9], these will be included on the phase diagram.

EXPERIMENTAL

Experiments were performed using a UHV electron microscope (modified JEM100B)[11]. Si(111) substrate crystals were heated and cleaned by passing a DC current through them. Lead was evaporated from a tungsten filament and the amount deposited was monitored by a quartz oscillator. The deposition rate was 1-3 ML/m, where 1 ML(monolayer) corresponds to 7.83×10^{14} atoms/cm², the atomic density of a bulk-terminated Si(111)1x1 surface. The azimuthal directions of the incident electron beams for the REM images and RHEED patterns were close to the $\langle 11\bar{2} \rangle$ direction.

Adsorption at Low Temperature

Temperature ($^{\circ}\text{C}$)

Deposited Amount of Pb (mL)

Regions: H, M, L

Equations for boundaries:

- $7 \times 7 + \sqrt{3} - H$
- $7 \times 7 + '1 \times 1'$
- $7 \times 7 + 2D + \delta - 7 \times 7$
- $\sqrt{3} - H$
- $\sqrt{3} - L$
- $2D + \delta - 7 \times 7 + 3D$

Labels: [a'], [a]

Fig. 1 Phase diagram of Si(111)-Pb surface. Abscissa represents the deposited amount of Pb. The coverage may be reduced from the deposited amount in high temperature range. Horizontal chain lines ($\approx 240^\circ$ and $\approx 360^\circ\text{C}$) represent the temperatures where irreversible transitions occur from the lower to higher temperature phase by annealing. Incommensurate phase α is formed by the additional deposition of Pb on the $\sqrt{3}$ -L or $\sqrt{3}$ -H surfaces. The hatched region (250° - 280°C) represents phase transition between the α and α' phases.

the $(m/7, n)$ and $(m, n/7)$ reflections, where m and n are integers, are strong and the other 7×7 reflections become weak. The δ - 7×7 was found to be formed by the adsorption of alkaline metal or hydrogen atoms on the $\text{Si}(111)7 \times 7$. This indicates that the stacking-fault layer of the DAS structure[15] is left at the interface, and so the 2D-Pb(111) layer is influenced by the 7×7 periodicity.

Upon further deposition, three dimensional(3D-) Pb(111) islands of the bulk lattice parameter are formed on the 2D-Pb(111) layer (the Stranski-Krastanov growth mode).

The 2D-Pb(111) layer transforms irreversibly to $\sqrt{3}$ -L by heating beyond the lower chain line in the phase diagram into "M" range. At the same time, reflections from the δ - 7×7 structure disappear. This indicates the stacking-fault layer at the interface disappears.

Adsorption at High Temperature

When Pb is deposited on a substrate at about 400°C , "H" range in the phase diagram, domains of the $\sqrt{3}$ structure are formed and expanded. The 3D islands are not formed by further deposition. This is because the desorption rate is high in this temperature range. The $\sqrt{3}$ -H structure is stable in the temperature range between room temperature and "H" range. By heating beyond 500°C the desorption of Pb becomes remarkable and the surface structure returns to the 7×7 phase of the clean surface.

Adsorption at Intermediate Temperature

When Pb is deposited on a substrate at $240^\circ - 360^\circ\text{C}$, "M" range in the phase diagram, small domains are formed on terraces. Correspondingly, the 7×7 superlattice reflections become streaky in the RHEED pattern. However, no other extra spots appear in the pattern. Thus, we labeled the structure of the domains formed as "1x1". Upon further deposition, the 7×7 superlattice reflections weaken and streaks from the $\sqrt{3}$ structure appear. This structure is labeled as $\sqrt{3}$ -L as distinct from the $\sqrt{3}$ -H structure. The intensities of the extra streaks from the $\sqrt{3}$ -L structure decrease on cooling below 200°C , unlike the $\sqrt{3}$ -H structure. This is characteristic of the $\sqrt{3}$ -L structure.

When Pb of about 1 ML was deposited at 240°C , low temperature in the "M" range, the RHEED pattern was seen to be changed from the 7×7 to "1x1" immediately after the deposition and the extra streaks due to the $\sqrt{3}$ -L structure appeared a few minutes later. This indicates the low mobility of the surface atoms and that it requires time to form the $\sqrt{3}$ -L structure at this temperature.

By heating beyond 360°C , the upper chain line in the phase diagram, into the "H" range, the $\sqrt{3}$ -L structure transforms irreversibly to the $\sqrt{3}$ -H structure. The intensities of the $\sqrt{3}$ streaks once weaken on the way of the phase transition, where the coverage of Pb may be reduced.

Incommensurate Structures

Figure 2a shows a RHEED pattern from a $\sqrt{3}$ -L surface (190°C) which was prepared by the deposition of Pb of 11/7 ML at 240°C and annealed at 330°C . Figure 2b shows a RHEED pattern after the additional deposition of Pb of 5/7 ML at 190°C . Intense streaks appear as indicated by the large arrow. The r value of the streak is not $2/3$ as expected for the $\sqrt{3}$ structure but 0.65. This indicates clearly that the structure is not $\sqrt{3}$ but incommensurate with the substrate surface, as reported[8]. The r value is close to the value obtained by Grey et al. from X-ray diffraction; $r=0.652$ [7]. This streak corresponds to the $(1,0)$ reflection of the two-dimensional Pb(111) layer (α layer) with the orientation of $\text{Pb}[110]//\text{Si}[211]$. The α layer is rotated by 30° about the surface normal from the 2D-Pb(111) layer formed by the deposition in "L" range. The Pb-Pb distance is contracted by 2.6% from that of the bulk(111) plane. The $(2,0)$ streak is seen at $r=1.30 (= 2 \times 0.65)$ as indicated by a medium-sized arrow. The intensity is much weaker than that of the $(1,0)$ streak. Furthermore, streaks are seen

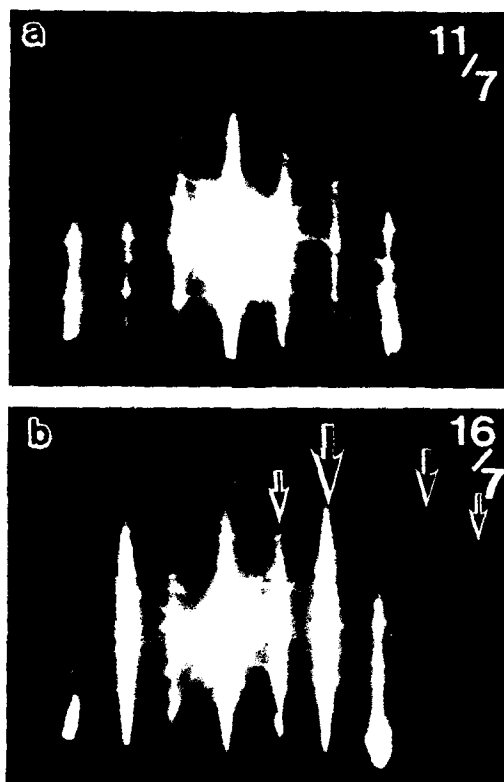


Fig.2 RHEED patterns from (a) v_3 -L surface and (b) α surface. The α structure was formed by the additional deposition of Pb of 5/7 ML on the v_3 -L surface at 190°C. Note the shift of the position of the streaks from (a) to (b): The r value of the streak indicated by a big arrow is not 2/3 but 0.65. The α is an incommensurate structure.

at $r=0.35$ ($\approx 1-0.65$) and 1.65 ($\approx 1+0.65$) as indicated by small arrows.

The α structure is also formed by additional deposition on the v_3 -H structure in "L" range. Figure 3a is a RHEED pattern from a v_3 -H surface at 180°C. The surface was prepared by annealing at 450°C of the surface having the 2D-Pb(111) layer with 3D islands by the deposition of Pb of 2 ML at 190°C. By the deposition of Pb of 5/7 ML on the v_3 -H surface, weak diffuse streaks due to the α structure appear as indicated by an arrow in fig.3b. The streaks from the α structure become sharper in a RHEED pattern taken 10 minutes after the deposition as shown in fig.3c. The streaks from the 3D-Pb(111) islands are also seen at $r=1.10$, as indicated by the large arrow in fig.3c. Thus, the 3D islands grown on the α layer have a lattice parameter of the bulk Pb crystal and the epitaxial orientation is parallel to the substrate, which is the same as that of the 3D islands grown on the 2D-Pb(111) layer. It takes a long time to form the α layer and the 3D islands at 180°C. The formation of the 3D islands on the α layer is directly seen in REM images of fig.4. Figures 4a and 4b are REM images from an α surface and the same surface after the deposition of Pb of 9/7 ML at 180°C,

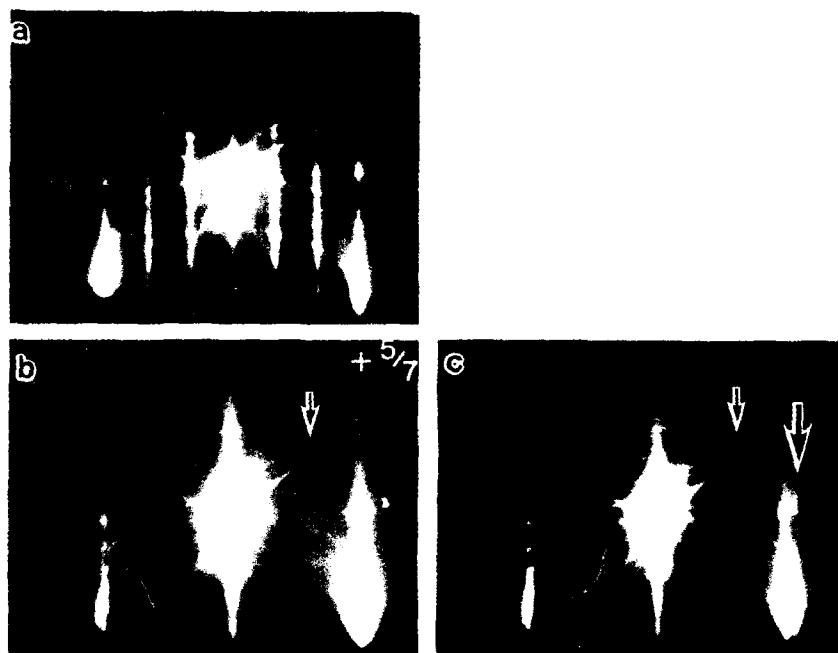


Fig.3 RHEED patterns from (a) $v3-H$ surface; (b) surface immediately after deposition of 5/7 ML of Pb on the $v3-H$ surface; (c) 10 min. after deposition. Substrate temperature was 180°C . Streaks from α layer appear as indicated by small arrows in (b) and (c). The streaks become sharper from (b) to (c). The streaks from the 3D-Pb(111) islands are also seen in (c), as indicated by the large arrow.

respectively. 3D-Pb(111) islands grown on the α surface are seen to be dark in fig.4b.

The α structure was changed to another incommensurate structure labeled as α' by heating beyond $250-280^{\circ}\text{C}$. Fig.5a is a RHEED pattern from an α surface at 190°C . The streak from the α structure indicated by an arrow is clearly seen at $r=0.654$. By heating up to 290°C , the streak indicated by an arrow became broad and weak and its position shifted to $r=0.625$ as shown in fig.5b. The diffuse streaks seen in the RHEED pattern from the α' structure are similar to those from a high temperature phase of Ge(111)-Pb surface[16]. The r value (0.625) of the diffuse streak indicated by the arrow in fig.5b corresponds to the reciprocal distance of $q = (2\pi/d) = 20.3 \text{ nm}^{-1}$. The distance is close to $20.5 - 20.6 \text{ nm}^{-1}$ which has been reported for the position of the first diffuse rod seen in the RHEED pattern from the high temperature phase of Ge(111)-Pb surface[16]. Figures 5c, 5d and 5e are the RHEED patterns which were taken immediately, and after 1 min. and 5 min., respectively, after cooling to 195°C . The streak became sharp and strong again and the position returned to that of the α structure gradually. The r values for the streaks shown in figs.5c, 5d and 5e are 0.624, 0.637 and 0.645, respectively. The position (r value) and the width of the streak changed gradually in several minutes. This is due to the low mobility of the Pb atoms at 195°C .

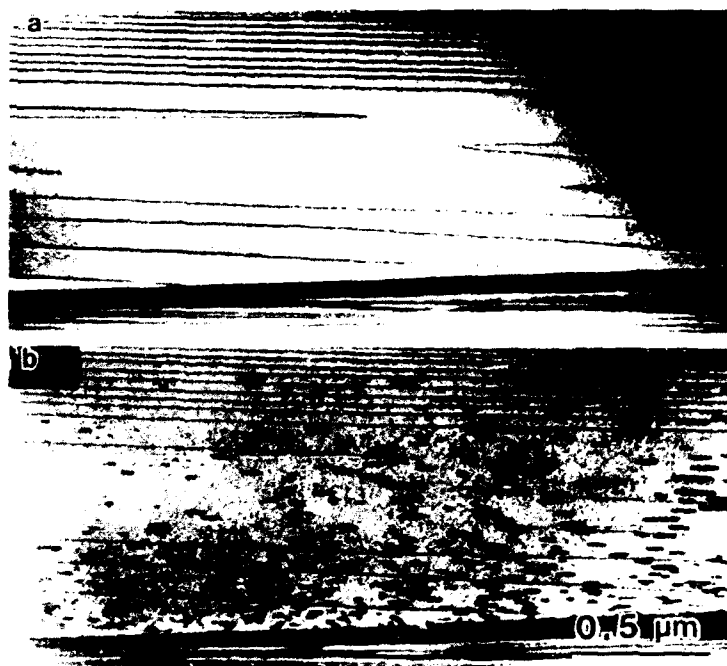


Fig.4 REM images from (a) α surface and (b) same surface after deposition of Pb of 9/7 ML at 180°C. The 3D islands are seen to be dark in (b). Images are foreshortened by 1/50 in the vertical direction due to the glancing exit of imaging electrons.

DISCUSSION

It is readily apparent from RHEED that the α layer has an incommensurate structure relatively to substrate surface, as previously reported by Grey et al.[7], the present authors[8] and Ganz et al.[10]. The framework of the α structure is a rotated (111) layer adsorbed on the surface, $\text{Pb}[1\bar{1}0]//\text{Si}[2\bar{1}1]$, from the parallel orientation ($\text{Pb}[1\bar{1}0]//\text{Si}[1\bar{1}0]$). Since the r value of the streak due to the α structure was 0.64 – 0.65, the α layer was found to be contracted by 1 – 3% from the bulk. The large contraction of 5% is needed to form the commensurate $\sqrt{3}$ ($\sqrt{3}\alpha$) structure on this model, where the interatomic distance between Pb atoms is compressed to be half of the $\sqrt{3}\times\sqrt{3}$ unit mesh length. Hence, the incommensurate structure α may be formed to relieve the elastic strain energy in the Pb layer. The compression of 1 – 3% is smaller than 4% for the 2D-Pb(111) layer formed on δ -7 \times 7 in "L" range. A structure similar to the α structure but having the $\sqrt{3}$ periodicity was reported to be formed on the Ge(111)-Pb surface[16], where the Pb layer is contracted by only 1.0% to form a commensurate $\sqrt{3}$ structure.

The intensity of the (2,0) streaks from the α layer was much weaker than that of the (1,0) streak as shown in fig.2b. This indicates that Pb atom positions in the α layer are modulated from those of the uniformly contracted layer by the substrate corrugation potential. The streaks at $r=0.35$ and 1.65 seen in fig.2b may be caused by the modulation, as has been suggested for the explanation of the appearance of the extra spots around the (1/3,1/3) in LEED by Ganz et al.[10]. However, the RHEED intensi-

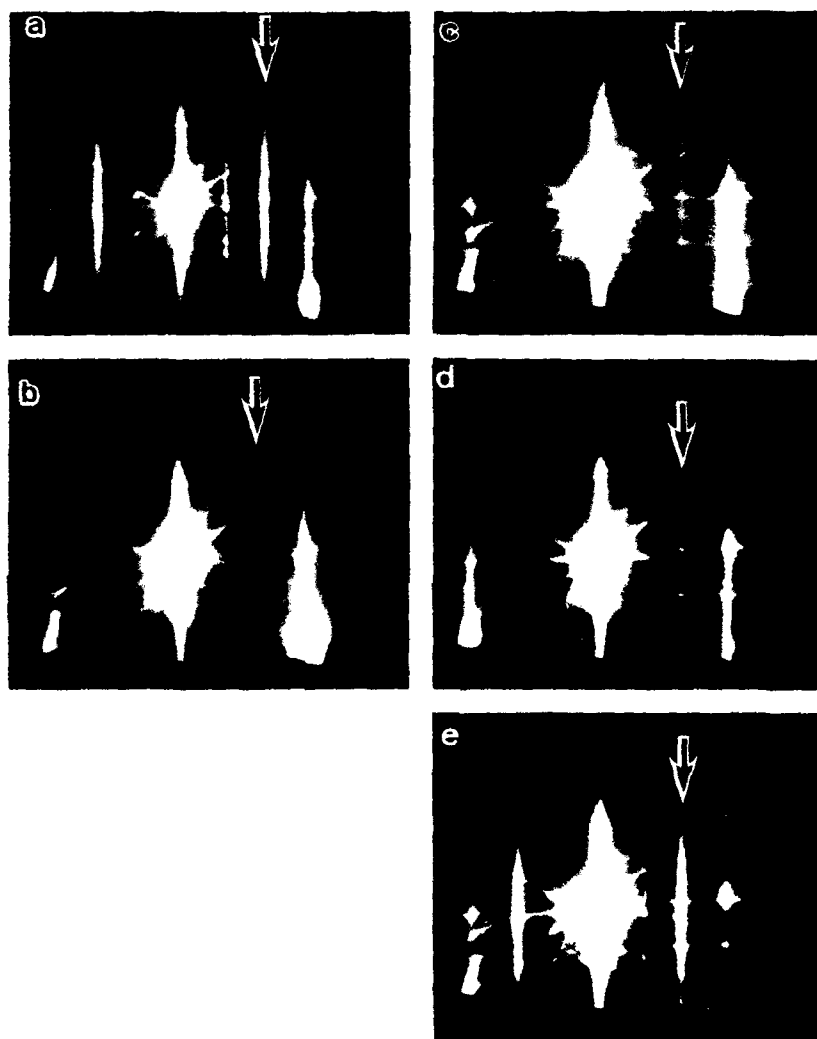


Fig.5 RHEED patterns from (a) α surface at 190°C ; (b) α' surface after heating to 290°C ; (c) immediately, (d) 1 min. and (e) 5 min. after cooling to 195°C . Note the change of the intensity and position of the streak indicated by arrows. The r values in (a) to (e) are 0.654, 0.625, 0.624, 0.637 and 0.645, respectively.

ties of the streaks as well as LEED intensities should be much influenced by dynamical diffraction effects. Thus, further study using X-ray diffraction or transmission electron diffraction in which the diffraction intensity can be treated using the kinematical approximation is needed for analysis of the modulation of the α layer.

The density in the α layer was reported to increase as the coverage increased, until the 3D island formation began[10]. Although the r value observed was scattered in the range of 0.64 – 0.65, such a relation was not seen in the present observation: The r value did not decrease by additional deposition on the α surface.

It was noticed that the r value of the streaks from the α structure increased gradually in several minutes after cooling from the α' structure. The structure change to reach on equilibrium required several minutes. The slow structure change was also seen in the formation of the $\sqrt{3}$ -L structure at 240°C and the formation of the α layer and 3D islands at 180°C. These times are due to the low mobility of surface atoms at low temperature.

The diffuse streaks seen in RHEED patterns from the α' structure of Si(111)-Pb surfaces were similar to those from the high temperature phase on Ge(111)-Pb surface. The latter phase has been reported to be 2D liquid of Pb on Ge(111) surface by Ichikawa[16]. Although the lattice parameter for Ge and Si substrates is different by 5%, the position of the first diffuse streak in RHEED patterns was much the same. Thus, it appears that the α' phase is 2D liquid on the Si(111) surface and that the phase transition from the α to the α' phase is 2D melting transition. Although the structure of the α' layer has not yet been analyzed, correlation lengths of the atoms in the Pb layers on Si and Ge substrates are similar.

It has been reported in our previous papers[8,9] that the $\sqrt{3}$ structure is classified into the $\sqrt{3}$ -L and $\sqrt{3}$ -H structures. Recently Ganz et al.[10] reported two kinds of the $\sqrt{3}$ structures on annealed surfaces which were named $\sqrt{3}$ -standard ($\theta=1/3\text{ML}$) and $\sqrt{3}$ -mosaic($\theta=1/6\text{ML}$) phases. Since the $\sqrt{3}$ -mosaic phase has been reported to be stable between RT and 600°C, the $\sqrt{3}$ -mosaic structure is considered to correspond to the $\sqrt{3}$ -H. The $\sqrt{3}$ -standard phase, then, appears to be the $\sqrt{3}$ -L. However, they reported also 1x1 overlayer of Pb in the range of coverage between $1/3 - 1 \text{ ML}$ on annealed surfaces. We also observed the "1x1" phase, but the domains of the "1x1" phase were formed at the initial stage of the deposition before the formation of the $\sqrt{3}$ -L structure. No contrast for such domains were seen in REM images after the $\sqrt{3}$ -L structure covered the whole surface. Since the displacement of the atoms in the $\sqrt{3}$ -L structure occurs to weaken the extra streaks upon cooling below 200°C, there is a possibility that the 1x1 overlayer in their observation performed at room temperature corresponds to the $\sqrt{3}$ -L phase at low temperature.

CONCLUSIONS

The structure changes caused by the deposition of lead on the Si(111)7x7 surface at different substrate temperatures, by heat treatment and by additional deposition on the annealed surface are summarized as a "phase diagram". The 2D-Pb(111) layer is formed on the δ -7x7 interface in "L" range. It is a metastable structure with a stacking-fault layer remaining at the interface and it attains lattice matching to the 7x7 unit mesh by a compression of 4.0%. The "1x1" and $\sqrt{3}$ -L structures are formed in "M" range, and the $\sqrt{3}$ -H is formed in "H" range. The 2D-Pb(111) layer transformed irreversibly to the $\sqrt{3}$ -L by annealing in "M" range, and the $\sqrt{3}$ -L transformed irreversibly to the $\sqrt{3}$ -H by annealing in "H" range. Incommensurate structure of rotated and 1-3 % compressed Pb(111) monolayer (the α) is formed by the additional deposition on the $\sqrt{3}$ -L and $\sqrt{3}$ -H surfaces in "L" range. The phase transition between the incommensurate structures of the α and the α' occurs at about 250°-280°C. By further deposition of Pb on the 2D-Pb(111) layer or the α layer, the 3D-Pb(111) islands of the bulk lattice parameter grow in the parallel orientation (the Stranski-Krastanov growth mode).

REFERENCES

1. D.R.Heslinga, H.H.Weitering, D.P.van der Werf, T.M.Klapwijk and T.Hibma, *Phys.Rev.Lett.* **64**, 1589 (1990).
2. P.J.Estrup and J.Morrison, *Surface Sci.* **2**, 465 (1964).
3. M.Saitoh, K.Oura, K.Asano, F.Shoji and T.Hanawa, *Surface Sci.* **154**, 394 (1985).
4. G.LeLay, J.Peretti, M.Hanbücken and W.S.Yang, *Surface Sci.* **204**, 57 (1988).
5. H.Yaguchi, S.Baba and A.Kinbara, *Appl.Surface Sci.* **33/34**, 75 (1988).
6. G.Quentel, M.Gauch and A.Degiovanni, *Surface Sci.* **193**, 212 (1988).
7. F.Grey, R.Feidenhans'l, M.Nielsen and R.L.Johnson, *J.Phys.(Paris) Colloq.* **C7**, 181 (1989).
8. Y.Tanishiro, M.Fukuyama and K.Yagi, in *Abstract of 3rd.Int.Conf. on Structure of Surfaces(ICSOS III)*, (Milwaukee, 1990) PWM1.
9. Y.Tanishiro, M.Fukuyama and K.Yagi, in *The Structure of Surfaces III*, edited by S.Y.Tong, M.A.Van Hove, K.Takayanagi and X.D.Xie (Springer-Verlag, 1991)p.623.
10. E.Ganz, I.S.Hwang, F.Xiong, S.K.Theiss and J.Golovchenko, *Surface Sci.* **257**, 259 (1991).
11. K.Takayanagi, K.Kobayashi, K.Yagi and G.Honjo, *J.Phys.* **E11**, 441 (1978).
12. H.Daimon and S.Ino, *Surface Sci.* **164**, 320 (1985).
13. A.Ichimiya and S.Mizuno, *Surface Sci.* **191**, L765 (1987).
14. Y.Horio, A.Ichimiya, S.Kohmoto and H.Nakahara, *Surface Sci.* **257**, 167 (1991).
15. K.Takayanagi, Y.Tanishiro, S.Takahashi and M.Takahashi, *Surface Sci.* **164**, 367 (1985).
16. T.Ichikawa, *Solid State Commun.* **46**, 827 (1983); **49**, 59 (1984).

THE SURFACE STRUCTURE OF OXIDES STUDIED WITH REFLECTED HIGH ENERGY ELECTRONS

Tung Hsu
P.O. Box 58364, Salt Lake City, Utah 84158-0364, U.S.A.

ABSTRACT

Reflected high energy electrons have been employed for studying surfaces of single crystal oxides in real and reciprocal space. The techniques used include reflection high energy electron diffraction (RHEED), reflection electron microscopy (REM), scanning reflection electron microscopy (SREM), and reflection electron energy loss spectroscopy (REELS). These methods have provided much information on surface morphology as well as the atomic and electronic structure of MgO, α -Al₂O₃, α -Fe₂O₃, SiO₂, TiO₂ (rutile), and ZnO single crystals. Analyses for chemical composition and electronic states are possible using SREM and REELS. Surfaces terminating at different atomic layers of large-unit-cell materials have been determined in REM images and also in REELS data obtained under REM and SREM. Surface modification due to bombardment with the incident electron beam is pronounced on some oxide surfaces. These processes have been investigated with the REM imaging and REELS techniques.

INTRODUCTION

Most oxides are good insulators. Consequently, surface charging is an obstacle when an electron beam is employed for the study of oxide specimens. Coating the surface with a conducting material is acceptable only when the desired information is not to be obscured by coating, as in the case of conventional SEM for morphological data. Low energy electron diffraction (LEED) investigations of oxide surfaces have been published but are not very extensive. Crystalline data, as obtained from the averaged diffraction intensity distributions in LEED patterns. In the case of the recent additions to the arsenal of surface techniques, scanning tunneling microscopy (STM) requires good electrical conductivity of the specimens, and while atomic force microscopy (AFM) is good for insulators and has been applied to the study of oxide surfaces, its lateral spatial resolution is somewhat limited in comparison with resolution of electron microscopy. It is therefore worthwhile to examine closely what REM, a 60-year-old technique [1], can do in investigating the atomic structure of oxide surfaces.

It should be noted that this paper considers only the surfaces of bulk oxide single crystals. The initial stages of oxidation of metals and semiconductors is of vital importance in materials research and has been investigated with the REM and RHEED methods extensively, but will not be discussed here. Interested readers should consult the many publications by Yagi and other workers [2, 3, 4, 5].

IMAGING CRYSTAL SURFACES USING FORWARD SCATTERED HIGH ENERGY ELECTRONS

Figure 1 illustrates a comparison of the three techniques generally regarded as "surface techniques" by workers in different fields: In SEM, the secondary electron (SE) or back scattered electrons (BSE) are collected by the detector to form the image of the specimen. Since SE and BSE are emitted from a surface layer of a few tens of nanometers, SEM is surface-sensitive.

The energy spectrum and the angular distribution of the scattered electrons depend strongly on the incidence angle of the primary electron beam. By choosing a small incidence angle and adding an energy filter in front of the detector to allow only these electrons with energies slightly lower than that of the primary electrons to be detected, Wells et al have accomplished the low-loss SEM [6]. These low-energy-loss electrons originate from a surface layer only a few nanometers thick, thus the technique represents an improvement in surface sensitivity.

If low-loss is good for the surface sensitivity, wouldn't no-loss be even better? Obviously, adjusting the filter to detect only the zero-loss electrons would not be a good way of no-loss-EM since the intensity would be very low. In fact, no-loss scattering can be easily achieved if the specimen is crystalline: Just detect the Bragg diffracted electrons from the surface. These electrons are diffracted from only a few atomic layers close to the surface into a well-defined direction and they can be detected using a small aperture which filters out other

diffracted and diffuse scattered electrons. Since they are diffracted by the periodic structure of the specimen, these elastically scattered electrons carry information about the crystalline structure of the surface in addition to morphological information.

Diffracted electrons are obviously not all elastic, but in most of this paper, we take the approximation of elastically diffracted beams, except when discussing REELS.

The combined REM and RHEED techniques, as performed in an electron microscope, have been explained previously [7]. It is sufficient to state here that the technique is similar to dark field (DF) TEM except that the specimen is semi-infinite and the surface to be observed is oriented in the microscope to make a small angle with respect to the incident electron beam.

This particular geometry presents some difficulty in microscope operation, but after learning the relative movements of the beam and the specimen, the operator can usually secure good diffraction conditions and obtain good RHEED patterns and REM images within a few minutes.

For reasons not yet completely understood, charging is not a problem even for oxide specimens. One may sometimes experience charging, as evidenced by drifting or even flickering of the beam during the initial alignment stage, but a stable RHEED pattern and REM image can always be obtained after good diffraction conditions have been secured. Using reduced beam current is helpful in reducing the instability of the beam due to charging. Mica is the only insulator that has not been successfully imaged under REM because of charging. All other insulators tried were stable under the electron beam, at least under the REM condition.

2. SURFACE MORPHOLOGY AND CRYSTALLINE STRUCTURE

When the surface is rough, its morphology can usually be intuitively interpreted from the REM images, similar to the interpretation of a low angle BES image obtained with an SEM. The paths of the incident and diffracted electrons can be traced as straight lines which may be blocked by surface height variations. The image thus consists of dark "shadows" in addition to well-illuminated bright areas [8]. An image of a polished and annealed α - Al_2O_3 is shown in Figure 2, where the faceted surfaces are shown in areas of different degrees of brightness.

Fig. 2. This image of a polished and annealed α - Al_2O_3 shows the (1120) facets (bright) and the (2243) (gray) facets.

0.2 μm

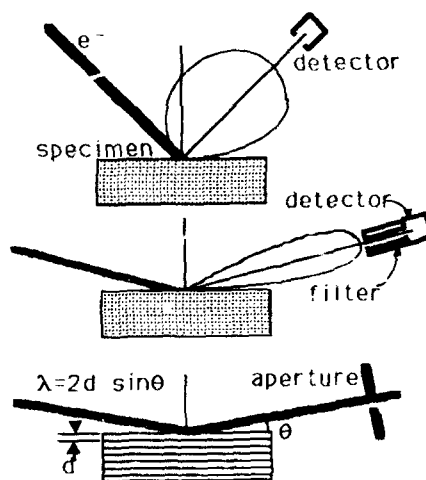


Fig. 1. From SEM (top) to low-loss SEM (middle) to REM (bottom). Surface sensitivity increases from top to bottom.

The situation is complicated by the phenomenon of refraction when the electron beam crosses the crystal/vacuum interface at a small angle. Bright or dark contrast may be reversed by very slight translation of the objective aperture or specimen/beam tilt when the surface of a single crystal specimen consists of facets of slightly different orientations [9, 10]. The contrast in Figure 2, for example, can be reversed with a light translation of the objective aperture.

The diffraction contrast in REM, which depends on the reflected electron intensities from crystalline surfaces, is similar to that in TEM(DF). It should be noted that the REM image is a projection of a generally 3-dimensional surface, where the direction of projection is usually no more than 5° above the surface. Therefore, the REM image is foreshortened by a factor of 20 to 50 along the beam direction. This foreshortening effect causes the image appearance to change markedly when the surface is rotated while maintaining the Bragg condition.

The index of the spot in the RHEED pattern used to form the REM image gives information about the direction from which the specimen surface is viewed. Since the viewing point is from a direction opposite to the reflected beam, the crystalline index of a straight line or a flat area on the surface can be determined from the index of the reflected beam used for imaging. Consequently, accurate measurements of the surface features are possible without depending upon the goniometer readings of the specimen holder. Protruding features present a complication, but using computer simulation it is possible to reconstruct the three-dimensional structure on the surface [11].

In Figure 2, the regular micro-facetting are shown as bright or dark parallelograms. Through calculation and computer simulations these facets are indexed as (1120) and (2243).

ATOMIC STEPS AND DEFECTS

The ability to detect atomic steps with high spatial resolution and high contrast is one of the most important features of REM. Images of atomic steps have been recorded on all specimens examined with the REM technique. In addition to revealing the fine details of the crystal surfaces, these features are also ideal for the development of contrast theory [12 - 20]. Step heights have been determined in simple crystals such as Si [16], Au [20, 21], Pt [18, 20, 22, 24], and GaAs [23, 24]. For oxides, step height measurement is not always possible due to the more complicated unit cells, although most of the time it is reasonably certain that the observed steps are "one or a few" atom layers high and thus called "atomic steps." The term "one-atom-high steps" is strictly reserved for steps known to be of only one atomic layer high.

Dislocations intersecting the surface are often associated with the surface steps. This feature has been used to determine the step height and the Burger's vector. The step height is equal to the Burger's vector projected in the surface normal. As illustrated in Figure 3 an intersecting dislocation on the (111) surface of an fcc metal or Si is associated with a one-atom-high step (Burger's vectors b1, b2, and b3) or is not associated with a step at all (Burger's vector b4).

For the (110) surface of crystals with the zinc blende structure, the situation is more complicated. Of the 6 most likely Burger's vectors, one leaves no steps, one leaves a two-atom-high step and the other four leave one-atom-layer steps. Since a two-atom-high step shows stronger image contrast than the one-atom-high step, when compared side by side, it was possible to determine some of the steps on the cleaved GaAs(110) surface being one-atom-high [23, 25].

The complicated structure of $\alpha\text{-Al}_2\text{O}_3$ and its dislocation system make it impossible to determine the step height as are the cases for Si(111), Pt(111), and GaAs(110). For example, the height of the step terminating at a dislocation as shown in Figure 4a has not been determined [26]. Using additional information, the regularly distributed steps on $\alpha\text{-Al}_2\text{O}_3$ (1102) have been determined to be three oxygen layers (Figure 4b) [27]. This is in agreement with result from AFM study [28].

Layer-by-layer sublimation or growth provides further evidence for surface steps being one-atom-high. REM images recorded in real time show steps moving across the surface of Si as the crystal grows or evaporates at the steps [16, 29]. These in situ experiments are more difficult to perform on oxide crystal surfaces because of the much higher temperature required. It is also not known if the compound oxide crystals evaporate one atom layer at a time. Recently, Wang et al. have shown step movements due to sublimation by in situ heating of MgO up to 1500°K [30] and $\alpha\text{-Al}_2\text{O}_3$ up to 1670°K [31].

For MgO [30, 32 - 35], ZnO [35, 36], and other oxides of simpler structures, atomic steps

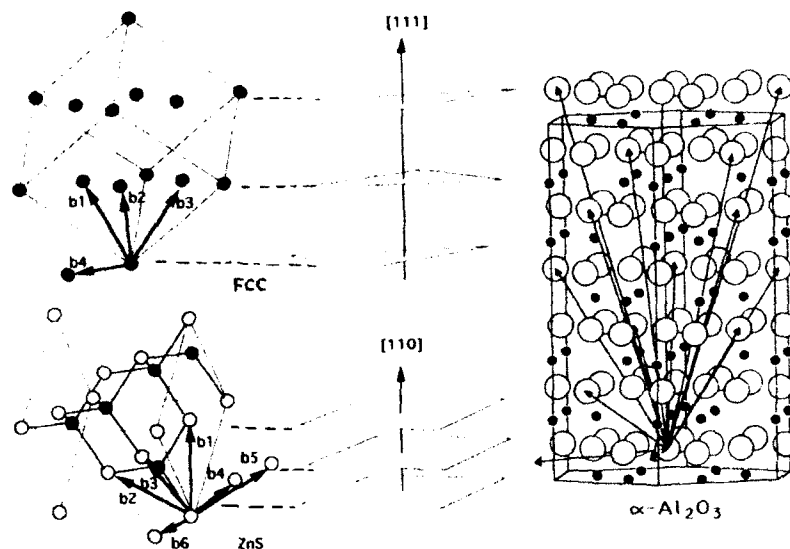


Figure 3. The height of a surface step at a dislocation is equal to the projection of the Burger's vector in the surface normal. Models of fcc and zinc blend structures show that the dislocations intersecting the surface can produce steps of zero, one, or two atomic layers. For the case of $\alpha\text{-Al}_2\text{O}_3$, the dislocation system is much more complicated and usually it is not possible to determine the step heights from the observation of the dislocations.

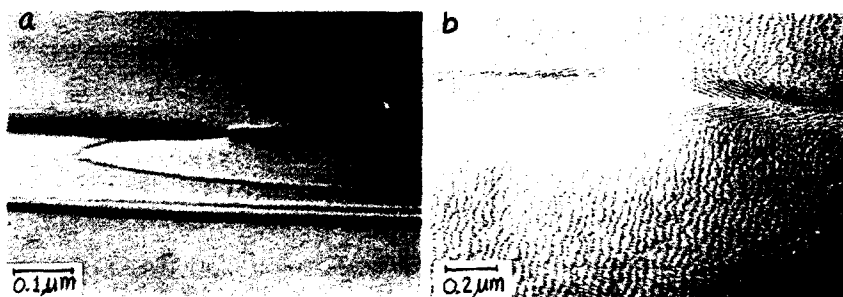


Fig. 4. Step and dislocation on. (a) The step on $\alpha\text{-Al}_2\text{O}_3(0001)$ ends at a dislocation, but the step height is not known. (b) These steps on $\alpha\text{-Al}_2\text{O}_3(1102)$ have been determined to be 0.35 nm, equivalent to 3 layers of oxygen atoms.

with the lowest contrast in the REM images are very likely to be one-atom-high. The distribution of these steps has been observed and on the basis of which dynamic processes and other surface reactions have been reduced.

Some encouraging results have come from the computer simulation of REM images of surface dislocations of different Burger's vectors [37, 38]. It will be useful if this kind of analysis can be further extended to oxide crystals. Another new development is reflection electron holography [18, 20], in which the surface step height on GaAs(110) has been measured based on the mean inner potential of the crystal and the phase shift of reflected electron waves [24].

In general, step height cannot be determined by visual inspection of the REM image; careful analysis is required, especially in the case of complicated structures such as many oxides. It is unlikely that an accurate method of determining the surface step height will be found that is completely independent of knowledge of the specimen. This is another good example of "The more you know about your specimen, the more accurate is your analysis. If you know everything about your specimen, then your analysis is 100% accurate [39]."

RECONSTRUCTIONS

The $\alpha\text{-Al}_2\text{O}_3(11\bar{2}0)$, $\text{MgO}(111)$, and the TiO_2 (rutile) surfaces have been found to be reconstructed [40, 32, 41]. An REM image of the reconstructed surface of $\alpha\text{-Al}_2\text{O}_3(11\bar{2}0)$ is shown in Figure 5. The interesting nature of these reconstructions surviving air exposure has not been fully explored. Moreover, while no explanation of the origin or atomic structure of these reconstructions has been offered, it should be pointed out that since these experiments were not conducted in an extremely clean or UHV environment, the possibility of adatoms forming the observed fringes should not be completely ruled out. Etching by water molecules, possibly enhanced by electron beam exposure has been reported on the $\alpha\text{-Al}_2\text{O}_3$ surfaces [43, 44, 45]. How these reaction could affect the reconstructions remains to be investigated.



Fig. 5. Reconstructed $\alpha\text{-Al}_2\text{O}_3(11\bar{2}0)$ showing 1.7 nm fringes. Arrows point to irregularities which are probably steps, out-of-phase boundaries, or else.

The image in Figure 5 shows clearly resolved fringes 1.7 nm apart. The theoretical limit of resolution of REM is estimated to be about 0.7 nm. Experimental results have shown about 0.9 nm on a regularly stepped Au surface [21]. Since lattice resolution depends only on the stability of the instrument, it is known in TEM that, by using a sufficiently large objective aperture, atomic lattice spacing would be resolved. However, the situation in REM is different, because the specimen surface has a very large depth of field. In order to record an image showing a wide region under the same focal condition, the objective aperture must be small. A larger aperture may be used to include two or more superlattice spot for forming the superlattice image, but if one used an even larger aperture to include two principal diffraction spots, then the in-focus region in the REM image becomes very narrow.

This situation is illustrated in Figure 6: A small aperture placed at spot 1 or 2 produces image 1 or 2. When both spots are selected with a large aperture, the image is a superposition of the two single aperture images. The small depth of field makes only a narrow region in focus, within which the lattice image is shown, but the rest of the image gives no useful information. This has been demonstrated on a high voltage electron microscope [46].

TERMINATION IN A UNIT CELL

Since REM is sensitive to one-atom-high steps on a crystal surface and monolayers of adatoms or reconstructed atoms, it is expected that, for a single crystal consisting of more than one species of atoms, it should also be possible to differentiate which species of atoms are exposed on the surfaces. To accomplish this we depend on two types of information: the contrast in the REM image as a function of the diffraction condition, and the RFEIS data.

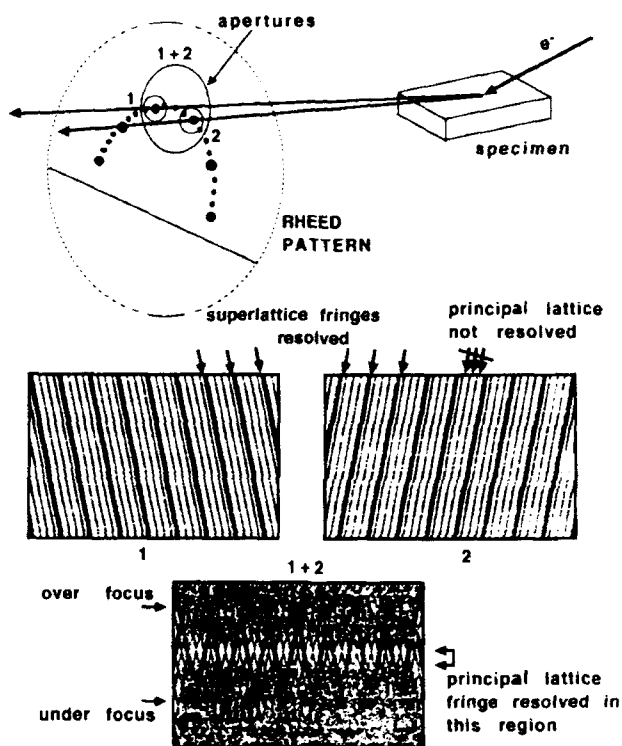


Fig. 6. Lattice resolution is possible if the depth of field is sacrificed. For the purpose of illustration, the unresolved principal lattice is shown in images 1 and 2. The image 1+2 is in fact not a simple addition of image 1 and image 2. This illustration only indicates that including two principal diffraction spots is equivalent to simultaneously observing the surface from two directions.

The REM image recorded under the resonance condition is particularly sensitive to the topmost layer of atoms, because there is at least one resonance beam propagating parallel to the crystal surface. Therefore, even if the specimen is a single crystal, contrast in the REM image may differ from area to area provided that these areas are terminated at different layers of the unit cell. This phenomenon has been observed on $\alpha\text{-Al}_2\text{O}_3$ [26].

The REELS analysis under the resonance condition allows the resonance beam to interact with the topmost layer of atoms and it therefore carries chemical information about these atoms. It has been found that REELS could differentiate oxygen-terminated from aluminum-terminated surfaces on $\alpha\text{-Al}_2\text{O}_3$ [47]. Likewise, REELS has given information that the $\text{MgO}(111)$ surface is likely to be Mg-terminated [42].

BEAM INDUCED DAMAGES/REACTIONS

Although the various oxide crystals are stable under the REM imaging condition, the contrast does change with time to different degrees. Other than the step movement due to sublimation at

high temperature, as mentioned previously, there were other contrast changes recorded [27, 34, 48, 49, 50]. The possibility of combined contamination, beam induced damage, and chemical reactions makes it difficult to determine the prevailing mechanism. Since none of the observations reported were performed under UHV or other well controlled environment, definitive conclusions are difficult to make.

CONCLUSION

The REM technique has been shown to be useful in imaging oxide surfaces. It is possible to measure surface features such as facet orientations, step heights, etc., quantitatively. Surface processes have been observed from step and dislocation distributions and their motion. Segregation of impurity atoms, terminations within unit cells, beam-induced damage, etc., can be observed with REM imaging with added information provided from REELS analysis. Some new reconstructions stable after air exposure have been found.

In situ experiments of REM in UHV electron microscopes have been applied to the initial stage of oxidation process on Si and other materials. Continued research in this direction, as well as better controlled environments for bulk crystals, should provide even more insight into the surfaces of oxide crystals. The true nature of some unexplained contrast changes and the structure and energy calculation of the reconstructed α - Al_2O_3 and MgO surfaces also demand further investigation, preferably under UHV.

ACKNOWLEDGMENT

Partially supported by the NSF Grant DMR-8717376, the University of Utah, Fritz-Haber-Institut of Max-Planck-Gesellschaft in Berlin, and Institute of Physics, University of Oslo. This work includes result from many years of collaborated research with Dr. Y.T. Kim, now at Kyonggi University, Rep. of Korea. The author thanks Union Carbide Corp. for providing the α - Al_2O_3 specimens, Ms. Nancy Blachman of Variable Symbols for her help in Mathematica programing and Drs. L.-M. Peng, Z.L. Wang, and D.J. Smith for critically reading the manuscript.

REFERENCES

1. E. Ruska, Z. Physik, 83: 492 (1933).
2. J. Beauvillian, A. Clavier, and B. Jouffrey, J. Crystal Growth, 64, 549 (1983).
3. H. Kahata and K. Yagi, Surface Sci., 220, 131 (1989).
4. N. Shimizu, Y. Tanishiro, K. Kobayashi, K. Tagayanki, and K. Yagi, Ultramicroscopy, 18, 453 (1985).
5. Y. Uchida and G. Lehmppuhl and R. Imbihl, Surface Sci., 234, 27 (1990).
6. O.L. Wells, A. Boyde, E. Lifshin, and A. Resanowich, in "Scanning Electron Microscopy" (McGraw-Hill, New York, 1974) pp. 139-150, 60-179.
7. T. Hsu, Microscopy Research and Technique, 20, 318 (1992).
8. M.E. Haine and W. Hirst, British J. Appl. Phys., 4, 239 (1953).
9. T. Hsu and G. Lehmppuhl, Ultramicroscopy, 27, 359 (1989).
10. T. Hsu and S.R. Nutt, in "Materials Problem Solving with the Transmission Electron Microscope", eds. L. W. Hobbs, K. H. Westmacott, and D. B. Williams, Materials Research Society, pp. 387-394 (1986).
11. T. Hsu and Y.T. Kim, Ultramicroscopy, 32, 103 (1990).
12. Nan Yao and John. M. Cowley, Microscopy Research and Technique, 20, 413 (1992).
13. L.-M. Peng, J.M. Cowley, and T. Hsu, Micron and Microscopia Acta, 18, 3, 179 (1987).
14. T. Hsu and L.-M. Peng, Ultramicroscopy, 22, 217 (1987).
15. N. Osakabe, T. Matsuda, J. Endo and A. Tonomura, Jpn. J. Appl. Phys., 27, L1772 (1988).
16. N. Osakabe, Y. Tanishiro, K. Yagi, and G. Honjo, Surface Sci., 102, 424 (1981).
17. L.-M. Peng and J.M. Cowley, Acta Cryst., A42, 545 (1986).
18. N. Osakabe, Microscopy Research and Technique, 20, 457 (1992).
19. Y. Uchida and G. Lehmppuhl, Ultramicroscopy, 23, 53 (1987).
20. H. Banzhof, K.H. Hermann, and H. Lichte, Microscopy Research and Technique, 20, 450 (1992).

21. T. Hsu, *Ultramicroscopy*, 11, 167 (1983).
22. Tung Hsu and J.M. Cowley, *Ultramicroscopy*, 11, 239 (1983).
23. T. Hsu, S. Iijima, and J.M. Cowley, *Surface Sci.*, 137, 551 (1984).
24. N. Osakabe, in *Proceedings of the 5th Asia-Pacific Electron Microscopy Conference*, Vol. I, 78 (1992, Beijing).
25. L.-M. Peng, J.M. Cowley, and T. Hsu, *Ultramicroscopy*, 29, 135 (1989).
26. Y.T. Kim and T. Hsu, *Surface Sci.*, 258, 131 (1991).
27. Y.T. Kim and T. Hsu, *Surface Sci.*, 275, 339 (1992).
28. M.D. Antonik and R.J. Lad, *J. Vac. Sci. Technol. A* 10, 669 (1992).
29. A. V. Latyshev, A. L. Aseev, A.B. Krasilnikov, and S.I. Stenin, *Surface Sci.*, 227, 24 (1990).
30. Z.L. Wang, J. Bentley, E.A. Kenik, L.L. Horton, and R.A. McKee, *Surface Sci.*, 273, 88 (1992).
31. Z.L. Wang and J. Bentley, in *Mat. Res. Soc. Symp. Proc. Vol. 208*, pp. 155-160 (1991).
32. M. Gajdardziska-Josifovska, P.A. Crozier and J.M. Cowley, in "The Structure of Surfaces III", S.Y. Tong, M. A. Van Hove, K. Takayanagi, X.D. Xie, Eds., Springer-Verlag, Berlin, pp. 660-664 (1991).
33. P.A. Crozier, M. Gajdardziska-Josifovska and J.M. Cowley, *Microscopy Research and Technique*, 20, 426 (1992).
34. Z.L. Wang, *Materials Letters*, 6, 4, 105 (1988).
35. J. Liu and J.M. Cowley, *Ultramicroscopy*, 37, 50 (1991).
36. L.-M. Peng and J.T. Czernuszka, *Philos. Mag.*, A 64, 533 (1991).
37. L.-M. Peng, J.M. Cowley, *Micron and Microscopia Acta*, 18, 3, 171 (1987).
38. L.-M. Peng, J.M. Cowley, and T. Hsu, *Micron and Microscopia Acta*, 18, 3, 179 (1987).
39. This quote, which may not be precise, comes from a MAS Annual Meeting. The author regrets not being able to give the exact reference.
40. Tung Hsu and Yootae Kim, *Surface Sci.*, 258, 119 (1991).
41. L. Wang, J. Liu, and J.M. Cowley, in *Proceeding of the 50th Annual Meeting of EMSA*, pp. 1462-1463 (1992).
42. M. Gajdardziska-Josifovska, P.A. Crozier, and J.M. Cowley, *Surface Sci. Lett.*, 248, L259 (1991).
43. L.A. Bursill, Peng Ju Lin, and D.J. Smith, *Ultramicroscopy* 23, 223 (1987).
44. J. E. Bonevich and L. D. Marks, *Ultramicroscopy* 35, 161 (1991).
45. Y. Tomokiyo, T. Kuroiwa, and C. Kinoshita, *Ultramicroscopy* 39, 213 (1991).
46. H. Koike, K. Kobayashi, S.-I. Ozawa, and K. Yagi, *Jpn. J. Appl. Phys.*, 28, 861 (1989).
47. Z.L. Wang and J. Bentley, *Microscopy Research and Technique*, 20, 390 (1992).
48. L.-M. Peng and J.T. Czernuszka, *Surface Sci.*, 243, 210 (1991).
49. Z.L. Wang and A. Howie, *Surface Science* 226, 293 (1990).
50. Z.L. Wang, *J. Microscopy*, 163, 261 (1991).

APPLICATION OF Z-CONTRAST IMAGING TO OBTAIN COLUMN-BY-COLUMN SPECTROSCOPIC ANALYSIS OF MATERIALS

NIGEL D. BROWNING AND STEPHEN J. PENNYCOOK

Solid State Division, Oak Ridge National Laboratory, Oak Ridge, TN 37831-6030

ABSTRACT

Z-contrast imaging has been shown to be an effective method for obtaining a high-resolution image from a scanning transmission electron microscope (STEM). The incoherent nature of the high-angle scattering makes image interpretation straightforward and intuitive with the resolution limited only by the 2.2 Å electron probe. The optimum experimental conditions for Z-contrast imaging also coincide with those used for analytical microscopy, enabling microanalysis to be performed with the same spatial resolution as the image. The detection limits afforded by a parallel detection system for electron energy loss spectroscopy (EELS) allows column-by-column core-loss spectroscopy to be performed using the Z-contrast image to position the electron probe. Preliminary results from the study of $\text{YBa}_2\text{Cu}_3\text{O}_{7.8}$ illustrate the spatial resolution available with this technique and the potential applications for materials science.

INTRODUCTION

The electron microscope provides the ideal tool to investigate materials properties approaching the atomic scale. However, for conventional microscopic techniques, the spatial resolution of the analytical signal is an order of magnitude poorer than that of the image (~10–20 Å compared with 1–2 Å for a high-resolution image). Additionally, the coherent method of image formation in the conventional transmission electron microscope (CTEM) is very sensitive to operating parameters so that unknown structures cannot be directly interpreted in terms of atomic column locations and compositions.

The development of Z-contrast imaging [1] has facilitated a new approach to atomic-resolution microanalysis by the addition of a high-resolution imaging capability to the scanning transmission electron microscope (STEM), which is primarily used for nanometer scale microanalysis [2,3]. The VG HB501 UX dedicated STEM utilizes a focused 2.2 Å probe, which is scanned across the specimen while the integrated output from various imaging detectors is displayed on a TV screen, scanning at the same rate to form an image. This image formation process means that the spatial resolution of both the image and the analytical signal (when the scan is switched off) are limited only by the effective size of the probe. The detector arrangement in the STEM also has the advantage that the Z-contrast images can be recorded simultaneously with EELS and Energy Dispersive X-ray (EDX) signals.

EXPERIMENTAL TECHNIQUE

The Z-Contrast Image

As is illustrated in Fig. 1, the Z-contrast signal is collected from a high-angle annular detector. The annular detector collects scattered electrons in the range of 75–150 mrad, where the dominant contribution to the detected intensity is from thermal diffuse scattering. In this high-angle regime, lateral coherence between the atomic columns in the specimen will be destroyed by detecting over a large angular range, and coherence between atoms in the same column will be averaged out by thermal vibrations. This high-angle diffuse scattering is, therefore, proportional to the electron intensity at each atom site, and as any coherent scattering of the outgoing electrons will also be averaged by the large angular range of the annular detector, the output signal is proportional to the integrated electron intensity at all atom sites under the beam. The detected intensity will, therefore, consist of a convolution of the probe profile and an object function which is strongly peaked at the atom sites. The width of this object function is typically ~0.1 Å and is dependent on the number of atoms in the projected columns and their atomic number Z . The spatial resolution of this signal is, therefore, limited only by the 2.2 Å probe size of the VG HB501 UX dedicated STEM. For a thin crystalline specimen in a major zone-axis orientation, when the probe is smaller than the

atomic column separations, a map of the location of the atomic columns can therefore be generated with the relative intensities of each column reflecting changes in composition [4].

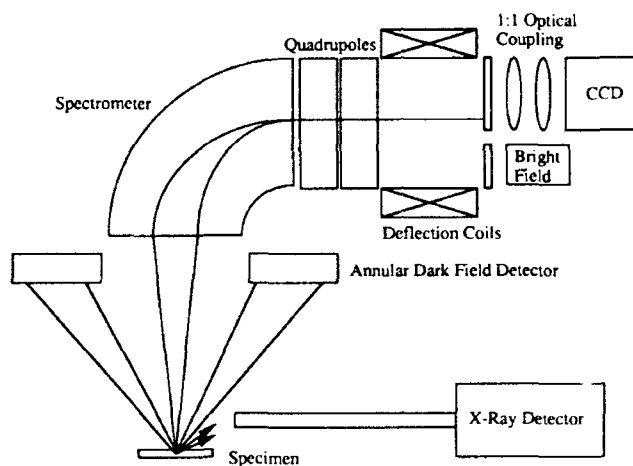


Fig. 1. STEM schematic showing the simultaneous acquisition of Z-contrast image, EELS, and EDX

This incoherent nature of the Z-contrast image makes it an ideal reference signal on which to base atomic-resolution microanalysis. The effect of increasing thickness is initially to scale the intensity as more atoms contribute to the image, although eventually the contrast reduces as the beam gets depleted by scattering effects. The effect of changing focus is also intuitively understandable as the focus control effectively alters the probe profile (Fig. 2). Changing the focus away from the Scherzer incoherent condition [5], the probe either broadens for lower defocus causing the individual columns to be unresolved or narrows with the formation of more intense tails for higher defocus causing a sharper image but compositional smearing. The optimum focus condition, therefore, represents a compromise between high-resolution (narrow probe profile) and the desire for a highly local image (no significant tails to the probe). As can be seen from Fig. 2, changes in focus do not cause contrast reversals, making the optimum condition experimentally straightforward to identify. These easily interpretable thickness and focus changes allow the unambiguous identification of the atomic column sites.

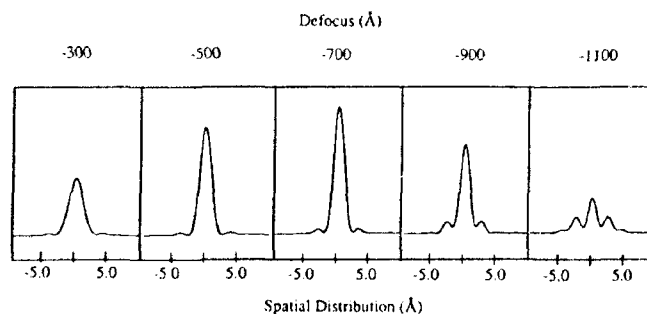


Fig. 2. Probe profile as a function of defocus. The central profile corresponds to the Scherzer condition.

Electron Energy Loss Spectroscopy (EELS)

In order to achieve atomic-resolution analysis, the range over which a fast electron can cause a particular excitation event must be less than the interatomic spacing. This range is described classically by the impact parameter, b , an approach which has been shown to be valid for applications in STEM imaging [6,7]. A root-mean-square impact parameter, which gives the effective spatial range of the inelastic scattering signal, can be defined [8] as

$$b_{\text{RMS}} = \frac{\hbar v \theta_{\text{max}}}{\Delta E \left[(\theta_{\text{max}}^2 + \theta_E^2) \ln \left(1 + \frac{\theta_{\text{max}}^2}{\theta_E^2} \right) \right]^{1/2}} \quad (1)$$

where ΔE is the energy loss and $\Delta E \ll E$, v the electron velocity, θ_{max} is the aperture limited cut-off angle, and $\theta_E = \Delta E/2E$ (E = incident beam energy). In the STEM, the experimental spatial resolution limit is therefore given by adding the probe size and the impact parameter in quadrature (Fig. 3). For energy losses above ~ 300 eV and a collection angle of 30 mrad, the spatial resolution of the energy loss signal approaches the probe size.

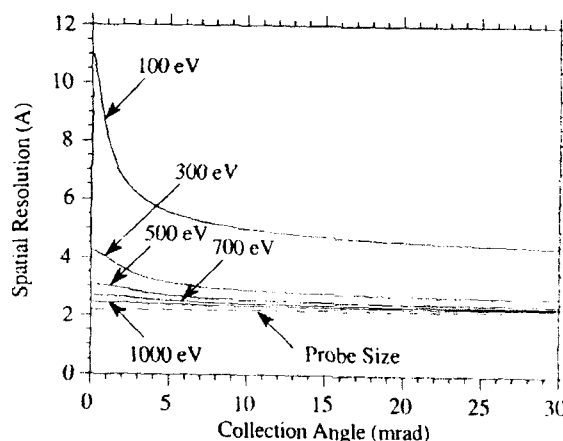


Fig. 3. The effective spatial resolution for various energy losses as a function of collection angle.

The detection limits of the system are of critical importance in atomic-resolution studies. The signal count rate for EELS is given by [9]

$$S = J N_A n_{\Delta} \sigma \quad (2)$$

where J is the number of electrons/m², N_A is the number of atoms under the beam, n_{Δ} is the efficiency of collecting a given event over a finite range of energy and angle, and σ is the total scattering cross-section. Typically, for Z-contrast applications, the beam current is ~ 0.01 nA, the probe diameter is 2.2 Å, and the collection angle is limited to ~ 30 mrad by the inner angle of the dark field detector. The other factors are dependent on the particular energy loss, but for example, the oxygen K-edge ($\Delta E = 530$ eV) at the maximum useful quadrupole dispersion (0.1 eV/channel), where σ is $\sim 10^{-24}$ m², $n_{\Delta} \sim 6 \times 10^{-4}$, and $N_A \sim 100$ atoms gives a count rate of

$$S \sim 100 \text{ electrons / channel / second} \quad (3)$$

The dark current of the CCD is only ~ 0.05 electrons for a multiphase pinned (MPP) chip, which is negligible when compared to the fact that each incident fast electron produces 10 CCD charges. For this chip, the signal-to-noise ratio (expressed in equivalent fast electrons) is ~ 10 . Using the criterion that the signal-to-noise ratio should be at least 4 for a signal to be observable above random noise, the CCD is working within reasonable limits for this low current operation. For more practical conditions, i.e., 0.2 eV/channel dispersion and a 5-second acquisition time, the signal-to-noise ratio is ~ 32 , indicating that as well as elemental identification, it should be possible to observe the spectral fine structure.

As for the Z-contrast image, by collecting the scattered signal up to a fairly large angle, ~ 30 mrad, the scattering is effectively localized at the atom cores in the core loss region of the spectrum, and the large angular range averages any coherent effects on the outgoing electrons. For relatively thick specimens, as in the above example where the atomic column consists of 100 atoms, elastic scattering of the energy loss electrons outside of the angular range of detection may reduce the detected signal intensity. However, the detection limits of the system are such that even if this signal is depleted by as much as a factor of 5, it is still observable above the random background noise.

RESULTS AND DISCUSSION

A typical Z-contrast image of $\text{YBa}_2\text{Cu}_3\text{O}_{7.8}$ oriented with the c-axis perpendicular to the beam is shown in Fig. 4. The barium columns and the copper columns in the copper-oxygen chains are clearly resolved. The yttrium columns and the copper columns in the copper-oxygen planes are more difficult to resolve due to the poor signal-to-noise of the image. However, the image does provide a map of the atomic structure of the material and can be used as a reference for positioning the probe. By setting the quadrupole dispersion so that both the Ba $M_{4,5}$ and the Cu $L_{2,3}$ edges are present on the same spectrum (780 and 930 eV, respectively), the relative peak intensities can be measured as the probe is positioned on different atomic columns in the unit cell. Figure 5 shows the relative peak intensity of the barium edge to the copper edge as the probe is positioned on different atomic planes. The result clearly maps out changes in composition on the scale of a few Ångströms, with a change in the intensity ratio by a factor of ~ 3 in moving from the barium planes to the copper planes.

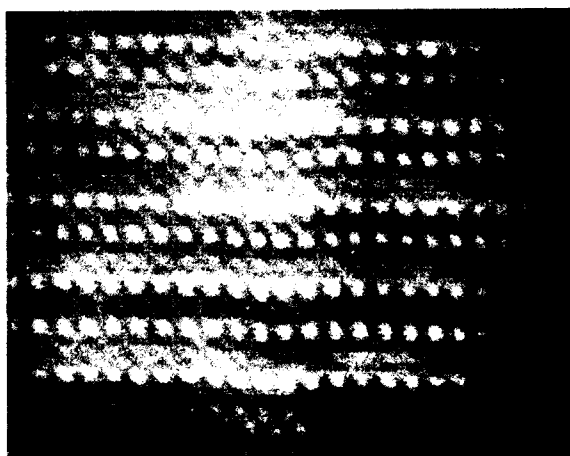


Fig. 4. Typical Z-contrast image of $\text{YBa}_2\text{Cu}_3\text{O}_{7.8}$.

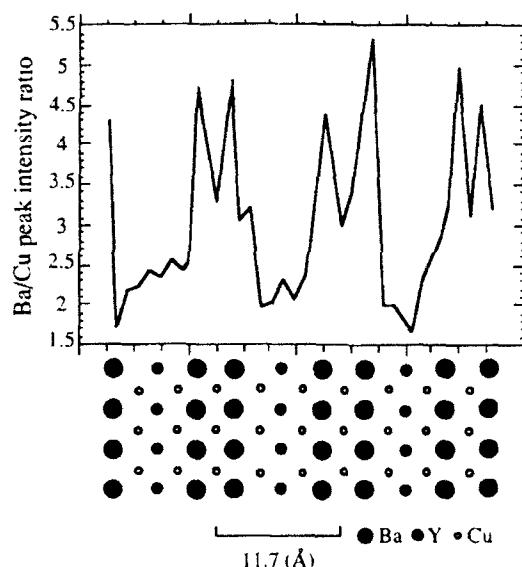


Fig. 5. Ba/Cu edge intensity ratio as the probe is moved across three unit cells on the image.

While the result shows a spatial resolution which is on the sub-unit-cell scale, it is not the atomic-resolution spectrum expected from the calculations. For the ideal probe profile, an order of magnitude change in intensity ratio is expected in moving from the copper to the barium planes. The complete disappearance of one of the edges when the probe is centered on the other plane is unlikely due to the contribution to the spectral intensity of the probe tails (Fig. 2) on the surrounding columns. The extent of this contribution will be dependent on the atomic spacing of the material and also the composition of the column as the energy filtering of the spectrometer means that only surrounding columns containing elements with core-edges in the same region of the spectrum will affect the result. The calculations of spatial resolution for the energy loss signal also assume a very thin sample and ignore any beam broadening effects. For thicker specimens beam broadening effects have been observed experimentally for EELS by measurements on specimens in random orientations [10]. However, for a zone-axis orientation, the Z-contrast result [1] shows that if the scattering event takes place in close proximity to the atom cores, the effect of beam channeling preserves the spatial resolution of the signal (Fig. 6) (this non-broadening of the beam in specimens on or near zone-axis orientations has been observed in the x-ray measurements of Furdanowicz et al. [11]). While these factors, and the presence of an amorphous layer on the surface caused by the thinning technique, may degrade the resolution slightly, the overriding factor in this case is the mechanical shutter on the CCD which, when opening to acquire the spectrum, causes mechanical vibrations that move the probe during acquisition. Even with this mechanical vibration, which can be corrected by employing an electrical shift to move the beam off the CCD, rather than a shutter, the effective spatial resolution of the signal can be estimated, with reference to the image, to be ~ 5 Å.

CONCLUSIONS

Atomic-column spectroscopy can aid the understanding of materials at the fundamental atomic level. Using this technique, it will be possible to unambiguously locate the atomic columns in the complicated interfacial structures present in real materials, to measure

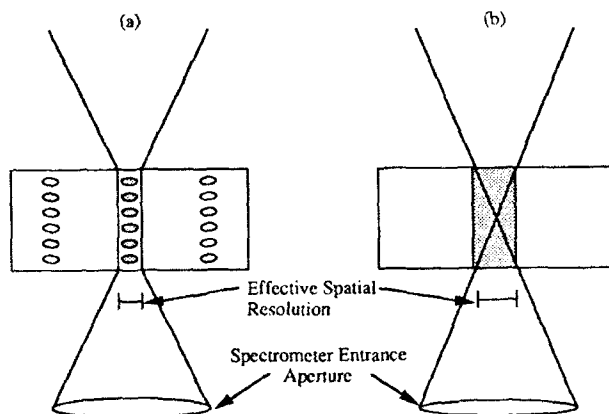


Fig. 6. Spatial resolution in the zone-axis orientation (a) is maintained by electron channeling effects, whereas for an amorphous or randomly oriented crystalline material (b), beam broadening occurs.

individual column composition and to determine local band structure. This capability will have applications in all fields of materials science. For example, the mechanical properties of steels, high-temperature intermetallics and nanophase ceramics are all controlled by segregation to dislocation cores at grain boundaries. Local changes in hole doping and atomic structure can now be studied simultaneously in the high-temperature superconductors on the same scale as the coherence length. This ability to study phenomenon at the atomic level will also provide a test for the atomistic simulations of interfaces and dislocations now being developed (*ab-initio*, molecular dynamics and Monte Carlo).

ACKNOWLEDGEMENTS

We would like to thank T. C. Estes, J. T. Luck and S. L. Carney for technical assistance. This research was sponsored by the Division of Materials Sciences, U.S. Department of Energy, under contract No. DE-AC05-84OR21400 with Martin Marietta Energy Systems, Inc., and supported in part by an appointment to the Oak Ridge National Laboratory Postdoctoral Research Program administered by the Oak Ridge Institute for Science and Education.

REFERENCES

1. Pennycook, S. J. and Jesson, D. E., *Phys. Rev. Lett.* **64**, 938 (1990).
2. Brown, L. M., *J. Phys. F* **11**, (1981).
3. Colliex, C. and Mory, C., *Quantitative Electron Microscopy*, J. N. Chapman and A. J. Craven, eds., SUSSP Publications, Edinburgh, 1984, pp 149-216.
4. Pennycook, S. J. and Jesson, D. E., *Ultramicroscopy* **37**, 14 (1991).
5. Scherzer, O., *J. Appl. Phys.* **20**, 20 (1949).
6. Ritchie, R. H. and Howie, A., *Philos. Mag.* **58**, 753 (1988).
7. Allen, L. J. and Rossouw, C. J., *Phys. Rev. B* **42**, 11644 (1990).
8. Pennycook, S. J., *Contemp. Phys.* **23**, 371 (1982).
9. Collett, S. A., Brown, L. M. and Jacobs, M. H., *Inst. Phys. Conf. Ser.* **68**, 103 (1984).
10. Isaacson, M. and Johnson, D., *Ultramicroscopy* **1**, 33 (1975).
11. Furdanowicz, W. A., Garratt-Reed, A. J. and Vander Sande, J. B., *Inst. Phys. Conf. Ser.* **119**, 437 (1991).

Author Index

- Aihara, Ryuso, 23, 201
 Arnold, George W., 139
 Baek, K.K., 189
 Bocquet, A., 219
 Böhringer, M., 207
 Bonnell, Dawn A., 29
 Booker, G.R., 121
 Bourret, A., 71
 Braue, W., 183
 Browning, Nigel D., 279
 Buckett, M.I., 109
 Campbell, Geoffrey H., 83, 97
 Carpenter, R.W., 183
 Carter, C. Barry, 173
 Chen, Fu-Rong, 167
 Chen, Wen-Jauh, 167
 Chonko, Mark A., 65
 Chuvilin, A.L., 179
 Cosandey, F., 91
 Cowley, J.M., 253
 Das Chowdhury, K., 183
 Daw, M.S., 91
 De Hosson, J.Th.M., 15
 Deckman, H.W., 151
 Denecke, R., 219
 Dow, John D., 9
 Dravid, Vinayak P., 115
 Drucker, J.S., 253
 Eby, Ray K., 139
 Eckstein, R., 219
 Feuillet, G., 71
 Foiles, S.M., 97
 Fonda, Richard W., 161
 Fukuyama, Masahiko, 261
 Furuno, Taiji, 145
 Ganz, Eric, 41
 Golovchenko, Jene, 41
 Hara, Masahiko, 145
 Hegde, Rama I., 65
 Hembree, G.G., 253
 Henderson, Grant S., 139
 Hobbs, L.W., 195
 Höche, T., 103
 Hsu, Tung, 271
 Hwang, Ing-Shouh, 41
 Idzerda, Y.U., 225
 Iwatsuki, Masashi, 3, 59, 157
 Jayaram, Raman, 247
 Jimenez, J.R., 231
 Kawai, Shichio, 35
 Kawai, Tomoji, 35
 Kenway, P.R., 103
 King, Wayne E., 83, 97
 Kleebe, H.-J., 103
 Knoll, Wolfgang, 145
 Kreuzer, H.J., 235
 Kryukova, G.N., 179
 Landis, William J., 243
 Leckey, R., 219
 Lee, E.Y., 231
 Ley, L., 219
 Li, Hua, 213
 Liang, Yong, 9, 29
 Liu, J., 127, 253
 Long, N.J., 121
 Lu, Ping, 133
 Luzzi, David E., 161
 Mallard, R.E., 121
 Matsumoto, Takuya, 35
 McKernan, Stuart, 173
 Medlin, D.L., 91
 Merkle, Karl L., 109
 Miki, K., 3
 Miller, M.K., 247
 Mills, M.J., 91
 Mimura, Ryou, 23, 201
 Molinàs-Mata, P., 207
 Morita, Y., 3
 Ohnishi, Satomi, 145
 Packard, William E., 9
 Pan, M., 127
 Pennycook, Stephen J., 279
 Plano, R.J., 151
 Ramaker, D.E., 225
 Ravikumar, V., 115
 Riley, J., 219
 Rühle, M., 97, 103
 Sadykov, V.A., 179
 Sasabe, Hiroyuki, 145
 Sato, Tomoshige, 3, 59, 157
 Sawaragi, Hiroshi, 23, 201
 Scarrott, K., 121
 Scheinfein, M.R., 253
 Schowalter, L.J., 231
 Selloni, A., 207
 Shaffer, J.P., 109
 Siperko, Lorraine M., 243
 Smith, David J., 133
 Solorzano, I.G., 189
 Spinnler, G.E., 127
 Stobbs, W.M., 91
 Sueyoshi, Takashi, 3, 59, 157

- Tokai, Mikio, 23, 201
Takaoka, Katsuya, 59, 157
Takeuchi, N., 207
Tanaka, Hiroyuki, 35
Tanishiro, Yasumasa, 261
Theiss, Silva K., 41
Thrush, E.J., 121
Tobin, J.G., 213
Tobin, Philip J., 65
Tokumoto, H., 3
Tong, S.Y., 213
Tsong, Tien T., 49
Tuller, H.L., 189
Turner, B.R., 231
Van Babel, G.P.E.M., 15
VanDer Sande, J.B., 189
Vogl, R., 133
Waddill, G.D., 213
Weiss, J.K., 253
Wicks, Fred J., 139
Yagi, Katsunichi, 261
Yang, H., 225
Yao, Takafumi, 59, 157
Yokoi, Naoki, 23
Yoshimura, Masamichi, 59, 157
Zegenhagen, J., 207
Zhou, Chuxin, 195

Subject Index

- aberrations, 23
- adatom rearrangement, 3
- Al- $\sqrt{3} \times \sqrt{3}$, 59
- Al adsorbed Si(111), 157
- α -7 \times 7 phase, 157
- α -Al₂O₃ bicrystals, 103
- aluminum, 91
- amorphous to crystalline structure, 65
- analytical, 183
- angle-resolved electron, 225
- anisotropy, 195
- artifacts, 151
- at heterostructures, 71
- atom probe field ion microscope, 247
- atomic(-)
 - force
 - microscope (AFM), 65, 145, 151
 - microscopy, 243
 - resolution microanalysis, 279
 - steps, 271
 - structure(s), 109, 115
 - of defects, 97
- atomistic simulations, 97, 103
- Auger, 225
- background, 83
- ballistic electron emission
 - microscopy, 231
 - spectroscopy, 231
- biological materials, 243
- body centered cubic (bcc) transition metals, 97
- brushite, 243
- calculated STM topographs, 15
- catalysts microcrystals, 179
- CdTe, 133
- CDW, 15
- charge density waves, 15
- charged polypeptide, 145
- coincidence electron spectroscopy, 253
- column-by-column core-loss spectroscopy, 279
- constrained-coincidence-site-lattice (CCSL)
 - model, 167
- crystalline-to-amorphous transition, 139
- Cu-1.5%Sb, 161
- defocus, 83
- delocalization, 253
- dichromatic patterns, 167
- diffusion, 195
- distributions, 225
- domain boundary, 59
- dynamic surface processes, 133
- electron
 - beam irradiation, 179
 - energy loss spectroscopy, 279
 - microscope, 235
 - microscopy, 127, 189
 - electrostatic-binding, 145
 - elevated temperatures, 133
 - embedded atom method, 91
 - epitaxial growth, 127
 - equilibrium crystal shape, 49
- ferritin, 145
- field
 - evaporation, 49
 - gradient induced diffusion, 49
 - first-principles calculations, 207
 - focusing characteristics, 23
 - Fourier transform, 213
 - fractal, 247
- GaAs, 219
- Ge, 173
- Ginzburg-Landau, 15
- grain(-)
 - boundaries, 115, 189, 247
 - boundary, 161
 - structure, 103
- grazing incidence x-ray, 71
- growth, 65
- heterophase interfaces, 109
- hetero-twin interface structure, 167
- high(-)resolution
 - electron
 - micrographs, 83
 - microscope, 133
 - microscopy, 109, 179
 - image, 279
 - transmission electron microscopy, 97, 103
- 2H-NbSe₂, 15
- holographic imaging, 213
- holography, 235
- hot electron transport, 231
- HREM, 71, 109, 121, 161, 173, 183
- HRTEM, 91, 167
- hydrogen desorption, 3
- hydroxyapatite, 243
- image(-)
 - artifacts, 151
 - simulation(s), 109, 167, 173
- imaging with photoelectron diffraction, 213
- incommensurate
 - phases, 157
 - structure, 261
- in-diffusion, 189
- inorganic oxide materials, 151
- InP, 9
- interdiffused multilayer interfaces, 121
- interface(s), 71, 109, 183, 247
 - structure, 167
- intergrowth, 195
- interlocking, 195
- ion-bombarded, 139

- layered transition metal dichalcogenides, 15
- LDOS, 207
- least squares, 83
- LEED, 207
- liquid metal ion source, 201
- low kinetics energies, 219
- LPCVD silicon, 65
- LTMD, 15
- metal/metal-oxide interfaces, 109
- metal/semiconductor interface, 231
- MgO microcubes, 127
- mineralization, 243
- MINPACK-1, 83
- mirror plane symmetry, 207
- misfit dislocations, 157
- MOCVD, 121
- morphology, 247
- muscovite, 139
- Nb, 83
- $\text{Nb}_{1-x}\text{S}_x$, 195
- near $\Sigma 11$ grain boundary, 103
- non-stoichiometry, 195
- nuclear microprobe, 201
- nucleation and growth of Ag, 127
- octahedral $-S_6-$ coordination, 195
- ordered arrays, 145
- oxide(s), 29
 - surfaces, 271
- oxygen vacancies, 35
- Pd/NiO, 109
- phase transition, 59, 261
- photoelectron
 - diffraction, 213, 219
 - holography, 213, 219
 - scattering, 225
- platelets, 195
- point source, 235
- Pr segregation, 189
- production pathways, 253
- RBS
 - mapping, 201
 - tomography, 201
- reaction-bonded SiC, 183
- real-time viewing, 133
- reconstruction(s), 235, 271
- reflection
 - electron
 - energy loss spectroscopy, 271
 - microscopy, 271
 - high energy electron diffraction, 271
- REM, 261
- RHEED, 261
- Rutherford backscattering (RBS), 201
- scanning
 - microscopy, 139
 - tunneling microscopy (STM), 3, 9, 15, 59, 157
- Schottky(-)
 - barrier heights, 231
 - emission, 23
- second phase particles, 183
- secondary electrons, 253
- SEM, 23
- Si(111)-Pb, 261
- Si(111)- $\sqrt{3} \times \sqrt{3} R30^\circ$, 3
- Si(111)- 7×7 , 59
- SiC grains, 183
- $\Sigma = 3$, 161
- $\Sigma = 3 \{112\}$ incoherent twin boundary, 91
- small Ag particles, 127
- spatial resolution, 253
- SrTiO_3 , 29
- $\text{SrTiO}_3(100)$, 35
- $\text{Sr}_{n+1}\text{Ti}_n\text{O}_{3n+1}$, 29
- stacking sequence, 195
- STEM, 121
- step(s), 9
 - roughening, 49
- STM, 15, 23, 29, 207
- STM/STS, 35
- strontium titanate, 115
- structural units, 173
- structure, 161
- $\sqrt{5} \times \sqrt{5}$ structure, 35
- sulfur vacancy, 195
- (110) surface, 9
- surface(s), 29
 - analysis techniques, 127
 - diffusion, 49
 - granularity, 65
 - morphology, 65, 271
 - of MgO, 127
 - profile imaging, 133
 - roughness, 65
 - segregation, 49
 - structure, 179
- surfactant effect, 3
- thickness, 83
- Ti-oxygen vacancy, 35
- toroidal analyzer, 201
- 1T-TaSe₂, 15
- 1T-TiS₂, 15
- twin boundaries, 173
- 2-D sublimation, 49
- UHV, 23, 29
 - STEM, 127
- Voter and Chen aluminum potential, 91
- Z-contrast imaging, 279
- ZnO:Pr:Co varistor, 189